



*First Latino-American Seminar on
Radar Remote Sensing*

Primeras Jornadas Latinoamericanas
de Percepción Remota por Radar

*Image Processing
Techniques*

Técnicas de
Procesamiento
de Imágenes

Buenos Aires, Argentina
2-4 December 1996

GEN32

esa SP-407
February 1997
ISBN 92-9092-311-3

*First Latino-American Seminar on
Radar Remote Sensing*

**Primeras Jornadas Latinoamericanas
de Percepción Remota por Radar**

Image Processing Techniques

**Técnicas de Procesamiento
de Imágenes**

**Buenos Aires, Argentina
2-4 December 1996**

Cosponsored by:
CONAE, INPE, ESA, SELPER, CIDA, DI-UFPe

**European Space Agency
Agence spatiale européenne**

Cover image: Buenos Aires

Enlargement of an ERS-1 SAR multitemporal image of the town of Buenos Aires, Argentina. This was generated by superimposing two precision images, taken on 26 May 1996 (blue) and on 20 August 1996 (green and red), respectively. The SAR signal patterns depict areas with different urbanisation and indicate the main features of the road network. Similarly, backscatter patterns in the Rio de La Plata indicate different surface-wind conditions on the two dates and the effect of currents in River Lujan merging with the waters of the Rio de La Plata (top-left).

**ESA SP-407: Proceedings of the First Latino-American Seminar on
Radar Remote Sensing: Image Processing Techniques
(Buenos Aires, Argentina, 2-4 December 1996)**

Published by: ESA Publications Division
 ESTEC, Noordwijk, The Netherlands

Compiled by: T.-D. Guyenne

Price Code: 80 Dfl.

Copyright © 1997 European Space Agency

ISBN 92-9092-311-3 Printed in The Netherlands

CONTENTS

Data Generation, Calibration & Interferometry

Chairmen/Presidentes:

Shaun Quegan & Joao R. Moreira

AIRBORNE SAR: IMAGE GENERATION AND HIGH-PRECISION DEM GENERATION Joao Moreira, <i>Aero-Sensing Radarsysteme GmbH</i>	9
POSSIBILITIES AND LIMITS OF SAR INTERFEROMETRY Fabio Rocca & al., <i>Politecnico di Milano</i>	15
AN INTERFEROMETRIC QUICK-LOOK PROCESSOR F. Gatelli & al., <i>Politecnico di Milano</i>	27
TRATAMIENTOS DE IMAGENES RADAR PARA OPTIMIZAR SU APLICACION S. Torrusio & E. Bozzarello, <i>Dirección de Aplicación de Imágenes</i>	31
SENSORIAMENTO REMOTO POR RADAR SAR: PRE-PROCESSAMENTO DE IMAGENS RADARSAT ('FINE MODE') NA REGIAO DA FLORESTA NACIONAL DO TAPAJOS S.Amaral & al., <i>INPE & CCRS</i>	37
EVALUATION OF THE PHASE NOISE REDUCTION FILTERS IN SAR INTERFEROMETRY J.Cl. Mura & al., <i>INPE & Aero-Sensing Radarsysteme GmbH</i>	43
RADARSAT AND IFSARE – COMPLEMENTARY SAR SOURCES FOR DEMS J. Bryan Mercer & A. Kahil, <i>Intermap Technologies Ltd.</i>	47
COMPARISON BETWEEN ERS-1/2 AND RADARSAT AGRICULTURAL DATA H. Mehl & al., <i>DLR, AGF, CONAE & UNER</i>	53

Statistics, Filtering & Data Fusion

Chairmen/Presidentes:

Jorge Lira & Nelson D.D. Mascarenhas

EL MODELO MULTIPLICATIVO PARA EL ANALISIS DE IMAGENES SAR A.C. Frery & al., <i>UFPE & INPE</i>	63
AN OVERVIEW OF SPECKLE NOISE FILTERING IN SAR IMAGES N.D.A. Mascarenhas, <i>Federal University of Sao Carlos</i>	71
ROBUST STATISTICS IN SAR IMAGE PROCESSING O.H. Bustos, <i>Universidad Nacional de Cordoba</i>	81
SAR DATA FUSION M. Manore & al., <i>CCRS & Geological Survey of Canada</i>	91
MAXIMUM LIKELIHOOD FITTING OF EXTREMELY HETEROGENEOUS RADAR CLUTTER K. Vasconcellos & A.C. Frery, <i>Universidade Federal de Pernambuco</i>	97
BITSLICE NOISE REDUCTION USING MATHEMATICAL MORPHOLOGY A.L. Bezerra Candeias & A.C. Frery, <i>INPE</i>	103
DIGITAL FILTERING OF SAR IMAGES THROUGH LOCALISATION OF MINIMUM SPECKLE INDEX REGIONS P.D. Ruiz & H.J. Rabal, <i>Universidad Nacional de Salta & de La Plata</i>	109
INTEGRAÇÃO DE DADOS MULTIESPECTRAIS LANDSAT-5 TM COM IMAGENS SAR JERS-1, PARA FINS CARTOGRAFICOS S. Monteiro Soares & al., <i>INPE & DSG</i>	115
INTEGRAÇÃO DE DADOS DE RADAR ADQUIRIDOS COM DIFERENTES ANGULOS DE INCIDENCIA PARA ESTUDOS DE RESERVATORIO NA AMAZONIA M. Pereira de Farias Costa & al., <i>INPE & CCRS</i>	125
APORTE EN LA INTERPRETACION VISUAL DEL USO DE LA TIERRA, DADO POR LA COMBINACION DEL SENSOR PASIVO TM LANDSAT-4 Y EL SENSOR ACTIVO SAR ERS-1 J.R. Prieto Gómez, <i>Instituto de Ingeniería</i>	133

Segmentation, Classification, GIS

Chairmen/Presidentes:

Laura Frulla & Manuel Vierna Monteiro

SEGMENTATION AND CLASSIFICATION IN SAR IMAGERY

S. Quegan, *University of Sheffield*

141

MORPHOLOGY OF SEGMENTED REGIONS IN SAR IMAGES BY MEANS OF A REGION GROWING ALGORITHM

J. Lira & al., *Instituto de Geofisica-UNAM & CONICET*

153

CLASSIFICAÇÃO DE CULTURAS IRRIGADAS NA REGIAO DE BEBEDOURO, PE, BRASIL, USANDO A INFORMAÇÃO POLARIMETRICA DAS IMAGENS DA MISSAO SIR-C/X-SAR

S.P. Castellari Ribeiro & al., *INPE*

165

UTILIZAÇÃO DE MEDIDAS TEXTURAIS NA DISCRIMINAÇÃO DE CLASSES DE USO DO SOLO DO PERIMETRO IRRIGADO DE BEBEDOURO, PERNAMBUCO, BRASIL, UTILIZANDO-SE IMAGENS SAR

C. Daleles Rennó & J. Viane Soares, *INPE*

171

UM SISTEMA DE ANALISE E CLASSIFICAÇÃO ESTATISTICAS PARA IMAGENS SAR

P. Ronalt Vieira & al., *INPE & UFPE*

179

ESTUDO COMPARATIVO DE ALGUNS CLASSIFICADORES UTILIZANDO-SE IMAGENS RADARSAT DA REGIAO DE TAPAJOS

S.J.S. Sant'Anna & al., *INPE & UFPE*

187

SOIL MOISTURE RETRIEVAL FROM ACTIVE MICROWAVE REMOTE SENSING

J. Viane Soares & C. Daleles Rennó, *INPE*

195

SPECKLE REDUCTION IN SAR IMAGES BY USING DISCRETE WAVELET TRANSFORM

S. Leguizamón, *CONAE*

205

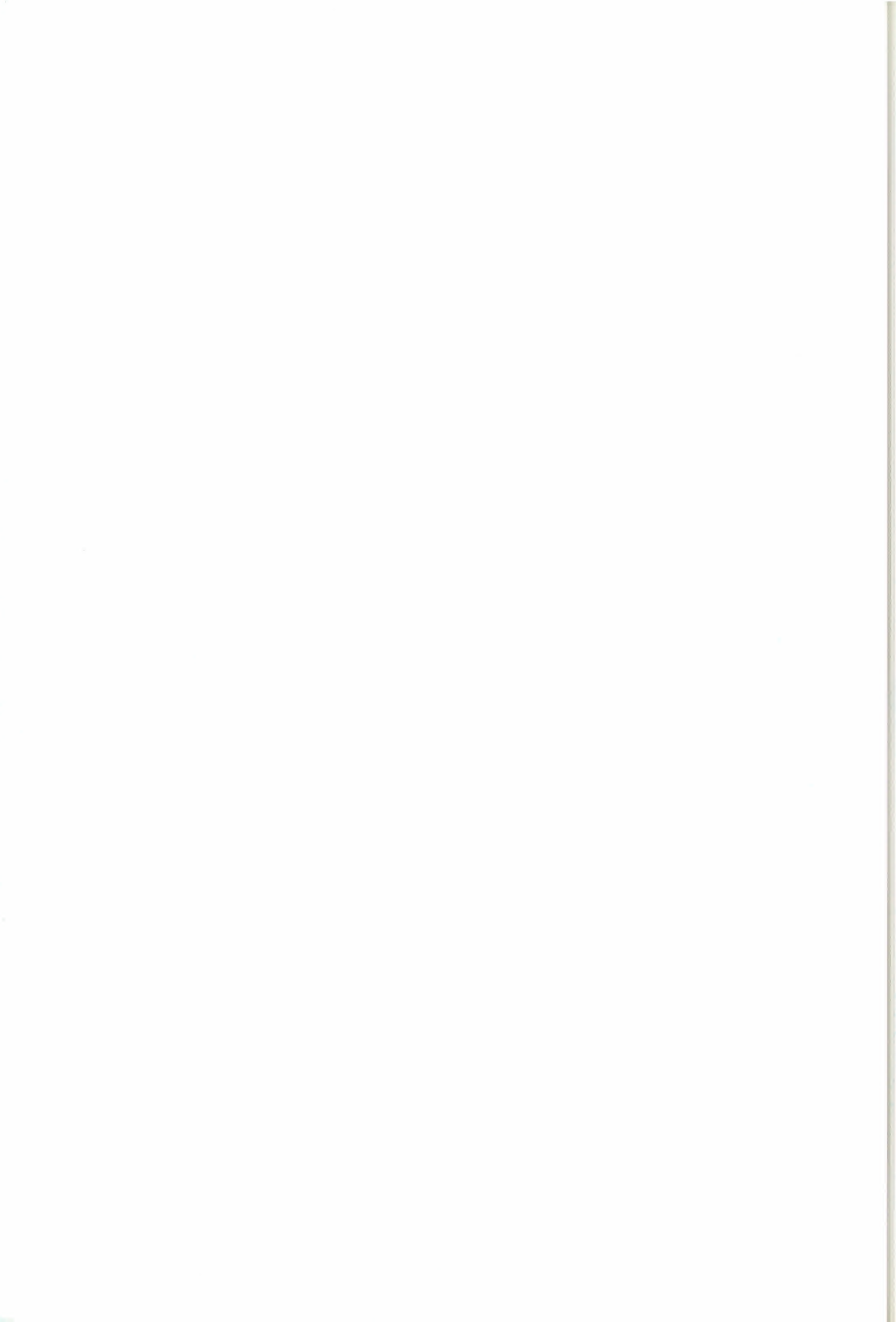
REDE NEURAL NAO SUPERVISIONADA BASEADA EM TRANSFORMADA KARHUNEN-LOEVE PARA PROCESSAMENTO, COMPRESSAO E RECONHECIMENTO DE IMAGENS

J. F. Marar & al., *UNESP & UFPE*

211

Participants

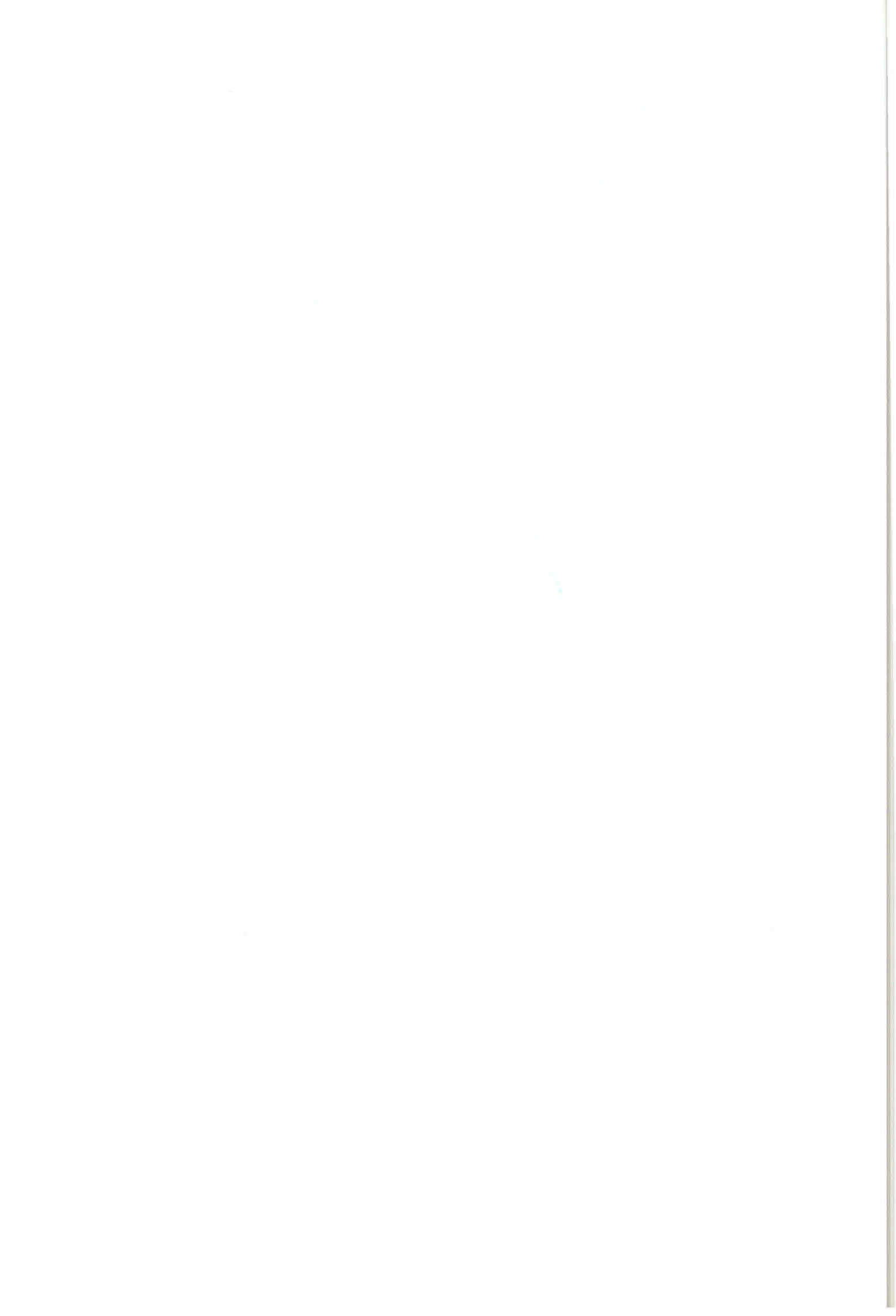
217



Data Generation, Calibration & Interferometry

Chairmen/Presidentes:

Shaun Quegan
Joao R. Moreira



AIRBORNE SYNTHETIC APERTURE RADAR: IMAGE GENERATION AND HIGH PRECISION DIGITAL ELEVATION MODEL GENERATION

João Moreira

Aero-Sensing Radarsysteme GmbH
 c/o DLR Research Centre
 82230 Oberpfaffenhofen, Germany
 phone: +49 8153 28 1542, fax: +49 8153 28 1543
 email: joao.moreira@dlr.de

ABSTRACT

This paper describes the Interferometric SAR (InSAR) of Aero-Sensing, AeS-1. The system AeS-1, designed and manufactured at Aero-Sensing, is mainly used for generation of fully geocoded SAR images and Digital Elevation Models (DEM). AeS-1 has a maximal ground resolution of 0.5 m x 0.5 m and a height accuracy up to 5 cm. AeS-1 had the first test flight in August 1996 and is operational since November 1996. High resolution images and DEM are finally shown.

1. INTRODUCTION

Aero-Sensing Radarsysteme GmbH is engaged in the field of microwave remote sensing by making use of Synthetic Aperture Radar (SAR) systems on both air- and spaceborn platforms. It is a private enterprise founded in early 1996 by former scientists of the German Aerospace Research Establishment (DLR), who were involved in the design and construction of the E-SAR, the Experimental Airborne SAR-System of DLR.

2. THE INTERFEROMETRIC SAR

The Interferometric SAR (InSAR) of Aero-Sensing, AeS-1, designed and manufactured at Aero-Sensing, is mainly used for generation of fully geocoded SAR images and Digital Elevation Models (DEM). The instrument has been already installed on board a Cessna 207A, a Dornier Do-228 and a Rockwell Aerocommander 685 aircraft. They are small aircrafts, offering the advantage of low costs. The radar had the first tests in August 1996 and is operational since November 1996. It operates in the interferometric mode as following:

- operating frequency: 9.6 GHz
- baseline: 1.5 m (orthogonal to line of sight direction)
- system bandwidth: 400 MHz
- ground resolution: up to 0.5 m x 0.5 m

- swathwidth: 1 to 14.8 km
- flight velocity: 60 - 120 m/s
- flight altitude over NN: 1000 to 3500 m

In general, the radar allows an aircraft velocity range between 50 and 200 m/s and a flight altitude range of 100 to 10.000 m over ground.

The preliminary estimation of the height accuracy measurement is around 0.5 m for a ground resolution of 0.5 m x 0.5 m and 0.05 m for a ground resolution of 5 m x 5 m. The navigation system used for SAR motion compensation is composed by a strap-down inertial system, a differential on-line GPS, D-GPS, and a radar altimeter. The Flight Control System of IGI, Aero-Control, processes the data of the navigation units by using Kalman filter techniques and delivers the aircraft motion to the interferometric processor.

Table 1 shows the main imaging configurations of the AeS-1-System. The ground and radiometric resolutions can be set to the following values:

- 0.5 x 0.5 m with 4 looks
- 1.0 x 1.0 m with 8 looks and
- 2.0 x 2.0 m with 16 looks.

The throughput of the processing chain was calculated considering an array of 6 units of IBM-PC Pentium Pro 200 MHz with 128 Mbyte RAM each.

3. THE INTERFEROMETRIC PROCESSOR

The interferometric processor consists on the SAR processing, interferometric and geocoding chain. The SAR processing chain has full motion compensation capability. The interferometric chain uses a new approach for phase unwrapping (Fornaro et al., 1996). A fusion procedure of strong-filtered and less-filtered unwrapped phases using Kalman filter technique is used (Lanari et al., 1996). These algorithms allow the full automation of the DEM generation process, making the SAR interferometry an attractive tool for topographic purposes. Due to the absolute position accuracy given by the D-GPS, the transformation

AeS-1 Parameter	Swath Mode				
	A	B	C	D	E
Spatial Resolution (m)	0.5-2.0	0.5-2.0	0.5-2.0	0.5-2.0	0.5-2.0
Height Accuracy (m)	< 0.5	< 0.5	< 0.5	< 0.5	< 0.5
Swath Width (km)	1	2	4	7.4	14.8
Radiometric Resolution (dB)	< 1.8	< 1.8	< 1.8	< 1.8	< 1.8
Throughput of the Processing Chain (km ² /day)	120	240	480	880	1760

Table 1. Main parameters of the AeS-1-System.

„phase to height“ and geocoding become straight forward procedures.

4. PRODUCTS

Due to the high ground resolution and height accuracy, one can have the following products from the AeS-System:

- Fully geocoded DEM's with following parameters:
 - Grid of 0.25 m and height accuracy of 0.5 m
 - Grid of 2.5 m and height accuracy of 0.05 m
- Fully geocoded SAR images, i.e. Orthoimages, with following parameters:
 - Grid of 0.25 m and a geometric distortion less than 0.5 m
 - Grid of 2.5 m and a geometric distortion less than 2.5 m
- Topographical maps in scale of 1:25,000 and larger;
 - with contour lines having a spacing of 0.1 m and larger.
- Transformation of SAR products into thematic and topographic maps showing, for example, roads, urban areas, forest types or other area features on the scale of 1:25,000 and larger as well as printed and/or coded data for specific subsequent treatment.
- Detailed measurement of the extent of local or area flooding to assist in the avoidance and/or protection from high water, representation of flood containment areas as well as cartographic representation of other environmental catastrophies and their chronological development.
- Update of geographical, topographic, land use, or other data banks and comparison between present and historical (also optical) data.
- Classification and representation of land surface as well as of vegetation and its change over time.

- Volume calculations of trash dumps, land fills, coal heaps, and other such areas.
- Measurements of the flow velocity of rivers and canals to an accuracy of 0.1 m/s with the along track interferometry technique.
- Evaluation of optimum sites for telecommunication stations

5. RESULTS

First results of the AeS-1 system are presented. Figs. 1 and 2 are generated from the raw data acquired on 6th Setember 1996 in Oberpfaffenhofen, Germany. Figs. 3, 4, 5 and 6 are from flight on the 11th Setember 1996 in Solothurn, Switzerland. Both flights were carried out with 400 MHz bandwidth and with the Cessna 207 A.

Fig. 1 is a 48 look image with 2 x 2 m resolution. Fig 2 is a 1 look image with 0.5 x 0.5 m resolution and is the small city shown in the right middle part of Fig. 1.

Fig. 3 is a 8 look image with 2 x 2 m resolution. Fig 4 shows the respective interferogram phase. Fig. 5 shows the terrain model derived from the interferogram. Fig. 6 shows the topographic map derived from the full geocoded SAR image from a parallel track of Fig. 3.

6. REFERENCES

G. Fornaro, G. Franceschetti, R. Lanari,
„Interferometric SAR phase unwrapping using Green's formulation“, *IEEE Transactions for Geosc. and Remote Sensing*, to be printed in May 1996.

R. Lanari et al., „Generation of Digital Elevation Models by using SIR-C/X-SAR Multifrequency Two-pass Interferometry: the Etna Case Study“, *IEEE Transactions for Geosc. and Remote Sensing*, to be printed in September 1996.

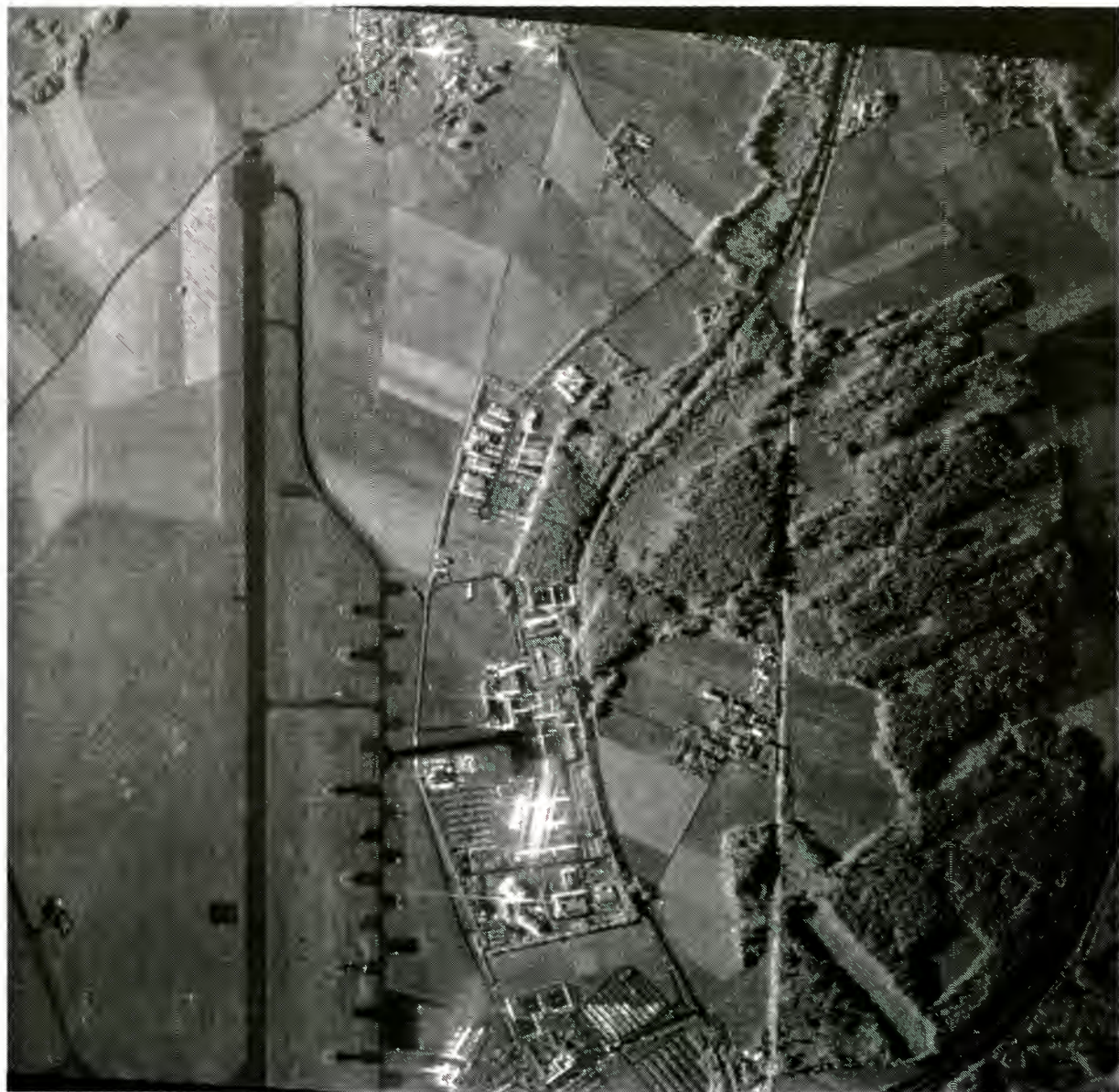


Figure 1. AeS-1 image over the Oberpfaffenhofen area in Germany. Image parameters: flight date: 6.9.96, flight velocity: 70.5 m/s, flight height: 11.000 feet, drift: -5.6 °, azimuth bandwidth: 200 Hz, range bandwidth: 400 Mhz, PRF: 8 kHz, transmitting frequency: 9.6 Ghz, number of looks: 48, resolution: 2 x 2 m.



Figure 2. AeS-1 image of Weichselbaum in Germany. Image parameters as Fig. 1. Number of looks: 1, resolution: 2 x 2 m. One can see the rails of the train (vertical lines), the houses of the village and the differentiation between coniferous and pine forest.



Figure 3. AeS-1 image of Solothurn in Switzerland. Image parameters: flight date: 11.9.96, flight velocity: 54.5 m/s, flight height: 11.000 feet, drift: -0.8 °, azimuth bandwidth: 200 Hz, range bandwidth: 400 Mhz, PRF: 8 kHz, transmitting frequency: 9.6 GHz, number of looks: 8, resolution: 2 x 2 m.



Figure 4. Interferogram phase of Fig. 3. One can see clearly the different height of the crop fields.

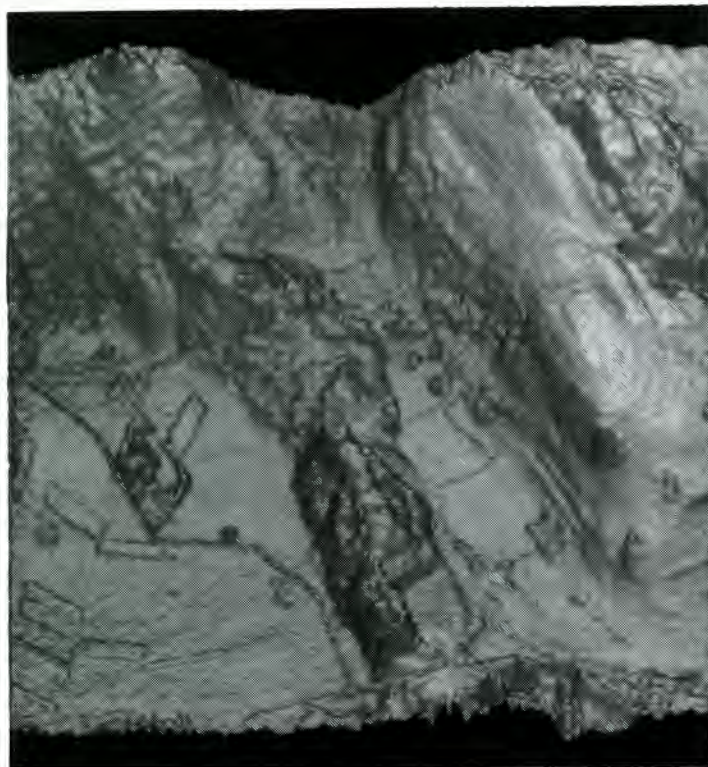


Figure 5. Digital elevation model derived from Fig. 4. The height axis is exaggerated. One can see clearly the different height of the crop fields also present in Fig. 4.

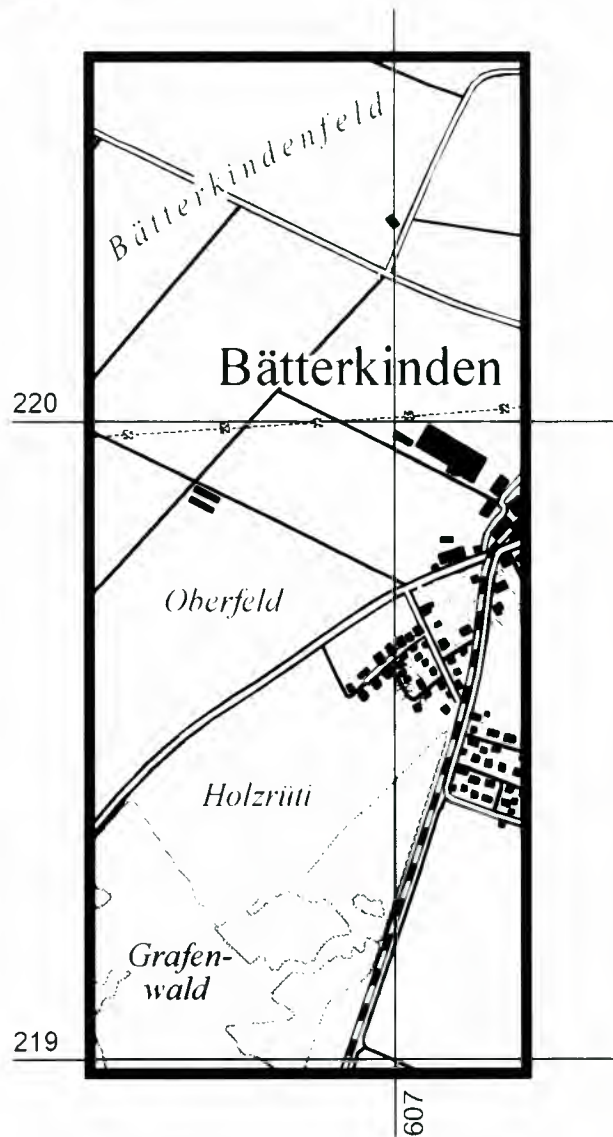


Figure 6. Topographic map derived from a full geocoded image of a parallel track of Fig. 3.

POSSIBILITIES AND LIMITS OF SAR INTERFEROMETRY

Fabio Rocca, Claudio Prati, Andrea Monti Guarnieri

Dipartimento di Elettronica e Informazione- Politecnico di Milano

Pzza. L. da Vinci, 32, 20133 Milano. Italy

Tel: +39-2-23993573 Fax: +39-2-23993413

E-mail: rocca@elet.polimi.it

March 6, 1996

1. Summary

In this presentation we summarize the impact of interferometry on the design of SAR surveys, its possibilities and limits. From the fringes a very good DEM is obtainable, with a vertical resolution that could be in the meter range or even less from airborne platforms. Millimetric motion of large areas of the terrain or of corner reflectors can be measured with good reliability and therefore the possibility of using the system to measure subsidence, landslides, coseismic motions has been demonstrated. The coherence of the interferometric pair is an important clue, that combined with the more usual backscatter amplitude, leads to high quality images segmentation. The wavenumber shift concept is finally introduced that may lead to a 3 dimensional view of the terrain. The same principle can be invoked to improve the resolution of objects that do not change with time.

2. Introduction

Synthetic Aperture Radar (SAR) systems record both amplitude and phase of the backscattered echoes. The phase of each pixel (ground resolution cell) of a focused SAR image is the sum of three distinct contributions:

1 - the two-ways travel path (sensor-target-sensor: hundreds of kilometers in the satellite case) that, divided by the used wavelength (a few centimeters), corresponds to millions of cycles;

2 - the interaction between the incident e.m. waves and the scatterers within the ground resolution cell;

3 - the phase shift induced by the processing system used to focus the image.

Therefore, the phase of a single SAR image is of no practical use. On the contrary, if two SAR images from slightly different viewing angles are considered (*interferometric pair*) their phase difference (*interferometric fringes*) can be usefully exploited to generate Digital Elevation Maps (DEMs), to monitor terrain changes and to improve the range resolution. The interferometric fringes image is derived as the phase of the

SAR *interferogram*, that is the complex image formed by cross-multiplying the two SAR images. The relation between the interferometric fringes and ground elevation is usually explained by means of the *monochromatic approach* [1, 2]. It is based on the assumption that the RF bandwidth is so small (and this is the case of most satellite systems including SEASAT, ERS-1, JERS-1, ERS-2 and RADARSAT) to be negligible. Thus the system is considered monochromatic. However, if the finite bandwidth of the system is considered (*wavenumber shift approach*), a relative shift of the ground wavenumber spectra dependent on the baseline and the local slope is found. A few important consequences come out from this result [3, 4, 5]. Using the simpler monochromatic approach we show the relationship between the relative terrain elevation and the interferometric fringes. Then we will determine the quality of the Digital Elevation Model derived from interferometry. Two sections 6 and 9.1 will be dedicated to the description of other applications of SAR interferometry: small terrain motion detection and uses of the coherence for image segmentation. In section 9 a deeper insight into SAR interferometry will be given by exploiting the wavenumber shift approach and the slant range resolution enhancement that can be obtained by using it. Symbols that will be used through the text and the main parameters values of the ERS-1 SAR system (that will be assumed as typical parameters of SAR from satellites) are shown in table 3.1.

3. The monochromatic approach

Let us consider two complex SAR images from two slightly different viewing angles (see figure 3.1), v_1 and v_2 . Even if non simultaneous acquisitions are considered, we shall suppose, for now, that the terrain backscatter did not change.

Let us now exploit the "monochromatic approximation": the relative system bandwidth is so small (i.e. in the ERS-1 case its value is $3 \cdot 10^{-3}$) to be neglected. Thus, the phase difference ϕ between correspondent complex pixels in v_1 and v_2 is proportional to the travel

Paper presented at the AGARD SPP Symposium on "Remote Sensing: A Valuable Source of Information", held in Toulouse, France from 22-25 April 1996, and published in CP-582.

Symbol	Meaning
λ	wavelength
$f_o = c/\lambda$	central frequency
W	system bandwidth
f_s	sampling frequency
$f_{Ny} = f_s/2$	Nyquist frequency
θ	off-nadir angle
α	local terrain slope (range)
H	platform altitude
ρ_s	slant range resolution
Δr	slant range sampling interval
ρ_g	ground range resolution
B	baseline
B_n	normal baseline
B_r	radial baseline
B_{nc}	critical baseline
r	slant range axis
r_o	sensor-target distance
y	ground range axis
z	elevation axis
k_y	ground range wave number
ϕ	interferometric phase
Symbol	ERS-1 value
λ	5.66cm
$f_o = c/\lambda$	5.3GHz
W	16MHz
f_s	18.96MHz
θ	23deg.
H	780km
ρ_s	9 meters
B_{nc}	1100 meters

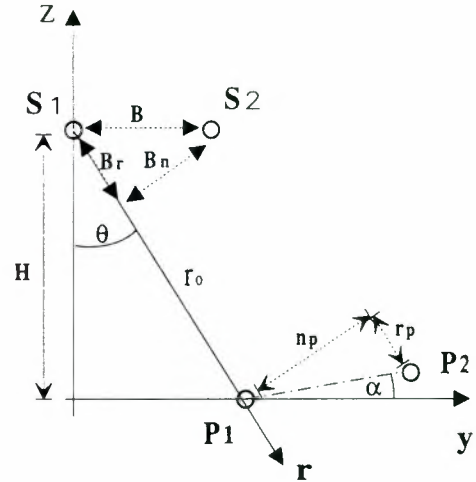
Table 3.1: List of symbols and values for ERS-1

path difference $2\Delta r_o$ (the factor 2 accounts for the two ways travel path):

$$\phi = \frac{4\pi}{\lambda} \Delta r_o \quad (3.1)$$

(λ is a constant). The interferometric phase ϕ of a single pixel is still of no practical use. The travel path difference $2\Delta r_o$ is usually much greater than the wavelength λ (in most of the practical cases, the travel path difference from the satellite can be as large as a few hundred meters whereas the used wavelength is of the order of a few centimeters) and the measured phase ϕ shows an ambiguity of many cycles. On the other hand, passing from one pixel to its neighbor (only a few meters apart in the slant range direction), the variation of the travel path difference ($\Delta(\Delta r_o)$) may be much smaller than λ and the variation of the interferometric phase $\Delta\phi$ is not ambiguous. Moreover, a simple relation between $\Delta\phi$ and the relative terrain elevation can be derived.

In figure 3.1 we have indicated the position of the

Figure 3.1: Interferometric SAR geometry in a plane orthogonal to the rectilinear platforms (S_1 and S_2) trajectory.

two SAR sensors (S_1 and S_2) and their relative displacements parallel (B_r) and normal (B_n) to the slant range direction. We have also indicated the position of two point scatterers and their relative displacements parallel (r_p) and normal (n_p) to the slant range direction. Let us assume as a reference the positions of S_1 and P_1 with their relative distance r_o . By changing the sensor and target position by (B_n, B_r) and (r_p, n_p) respectively the sensor-target distance becomes:

$$r = \sqrt{(r_o + r_p - B_r)^2 + (n_p - B_n)^2} \quad (3.2)$$

Since the distance between the two SAR sensors is generally much smaller than the sensor-target distance r_o (a few hundred meters compared with 800km, in the ERS-1 case), the following expression of the interferometric phase variation holds:

$$\Delta\phi = \frac{4\pi}{\lambda} \Delta(\Delta r_o) = \frac{4\pi \cdot B_n \cdot n_p}{\lambda \cdot r_o} \quad (3.3)$$

This result shows that if we know the relative displacement of the two orbits normal to the slant range direction B_n , the distance r_o and the value of the SAR wavelength λ , then the phase difference $\Delta\phi$ depends only on the n_p value, i.e. the elevation difference between the points displayed in figure 3.1, measured in the direction normal to the slant range axis. Thus the interferometric phase image represents a map of the relative terrain elevation with respect to the slant range direction. A linear term can then be subtracted from the interferometric phase so that the phase corresponding to the flat horizontal terrain is a constant. After some algebra, the version of equation 3.3 that refers to the relative elevation $q = \Delta z$ with respect to a flat terrain becomes:

$$\Delta\phi = \frac{4\pi \cdot B_n \cdot q}{\lambda \cdot r_0 \cdot \sin \theta} = K \cdot q \quad (3.4)$$

4. Phase unwrapping

Up to now it has been assumed that the phase difference $\Delta\phi$ of equation 3.4 would be directly obtained from the interferometric fringes. However such an assumption is in some way misleading. In fact, from the interferogram, the complex values $e^{j\Delta\phi}$ can be determined but not the $\Delta\phi$ values themselves. What is measured is not the phase difference value $\Delta\phi$, but its principal value $\Delta\phi_p$, limited between $-\pi$ and $+\pi$. The interferometrical fringes show typical discontinuities like those shown in figure 4.1.



Figure 4.1: ERS-1 - Mt. Vesuvius (Italy) August 27th and September 5th, 1991. - Interferometric fringes. The estimated normal baseline is $B_n = 193$ meters.

Two adjacent discontinuities separated by a constant elevation increment, corresponding to a 2π phase drop, represent the height contours of the terrain elevation map. However, since the real phase values are "wrapped" around a 2π interval, to obtain the correct map (and, thus, the correct labels of each contour line), a map of the multiples of 2π to be added to the "wrapped" phase should be carried out (*phase unwrapping*). At the beginning of the studies on SAR interferometry (1988-89), the phase unwrapping problem was investigated assuming that only two SAR images were available. That was the actual situation at that time since the only few interferometric SAR images were from the SEASAT and the JPL single pass airborne systems. Many techniques of phase unwrapping of interferometric SAR images have been proposed [6, 7, 8]. A summary of these techniques is out of the scope of this paper. Nonetheless the following con-

clusion came out from these works: phase unwrapping can be either trivial or practically impossible depending on the coherence of the images (see section 8) and on the presence of foreshortening and layover (see section 5). More recently, however, a different strategy to solve the phase unwrapping problem has been considered. With the huge amount of SAR images from the European satellites ERS-1 and ERS-2 together with the availability of Digital Elevation Models (typically from the optical stereo SPOT) the basic assumption changed: all the available information should be exploited to get a DEM [9]. Then, an available Digital Elevation Model (DEM) can be transformed into the SAR geometry and subtracted from the interferogram. Depending on the DEM accuracy and on the normal baseline B_n the phase of the residue can be so small to show a single fringe with no need of phase unwrapping. On the other hand, if more interferograms are available the linear relation between the baseline and the interferometric phase (see equation 3.4) can be exploited together with the theorem of the "chinese remainder" to reduce the wrapped phase ambiguity. As a conclusion, even if a fully automatic phase unwrapper that works in every condition is not available yet, phase unwrapping does not appear to represent a serious problem in SAR interferometry anymore.

5. Digital Elevation Map preparation

The elevation map derived from SAR interferometry lies on a plane where the reference axes correspond to the azimuth and slant range directions.

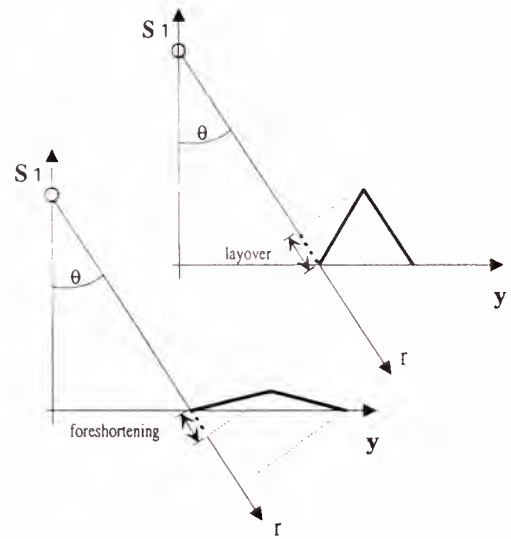


Figure 5.1: Typical geometric deformations introduced by SAR (foreshortening and layover).

Such a coordinates system is completely different from the reference systems in the azimuth-ground range plane used in the usual el-

elevation maps. Thus it is necessary to transfer the unwrapped phase from the slant range coordinates system to the ground range system; the obtained values must be interpolated and resampled in terms of uniform ground range cells.

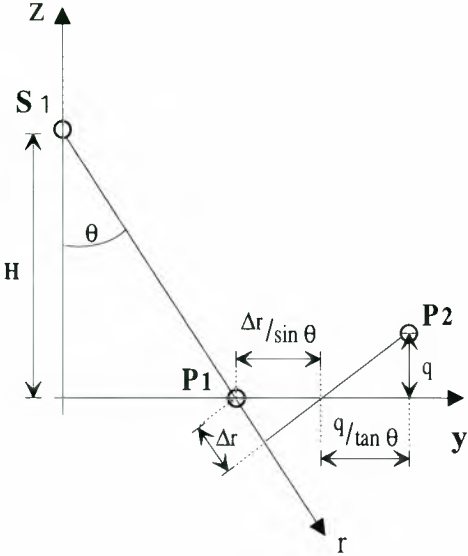


Figure 5.2: Cross-section of the SAR system geometry normal to the azimuth direction. The ground range coordinate depends on both the range position and the point elevation.

5.1. Rectification of the elevation map

From Figure 5.2 it is evident that the horizontal position of a backscatterer depends on both the slant range coordinate and the elevation. Through simple geometrical expressions the relation between these three parameters can be found. The ground range coordinate with respect to the initial point, indicated by y , is the sum of two components: the first is the horizontal displacement in the case of flat terrain, the second caused by a non-zero elevation drop.

$$y(r, q) = \frac{\Delta r}{\sin \theta} + \frac{q(r)}{\tan \theta} \quad (5.1)$$

Since the position of the points depends on its elevation, the correspondence between ground range and slant range is quite irregular. In fact, the well known foreshortening effect causes a compression of the areas with ascending slope and a spread of the descending areas. As a consequence the ground difference, corresponding to a constant slant range displacement, will be much larger in the case of ascending slopes. Furthermore, when layover effects occur several areas of the earth's surface can disappear from the SAR image (see figure 5.1).

In a ground range reference system the obtained elevation map will have a quite uneven sampling inter-

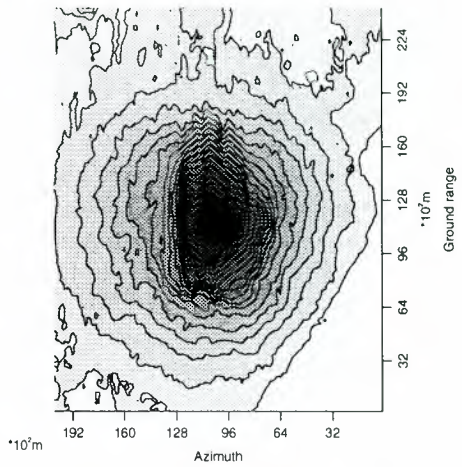


Figure 5.3: A topographic map of the area of Vesuvius obtained from the unwrapped and rectified phase, shown in the previous picture.

val. Thus to obtain a regular sampled map the elevation values must be interpolated. For our purposes a linear interpolation is quite adequate. In fact, in flat or descending areas the interpolating points are fairly close, whereas with an ascending slope the foreshortening effect produces such a large slant range compression that the interpolating points lie much further away and no interpolator would operate correctly. For example, for geometrical parameters like the ERS-1 mission, a slant range sampling $\delta r \simeq 8\text{m}$ corresponds to a ground range step $\delta y = \delta r / \sin \theta \simeq 20\text{m}$ for flat terrain; on the contrary for a terrain slope $\alpha = 15^\circ$, the ground range step is $\delta y = \delta r \cos \alpha / \sin(\theta - \alpha) \simeq 60\text{m}$. The results of the rectification process, performed for the SAR image of the area near the Vesuvius is shown in figure 5.3. Contour lines correspondent to descending orbits are shown.

5.2. Combination of ascending and descending orbits data

Any current DEM estimate is very useful for unwrapping. In fact, data from different takes and therefore with different baselines can be combined, but only if properly positioned in space; in the case of a flat region, uninteresting for the unwrapping problem, the coregistration can be carried out using ephemerides. Not so in complex topography situation, where the registration is DEM dependent. We arrive to an iterative procedure where the available data are combined in such a way to achieve a progressive improvement of the DEM. In this operation, the combination of data from ascending and descending orbits could be very helpful. First, to unravel the layover areas, that, if not in shadow, may appear well behaved with the other orbit. Second, and equally relevant, the combination of the two views is only possible if the DEM is correct; hence, it is a pow-

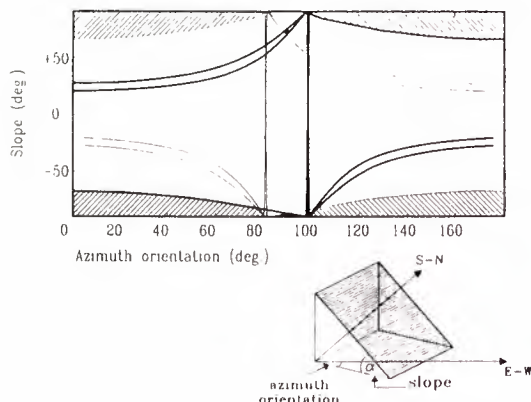


Figure 5.4: Combinations of slope and azimuth orientation that cannot be recovered from ERS-1 data. With ascending orbits (gray and shaded areas). With both ascending and descending orbits (shaded areas only). With layover separation (black areas).

erful check of its quality, to remove blunders, reduce the elevation dispersion, etc.

5.2.1. Slopes coverage improvement

Ascending and descending orbits combination is essential for slopes coverage in SAR interferometry. As an example, the different curves of figure 5.4 identify terrain slopes α recoverable from ERS-1 as a function of their azimuth orientation (see the lower part of figure 5.4). Thick and thin lines refer to ascending and descending passes respectively (here a baseline of 100 meters has been assumed both for ascending and descending passes). If just ascending passes are used, slopes that can be recovered from ERS-1 (at the equator in this example) are contained in the white area. To understand how that plot has been generated, let us consider a 9 degrees azimuth orientation (i.e. the orbit orientation) and let us consider slopes ranging from -90 to $+90$ degrees (i.e. from the lower to the upper limits of the plot). It is clear that, if we consider an incident angle of 23 degrees for flat terrain, slopes from -90 to -67 degrees will not be observed since in shadow (lower shaded areas). On the other hand, slopes from 20 to 26 degrees will not be observable since the interferometric images are uncorrelated [5] (this is the region between the two thick lines). Finally, slopes from 26 to 90 degrees are in layover (upper gray and shaded area). These simple considerations can be repeated for every azimuth orientation and for descending ERS-1 orbits. Then, if both ascending and descending passes are used, the unrecoverable areas are represented by the shaded areas only. Those areas affected by foreshortening and layover in one image are well covered (if not in shadow) in the other image. Finally, if layover areas could be separated from the rest of the image (an operation not always possible), the

irrecoverable slopes are further reduced to the small black areas shown in figure 5.4.

The results of the rectification process, performed for the SAR image of the area near the Vesuvius using both ascending and descending orbit data are shown in Figure 5.5.

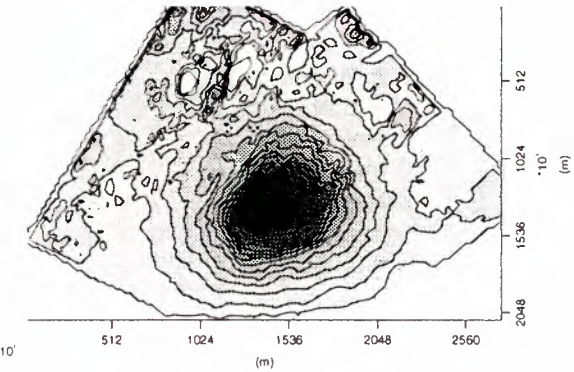


Figure 5.5: A topographic map of the area of Vesuvius obtained from the unwrapped and rectified phase using both ascending and descending orbits.

6. Monitoring terrain changes

If the SAR acquisitions are not simultaneous, the interferogram phases (*fringes*) are also affected by the possible terrain changes. Two types of temporal terrain evolution can be identified by means of multitemporal interferometric SAR images: decorrelation changes and small terrain motions.

Decorrelation changes. A random change of the position and physical properties of the scatterers within the resolution cell can be detected as low coherence of the images and will be dealt with in section 8.

Small terrain motions. Centimetric slant range relative motions of local areas that occur between two SAR acquisitions, generate large local phase shifts in the interferogram. The phase difference $\Delta\phi$, generated by small terrain relative motions is governed by a mathematical relation completely different from that of the interferometric fringes (that, in order to avoid any confusion we shall indicate with $\Delta\phi_T$) described by equation 3.3. It is, in fact, proportional to the ratio between the relative motion Δs along the slant range direction and the transmitted wavelength λ . Thus, if we have a non simultaneous interferometric SAR pair with a given baseline B_n and a small terrain relative motion occurs between the two acquisitions, the following expression of the interferometric phase difference holds:

$$\Delta\phi = \Delta\phi_T + \Delta\phi_s = \frac{4\pi B_n n_p}{\lambda r_o} + \frac{2\Delta s}{\lambda} \quad (6.1)$$

From equation 6.1, it is clear that the two terms $\Delta\phi_T$ and $\Delta\phi_s$ should be separated in order to recover the terrain relative motion. The simplest way to estimate small motions consists of choosing an image pair with a very small baseline (zero or a few meters would be sufficient in the case of ERS-1) so that the first term is much smaller than the second. An interesting example of such a solution is shown in figure 6.1. Two ERS-1 images of the area of Nice on the border between France and Italy, with a time interval of 9 days and a baseline $B_n = 6m$, have been used to generate an interferogram. In figure 6.1 the interferometric fringes are shown. Due to the very small baseline the fringes do not show rapid variations (even if the topography of that area is not flat at all) but for a small area close to the center of the map. In that area a very active landslide has being monitored by the group of the Institute de Physique du Globe (IPG) in Paris. From the ERS-1 interferometric data, an average landslide velocity of about 1cm per day has been estimated. The result is in good agreement with the data provided by the IPG group. Moreover, the ERS-1 interferometric SAR image provides a set of measurements of the landslide relative motion on a very dense grid (4×20 meters) at a cost that is much smaller than that of any other traditional techniques. The accuracy of the motion measurement offered by such a technique has been recently tested with an ERS-1 experiment (the "Bonn experiment"), where elevation change as small as 9 mm of a few artificial radar targets (corner reflectors) has been detected with no ambiguity [10, 11, 12].

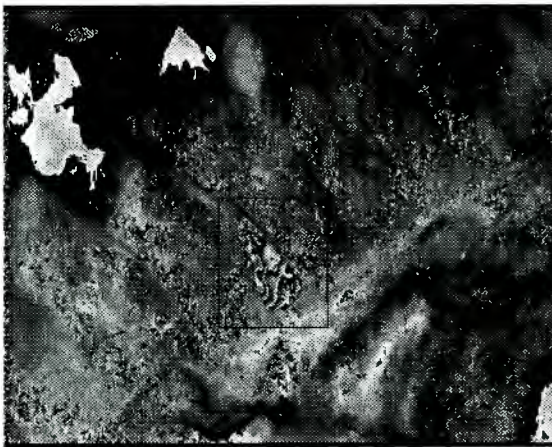


Figure 6.1: ERS-1 SAR interferometry. Fringes generated from two images of the area of Nice on the border between France and Italy, with a time interval of 9 days and a baseline $B_n = 6m$.

If a stereo SAR pair with a very small baseline is not available, the topography contribution to the inter-

ferometric phase ($\Delta\phi_T$) must be subtracted from the fringes. It can be accomplished in two different ways. If a topographic map of the area of interest is available, it has to be transformed in the azimuth slant range coordinates and scaled proportionally to the baseline of the interferometric pair in order to have an estimate of the phase component $\Delta\phi_T$. Then, it should be subtracted from the fringes (an impressive example of this technique has been shown at CNES [13] for the Landers earthquake). As an alternative, an additional SAR image can be exploited in order to have an interferometric SAR pair with no terrain changes [14]. For the sake of simplicity, let us label the three SAR images with 1, 2 and 3 with no regard to their time consecution. Let us also assume that during the first two images no terrain changes occur. Thus, the fringes generated from the first two images will be proportional to the phase $\Delta\phi_t$ to be subtracted from the fringes generated either from the couple 1 – 3 or 2 – 3. From equation 3.3, it is clear that the proportionality coefficient is given by the ratio of the two baselines B_{n12} and B_{n13} (or B_{n23}). However, since the proportionality holds on the phases and not on their principal values¹, the fringes obtained from the couple 1 – 2 must be first unwrapped and then scaled.

7. Atmospheric effects

In repeated pass SAR interferometry from satellite, different propagation velocities along the scene due to atmospheric changes (at the time of the two surveys) could be responsible of interferometric phase variations that cannot be related neither to the topography nor to relative terrain motions. The above said effects can be clearly seen on the interferometric phase shown in figure 7.1.

This phase image has been generated from two ERS-1 images of the black forest near Freiburg (a quite stable area) taken on August 17 and 20, 1991. The normal baseline is 9 meters (i.e. a 2π phase change corresponds to more than 1000 meters relative elevation). The phase variations with very low spatial frequency visible in figure cannot be associated either to the topography or to terrain deformations and might be generated by evapotranspiration phenomena, atmosphere or soil moisture changes within the two surveys. These effects appear to be the major limitation to the use of SAR interferometry as a technique for generating highly accurate Digital Elevation Models and for detecting small surface deformations. However some considerations should be made at this regard showing that in both applications these parasitic effects can be strongly reduced if many independent interferograms are available. Let us first consider the DEM generation case. The interferometric phase depends on the relative elevation through a coefficient that is directly propor-

¹Apart from the special case of an integer ratio between B_{n12} and B_{n13} (or B_{n23})



Figure 7.1: Phase image generated from two ERS-1 images of the black forest near Freiburg (a quite stable area) taken on August 17 and 20, 1991. The normal baseline is 9 meters.

tional to the baseline (see equation 3.3): the higher the baseline, the higher the phase variation correspondent to the same topography. On the other hand, the phase variations due to atmospheric changes are independent of the baseline. Thus, the higher is the baseline of the interferometric pair the smaller is the topographic error due to parasitic effects. Moreover, if many interferometric pairs of the same area are available (as in the case of ERS-1/ERS-2 Tandem mission) "outliers" can be identified and eliminated from the database. The remaining results can be combined to "filter out" the effects of atmospheric changes. The availability of an interferograms database can be also exploited to improve the measurements accuracy of surface deformations. In this case the interferometric phase variations due to surface deformation is independent of the baseline. However, if a model of the deformation development with time is available, the interferometric images can be used to identify the parameters that fit the model to the time series. Clearly, the larger the available interferograms time series the more accurate the parameters estimation. Also in this case outliers can be identified and eliminated. As a conclusive remark of this section, it should be pointed out that an attempt of modeling the phase variations due atmospheric changes is being carried out at CNES [13]. A simplified model has been supposed where the interferometric phase variation is the sum of two terms: the phase variation due to the different travel paths in two atmospheres with a different refraction index (there assumed to vary linearly with the altitude) and phase variations due to localized atmospheric changes (i.e. clouds, fog ...). Due to the first contribution, a moderate phase variation among interferograms (linearly dependent on the elevation) is generated. This effect can be strongly reduced if many interferograms are available. On the contrary, the second contribu-

tion is unpredictable and can be so strong to make the interferometric pair useless. In this case such an interferometric pair should be eliminated from the database as an outlier.

8. Coherence

8.1. Generalities

The quality of the interferometric phase depends on the amount of noise that, in general, comes from distinct sources [2, 15]: i- system noise; ii- terrain change (non simultaneous acquisitions); iii- images misregistration; iv- approximate and unequal focusing of the two passes; v- decorrelation due to the baseline ("geometric" decorrelation). It is obvious that there is no way to avoid the first two sources of noise. On the other hand, as far as the last three sources are concerned, they can be taken under control. In other words, since in most cases the system noise is quite small compared with the usually sensed signals, and the processor noise is well under control if it is designed to be **phase preserving** [2], it will be shown that the fringes quality is degraded by scattering change in time and volumetric effects (see section 9.2) only. The coherence γ of two complex SAR images v_1 and v_2 , is defined as follows [3]:

$$\gamma = \frac{E[v_1 v_2^*]}{\sqrt{E[|v_1|^2]E[|v_2|^2]}} \quad (8.1)$$

where $E[\cdot]$ means the expected value (that in practice will be approximated with a sampled average) and $*$ the complex conjugate. The absolute value of γ is a fundamental information on the exploitability of SAR interferograms. The signal (usable fringes) to noise ratio Ξ can be usefully expressed as a function of the coherence:

$$\Xi = \frac{|\gamma|}{1 - |\gamma|} \quad (8.2)$$

Thus, it is clear that every effort should be dedicated to avoid coherence loss during the interferogram generation process (section 8.1).

The statistical confidence of the estimated coherence (sampled coherence) and of the derived measurements, depends on the number of independent samples (n) that can be combined for the computation. As a first approximation, the standard deviation of the estimator is proportional to $1/\sqrt{n}$. Thus, whenever uniform areas (in the statistical sense) are identified, the sampled coherence can be computed as:

$$\gamma = \frac{\sum_n v_1 v_2^* e^{-j\phi}}{\sqrt{\sum_n |v_1|^2 \sum_n |v_2|^2}} \quad (8.3)$$

In fact, since the coherence is estimated from the combination of the phases of a few pixels at the very least, the topography effects on the interferometric phase ϕ proportional to the known terrain changes have



Figure 8.1: Coherence map of Mt. Vesuvius.

to be removed from the result. Thus, in order to compensate this unwanted effect, the vectors at the numerator of equation 8.3 must be *deskewed* before summing. It is also clear that, in order to generate an interferogram, the pixels of the images gathered in the two different images must be registered accurately, so that the random variates corresponding to the reflectivity are properly aligned. A single pixel shift, if the focusing processor is a good one, is enough to practically zero the correlation. In the following we will not consider the effects due to misregistration and system noise, since they can be avoided with a good system or with a proper processing. The elevation error σ_n of maps generated by means of SAR interferometry will follow the value of Ξ as:

$$\sigma_n = \frac{\lambda r_o \sin \theta}{2\pi n_s} \sqrt{\frac{1}{2\Xi}}$$

As an example, the coherence map of the area of Mt. Vesuvius in Italy observed from ERS-1 on August 27th and September 5th 1991 is shown in figure 8.1 (see also the fringes obtained with the same passes that are shown in figure 4.1). The sampled coherence has been computed on small rectangles 16×4 (azimuth, slant range) pixels large ($n = 64$) that reasonably belong to uniform areas. The coherence map can be converted into an elevation error map (apart from systematic errors). As expected, areas covered by thick vegetation or in foreshortening or layover show an almost zero coherence and are not usable for SAR interferometric applications (e.g. DEM generation and super-resolution).

8.2. Applications to image segmentation

SAR coherence is an additional source of information with noticeable diagnostic power. In the following we

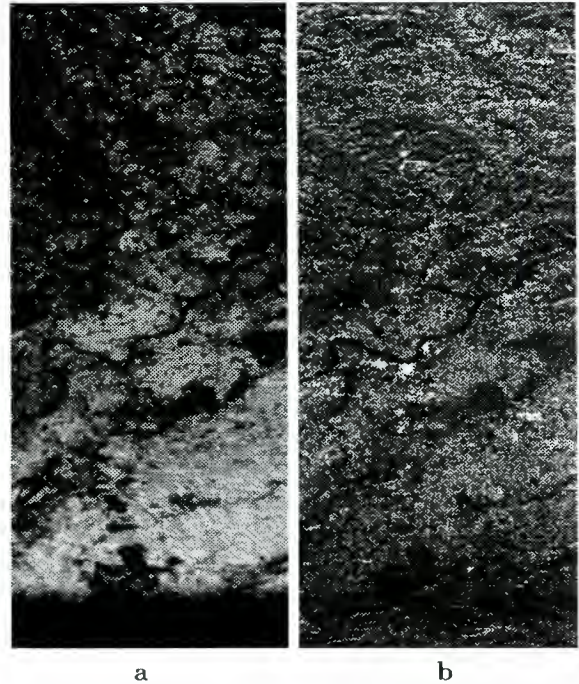


Figure 8.2: **a** - Coherence map of the Bonn area. The Rhein river is clearly visible crossing from left to right the image. **b** - ERS-1 detected image of the same area.

shall enumerate some of the most relevant applications. In [12] it was first observed that forests, that appeared with variable reflectivity in the ERS - 1 detected images, appeared almost black in the coherence images: this effect is due to the scarce penetration of C band radiation in the vegetated canopy, so that small variations of the positions of leaves and smaller branches were enough to change the disposition of the scatterers and therefore practically annihilate coherence; likewise happens for water bodies, that appear always with negligible coherence. In [16, 17, 18] it was also observed that cultivated field changed their coherence after plowing, harvesting etc., so that it was possible to detect anthropogenic effects in multitemporal sequences of takes of the same area, by looking at sudden coherence losses. In general, the combination of multitemporal observation both of detected images and coherence allows a very good segmentation of agricultural areas; it is thus possible to identify cultures (potatoes are harvested in that month, whereas corn matures in that other ..). The coherence map, achieved from interferometric quick-look processing, generated from two ERS-1 images of the Bonn area taken 3 days apart in time (March 8th and March 11th 1992) is shown in figure 8.2. Notice the black curve (low coherence) that corresponds to Rhein river crossing from left to right figure 8.2. For comparison, also the detected image is shown in figure 8.2. Other authors [19] observe that from the phase of the interferometric takes the height of the trees and therefore the biomass can be estimated.

8.2.1. Identification of exposed rocks

The coherence image of Mt. Vesuvius 8.1 shows interesting features that are not visible in the detected image of the same area. Apart from the already mentioned zero-coherence areas, a very bright stripe (high coherence) is visible on the left hand side of Mt. Vesuvius. This area that is not identified on the absolute value image, has a geological peculiarity: it is an old lava flow (year 1944). Since exposed rocks are coherent even after years, such areas can be easily identified by using SAR coherence.

9. The wavenumber shift approach

The above described monochromatic approximation, notwithstanding its simplicity, hides an important aspect of the interferogram generation mechanism that will be discussed in this section. Let us consider the approximated relation between the frequency f and the ground wavenumber k_y (along the range direction y as shown in figure 9.1). It can be easily derived by projecting the transmitted wavelength λ , measured along the slant range direction, on the terrain. For sake of simplicity we shall suppose that the terrain has a constant slope α . Thus, as a first approximation, the wavelength λ projected on the terrain is scaled by the factor $1/\sin(\theta - \alpha)$. Then, the factor 2 accounting for the two ways travel path, the following expression of the ground wavenumber holds:

$$k_y = \frac{4\pi}{\lambda} \sin(\theta - \alpha) = \frac{4\pi f}{c} \sin(\theta - \alpha) \quad (9.1)$$

Thus, in general, a looking angle difference $\Delta\theta$ generates a shift and a stretch of the imaged terrain spectra. However, if the relative system bandwidth is small, the frequency f in the second term of equation 9.1 can be substituted with the central frequency f_o . The stretch can be neglected and the following equation holds.

$$\Delta k_y = \frac{4\pi f_o \Delta\theta}{c} \cos(\theta - \alpha) \quad (9.2)$$

Finally, since the radar is not monochromatic (we have a bandwidth W centered around the central frequency f_o), we can conclude that by changing the looking angle of the SAR acquisition, we get a different band of the ground reflectivity spectrum. Now, in order to compare the shift of the ground reflectivity spectrum with the SAR bandwidth W , it is worth to express the ground wavenumber shift of equation 9.2 as an equivalent frequency shift Δf . The following expression of Δf for an angular separation $\Delta\theta$ can be obtained by differentiation of equation 9.1 directly,

$$\Delta f = -\frac{f_o \Delta\theta}{\tan(\theta - \alpha)} = -\frac{c B_n}{r_o \lambda \tan(\theta - \alpha)} \quad (9.3)$$

We would like to stress again that equation 9.3 does not state that by changing the looking angle of the SAR

acquisition the radar bandwidth is shifted by Δf . It just says that by changing the SAR looking angle, the backscattered signal contains different spectral components of the ground reflectivity spectrum. In other words, if we look at the signals received by two SARs separated by an angle $\Delta\theta$, equation 9.3 states that the same spectral components of the first signal are found in the second spectrum shifted by Δf . In figure 9.1 the wavenumber shift principle is sketched.

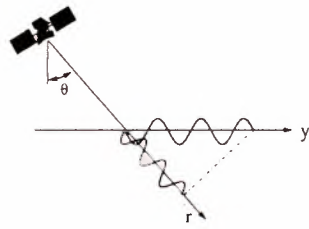


Figure 9.1: The wavenumber shift principle. By changing the looking angle of the SAR acquisition we get different wavenumbers of the ground reflectivity spectrum.

Different bands of the ground reflectivity spectrum (limited by the finite bandwidth of the SAR systems) observed from slightly different looking angles are shown. Notice that whenever the spectral shift Δf is smaller than the system bandwidth W , we have that only part of the ground reflectivity spectrum is common to both spectra. In the following, we shall refer to that as the "common band". In the case of distributed random scatterers, there can be a correlation of the two return signals only if there is such a common band; in such a case, by considering equation 9.3, it is clear that the spectral shift Δf between the two images can be measured and, if we know the geometric parameters B_n , θ and r_o , the local terrain slope α can be recovered. Then, by integrating the local terrain slope, the terrain topography can be derived. From equation 9.3, the expression can be easily derived of the critical baseline for which the two spectra become totally disjoint, the correlation of the two return signal goes to zero and the spectral shift cannot be computed. As an example, the ERS-1 critical baseline for flat terrain ($\alpha = 0$) can be computed is 1100 m.

9.1. Range resolution improvement

The range resolution achievable from a single SAR complex image is limited by the system bandwidth [3, 4]:

$$\rho_r = \frac{c}{2W}$$

However, we will show how the image bandwidth (and so the resolution) can be enhanced by combining multiple surveys from different view angles. As an example, in the case of two surveys, the spectral shift caused by

a change in the view angle of $\Delta\theta$ could give a single image with an enhanced bandwidth: $W_e = W + \Delta\omega/(2\pi)$.

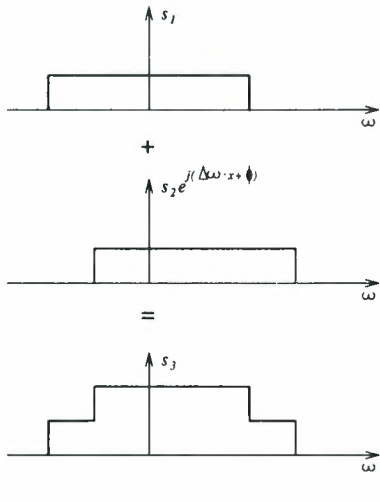


Figure 9.2: The wavenumber shift principle is used to improve slant range resolution.

This is shown in figure 9.2: it can be noted that the parts not common to the two range spectra, that were filtered out in the interferometric processing, now represent the innovation present in one image with respect to another. It's worth to note that the resulting band expansion, and hence the improvement of resolution in slant range is not constant in all the image points, but it is a function of the baseline and of the local slope angle of the ground α . In the points where α is positive, the spectrum shift and the obtainable improvement are maximum. The processing required to get the super-resolution image, i.e. the coherent superposition of the surveys, requires the compensation for each scatterer, of the phase rotation due to the travel path distance between the scatterer and the couple of interferometric sensors.

9.2. Volume scattering

Up to now, we have considered only surface scattering, neglecting the effect of volume scattering. However, when backscattering comes from targets with different elevation z within the resolution cell, volume effects cannot be ignored. Two SAR images from different angles (θ and $\theta + \Delta\theta$) represent different bands of the complex reflectivity spectrum. From figure 9.1, it is clear that, in order to observe the same k_y from the two acquisitions (i.e. the condition that allows coherent interferometry in case of surface scattering), the looking angle change $\Delta\theta$ should be compensated by the already mentioned spectral shift

$$\Delta\omega = -\omega\Delta\theta/\tan(\theta)$$

that is equivalent to the following k_z wavenumber shift

$$\Delta k_z \simeq -2\Delta\omega/(c \cos \theta) = 2\omega\Delta\theta/(c \sin \theta).$$

The coherence of interferometric images depends on the degree of spectral correlation between the measurements in k_z and $k_z + \Delta k_z$. If we consider, as a special case, the flat box ($\Delta z = 0$), the signal is impulsive in the z domain and we have total correlation of the different spectral components and unitary coherence. In general, with a finite volume and a non zero value of Δz , we shall have the following expression of the spectral correlation function:

$$\frac{\sin(\Delta k_z \Delta z/2)}{\Delta k_z \Delta z/2}$$

So, we can state that whenever $|\Delta z| \ll 2\pi/|\Delta k_z|$, volumetric effects can be neglected. A useful expression can be found as a function of transmitted wavelength, normal baseline and satellite altitude:

$$|\Delta z| \ll |\frac{\lambda H \tan \theta}{2B_n}| = |\Delta z_o|$$

If we consider the case of $|\Delta z| \geq |\Delta z_o|$, we have spectral decorrelation and low coherence. In the ERS-1 case with a baseline of 250 meters decorrelation is expected for $|\Delta z| \geq 38$ meters. From those observations, it is then possible to derive a LMS estimate of the surface and the volumetric contribution. These concepts have been further tested by means of the anechoic chamber at JRC-EMSL [20].

10. Interferometry from airplanes

Apart from satellites, airplanes are the other source of interferometric data: in this case, however, the instability of the platform makes it practically very difficult to achieve multi pass interferometry; in the single pass technique, the two antennas are placed on board at the maximum distance compatible with the airframe to increase the baseline. The coherence of the interferometric picture is basically equal to 1, so this is not a source of information. On the other hand the quality of the fringes is topmost and therefore the quality of the DEM that can be generated very high. There are still problems with layover, but reduced due to the fact that the off nadir angle can be higher than 45° , and at times close to 80° . Then shadows become important: In that case the coherence drops to 0, and there is no signal. The real problem with airplane data is again the instability of the platform and the uncertainty of the Doppler centroid and of the actual value of the baseline, that depends on the airplane position. The spatial resolution can be as high as 0.5×0.5 m [21]. The vertical resolution can be also very good due to the high quality of the fringes and to the very good signal to noise ratio. A big difference with the satellite is the swath, that can never be much beyond a few kilometers. This makes airplane surveys more expensive than those from satellites. The other application of airplane interferometry is along track instead of across track; in that case, the two antennas are displaced along the

flight direction, so that the image taken is the same, but for the objects that moved in the time interval correspondent to the sensor displacement (say 20 msec). Then it is possible to see that movements along range at the speed of say 1 m/sec correspond to fringes of about a wavelength in C band and therefore are very well visible. This leads to another very important application of interferometry [22] i.e. the measurement of sea currents.

11. The complete interferometric chain

In the case of multi pass interferometry a good control of the platform position and of the central frequency of the radar is needed to get good pictures; then the data should be processed with a phase preserving processor, i.e. without distorting or adding space varying phase shifts induced by inaccurate processing. Almost all processors can do as long as they are designed for that; we remember here the $\omega - k$ processor [2] but also range Doppler ones can be made to work [23]. Once the data are focused, then the two images have to be properly aligned in space; the precision of the alignment should be about .1 pixel or better; this is achieved by optimizing the quality of the fringes and using very high quality interpolators [24]; it is also possible to design the focusing processor to properly stretch the images avoiding too many interpolations [25]. The fringes thus generated have to be unwrapped: the problem can be solved either with a single very high quality image pair (the airplane case) or if we have several lower quality image pairs with different baselines (the satellite case); a precedent DEM is always useful. Finally the image has to be geocoded and if possible merged with other estimates of the DEM; but then this type of processing is not specific for interferometry anymore.

12. Actual and future missions

Many airborne systems have been designed to meet interferometric needs (AIRSAR - JPL; ESAR, DLR; EMISAR, TUDenmark; CV 580 - CCRS); satellite interferometry was found [1, 12] because the stability of the orbits and of the clocks were much beyond the specs. Recently, after many years of positive results with ERS - 1, the first mission is flying that was designed with interferometry as one of the main goals, namely the tandem mission where ERS - 1 and ERS - 2 satellites of the European Space Agency revisit the same area after 1 day (revisiting delays of about 30 min. and of 8 days could also be envisaged); the quality of the images is very good. It is also important to mention the SIR - C mission, where the final days were devoted to multifrequency interferometry (L, C, and X band), with one day revisiting time, with results similar to that of the Tandem mission, with advantage of the multifrequency and the disadvantage of a limited duration of the mission and therefore a limited

coverage of the globe. More satellite missions are envisioned: first ENVISAT, where a SCANSAR system will be available (the off nadir angle can be changed during the observation time), but then a mission with the shuttle where two C band and may be X band receivers will be available at the ends of a 60 feet boom, to achieve single pass interferometry from the satellite. This mission will merge the advantages of airplane and satellite interferometry, namely wide swath and unitary coherence. Further ahead in time, satellite fleets are being studied; the concept of the tandem mission will be exploited, i.e. the cooperation of two or more satellites to have images at a short time distance; the satellites may be staggered in frequency to have more resolution, in space to have the usual interferometry, in time to have along track interferometry, etc.

13. Conclusions

In this presentation we have tried to summarize the impact of interferometry on the design of SAR surveys, its possibilities and limits. First, interferometry is speckle free, since its effect disappears from the differential phase; the concept of radiometric resolution thus loses meaning. Further, we have seen that from the fringes, given short or zero revisiting times, a very good DEM is obtainable, with a vertical resolution that could be in the meter range or even less from airborne platforms. Millimetric motion of large areas of the terrain or of corner reflectors have been measured with good reliability and therefore the possibility of using the system to measure subsidence, landslides, coseismic motion has been demonstrated. However, several conditions have to be met, the most important being the maintenance of some coherence of the scatterers during the entire experience. This is possible in the case of exposed rocks, but in other cases artificial reflectors may be needed to link together scattering structures that may change due to vegetation, floods, storms, etc. Coherence is an important clue, that combined with the more usual backscatter amplitude, leads to high quality images segmentation. The wavenumber shift concept, finally, may lead to a 3 dimensional view of the terrain, provided that sufficiently low radio frequencies be used, that penetrate the target's internal structure. The same principle can be invoked to improve the resolution of objects that do not change with time, seeing them under different angles and therefore using the spotlight mode both in range and in azimuth. We have also presented the state of development of SAR interferometry. Codes have been developed that carry out automatic images registration (up to 1/100 of a pixel), fringe prefiltering and slope driven smoothing. Automatic phase unwrapping is not an easy goal with noisy or difficult images. However, the high quality of the tandem mission makes it likely that global DEM might be available soon in ERS - SAR geometry, so that only differential interferometry data with small phase deviations should be considered. However, both ascending

and descending passes are necessary to avoid foreshortening and layover effects. The combination of multiple images will allow improved resolution.

References

- [1] Zebker, H. Goldstein R., 1986, Topographic Mapping from SAR Observation, *Journal of Geophysical Research*, Vol. 91, pp. 4993 - 4999.
- [2] Prati C., Rocca F., Monti Guarnieri A., Damonti E., 1990, Seismic migration for SAR focusing: Interferometrical applications, *IEEE Transactions on GARS*, Vol.28, N.4, pp.627-640.
- [3] Prati C., Rocca F., Range resolution enhancement with multiple SAR surveys combination, *Proc. IGARSS'92*, Houston, May 1992.
- [4] Prati C., Rocca F., 1993, Improving slant range resolution of stationary objects with multiple SAR surveys, *IEEE Transactions on AES*, Vol. 29, No.1, 135-144
- [5] Gatelli F., Monti Guarnieri A., Parizzi F., Pasquali P., Prati C., Rocca F., 1994, Use of the spectral shift in SAR interferometry: applications to ERS-1, *IEEE Trans. on GARS*, Vol. 32 , No 4, July 1994, pp.855-865.
- [6] Goldstein R.M., Zebker H.A., Werner C.L., 1988, Satellite radar interferometry: Two-dimensional phase unwrapping, *Radio Science*, Vol.23, N.4, pp. 713-720.
- [7] Giani M., Prati C., Rocca F., 1992, "SAR interferometry and its applications", *ESA report N.8928/90/F/BZ*.
- [8] Spagnolini U., 1993, 2-D Phase Unwrapping and Phase Aliasing, *Geophysics*, Vol.58, N.9, pp.1324-1334.
- [9] Tarayre H., 1996, Extraction de modeles numeriques de terrain par interferometrie radar satellitaire: algorithmie et artefacts atmospheriques, *These de docteur de l'I. N. Polytechnique de Toulouse*.
- [10] Hartl Ph., Reich M., Thiel K., Xia Y., SAR Interferometry applying ERS-1 - Some preliminary test results, *Proc. First ERS-1 Symposium*, Cannes, 4-6 November 1992, pp. 219-222.
- [11] Prati C., Rocca F., Monti Guarnieri A., SAR interferometry experiments with ERS-1, *Proc. First ERS-1 Symposium*, Cannes, 4-6 November 1992, pp. 211-218.
- [12] Monti Guarnieri A., Parizzi F., Pasquali P., Prati C., Rocca F., Developments in ERS-1 SAR interferometry, *Proc. of 1st Workshop FRINGE*, ESA-ESRIN, Frascati, 12 Ottobre 1992.
- [13] Massonnet D. et al., The Displacement Field of the Landers Earthquake Mapped by Radar Interferometry, *Nature*, Vol.364, July 8, 1993, pp.138-142.
- [14] Gabriel A.K., Goldstein R.M., Zebker H.A., Mapping small elevation changes over large areas: differential radar interferometry , *J.G.R.*, Vol.94, N.B7, July 1989, pp.9183-9191.
- [15] Rodriguez E., Martin J.M., 1992, Theory and design of interferometric synthetic aperture radars, *IEE Proceedings-F*, Vol.139, No.2, pp.147-159.
- [16] Prati C., Rocca F., Monti Guarnieri A., 1994, Topographic Capabilities of SAR exemplified with ERS-1, *Geo-Information-Systems*, Vol. 7, No.1, February 1994, pp.17-22.
- [17] Werner C., Hensley S., Goldstein R.M., Rosen P.A., Zebker H.A., Techniques and applications of SAR interferometry for ERS-1: Topographic mapping, change detection, and slope measurement, *Proc. First ERS-1 Symposium*, Cannes, 4-6 November 1992, pp. 205-210.
- [18] Wegmueller U., and Werner C. L., 1995, Farmland monitoring with SAR interferometry, *Proc. IGARSS 1995*, Florence, Italy. pp. 544 - 546, 1995b.
- [19] Ulander L. M. H., Dammert, P. B. G., Hagberg, J. O., 1995, Measuring tree height using ERS - 1 SAR Interferometry, *Proc. IGARSS 1995*, Florence, Italy. pp. 2189-2191, 1995c.
- [20] Fortuny J., Holmer E., Sieber A. J., Pasquali P., Prati C., Rocca F., 1994, Validating SAR interferometry applications by using EMSL, *Proc. of IGARSS'94*, Pasadena (CA), pp.736-738.
- [21] Moreira J., 1996, personal communication.
- [22] Gray L., Van der Kooj M., Mattar K., Farris Manning P., Progress in the development of the CCRS along - track interferometer. *Proc. IGARSS 1994*, Pasadena, CA, pp. 2285 - 2287, 1994d.
- [23] Moreira J., et al., 1995, X-SAR Interferometry - First Results, in *IEEE Trans. on GARS*, vol 33, no. 4, pp 950-956, 1995.
- [24] Gatelli F., Monti Guarnieri A., Prati C., Rocca F., 1996, Medium Resolution Efficient Phase Preserving Focusing for Interferometry, in *Proc. IGARSS'96* (Lincoln, Nebraska,) 27-31 May, 1996.
- [25] Fornaro G., Franceschetti G., Marzouk E. S., 1994, A new approach for image registration in interferometric processing, in *Proc. IGARSS'94*, Pasadena, CA, Aug. 94, Vol. 4, pp. 1983-1985.

AN INTERFEROMETRIC QUICK-LOOK PROCESSOR

F. Gatelli, A. Monti Guarnieri, C. Prati, F. Rocca.

Dipartimento di Elettronica - Politecnico di Milano

Piazza L. da Vinci, 32 - 20133 Milano - Italy

Fax: +39-2-23993585, e-mail: monti@elet.polimi.it

Abstract – A real time technique to get strip-map SAR interferograms and coherence maps with common UNIX Workstations / PC is presented. For the ERS mission, the “real time” throughput corresponds to approximately 1/8 of PRF: e.g. approximately 3 min for processing a 100 x 100 km image pair. The proposed algorithm computes a multi-look averaged interferogram + coherence map (at a resolution 50 x 50 m) in 18 minutes by means of a low cost PC (Pentium Pro). This goal is achieved, at a price of some data loss, by exploiting fast techniques for presumming, focusing, image co-registration and coherence estimate.

INTRODUCTION

With the huge amount of interferometric SAR data that are now and potentially will be available from satellite SAR missions (ERS-1, ERS-2, RADARSAT, SIR-C/X-SAR III) [1], the computing time to obtain interferograms and coherence maps in a semi-operative scenario should be kept as short as possible. Thus, to select SAR pairs that actually can be exploited for interferometric applications the generation of fast, low-resolution surveys (e.g. fringes and coherence maps) should be carried out routinely on those pairs that show a suitable perpendicular baseline.

A “quick-look” processor is presented in this paper. The processor computes *interferogram and coherence maps* in blocks of 33 x 100 km, at a geometric resolution 45 x 45 m on the ground (for flat earth). A good altimetric accuracy has been achieved by averaging the interferograms of 5 azimuth looks. Several adjacent “blocks” are then mosaicked to get a continuous azimuth strip.

The processor performs near to real time on common low-cost machine: approximately 6 min are requested to compute a single block (32 x 100 km, 5 looks averaged) interferogram & coherence map, by using a *PC PENTIUM PRO 200* running under Unix. Real time processing, i.e. 8 x the survey time (including some margin for data ingestion from HDDT), would require a machine 5 times faster.

Efficiency has been obtained, at a cost of some quality loss, by designing fast techniques for:

- range and azimuth focusing,

- images co-registration,
- estimate of coherence maps.

PRESUMMING AND FOCUSING

The first processing step of the proposed algorithm consists of a range and azimuth presumming of the SAR raw data. The use of presumming allows to achieve the following advantages:

- (a) the data rate is reduced by discarding less correlated (and noisy) contributions both in azimuth and in range. For range presumming, the central frequency is tuned according to the spectral shift predicted by the baseline [3,4].
- (b) 2D wave-number domain focusing can be performed on smaller kernels and with “approximate” references. These kernels fit better in the processor cache. Moreover the cost of the Fourier Transforms is reduced.
- (c) The processor can be easily implemented on multi-processor machines.

The presumming cost is minimized by means of an integer implementation (e.g. by storing one complex sample in one 16 bit word) and by using polyphase filter banks [3].

The processing time is thus reduced by a factor of 2.2 times due to range presumming (half band is dropped), 2 times due azimuth presumming (3 of the possible 8 looks are discarded) and 1.3 due to approximate focusing. These improvements are achieved at the cost of some information loss: nominally 50 % of the signal (for very low baselines) is lost due to range presumming and almost nothing for azimuth baseline in the tandem case due to the 300 Hz Doppler shift.

As an example, for acquisitions with a baseline of 300 m the range spectral shift is ~5 MHz (for flat earth). A range presumming of 2 allows to recover 81% of the useful bandwidth (e.g. 9 MHz with respect of 11 MHz), if the center frequencies of the presumming filters are tuned according to the spectral shift [2,4]: $f_0 = \pm 2.5$ MHz. Yet, the data rate is halved with evident computational advantages.

The five sub-looks created by raw data presumming are

then range and azimuth focused. For ERS, an efficient 1-D range-Doppler processor has provided enough quality for the goal. That processor has passed the CEOS phase-preserving test (e.g. phase errors are one order of magnitude lower than the requirements).

COHERENCE ESTIMATE

A fast algorithm has been designed to compute coherence maps. The estimator achieves a computational time gain greater than 100, with respect of the conventional estimator, at the cost of a reduced statistical confidence (its accuracy being 3 to 5 times worse for coherence values > 0.4).

The proposed estimator exploits the images amplitudes, and it is based upon the relation between the absolute value of the complex coherence,

$$\gamma = \frac{|E[v_1 \cdot v_2^* \exp(j\phi(x,y))]|}{\sqrt{E[|v_1|^2] E[|v_2|^2]}}$$

(being $\phi(x,y)$ the averaged interferometric phase), and the normalized cross-correlation r of the detected SAR images:

$$r = \frac{E[(|v_1|^2) \cdot (|v_2|^2)]}{\sqrt{E[|v_1|^4] E[|v_2|^4]}}$$

The following expression [5]

$$r = \frac{\gamma^2 + 1}{2}$$

can be exploited to compute the complex coherence, given an estimate of the normalized cross-correlation of the amplitude image, r . The amplitude based coherence estimator is more efficient, since it does not require the knowledge of the interferometric phase (or local frequency). Moreover, it is not affected by possible local frequency estimation errors being insensitive to the interferometric phase.

It can be shown that the proposed estimator is strongly biased by amplitude non stationarities, however this bias can be effectively reduced by applying a sort of automatic gain control (AGC) to both detected images before computing the coherence estimate [5].

The proposed estimator can be efficiently implemented to compute a coherence map by exploiting overlapped Bartlett or Boxcar windows at a cost of 50 flops for each image pixel, independently of the window size.

IMAGES CO-REGISTRATION

An efficient image co-registration requires both a fast estimate of alignment parameters, and a low-cost image

resampling. In the ERS case, the following deformation model can be assumed between the two images:

$$\begin{bmatrix} x'' \\ r'' \end{bmatrix} = \begin{bmatrix} \cos \beta & -\sin \beta \\ \sin \beta & \cos \beta \end{bmatrix} \begin{bmatrix} x_1 & 0 \\ 0 & r_1 \end{bmatrix} \begin{bmatrix} x \\ r \end{bmatrix} + \begin{bmatrix} x_0 \\ r_0 \end{bmatrix} \underset{\beta \ll 1}{\approx} \begin{bmatrix} x_1 & -r_1 \beta \\ x \beta & r_2 \end{bmatrix} \begin{bmatrix} x \\ r \end{bmatrix} + \begin{bmatrix} x_0 \\ r_0 \end{bmatrix}$$

being x'', r'' the reference coordinate of one image and x, r those of the other. The images shift (x_0, r_0) , stretch (x_1, r_1) and skew (β) parameters can be estimated by exploring the relative shift of at least three small-windows, possibly close the corners of the images. The shifts between corresponding windows can be found by maximizing coherence (estimated basing on the images' absolute values). The accuracy can be $\ll 1/10$ of a resolution cell, that is enough for a medium resolution product, however the measured coherence should exceed a proper threshold to avoid larger errors. As an example, Fig.1 shows the probability that the estimated cross-correlation has a maximum for a random position, different from the right one.

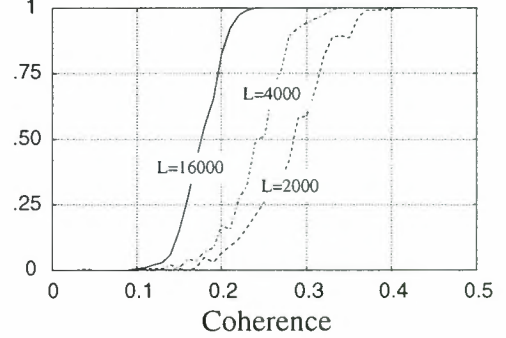


Figure 1: Probability of “correct detection” (e.g. the estimated shift is within ± 1 sample from the correct value) for different numbers of independent pixels, L .

Once that the parameters for images co-registration are known, the necessary images resampling can be implemented, together with 1:2 range oversampling by means of 1-D resampling along azimuth and then along range. These resampling can be given in the space domain by exploiting the FIR kernels:

$$h_{\Delta}(n) = h_{lp}(n) \cdot \frac{\sin(\pi(n - \Delta))}{\pi(n - \Delta)} \cdot \exp(-j2\pi f_{dc}(n - \Delta)) \exp\left(-j2\pi \frac{f_s}{N_l} \Delta d\right)$$

being Δ the local shift, f_{dc} the Doppler centroid, d the look number (N_l the number of looks), and $h_{lp}(n)$ a proper smoothing window. The two exponentials in the expression above are requested to shift the kernel spectrum

around the Doppler centroid (for azimuth resampling) and to compensate the phase offset due to looks' subsampling.

The size of the kernel, e.g. the extent of the window $h_{lp}(n)$, depends on the level of phase noise that can be tolerated. For example, it can be shown that a 6 samples window, gives a decorrelation of 0.1% ($SNR=27$ dB) for $\Delta = 0.5$ (that is the case of image range oversampling $\times 2$). In general, the optimum window size is a function of the azimuth power spectrum density and of the displacement Δ , therefore a Look-Up-Table of N kernels can be built by optimizing the kernels for the shifts: $\Delta = 0 \dots 1/N$. The noise due to the quantization of Δ can be made negligible ($SNR < 32$ dB) by assuming $N \geq 64$. Notice that the use of small kernels of 6-7 samples makes space domain resampling (and oversampling) more efficient than the frequency domain approach [6].

STRIP-MAP INTERFEROGRAM GENERATION

The generation of an interferogram is accomplished, as usual, by complex multiplication of two surveys after co-registration and range oversampling. At this step, it is possible to add in-phase the contribution of different looks. Then, the interferogram is flattened, low-pass filtered and subsampled. A strip-map interferogram is obtained by mosaicking small azimuth strips, say 32 km wide. In the ERS case, the variation of Doppler parameters in strips of that extent causes negligible defocusing (and phase distortion) at the edges of the blocks. There is no need of space registration if the images were registered at zero Doppler while focusing. The only phase registration necessary could be performed to compensate the variation of flattening functions in two adjacent blocks. However, that

COMPUTATIONAL COMPLEXITY

The computing time achieved by the interferometric quick-look (for a 33×100 Km image block) is summarized in table 1. CPU time are referred to a current PC PENTIUM PRO 200, running under UNIX.

The most time-consuming steps have been highlighted in italics. Note the advantage achieved with respect to the standard - public domain interferometric processor, due to a much more efficient way to compute coherence.

An example of a 5 looks averaged ERS-1/ERS-2 tandem interferogram got by mosaicking two strips of 32 km (azimuth) \times 100 km (range) is given in Fig.2,3.

ACKNOWLEDGMENTS

The authors would like to thank the European Space Agency and ACS for sponsoring the work.

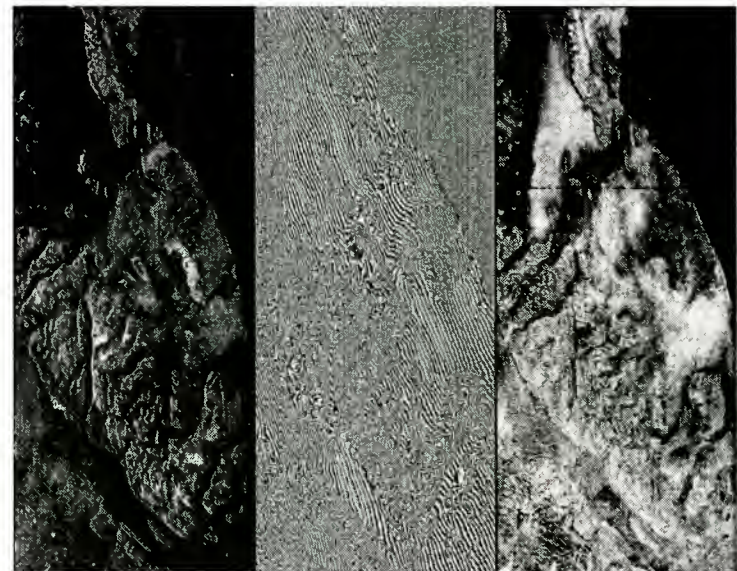


Figure 2: Low resolution interferogram from ERS-1/ERS-2 tandem mission (Jan '96), Greenland. Images' size is approximately 300 km (azimuth, vertical) \times 100 km (slant range, horizontal). Left: absolute value; center: fringes; and right: coherence map.

CONCLUSIONS

An algorithm for generating interferograms & coherence strips has been presented. It is intended for data screening and browsing. All the processing steps requested for generating the interferogram have been revisited - efficiency has been achieved by keeping coherence loss due to processing less than 5%. A "quick-and-dirty", phase-independent coherence estimator has been introduced. It requires 14" to compute a 33×100 km, 5 looks averaged coherence map.

Table 1: Computational complexity and computing time for the quick-look algorithm (30×100 km interferogram).

Processing Step	Quick-look Processor		Standard ISAR Processor (Polimi-ESA)
	CPU time [min:sec]	Mflops/s	CPU time [min:sec]
	1-look	5looks	single look from SLC
Doppler Centroid Estimate	0:01	0:01	-
Baseline Estimation	0:01	0:01	-
<i>Filtering and Subsampling</i>	<i>1:10</i>	<i>1:10</i>	<i>31</i>
<i>Focusing</i>	<i>0:36</i>	<i>3:00</i>	<i>27</i>
Registration parameters estimate	0:03	0:03	-
<i>Image #1 Resampling</i>	<i>0:20</i>	<i>1:40</i>	<i>27</i>
<i>Image #2 Oversampling</i>	<i>0:05</i>	<i>0:25</i>	<i>30</i>
Interferogram Generation	0:06	0:07	31
TOTAL	2:22	6:27	
Coherence Estimate	0:14	0:30	48:28

A 5 looks averaged, 33 x 100 km ERS interferogram can be computed in 6' with a 30 Mflops/s Workstation. A prototype processor, installed at ESRIN, has produced several interferograms and coherence strip-maps thousands of km long.

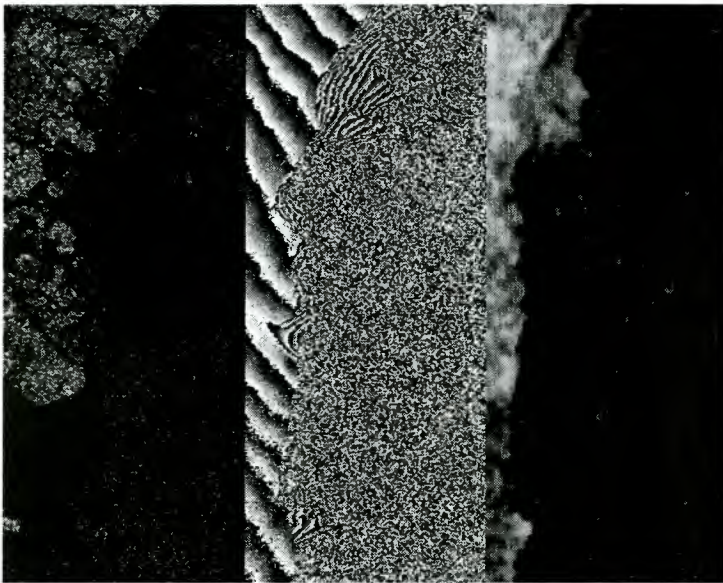


Figure 3: Enlargement of the previous image: an area of approximately 7 x 15 km has been shown. Note the fast fringes probably due to the motion of the ice detaching from the ice-shelf.

REFERENCES

- [1] Solaas G. A., *An Assessment of ERS SAR Low Resolution Imagery*, ESA rep. n. ES-TN-DPE-OM-GS01, Jul. 1993.
- [2] Rocca F., Prati C., Pasquali P., Monti Guarnieri A., *ERS-1 SAR Interferometry techniques and applications*, ESA report n.3-7439/92/HGE-I, 1994.
- [3] Monti-Guarnieri A., Prati C., F. Rocca F., *SAR interferometric quick-look* in *Proc. IGARSS' 93* (Tokyo, Japan), Aug. 93, Vol. 3, pp. 988-990.
- [4] Gatelli F., Monti Guarnieri A., Parizzi F., Pasquali P., Prati C., Rocca F., *The wavenumber shift in SAR interferometry* *IEEE Trans. on Geosci. and Remote Sens.*, Vol. 32, No. 4, pp. 855-865, Jul 1994.
- [5] Monti Guarnieri A., Prati C., *SAR Interferometry: a "Quick and Dirty" Coherence Estimator for Data Browsing*, to appear on *IEEE Trans. Geosc. and Remote Sensing*, (submitted: Jan. 1996).
- [6] G. Fornaro, G. Franceschetti, E. S. Marzouk, "A new approach for image registration in interferometric processing" , in *Proc. IGARSS' 94* (Pasadena, CA), Aug. 94, Vol. 4, pp. 1983-1985.

TRATAMIENTOS DE IMÁGENES RADAR PARA OPTIMIZAR SU APLICACIÓN.

Torrusio Sandra, Bozzarello Enrique.

Dirección de Aplicación de Imágenes Satelitarias-MOSP. Proyecto PNUD Arg. 91/017.

Av. 7 N° 1267, 2º piso, La Plata (1900), Buenos Aires, Argentina.

Tel: 54 21 294951. Fax: (54-21) 294952.

Email: capdis@isis.unlp.edu.ar

ABSTRACT

This is a complementary job of another referred to the use of SAR images, proceeding of ERS-1 and Radarsat, that in these years have had an important diffusion in those areas where either by cloud cover or short sunlight hours (tropical or polar zones) isn't possible to obtain optical data. Also in those regions with optical images, SAR data are an useful complement and in certain studies are being used alone (e.g. flooding).

In addition, we began to work with the first RADARSAT images of Argentine (Buenos Aires Province) and ERS-1 SAR images, in ERDAS Imagine 8.2, to optimize different treatments and to obtain more information from original data, these images were combined with TM images (synergism) and vectorial maps (realized with ARC/INFO), conforming the aims of this study.

The results of this work will allow to incorporate SAR data to studies of flooding, agriculture, land use, geology, coastal zones, multitemporal studies, etc.

RESUMEN

Este trabajo se complementa con uno previo referidos ambos al manejo de las imágenes obtenidas a partir del radar de abertura sintética, portado por satélites como RADARSAT, ERS-1 y 2, que en estos últimos años están cobrando difusión sobre todo en aquellas áreas en que la cobertura nubosa o las escasas horas de luz, (zonas tropicales o polares, respectivamente), no permiten la obtención de datos satelitarios provenientes de sistemas ópticos como Landsat y Spot. Así mismo, en aquellas regiones en que es posible contar con datos ópticos la imagen radar constituye un complemento importante y aún para determinados estudios es una herramienta de suma utilidad en sí misma (ej: inundaciones).

Estas razones motivaron que se comenzara a trabajar con las primeras imágenes RADARSAT de la República Argentina (Prov. de Buenos Aires) y con imágenes ERS-1, en ERDAS Imagine 8.2 y optimizar diversos tratamientos para extraer más información a partir de los datos originales. Se combinaron, además, con imágenes ópticas, realizando una interpretación a priori, mediante el análisis de color de las diferentes coberturas. Mapas vectoriales obtenidos con

ARC/INFO también se superpusieron, tanto sobre la imagen radar, como sobre el producto del sinergismo. Constituyéndose en los objetivos del estudio.

Al mismo tiempo se estableció un punto de partida para el entrenamiento de los usuarios e intérpretes referente a este nuevo tipo de imagen y a las posibilidades presentadas en este caso por ERDAS Imagine 8.2 para analizarlas.

Los resultados obtenidos a partir de este trabajo permitirán incorporar los datos SAR a los estudios aplicados al monitoreo de inundaciones, estimación de cultivos, uso del suelo, estudios geológicos y de zonas costeras, estudios multitemporales, etc.

1. INTRODUCCIÓN

En noviembre de 1995 fue lanzado exitosamente el satélite canadiense RADARSAT que lleva a bordo un sistema de imágenes de radar de abertura sintética (SAR). Mientras que se cuentan con datos ERS-1 ya desde el año 1991.

El SAR, a diferencia de los sistemas ópticos pasivos que dependen de la luz solar, transmite de manera activa una señal de microondas que interactúa con la cobertura terrestre y regresa una señal al satélite. La topografía del terreno, su orientación y otras características afectan a la señal de retorno produciendo cambios en su fase, amplitud y polarización (FAO/ESA, 1993). Mediante el procesamiento computarizado de estos elementos se obtiene una imagen del terreno. Para extraer información de la misma se examina el tono, la textura y la fuerza de la señal ya que se trata de imágenes en blanco y negro.

Para este trabajo se contó con imágenes ERS-1 del año 1993 y las primeras imágenes RADARSAT para la República Argentina de marzo de 1996 (con características similares a la imagen ERS-1, en cuanto a la resolución espacial, el ángulo de incidencia y un ancho de franja de 100 Km).

El objetivo de estudio fue procesar con ERDAS Imagine 8.2 las imágenes Radar y optimizar diversos tratamientos para extraer mucha más información de los datos originales, combinándolos con imágenes ópticas (Landsat TM) y mapas vectoriales obtenidos con ARC/INFO. Iniciando así una nueva etapa en lo que a tratamientos e interpretación de imágenes satelitarias respecta.

2. MATERIALES Y MÉTODOS

Área de estudio:

Las imágenes ERS-1 pertenecen al Partido de Pehuajó, provincia de Buenos Aires, Argentina. Es una zona con relieve plano interrumpido por dunas longitudinales de dirección NE-SO, entre las cuales se hallan cuerpos de agua siguiendo esa misma dirección. Se practican actividades agrícolas - ganaderas de forma extensiva, en las áreas más altas.

Las imágenes RADARSAT comprenden un sector del Delta del Paraná, área limítrofe entre las provincias de Buenos Aires y Entre Ríos. Con un paisaje muy particular en el que alternan zonas con antiguos depósitos marinos, zonas de erosión y deposición de sedimentos fluviales, islas con vegetación natural sobre los márgenes mientras presentan bajos en la parte central, áreas forestadas por el hombre y con actividades frutihortícolas.

Se emplearon:

- Imagen ERS-1/ SAR.PRI del 30 de noviembre de 1993 centrada en las coordenadas S -35.687 y W 62.563.
- Imagen LANDSAT TM Bandas 3,4,5 del 23 de diciembre de 1993, Path-Row 227-85.
- Cartas topográficas de IGM (Instituto Geográfico Militar) a escala 1:50.000 del área en estudio.
- Imágenes RADARSAT de la provincia de Buenos Aires, Argentina, del 6 de marzo de 1996.
- Imagen LANDSAT TM, bandas 3,4,5, del 10 de enero de 1994, path-row 225-84.

El procesamiento de imágenes se llevó a cabo con ERDAS Imagine 8.2.

Se trabajó sobre dos ventanas temáticamente diferentes:

- a) Delta del Paraná.
- b) Sector central del partido de Pehuajó

Los tratamientos aplicados fueron en algunos casos comunes a ambos, mientras que otros fueron exclusivos para cada uno de ellos.

Antes de poder utilizar la imagen ERS-1 fueron necesarios ciertos pasos:

- De formato exabyte se pasó a tape de back up.
- La imagen presentaba inversión de pares de bytes, otorgando una imagen caótica.
- Se le aplicó un programa (J.J. Verges) para restablecer el orden correcto de bytes.
- La imagen obtenida en el paso anterior presentaba una rotación respecto al eje vertical.
- Con ERDAS se lograba invertirla, pero no fue posible generar un nuevo archivo con la imagen en la posición correcta. Recién se pudo obtener después de la georreferenciación.
- Los procesos que se aplicaron sobre la imagen original de 16 bit, también se aplicaron a una de 8 bit.

Para observar si existían diferencias, ya que muchos procesadores de imágenes, que están en el mercado, asociados a sistemas de información geográfica (Iwris, Idrisi) tienen esta limitación para generarlas.

La imagen Radarsat resultó más accesible, en formato CD, se levantó con un programa especial para estas imágenes y se obtuvo la imagen lista para trabajar.

Se aplicaron diferentes filtros sobre la imagen ERS-1, como el de media, Frost, Lee, Map (comparados en Torrusio et al, 1996). resultando en este caso más favorable estadísticamente el de Frost.

Sobre la imagen Radarsat se aplicaron sólo el de Lee y el de Frost, resultando mejor el primero.

Las imágenes SAR fueron, luego del filtrado, (Dallemand et al, 1992) georreferenciadas mediante el método del vecino más cercano (nearest neighbor).

En el caso de la RADARSAT a partir de la cartografía en el Sistema de Proyección Gauss Kruger, con un error medio cuadrático (RMS) de 1,6 pixel ; mientras que la imagen ERS-1 fue ajustada a partir de la imagen LANDSAT TM, pues resultaba difícil encontrar buenos puntos de control directamente sobre la imagen radar (RMS=1,9).

Ambas imágenes LANDSAT fueron georreferenciadas (Fig. 1) por el mismo método (nearest neighbor) alcanzando un RMS menor a un pixel y remuestreadas a 15 m., para luego superponerlas con los datos SAR. En las dos áreas de estudio se combinaron (sinergismo) los datos SAR con las bandas 3 y 4 del Landsat TM (Dallemand et al, 1992, Perlant, 1992, Kohl et al, 1994) asignados a los canales azul, verde y rojo de manera respectiva. Por medio del análisis del color (Lichtenegger et al, 1991) de la imagen resultado se llega a una interpretación, a priori, del área de estudio. Fue importado de ARC/INFO un mapa vectorial (digitalizado a partir de la cartografía del Instituto Geográfico Militar, relevada en el año 1970) conteniendo vías de comunicación, curso de ríos y contornos de islas que fue superpuesto con la ventana del Delta del Paraná (Fig); y otro similar del área de Pehuajó, a partir de la cartografía IGM del año 1956. En este caso se digitalizaron de pantalla ciertos rasgos que dada la antigüedad de la cartografía no figuraban.

3. RESULTADOS Y CONCLUSIONES:

En cuanto a los filtros, resultó mejor en la zona de Pehuajó el filtro de Frost, pues mantiene la mayor cantidad de datos originales y sus estadísticos no son tan diferentes al de los otros filtros que tienen una fuerte pérdida radiométrica; factor a tener en cuenta cuando se emplea el análisis digital de la imagen, como por ejemplo una clasificación automática. Aquí se debe remarcar que esta mencionada pérdida radiométrica tiene suma importancia al tratarse de imágenes de solo 8 bit.

En la zona del delta, el filtro de Lee fue el elegido desde el punto de vista estadístico y visual. (Fig. 2)

Mediante la combinación de los datos SAR y Landsat TM se obtiene una imagen final, (Fig. 3) para cada zona, que enriquece el análisis e interpretación de los datos originales. Aportando información de la topografía (por ejemplo superficies lisas o rugosas) los primeros y del comportamiento espectral de los objetos los segundos.

Para la interpretación a priori de las dos ventanas se puede establecer que los colores rojo a magenta están asociados a una cubierta vegetal continua siendo superficies más rugosas aquellas próximas al magenta, pudiendo diferenciarse zonas de monte y/o áreas forestadas (observándose el aporte de la banda 4, IRC, y la rugosidad otorgada por los datos SAR).

Del rojo al amarillo se relacionan con la vegetación siendo más baja a medida que se aproxima a este último color.

Del verde al amarillo y al cian se corresponden con suelos recubiertos de una vegetación rala o suelos desnudos. A medida que el cian se aproxima al azul se observa el suelo desnudo en diferentes estados de preparación (rugosidad) y con distinto porcentaje de humedad, resultando difícil establecer cual de los dos factores influye más en la retrodifusión.

También es importante destacar en la ventana de Pehuajó que se distinguen diferentes tipos de agua según presenten alguna clase de vegetación en superficie o sedimentos, analizando la diferente coloración en la imagen final. Se destaca además en la misma imagen radar una alta retrodifusión en las lagunas observándose tonos de gris muy claros. Esto se ha debido probablemente a la presencia de viento en superficie que convirtió esa superficie plana originalmente, con retrodispersión prácticamente nula y de color negro (como se ve en la mayoría de los casos) en zonas rugosas, con retrodifusión más alta y de grises más claros.

El software empleado incluye, por medio de dos de sus aplicaciones (Blend y Swipe), la posibilidad de mezclar en distintos porcentajes ambos tipos de datos analizando así el ajuste y los aportes para cada cobertura de ambos sistemas.

De la superposición de la imagen SAR y TM con el mapa vectorial se distingue un buen ajuste. Se observa en la zona del Delta el cambio acontecido en el cauce de algunos cursos de agua al observarse la diferencia entre lo digitalizado a partir de la cartografía (1970) y el curso actual aportado por la imagen. (Fig.3).

En el área de Pehuajó la superposición (Fig. 4) se realizó sin complicaciones, ayudando en este caso la disminución de speckle (mediante el filtro de Frost), la identificación de nuevos rasgos ausentes en la cartografía junto a la adquisición progresiva de experiencia por parte del intérprete.

Se establece finalmente que el sinergismo entre SAR y TM es favorable para analizar de forma completa la

variabilidad presente en diferentes ambientes y así lograr un mejor monitoreo de éstos y de los recursos que sustentan. Además el manejo de estas imágenes y de archivos ARC/INFO con ERDAS Imagine 8.2 resulta amigable y operativo, una vez que los primeros tropiezos, siempre presentes al inicio de una temática nueva, son superados.

4. REFERENCIAS:

Dallemand, J. & al (1992). Combined analysis of ERS-1 SAR and visible/infrared remote sensing data for land cover/land use mapping in a tropical zone: a case study in Guinea. *Proceeding of the First ERS-1 Symposium - Space at the Service of our Environment*. Cannes, Francia. ESA SP-359. Vol II. pp 555-561.

FAO/ESA (1993). Radar imagery: theory and interpretation. *Remote Sensing Series N°67*. pp 103.

Lichtenegger, J. & al (1991). Cartographie de l'utilisation des sols en Tunisie. combinaison de différentes données. *Obsevation de la terre*. ESA Publications. N° 33, pp 1-6.

Perlant, F. (1992). Example of Spot/ERS-1 Complementarity. *Proceeding of the First ERS-1 Symposium - Space at the Service of our Environment*. Cannes, Francia. ESA SP-359. Vol II. pp 563-568.

Kohl, H. & al (1994). Crop acreage estimation with ERS-1 PRI images. *Earth observation quarterly N° 46*. pp 6-8-

5. AGRADECIMIENTOS

Los autores agradecen la participación y colaboración brindada por los sres. Calvanese G. y Platzeck G. de manera especial. Fue muy valioso el aporte recibido por el sr. J.J. Verges. Un agradecimiento, además a todos los profesionales de la DAIS que brindaron su ayuda.

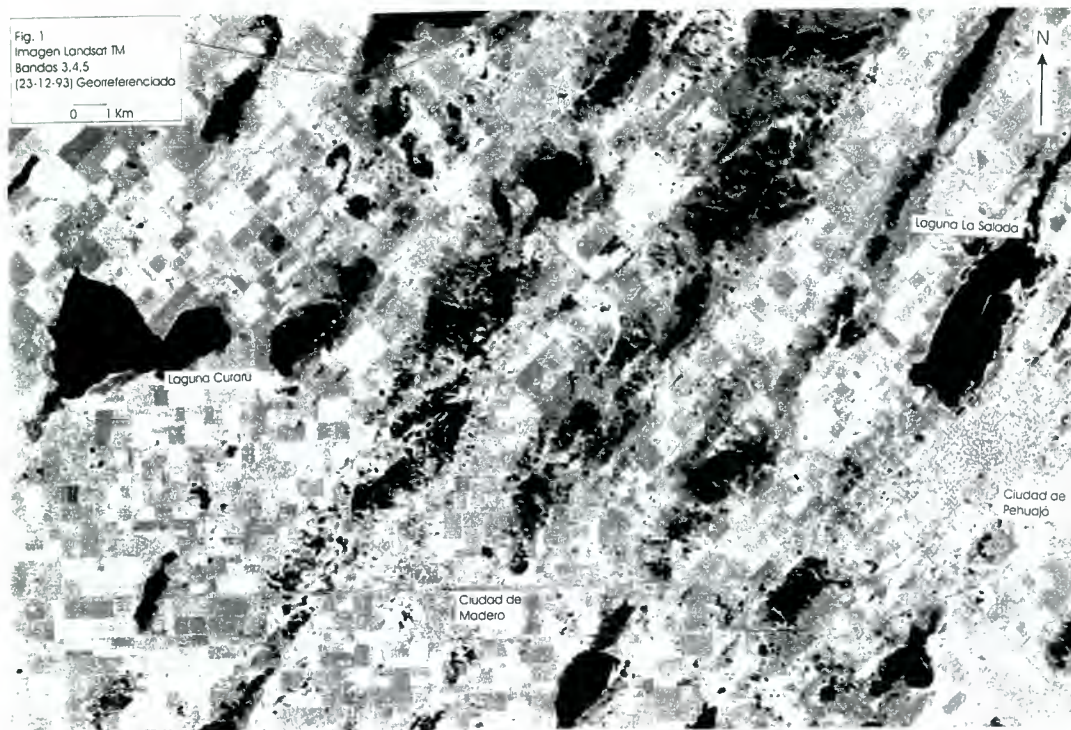


Figura 1. Imagen Landsat TM, bandas 3,4,5. Zona de Pehuajó. Georreferenciada.

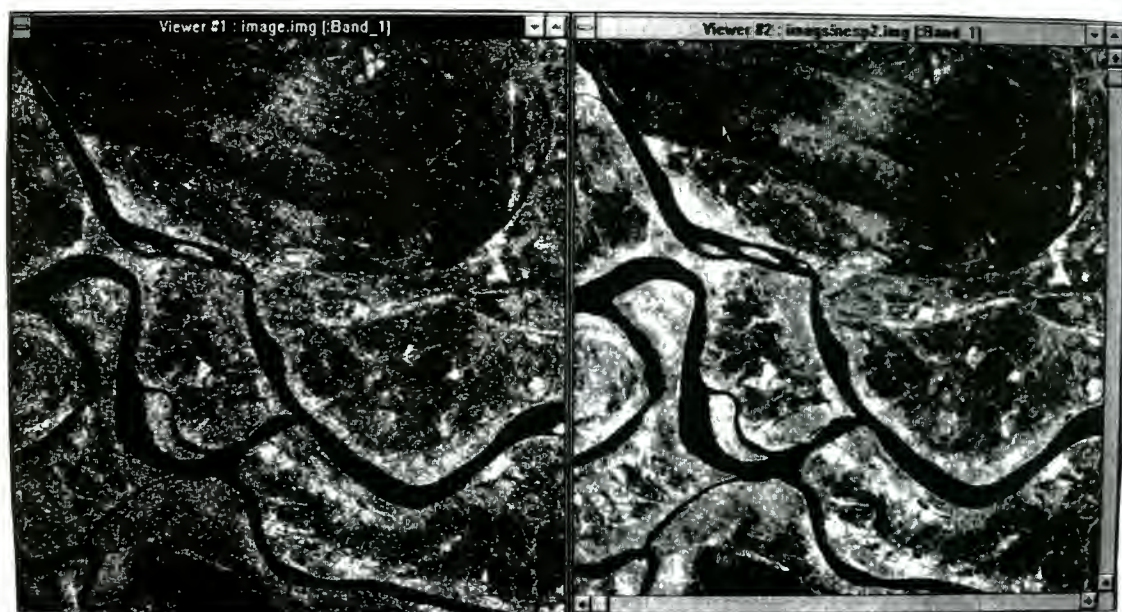


Figura 2. Comparación de la imagen Radarsat sin filtrar (izq.) y con filtro de Lee (der.)
Zona delta del Paraná.

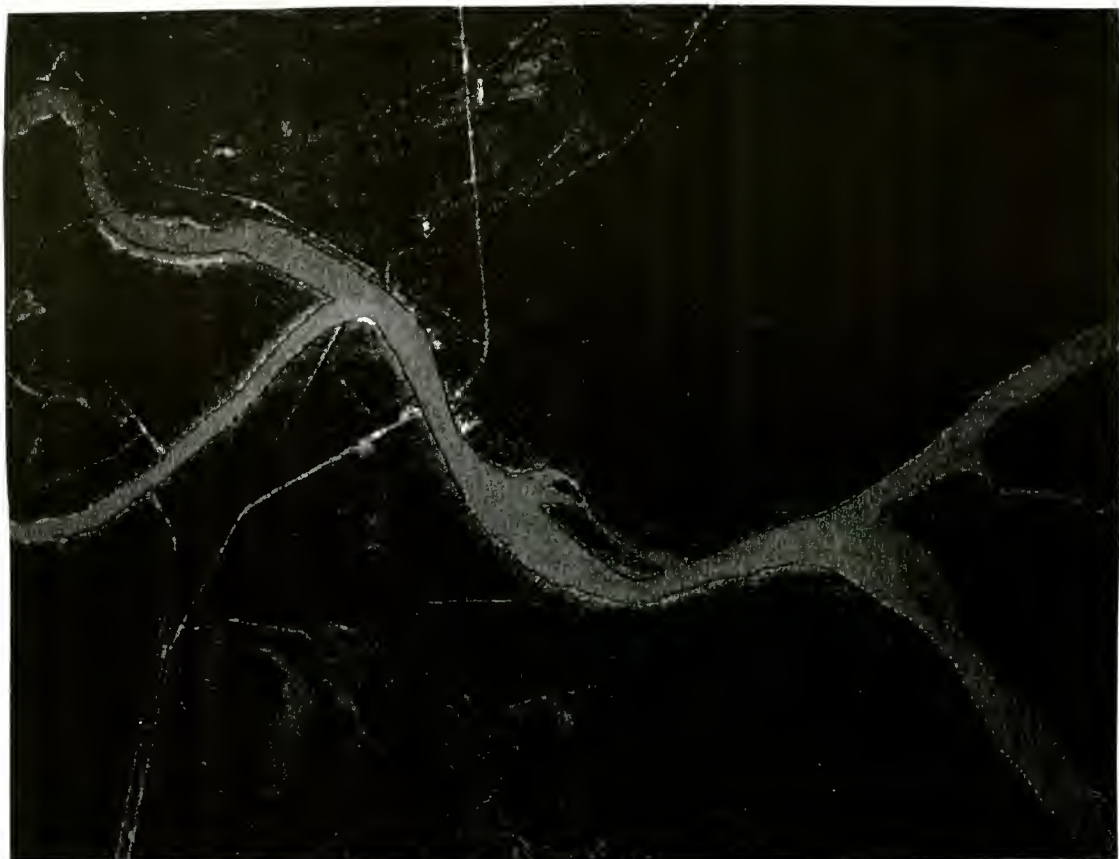


Figura 3. Imagen Landsat TM + ERS-1 + Mapa vectorial ARC/Info. Zona Delta del Paraná. Observar la diferencia en el curso del río (ángulo sup. izq.) con lo digitalizado del año 1970.

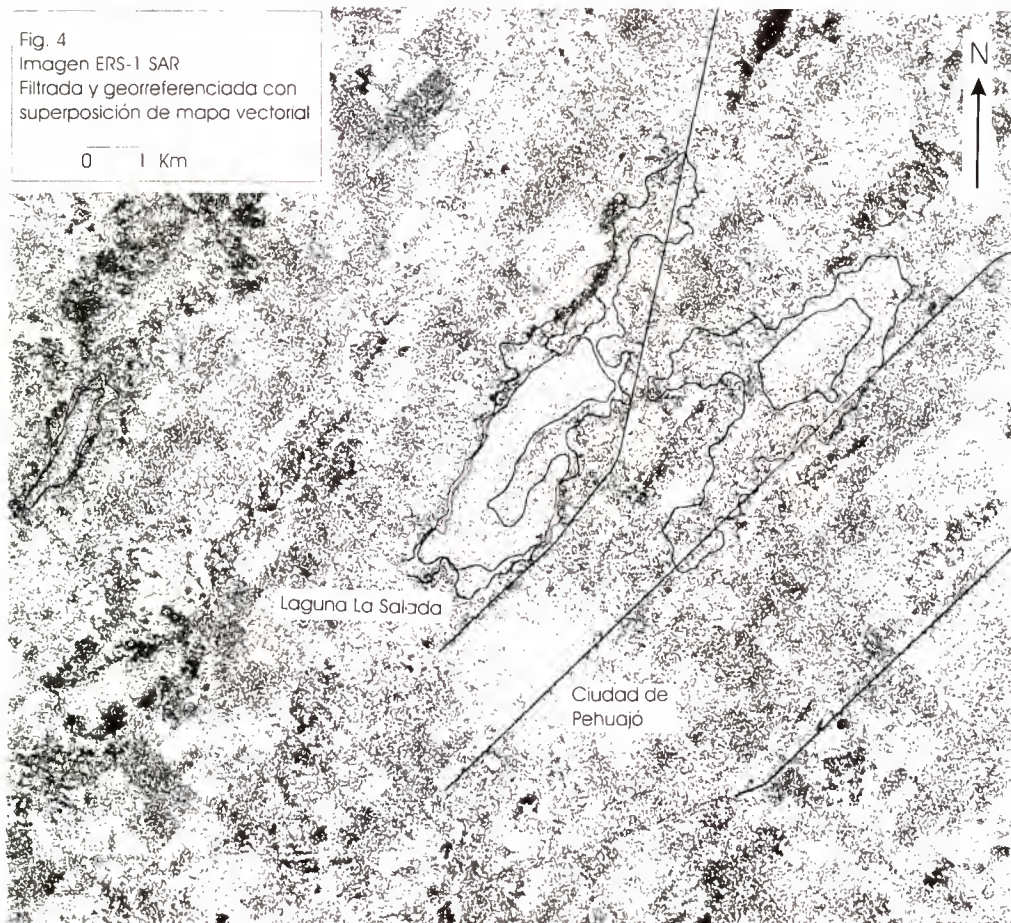
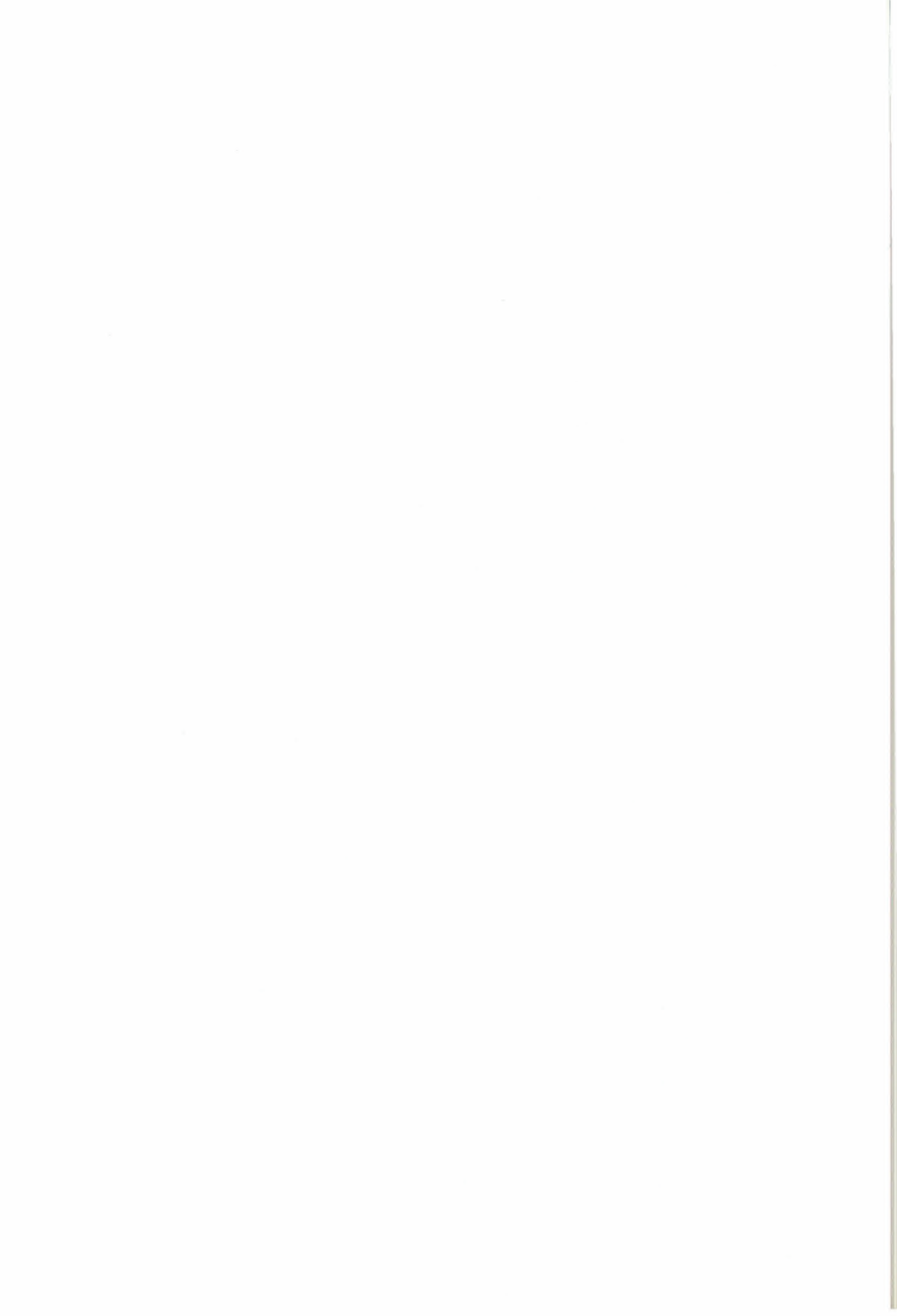


Figura 4. Imagen ERS-1 SAR. Filtrada, georreferenciada y con mapa vectorial ARC/Info.



SENSORIAMENTO REMOTO POR RADAR (SAR): PRÉ-PROCESSAMENTO DE IMAGENS RADARSAT ("FINE MODE") NA REGIÃO DA FLORESTA NACIONAL DO TAPAJÓS

Silvana Amaral e Yosio E. Shimabukuro

Instituto Nacional de Pesquisas Espaciais - INPE
 Caixa Postal 515, CEP 12227-010 São José dos Campos, SP, Brasil
 telefone: 55 12 325 64 83, fax: 55 12 325 64 68
 silvana@dpi.inpe.br, yosio@ltid.inpe.br

Thierry Toutin e Frank Ahern

Canada Centre for Remote Sensing - CCRS
 588, Booth Street, Ottawa, K1A 0Y7, Ontario, Canada
 Frank.Ahern@ccrs.emr.ca, Thierry.Toutin@ccrs.emr.ca

RESUMO

Este trabalho relata as primeiras atividades desenvolvidas no Projeto ADRO (CCRS/INPE) com imagens RADARSAT - "fine mode", para aplicações em área florestal. O Projeto ADRO tem como objetivo, a avaliação da potencialidade das imagens RADARSAT em diferentes áreas, para diferentes aplicações. Para esta aplicação (estudo de áreas florestais), a área de estudo compreende a Floresta Nacional do Tapajós, Santarém - PA. Foram utilizadas duas imagens RADARSAT, SGF- F2, de 20/05/96 e SGX-F5 de 03/05/96 e uma imagem TM/Landsat (WRS 227/62) de 07/08/95, bandas 3, 4 e 5. As imagens RADARSAT foram submetidas a calibração radiométrica relativa, orto-correção através de modelagem geométrica, considerando o modelo digital de elevação (MNT) do terreno, e integração com imagem TM/Landsat utilizando a transformação IHS. O procedimento metodológico e a avaliação visual do produto resultante da integração com imagem TM/Landsat são apresentadas quanto a capacidade de discriminar diferentes coberturas florestais e distúrbios na floresta.

1. INTRODUÇÃO

O sensoriamento remoto na região de microondas, coloca a disposição um valioso conjunto de dados para áreas onde a cobertura de nuvens é frequente, vantagem até então não disponível quando da utilização de dados provenientes das porções visível e infravermelho do espectro eletromagnético.

Esta característica é um dos fatores que motivam o desenvolvimento de técnicas para extração de informações a partir de imagens de radar para áreas como a Amazônia, onde a dimensão territorial e a cobertura de nuvens demandam dados com as características descritas para imagens de radar.

Contudo, para que imagens de radar sejam utilizadas, em projetos operacionais, para monitoramento ambiental por exemplo, é necessário que a comunidade de usuários conheça e domine as técnicas de correções (pré-processamento) básicas necessárias e as informações provenientes de cada produto disponível no mercado.

Este trabalho, insere-se no escopo de atividades previstas pelo projeto ADRO - INPE/CCRS, de avaliação das potencialidades das imagens RADARSAT, especificamente para aplicações florestais. O objetivo específico é descrever o processamento digital realizado em imagens RADARSAT-fine mode, para a correção radiométrica e geométrica das imagens, e posterior integração com dados TM/Landsat.

2. ÁREA DE ESTUDO

A área de estudo constitui-se da porção norte da Floresta Nacional (Flona) do Tapajós, no município de Santarém, PA - Brasil. A região de interesse encontra-se entre as coordenadas 55° 03' 23" e 54° 53' 11" de longitude oeste e 02° 52' 40" e 03° 01' 07" de latitude sul. A Flona é administrada pelo Instituto Brasileiro de Meio Ambiente e Recursos Naturais Renováveis (IBAMA) e é limitada pelo Rio Tapajós a oeste e pela BR-163 a leste (Figura 1).

A região é marcada por estações seca (agosto a novembro) e chuvosa (fevereiro a maio) bem definida com temperaturas variando de 20°C a 35°C, e mínimas ocorrendo durante a estação chuvosa. É caracterizada ainda por duas grandes unidades morfoestrutural - o Planalto Rebaixado da Amazônia (cotas de 100m) e o Planalto Tapajós/Xingu (cotas entre 120 a 170 m).

De acordo com o RADAMBRASIL (1976) a vegetação também é subdividida em duas regiões: Baixos Platôs da Amazônia, que por sua vez se divide

em Ecossistemas de Baixos Platôs e Ecossistemas de Baixos Platôs Dissecados, e os Altos Platôs dos Rios Xingu e Tapajós. Ambas regiões apresentam floresta tropical densa com espécies de alto valor econômico, sendo estas mais abundantes nos Altos Platôs.

A Flona, como unidade de conservação pode ser manejada e provavelmente terá parte de seus recursos madeireiros explorados, através de metodologia de manejo sustentado desenvolvida pelo IBAMA.

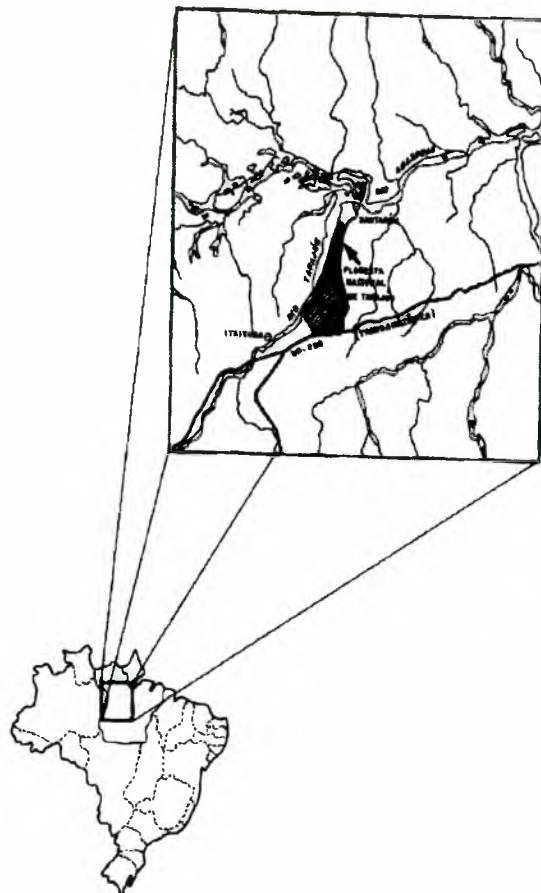


Figura 1. Localização da Floresta Nacional do Tapajós

Apresenta-se atualmente ocupada por muitos colonos estabelecidos ao longo do Rio Tapajós e da estrada que comunica a BR-163 com o vilarejo de Tauari, atravessando o povoado de São Jorge. Estes colonos mantêm atividades de agricultura e pastagem, alterando a cobertura florestal original.

3. RADARSAT

RADARSAT é o primeiro satélite canadense de observação da Terra desenvolvido para aplicações de manejo e monitoramento dos recursos naturais. O sensor de radar a bordo do satélite opera numa única frequência de microondas - banda C, com frequência de 5,3 Ghz (5,6 cm de comprimento de onda),

polarização HH, e tem a possibilidade de 7 modos de imageamento de acordo com a faixa imageada e a resolução disponível (modos: "scansar wide", "scansar narrow", "extended low", "wide", "standard", "extended high" and "fine") (RADARSAT, 1995).

Para cada um dos modos de imageamento é possível selecionar uma posição do ângulo de incidência disponível. Por exemplo, para as imagens "fine mode", de 10 m de resolução nominal e 50 x 50 km de faixa imageada, é possível selecionar 5 posições de ângulo de incidência: de F1 (37 a 40 graus) a F5 (45 a 48 graus).

Para este trabalho foram utilizadas duas imagens RADARSAT - "fine mode", cujas características são apresentadas na Tabela 1.

Tabela 1 - Imagens RADARSAT utilizadas

	F5 - SGX	F2 - SGF
Data	03/05/1996	20/05/1996
Modo	F5 - SGX	F2 - SGF
Ângulo de Incidência (graus)	45-48	39-42
Resolução	10m	10m
Nominal (m)	(8,8 a 9,0m)	(8,8 a 9,0m)
Tamanho do Pixel (range, azimute)	3,125 x 3,125	6,25 x 6,25
Latitude central (graus)	-3,07936	-2,91194
Longitude central (graus)	-54,96849	-43,83519
Número de Pixels	12166	6770
Número de Linhas	13766	8100
Número de Looks	1	1

As imagens RADARSAT são disponibilizadas em diferentes níveis de processamento. A imagem F2 utilizada neste trabalho é uma "path image" - SGF, ou seja a imagem foi alinhada paralela à órbita do satélite e teve as coordenadas (latitude e longitude) iniciais, finais e central adicionadas a cada linha do dado. A imagem F5 por sua vez é um produto do tipo "path image plus" - SGX, que difere do anterior apenas quanto ao procedimento de amostragem utilizado. Produtos SGX utilizam um tamanho de pixel menor para manter a resolução plena.

Quanto à direção de visada, o satélite RADARSAT pode imagear a Terra com a visada para leste quando a órbita é ascendente (6:00 a.m. horário de cruzamento do Equador) e para oeste quando a órbita é descendente (6:00 p.m. horário de cruzamento do Equador). As duas imagens utilizadas foram adquiridas em órbita descendente.

4. FUNDAMENTAÇÃO TEÓRICA

Por calibração radiométrica absoluta de imagens de radar, entende-se a extração dos valores do retroespalhamento (σ^0) a partir dos níveis digitais de amplitude presentes nas imagens. Esta calibração possibilita a compreensão dos processos de retroespalhamento dos alvos e consequentemente a comparação entre imagens de datas e passagens distintas. Contudo, esta calibração absoluta ainda não está disponível para as imagens RADARSAT. Apenas a calibração relativa encontra-se disponível, e consiste na eliminação de uma "look up table" (valores de ganho e off-set) que foi aplicada na imagem no processo de gravação, e na conversão dos valores digitais de magnitude em potência. Esta calibração, apresentada sumariamente a seguir, encontra-se detalhadamente descrita em Shepherd et al (1995).

No "header" da imagem (campos 12 a 531) encontram-se os valores de ganho e offset que foram incorporados e desta forma os valores de brilho da imagem podem ser calculados por:

$$\beta^0_{(R)} = 10 * \log_{10} [\{DN^2 + A_0\} / A_{(R)}] \text{ dB}$$

onde:

$\beta^0_{(R)}$ = brilho do pixel - ground range (R)

DN = número digital

A_0 = offset fixo (look up table)

$A_{(R)}$ = ganho para o pixel "ground range" (R)

Para calcular os valores de brilho de toda a imagem, deve-se considerar o ângulo de incidência para cada coluna da imagem, e o retroespalhamento (σ^0) pode então ser obtido corrigindo-se os valores de brilho para os ângulos de incidência $I_{(R)}$, onde I é uma função do "range" r:

$$\sigma^0 = \beta^0_{(R)} + 10 * \log_{10} \{\operatorname{sen} I_{(R)}\} \text{ dB}$$

A partir desta imagem, os valores de nível digital de potência podem ser obtidos a partir de σ^0 através da relação: $\sigma^0 = 10 \log_{10} DN_{(P)}$.

Atenção especial deve ser dispensada à imagens de órbita descendente, como às utilizadas neste trabalho, uma vez que a "look up table" estava sendo aplicada indiscriminadamente do sentido da órbita. Estas imagens deveriam ser espelhadas antes de se aplicar a correção relativa e depois novamente espelhadas para representarem fidedignamente a superfície.

As imagens RADARSAT - SGF e SGX são fornecidas em "ground range" porém necessitam de correção geométrica. Esta correção faz-se necessária quando se deseja eliminar efeitos de relevo (lay-over e sombra) ou mesmo utilizar as imagens para

integração com outros tipos de imagens, como no caso imagens TM/Landsat.

Em substituição ao tradicional registro polinomial de imagem com mapa ou imagem-imagem, aconselha-se o uso da modelagem geométrica unificada e integrada para a correção das imagens (Toutin, 1995). Ao invés de corrigir localmente a imagem ajustando um modelo polinomial a partir dos pontos de controle, o modelo geométrico corrige globalmente a imagem considerando as distorções da plataforma (posição, velocidade e orientação), do sensor (ângulo de orientação e integração do sinal), da Terra (geóide e elipsóide, incluindo elevação) e da projeção cartográfica (plano cartográfico e elipsóide).

O procedimento de orto-correção utilizando o modelo geométrico apresenta-se esquematizado na figura 2.

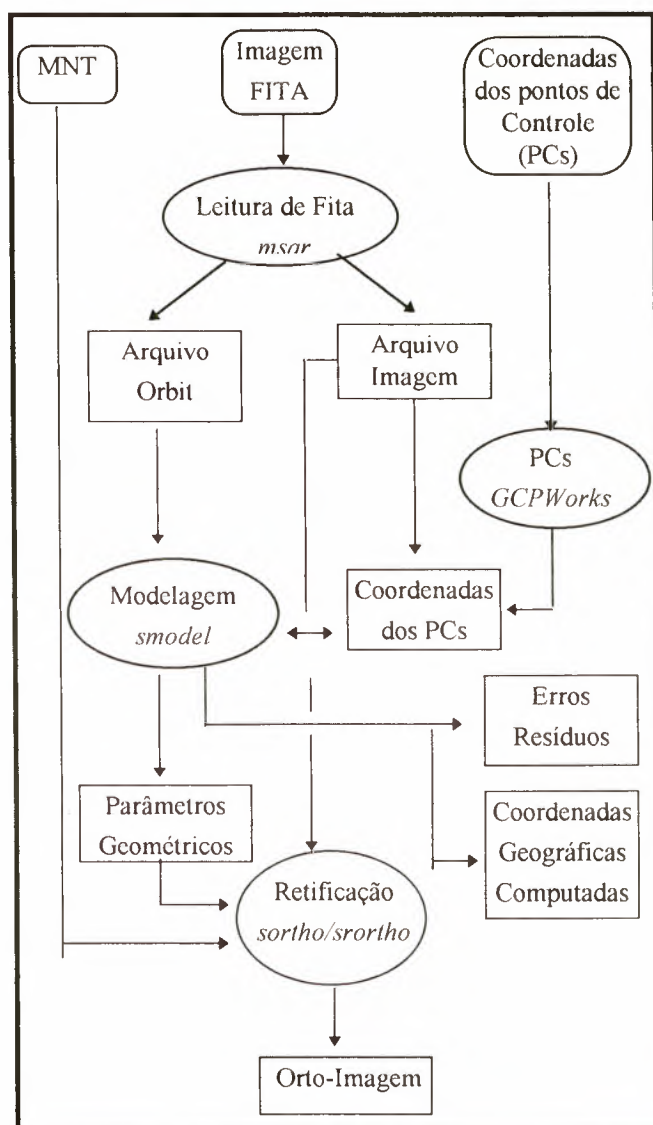


Figura 2. Fluxograma do procedimento utilizado para correção geométrica das imagens RADARSAT e TM/Landsat.

O procedimento básico consiste inicialmente na leitura da imagem, onde as informações de altitude, efeméride e geometria de visada são extraídas. Na sequência, um mínimo de 12 pontos de controle com coordenadas X, Y e Z devem ser coletados para a imagem, e o modelo pode ser computado. Os parâmetros orbitais são usados para inicializar o modelo e então um ajuste interativo de mínimos quadrados é utilizado para resolver a equação com os pontos de controle (7 pontos são usados para resolver a equação de imagens SAR). Como resultado obtém-se os parâmetros do modelo geométrico, os resíduos dos pontos de controle, os erros dos pontos de teste e as coordenadas geográficas computadas para cada ponto.

Uma vez gerado o modelo, a imagem pode ser orto-corrígida para um sistema de projeção geométrica definido e um Modelo Digital de Elevação pode ser utilizado para computar as distorções de elevação para cada pixel da imagem. Para a reamostragem final da imagem pode-se selecionar um filtro de eliminação de "speckle" substituindo os interpoladores (vizinho mais próximo, bilinear ou bicúbico), gerando assim uma imagem orto-corrígida e com efeito de speckle minimizado, evitando assim múltiplas interpolações.

5. METODOLOGIA

Para a integração com as imagens RADARSAT, foi utilizada uma imagem TM/Landsat-5, WRS - 227/62, de 7 de agosto de 1995, bandas 3,4 e 5.

Utilizou-se um modelo numérico de terreno da altimetria da região, para a correção geométrica. Foram utilizadas as isolinhas com valores de cota, digitalizadas no sistema de informação geográfica SGI pelo projeto Funatura (Hernandez Filho et al, 1993). As isolinhas foram interpoladas no software Spring através de triangulação para gerar uma grade regular, com resolução de 30 m. Esta grade regular deu origem a uma imagem onde os valores de nível digital correspondem aos valores de altimetria, que foi utilizada na orto-correção.

Para o processamento de imagens utilizou-se o software PCI. Inicialmente as imagens RADARSAT foram lidas com o algoritmo *msar*. O ângulo de incidência foi calculado para as colunas utilizando o *sarincid*, e o retroespalhamento obtido através do *sarsigma*. Através da opção *model*, os valores de retroespalhamento foram convertidos de retroespalhamento- σ^0 (decibeis) para potência (nível digital), através da expressão:

$$\text{Potência} = 10^{\frac{1}{2}} (\text{Retroespalhamento}/10).$$

Para avaliar o efeito da órbita descendente com "Look up table" de imagem ascendente, um teste foi

realizado espelhando-se a imagem original (*mirror*) após a leitura da imagem e o mesmo procedimento de calibração relativa e efetuado.

Para a correção geométrica, os pontos de controle (PCs) foram coletados nas cartas topográficas na escala de 1:100.000. Os algoritmos utilizados para cada uma das etapas da orto-correção estão indicados na figura 2 (em *italico*). O modelo foi computado para cada imagem, e apenas os pontos de controle que apresentaram erro quadrático médio inferior a três vezes o erro quadrático médio total foram utilizados. As imagens foram reamostradas para pixels de 12,5 m utilizando filtros de eliminação de speckle e a imagem de modelo numérico de elevação.

Para a eliminação do ruído speckle, os filtros de mediana, Gama e Lee foram testados sobre as imagens, utilizando-se janelas de diferentes tamanhos.

A imagem TM/Landsat também foi orto-corrígida através do mesmo procedimento descrito para as imagens RADARSAT, utilizando interpolação bilinear. Para a integração, esta imagem também foi reamostrada para 12,5 m.

Para a integração de dados RADARSAT e TM/Landsat procedeu-se a transformação IHS, utilizando-se a composição TM bandas 3, 4 e 5 nos canais azul, verde e vermelho respectivamente. Para a conversão IHS-RGB, a banda de intensidade foi substituída pelas imagens RADARSAT gerando assim duas novas imagens híbridas TM-RADARSAT. Devido a presença de nuvens na imagem TM, o canal de matiz (H) não foi utilizado na transformação IHS-RGB, sendo substituído pelo canal de intensidade.

6. RESULTADOS E DISCUSSÃO

A imagem resultante da calibração radiométrica é apresentada na figura 3. Observa-se o aspecto ruidoso da imagem, demandando uma filtragem do speckle. Comparando-se a calibração radiométrica relativa realizada sobre a imagem original e sobre a imagem espelhada, observou-se uma diferença de 10% entre os valores de potência nas margens da imagem, e diferenças de 5% no região central da imagem. Esta diferença era esperada uma vez que a "Look up table" varia ao longo do imageamento ("range"). Para aplicações como integração de dados para posterior classificação, estas diferenças podem ser desconsideradas, o que não é válido para aplicações onde os valores de backscatter serão associados as medidas de campo.



Figura 3 - Imagem potência SGF-F2 após calibração relativa

O filtro gama, com uma janela de 9x9 foi o que apresentou melhor resultado na eliminação de speckle, quando visualmente comparado com os outros filtros testados. Contudo pixels saturados ainda são observados na imagem (Figura 4). Estes pixels correspondem a valores de potência maiores que 1, o que poderia ser atribuído a alguma saturação no processo de geração da imagem e as variações do terreno como “double bounce” e efeitos de relevo. Esta observação é confirmada observando-se que mesmo após a aplicação de um filtro mediana, de janela de 11x11, estes pixels saturados continuam presentes.



Figura 4 - Imagem SGF-F2 após filtro gama 9x9

As figuras 5 e 6 apresentam as imagens F2 e F5 respectivamente após a ortocorreção, com a utilização do filtro mediana para a interpolação. Comparando-se as imagens F2 e F5, observa-se que a rugosidade do dossel e o efeito de “double-bouncing” é mais evidente na imagem F5, devido ao maior ângulo de incidência. Por consequência, os limites entre feições da imagem como floresta e áreas desmatadas são evidenciados, indicando esta imagem como mais apropriada para interpretação visual, especialmente para identificar áreas de alterações na cobertura florestal.



Figura 5- Imagem SGF-F2 após orto-correção



Figura 6- Imagem SGX-F5, após orto-correção

A figura 7 apresenta as imagens resultantes da orto-correção integradas com a imagem TM/Landsat após a transformação IHS. Observa-se que algumas feições não estão completamente ajustadas, o que se deve ao caráter de correção global da imagem e não local. O mapa utilizado para a aquisição de pontos de controle apresenta uma precisão de 50 m. Os erros quadráticos dos resíduos computados para F2 e F5 foram de 37 m e 29 m respectivamente, e de 57,5 m para a imagem TM.



Figura 7 - Imagem SGX-F5 e TM/Landsat após IHS

O erro de posicionamento observado na imagem é de aproximadamente 2 pixels, ou seja 25 m, inferior à precisão da carta. Resultado este que supera as expectativas, considerando a dificuldade de localização de pontos de controle na área e a precisão da carta utilizada. Para que melhores resultados sejam obtidos na correção geométrica, aconselha-se a utilização de pontos de controle coletados com GPS diferencial no campo.

A informação tonal (espectral), introduzida com a imagem TM/Landsat, auxilia a interpretação das imagens e identificação dos alvos, antes apenas distintos pelos limites associados à variação de altura da cobertura vegetal. A identificação de feições nas imagens RADARSAT, como áreas de clareira e desmatamento, e variações das formações florestais é realizada após a integração com dados TM.

7. CONSIDERAÇÕES FINAIS

O procedimento de pré-processamento das imagens RADARSAT, calibração radiométrica relativa e orto-correção geométrica, utilizando a modelagem geométrica com Modelo Numérico de Terreno foi apresentada. Este processo, apesar de demandar

tempo de processamento é fundamental para o uso das imagens para qualquer aplicação.

A integração com imagem TM/Landsat proporciona um produto mais apropriado para interpretação visual das imagens, facilitando o reconhecimento das diferentes coberturas.

De modo a otimizar a correção geométrica, aumentando a precisão de posicionamento, este procedimento deverá ser repetido utilizando-se pontos de controle adquiridos no campo, com precisão.

As imagens RADARSAT, pela característica da banda C, refletem a variação da estrutura superior da cobertura, do dossel no caso da cobertura florestal. A rugosidade do dossel será avaliada a partir de dados de campo, onde a variação da altura das árvores emergentes será modelada e comparada com a resposta obtida nas imagens. Esta análise proporcionará a avaliação da textura das coberturas florestais e orientará a extração de informações florestais a partir das imagens RADARSAT.

Acredita-se que estas imagens constituam uma valiosa fonte de dados para identificação da variação de dossel em áreas de floresta tropical, para auxiliar no manejo e/ou preservação destas áreas.

8. AGRADECIMENTOS

Os autores agradecem à CIDA (Canadian International Development Agency) pelo suporte financeiro e pela oportunidade de apresentação deste trabalho.

9. REFERÊNCIAS

Hernandez Filho et al., 1993. Relatório Final: Projeto de Inventário Florestal na Floresta Nacional do Tapajós. Projeto de Cooperação Técnica desenvolvido pelo INPE/IBAMA/FUNATURA/IITO, INPE, São José dos Campos (INPE-5423-PRP-171).

Projeto RADAMBRASIL. Folha S/A 21 - Santarém. Rio de Janeiro, DNPM 1976. (Levantamento dos Recursos Naturais, v.10).

RADARSAT International, 1995. RADARSAT-Illuminated - Your guide to products and services.

Shepherd, N.W. and Associates., 1995. CDPF Output Data Calibration. Technical Note No. 4.2.

Toutin, T. 1995. Multisource data fusion with an integrated and unified geometric modelling. EARSil Advances in Remote Sensing. Vol.4, N2 - X., p. 118-129.

Evaluation of the phase noise reduction filters in SAR Interferometry

José Claudio Mura¹
 Ana Lucia Bezerra Candeias¹
 Luciano Vieira Dutra¹
 João Roberto Moreira²

¹INPE - Instituto Nacional de Pesquisas Espaciais
 EMail:[mura;analucia;dutra]@dpi.inpe.br

²Aero-Sensing Radarsysteme GmbH
 Email: joão.moreira@dlr.de

Abstract

The Digital Elevation Model (DTM) is one of the products generated by SAR Interferometry. The phase unwrapping is the processing step which transforms the wrapped phase (modulo 2π), known as *interferogram*, into an absolute phase map, which is related with the terrain elevation. Noise in the interferogram disturbs the phase unwrapping process and to overcome this problem one applies a low pass filter on the complex interferometric data before relative phase generation. This paper compares three different non linear methods, which filter the wrapped phase in order to improve the phase unwrapping process. The methods are the pivoting median filter, mode filter and the pivoting alternating sequential filter, which is a modified morphological filter. These modified filters are built considering the periodic character of the wrapped phase function. Results using simulated data are presented for the three filters and showed that the proposed filters are very effective in reducing unwrapping phase errors due to interferometric noise.

1 - Introduction

The phase unwrapping process [1] is disturbed by the noise buried in the interferogram, originated from thermal and speckle noise, processing errors, temporal and spatial decorrelation, etc. Low pass filter is commonly applied to the complex interferometric data [2] to improve the phase unwrapping process. However, it is not possible to enlarge the box size of the low pass filter without losing the resolution and even connecting some fringes presented in the interferogram.

In order to improve the phase unwrapping process, the interferogram is filtered by non linear filters [3]. These filters are the pivoting median, mode and pivoting alternating sequential filter (P-ASF),

developed to take into account the statistical characteristics of the circular data, such as the interferogram.

The probability density function (pdf) of the phase noise has a 2π base interval [4]. If this interval is chosen around the mean value, the pdf will be symmetrical and the variance will not depend on the base interval. These characteristics are desirable for low-pass filtering because low-pass filtering should not move the location of the distribution. So, the key problem of the phase filtering is to determine the location of the local noise distribution.

The first step in the phase field processing is the calculation of the mean value. The natural way of combining vectors is by vector addition, given what is known as the mean direction. This processing, however, involves the computation of the transcendental functions [5]. More practical alternatives are the use of the others location measures, such as the sample median direction or the sample modal direction. In the filters described in [3], it was used the sample modal direction as an estimate of the mean direction.

The applied filters are defined as shown in the following. Let us assume $E = \{(i,j): i,j = 1, \dots, N\}$, the support of an $N \times N$ random phase field $f(\cdot)$ whose range of the values is $(-\pi, \pi)$, and M_p is an $L \times L$ mask centred in $P = (i,j) \in E$. Each filter of $f(\cdot)$ over M_p , has been designed to consider the characteristics of the circular data. An analogous version of the median filter, called here pivoting median filter (P-Median) and analogues to the morphological erosion and dilation filters, called here pivoting erosion (P-Erosion) and pivoting dilation filter (P-Dilation) are defined by the following equations:

Median:

$$\mu_{MD}(f)(P) = \text{Mode}(M_p) + MD\left\{\left(f(Q) - \text{Mode}(M_p)\right), Q \in M_p \cap E\right\} \quad (1)$$

Erosion:

$$\mu_{ER}(f)(P) = \text{Mode}(M_p) + \min\left\{\left(f(Q) - \text{Mode}(M_p)\right), Q \in M_p \cap E\right\} \quad (2)$$

Dilation:

$$\mu_{DL}(f)(P) = \text{Mode}(M_p) + \max\left\{\left(f(Q) - \text{Mode}(M_p)\right), Q \in M_p \cap E\right\} \quad (3)$$

Where $\langle \rangle$ is the modulo 2π operator, defined in the $[-\pi, \pi]$ range and MD is the median operator.

The mode filter is a filter by its own, that is substituting the centre pixel of a mask by its mode, which is also a non linear low pass filter.

2 - Methodology and results

The diagram in Figure 1 depicts the filtering process for each type of filter, and the P-ASF is shown in the Figure 2.

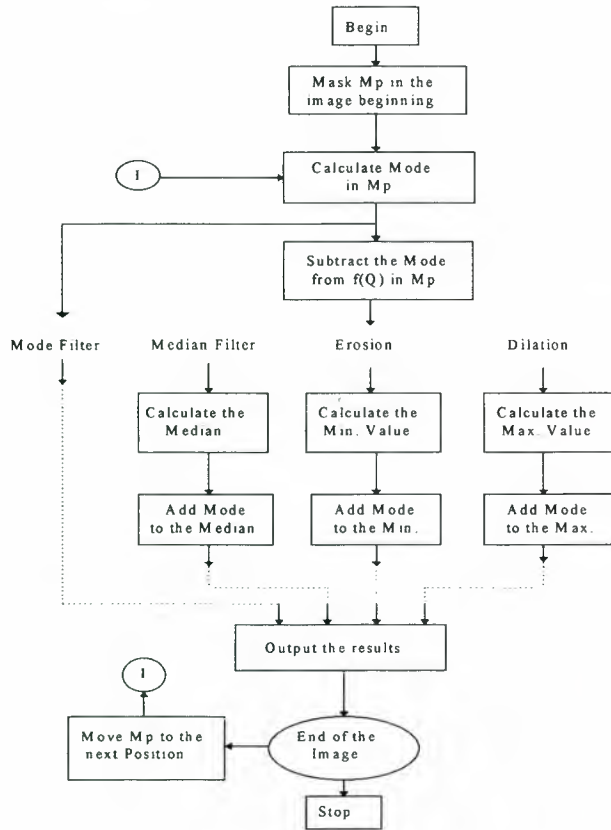


Figure 1 - Diagram of the filters

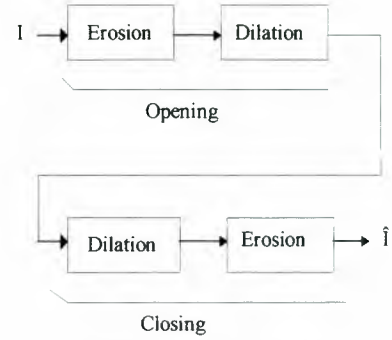


Figure 2 - P-ASF filter

The filters are evaluated using simulated interferogram data, which is corrupted by a noise whose probability density function (pdf) is described in [4]. Several levels of noise are selected and added to the uncorrupted data.

The inversion method [6] was used to generate a three noise fields with $\gamma = 0.9$, $\gamma = 0.7$ and $\gamma = 0.5$, where γ is the coherence between complex channels [4]. These noise fields are added modulo 2π to the noiseless interferogram.

Normally, in INSAR processing the interferogram is first filtered in complex domain. In this case all noisy interferograms were transformed to complex domain, box filtered and transformed back to phase domain.

Figure 3 shows the noiseless interferogram simulating a pyramid with variable slope. Figures 4, 5 and 6 show the noisy interferograms filtered in complex domain for $\gamma = 0.9$, $\gamma = 0.7$ and $\gamma = 0.5$, respectively.



Figure 3 - Original Interferogram



Figure 4 - Interferogram with $\gamma = 0.9$

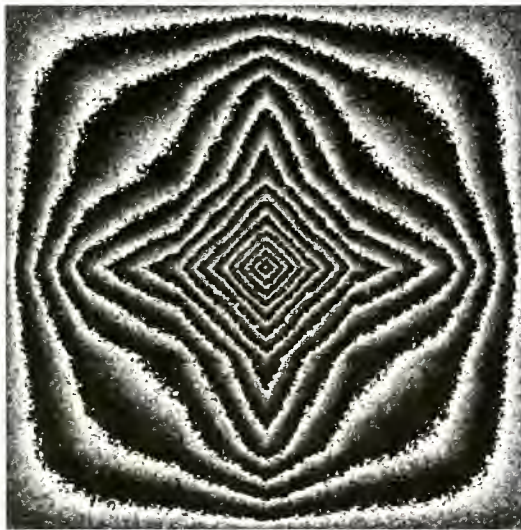


Figure 5 - Interferogram with $\gamma = 0.7$

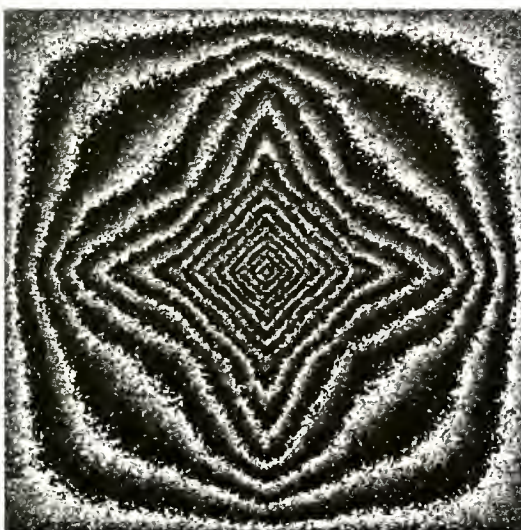


Figure 6 - Interferogram with $\gamma = 0.5$

The three noisy interferograms were filtered using the Mode filter, P-Median filter and P-ASF. The absolute phase were calculate for all data, using the phase unwrapping algorithms described in [1], the Green Function Method. Figure 7 shows profiles of the unwrapped phase corresponding to each one of the filters used, for $\gamma = 0.5$.

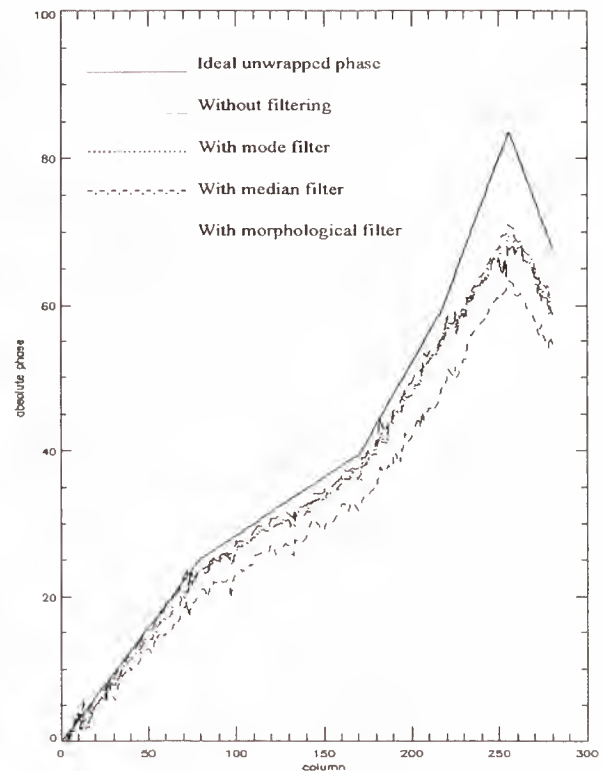


Figure 7 - Phase unwrapped for $\gamma = 0.5$

The Table 1 shows the rms. error between the ideal unwrapped phase and which one of the unwrapped phase for all cases of the filters and coherence.

γ	0.9	0.7	0.5
Without Phase Filter	0.21	1.22	3.98
Mode Filter	0.21	0.92	1.96
P-Median Filter	0.18	0.88	1.92
P-ASF Filter	0.25	0.57	1.54

Table 1 - Unwrapped phase rms error

One of these filters, the pivoting median was used to filter the interferometric data of SIR-C/XSAR mission over the Etna volcano for X, C and bands with promising results [7].

4 - Conclusions

Although the results of these filters are dependent not only on the noise level, but also on other factors like fringes density, some conclusions can be drawn.

For the low coherence case ($\gamma = 0.7$, $\gamma = 0.5$), the P-Median and Mode filters showed similar results, being the P-Median filter somewhat better. P-ASF filter had a better overall performance, probably due to a large mask support area resulting from the filtering sequence (ASF). However, in high fringes density its performance is worse than the former ones, as seen in the Figure 7.

For the high coherence case ($\gamma = 0.9$) P-Median filter had the best performance. The P-ASF filter was not good in this case because the result is even worse than the non filtering case.

Given the fact that normally interferograms have regions with different coherence levels, the use of the P-Median seems to give better average results.

5 - Acknowledgement

This work was partially funded by CNPq under contract # 680.061/94-1 (Geotec).

6 - References

- [1] Fornaro, G.; Franceschetti, G.; Lanari, R., "Interferometric SAR phase unwrapping using Green's Formulation", IEEE Trans. on Geoc. and Rem. Sensing, Vol. 34, No. 3, pg. 720-727, may 1996.
- [2] Rodriguez, E. R., "Maximum likelihood estimation of the interferometric phase from distributed targets", IEEE Trans. on Geoc. and Rem. Sensing, 1992.
- [3] Candeias, A. L. B.; Mura, J. C.; Dutra, L. V. and Moreira J. R., "Interferogram phase noise reduction using morphological and modified median filters", Proceeding IGARSS'95, Vol.1, pg. 166-168, 1995.
- [4] Just, D. and Bamler, R., "Phase statistics of interferograms with applications to synthetic aperture radar", Applied Optics, Vol. 33, No. 20, pg. 4361-4368, July 1994.
- [5] Press, W. H. and Flannery B. P., "Numerical Recipes in C: The Art of Scientific Computing", 2nd ed. Cambridge: Cambridge Univ. press, 1992.
- [6] Bustos, O.,B. and Frery, A.C., "Stochastic Simulation: Theory and Algorithms", IMPA, Brazil, 1992.
- [7] Coltell, M.; Dutra, L.; Franceschetti, G.; Lanari, R.; Migliaccio, M.; Moreira, J.; Papathanassiou, K.; Puglisi, G.; Riccio, D. and Schwabisch, M., "SIR-C/XSAR Interferometry over Mt.Etna:DEM Generation, Accuracy Assessment and Data Interpretation", Internal Report - DLR-FB 95-48, Oberpfaffenhoffen, Germany, 1996. ISSN 0939-2963.

RADARSAT and IFSARE - Complementary SAR Sources for DEMs

J.Bryan Mercer and Alain Kahil

Intermap Technologies Ltd.
900, 645 - 7th Avenue S.W.
Calgary, Alberta, Canada T2P 4G8
Tel (403) 266-0900, Fax (403) 265-0499, e-mail bmercer@intermap.ca

ABSTRACT

Technology has recently become available that enables users to obtain high quality Digital Elevation Models (DEMs) almost anywhere in the world and with delivery times that are much shorter than the mapping industry normally experiences. This new capability is timely because DEMs are being used increasingly in a host of applications ranging from GIS-based topographic data bases to tower-siting in the telecommunications industry. Synthetic Aperture Radar (SAR), because of its cloud-penetrating capability, allows data acquisition in large parts of the tropics where imaging with conventional optical systems has previously been problematic and expensive.

In this paper we describe two solutions that are being offered by Intermap Technologies Ltd. Using RADARSAT stereo, DEMs can be created at levels of detail appropriate to 1:100,000 or possibly 1:50,000 mapping scales. This can be done over wide areas, quickly and at low cost. On the other hand, IFSARE, an interferometric SAR carried aboard a LearJet, creates DEMs of much greater detail, with sample spacing of 5 meters or less and vertical accuracy tested to less than 2 meters. This is appropriate to mapping scales of 1:10,000 or better. The solution selected for any particular application depends on the scale or level of detail that is needed and the nature of the application.

A description is given of these two complementary systems, including specifications, test results and visual examples. Some comments are included with respect to cost versus detail of the associated products.

1. INTRODUCTION

Despite broad recognition of the need for creation of spatial data bases in support of resource and infra-structure development, parts of the world remain poorly mapped at scales of 1:100,000 and larger (U.N. Cartographic Conference, Beijing, 1994). This is particularly the case in areas of persistent cloud-cover where aerial photography becomes prohibitively expensive and the ground is often obscured to view from optical satellites. Imaging radar has been used for small scale mapping for several

decades in these areas because of its cloud-penetrating characteristics. In the first half of the 1990's, the STARMAP process of Intermap (formerly 'Intera') Technologies Ltd., using digital stereo imagery from its STAR-1 airborne SAR system, provided DEMs (Digital Elevation Models), contour maps, Ortho-Rectified Images (ORIs) and Image Map mosaics in many areas (total area over 300,000 kmsq) of SE Asia, South America and Central Africa (Mercer and Griffiths, 1993).

Intermap has replaced the STARMAP process by two new, but related, technologies which are both being offered commercially and have just commenced operations after a period of test and demonstration. The STARMAP stereo process has been modified and migrated to TOPOSAR™, a stereo-based capability to create DEMs from RADARSAT. As will be demonstrated, this enables DEMs with vertical accuracies in the 10-15 meter (1σ) range to be created over large areas relatively inexpensively. At the same time STAR3i is an airborne interferometric SAR (developed by ERIM - the Environmental Research Institute of Michigan - under the name IFSARE), which provides DEMs and ORIs at a level of detail 5 - 10 times finer than the TOPOSAR™ products, but at greater cost. The two technologies are complementary: The RADARSAT / TOPOSAR™ products are appropriate for large area mapping at scales of 1:100,000 to 1:50,000, while the STAR3i products are designed for mapping scales of 1:10,000 - 1:25,000. Because of the near-global coverage of RADARSAT and the flexibility, responsiveness and range of the LearJet hosted STAR3i, it is now possible to create spatial data base products in this desirable range of mapping scales over most of the planet's terrain, irrespective of cloud-cover, and with delivery time scales of weeks rather than years.

It should be noted that at the relatively short wavelengths of these systems (C-band for RADARSAT and X-band for STAR3i), the scattering is generally off the top layer of foliage or other scattering surface that the incident radar beam might encounter. The derived DEM is therefore with respect to this layer and might more accurately be termed a 'surface model'. In instances of dense forest canopy, the underlying 'bald earth' elevation model would

be obtained by removing the tree height through some procedure.

In sections two and three, some of the specifications of these two technologies will be summarised and graphical examples provided. In section four and five, cost vs. detail issues will be contrasted for these two technologies in the context of more familiar technologies.

2. DEMs from RADARSAT Stereo Images

2.1 Background: The principles associated with elevation derivation from stereo radar images has been widely reviewed (in particular see Leberl, 1990). A practical, operational implementation for airborne SAR has been described in Mercer and Griffiths(1993). This approach was modified for satellite SAR and prior to the RADARSAT launch, tested with stereo pairs combined from the ERS-1 experimental roll/tilt and normal mode imagery, the geometry of which approximated a RADARSAT S1/S4 combination. The resulting DEMs in two Canadian test situations (Ottawa and Mission, B.C.) were compared with government DEMs as well as GCPs (Ground Control Points) extracted from government maps. Vertical accuracies of 10-15 meters (1σ) were obtained in moderate terrain. In steeper areas, layover became a problem and it was recognized that it would be necessary to merge the elevation data from pairs of ascending and descending satellites (approximately opposite-viewing at low latitudes) in order to fill in data gaps. More recently the software and procedures have again been modified to utilize RADARSAT 'Path Image' pairs.

2.2 TOPOSAR™ Methodology: The current methodology is based upon a digital stereo-viewing, UNIX-based workstation; the procedures are partially automated but allow for operator intervention at key stages (Mercer et al., 1994). The stereo model is densely sampled using various point collection strategies (grid, breakline, random, etc.) in this partly automated, partly interactive acquisition stage. The resulting aggregate of points, individually identified by their (line, pixel) coordinates, is then processed in the radargrammetry module, using a range-doppler solution, to obtain ground coordinates with respect to the ellipsoid. This process requires calculation of satellite position and velocity (based upon detailed ephemeris information), which together with the point co-ordinates are input into the module. The resulting irregular grid of ground coordinates, after some automated editing, is then processed into a regular DEM in the chosen projection. If dual ascending/descending pairs of images have been used, the process is performed on each and the resulting points combined at this stage. The DEM is used to ortho-rectify the input images, and create elevation contours. The final stage is to perform QA and editing functions on the DEM. This is

done by overlaying the contours on the ORIs and, using a suite of editing tools, to modify the contours to better conform to the observed terrain where necessary. The modified contours are then reflected back into the DEM. While this description characterizes the current process, it should be noted that substantial TOPOSAR™ development is underway with a view to improving production efficiency through increased automation and other factors in order to reduce processing time and cost.

2.3 Accuracy Issues: The key factors determining vertical accuracy include (1) viewing angle geometry, (2) resolution, (3) target matching accuracy, and (4) instantaneous accuracy of satellite position and velocity. Because (1) and (3) make opposing demands (Mercer et al., 1994) on the 'intersection angle' (figure 1), it is usual to use same-side stereo pairs but with as large an angle as possible depending on the steepness of the terrain. RADARSAT's 'Standard' beam is generally used in preference to its 'Fine' beam because the geometry advantage of using Standard beam is greater than the resolution advantage of using Fine beam.

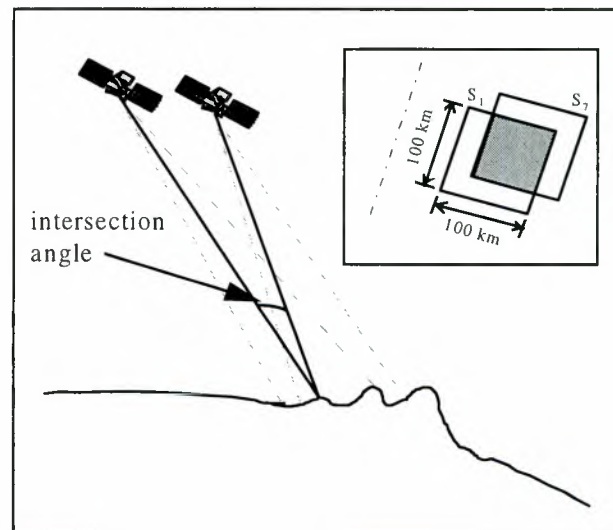


Figure 1 - RADARSAT Stereo Geometry

2.4 Test Results and Discussion

A number of tests of the vertical and horizontal accuracies achievable with various RADARSAT beam geometry and resolution combinations for different terrain types are planned. The first results available include the Ottawa site using an S1/S7 beam combination.

Table 1.

<i>Parameter</i>	<i>S1 Mode</i>	<i>S7 Mode</i>
Acquisition Date	Dec. 13/95	Feb. 10/96
Scene Centre	45.3 N, 75.4W	45.2 N, 75.6W
Inc. Angle	23 deg.	47 deg.
Pix. Spacing (Rg.xAz.)	12.5m x 12.5m	12.5m x 12.5m
Pix. Res. (nom)	25m x 28m	25m x 28m
Orbit	Descending	

Table 2.**Test #1: Comparison With Government DTMs
(ie "Truth")**

<i>Source</i>	<i>Area</i>	Δ <i>RMS</i>	Δ <i>Mean</i>
Fed DTED	(80km x 80km)	14.9m	36.1m
OBM	(5 sites @ 6km x 6km)	14.3m	38.0m

Notes:

1. Δ = (Radarsat - "truth");
2. No GCPs used
3. OBM = Ontario Base Map (1:10,000)
4. Min, Max $\approx 3\sigma$

Table 3.**Test #2: Comparison With Check Points (ie "Truth")**

ΔE		ΔN		ΔH	
<i>RMS</i>	<i>Mean</i>	<i>RMS</i>	<i>Mean</i>	<i>RMS</i>	<i>Mean</i>
32.4	-18.0	15.7	-10.1	13.0	35.3 m

Notes:

1. Δ = (Radarsat - "truth")
2. 28 points taken from 1:50,000 scale NTS map

Details of the test are shown in Table 1 and results of two types of test are summarised in Tables 2 and 3. The former used federal and provincial government DEMs for comparison and described the difference in terms of mean and standard deviation. The latter compared target coordinates on the associated ORI with those on 1:50,000 government topo maps in order to determine horizontal accuracies in particular. In both of these, the government reference will contribute a portion of the observed difference statistics. For example, due to generalization alone, the horizontal coordinates of the test points digitized from the topo map are expected to be uncertain to about 10-15 meters RMS. These statistics therefore over-

state the uncertainty of coordinates derived by TOPOSAR™.

It should be noted that the two images were unfortunately acquired two months apart during a wet-snow winter. This meant that image matching was difficult in some areas due to change in scene content and that above normal noise would therefore have contributed to the 14 meter vertical uncertainty. By comparison the above-mentioned ERS-1 test in an adjacent area got better results despite poorer geometry. It is planned to reproduce this test using a shorter intervening time gap which would be the normal operating mode in changing conditions.

Moreover, the results were obtained without the use of ground control. The control points were used only as test points and did not appear in the radargrammetric solution. The mean offsets are believed to represent mainly the uncertainty of the satellite along-track position derived from the ephemeris data. This suggests that in areas where ground control cannot be acquired easily, it will still be possible to obtain reasonable DEMs with offsets in the 30-40 meter range; these offsets can be largely removed when control does become available.

Support for this approach has come from a second test in Papua New Guinea (PNG) in which independent data sets from ascending and descending stereo pairs were compared. In the valley areas where data coverage was complete from both sets, the difference in the vertical was about 10 meters (1σ), with about 30 meters mean vertical difference and about 60 meters horizontal (mainly along-track) mean difference suggesting a persistent 30 meter 'lag' in the satellite orbital positioning. There was no ground truth available for comparison. A wire mesh perspective view of the PNG DEM is shown in figure 2. The image is shown draped upon the DEM in figure 3 colored according to elevation (in the original).

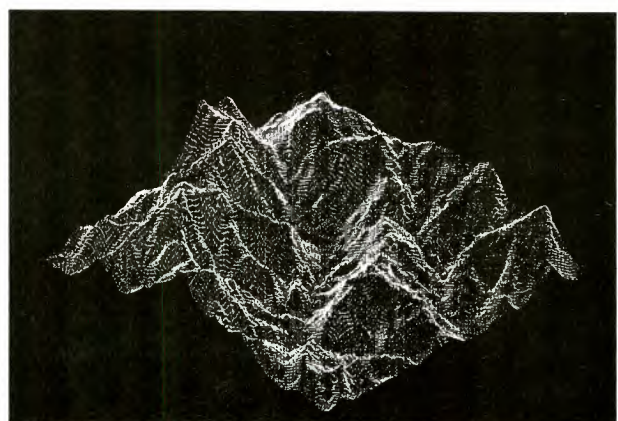


Figure 2 - TOPOSAR/RADARSAT wire mesh view of DEM in Western Papua New Guinea.

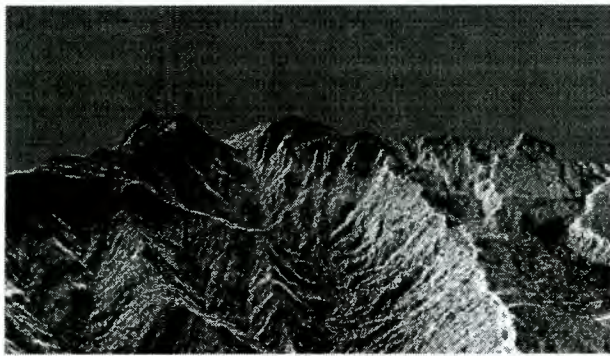


Figure 3 - Perspective view of image draped over DEM in Western Papua New Guinea.

In summary, the test results to date indicate a 10-15 meter uncertainty at the 1σ level with mean offsets in vertical and along-track directions of about 30 meters. The offsets can be largely removed through use of ground control.

3. DEMs from Airborne Interferometric SAR

3.1 Background: The interferometric process has been widely discussed in the literature, particularly for the case of repeat pass interferometry (e.g. Zebkor and Villesenor (1992), Goldstein (et al., 1988). Some of the general issues associated with airborne interferometry have been discussed, for example, in Gray and Farris-Manning (1993).

The principle, depicted in figure 4, is based upon measurement of the *phase difference* between the backscattered wave fronts from a common target pixel, arriving at two spatially separated antennas. The *phase difference* is determined by the *path difference* between these wave fronts. Calculating the path difference from the observed phase difference, and with knowledge of the antenna separation or *baseline*, its orientation with respect to nadir, and the height of the platform above the reference geoid, it is then possible from simple geometry to calculate the height of the target pixel (in principle, at least). In practice, the phase is determined from an ‘interferogram’, which is mathematically the complex product of the complex images received from each of the two antennas. Because the phase difference can only be measured between 0 and 2π (modulo 2π), there is an absolute phase ambiguity which is normally resolved with the aid of ground control and a ‘phase unwrapping’ technique (e.g. Goldstein et al, 1988). Thus the extraction of elevation is performed on the ‘unwrapped’ phase.

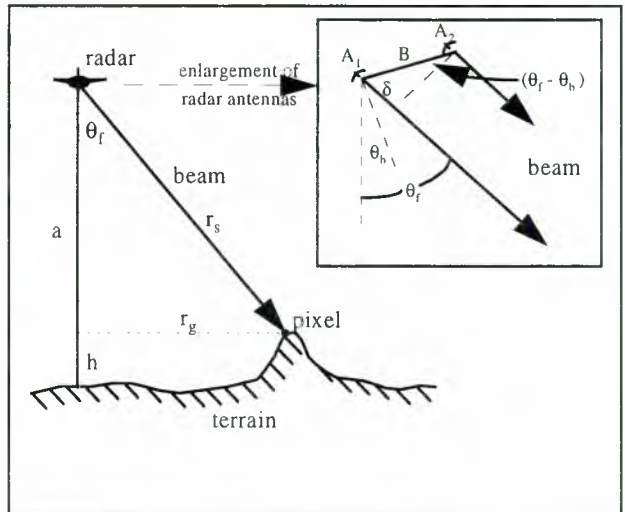


Figure 4 - Interferometric Airborne SAR Geometry

In the airborne case, both antennas are located on the same platform. The prime advantage of this configuration is that it is a single-pass system. Thus the target is viewed by both antennas simultaneously. (This is in contrast to the situation for repeat-pass interferometry for which scene and atmospheric changes between satellite passes can limit the practical application for DEM production over many of the geographical areas of interest).

3.2 STAR3i: Intermap Technologies, through agreements with ERIM and DARPA (Defense Advanced Projects Agency), have obtained exclusive rights to market and operate the IFSARE airborne SAR system developed by ERIM. The system has been re-named STAR3i. Over a two year test and operational validation period, the system has been flown by ERIM over a dozen sites and mapped well over a hundred thousand kmsq in the US and abroad. The IFSARE system was described by Sos, et al. (1994), and is briefly summarised from an operational point of view in the following paragraphs. The first commercial operations of STAR3i are to commence in December, 1996.

The radar, an X-band interferometric SAR, is carried in a LearJet 36 and is capable, under ideal circumstances, of imaging 30,000 kmsq in a single operational day. Positioning and motion compensation are achieved through use of a laser inertial reference platform and GPS which is differentially post-processed. Its normal operational mission mode would be performed at 40,000' (12.2 km) ASL and in this mode would collect 2.5 meter pixels across a 10 km ground swath. The DEM created from the interferometric data is post-processed, and an orthorectified image is simultaneously produced. Typically the DEM is produced at 5 meter postings. In a rigorous test performed by the US Government in the Chalone Hills of California, the IFSARE DEM was compared with a

large area (10km x 15km), photogrammetrically derived DEM. Statistically, the vertical difference was about 1.6 meters (1σ) with mean vertical offset of about 1.4 meters (Carlisle, 1996). These test results were created without the use of in-scene ground control. Vegetation (6% of the total area) was masked out of the results to ensure bald earth comparison. With this performance the system can create standard mapping products at 1:10,000 scale or smaller. Flying at a lower altitude (20,000' ASL), the system has demonstrated the ability to derive a DEM with significantly lower *relative* vertical uncertainty because of the improved signal-to-noise ratio. Of course this is achieved at the cost of a narrower swath.

Because of its altitude capability, it is able to operate over mountainous terrain. The moderate viewing geometry (approximately 45°) reduces the problems of lay-over, although not eliminating it in steep mountain regimes. Because of the 400 knot cruising speed, and 5 hour flying range, the LearJet can be rapidly deployed world-wide.

Examples of the imagery and DEM created in the Chalome Hills tests are displayed in figures 5 and 6.



Figure 5: STAR3i Ortho-Rectified Image of Avenal Area of Chalome Hills, California



Figure 6: STAR3i - Perspective View of Image Draped Over DEM of Avenal Area of Chalome Hills, California (original color-coded for elevation)

4. Cost / Performance Issues and Tradeoffs

Normally the user is forced to make choices among various factors which affect his or her spatial data base application. One of the major factors is cost and another is level of detail. Level of detail can often be quantified according to mapping scale, resolution, accuracy or similar parameters. In figure 7 we show a plot which graphically portrays the relationship between detail, as quantified by DEM accuracy (at the 1σ level), and unit price. This figure shows the relationship not only of the RADARSAT/TOPOSAR™ and STAR3i products but where they stand in relationship to other technologies such as SPOT and aerial photogrammetry. The numbers are not exact, of course, owing to the project-specific nature of most costs.

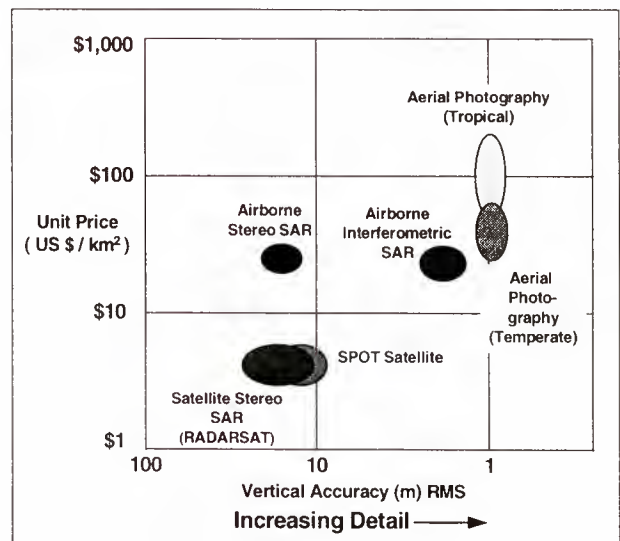


Figure 7 - DEMs - price vs. detail

Another factor for many users is delivery schedule or turn-around time. Mapping institutes have often been working on time scales of years owing to technology limitations and other disincentives, but recent advances in information technology, highly competitive industries, national prerogatives and other factors have created demand for much faster response to stated needs. For example the telecommunications industry may require response times of only a few weeks for delivery of DEM and other spatial data products. Thus the ability to respond on these time periods is an important pre-requisite for successful commercial operation of the RADARSAT /TOPOSAR™ and STAR3i systems. For both of these technologies, turnaround time in cloud-covered areas is significantly less than for competing technologies. In spite of this, efforts are underway to further reduce turn-around time to days/weeks from what is now weeks/months depending on project size.

5. Availability

DEM, ORIs, Image maps and related products from STAR3i and RADARSAT/TOPOSAR™ are both being currently offered as commercial services. Additionally, the TOPOSAR™ software will be offered as a stand-alone or bundled package in 1997.

6. Conclusions

Two new, commercially operational technologies for creation of DEMs and ORIs from radar have been described. They allow rapid acquisition over most of the world of the information needed for spatial data bases at the mapping scales of 1:10,000 to 1:100,000 (or smaller). Tests have demonstrated DEM accuracies (at the 1σ confidence level) of less than 2m for the STAR3i interferometric airborne SAR and 10-15 meters (in moderate terrain) for RADARSAT stereo pairs processed by TOPOSAR™. These complementary technologies allow cost / accuracy tradeoffs for large area topographic mapping projects. Level of detail and cost differ by a factor of about ten between the two solutions. Both are being currently offered commercially as services by Intermap, and the TOPOSAR™ software will be made available shortly.

7. Acknowledgments

We wish to express our gratitude to our colleagues in the development and production groups at Intermap for providing materials and information related to both technologies. Similarly, the interferometric examples shown were acquired and processed by ERIM. We are grateful to the RDDP program of CCRS and the RUDP program of CSA (Canada Space Agency) for financial support. The RADARSAT images (copyright CSA) were provided by Dennis Nazerenko of RSI (RADARSAT International).

8. References

- Carling, Robert, (1996). GeoSAR Program; IFSAR Validation and Terrain Classification from Polarimetry. Presentation to the SPIE Conference, Orlando
- Gray, Laurence A., and P. J. Farris-Manning, (1993). Repeat-Pass Interferometry with Airborne Synthetic Aperture Radar. IEEE Transactions on Geoscience and Remote Sensing. Vol. 31: Number 1, pp 180-191.
- Goldstein, R. M., H. A. Zebker, and C. Werner, (1988). Satellite Radar Interferometry: two dimensional phase unwrapping. Radio Sci, Vol23: Number 4, pp 713-720
- Leberl, F. (1990). Radargrammetric Image Processing. Artech House, Boston Mass.
- Mercer, J. B. and S. Griffiths, (1993). Operational Topographic Mapping from Airborne SAR Data (Presented at the International Symposium "Operationalization of Remote Sensing", 19-23 April 1993, ITC Enschede, The Netherlands)
- Mercer, J. Bryan, Stephen Griffiths and Scott Thornton, (1994). Large Area Topographic Mapping Using Stereo SAR. Proceedings of the First International Airborne Remote Sensing Conference and Exhibition, Strasbourg, France, Vol I, pp 269-280
- Sos, G. Tim, Herbert W. Klimach and Gary F. Adams, (1994). High Performance Interferometric SAR Description and Capabilities. Tenth ERIM Thematic Conference on Geologic Remote Sensing, San Antonio, Texas, Vol II, pp 637-649
- Zebker, Howard A., and J. Villasenor, (1992). Decorrelation in Interferometric Radar Echoes. IEEE Transactions on Geoscience and Remote Sensing, Vol 30: Number 5, pp 950-959.

COMPARISON BETWEEN ERS-1/2 AND RADARSAT AGRICULTURAL DATA

H. Méhi^{*/}, J. Aiello^{***}, A. Brizuela^{****}, O. Peinado^{***/**}, J. Kuba^{***}**

*** DLR (Deutsche Forschungsanstalt für Luft-und Raumfahrt)**

**** AGF (Arbeitsgruppe Fernerkundung, Universität München)**

***** CONAE (Comisión Nacional de Actividades Espaciales)**

****** UNER (Universidad Nacional de Entre Ríos)**

ABSTRACT

The objective of the project "ERS-1/2 Agricultural Monitoring Experiment in Entre Ríos, Argentina", is to obtain accurate and updated information on agricultural production, to be able to take decisions in the different policies of the agricultural administration, developing these applications with radar images. The project is divided in three areas: remote sensing, in charge of the AGF/DLR, GIS in charge of CONAE and field work, carried out by the UNER. The information is very efficiently exchanged via Internet, with CONAE as the concentration and distribution node for all the messages and data interchange.

ERS-1 (SLC and PRI) and RADARSAT images have been used in this paper, to use the information given by each one as they have different incidence angles and polarization. Data integration and comparison were made in a test zone aided by field data. After testing different types of filters, the MAP (Maximum A Posteriori) filter was chosen to reduce image speckle. This filter is a variation of the Lee-Sigma filter, for a non-correlated noise, as its application reduces very well the speckle without losing much information. The objective of working with these filters is to achieve homogeneous fields with the least content of noise, preserving details such as routes and roads for later classification and multitemporal studies.

The spatial resolution of the data from ERS-1 and RADARSAT is here compared with the different incidence angles over an inhabited zone and over cultivated areas comparing each one's advantages for each sector and the type of structures able to be verified with each satellite in these areas.

1. INTRODUCTION

The Province of Entre Ríos is part of a national agroproductive area participating with important volumes of animal and vegetable production mainly destined to satisfy the feeding needs of the region and other markets. Wheat, corn, soya beans, rice, are some

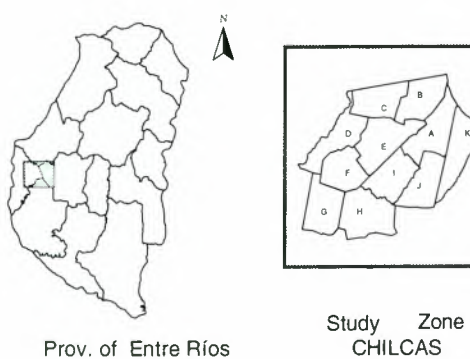
crops with economical relevance. The information about agricultural production is not available at the time of taking decisions and executing programmes; this situation happens in state and private areas. There are no doubts about the need of having accurate and reliable statistics. The conventional methods used to obtain these statistics are expensive, slow, inaccurate and not suitable for production estimations and follow-up. Satellite data, with a good coverage frequency and field data, obtained simultaneously on the ground, shall be used to monitor and update agricultural statistics. These data shall be integrated in a Geographical Information System oriented towards agricultural resources to fulfill the information demands.

The objectives of the project are linked with the methodologic development and test of an agricultural GIS. Simultaneously, the plan is to have a GIS able to obtain temporal and spatial information to carry out an adequate diagnosis of the District's agricultural situation. Due to serious problems with the image receptions, intermediate goals have to be changed for the time being. The request comprised ERS-1 images every 35 days, starting June 1994, and from July 1995, images from ERS-2 (tandem mission). But the ESA only confirmed 16 images through their descview software and by fax; from these 16 images only 3 images from ERS-1 were received and none from ERS-2, with an average delay of 14 months due to the problems with the antenna in Cuiabá, Brazil. Obviously, this situation completely stopped the work with interferometry, as the minimum difference between two scenes is 35 days; this implies too many changes to be able to obtain a coherent image with scientifically credible results. It was neither possible to carry out a proper multitemporal study. On the other hand, a Radarsat image was received in time. The image was type F3 and work started with this image, discovering a structural problem which is being studied by the Canadian Space Agency experts. No logical explanation has been achieved up to this moment. As it is very well known, due to technical problems in the satellite, Radarsat images cannot be received for the time being.

image available (the others are SLC) and the Radarsat image, to see the differences between both satellites. It was a visual comparison, as these images have a difference of two years and it is not possible to make a mathematical comparison with a sound scientific support.

2. WORKING AREA

It was chosen the district of Chilcas, in the province of Entre Ríos, south of the provincial capital city, with coordinates $32^{\circ} 13'$ and $32^{\circ} 21'$ SL and between $60^{\circ} 20'$ and $60^{\circ} 08'$ WL. The district comprises an area of 20 Km x 20 Km; 11 zones were defined, from Zone A to Zone K.



Graph 1: Study Zone

3. GEOGRAPHIC INFORMATION SYSTEM (GIS)

The current status of the project presents 3 out of 11 zones already digitized, with their corresponding codifications. A group of agricultural variables has been defined and is currently under study. This study shall be done for a limited number of plots in which each zone is divided, and that are the result of a typical sampling to be applied upon all the zones during the future development of the project. Another alternative to be studied in the future is that these plots are geographically fixed, being representative in the statistical sense of the agricultural activity of the district of Chilcas. Each variable constitutes a field of each record of the Data Base associated to the above mentioned GIS coverage. For each field campaign a new Data Base is defined and identified with the date of the field campaign. This method produces a continuous updating of the parameters that govern the project and simplifies the interrogation of the different variables.

4. FIELD WORK

Field work implies periodic visits to the chosen plots in Chilcas. It is foreseen to take three groups of 30 plots (conglomerates) to be visited every 15 days -if necessary- observing crops, soil and other features as indicated below. Place and seasonal representative crops, as well as phenological and general condition of the ground, shall be photographed. The parameters to be studied are:

- Type of crop: to know the relation between the crop and the response of the radar wave.
- Estimation of the sown area: to improve the estimations complementing the information with the data from Landsat and Spot satellites. Accuracy shall be examined, using ERS-1/2 and Radarsat data.
- Condition of the crop and yield: to study the capacity of providing information on the condition of the crops and probable yields (based on multitemporal and phenologic data plus other field observations).
- Soil changes and morphology: Combining data from Landsat TM -for pedologic units- and ERS-1/2 and Radarsat -for morphology and soil physical properties dynamics- the interest is to study soil aspect and drainage patterns, erosion, seasonal changes of soil humidity, roughness effect and incidence angle of radar waves.

5. REMOTE SENSING

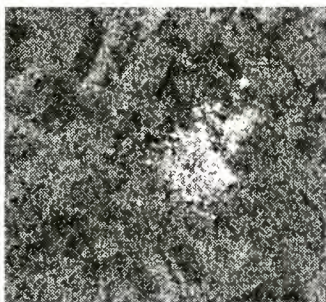
With these few data, intensive work was done, testing filters and radiometric correction algorithms, obtaining a multitemporal image for visual interpretation to integrate with the GIS; to achieve this it was necessary to develop a special method to work with SLC images as PRI. The images received up to this date are the ones showed in table 1. As it can be observed, between SLC images from 1994 and 1995 there is a difference of one year; therefore, the phase information cannot be used, and the images from 1995 have a difference of 35 days: this makes the interferometry work practically impossible (PRATI, 1990); neither a multitemporal study with investigation purposes can be done. The track shows a difference not noticed at the time of ordering the image (only the Frame was checked) and consequently, the image of 1994 belongs to the second quadrant of the descending path image and the image of 1995 belongs to the first quadrant. This effect is reflected in the incidence angle in the centre of the image and partially explains the contrast difference in the cities, the effect of "dark cities" observed in the images of 1995.

Date	07.24.94	05.13.95	06.17.95	04.23.96
Type	SLC / PRI	SLC	SLC	SGX,F3 (Radarsat)
Frame	4257	4257	4257	2441
Track	842	482	482	
Resolution	23 m / 12,5 m	23 m	23 m	4 m x 4 m
Incidence Angle	25,003	21,579	21,579	42,978
Variation coefficient	0,185448/0,217036	0,182006	0,183047	0,2140354

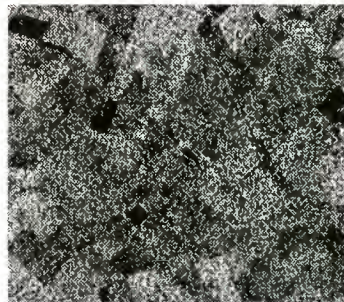
Table 1: Images received.

This situation is being studied by ESA's D-PAF in Oberpfaffenhofen, based on the raw data received from Brazil to see if there is an recording error or is an antenna effect. (Graph 2). The two cities that can be observed in the working area, Aranguren and Villa General Ramirez, have wide streets. Aranguren has dirt streets, while General Ramirez has paved streets, with trees, ground-floor houses, one-slope flat roofs, made of roof slabs or sheet zinc. The "dark cities" effect observed in the images from 1995 (Graph 2), apart from the probable processing error, can be the result of

a smaller incidence angle producing a higher Bragg resonance effect (RADARSAT 1992) in the dirt streets in one case, and, combined with the volume speckle of the trees in the other, reduces the contrast of the city. A very similar effect can be observed in the Radarsat image from 1996, with an incidence angle of 43 °. Note that no reflective cones can be observed in these two images, but this does happen and very clearly in the image from 1994.



PRI Image (City)



Radarsat Image (City)

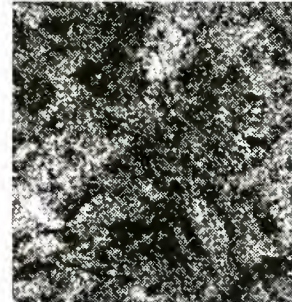


Image from 1995 (Dark city)

Graph 2: Comparison of images

As there were no PRI images available to obtain a multitemporal image, it was used the intensity and phase information from the SLC images to generate PRI images of 5 looks, with the following method:

- The images were imported to Erdas Imagine considering that the data are of 16 bits signed; therefore, the number of columns in the Headers file must be divided by 4, deducting 12 bytes by line as these are not part of the image. In this way, an image of 2 bands of 16 bits each is created (BIP format), (ESA, 1995).

- Depending on the platform used, the image must be reduced to 8 bits, as many filters only function with that resolution and if possible, it is desirable to work with 16 bits as this provides much more information.

- The transformation to PRI consists in taking the square root of the square of the amplitude and phase components. In other words, consists in taking the absolute value of a complex image.

- For the correction in Azimuth a 5 x 1 low pass filter was applied and then reduced in azimuth 5 times, obtaining a new image where each row is the average of the previous 5 rows.

- Radiometric calibration of the data was then made using the formulas provided by ESA in the correction of the PRI data, that, in this case and specially for the scene from 1994, is relatively very important. The formula is the following: ESA, 1996, S. Lehner 1996):

$$\sigma_0 = \frac{\langle I \rangle \sin(\alpha) \text{ Image Replica Power}}{\text{Power Loss}}$$

$$\text{K sin } (\alpha_{\text{ref}}) \text{ Reference Replica Power}$$

$\langle I \rangle$ = Square amplitude

$\sin(\alpha)$ = Incidence angle, in the centre of the image (between 19.5 y 26.6 °)

$\sin(\alpha_{\text{ref}})$ = Reference angle (23°)

K = Calibration constant, is different according to the data and processing centre, e.g. DPAF is 666110 for ERS-1 and 944064 for ERS-2.

Image Replica Power = It is an internal correction factor showed in the image header file.

Reference Replica Power = It is a constant equal to 205229 for ERS-1 and 156000 for ERS-2.

Power Loss = For each pixel it is determined by a look up table that relates the intensity value with the correction value. (Instantaneous antenna illumination area).

In the study zone the difference of angles between near and far range is 6° 22'', considering that in a flat zone the radiometric correction is +1.2 db in the ends. The corrections are based in alinealities in the ADC and variations in the Replica pulse power, as well as inaccurate application of the elevation antenna pattern in the PAF (Processing and Archiving Facilities). The pixel intensity value is proportional to the radar luminosity (β) in the illuminated scene. This value is $\sigma = \beta \cdot \sin(\alpha)$ where α is the incidence angle for a flat surface (as in the zone under study). The power loss occurs when the input signal to the AD converter is very high, this is then saturated (codifies in 5 bits = 32 levels) and the output value is lower than the input: this is a power loss. If the input signal is very low, a quantization noise occurs, this is a case of gain of power, as the output is higher than the input. The correction is provided by a look up table. The power loss value was reduced for the ERS-2 images from 13 July 1995, due to the corrections made in the ADC. (ESA, 1996).

- Always with the aim of obtaining homogeneous fields for a future multitemporal classification, and after some 150 tests with different filters such as the Kuan, Lee, Lee-2, Frost, Lee-Sigma, adaptive filters developed in the AGF, texture filters like the ones for typical deflection, variation coefficient, kurtosis, contrast, correlation, second angular moment, entropy and different types of convoluting filters, the MAP filter was chosen. After working with different window sizes (7x7, 5x5 and 3x3) the 3x3 size was chosen. The MAP filter is based on the Lee-Sigma filter (LEE, 1981), for that reason it also uses the variation coefficient showed in table 1 and is very near the theoretical value of an image of 6 looks, considering that, in this case, it is an image of 5 looks. Lee-Sigma and Lee filters use the DN statistical distribution within the moving window to determine the interested pixel value. These filters assume that the media and variance of the interested pixel are equal to the variance within the moving window. Noise is considered to have the multiplying

model with mean equal to 1, therefore it should be given a value of σ , the variation coefficient within the interested scene. The variation coefficient varies from .52 for images of 1 look to .18 for images of 8 looks, this based on the Rayleigh's distribution.

$$\text{Coef. of } \sigma_0 = \frac{\sqrt{\text{Variance}}}{\text{Media standart}} = \text{Deflection variation}$$

Media standart

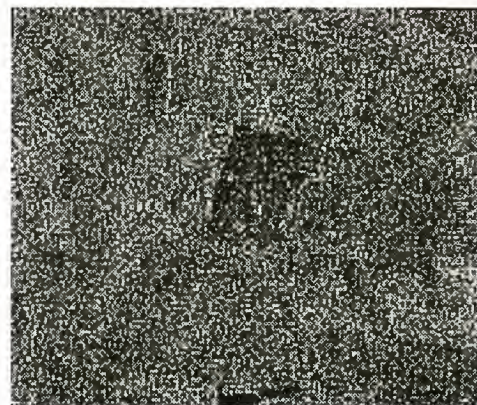
The filter maximizes a posteriori the function of density of probability. This filter was chosen because it gave the best results when working with images of 16 bits, reducing noise without losing details and, as it is a standard filter already incorporated to the software, is ideal for team work via internet, as used in this project. Due to the kind of images available, the use of chain filters is not convenient due to loss of resolution.

- The image was then reversed 180° and geocodified using ground control points, 40 for each image, identified in the image and in IGM charts with 1:50.000 scale and in IGM charts made with Landsat cloud free images from 1995. It is important to use the nearest neighbor method at the time of making the geocodification, so that the pixels from the corrected image keep the original value. The parameters used for the codification belonged to the Gauss-Kruger projection. The corrections were systematized so that when there is data available, the images register between themselves at pixel level, with only 4 control points.

By processing the three images with this method it was possible to obtain a multitemporal image. Aided by field data of the pilot zone, designated as zone D, within the Chilcas district, the digitized plots were identified, specially the change in using the ground in some plots (plots with corn changed to alfalfa).



PRI (Rivers from N to S)



Radarsat (Rivers from N to S)

Graph 3: River courses.

As it can be observed very clearly in the zone around the Doll creek, the ground has a completely different texture than the zone towards the north of the creek, where the ground shows more clay and the field's structure is different. (Graph 4). The city of Aranguren can be observed very clearly as well as the paved route 36, same as the provincial route 11, to the south of the image; both routes are very distinctive in the image. The multitemporal image is at 1:50.000 scale with band composition of 07.21.94 in red, 06.17.95 in green and 05.13.95 in blue. Spatial resolution is approximately 23 metres. In the Radarsat image, an F3 type, SGX product, which means fine resolution with an angle between 41 and 44 ° and a standard resolution of 10 m x 10 m, (effective of 4 m x 4 m in this case), with a coverage area of 50 km x 50 km (RADARSAT, 1995). Comparing the PRI image from 1994 with the Radarsat image from 1996, some features should be mentioned:

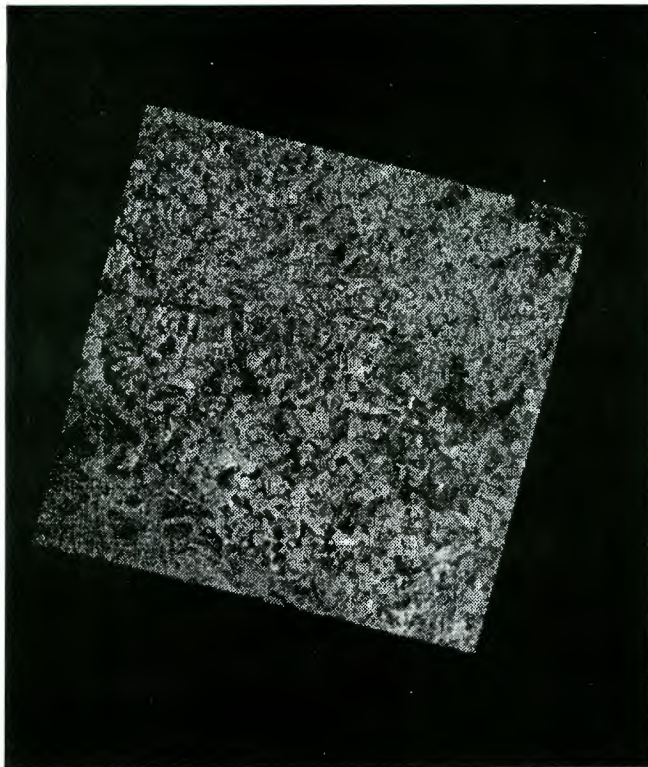
- Water courses running from east to west can be observed very clearly, in perpendicular direction to the satellite path, but the ones running parallel to the satellite path are not so clear. This case is opposite to the ERS-1 case, where the water courses running in the N/S direction can be observed much better. (Graph 3).
- Due to the spatial resolution, there are more details, roads and fields' limits that can be observed much better but there is less contrast than in the ERS-1 image. Therefore, for a general view, the ERS images present more contrast.

- Lagoons and stemmed waters can hardly be seen in RADARSAT images while in ERS-1's these appear very clear. (Graph 3).

- Radarsat images have an excellent definition in cities (4 metres); streets can be observed very clearly but the contrast with the contour is very low, while in the ERS images this contour is clearer and the detail degree is less (12,5 metres); there are also reflective cones, this phenomenon does not happen in any city in the Radarsat image. (Graph 2).

- With such temporal difference (2 years), different times of the year, different humidity conditions (it rained two days before the image of 1994 was obtained), different sensors, different polarization and different incidence angle, it is not possible to achieve any scientific deduction applied to agriculture, but it is useful to observe the basic differences between sensors.

- While processing the Radarsat image, a completely unusual structure was found when observed with a 1 to 1 zoom; the structure looks like snakes or curls. After consulting the Canadian Space Agency, their experts recognized the strange structure but they are still unable to find a solution to this problem. When some work was done directly on the image, the result was a disaster; therefore, it became necessary to filter the image with lowpass filters before carrying out any other operation.



6. CONCLUSIONS

Due to the serious problems with the reception of images, intermediate goals of the project have to be changed for the time being. The request comprised ERS-1 images every 35 days from June 1994, and from July 1995, images from the ERS-2 (tandem mission). But the ESA only confirmed 16 images through their descview software and by fax; from these 16 images, only 3 images from ERS-1 were received and none from ERS-2, with an average delay of 14 months due to the problems with the antenna in Brazil. Obviously, this situation completely stopped the work with interferometry, as the minimum difference between two scenes is 35 days; this implies too many changes to be able to obtain a coherent image with scientifically credible results. It was neither possible to carry out a proper multitemporal study. On the other hand, a Radarsat image was received in time. The image was type F3 and work started with this image, discovering a structural problem which is being studied by the Canadian Space Agency experts. No logical explanation has been achieved up to this moment. As it is very well known, due to technical problems in the satellite, Radarsat images cannot be received for the time being.

Anyhow, with these few data, and with the field information and after an intense work testing filters and radiometric correction algorithms, it was possible to obtain a multitemporal image for visual interpretation. Comparisons were also made between the only PRI

Graph 4: Multitemporal Image

image available (the others are SLC) and the Radarsat image, to see the differences between both satellites. It was a visual comparison, as these images have a difference of two years and it is not possible to make a mathematical comparison with a sound scientific support.

When the relevant data are available, it is foreseen to work with the interferometry and differential interferometry technics and with multitemporal classifications using data from the optical sensors and from the Radarsat using fuzzy logic technics and ancillary data. Otherwise, work will continue systematizing the generation of maps, with the digital processing and the systematizing of filtering and corrections. Combination with other sensors may offer interesting possibilities in the planning of resources, agricultural and ecological environmental monitoring as well as a good visual interpretation and digital classification. The aim is to obtain better image combinations, updated thematic maps, to improve image processing methodologies and environmental monitoring. The development of the project shall be to obtain the structure and support of a geographic information system to be used by institutions, private companies, technicians or producers with minimum requirements and low costs. The aim is to work with Radarsat and ERS multitemporal data and establish their advantages and to work with images from both satellites with very little temporal difference using the information provided by each one.

Indeed, as this activity started very recently, there is no intention at the present time to reach analysis tools and obtain conclusions; anyhow, it is very important to show the integration of the Data Base (with the currently existing variables) through the georeferentiation and registration with a radar image to visualize the ground.

7. BIBLIOGRAPHY

ESA, 1996, "ERS SAR CALIBRATION. Derivation of the Backscattering Coefficient σ_0 in ESA ERS SAR Products", Document No: ES-TN-RS-PM-HL09, Issue 2, Rev. 2 , 28 June, ESRIN.

A, 1992, "ERS-1 Product Specifications", ESA SP-1149, issue 3. ESA Publication Division.

ESA, 1995, "ERS SAR.SLC CTT and EXABYTE", ESA ER-IS-EPO-GS-5902.3.

PRATI, C., GIANI, M. y LEURATTI, N. ,1990, " SAR interferometry: a 2-D Phase unwrapping technique based on phase and absolutes values information", Proceedings ICGARS'90, 2043.

LEE, J-S, 1981, "Speckle analysis and smoothing of Synthetic aperture radar images". Computer Graphics and Image Processing Vol. 17, 24-32.

S.Lehner, J.Horstmann, W.Rosenthal, W.Koch, 1996, "Mesoscale Wind Measurements Using Recalibrated ERS-SAR Images", DLR /DFD.

RADAR REMOTE SENSING, a Training Manual, 1992, Dendron Resources Surveys Inc., Radarsat International.

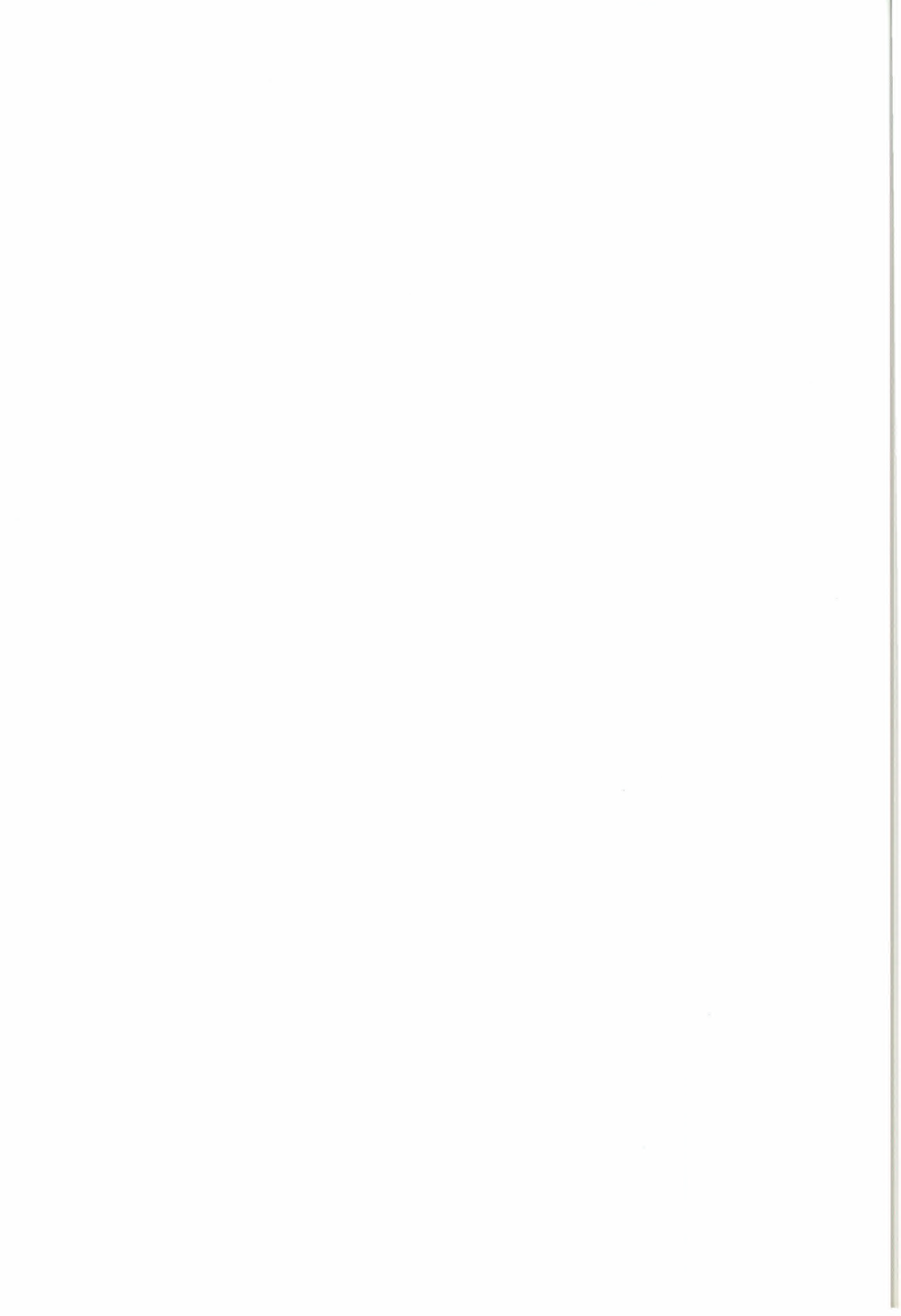
RADARSAT ILLUMINATED, YOUR GUIDE TO PRODUCTS AND SERVICES, 1995, RADARSAT International.

Statistics, Filtering & Data Fusion

Chairmen/Presidentes:

Jorge Lira

Nelson D.A. Mascarenhas



EL MODELO MULTIPLICATIVO PARA EL ANÁLISIS DE IMÁGENES SAR

Alejandro C. Frery[†]
 Corina da C. F. Yanasse[‡]
 Sidnei J. S. Sant'Anna[‡]

[†]UFPE – Universidade Federal de Pernambuco
 DI – Departamento de Informática
 CP 7851
 50732-970 Recife, PE, Brasil
 frery@di.ufpe.br

[‡]INPE – Instituto Nacional de Pesquisas Espaciais
 DPI – Divisão de Processamento de Imagens
 Avenida dos Astronautas, 1758
 12227-010 São José dos Campos, SP, Brasil
 {corina; sidnei}@dpi.inpe.br

ABSTRACT

In this paper a review of the multiplicative model and its associated distributions is made for SAR image analysis. The class of \mathcal{G} distributions is introduced for the return, using the Generalized Inverse Gaussian distribution for the intensity backscatter. Several particular cases of special interest are derived, such as \mathcal{K} and \mathcal{G}^0 distributions. Relationships among these and other distributions are presented, along with estimators for their parameters. Applications to the assessment of target homogeneity through parameter estimation are shown.

Keywords: multiplicative model; SAR; statistical modelling.

1. INTRODUCCIÓN

Es bien sabido que la gran mayoría de los datos provenientes de imágenes de radar de apertura sintética (*Synthetic Aperture Radar – SAR*) no obedece la distribución Gaussiana. Ésto se debe a que la iluminación que se utiliza para formar tales imágenes es del tipo coherente, en el que aparecen fenómenos de interferencia constructiva y destructiva de la señal devuelta al sensor [Goodman 1982; Tur et al. 1982].

El modelo multiplicativo para la señal de retorno ha probado ser muy exitoso para datos SAR. De él de-

vienen, entre otras, las distribuciones Rayleigh, Raíz de Gamma, Exponencial, Gamma, y la clase de las distribuciones \mathcal{K} . Estas distribuciones han recibido mucha atención en la literatura especializada (ver, por ejemplo, [Lee et al. 1994; Oliver 1991]). Recientemente fue propuesta una extensión para las distribuciones asociadas al modelo multiplicativo, que lleva a la clase de distribuciones \mathcal{G} y a la subclase de distribuciones \mathcal{G}^0 , útiles para el modelado de una gran variedad de blancos:

En este trabajo presentamos las distribuciones que devienen del modelo multiplicativo para los tres principales formatos de imágenes SAR multilook: complejo, intensidad (detección cuadrática) y amplitud (detección lineal). Se hace énfasis en las relaciones que vinculan estas distribuciones entre sí, lo que posibilita analizar la rugosidad de muestras a través de la estimación de parámetros.

La importancia de caracterizar estadísticamente una muestra, sea dentro o fuera del modelo multiplicativo, no se reduce a la posibilidad de clasificarla. Tal caracterización también puede redundar en la propuesta de técnicas novedosas (y mejores) para la reducción del ruido *speckle*, para la detección de alteraciones temporales, y para la extracción de parámetros biofísicos de datos SAR.

Conjeturada una distribución para una colección de datos, la estimación de parámetros es el paso que permite tanto verificar la hipótesis de trabajo como cuantificar la heterogeneidad del área observada. En este trabajo damos estimadores para los parámetros

de las distribuciones que más aparecen en la práctica.

2. MODELO MULTIPLICATIVO Y RUIDO SPECKLE

El modelo multiplicativo es una de las herramientas más frecuentemente usadas en el modelado estadístico de datos obtenidos con radiación coherente, tal como es el caso de imágenes SAR. Este modelo supone que el valor observado en cada coordenada de la imagen es el resultado de observar la variable aleatoria Z que, a su vez, es el producto de otras dos variables aleatorias independientes, X e Y . La variable aleatoria X modela el *backscatter* del terreno (cantidad vinculada a la constante dieléctrica del mismo, que relaciona el pulso de energía incidente con la señal devuelta al sensor), mientras que la variable aleatoria Y modela el ruido *speckle* característico de estas imágenes. Así siendo, el retorno es dado por observaciones de la variable aleatoria $Z = X \cdot Y$. En este trabajo los vectores serán denotados en negrito, las variables aleatorias en mayúsculas y sus eventos en minúsculas.

Pueden hacerse varias hipótesis para las distribuciones de X y de Y , y dependiendo de éstas será más o menos tratable y más o menos adecuada la distribución de Z para los datos que están siendo analizados. También puede suponerse una estructura de correlación espacial para el proceso $(X_s)_{s \in S}$, donde S denota el conjunto de coordenadas sobre el que está definida la imagen (el *soporte* de la imagen). Aunque ésta es un área de investigación importante, en este trabajo no abordaremos el modelado de la correlación espacial de los datos (es común suponer que el *speckle* puede ser considerado como formado por variables aleatorias independientes entre sí e independientes del *backscatter*).

La literatura ofrece una gran variedad de trabajos sobre las propiedades estadísticas del ruido *speckle* [Frery et al. 1996; Frery et al. 1995a; Frery et al. 1995b; Goodman 1982]. Se suele suponer que este ruido, en formato complejo (estamos tratando señales electromagnéticas, por naturaleza caracterizadas por dos componentes: una eléctrica y una magnética), tiene distribución normal bivariada de componentes independientes e idénticamente distribuidas de varianza $1/2$. Denotaremos en este trabajo esta situación como $\mathbf{Y}_C = (Y_R, Y_S) \sim \mathcal{N}2(0, 1/2)$. Para evitar confusiones utilizaremos los subíndices “ C ”, “ I ” y “ A ” para los formatos complejo, de intensidad y de amplitud respectivamente.

El *speckle multilook* de intensidad aparece tomando la media de n observaciones independientes del módulo cuadrado del *speckle* complejo \mathbf{Y}_C . Así siendo, la variable aleatoria resultante $Y_I = n^{-1} \sum_{i=1}^n \|\mathbf{Y}_C(i)\|^2$ tendrá distribución Gamma con densidad

$$f_{Y_I}(y) = \frac{n^n}{\Gamma(n)} y^{n-1} \exp(-ny), \quad y, n > 0,$$

denotada aquí $Y_I \sim \Gamma(n, n)$. Un caso particular de interés es cuando $n = 1$, para el cual Y_I tiene distribución exponencial de media unitaria.

El *speckle multilook* de amplitud aparece tomando la raíz cuadrada del respectivo *speckle multilook* de intensidad, esto es $Y_A = Y_I^{1/2}$. La distribución resultante, denotada $Y_A \sim \Gamma^{1/2}(n, n)$, se conoce como “raíz cuadrada de Gamma” y es caracterizada por la densidad

$$f_{Y_A}(y) = \frac{2n^n}{\Gamma(n)} y^{2n-1} \exp(-ny^2), \quad y, n > 0. \quad (1)$$

Para caracterizar esta manera de generar imágenes multilook podríamos utilizar la siguiente forma

$$Z_A = Z_I^{1/2} = \sqrt{\frac{1}{n} \sum_{i=1}^n Z_i}, \quad (2)$$

donde Z_i es el retorno de intensidad de un look.

Este modelo de generación de datos *multilook* de amplitud no es el único posible. Algunas imágenes de amplitud son formadas tomando el promedio de n datos de amplitud de un *look* cada uno [Grover and Quegan 1993]. Usando una representación análoga a la utilizada en la ecuaci'on (2) tenemos que, según este método,

$$Z_A = \frac{1}{n} \sum_{i=1}^n \sqrt{Z_i}, \quad (3)$$

donde Z_i es el retorno de intensidad de un look, pero este modelo presenta un problema teórico.

La raíz cuadrada de una variable aleatoria con distribución exponencial obedece una ley Rayleigh. Para esta distribución sólo se conoce una expresión cerrada para la densidad de convoluciones cuando $n = 2$ [Yanasse et al. 1995]. Aún en el caso $n \geq 3$, la distribución dada por la densidad (1) puede usarse como una buena aproximación para la densidad de la variable aleatoria definida en la ecuación (3), resolviendo parcialmente así este problema.

Aunque el número de looks n debería, en principio, ser un entero raramente se observa ésto al estimar esta cantidad a partir de datos reales. Una de las razones para ello es que los datos que se promedian para formar la imagen multilook no son independientes debido, entre otros factores, a las características no ideales del sensor. En [Vieira 1996; Yanasse et al. 1993] se muestra como estimar n , llamado de ahora en más “número equivalente de looks”, a partir de imágenes SAR reales.

Es importante destacar que la manera presentada para obtener el modelo multiplicativo no es la única posible. Otro abordaje consiste en construir la variable aleatoria del retorno en amplitud Z_A através de un paseo aleatorio multidimensional, observando la distancia del proceso al origen cuando el número de

pasos crece indefinidamente. Esta derivación se basa en el modelado del número medio de reflectores elementales que constituyen cada célula de resolución.

3. BACKSCATTER DE AMPLITUD

En la literatura se encuentran dos modelos para el *backscatter* de amplitud: una constante, asociada a áreas homogéneas y que lleva a un retorno distribuido según una ley raíz cuadrada de Gamma, y una distribución raíz de Gamma, asociada a áreas heterogéneas y que lleva a un modelo \mathcal{K}_A para el retorno. En varios trabajos [Lopes et al. 1990; Ulaby et al. 1986] se verificó que la heterogeneidad expresaible por este último modelo no es suficiente para algunas áreas y sensores, llevando a la necesidad de extenderlo.

El modelo multiplicativo más general que los autores conocen es el que se obtiene al utilizar la distribución raíz de Gaussiana inversa generalizada para el *backscatter* de amplitud (propuesta en [Frery et al. 1996]). Se dice que la variable aleatoria X_A obedece la distribución raíz de Gaussiana inversa generalizada con parámetros α , γ y λ si su densidad es dada por

$$f_{X_A}(x) = \frac{(\lambda/\gamma)^{\alpha/2}}{K_\alpha(2\sqrt{\lambda\gamma})} x^{2\alpha-1} \cdot \exp\left(-\frac{\gamma}{x^2} - \lambda x^2\right), \quad x > 0, \quad (4)$$

donde K_α denota la función de Bessel modificada de tercer tipo y orden α . El espacio de variación de los parámetros es el conjunto definido por

$$\begin{cases} \gamma > 0, \quad \lambda \geq 0 & \text{si } \alpha < 0, \\ \gamma > 0, \quad \lambda > 0 & \text{si } \alpha = 0, \\ \gamma \geq 0, \quad \lambda > 0 & \text{si } \alpha > 0. \end{cases} \quad (5)$$

Esta situación será denotada $X_A \sim \mathcal{N}^{-1/2}(\alpha, \gamma, \lambda)$. Los momentos de orden r de esta variable aleatoria son dados por

$$E(X_A^r) = \left(\frac{\gamma}{\lambda}\right)^{r/4} \frac{K_{\alpha+r/2}(2\sqrt{\gamma\lambda})}{K_\alpha(2\sqrt{\gamma\lambda})}.$$

Si $X_A \sim \mathcal{N}^{-1/2}(\alpha, \gamma, \lambda)$ entonces se dice que $X_I = X_A^2$ sigue una distribución Gaussiana inversa generalizada. Varias propiedades y aplicaciones de esta última pueden verse en [Barndorff-Nielsen and Blæsild 1981; Jørgensen 1982].

Algunas de las ventajas de usar para X_A la distribución caracterizada por la densidad dada en (4) son las siguientes:

- la densidad que caracteriza la distribución resultante de multiplicar X_A por una variable con distribución $\Gamma^{1/2}(n, n)$ (que, como ya vimos, es un modelo interesante para el *speckle multilook* de amplitud) puede obtenerse analíticamente;

- la distribución raíz cuadrada de Gaussiana inversa generalizada se reduce a los siguientes casos particulares
 - a una distribución raíz cuadrada de Gamma, llevando a un retorno con distribución \mathcal{K}_A ;
 - a la distribución de la reciproca de una variable aleatoria distribuida como una raíz cuadrada de Gamma, llevando a un retorno con distribución \mathcal{G}_A^0 , cuya definición e importancia serán vistas en las próximas secciones;
 - a una constante, que redunda en *speckle* puro, esto es, a retorno distribuido según una raíz cuadrada de Gamma.

Estas relaciones y casos particulares se resumen en la Figura 1, donde “ $\xrightarrow{\mathcal{D}}$ ” y “ $\xrightarrow{\Pr}$ ” denotan convergencia en distribución y en probabilidad, respectivamente. Es importante notar que estas propiedades permiten, por lo menos en tesis, realizar el modelado del *backscatter* de cualquier tipo de área (suponiendo datos de amplitud bajo el modelo multiplicativo) con la distribución $\mathcal{N}^{-1/2}(\alpha, \gamma, \lambda)$, escogiendo convenientemente sus parámetros

La distribución $\Gamma^{-1/2}$ está asociada al *backscatter* de áreas extremadamente heterogéneas dado que las modelan muy exitosamente [Frery et al. 1996]. De hecho, fue la búsqueda de modelos para áreas urbanas, dentro del referencial multiplicativo, que llevó a proponer el uso de la distribución $\mathcal{N}^{-1/2}$, y como caso particular de la $\Gamma^{-1/2}$, para el *backscatter* de este tipo de áreas.

4. RETORNO DE AMPLITUD

Puede probarse [Frery et al. 1996] que si $X_A \sim \mathcal{N}^{-1/2}(\alpha, \gamma, \lambda)$ y si $Y_A \sim \Gamma^{1/2}(n, n)$ son independientes, entonces $Z_A = X_A \cdot Y_A$ obedece una distribución denominada G-Amplitud con parámetros $\alpha, \gamma, \lambda, n$, denotada por $\mathcal{G}_A(\alpha, \gamma, \lambda, n)$, cuya densidad es dada por:

$$f_Z(x) = \frac{2n^n (\lambda/\gamma)^{\alpha/2}}{\Gamma(n) K_\alpha(2\sqrt{\lambda\gamma})} x^{2n-1} \left(\frac{\gamma + nx^2}{\lambda}\right)^{\frac{\alpha-n}{2}} \cdot K_{\alpha-n}(2\sqrt{\lambda(\gamma + nx^2)}), \quad x \in \mathbb{R}, \quad (6)$$

y con el espacio de parámetros dado en (5).

Sus momentos de orden r son dados por:

$$E(Z^r) = \left(\frac{\gamma}{n^2\lambda}\right)^{r/4} \frac{K_{\alpha+r/2}(2\sqrt{\gamma\lambda}) \Gamma(n+r/2)}{K_\alpha(2\sqrt{\gamma\lambda}) \Gamma(n)}.$$

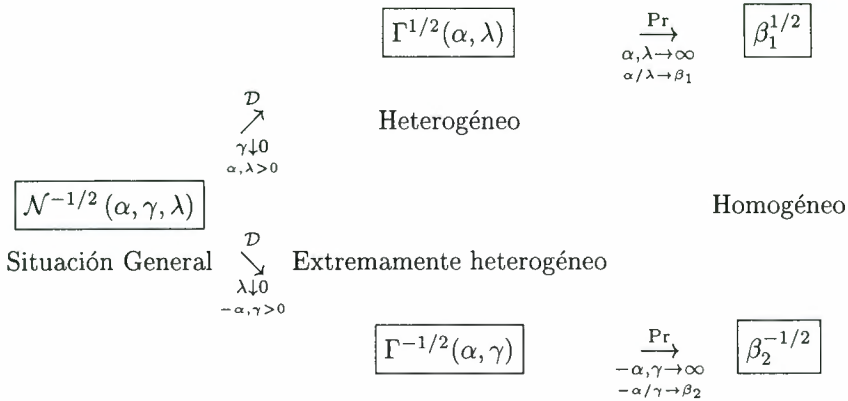


Figura 1: Resumen de las relaciones entre las distribuciones para el *backscatter* en formato de amplitud asociadas al modelo multiplicativo.

Tal como anteriormente mencionado, la distribución \mathcal{G}_A posee como casos especiales las siguientes distribuciones:

1. la distribución $\mathcal{K}_A(\alpha, \lambda, n)$, cuando $\gamma \rightarrow 0$ con $\alpha, \lambda > 0$, cuya densidad es dada por:

$$f_Z(x) = \frac{4\lambda nx}{\Gamma(\alpha)\Gamma(n)} (\lambda nx^2)^{(\alpha+n)/2-1} \cdot K_{\alpha-n}(2x\sqrt{\lambda n}), \quad \alpha, \lambda, n, x > 0; \quad (7)$$

2. la distribución $\mathcal{G}_A^0(\alpha, \gamma, n)$, cuando $\lambda \rightarrow 0$ con $-\alpha, \gamma > 0$, cuya densidad es dada por:

$$f_{Z_A}(x) = \frac{2n^n \Gamma(n-\alpha) \gamma^{-\alpha} x^{2n-1}}{\Gamma(n)\Gamma(-\alpha)(\gamma + nx^2)^{n-\alpha}}, \quad -\alpha, \gamma, n, x > 0. \quad (8)$$

3. la distribución $\Gamma^{1/2}$, que tanto puede venir de (7), cuando $\alpha, \lambda \rightarrow \infty$, con $\alpha/\lambda \rightarrow \beta_1$, como de (8), cuando $-\alpha, \gamma \rightarrow \infty$, con $-\alpha/\gamma \rightarrow \beta_2$.

Estas relaciones están resumidas en la Figura 2, donde “ $\xrightarrow{\mathcal{D}}$ ” y “ $\xrightarrow{\text{Pr}}$ ” denotan convergencia en distribución y en probabilidad, respectivamente. Es importante notar que estas propiedades permiten, por lo menos en tesis, reducir cualquier estimación de parámetros (suponiendo datos de amplitud bajo el modelo multiplicativo) a la estimación de α , γ y λ (supondremos n conocido o previamente estimado) para la distribución \mathcal{G}_A . Realizada esta estimación, el área bajo estudio es clasificada según los valores observados. Las funciones de distribución acumuladas de las distribuciones \mathcal{K}_A y \mathcal{G}_A^0 pueden consultarse en [Frery et al. 1996; Yanasse et al. 1995]. En esta última referencia se discuten con detalle los problemas numéricos asociados al uso de la distribución \mathcal{K}_A .

La distribución \mathcal{G}_A^0 está asociada a áreas extremadamente heterogéneas por los mismos argumentos expuestos al final de la sección 3.

En particular, dado que en [Frery et al. 1996] se verificó que es suficiente utilizar los modelos \mathcal{K} y \mathcal{G}_A^0 , basta observar el valor estimado del parámetro α para tener una idea de la homogeneidad del área bajo estudio: valores estimados “cercanos” a cero indican un área heterogénea, mientras que valores absolutos “grandes” indican un área homogénea. Más adelante serán vistos algunos de estos valores estimados con datos reales.

En la Fig. 3 se muestran algunas densidades \mathcal{G}_A^0 de un look, con media unitaria. La distribución $\Gamma^{1/2}$ se muestra como caso límite de la \mathcal{G}_A^0 , según se ve en las propiedades mostradas en la Fig. 2. El uso de escala doblemente logarítmica para la comparación de densidades puede verse en [Barndorff-Nielsen and Blæsild 1981]. De estas figuras puede verse que a medida que $\alpha \rightarrow 0$ las modas se acercan al origen y, simultáneamente, el decrecimiento asintótico de las densidades se vuelve más lento. Las consecuencias de este comportamiento quedan en evidencia al verificar que sólo se tienen momentos de orden r para la distribución \mathcal{G}_A^0 si $r < -2\alpha$.

La fuerte influencia que el número equivalente de looks tiene en esta distribución se ilustra en la Fig. 4, donde se dibujaron varias densidades de la distribución \mathcal{G}_A^0 de media unitaria con $\alpha = -1$ y varios valores de n . De esta figura queda en evidencia que cuanto mayor n más simétrica es esta densidad, pareciéndose cada vez más a una normal. Así siendo, se verifica que cuanto menor n más crítico es el desvío de la hipótesis Gaussiana.

Las distribuciones en formato de intensidad, tanto para el *backscatter* como para el retorno, surgen fácilmente de aplicar la transformación de densidades dada por $f_{X_I}(x) = f_{X_A}(\sqrt{x})/(2\sqrt{x})$ a las respectivas densidades en formato de amplitud.

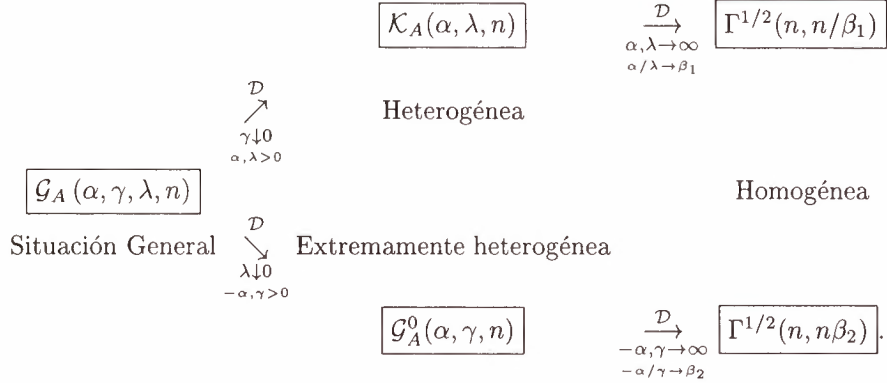


Figura 2: Resumen de las relaciones entre las distribuciones asociadas al modelo multiplicativo para datos en formato de amplitud.

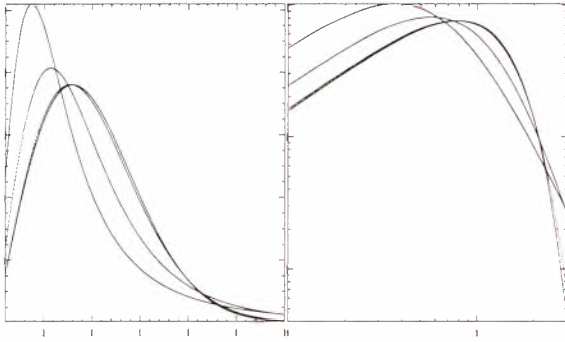


Figura 3: Densidades, en escalas lineal y doble-logarítmica, de las distribuciones $\mathcal{G}_A^0(-1, 4/\pi^2, 1)$ (línea continua), $\mathcal{G}_A^0(-2, 1.621, 1)$ (guiones largos), $\mathcal{G}_A^0(-20, 24.512, 1)$ (guiones) y $\Gamma^{1/2}(1, \pi/4)$ (guion-punto-punto-punto).

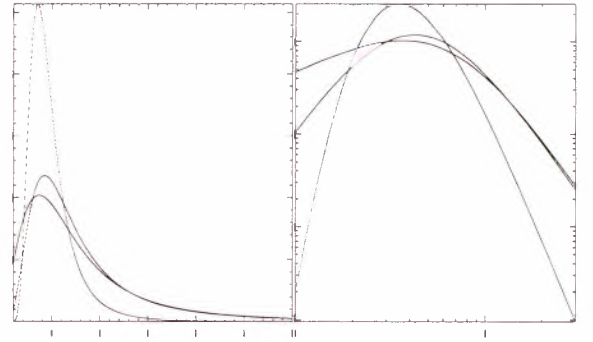


Figura 4: Densidades, en escalas lineal y doble-logarítmica, de las distribuciones $\mathcal{G}_A^0(-1, 4/\pi^2, 1)$ (línea continua), $\mathcal{G}_A^0(-1, 0.360, 2)$ (guiones largos) and $\mathcal{G}_A^0(-1, 0.328, 8)$ (guiones).

5. FORMATO COMPLEJO

Aunque en la mayoría de las aplicaciones de imágenes de radar a percepción remota raramente se utilizan datos en este formato, tales imágenes tienen interés práctico pues, entre otras cosas, permiten verificar el funcionamiento del sistema sensor [Yanasse 1991]. Así siendo, a seguir se presentan las densidades que caracterizan las distribuciones asociadas al retorno complejo resultantes de los *backscatters* caracterizados en la Figura 1.

Las distribuciones denotadas \mathcal{G}_C , \mathcal{G}_C^0 y \mathcal{K}_C en la Figura 5 están caracterizadas, respectivamente, por las siguientes densidades:

$$f_{Z_0}(x) = \frac{1}{K_\alpha(2\sqrt{\lambda\gamma})} \sqrt{\frac{(\lambda/\gamma)^\alpha}{\pi}} \left(\frac{\gamma + x^2}{\lambda} \right)^{\frac{\alpha-1}{2}}.$$

$$\begin{aligned} f_{Z_0}(x) &= \frac{\Gamma(1/2 - \alpha)}{\sqrt{\pi\gamma^\alpha}\Gamma(-\alpha)} (x^2 + \gamma)^{\alpha - \frac{1}{2}}, \\ f_{Z_0}(x) &= \frac{2}{\Gamma(\alpha)} \sqrt{\frac{\lambda^{\alpha+1/2}}{\pi}} |x|^{\alpha - \frac{1}{2}} K_{\alpha - \frac{1}{2}} \left(2|x|\sqrt{\lambda} \right), \end{aligned}$$

donde $x \in \mathbb{R}$ y los parámetros α , γ y λ pertenecen al conjunto especificado en (5). Estas distribuciones son las marginales de los datos en formato complejo, y Z_0 denota tanto la componente real como la imaginaria.

La distribución \mathcal{G}_C^0 está asociada a áreas extremadamente heterogéneas por los mismos argumentos expuestos al final de la sección 3.

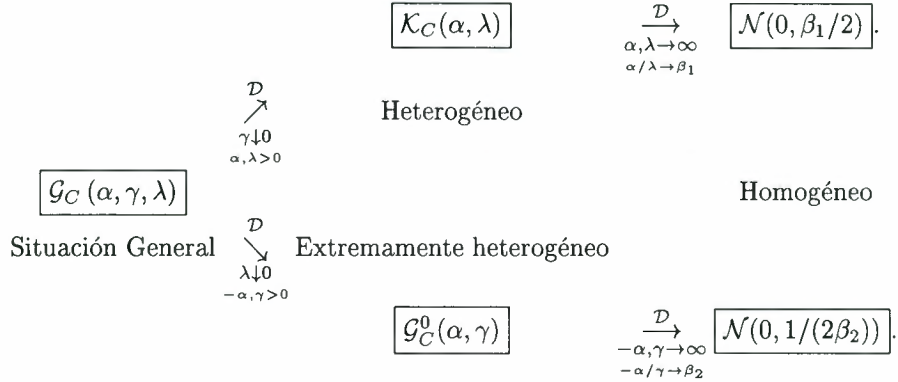


Figura 5: Resumen de las relaciones entre las distribuciones asociadas al modelo multiplicativo para datos en formato de complejo.

6. ESTIMACIÓN PARA EL FORMATO DE AMPLITUD

El problema de estimación de los parámetros de las distribuciones asociadas al modelo multiplicativo no está ni satisfactoria ni totalmente resuelto en la literatura. Los problemas encontrados son varios, siendo uno de los principales la notable dificultad [Joughin et al. 1993] (o, en la mayoría de los casos, imposibilidad) de encontrarse formas computacionalmente tratables para los estimadores de máxima verosimilitud.

Por estos motivos suele usarse el método de los momentos como alternativa para estimación de parámetros. Queda por resolver el problema de **cuáles** momentos involucrar en la estimación, pero éste es otro de los muchos problemas en abierto.

Suponiendo conocido el número equivalente de looks n , algunos estimadores para los parámetros de las distribuciones $\Gamma^{1/2}(n, n/\beta)$, $\mathcal{K}_A(\alpha, \lambda, n)$ y $\mathcal{G}_A^0(\alpha, \gamma, n)$ basados en este método son, respectivamente, las soluciones de los siguientes sistemas de ecuaciones:

$$\hat{\beta} = \widehat{m}_2;$$

$$\left\{ \begin{array}{l} \frac{\Gamma(n)\Gamma(n+1/2)\Gamma(\hat{\alpha})\Gamma(\hat{\alpha}+1/2)}{(\Gamma(n+1/4)\Gamma(\hat{\alpha}+1/4))^2} - \frac{\widehat{m}_{1/2}^2}{\widehat{m}_1^{1/2}} = 0 \\ \hat{\lambda} = \left(\frac{\Gamma(n+1/2)\Gamma(\hat{\alpha}+1/2)}{\Gamma(n)\Gamma(\hat{\alpha})\widehat{m}_1} \right)^2 \frac{1}{n} \end{array} \right.$$

$$\left\{ \begin{array}{l} \frac{\Gamma^2(-\hat{\alpha}-1/4)\Gamma^2(n+1/4)}{\Gamma(-\hat{\alpha}-1/2)\Gamma(n+1/2)\Gamma(-\hat{\alpha})\Gamma(n)} - \frac{\widehat{m}_{1/2}^2}{\widehat{m}_1^2} = 0 \\ \hat{\gamma} = n \left(\frac{\widehat{m}_1\Gamma(-\hat{\alpha})\Gamma(n)}{\Gamma(-\hat{\alpha}-1/2)\Gamma(n+1/2)} \right)^2, \end{array} \right.$$

donde \widehat{m}_j denota el momento muestral de orden j dado por $\widehat{m}_j = \sum_{i=1}^N z_i^j$.

7. APLICACIÓN A UNA IMAGEN REAL

El ejemplo de aplicación que se seguirá fue mostrado en [Frery et al. 1996]. Los datos provienen del sensor JERS-1, y corresponden a una región del Amazonas brasileño conocido como Reserva Florestal de Tapajós, estado de Pará. En la Fig. 6 se observan tres clases vegetales: selva virgen con relieve ondulado, selva virgen con relieve plano y una región que sufrió desflorestamiento.

A cada uno de esos conjuntos de datos se le estimó los parámetros de las distribuciones $\Gamma^{1/2}$, \mathcal{K}_A y \mathcal{G}_A^0 , además del coeficiente de variación. Los valores estimados se muestran en la Tabla 1. La última columna de esta tabla muestra los p -valores resultantes de aplicar el test χ^2 a los tres ajustes mencionados.

De la Table 1 y de los ajustes mostrados en la Fig. 7 puede concluirse que el parámetro α de la distribución \mathcal{G}_A^0 está fuertemente relacionado al grado de homogeneidad de los datos, y que es menor para áreas más homogéneas. El parámetro *alpha* de la distribución \mathcal{K}_A también mide la homogeneidad de las áreas, siendo mayor para aquellas más homogéneas. Como previsto por el modelo, la distribución $\Gamma^{1/2}$ sólo se ajusta bien a datos de alta heterogeneidad.

El ajuste por la distribución \mathcal{G}_A^0 siempre es posible, mientras que no ocurre lo mismo con la distribución \mathcal{K}_A . Esta adaptabilidad (aún más notable en el análisis de áreas urbanas presentado en [Frery et al. 1996]), sumada a las ventajas analíticas de la primera distribución en relación a la segunda, hacen que la distribución \mathcal{G}_A^0 sea una seria candidata a reemplazar a la distribución \mathcal{K}_A en varias aplicaciones.

8. EXTENSIONES

Se desconocen técnicas de estimación computacionalmente viables para los parámetros α, γ, λ de la dis-

Tabla 1: Parámetros estimados en las regiones vegetales de Tapajós

Área	\widehat{CV}	$\widehat{\beta}$	$(\widehat{\alpha}, \widehat{\lambda})$	$(\widehat{\alpha}, \widehat{\gamma})$	$\Gamma^{1/2}$	p_{X^2}	\mathcal{K}_A	\mathcal{G}_A^0
Relieve ondulado	0.463	1361240	$(2.254, 1.877 \cdot 10^{-6})$	$(-3.040, 2819050)$	0.00	0.01	0.04	
Relieve plano	0.335	1303020	$(13.652, 1.048 \cdot 10^{-5})$	$(-14.290, 17314500)$	$5 \cdot 10^{-4}$	0.78	0.81	
Deforestamiento	0.318	684111	$(21.157, 3.083 \cdot 10^{-5})$	$(-21.657, 14180400)$	0.69	0.84	0.48	

tribuciones \mathcal{G} , ni se dispone de ningún resultado que permita llegar a estas distribuciones para el retorno a través de los paseos aleatorios mencionados al final de la sección 2. de este trabajo. Las propiedades de varias alternativas de estimación de los parámetros de las distribuciones \mathcal{K}_A , \mathcal{G}_A^0 y \mathcal{G}_I^0 están siendo estudiadas. Los autores no conocen ningún trabajo que aborde las distribuciones \mathcal{G} multidimensionales ni tampoco variables aleatorias correlacionadas con estas distribuciones.

AGRADECIMIENTOS

Los autores agradecen el apoyo del CNPq-Brasil a través del proyecto PROTECM-CC GEOTEC (Proceso 680.061-94-0).

REFERENCIAS

- O. E. Barndorff-Nielsen and P. Blæsild. Hyperbolic distributions and ramifications: contributions to theory and applications. In C. Taillie and B. A. Baldessari, editors, *Statistical distributions in scientific work*, pages 19–44. Reidel, Dordrecht, 1981.
- A. C. Frery, H. J. Müller, C. C. F. Yanasse, and S. J. S. Sant’Anna. A model for extremely heterogeneous clutter. *IEEE Transactions on Geoscience and Remote Sensing*, 1996, in press.
- A. C. Frery, C. C. F. Yanasse, and S. J. S. Sant’Anna. Alternative distributions for the multiplicative model in sar images. In *Quantitative remote sensing for science and applications*, pages 169–171, Florence, Jul. 1995. IEEE. IGARSS’95 Proc.
- A. C. Frery, C. C. F. Yanasse, and S. J. S. Sant’Anna. Statistical characterization of SAR data: the multiplicative model and extensions. In *Latinoamérica evaluada desde el espacio*, pages 502–515, Mexico, Nov. 1995. SELPER.
- J. W. Goodman. Statistical properties of laser speckle patterns. In J. C. Dainty, editor, *Laser speckle and related phenomena*, chapter 2. Springer-Verlag, Berlin, 1982.
- K. D. Grover and S. Quegan. Image quality, statistical and textural properties of SAREX data from the Tapajós test site. In M. Wooding and E. Attema, editors, *SAREX-92: South American Radar Experiment*, pages 15–24, Paris, 1993. ESA.
- B. Jørgensen. *Statistical properties of the generalized inverse Gaussian distribution*, volume 9 of *Lecture Notes in Statistics*. Springer-Verlag, New York, 1982.
- I. R. Joughin, D. B. Percival, and D. P. Winebrenner. Maximum likelihood estimation of K distribution parameters for SAR data. *IEEE Transactions on Geoscience and Remote Sensing*, 31:989–999, 1993.
- J. S. Lee, K. W. Hoppel, S. A. Mango, and A. R. Miller. Intensity and phase statistics of multi-look polarimetric and interferometric SAR imagery. *IEEE Transactions on Geoscience and Remote Sensing*, 32:1017–1027, 1994.
- A. Lopes, H. Laur, and E. Nezry. Statistical distribution and texture in multilook and complex SAR images. In *Remote sensing science for the nineties*, pages 2427–2430, New York, May 1990. IEEE.
- C. J. Oliver. Information from SAR images. *Journal of Physics D: Applied Physics*, 24:1493–1514, 1991.
- M. Tur, K. C. Chin, and J. W. Goodman. When is speckle noise multiplicative? *Applied Optics*, 21:1157–1159, 1982.
- F. T. Ulaby, F. Kouyate, B. Brisco, and T. M. Williams. Textural information in SAR images. *IEEE Transactions on Geoscience and Remote Sensing*, GE-24:235–245, 1986.
- P. R. Vieira. Desenvolvimento de classificadores de máxima verossimilhança pontuais e ICM para imagens de radar de abertura sintética. Master’s thesis, Instituto Nacional de Pesquisas Espaciais, São José dos Campos, SP, Brazil, 1996.
- C. C. F. Yanasse. *Statistical analysis of synthetic aperture radar images and its applications to system analysis and change detection*. PhD thesis, University of Sheffield, Sheffield, UK, 1991.
- C. C. F. Yanasse, A. C. Frery, and S. J. S. Sant’Anna. Stochastic distributions and the multiplicative model: relations, properties, estimators and applications to SAR image analysis. Technical Report 5630-NTC/318, INPE, São José dos Campos, SP, Brazil, 1995.
- C. C. F. Yanasse, A. C. Frery, S. J. S. Sant’Anna, P. F. Hernandez, and L. V. Dutra. Statistical analysis of SAREX data over Tapajós - Brazil. In M. Wooding and E. Attema, editors, *SAREX-92: South American Radar Experiment*, pages 25–40, Paris, 1993. ESA.

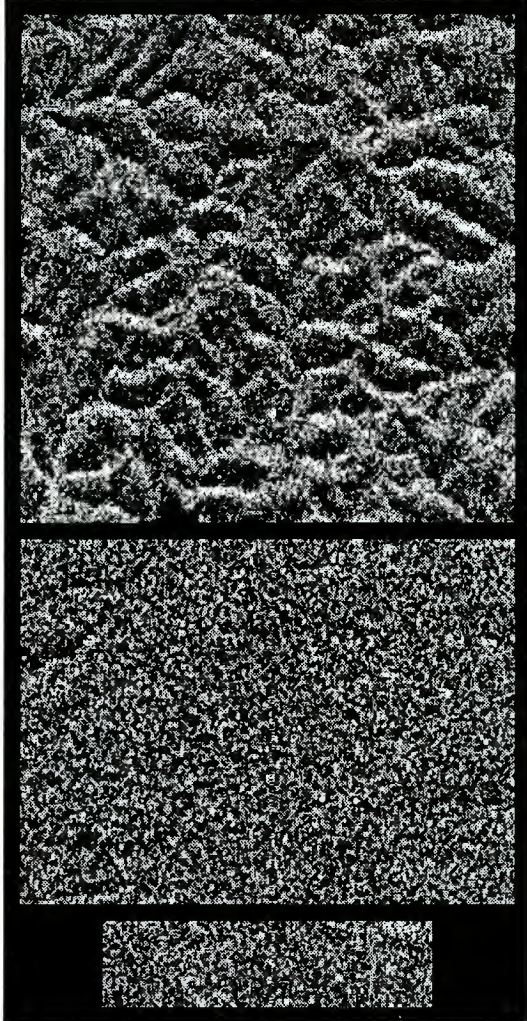


Figura 6: Áreas vegetales de selva con relieve ondulado, selva con relieve plano y región desforestada.

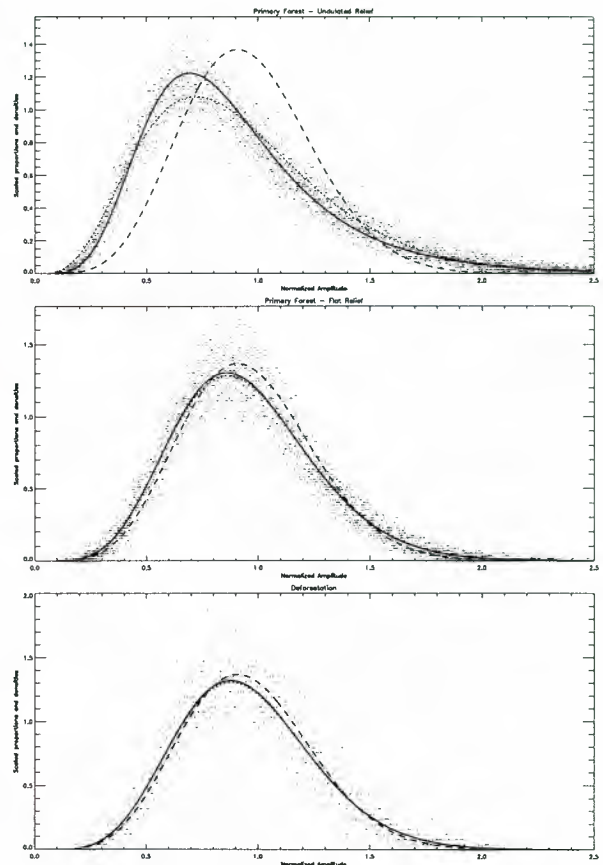


Figura 7: Ajustes por tres densidades a los datos de las áreas vegetales: $\Gamma^{1/2}$ (guiones), \mathcal{K}_A (guiones largos) and \mathcal{G}_A^0 (línea continua).

AN OVERVIEW OF SPECKLE NOISE FILTERING IN SAR IMAGES

Nelson D. A. Mascarenhas

Federal University of São Carlos
 Computer Department
 Architecture, Signal and Image Processing Group
 Via Washington Luis, km 235
 Caixa Postal 676
 CEP 13565-905 São Carlos, SP, Brazil
 Tel/Fax: +55-16-274-8233
 E-Mail: nelson@dc.ufscar.br

ABSTRACT

Synthetic Aperture Radar Images are corrupted by a signal-dependent noise called speckle, that decreases the potentiality of these images for human or automatic interpretation. This degradation is due to the coherent nature of the radiation that is used and its interaction with the roughness of the terrain. In this paper, a survey of the techniques that have been proposed for reducing speckle noise in a SAR image is presented. First, a statistical model for the speckle noise is presented. This model, multiplicative in its nature, leads to the majority of the algorithms for speckle noise reduction. We describe the Lee, Kuan, Frost and adaptive versions of the last three filters, which are the most well known algorithms, as well as the MAP filter and some heuristic filters. We also briefly present new algorithms based on the theories of Markov Random Fields and Robust Estimation. Finally, we describe techniques for the evaluation of speckle reduction filters.

1. INTRODUCTION

Speckle noise corrupts images that are obtained by coherent radiation, like SAR, ultrasound, laser, sonar, etc. The presence of this type of noise decreases the usefulness of these images for both human and automatic interpretation. In this paper we review the main algorithms that have been proposed for speckle noise reduction. We shall concentrate our review on single band images, ie, filters for multipolarization or multifrequency images will not be covered. Previous reviews of this subject were published by Durand et al [Ref. 1], Sadjadi [Ref. 2], Dewaele et al [Ref. 3] and Lee et al [Ref. 4].

2. A Statistical Model for Speckle

The statistical model for speckle noise is usually based on the assumption that the resolution cell contains a large number of scatterers of radiation with a wavelength that is comparable to the roughness of the terrain. In this case, the returned wave is the result of the superposition of all these reflected components. If we represent each of these reflected waves by a phasor, we have the following diagram that is a realization of a random walk process in the plane:

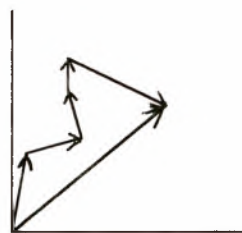


Figure 1- Phasor diagram showing the addition of the contributions of different scatterers.

The signal due to the i^{th} scatterer can be expressed by:

$$V_i \exp[j(wt + \theta_i)] = V_i \exp(j\phi_i) \quad (1)$$

where V_i is the magnitude and ϕ_i is the instantaneous phase. The return from N scatterers results in a instantaneous voltage given by:

$$V = \sum_{i=1}^N V_i \exp(j\phi_i) \quad (2)$$

We can express V in the following polar form:

$$V = V_e \exp(j\phi) \quad (3)$$

V can be decomposed in the two cartesian components V_x and V_y . For a large value of N, it is possible to apply the Central Limit Theorem and these components will have a Gaussian distribution. It is easily seen that V_x and V_y have zero means and are non-correlated. As a consequence, the joint probability density function of V_x and V_y will be given by:

$$f(V_x, V_y) = \frac{1}{2\pi\sigma^2} \exp\left(-\frac{V_x^2 + V_y^2}{2\sigma^2}\right) \quad (4)$$

There are two kinds of detection systems employed in SAR. In the first one, called linear detection, the envelope voltage V_e determines the brightness of the pixel in the image. In the second detection system, called quadratic detection, the square of V_e is used for this purpose.

In the first case, it is possible to derive the joint probability density function of V_e and ϕ and to conclude that they are independent random variables, V_e being Rayleigh distributed and ϕ being uniformly distributed between 0 and 2π . In the second case, V_e^2 has an exponential distribution.

Under the linear detection, the ratio of the standard deviation to the expected value over homogeneous areas (no signal variation) is constant and equal to .5227, with one look. Under quadratic detection, this ratio is equal to one. In any case, the standard deviation is proportional to the expected value, and this fact is the basis for the multiplicative model of the speckle noise. At the same time, it also implies that speckle is a signal-dependent noise.

It is possible to reduce the standard deviation of the speckle by dividing the synthetic aperture into N parts, generating N images of the same scene with independent noise and obtaining the mean of these images. The reduction of the standard deviation is by a factor of $N^{1/2}$. The price being paid is a reduction by a factor of N of the resolution in the azimuth direction. Better results are obtained by using the information content of the image on the speckle reduction process, as it happens with several of the filters that will be described in this article.

3. Heuristic Filters

It is possible to devise heuristic schemes to reduce the speckle, without taking into consideration any statistical criterion.

A simple moving average (eg, 3x3, 5x5 window) over the image tends to reduce the speckle, due to the fact that there is a tendency for a moderately low correlation between adjacent speckle samples, if the point spread function of the sensor is not too wide. However, this low-pass filter tends to indiscriminately blur the image. The geometrical filter [Ref. 5] or the analogous morphological filter [Ref. 6] have also been proposed for speckle reduction. Like the moving average filter, they are efficient over homogeneous areas. However, although they tend to preserve edges well, these two filters erase point target responses, thin curvilinear structures and high frequency texture variations [Ref. 7]. Median filters have also been proposed on a heuristic basis, but, as will be described later in this paper, they can be introduced through the formal framework of robust estimation theory.

The most effective filters for speckle reduction are adaptive and based on appropriate models for the backscatter and the speckle statistical properties.

4. The Multiplicative Model

The fact that, over homogeneous areas, the standard deviation is proportional to the mean suggests a multiplicative model for the speckle that has been widely used for deriving speckle reduction schemes. It has been expressed as:

$$z_{i,j} = x_{i,j} \cdot n_{i,j} \quad (5)$$

The subscripts i and j represent the spatial position of the pixel over the image; z represents the noisy observed value of the pixel, x is the original signal (backscatter) and n is the speckle noise,, with unitary mean and described by a probability density function that depends on the type of detection and the number of looks. The random variables x and n are independent.

The multiplicative model suggests that a possible method for filtering the speckle would be based on homomorphic techniques. It is based on taking the logarithm to transform the multiplicative noise into an additive one. Omitting the subscripts for simplicity, one obtains the following relation:

$$\log z = \log x + \log n \quad (6)$$

Once the additive model is obtained, there is a large number of techniques that could be used to derive noise reducing filters. At the final stage, an exponential operation is performed to obtain an estimate of the original image. Homomorphic filters have been used for speckle removal with some success by Jain and Christensen [Ref. 8], Lim and Nawab [Ref. 9], Arsenault and Denis [Ref. 10], Arsenault and Levesque [Ref. 11], Harvey and April [Ref. 12] and Franceschetti et al [Ref. 13]. It should be noted that, when the image intensity is integrated with a finite aperture and logarithmically transformed, the speckle noise is approximately Gaussian additive noise and it tends to a normal distribution much faster than the intensity distribution. This fact was used by Guo et al [Ref. 14] in their wavelet-based method for speckle reduction.

5. Lee's Filter

Lee [Ref. 15] developed a widely used local statistics filter for speckle noise reduction. A pointwise linear filter minimizing the mean square error has the form:

$$x' = x_m + b(z - x_m) \quad (7)$$

where

$$b = \text{var}(x)/\text{var}(z) \quad (8)$$

and x_m and $\text{var}(x)$ (a priori mean and variance of the original signal) can be estimated through measurements of the sample mean and sample variance of the noisy image and knowledge of the type of detection and number of looks by the expressions:

$$x_m = z_m/n_m = z_m \quad (9)$$

and

$$\text{var}(x) = \frac{\text{var}(z) - z_m^2 \sigma_n^2}{\sigma_n^2 + 1} \quad (10)$$

In the derivation of Lee's filter a first order Taylor expansion for the multiplicative model (eq. 5) is performed around the mean value. In this case, the b term of eq. (7) has the form:

$$b' = \text{var}(x)/[z_m^2 \sigma_n^2 + \text{var}(x)] \quad (11)$$

In order to apply the filter, one has to check if the value of $\text{var}(x)$ given by eq. (10) is negative. In this case, we have a very homogeneous area, $\text{var}(x)$ should be set to zero and the estimate x' is given by the local mean z_m . On the other hand, if the numerator of eq. (10) is very large, this indicates a very high contrast region (or an edge presence) and $x' = z$. These extreme cases are in accordance with the bayesian approach that is adopted in this linear minimum mean square error filter.

6. Kuan's Filter

Kuan et al [Ref. 16] and Nathan and Kurlander [Ref. 17] also developed a local linear minimum mean square error filter under multiplicative noise. The difference with respect to Lee's filter is that there is no approximation involved. The multiplicative model is exactly transformed into an additive model with uncorrelated signal and noise and the pointwise Wiener filter is derived. The local statistics are computed by the same expressions as with Lee's filter (eqs. 9 and 10) and the b term in the filter expression (eq. 7) has the exact expression:

$$b = \text{var}(x)/[z_m^2 \sigma_n^2 + (1 + \sigma_n^2)\text{var}(x)] \quad (12)$$

The same observations that were made for the limit cases in the bayesian estimation procedure for the Lee's filter are valid for Kuan's filter. In practice, it has been observed that Lee's and Kuan's filters display a very similar performance.

7. Adaptation Procedures

Several adaptation procedures were proposed to cope with space varying statistics and the presence of features like edges. Li [Ref. 18] introduced the variance ratio given by $R = \sigma_x^2/\sigma_z^2$ as a means of controlling the size of the window for computing the statistics given by eqs. (9) and (10). Under the multiplicative model, this ratio is given by:

$$R = \frac{1 - (z_m \sigma_n / \sigma_z)^2}{1 + \sigma_n^2} \quad (13)$$

This ratio varies from zero (very homogeneous areas) to one (strong contrast areas) and determines the size of the used window. Small (large) values of R indicate the use of large (small)

windows. The problem with this technique is the empirical choice of the thresholds on R to determine the window sizes.

Lopes et al [Ref. 19] proposed a modification on Lee's filter to include a lower limit (equivalent to the estimated $\text{var}(x)$ being greater or equal to zero in eq. (10)) and an upper limit on scene homogeneity, measured by the coefficient of variation σ_z/z_m . This upper limit is set experimentally or theoretically, based on several factors, like the number of looks, spatial resolution, scene properties, etc [Ref. 4]. Lopes et al [Ref. 7] introduced the use of edge detectors like the ratio detector of Touzi et al [Ref. 20] to be used in conjunction with that upper limit in order to define the shape and size of the window.

The same philosophy of limiting the size of the window was adopted by Lee [Ref. 21] in his Refined Local Statistics Filter, through the use of edge detection or by Wu and Maitre [Ref. 22] by determining the window size as a function of the maximum homogeneous region.

Lee [Ref. 23] introduced the idea of limiting the size of the averaging window to filter the speckle, by assuming a gaussian distribution and only averaging over those pixels that lie in the range of two standard deviations of the center pixel within a scanning window (that includes 95.5% of the distribution). Under the multiplicative model, this range is given by $(z - 2\sigma_n z, z + 2\sigma_n z)$, by assuming that z is the mean of the distribution.

8. Frost's Filter

A linear minimum mean square error convolutional filter for multiplicative noise reduction was proposed by Frost et al [Ref. 24]. The observed process is assumed to be further convoluted by a point spread function $h(t)$, although this blurring is ignored in the derivation of the filter, which has the form:

$$x'(t) = z(t) * m(t) \quad (14)$$

where $m(t)$ is an isotropic impulse response of the spatial filter given by an exponential expression:

$$m(t) = K_1 \alpha \exp(-\alpha|t|) \quad (15)$$

K_1 is a normalizing constant that guarantees the preservation of the mean value and α is given by:

$$\alpha^2 = (2a/\sigma_n^2)[\text{var}(x)/(\text{var}(x) + x_m^2)] + a \quad (16)$$

where x_m and $\text{var}(x)$ are evaluated by eqs. (9) and (10), respectively, over a 5×5 window and $\exp(-a)$ is the correlation coefficient between adjacent pixels of the original image $x(t)$. By assuming an autoregressive model for the original non-noisy backscatter image, Quelle and Boucher [Ref. 25] proposed an implementation of Frost's filter including an estimation of that correlation coefficient.

Although Frost's filter was shown to be not optimal [Ref. 26], it has been widely used for speckle noise reduction.

9. The Pointwise MAP Filter

An adaptive non-linear pointwise filter that satisfies the criterion of maximum a posteriori was proposed by Kuan et al [Ref. 27]. The authors assumed the multiplicative model for the speckle, one look and quadratic detection, which implies that the conditional probability density function $f(z/x)$ is exponential, with parameter x . The a priori probability density function for the signal x was supposed to be gaussian, with mean x_m and variance $\text{var}(x)$. Under these conditions, the estimate for x (x') must maximize the a posteriori probability density function $f(x/z)$, which is obtained by the Bayes rule. The estimate x' is a solution of the following third order equation:

$$x'^3 - x_m x'^2 + \text{var}(x)x' - \text{var}(x)z = 0 \quad (17)$$

The estimates for x_m and $\text{var}(x)$ are obtained by eqs. (9) and (10), respectively. Out of the three roots of the equation, x' is selected as the real, positive value that lies between x_m and z . This is in accordance with the bayesian approach of the MAP criterion, which gives a balance between the observation and the a priori mean..

The gaussian a priori density function is not a very appropriate model for describing the backscatter, which is necessarily a non-negative quantity. Therefore, Lopes et al [Ref. 28] proposed MAP estimates with densities defined on the non-negative real line, like the beta and gamma densities. The latter one has been proposed by several authors to describe the backscatter and, in the quadratic detection situation, it implies a K-distribution for the noisy signal [Refs. 29-31].

10. The ICM Filter

The natural extension of the pointwise MAP filter is to develop block filtering, taking into

consideration the correlation properties of the backscatter and/or the speckle. This possibility faces numerical difficulties due to the non-linearity of the system of equations and it was examined by Luttrell [Ref. 32].

Another possibility comes from the theory of Markov Random Fields. In this case, a bayesian framework is also adopted and the a priori global distribution of the backscatter is chosen as a Gibbs distribution. By choosing the MAP criterion, the direct solution involves a very large number of variables and the technique of simulating annealing associated with the Gibbs Sampler of Geman and Geman [Ref. 33] could be used, but with a very high computational load.

A method that provides a local optimum is the ICM (Iterated Conditional Modes), originally proposed by Besag [Ref. 34]. This method was used by Frery and Mascarenhas [Ref. 35] for the binary segmentation of SAR images and later, by increasing the number of levels of the a priori model (Multilevel Logistic or the Potts-Strauss model), by Mascarenhas and Frery [Ref. 36] for speckle filtering.

The ICM algorithm uses both the conditional probability density of the noisy observation, given the backscatter (given by the Rayleigh distribution in the case of one look and linear detection) and the conditional probability of the backscatter x at a certain pixel, given the values of the backscatter values over the neighborhood (δx) of this pixel. This last expression has the form:

$$\Pr(x/\delta x) = \exp(\beta \cdot \#(t \in \delta x : x = x_t)) \quad (18)$$

Therefore, the expression to be maximized by the choice of x at each pixel in the iterative procedure is given by:

$$\exp(\beta \cdot \#(t \in \delta x : x = x_t) \cdot (z/x^2) \exp(-z^2/2x^2)) \quad (19)$$

The 4-neighborhood was chosen and the parameter β was estimated at each cycle of the iteration by the maximum pseudolikelihood estimation procedure[Ref. 37].The iteration process was started by the pointwise maximum likelihood classification of the pixels in one of the selected number of backscatter values (from 16 to 256), using the Rayleigh probability density function.

An airborne SAR-580, L-Band, HH polarization, one-look, linear detected image over Freiburg, Germany, was used to test the ICM algorithm. Figure 2 shows the original 128x128 image and

the result of applying the Nagao Matsuyama filter [Ref. 38], for comparison. Figure 3 displays the results of the ICM with 16 and 32 levels and Figure 4 with 256 levels. There is an effective noise reduction with the ICM, as compared to the original image. It is also noticeable the effect of blocking, i.e., the noise reduction is performed by the grouping of observations with similar grey levels. The blocking effect is more pronounced with the Nagao-Matsuyama filter, yielding a visually less natural solution.

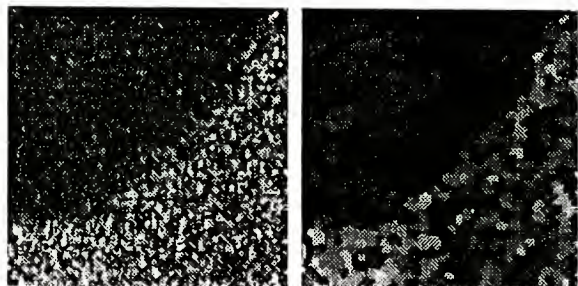


Figure 2- Original Image (l), 256 levels, and the result of applying the Nagao-Matsuyama filter (r).

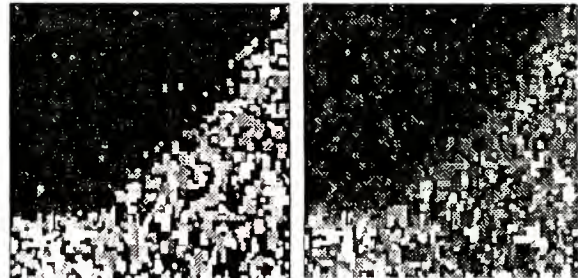


Figure 3- Filtered image with the ICM algorithm: 16 and 32 levels.

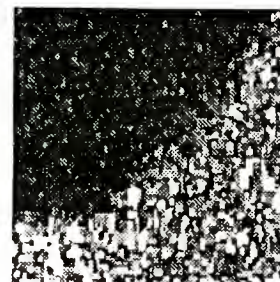


Figure 4- Filtered image with the ICM algorithm: 256 levels.

11. The Robust Filters

In general, the proposed filters for speckle noise reduction assume that all the samples come from the same distribution (eg, the Rayleigh distribution over homogeneous areas, with linear detection and one look) and are independent, given the backscatter. These assumptions may be violated, for example, over edges between different regions, by mixture of distributions, or by correlation between speckle values, due to the point spread function of the sensor. In these cases, it may be useful to derive estimators that are robust to the contamination of the samples.

Frery and Sant'Anna [Ref. 39] proposed speckle reduction filters based on the theory of robust estimation [Ref. 40]. Two kinds of robust estimators were considered: two based upon the idea of trimming extremal observations and three based on order statistics, including the median filter.

Figure 5 displays the histogram of the original image over the same area of Figure 2. It can be seen that, even though there are two distinct backscatter areas, the speckle noise completely masks the valley of the histogram. Figure 6 shows the image obtained with one of the robust filters, the trimmed maximum likelihood filter, while Figure 7 displays the corresponding histogram. The reduction of the speckle noise is quite clear, by observing the valley in the histogram.

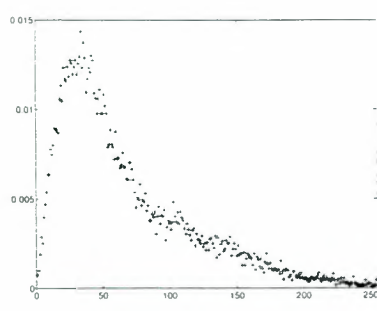


Figure 5- Histogram of the original image

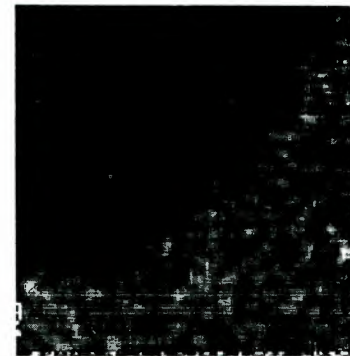


Figure 6- Trimmed maximum likelihood filtered image

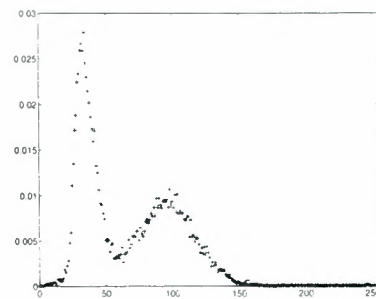


Figure 7- Histogram of the trimmed maximum likelihood filtered image

12. Filter Evaluation

The evaluation of a filter performance should consider several factors [Ref. 4]: retention of mean value over homogeneous areas, (unbiasedness), speckle reduction capability, edge sharpness and thin features preservation, point target preservation, texture preservation, computational efficiency and implementation complexity.

The speckle reduction capability is usually measured by the equivalent number of looks (ENL). For the linear detection, this quantity is evaluated over homogeneous areas by the expression:

$$\text{ENL} = 0.2732 \left(z_m^2 / \text{var}(z) \right) \quad (20)$$

For the quadratic detection the expression is:

$$\text{ENL} = (p_m^2 / \text{var}(p)) \quad (21)$$

where $p = z^2$.

An experiment was performed [Ref. 41] using the SAR-580 image, part of which is displayed in Figure 2. The image was filtered using the mean, the median, Lee, Kuan and Frost filters with a 5x5 window, as well as the filters by Lee and Kuan by incorporating Li's adaptation procedure. The number of looks was measured over homogeneous areas, where the fit of the histogram to the Rayleigh distribution was quite good. The results are summarized in Table 1 below.

Image	ENL
Original	1.0
Mean	5.5
Median	4.3
Lee	5.1
Lee - Adapt. Wind.	8.2
Kuan	5.1
Kuan - Adapt. Wind.	8.6
Frost - $\rho = 0.6$	3.8
Frost - $\rho = 0.8$	4.4

Table 1 - Equivalent number of looks for several filters, over homogeneous areas.

Edge sharpness was measured by Lee et al [Ref. 4] by using three pixel wide strips on both sides of the edge, taking the sample means and variances over these strips and the absolute difference in the means as the measure of edge sharpness. The square root of the sum of the two variances is a measure of the speckle noise level along both sides of the edge. Sant'Anna and Mascarenhas [Refs. 42, 43] used two edge detectors: a) the coefficient of variation over a 3x3 window, thresholded to the average of the three-pixel wide strip around the edge of the non-noisy image on the simulation and b) the parametric edge detector proposed by Bovik and Munson [Ref. 44]. In the first case, the figure of merit of Abdou and Pratt [Ref. 45] was used and in the second case a measure depending on the percentage of correctly and incorrectly detected as well as the percentage of non-detected edge pixels was computed.

The evaluation of one pixel wide line targets by Lee et al [Ref. 4] was made by estimating the contrast between the line and its background by using the line pixels and two one-pixel wide strips on both sides of the line. The difference between twice of the mean value of the line pixels and the mean value of the background pixels is the

measure of line preservation. A similar measure was adopted for point target preservation. Sant'Anna and Mascarenhas [Ref. 40] measured the widening of the point spread of an airborne radar to evaluate the point target preservation of different speckle reduction filters.

Retention of texture information is difficult to quantify, so the judgement is usually performed by visual inspection. In general, filters using small windows (3x3 or 5x5) have a better performance in this respect.

13. Concluding Remarks

In this paper, a brief overview of several speckle reducing filters was presented. It is very difficult to make a statement about which filter is the best. The ideal filter should perform well with respect to all items of last section.

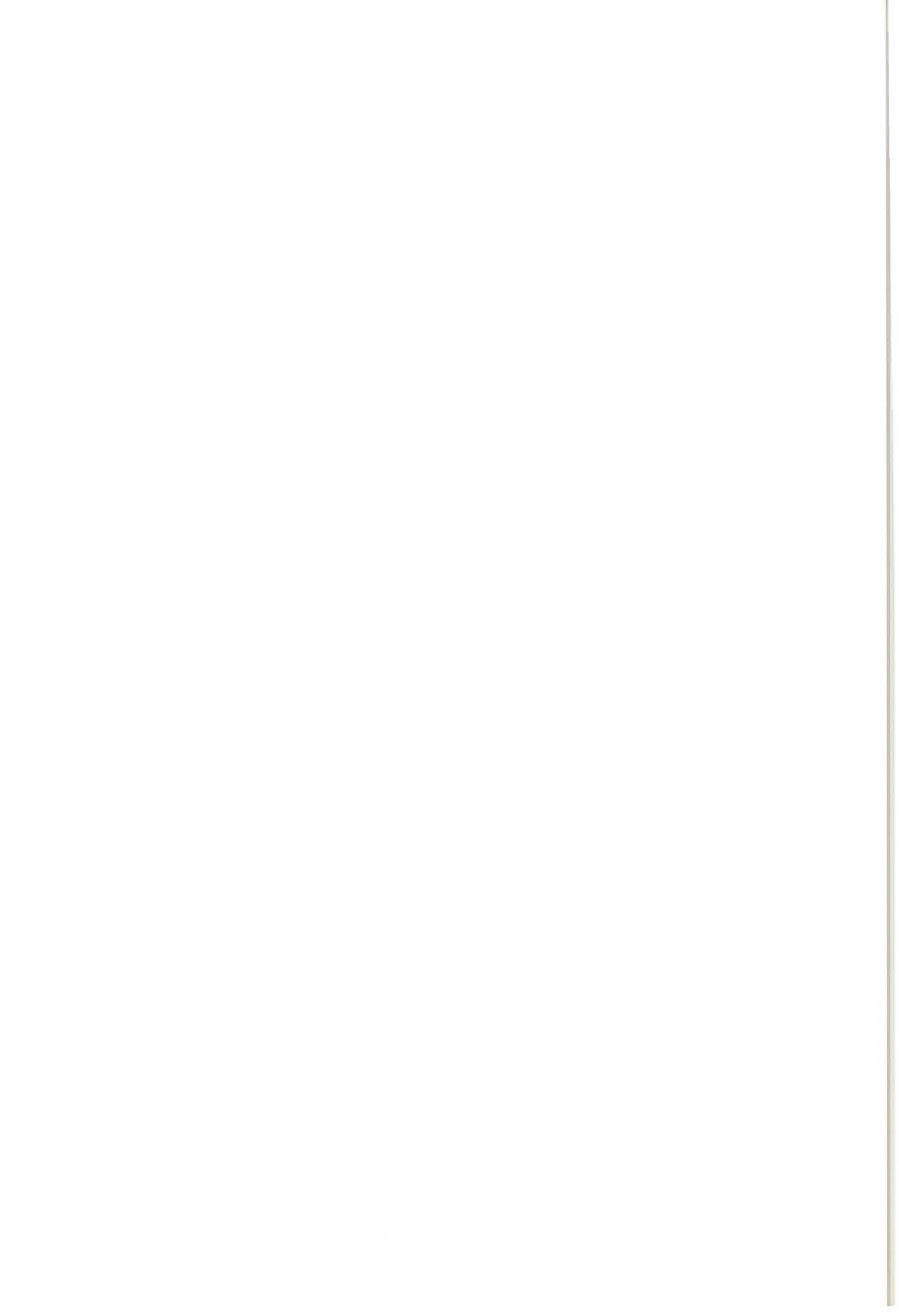
Lee et al [Ref. 4] consider the Refined Lee Filter very adequate for visual interpretation, due to preservation of edges, linear features, point targets and texture information. For segmentation, the Geometrical Filter and most of the adaptive filters, iteratively applied, are adequate, due to their very good speckle smoothing capability.

14. References

1. Durand, J. M., Gimonet, B. J. and Perbos, J. R. 1987, Speckle Filtering in SAR Images: An Evaluation of Filtering Techniques, *Adv. Space Res.*, Vol. 7, No. 11, pp. 301-304.
2. Sadjadi, F. A. 1990, Perspective on Techniques for Enhancing Speckled Imagery, *Optical Engineering*, Vol. 29, No. 1, pp. 25-30.
3. Dewaele, P., Wambacq, P., Oosterlinck A. and Marchand, J. L. 1990, Comparison of Some Speckle Reduction Techniques for SAR Images, *International Geoscience and Remote Sensing Symposium (IGARSS'90)*, pp. 2417-2422.
4. Lee, J. S., Jurkevich, I., Dewaele, P., Wambacq P. and Oosterlinck A. 1994, Speckle Filtering of Synthetic Aperture Radar Images: A Review, *Remote Sensing Reviews*, Vol. 8, pp. 313-340.
5. Crimmins, T. R. 1985, Geometric Filter for Speckle Reduction, *Applied Optics*, Vol. 24, No. 10, pp. 1438-1443.
6. Safa, F. and Flouzat, G. 1989, Speckle Removal on Radar Imagery Based on Mathematical Morphology, *Signal Processing*, Vol. 16, pp. 319-333.

7. Lopes, A., Nezri E., Touzi, R. and Laur, H. 1993, Structure Detection and Statistical Adaptive Speckle Filtering in SAR Images, International Journal of Remote Sensing, Vol. 14, No. 9, pp. 1735-1758.
8. Jain, A. K. and Christensen, C. R. 1980, Digital Processing of Images in Speckle Noise, SPIE Vol. 243, Applications of Speckle Phenomena, pp. 46-50.
9. Lim J. S. and Nawab, H. 1980, Techniques for Speckle Noise Removal, SPIE Vol. 243, Applications of Speckle Phenomena, pp. 35-41.
10. Arsenault, H. H. and Denis, M. 1983, Image Processing in Signal-Dependent Noise, Canadian Journal of Physics, Vol. 61, pp. 301-317.
11. Arsenault, H. H. and Levesque, M., Combined Homomorphic and Local-Statistics Processing for Restoration of Images Degraded by Signal-Dependent Noise 1984, Applied Optics, Vol. 23, No. 6, pp. 845-850.
12. Harvey, E. R. and April, G. V. 1990, Speckle Reduction in Synthetic-Aperture -Radar Imagery, Optics Letters, Vol. 15, No. 13, pp. 740-742.
13. Franceschetti, G., Pascazio, V. and Schirinzi, G. 1995, Iterative Homomorphic Technique for Speckle Reduction in Synthetic-Aperture Radar Imaging, Journal of the Optical Society of America A, Vol. 12, No. 4, pp. 686-694.
14. Guo, H., Odegard, J. E., Lang, M., Gopinath, R. A., Selesnick, I. W. and Burrus, C. S. 1994, International Conference on Image Processing, Austin, Texas, pp. 75-79.
15. Lee, J. S. 1980, Digital Image Enhancement and Filtering by Use of Local Statistics, IEEE Trans. on Pattern Analysis and Machine Intelligence, Vol. 2 , No. 2, pp. 165-168.
16. Kuan, D. T., Sawchuck, A. A., Strand, T. C. and Chavel, P. 1985, Adaptive Noise Smoothing Filter for Images with Signal-Dependent Noise, IEEE Trans. on Pattern Analysis and Machine Intelligence, Vol. 7, No. 2, pp. 165-177.
17. Nathan, K. S. and Curlander, J. C. 1987, Speckle Noise Reduction of 1-Look SAR Imagery, International Geoscience and Remote Sensing Symposium (IGARSS'87), pp. 1457-1462.
18. Li, C. 1988, Two Adaptive Filters for Speckle Reduction in SAR Imagery by Using the Variance Ratio, International Journal of Remote Sensing, Vol. 9, No. 4, pp. 641-653.
19. Lopes, A., Touzi, R. and Nezry, E. 1990, Adaptive Speckle Filters and Scene Heterogeneity, IEEE Trans. on Geoscience and Remote Sensing, Vol. 28, No. 6, pp. 992-1000.
20. Touzi, R., Lopes, A. and Bousquet, P. 1988, A Statistical and Geometrical Edge Detector for SAR Images, IEEE Trans. on Geoscience and Remote Sensing, Vol. 26, pp. 764-773.
21. Lee, J. S. 1981, Refined Filtering of Image Noise Using Local Statistics, Computer Graphics and Image Processing, Vol. 15, pp. 380-389.
22. Wu, Y. and Maître, H. 1990, A Speckle Suppression Method for SAR Images Using Maximum Homogeneous Region Filter, International Geoscience and Remote Sensing Symposium (IGARSS'90), pp. 2413-2416.
23. Lee, J. S. 1983, Digital Smoothing and the Sigma Filter, Computer Vision, Graphics and Image Processing, Vol. 24, pp. 255-269.
24. Frost, V., Stiles, J. A., Shanmugan, K. S. and Holtzman, J. C. 1982, A Model for Radar Images and its Application to Adaptive Digital Filtering of Multiplicative Noise, IEEE Trans. on Pattern Analysis and Machine Intelligence, Vol. 4, no. 2, pp. 157-166.
25. Quelle, H. C. and Boucher, J. M. 1990, Combined Use of Parametric Spectrum Estimation and Frost Algorithm for Radar Speckle Filtering, International Geoscience and Remote Sensing Symposium (IGARSS'90), pp. 295-298.
26. Woods., J. W. and Biemond, J. 1984, Comments on "A Model for Radar Images and its Application to Adaptive Filtering of Multiplicative Noise", IEEE Trans. on Pattern Analysis and Machine Intelligence, vol. 6, No. 5, pp. 658-659.
27. Kuan, D. T., Sawchuck, A. A., Strand, T. C. and Chavel, P. 1987, Adaptive Restoration of Images with Speckle, IEEE Trans. on Acoustics, Speech and Signal Processing, Vol. 35, No. 3, pp. 373-383.
28. Lopes, A., Nezry, E., Touzi, R. and Laur, H. 1990, Maximum a Posteriori Speckle Filtering and First Order Texture Models in SAR Images, International Geoscience and Remote Sensing Symposium (IGARSS'90), pp. 2409-2412.
29. Jackeman, E. and Pusey, P. N. 1976, A Model for Non-Rayleigh Sea Echo, IEEE Trans. on Antennas and Propagation, Vol 24, No. 6, pp. 806-814.
30. Jackeman, E. 1980, On the Statistics of K-Distributed Noise, Journal of Physics A: Math. Gen., Vol 13, No. 1, pp. 31-48.
31. Jao, J. K. 1984, Amplitude Distribution of Composite Terrain Radar Clutter and the K-Distribution, IEEE Trans. on Antennas and Propagation, Vol. 32, No. 10, pp. 1049-1061.
32. Luttrell, S. P. 1991, The Theory of Bayesian Super-Resolution of Coherent Images: A Review, International Journal of Remote Sensing, Vol. 12, pp. 303-314.

33. Geman, S. and Geman, D 1984, Stochastic Relaxation, Gibbs Distribution and the Bayesian Restoration of Images, *IEEE Trans. on Pattern Analysis and Machine Intelligence*, Vol. 6, pp. 721-741.
34. Besag, J. 1986, On the Statistical Analysis of Dirty Pictures (with Discussion), *Journal of the Royal Statistical Society B*, Vol. 48, pp. 259-302.
35. Frery, A. C. and Mascarenhas, N. D. A. 1992, Binary Segmentation of SAR Images Through the ICM Algorithm, *V Brazilian Symposium on Computer Graphics and Image Processing*, pp. 73-79 (In Portuguese).
36. Mascarenhas, N. D. A. and Frery, A. C. 1994, SAR Image Filtering with the ICM Algorithm, *International Geoscience and Remote Sensing Symposium (IGARSS'94)*, pp. 2185-2187.
37. Jensen, J. L. and Møller (s.d.) Pseudolikelihood for Exponential Family of Spatial Processes, Department of Theoretical Statistics, Institute of Mathematics, University of Arhus, Denmark.
38. Nagao, M. and Matsuyama, T. 1979, Edge Preserving Smoothing, *Computer Graphics and Image Processing*, Vol. 9, No. 4, pp. 394-407.
39. Frery, A. C. and Sant'Anna, S. J. S. 1993, Non-Adaptive Robust Filters for Speckle Noise Reduction, *VI Brazilian Symposium on Computer Graphics and Image Processing*, pp. 165-174.
40. Huber, P. S. 1981, *Robust Statistics*, John Wiley.
41. Mascarenhas, N. D. A., Ono, S. E., Fernandes, D. and Kux, H. J. H. 1991, A Comparative Study of Speckle Reduction Filters in SAR images and their Application for Classification Performance Improvement, *24th International Symposium on Remote Sensing of Environment*, Rio de Janeiro, vol. II, pp. 911-923.
42. Sant'Anna, S. J. S. and Mascarenhas, N. D. A. 1994, A Comparative Evaluation of the Resolution Loss of Speckle Noise Reduction Filters, *VII Brazilian Symposium on Computer Graphics and Image Processing*, pp. 141-148 (In Portuguese).
43. Sant'Anna, S. J. S. and Mascarenhas, N. D. A. 1996, A Comparison of the Performance of Speckle Reduction Filters, *VIII Brazilian Symposium on Remote Sensing*, article t-122 (In Portuguese).
44. Bovik, A. C. and Munson, Jr. D. C. 1986, Optimal Detection of Object Boundaries in Uncorrelated Speckle, *Optical Engineering*, vol. 25, No. 11, pp. 1246-1252.
45. Pratt, W. K. 1978, *Digital Image Processing*, John Wiley, pp. 495-499.



ROBUST STATISTICS IN SAR IMAGE PROCESSING

Oscar Humberto Bustos

Facultad de Matemática, Astronomía y Física

Universidad Nacional de Córdoba

Ph.N. 54+51+334051 - FAX 54+51+334054

e-mail bustos@mate.uncor.edu

Buenos Aires - December 3rd. 1996

Abstract

Multiplicative models are widely used to model statistical variations in SAR images. In this work we will study some distributions that work satisfactorily in adjusting SAR images. It is however important to point out that these models are based on assumptions that are not always met. In almost any conceivable image there are pixels where the value does not meet the proposed distribution. Due to this fact the usual estimators and the filters based on these models do not always perform as expected. It is therefore necessary to build models that account for this contamination. We shall see three classes of such *contamination* models that seem to be adequate for many practical situations.

1 Statistics and Robust Inference

According to Cramer (CRAMER [1]) the main objective of Statistics is to draw valid inferences from a data set. To do this in a systematic way we must propose a mathematical model. In order to do this assumptions must be made. Since we can never be sure that these assumptions are completely satisfied, it is natural looking for techniques that withstand deviations from the hypothesis. In recent years such technics have been referred to as *robust*.

It can be said (MOSTELLER and TUKEY [2]) that the history of statistical inference is a blend of optimism and skepticism about the hypothesis that the observations follow a particular distribution. A central role has been played by the normal (or Gaussian) distribution. This distribution was introduced by C. F. Gauss, who used it to adjust data involved in the determination of celestial bodies orbits. He chose the normal distribution to privilege the statistical technique that he considered most appropriate to deal with the data he was handling: the sample mean. Since then this distribution was used rather indiscriminately by the scientists. In many cases, observations that did not fit this distribution

were considered spurious and therefore discarded. Early efforts made to remedy this situation were hindered by the fact that the implementation of alternative technics lead to cumbersome computations. The historic aspects of the early period of robust estimation can be found in STIGLER [4], HUBER [6], HAMPEL [7], etc.. The articles written by HARTER ([5]). are also of interest. The spread of electronic computers and the development of non-parametric technics (in the late 50's) triggered a change of attitude towards these robustness.

Nowadays it is widely recognized the need of robust techniques in most branches of statistical inference. Some difficulties in the application of robust technics are: complexity of both, theoretical foundations and algorithms that are used to implement the techniques; lack of thorough validation of data and models, and the fact that these technics are not yet known outside the community of statisticians.

The goal of this article is to contribute to the applications of these technics in the area of analysis and processing of SAR images.

It is sometimes suggested (see HOGG [10]) that the following steps should be followed whenever a statistical analysis is carried out:

- 1) Use classic technics, for instance maximum likelihood estimation, moments estimation, least squares mean, maximum likelihood ratio test, etc.
- 2) Choose and apply a robust technique, based on a careful study of the models being applied.
- 3) If the results obtained using the robust technique do not agree with those obtained when using the standard methods, then a complete revision of both, model and data, is in order. After a careful analysis an alternative classical method can be proposed. Also a new robust technique can be set. It is important to notice that the robust method must yield results consistent with both models: the original and the alternative.

The goal is not to decide if the original model is better than the alternative one, but to cast doubts on both models, and on the data.

The best known model is the so called "measurement model". Although this model is too simple and of rather

limited applicability, it is inspiring and can suggest robust technics to be applied to more complex situations. See ANDREWS et al. [11], HUBER [12], [6], HAMPEL et al. [13], ROUSSEEUW and LEROY [9], etc.. The advantage of using a robust technique is illustrated in RELLES and ROGERS [14].

Deviations from the assumptions made a priori are more common than it is usually believed. The effects of such deviations are sometimes so severe that they can invalidate the conclusions obtained by using standard technics (see for instance HAMPEL [7] and [15]).

Deviations are introduced by the following causes: 1) discretization; 2) coarse errors like data misreading; 3) deviations from the proposed distribution; 4) preliminary condition of the model; the model is just a first approximation to the real problem.

It is interesting to mention that according to Hampel (op. cit.), data in engineering applications usually have 10 % of coarse errors. In industry related data these values may vary from 1% to 10%, and in some cases may even reach 20%. Data obtained from carefully controlled measurements in physics and astronomy are not free of such errors (from 5% to 10%). It seems that it has been a frequent practice in geodesy and astronomy to force data to fit a normal distribution. In Hampel's book we read: "normality is a myth, there has never been a normal distribution (of observations)" (GEARY [16]).

2 The Multiplicative Model

2.1 1-look Images

The multiplicative model is very successful to deal with SAR images. The basic idea is to represent each pixel by a random variable Z . If we denote the variable of interest by X the relationship between these two variables is expressed by the equation $Z = X \cdot Y$, where Y represents the noise speckle. X is a real non-negative random variable and Y is a complex random variable. RY and IY denote the real and imaginary parts of Y respectively. What is known is not usually Z , but $Z_I = |Z|^2$ or $Z_A = |Z| (= \sqrt{Z_I})$. The following notation is standard: $|Z_I|$ is the intensity image, $|Z_A|$ is the amplitude image, Y_I is the speckle intensity and Y_A is the speckle amplitude. We then have $Z_I = X^2 Y_I$ and $Z_A = X Y_A$.

In figure 1 we see an example of a SAR image.

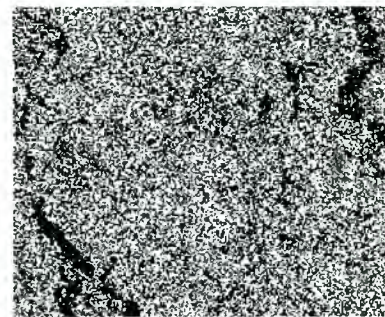


Figure 1. SAR original image

There are three types of SAR images: homogeneous, heterogeneous and very heterogeneous. Each of these type of images corresponds to a different kind of area on the earth surface. An urban area for instance yields a very heterogeneous SAR image.

The correspondences between the type of image and the variable X that are most often assumed follow. Completely homogeneous areas are represented by a constant X , let's say $\sqrt{\beta}$; in other words, X has mass 1 on $\sqrt{\beta}$, $\beta > 0$. Heterogeneous areas are represented by X with distribution $\sqrt{\Gamma}(\alpha, \lambda)$, where α and λ are positive. For very heterogeneous areas the X has distribution $N^{-\frac{1}{2}}(\alpha, \gamma, \lambda)$ (square root of an inverse Gaussian distribution).

Moments and other properties of these variables can be found in FRERY et al. [18].

It is reasonable to postulate that RY and IY are non-correlated Gaussian distributed, with zero mean and variance $1/2$. From here we can conclude that Y_I has distribution $E(1)$ (exponential with parameter 1). Y_A is $R(1)$ (Rayleigh with parameter 1) distributed. In Section 2.2 we will obtain from this the distributions of the variables Z_I and Z_A . Figure 2 shows the effect of the speckle on borders between homogeneous areas.

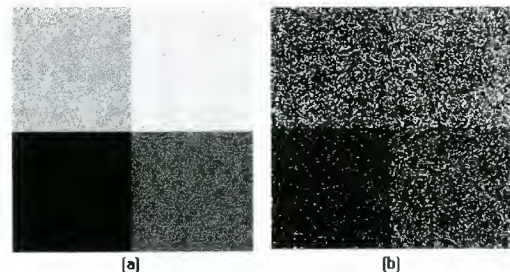


Figure 2. (a) "Original" image composed by four homogeneous field .
(b) Speckled simulated SAR image of (a)

In Figure 3 we can see the effect of the speckle on sharp edges and on point targets.

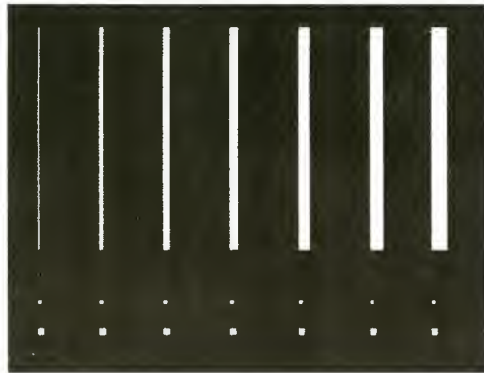


Figure 3. Original images of lines and point targets

This Figure is based on an idea found in LEE et. al. [19]. It consists of seven lines and some dots on a dark background (50.0 bytes). The lines are 1, 3, 5, 7, 9, 11 and 13 pixels wide respectively. In the bottom of the figure there are point targets of 3x3 and 5x5 pixels. In Figure 4 we see the same image with speckle.



Figure 4. Speckled simulated SAR image of Figure 3.

In statistical modelling the errors are usually considered to be additive. Therefore it is natural to look for a transformation that changes our model into an additive one. This can be done by taking logarithms: $Z = XY$ is transformed into $\log(Z) = \log(X) + \log(Y)$. Both images, the original corresponding to Z , and the transformed one (that corresponds to $\log(Z)$) are shown in Figure 5.

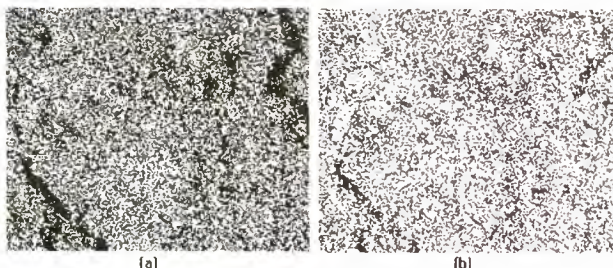


Figure 5. (a) SAR image of Figure 1. (b) Image of $\log(a)$

It is clearly seen in this example that some resolution is lost when the transformation is applied. At this moment it is interesting to call the attention to LEE et. al. [19]:

"Arsenault et al. ([20]) applied a logarithmic transformation to convert the multiplicative noise model ... to the additive noise model ... The main drawback is that the dynamic range of the original image has been logarithmically compressed. The strong signals are severely suppressed relative to the weak signals."

2.2 N-look images.

An usual technique used to reduce the speckle noise is to take the average of several independent looks of the image.

In Figure 6 we can see the result of 1-look speckle and 4-look when applied to images of very heterogeneous areas.

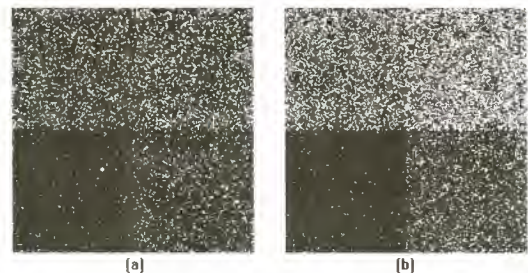


Figure 6. (a) Speckled 1-look simulated SAR image. (b) Speckled 4-look simulated SAR image.

In Figure 7 the original, the original with 1-look speckle and the original with 4-look speckle are superimposed (the image that is being processed is the upper left quadrant of Figure 6). It is clear that the distribution of the original with 4-look speckle is a better approximation to the original than the original with 1-look speckle.

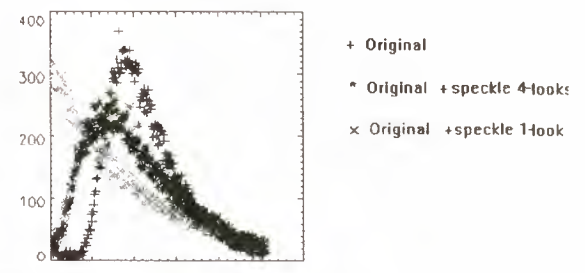


Figure 7. Comparisons of histograms.

A common practice is to obtain N independent images of the same scene (N -look) using some kind of diversity in the process of echo generation (details can be found in FERNANDES [21]). Each pixel of the intensity image of the scene is the average of the N independent intensity images (intensity look) of the same scene.

Taking into account that the backscatter function does not depend on any particular look we have: $Z_{I,N} = X^2Y_{I,N}$, where $Z_{I,N}$ is the N -look intensity speckle. The N -look amplitude speckle can be defined in two different ways: 1) as the average of N independent ampli-

tude speckle images. 2) as the square root of the N-look intensity speckle image. Accordingly there are two different ways of obtaining the N-look amplitude image. In the first case the distribution of the N-look amplitude speckle image is the convolution of Rayleigh distributions, and consequently we cannot put it in a closed form, it is therefore more convenient to adopt the second definition: $Z_{A,N} = XY_{A,N} = \sqrt{Z_{I,N}} = \sqrt{X^2Y_{I,N}}$, where $Z_{A,N}$ is the N-look amplitude image and $Y_{I,N}$ is the N-look amplitude speckle.

In LEE et. al. [19] it is pointed out that we would not obtain a reduction of the speckle if we sum the complex images. The reason for this is that the process would be equivalent to the sum of the total number of elemental sources of dispersion of the N images.

The N-look speckle intensity image is the mean of the N independent 1-look intensity images. Then the distribution of $Y_{I,N}$ is $\Gamma(N, N)$. On the other hand, and according to the definition of N-look amplitude speckle image adopted in this work, we have that $Y_{A,N}$ has distribution $\sqrt{\beta}(N, N)$. For the intensity image we have: completely homogeneous areas: If X has mass 1 on $\sqrt{\beta}$, then $Z_{I,N}$ has distribution $\Gamma(N, N/\beta)$. Heterogeneous areas: If X^2 has distribution $\Gamma(\alpha, \lambda)$ then $Z_{I,N}$ has distribution $K_I(\alpha, \lambda, N)$. Extremely heterogeneous areas: If X has distribution $N^{-1/2}(\alpha, \gamma, \lambda)$ then $Z_{I,N}$ has distribution $G_I(\alpha, \gamma, \lambda, N)$ (definitions and properties of the last two distributions can be found in FRERY et al. [18]). Regarding the amplitude image, for completely homogeneous areas, if X has mass 1 on $\sqrt{\beta}$, then $Z_{A,N}$ has distribution $\sqrt{\Gamma}(N, N/\beta)$. For heterogeneous areas, if X^2 has distribution $\sqrt{\Gamma}(\alpha, \lambda)$ then $Z_{A,N}$ has distribution $K_A(\alpha, \lambda, N)$. And for extremely heterogeneous areas, if X has distribution $N^{-1/2}(\alpha, \gamma, \lambda)$ then $Z_{A,N}$ has distribution $G_A(\alpha, \gamma, \lambda, N)$ (see FRERY et al. [18]).

Empirical evidence supports the fact that X is

$N^{-1/2}(\alpha, \gamma, 0)$ distributed, with $\alpha < 0$ and $\gamma > 0$.

The following result is often used in theoretical developments and in simulation as well: If Y is a random variable with distribution $\sqrt{\Gamma}(\eta, \gamma)$ (η and γ positive), then $X = 1/Y$ has distribution $N^{-1/2}(-\eta, \gamma, 0)$.

According to FRERY et al. [18], if $|\alpha_1|$ is strictly less than $|\alpha_2|$, then the distribution $N^{-1/2}(\alpha_1, \gamma, 0)$ corresponds to an area that is more heterogeneous than the area modeled by $N^{-1/2}(\alpha_2, \gamma, 0)$.

3 Contamination Models

Many problems may affect SAR images data and its hypothetical distributions. For instance the number of variability sources in a cell could be too small. Besides, different variability sources could contribute differently to global dispersion of the terrain backscatter.

A rather detailed exposition about this topic could be found in YANASSE [22]. In JAKEMAN and PUSEY [24] a Poisson model is proposed for SAR images. In JAKEMAN [25] it is proposed a negative binomial distribution to account for the effect of variability sources. References JAKEMAN and PUSEY [26] and OLIVER [27] consider alternatives to the multiplicative model defined and analyzed in the previous section. A model for the N-look intensity speckle for SAR multilook is proposed in APRIL and HARVEY [30]. This model is based in experimental measurements of signal-noise rate and empirical distribution of data regarding intensity images. It takes into account the correlation among different underlying looks. In YANASSE [22] it is shown that many faults can be traced to a malfunction of the remote perception system used to obtain the images globally. Data coming from wide homogeneous areas could be of help to detect the mentioned malfunction and to calibrate the system as well. Among the different classes of perturbations, those with non-zero mean in the complex images are relevant. As it was seen in Section 1, in the case of homogeneous areas, it is assumed that the observed complex image, $Z = RZ + iIZ$, satisfies that RZ and IZ are independent and identically distributed with distribution $N(0, \beta/2)$. In the case of the mentioned perturbation it is possible that $E(RZ) \neq 0$, and/or $E(iIZ) \neq 0$ due to noise in the perception system. In that case, YANASSE [22] shows that the parameters estimated by both, the Maximum Likelihood and the Moments methods, have large variances. Therefore it will not be always possible to determine if $E(RZ)$, and/or $E(iIZ)$ are different from zero.

A problem closely related to parameter estimation is Image Filtering. This problem could be assimilated as a parameter estimation problem in a moving window of just a few pixels wide.

Independence and equal distribution of observation are not fulfilled in practice. For instance in filtering windows some processed pixels could come from a region where the reigning underlying distribution varies. In this case, classical filters will just blur the borders of the fields. A reason for non independence could be correlation among the observations due to globally considered perception system. In this work we will consider only the first problem. We will follow FRERY et al. [23]. Finally we present the ϵ -contamination model. Usually the hypothesis of normality is derived from the Central Limit Theorem applied to many small perturbations. But in practice the empirical distributions have heavier tails than the Gaussian one.

The three types of “contaminated” models we will see in this review are alternative models to the standard one seen in Section 2. The standard model only allows for the possibility that the underlying distribution is not the

proposed one but some other distribution to it. It still needs the unrealistic hypothesis that pixels are independent. To achieve something closer to pixel independence it is a common practice to subsample the original images, lowering the correlation but leaving aside information. It is worth mentioning what LEE et al. [19] and ULABY [31] say: If the distance among pixels exceed the spatial resolution, then the correlation among neighboring pixels is negligible. And it continues: ... if such distance is between $r/2$ and r -where r is the spatial resolution- then there will be correlation among immediate neighboring pixels, but such correlation will again be negligible for pixels which are distant more than a pixel distance.

Besides the mentioned bibliography, for more information see RANEY and WESSELS [32] and GOLDFINGER [33].

3.1 Complex image with non zero mean

In the case of $E(RY) \neq 0$, and/or $E(IY) \neq 0$, density function of intensity image and speckle amplitude are difficult to obtain.

Let us suppose that RZ has a distribution $N(\mu_a, \sigma_a^2)$ and IZ has a distribution $N(\mu_b, \sigma_b^2)$ with $\sigma_a^2 = \sigma_b^2 = \sigma^2$. In this framework the analysis becomes simpler (see YANASSE [22]).

Below we can see the picture of the superimposed histograms of the lower left (dark area) and upper left (clear area) quadrants of the homogeneous area images. The contamination for this picture was given by a distribution with $\mu_a = 100$, $\mu_b = 0$ and $\sigma_a^2 = \sigma_b^2 = 1$.

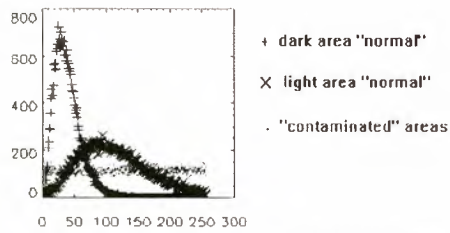


Figure 8. Comparisons of histograms of 4-look speckled SAR images.

It is remarkable the effect of this contamination in the amplitude image of edges and point targets.

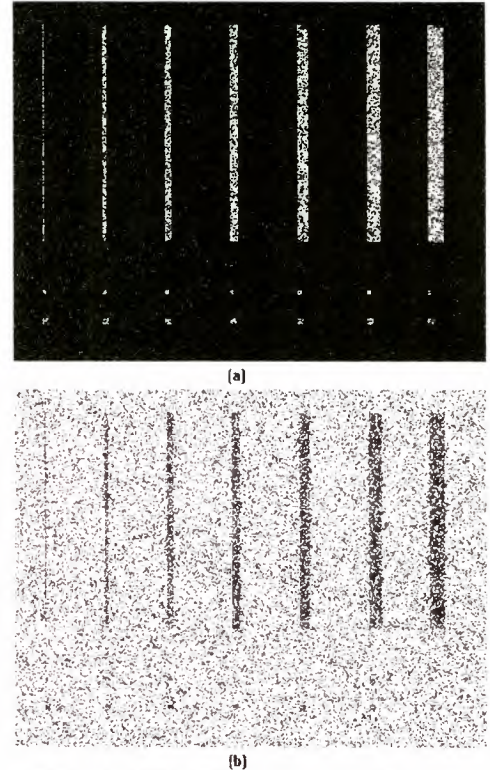


Figure 9. (a) "normal" image. (b) "contaminated" image

Our example fully agrees with the thorough analysis carried out by YANASSE [22] about the difficulty for distinguishing contaminated images with contaminated noise speckle.

Regarding distributions, under the previous hypothesis, Y_I and Y_A have respectively Ricean and Ricean modified distributions with parameters μ and σ .

3.2 Model with non identically distributed random variables

In FRERY et al. [23] it is analyzed the behavior of some filters and estimators for the case of 1-look amplitude images for homogeneous areas. It is assumed that the variables in the filter window follow a Rayleigh distribution, though not necessarily with same parameters.

Let us suppose that $Z_{A,1}, \dots, Z_{A,n}$ are random variables that represent the amplitude image in n pixels. The usual mode —let us say pure— considers that they are i.i.d. with Rayleigh distribution of parameter ξ . The alternative model -contaminated- is defined as follows: Let $\alpha > 0$, $\beta > 0$, with $\alpha + \beta < 1/2$ and $0 < \xi_0 < \xi < \xi_1$. It is assumed that $Z_{A,1}, \dots, Z_{A,[\alpha n]}$ are i.i.d. with Rayleigh distribution of parameter ξ_0 . $Z_{A,[\alpha n]+1}, \dots, Z_{A,n-[\beta n]}$ are i.i.d. as well, with Rayleigh distribution of parameter ξ . Finally, $Z_{A,n-[\beta n]+1}, \dots, Z_{A,n}$ are assumed to have Rayleigh distribution with parameter ξ_1 .

3.3 ε -contamination Model

The importance of the ε -contamination models has been

legitimated by numerous publications about applied works in the area of image processing and image analysis. See for instance KASHYAP and EOM [28] and COYLE et al. [29].

Let us see a basic example of this model. We will suppose that RY and IY are independent and identically distributed with distribution $NC(\mu_1, \sigma_1^2, \mu_2, \sigma_2^2, \varepsilon)$. We will refer to this distribution as the contaminated normal and its density will be given by $f(t) = (1 - \varepsilon)\varphi(t; \mu_1, \sigma_1^2) + \varepsilon\varphi(t; \mu_2, \sigma_2^2)$ where $\varphi(t; \mu, \sigma^2)$ is the density of normal distribution with mean μ and variance σ^2 . Therefore an observation will be generated by the distribution $N(\mu_1, \sigma_1^2)$ with probability $1 - \varepsilon$, and by the distribution $N(\mu_2, \sigma_2^2)$ with probability ε .

A more general contamination model is obtained by assuming that the observations $Z_{I,N}$ —in the N-look case— is not the theoretical one ($\Gamma(N, N/\beta)$ for homogeneous areas, $K_I(\alpha, \lambda, N)$ for heterogeneous areas and $G_I(\alpha, \gamma, \lambda, N)$ for very heterogeneous areas) but it is of the form $G = (1 - \varepsilon)F + \varepsilon H$, where F represents the distribution of the theoretical model and H the distribution of a “contaminant” variable.

The pictures below are similar to those presented above but with an ε -contamination defined by $\mu_1 = \mu_2 = 0$, $\sigma_1^2 = 0.5$, $\sigma_2^2 = 2.5$ and $\varepsilon = 0.1$.

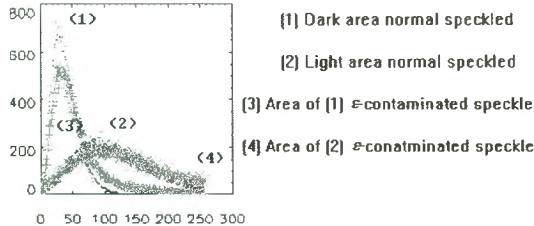


Figure 10. Comparisons of histograms.

It is worth pointing out that in this graphic, dark areas are more affected than clear areas by the contamination effects.

The ε -contamination does not affect $E(Z_{I,N})$ but it increases $Var(Z_{I,N})$. Therefore the efficiency of the Maximum Likelihood and Moments estimators will be decreased.

Regarding images with “edges” and “point targets” we can see the Figure 11.

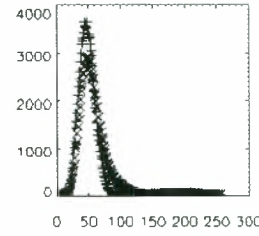


Figure 11. Comparisons of histograms from speckled images of Figure 3. {+} normal speckle. {x} ε -contaminated speckle.

In the working paper LUCINI [34] the distributions and moments of Y_I and Y_A are computed under ε -contamination model.

4 “Classic” and robust filters and estimates

We will begin this section with the basics of Parametric Inference.

Suppose we have n observations (Z_1, \dots, Z_n) from the random variable Z with density f_Z . We suppose that Z_1, \dots, Z_n are i.i.d. and distributed as Z .

Let Θ be a subset R^k ($k \geq 1$) — Θ is called the parameter space—and $f : Rx\Theta \rightarrow [0, +\infty)$ a function such that for each $\theta \in \Theta$, $f(., \theta)$ is a density. Besides, let $f(., .)$ satisfy the following condition: if θ and θ' are two different points of Θ , then the probabilities induced by $f(., \theta)$ and $f(., \theta')$ are different. As we see, the basic assumption of parametric statistics is to assume that there is a unique θ_0 such that f_Z is $f(., \theta_0)$.

Moment Method.

Let $g : R \rightarrow R$ be a real function. Suppose that $m_g(\theta) = \int g(x)f(x, \theta)dx$ exists and it is well defined for each $\theta \in \Theta$. We say that $\hat{\theta} = \hat{\theta}(Z_1, \dots, Z_n)$ is an estimator of θ_0 based on the moment of order 1 of g if $m_g(\hat{\theta}) = \frac{1}{n} \sum_{i=1}^n g(Z_i)$.

As a rule, if Θ is an open set of R^k , k functions g_1, \dots, g_k will be needed. In this case we say that $\hat{\theta} = \hat{\theta}(Z_1, \dots, Z_n)$ is an estimator of θ_0 based on the moments of order 1 of g_1, \dots, g_k if $m_{g_j}(\hat{\theta}) = \frac{1}{n} \sum_{i=1}^n g_j(Z_i)$, $j = 1, \dots, k$. In the case of $g(t) = t^r$ for $r \geq 1$ integer, it is customary to write m_r instead of m_g .

Maximum Likelihood Method.

Let $L : R^n \times \Theta \rightarrow [0, +\infty)$ the function defined by $L((z_1, \dots, z_n), \theta) = \prod_{i=1}^n f(z_i, \theta)$. We say that $\theta^* = \theta^*(Z_1, \dots, Z_n)$ is a maximum likelihood estimator of θ_0 if $L((Z_1, \dots, Z_n), \theta^*) \geq L((Z_1, \dots, Z_n), \theta)$ for all θ in Θ . If it exists $I \subset R$ an open interval such that $f(z, \theta) > 0$ for all $\theta \in \Theta$ and $z \in I$; and $f(z, \theta) = 0$ for all $z \notin I$, then θ^* could be equivalently defined

by $l((Z_1, \dots, Z_n), \theta^*) \geq l((Z_1, \dots, Z_n), \theta)$, for all $\theta \in \Theta$, where $l((z_1, \dots, z_n), \theta) = \log(L((z_1, \dots, z_n), \theta)) = \sum_{i=1}^n -\rho(z_i, \theta)$, con $\rho(z, \theta) = -\log(f(z, \theta))$. In the case of “regularity” -meaning that $f(z, .)$ is differentiable in Θ (open set in R^k)- for all $z \in I$, θ^* is determined by $\sum_{i=1}^n \psi(Z_i, \theta^*) = 0$. Where $\psi(z, \theta) = \frac{\partial}{\partial \theta} \rho(z, \theta) = \frac{\partial}{\partial \theta} f(z, \theta)/f(z, \theta)$ for all $\theta \in \Theta$ and $z \in I$.

Robust Methods: L- and M- estimators.

Without loss of generality we can suppose that $Z_i \neq Z_j$ with probability 1 for $1 \leq i \neq j \leq n$ — Z has a density—. By $(Z_{(1)}, \dots, Z_{(n)})$ let us denote the sorted observations (Z_1, \dots, Z_n) in such a way that $Z_{(1)} < \dots < Z_{(n)}$. Let a_1, \dots, a_n be real numbers such that $\sum_{i=1}^n a_i = 1$. We say that

$\bar{L} = \bar{L}((Z_1, \dots, Z_n); (a_1, \dots, a_n)) = \sum_{i=1}^n a_i Z_{(i)}$ is the L-statistics of (Z_1, \dots, Z_n) (or L-estimator) based on (a_1, \dots, a_n) .

The rationale beyond this method is that choosing an adequate vector (a_1, \dots, a_n) we can selectively weight each observation. Many classical estimators are just a particular case of L-estimators. For instance if $(a_1, \dots, a_n) = (1/n, \dots, 1/n)$ then $\bar{L} = \frac{1}{n} \sum_{i=1}^n Z_i$, what is just the sample mean. The median is an L-estimator as well.

If α is a number between 0 and $1/2$, we obtain the α -trimmed estimator by taking (a_1, \dots, a_n) in such a way that $\hat{L} = \frac{1}{n-2[\alpha]} \sum_{i=[\alpha]+1}^{n-[\alpha]} a_i Z_{(i)}$.

The M-estimators are an extension of the Maximum Likelihood Method. Let succinctly describe its rationale. It is easy to verify that if $f(z, \theta) = \frac{1}{\sqrt{2\pi}} \exp(-(z-\theta)^2/2)$ with $\theta \in R$ (density of a normal distribution with mean θ and variance 1), then θ^* is defined by:

$$\sum_{i=1}^n \rho(Z_i, \theta^*) \leq \sum_{i=1}^n \rho(Z_i, \theta),$$

where $\rho(z, \theta) = (z-\theta)^2$. Which renders $\theta^* = \frac{1}{n} \sum_{i=1}^n Z_i$. ($Z_i - \theta^*$). It is clear that those Z_i with large $(Z_i - \theta^*)^2$ — Z_i far away from the Z_1, \dots, Z_n sample mean—, will have excessive weight in the determination of the Maximum Likelihood Estimator. Taking this into account we will consider estimators of θ_0 that minimize $\theta \mapsto \sum_{i=1}^n \rho(Z_i, \theta)$ but with a more adequate ρ —instead of $\rho = -\log(f(z, \theta))$ —. After this motivation we can state the definition of an M-estimator.

Let $\rho : Rx\Theta \rightarrow [0, +\infty)$ be a real function. We say that $\theta_M = \theta_M(Z_1, \dots, Z_n)$ is an M-estimator of θ_0 defined by ρ if $\sum_{i=1}^n \rho(Z_i, \theta_M) \leq \sum_{i=1}^n \rho(Z_i, \theta)$, for all $\theta \in \Theta$. In the case that $\rho(z, .)$ is differentiable en Θ , θ_M is equivalently defined by $\sum_{i=1}^n \psi(Z_i, \theta_M) = 0$, where $\psi(z, \theta) = \frac{\partial}{\partial \theta} \rho(z, \theta)$ for all $\theta \in \Theta$ and $z \in R$.

The choice of ρ depends on the underlying model. For instance in the case $k = 1$ and $f(z, \theta) = f_0(z - \theta)$ where f_0 is a symmetric density function, it is convenient to choose $\rho(z, \theta) = \rho_0(z - \theta)$, with ρ_0 convex, symmetric, such that $\rho_0(|t|) \rightarrow +\infty$ when $|t| \rightarrow +\infty$.

If ρ_0 is differentiable, it follows that θ_M is defined by $\sum_{i=1}^n \psi_0(Z_i - \theta_M) = 0$, where ψ_0 is the derivative of ρ_0 . Notice that in the case of $\psi_0(t) \equiv t - \rho_0(t) \equiv t^2 -$, θ_M is the sample mean of (Z_1, \dots, Z_n) , while in the case of $\rho_0(t) \equiv |t|$, θ_M is the sample median of (Z_1, \dots, Z_n) . Is then clear the reason why it is possible to choose more efficient estimators than the sample median as an alternative to the sample mean by the choosing of an adequate ψ_0 . Examples of such ψ_0 ’s follow. With the choice of $\psi_0(t) = \min(|t|, c).sign(t)$, it is defined the M-estimator with ψ of Huber, which will be denoted by θ_{MH} . With the choice $\psi_0(t) = t \left(1 - \left(\frac{|t|}{c}\right)^2\right)^2$ if $|t| < c$, and 0 if $|t| \geq c$, it is defined the M-estimator with bisquare ψ . It will be denoted by θ_{MB} . In this last examples, c is a calibration constant chosen to ensure that the obtained M-estimator does not have poor efficiency under both, the “pure” and the “contaminated” models.

Regarding estimation applied to SAR, the moments estimators of the parameters of $Z_{I,N}$ and $Z_{A,N}$ with known N (remember N is the number of looks) are discussed in FRERY et al. [18]. Here the estimation is analyzed for the three types of areas above mentioned. In the case of unknown N , YANASSE et al. [35] analyzes the case when $Z_{I,N}$ is distributed as $\Gamma(N, N/\beta)$ for homogeneous areas and as $K_I(\alpha, \lambda, N)$ for heterogeneous areas. The Maximum Likelihood Estimators for $K_A(\alpha, \lambda, 1)$ are computed in FRERY [36] and for $K_A(\alpha, \lambda, N)$ with known N in JOUGHIN et al. [37].

It is worth pointing out that the main goal of image filtering is the reduction of the speckle but without losing information. The “ideal” filter should smooth the noise in an adaptive way and preserve area borders and edges information. It should preserve as well distinguishable - though perhaps subtle- details. Filters based in mean and median estimators applied in a window that sweeps the image have proved not to be very useful in SAR image processing. A possible cause of this shortcoming could be the multiplicative nature of the noise. In LEE et al. [19] there is an extensive reference list regarding multiplicative models. FRERY et al. [23] deals with filters based on L-estimators. Unfortunately, no references are known by the author of this review about M-estimators applied to SAR images.

As an illustration we show below the output of the application of filters based on the M-estimator θ_{MB} to the “edge” and “point targets” images with superimposed 4-look speckles.

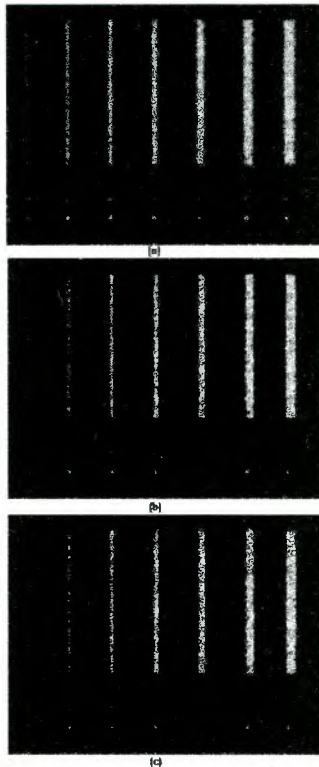


Figure 12. Filtered Images from image of Figure 9 [a].
[a] 5x5 mean filter. [b] 5x5 median filter. [c] 5x5 M-filter.

The θ_{MH} based filter was applied as well but with no major differences with the θ_{MB} output. The rather non satisfactory preliminary results could be attributed to the disregard of the multiplicative nature of the speckle. To overcome this deficiency and to make the Maximum Likelihood Estimator in SAR images more robust, it is worth implementing the use of M-estimators for the gamma distribution as proposed and analyzed in MARAZZI and RUFFIEUX [38].

5 References

- [1] CRAMER, H. (1946), Mathematical Methods of Statistics, Princeton, University Press, Princeton, New Jersey.
- [2] MOSTELLER, F. E. and TUKEY, J. W. (1977), Data Analysis and Regression, Addison Wesley, Reading.
- [3] DAVIS, C. H. (traductor) (1973), Gauss, K. F.: Theory of the Motion of the Heavenly Bodies Moving about the Sun in Conic Section, Dover Publications, Inc., New York.
- [4] STIGLER, S. M. (1973), Simon Newcomb, Percy Daniell and the history of robust estimation: 1885-1920, Journal of American Statistical Association, Vol. 68, pages. 872-879.
- [5] HARTER, H. L., The method of least squares and some alternatives, Int. Stat. Rev.; Vol. 42 (1974), pages. 147-174, 235-264, 282; Vol. 43 (1975), pages. 1-44, 125-190, 269-272, 273-278; Vol. 44 (1976), pages. 113-159.
- [6] HUBER, P. J. (1972), Robust statistics: a review, Annals of Mathematical Statistics, Vol. 43, pages. 1041-1067.
- [7] HAMPEL, F. R. (1973), Robust estimation: a condensed partial survey, Z. Wahrscheinlichkeitstheorie und Verw. Gebiete, Vol. 27, pages. 87-104.
- [8] BOX, G. E. P. (1979), Robustness in the strategy of scientific model building, in Robustness in Statistics, Launer and Wilkinson (eds.), Academic Press, New York.
- [9] ROUSSEEUW, P. J., and LEROY, A. (1987), Robust Regression and Outlier Detection, Wiley, New York.
- [10] HOGG, R. V. (1979), Statistical robustness: one view of its use in applications today, The American Statistician, Vol. 33, pages. 108-115.
- [11] ANDREWS, D. F. et alter (1972), Robust Estimation of Location: Survey and Advances, Princeton University Press, Princeton, New Jersey.
- [12] HUBER, P. J. (1964), Robust estimation of a location parameter, Annals of Mathematical Statistics, Vol. 35, pages. 73-101.
- [13] HAMPEL, F. R. et alter (1986), Robust Statistics: the Approach Based on Influence Functions, Wiley, New York.
- [14] RELLES, D. A., and ROGERS, W. H. (1977), Statisticians are fairly robust estimators of location, Journal of American Statistical Association, Vol. 72, pages. 107-111.
- [15] HAMPEL, F. R. (1977), Modern trends in the theory of robustness, Report No 13, Fachgruppe für Statistik, ETH, Zürich.
- [16] GEARY, R. C. (1947), Testing for normality, Biometrika, Vol. 34, pages. 209-242.
- [17] GRADSHTEYN, I. S. and RYZHIK, I. M. (1980), Table of integrals, series and products: corrected and enlarged edition, Academic Press, New York.
- [18] FRERY, A., C., MÜLLER, H., J., YANASSE, C., and SANT 'ANNA, S. J. S. (1995), A Model for Extremely Heterogeneous Clutter, to be published in IEEE.
- [19] LEE, J., S., JURKEVICH, I., DEWAELE, P., WAMBACQ, P., and OOESTERLINCK, A. (1994), Speckle Filtering of Synthetic Aperture Radar Images: a Review, en Remote Sensing Reviews, 1994, Vol. 8, pages. 313-340, Harwood Academic Publishers.

- [20] ARSENAULT, H. H. and LEVESQUE, M. (1984), Combined homomorphic and local-statistics processing for restoration of images degraded by signal-dependent noise, *Applied Optics*, Vol. 23 (6).
- [21] FERNANDES, D. (1993) Formação de Imagens de Radar de Abertura Sintética e Modelos da Relação “speckle”-textura, Tese de Doutorado em Ciências, Engenharia Eletrônica e Computação, Instituto Tecnológico de Aeronáutica, São José dos Campos, Brasil.
- [22] YANASSE, C. C. F. (1991), Statistical Analysis of Synthetic Aperture Radar Images and its Applications to System Analysis and Change Detection, Ph. D. Dissertation, Department of Probability and Statistics, University of Sheffield, Inglaterra.
- [23] FRERY, A., C., SANT'ANNA, S. J. S., MASCARENHAS, N., and BUSTOS, O. H. (1994), Robust Inference technics for Speckle Noise Reduction in 1-look Amplitud SAR Images, unpublished paper.
- [24] JAKEMAN, E., and PUSEY, P. N. (1973), The Statistics of Light Scattered by a Random Phase Screen, *J. Phys. A: Math., Nucl. Gen.*, Vol. 6, pages. 189-192.
- [25] JAKEMAN, E. (1980), On the Statistics of K-distributed Noise, *J. Phys. A: Math., Gen.*, Vol. 13, pages. 31-48
- [26] JAKEMAN, E., and PUSEY, P. N. (1976), A Model for Non-Rayleigh Sea Echo, *IEEE Trans. on Antennas and Propagation*, Vol. AP-24, pages. 806-814.
- [27] OLIVER, C. J. (1984), A Model for Non-Rayleigh Scattering Statistics, *Optica Acta*, Vol. 31, pages. 701-722.
- [28] KASHYAP, R. L., and EOM, K. (1988), Robust image modeling techniques with an image restoration application, *IEEE Trans. on Acoustics, Speech, and Signal Processing*, Vol. 36 (8), pages. 1313-1325.
- [29] COYLE, E. J., LIN, J., and GABBOUJ, M. (1989), Optimal stack filtering and the estimation and structural approaches to image processing, *IEEE Trans. on Acoustics, Speech, and Signal Processing*, Vol. 37 (12), pages. 2037-2066.
- [30] APRIL, G. V., and HARVEY, E. R. (1991), Speckle statistics in four-looking synthetic aperture radar imagery, *Optical Engineering*, Vol. 30 (4), pages. 375-381.
- [31] ULACY, F. T., et al. (1986), Texture information in SAR images, *IEEE Trans. Geo. Rem. Sen. Vol. 24 (2)*, pages. 235-245.
- [32] RANEY, R. K., and WESSELS, G. J. (1988), Spatial considerations in SAR speckle simulation, *IEEE Trans. Geo. Rem. Sen. Vol. 26 (5)*, pages. 666-672.
- [33] GOLDFINGER, A. D. (1982), Estimation of spectra from speckled images, *IEEE Transactions on Aerospace and Electronic Systems*, Vol. 18 (5), pages. 675-681.
- [34] LUCINI, M. M. (1996), Distribuciones y estadísticas para imágenes SAR bajo modelos de ϵ -contaminación, working paper.
- [35] YANASSE, C. C. F., FRERY, A. C., and SANT'ANNA, S. J. S. (1995), Stochastic distributions and the multiplicative model: relations, properties, estimators and applications to SAR image analysis, INPE-5630-NTC/318, INPE, São José dos Campos, Brasil.
- [36] FRERY, A. C. (1993), Some statistical tools for synthetic aperture radar image synthesis, processing and analysis, (PhD Thesis, in portuguese), INPE, São José dos Campos, Brasil.
- [37] JOUGHIN, I. R., PERCIVAL, D. B., and WINEBRENNER, D. P. (1993), Maximum likelihood estimation of K distribution parameters for SAR data, *IEEE Trans. Geo. Rem. Sen. Vol. 31 (5)*, pages. 989-999.
- [38] MARAZZI, A., and RUFFIEUX, C. (1996), Implementing M-estimators of the gamma distribution, in Robust Statistics, Data Analysis, and Computer Intensive Methods, R. Helmut (ed), Lecture Notes in Statistics 109, Springer-Verlag, Berlin.

SAR DATA FUSION

Michael Manore and Marc D'Iorio

Canada Centre for Remote Sensing
 588 Booth St., Ottawa, Ontario, Canada K1A 0Y7
 tel. +1-613-947-1281, fax. +1-613-947-1385
 email: mike.manore@ccrs.nrcan.gc.ca

Jeff Harris

Geological Survey of Canada
 1 Observatory Crescent, Ottawa, Ontario, Canada K1A 0Y7
 tel. +1-613-947-0790
 email: jeff.harris@gsc.nrcan.gc.ca

ABSTRACT

Synthetic Aperture Radar (SAR) systems can provide high-resolution, microwave brightness images of the earth's surface, typically in the 1GHz-10GHz frequency (1cm-60cm wavelength) range. These images are sensitive to the roughness, geometry and dielectric properties of targets, and thus provide geophysical measurements of the surface which are complementary to the spectral measurements captured by optical sensors, and to other sources of data such as geochemistry or rasterized colour maps. The fusion of SAR with other data sets is recognized as a useful approach for maximizing information extraction from remotely sensed data. This paper summarizes the rationale for SAR data fusion and will review image processing techniques to accomplish it. The advantages and limitations of techniques such as band combinations, band ratioing, statistical transforms and colour space transforms are discussed.

1. INTRODUCTION

Synthetic Aperture Radar (SAR) imagery such as that from ERS-1/2, RADARSAT, and aircraft provide images of radar brightness which are sensitive to the surface topography, small-scale roughness and dielectric properties of targets. Other remote sensing instruments, such as optical, thermal, and geophysical sensors measure targets in different regions of the electromagnetic spectrum or through other physical processes (e.g., gravity, magnetism). These sensors are sensitive to different target properties than the SAR, and thus provide information which is complementary and

may be usefully combined with SAR. The combination, or fusion, of these complementary data sources can result in a more complete characterization of the target than that accomplished by a single data source. This paper will identify the objectives of SAR data fusion and review common image processing techniques used to achieve it.

2. OBJECTIVES OF SAR DATA FUSION

The goal of SAR data fusion is to exploit the different information content about a target captured by SAR and other sensors in order to improve the recognition and discrimination of features in the scene. This is often accomplished by enhancing the visual interpretability of features, or through improved class separability in numeric classifications. The end-product of fusion through enhancement is typically a colour image in which the SAR and other data have been combined into an attractive, interpretable scene. The fusion of SAR for classification should result in improved classification accuracies for the classes of interest.

3. CONTRIBUTIONS FROM SAR DATA

The contributions from SAR to data fusion include target texture and landform structure, indicators of the dielectric properties of targets, and a high temporal reliability because of its all-weather imaging capabilities. In areas of moderate-to-high topographic relief, the dominant information content of SAR imagery is landform topography and geomorphology which provide useful terrain and structural information when combined with other data. In scenes of low topographic relief, SAR imagery provides good surface roughness and textural information about targets such as

variations in rock surface weathering, vegetation canopy structure and ocean surface features. The sensitivity of SAR to the dielectric properties of targets is usefully exploited for soil moisture determination in agricultural and rangeland areas, for wet snow detection in glacier mass-balance and hydrologic modelling applications, and for multi-year sea ice discrimination.

The temporal advantages of SAR over other sensors lie in the early detection of certain phenomena (e.g. early emergence of broadleaf crops versus grains [Brisco and Brown, 1995], detection of snow wetness, and the ability to image time-critical events under all weather conditions. Examples of the latter include fast-response imaging of transient phenomena such as oil spills and floods, and imaging during critical phenological windows for vegetation discrimination. Data fusion may also be applied in instances where optical imagery is unsuitable because of partial cloud cover. In this case information under the cloud may be retrievable from SAR data.

4. CONTRIBUTIONS FROM OTHER SOURCES

The information contributions from other data sources include the spectral properties of targets from optical data, thermal signatures from thermal infrared sensors, and geophysical data such as gravity and magnetics. From spectral properties general land cover classes may be derived, as well as assessments of vegetation type and condition. Thermal signatures may be used to derive sea surface temperature and ice thickness information, and may be usefully combined with SAR data to enhance ocean circulation features and sea ice structures. Thematic maps of soil or geologic units in a colour format are also common sources of detailed geophysical data that can be combined with SAR imagery. A further contribution from other data sources when fused with SAR is improved resolution. Often, optical data can provide a ‘sharpening’ effect because of the strong tonal contrasts between some classes in optical data when compared with SAR.

5. KEYS TO SUCCESS

There are a number of factors which significantly affect the success of data fusion. Harris *et al.* [1994] provide the following guidance:

- the integration strategy (i.e., the choice of data to combine and its presentation) must be driven by the detection or discrimination problem at hand. This requires that the key information content of the

different data sources be identified, and that they be preserved and enhanced in the fusion process. The identification of the key information content is entirely dependent on the data sources and the targets of interest.

- there should be a broad range of colours in an enhancement product in order to ease visual interpretability.
- the colours resulting from the data fusion should be interpretable and linked to the geophysical properties of the target of interest.
- the effectiveness of the integration relies on spatial and spectral combinations appropriate to the problem at hand.

6. PRE-PROCESSING

A common environment in which to perform SAR data fusion is within raster-based image analysis systems because SAR (and most other sources of data) originates in image format, and because the tools are available in most off-the-shelf software packages. Some ancillary data sources may originate in vector (e.g., thematic maps) or point (e.g., geochemical) format, for which conversion to raster is normally a required pre-processing step.

The data sets to be fused are required to be spatially registered, either through simple image-to-image co-registration, or more typically through geocoding to a map projection. Most software packages require that the data be resampled to a common pixel size. Data from SAR sensors should not be simply sub-sampled in order to increase the pixel spacing because this preserves speckle while reducing the useful signal in the imagery. A more appropriate procedure is to block-average the input pixels, or to Gaussian filter then sub-sample the input scene in order to increase the pixel spacing.

Filtering of SAR imagery for speckle reduction is a common pre-processing step. The choice of filters available is very large and dependent on the application. Typically, a simple median filter or statistically adaptive filter sensitive to SAR speckle distributions (e.g., Lee, Kuan, MAP) are used. Simple block averaging is also an effective speckle reduction technique if decreases in

resolution in the SAR data are acceptable for the application (e.g., small scale land use mapping, sea ice).

7. IMAGE PROCESSING TECHNIQUES

Image processing techniques for data fusion include [Harris *et al.*, 1994]:

- band combinations
- arithmetic combinations
- statistical transforms
- colour space transforms.

More recently the use of the wavelet transform for data fusion has been discussed because of its multi-resolution capabilities, but this is still considered experimental and will not be discussed in this paper. In addition, fusion may be achieved through the inclusion of SAR imagery in multi-channel classifications where the SAR (or multi-date SAR images) are treated as additional features. Also, where partial cloud affects the results of classifying an optical image, the results of a SAR-only classification may be logically combined with the incomplete optical classification in order to improve overall classification accuracy [Brisco and Brown, 1995].

Band Combinations

Band combination refers to the simple assignment of different channels of data to the Red, Green, and Blue (RGB) channels of the display device. For example:

$$\begin{array}{lcl} \text{SAR} & \rightarrow & \text{Red} \\ \text{TM4} & \rightarrow & \text{Green} \\ \text{TM3} & \rightarrow & \text{Blue} \end{array}$$

The fusion of the SAR data is achieved through simple visualization of the radar in combination with other data sets. The advantages of this technique is that it is fast, simple, easily changed and experimented with. The principle disadvantages of the technique are that only three channels of data may be combined, and that the combination may result in an unconventional and poorly-interpretable colours scheme.

Arithmetic Combinations

Arithmetic combinations of data involve the combination of multiple data channels through

arithmetic operations such as differences, ratios, and normalized differences. Common arithmetic combinations include the Normalized Difference Vegetation Index (NDVI) and the radar co-polarization ratio among many. In most cases of SAR data fusion, the SAR data is not arithmetically combined directly with optical data, but rather combinations of SAR and other data are combined then displayed in colour band combinations. An example of such a combination is:

$$\begin{array}{ll} \text{SAR (HH/VV)} & \rightarrow \text{Red} \\ \text{TM4} & \rightarrow \text{Green} \\ \text{TM5 - TM3} & \rightarrow \text{Blue} \end{array}$$

The advantages of arithmetic combinations is that they are computationally fast and simple, and they permit the integration of more than three channels. The disadvantage of this approach, like simple band combinations, is the interpretability of the unconventional colour scheme that may result from the process.

Statistical Transforms

Statistical transforms involve the transformation of original channels of data to new measurement axes in order to (typically) maximize the variance inherent in the data into the fewest possible uncorrelated channels. The most common statistical transform is Principal Component (PC) analysis. When employed for SAR data fusion, it is typically optical data that is transformed in order to reduce the number of uncorrelated features, then combined with SAR in a color band combination, such as:

$$\begin{array}{ll} \text{TM1} & \text{SAR} \rightarrow \text{Red} \\ \text{TM2} & \text{PC1} \rightarrow \text{Green} \\ \text{TM3} \Rightarrow & \text{PC2} \rightarrow \text{Blue} \\ \text{TM4} & \text{PC3} \\ \text{TM5} & \text{PC4} \\ \text{TM7} & \\ & \uparrow \\ & \text{Principal Component} \\ & \text{Transform} \end{array}$$

In this case, six optical bands from Landsat TM are reduced to four components, of which the first two are used in a band combination with SAR data. In many scenes, the first two components may account for 60%-80% of the variance within the scene, and thus represents a significant process of data reduction.

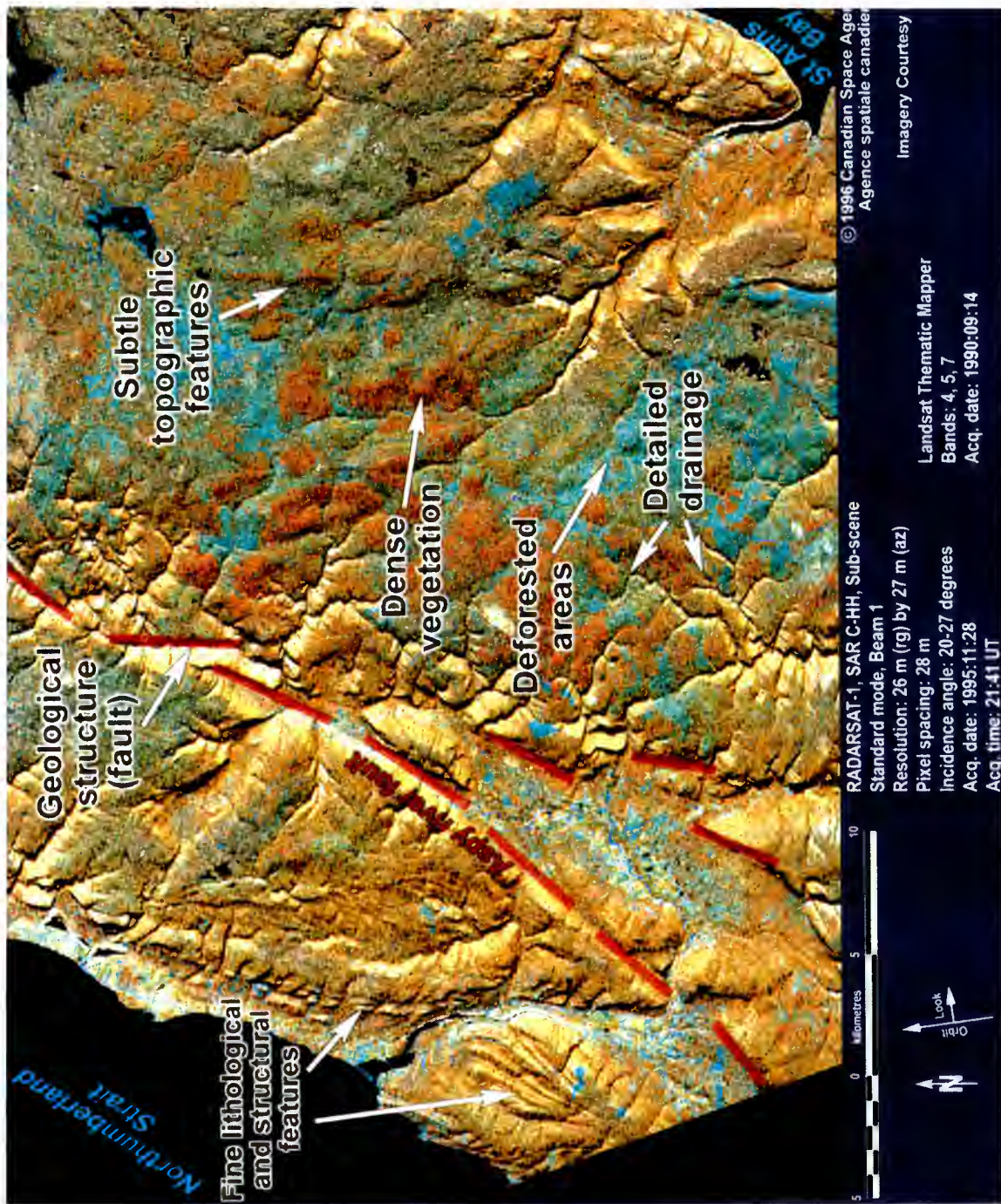
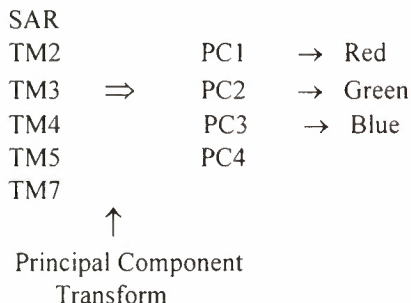


Plate 1: IHS Integration of RADARSAT SAR and Landsat TM for geology and forestry applications, Cape Breton Island, Nova Scotia, Canada. The colours in the original TM 4,5,7 band combination are preserved in this integration with SAR to facilitate interpretation. The major contribution of the SAR to the fused product is the enhancement of lithological structures and geomorphologic features.

Less common is the inclusion of SAR data (or multiple SAR images) in a statistical transform with optical data as illustrated below.



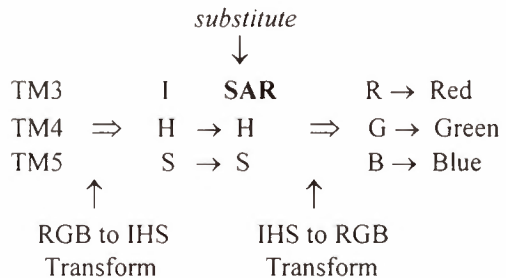
The advantages of statistical transforms is that they permit the integration of many channels of data and they reduce the information content of the original data into a small number of channels for display or classification. The disadvantages of this approach include the unconventional colours that may result in the display and the difficulty in relating these to the geophysical parameters measured in the original data set. In addition, statistical transformations are normally based on scene statistics and are therefore difficult to reproduce with different input scenes.

Colour Space Transforms

The use of colour space transforms for SAR data fusion takes advantage of the fact that single-channel SAR imagery is achromatic (i.e., without colour information), while the contribution from other sources of data is typically spectral or thematic information displayed in colour (e.g., multi-spectral imagery or colour thematic maps). Colour space transforms project the colour information represented in the Red-Green-Blue (RGB) colour space into a different set of measurement axes to describe the range of possible variations in colour tones. The most common of these alternate colour systems is the Intensity, Hue, Saturation (IHS) colour space which describes tones in terms of brightness (intensity), wavelength (hue), and the purity of the colour (saturation) [Harris *et al.*, 1990, Chavez *et al.*, 1991]. Figure 1 illustrates the relationship between the RGB and IHS colour spaces.

One result of the transformation of imagery to the IHS colour space is that all brightness information is isolated in the achromatic intensity axis. Virtually all the colour information of the original scene is captured in the hue and saturation axes. The most common technique for using the IHS transform for SAR integration involves

substituting the SAR data for the ‘intensity’ information from the original scene, and then applying the reverse transform to return the data to RGB representation. The technique is thus a two stage process as follows:



In this process, an original band combination that has a desirable colour presentation is transformed from RGB to IHS colour representation. The intensity channel is substituted with SAR imagery, and the data are transformed back to three conventional RGB channels for display. By this method the SAR imagery is imbedded in the resulting RGB channels while retaining the colours of the original band combination. Plate 1 illustrates an example of SAR fusion using the IHS transform.

Harris *et al.* [1994] describe a number of distortions and loss of information that may result from the substitution process. The principal effect that can be encountered is the loss of significant information about targets that are highly correlated in all three channels of the original band combination. These features appear achromatic (grey tones without colour) in the original image and are thus captured in the achromatic (intensity) channel in IHS colour space. When replaced by the SAR imagery, the information in the calculated intensity channel is discarded. Information about the correlated targets (which is likely to be significant) is also lost in this process. Mechanisms to overcome this inadvertent loss of information include the arithmetic combination of the calculated intensity channel with the SAR imagery (i.e., a ‘blending’ of the two sources [Harris *et al.*, 1994]), or substitution of a different IHS channel with the SAR. For instance, when substituted for Hue, the magnitude of the SAR backscatter determines the colour component of the output scene while the brightness (achromatic intensity) of the original data is retained [Kux *et al.*, 1995].

The main advantage of colour space transforms over other fusion techniques is its ability to imbed SAR information into a product while preserving the colours

of the original RGB band combination. This permits easier interpretation because of familiarity with the colours and their relationship to the geophysical properties of the target. Another attractive feature of the IHS transform is the control the user has over the degree of visibility of the SAR in the fused product through manipulation of the Saturation parameter [Harris *et al.*, 1994].

The disadvantages of colour space transforms for data fusion is their computational and conceptual complexity, the possible loss of information through substitution or distortion of hues, and that the process of achieving an attractive, satisfactory product is often one of trial-and-error. In general, there are not interactive software tools for experimenting with different transformation parameters so the process can be quite time consuming.

8. CONCLUSION

There is a large volume of literature which demonstrates the synergistic information content of SAR and other data sources, including optical imagery, geophysical and geochemical data, and thematic maps. This paper has described a number of the basic image processing techniques that may be used to fuse SAR with other data in order to fully exploit their combined information content. These techniques include visual enhancement, transformations and multi-dimensional classification, and all rely on a logical combination of the available data sources. All are commonly available in most off-the-shelf image processing systems. However, the creation of attractive fused products which preserve and enhance the information content of the input data sources remains a mix of *art* and *science*. Improved interactivity of the fusion tools and a more mature understanding of the synergistic information content of SAR and other data will be required to advance the state of the art in this area.

9. REFERENCES

Chavez, P., S. Sides, and J. Anderson 1991. *Comparison of Three Different Methods to Merge Multi-resolution and Multi-Spectral data: Landsat TM and Spot Panchromatic*, Photogrammetric Engineering and Remote Sensing, 57-3, pp 295-303.

Kux, H., F. Ahern, and R. Peitsch 1995. Evaluation of Radar Remote Sensing for Natural Resource Management in the Tropical Rainforests of Acre State,

Brazil, Canadian Journal of Remote Sensing, 21-4, pp 430-440.

Brisco, B. and R. Brown 1995. *Multidate SAR/TM Synergism for Crop Classification in Western Canada*, Photogrammetric Engineering and Remote Sensing, 61-8, pp 1009-1014.

Harris, J., R. Murray, and T. Hirose 1990. *IHS Transform for the Integration of Radar Imagery and Other Remotely Sensed Data*, Photogrammetric Engineering and Remote Sensing, 56-12, pp 1631-1641.

Harris, J., C. Bowie, A. Rencz, and D. Graham 1994. *Computer-Enhancement Techniques for the Integration of Remotely Sensed, Geophysical, and Thematic Data for the Geosciences*, Canadian Journal of Remote Sensing, 20-3, pp 210-221.

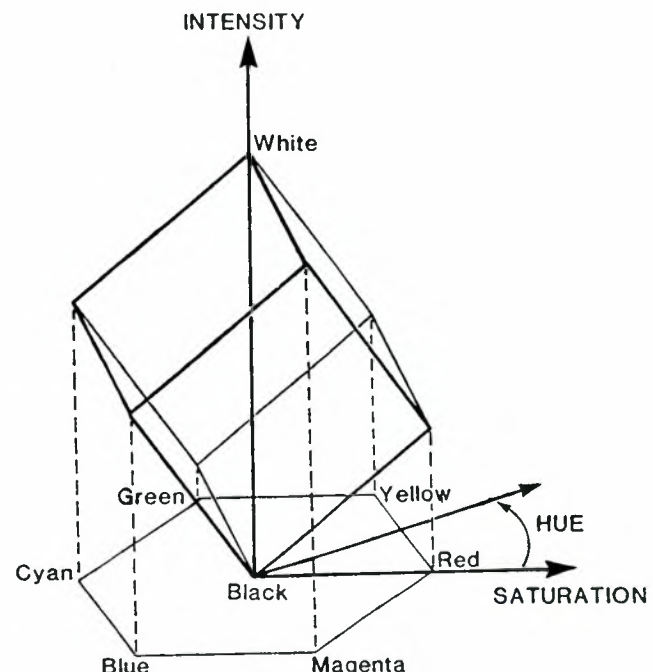


Figure 1: Relationship of RGB and IHS Colour Spaces
[from Harris *et al.*, 1990]

MAXIMUM LIKELIHOOD FITTING OF EXTREMELY HETEROGENEOUS RADAR CLUTTER

Klaus Vasconcellos†
Alejandro C. Frery‡

Universidade Federal de Pernambuco

†Departamento de Estatística
50740-540 Recife, PE, Brazil

‡Departamento de Informática
CP 7851
50732-970 Recife, PE, Brasil

ABSTRACT

The precise knowledge of the statistical properties of SAR data is widely recognized in the literature as a powerful tool for image analysis. However, little progress has been made beyond moment estimates usage for the multiplicative model. This can be explained by the difficulty of dealing with the class of \mathcal{K} distributions, which arise in this framework. A recent proposal, the family of \mathcal{G} distributions, allows the modelling of a very wide class of clutter heterogeneity. These new distributions also belong to the multiplicative model, and are characterized by as many parameters as their \mathcal{K} counterparts. A remarkable property of a particular subclass of these distributions, namely the \mathcal{G}_l^0 distributions for intensity multilook images, is that the maximum likelihood estimator of the shape parameter is attainable, given the number of looks and scaled data. This paper presents the derivation of this estimator, along with some theoretical and computational considerations about it. The second order bias of this estimator is established, therefore, yielding to an estimator which presents good sampling properties. A simulation study is conducted in order to verify that \mathcal{K}_l data designed to model extremely heterogeneous clutter can be well fitted by the \mathcal{G}_l^0 distribution.

1. INTRODUCTION

The precise knowledge of the statistical properties of SAR data plays a central role in image processing and understanding. These properties can be used to discriminate types of land use and to develop special-

ized filters for speckle noise reduction, among other applications.

The multiplicative model has been widely used in the modelling, processing and analysis of synthetic aperture radar images. This model states that, under certain conditions [Tur et al. 1982], the response results from the product of the speckle noise by the terrain backscatter. Several distributions could be used for the backscatter, aiming at modelling different types of classes and their characteristic degrees of homogeneity. For instance, for some sensor parameters (wavelength, angle of incidence, polarization, etc.), a pasture area is more homogeneous than a forest, which, in turn, is more homogeneous than urban areas.

A successful statistical model for heterogeneous areas is derived multiplying two Gamma-distributed random variables, which leads to the \mathcal{K} distribution for the intensity data. Though this distribution has proved being very useful, it has two major disadvantages: using it involves calculating the cumbersome modified Bessel function of the third kind, and the maximum likelihood estimators for its parameters cannot be obtained in a tractable form.

Many alternatives have been proposed in the literature, but most of them consist of abandoning the multiplicative model. This is not completely satisfactory, since the parameters of the distributions associated to the multiplicative model are fully interpretable in physical terms.

In this paper it is shown that a recent generalization of those distributions associated to the multiplicative model yields to a model with many advantages. It allows the modelling of extremely heterogeneous data

beyond what \mathcal{K} distributions could do, and it is also flexible enough to fit data with an underlying intensity \mathcal{K} law. It is also easy to obtain the maximum likelihood estimator of the heterogeneity parameter of this distribution, and to correct its bias up to the second order.

This paper is organized in the following manner: next section presents the multiplicative model and the distributions that arise under this assumption; section 3. presents the maximum likelihood estimator of the heterogeneity parameter of the \mathcal{G}_I^0 distribution and the second order correction of its bias is obtained; in section 4. the flexibility of this distribution is shown fitting it to \mathcal{K}_I data. Finally, section 5. presents the conclusions and possible extensions of this work.

2. MULTIPLICATIVE MODEL, SPECKLE NOISE AND INTENSITY RETURN

This section is based on [Frery et al. 1996; Frery et al. 1995a; Frery et al. 1995b; Yanasse et al. 1995]. The speckle noise is always associated to coherent-illuminated scenes, such as those obtained by microwaves, laser, ultrasonography, etc. This kind of noise appears due to interference phenomena between the incident and reflected signals.

The multiplicative model is a common framework used to explain the stochastic behavior of data obtained with coherent illumination. It assumes that the observations within this kind of images are the outcome of the product of two independent random variables X and Y , representing the terrain backscatter and the speckle noise, respectively. The former is frequently considered real and positive, while the latter can be complex (if the considered image is in complex format) or positive real (intensity format). In order to make a clear distinction between these formats, the subscripts “ C ” and “ I ” will be used for the complex and intensity cases, respectively. Vectors will be explicitly denoted in boldface.

Complex speckle, \mathbf{Y}_C , is usually assumed to have a bivariate normal distribution, with independent identically distributed components having zero mean and variance 1/2. Multilook intensity speckle appears by taking the average over n independent samples of $Y_I = \|\mathbf{Y}_C\|^2$, leading, thus, to a Gamma distribution denoted here as $Y_I \sim \Gamma(n, n)$ and characterized by the density

$$f_{Y_I}(y) = \frac{n^n}{\Gamma(n)} y^{n-1} \exp(-ny), \quad y, n > 0.$$

A recent proposal for the intensity backscatter X_I [Frery et al. 1996; Frery et al. 1995a; Frery et al. 1995b] consists of using the generalized inverse Gaussian distribution. This distribution is characterized

by the density

$$f_{X_I}(x) = \frac{(\lambda/\gamma)^{\alpha/2}}{2K_\alpha(2\sqrt{\lambda\gamma})} x^{\alpha-1} \cdot \exp\left(-\frac{\gamma}{x} - \lambda x\right), \quad x > 0, \quad (1)$$

where K_ν denotes the modified Bessel function of the third kind and order ν , with the domain of variation of the parameters given by

$$\begin{cases} \gamma > 0, \quad \lambda \geq 0 & \text{if } \alpha < 0 \\ \gamma > 0, \quad \lambda > 0 & \text{if } \alpha = 0 \\ \gamma \geq 0, \quad \lambda > 0, & \text{if } \alpha > 0. \end{cases} \quad (2)$$

The distribution defined above is denoted here as $X_I \sim \mathcal{N}^{-1}(\alpha, \gamma, \lambda)$. Its r -th order moments are given by

$$E(X_I^r) = \left(\frac{\gamma}{\lambda}\right)^{r/2} \frac{K_{\alpha+r}(2\sqrt{\gamma\lambda})}{K_\alpha(2\sqrt{\gamma\lambda})}.$$

This distribution can be reduced to several particular cases, but the following two are of special interest in our study:

1. the Gamma distribution, when $\gamma = 0$, denoted here as $\Gamma(\alpha, \lambda)$;
2. the distribution of the reciprocal of a Gamma distributed random variable, when $\lambda = 0$, denoted here as $\Gamma^{-1}(\alpha, \gamma)$.

The first special case leads to an *intensity K* distribution for the response, when the speckle is Gamma distributed [Yanasse et al. 1995]. The second yields to the model that will be discussed here. For detailed properties and applications of the $X_I \sim \mathcal{N}^{-1}(\alpha, \gamma, \lambda)$ distribution, the reader is referred to [Barndorff-Nielsen and Blæsild 1981; Jørgensen 1982].

If $X_I \sim \mathcal{N}^{-1}(\alpha, \gamma, \lambda)$ and $Y_I \sim \Gamma(n, n)$, then, the product $Z_I = X_I \cdot Y_I$ has a distribution which we call the *intensity G distribution*. This distribution will be denoted here by $\mathcal{G}_I(\alpha, \gamma, \lambda, n)$. It can be characterized by the density

$$f_{Z_I}(x) = \frac{n^n (\lambda/\gamma)^{\alpha/2}}{\Gamma(n) K_\alpha(2\sqrt{\lambda\gamma})} x^{n-1} \cdot \left(\frac{\gamma + nx}{\lambda}\right)^{\frac{\alpha-n}{2}} \cdot K_{\alpha-n}(2\sqrt{\lambda(\gamma + nx)}), \quad x > 0,$$

with $n > 0$ and $(\alpha, \gamma, \lambda)$ as in (2).

This distribution for the intensity response is quite general. On the other hand, its estimators are very hard to obtain by maximum likelihood. In [Frery et

al. 1996], it was shown that the particular case when $X_I \sim \Gamma^{-1}(\alpha, \gamma)$ leads to a special distribution for Z_I , denoted the $\mathcal{G}_I^0(\alpha, \gamma, n)$ distribution. This distribution has the following nice properties:

1. its density only involves simple functions, since it is given by

$$f_{Z_I}(x) = \frac{n^n \Gamma(n - \alpha) x^{n-1}}{\gamma^\alpha \Gamma(n) \Gamma(-\alpha) (\gamma + nx)^{n-\alpha}}, \quad (3)$$

with $-\alpha, \gamma, n, x > 0$.

2. it allows the modelling of homogeneous, heterogeneous and very heterogeneous clutter; specifically, data from deforested areas, from primary forest and from urban areas are very well fitted by this distribution;
3. its cumulative distribution function is easily obtained, since the \mathcal{G}_I^0 distribution is readily seen to be proportional to the well-known Snedecor F distribution, in the sense that

$$-\frac{\alpha}{\gamma} \mathcal{G}_I^0(\alpha, \gamma, n) \sim F(2n, -2\alpha).$$

As the F distribution arises in many important statistical problems, its cumulative distribution function is obtainable in a wide variety of statistical systems. We have, then, an easy form of obtaining the cumulative distribution function for the \mathcal{G}_I^0 distribution, by using standard statistical routines for the F distribution.

The relationships between the aforementioned distributions for intensity backscatter are summarized in Fig. 1, where “ $\xrightarrow{\mathcal{D}}$ ” denotes convergence in distribution.

The parameter α is of particular interest in this study, since it is directly related to the roughness of the target. It is easy to check that if the outcomes of N independent $\mathcal{G}_I^0(\alpha, \gamma, n)$ -distributed random variables are multiplied by the factor

$$\frac{(n-2)\mathbb{E}(Z_I^{-2})}{2\mathbb{E}(Z_I^{-1})} - \frac{(n-1)\mathbb{E}(Z_I^{-1})}{n}$$

then, the scaled observations are the outcomes of N independent $\mathcal{G}_I^0(\alpha, 1, n)$ -distributed random variables. Since the number of looks n is known (and can be assumed integer) and the k th-order moments of the sample can be easily obtained, it is enough to study the inference of the parameter α for the $\mathcal{G}_I^0(\alpha, 1, n)$ distribution. It must be stressed here that this procedure only works if $n > 2$, which guarantees that the moments in the above equation will be finite.

This scaling technique could also be performed with the aid of positive moments of Z_I , typically the first and the second ones. However this leads to restrictions on the values of α , which in practice becomes a serious problem since the true value of α is unknown.

3. MAXIMUM LIKELIHOOD ESTIMATOR

Maximum likelihood estimation for the aforementioned distributions is, in general, a difficult task. In particular, the K distribution was treated in [Joughin et al. 1993; Lombardo and Oliver 1994; Raghavan 1991]. In this section it will be shown that it is possible to derive the maximum likelihood estimator for the parameter α of the $\mathcal{G}_I^0(\alpha, 1, n)$ distribution, provided n is integer and known. Also, the second-order bias of this estimator is derived and, thus, a corrected version with better sampling properties is obtained.

Assume $\mathbf{z} = (z_1, \dots, z_N)$ are the outcomes of N independent identically distributed $\mathcal{G}_I^0(\alpha, 1, n)$ random variables where n is a known natural number.

From eq. (3), denoting $\eta = -\alpha$ and $w_i = \ln(1 + nz_i)$, it is immediate that the reduced log-likelihood of the sample is

$$\ell(\mathbf{w}, \eta) = N \ln \left(\frac{\Gamma(n + \eta)}{\Gamma(\eta)} \right) - \eta \sum_{i=1}^N w_i. \quad (4)$$

From eq. (4) it is possible to derive the maximum likelihood estimator of η , which is given by the solution $\hat{\eta}$ of the equation:

$$\sum_{p=0}^{n-1} \frac{1}{\hat{\eta} + p} = \bar{w}. \quad (5)$$

Since

$$\frac{\partial^2 \ell(\mathbf{w}, \eta)}{\partial \eta^2} = -N \sum_{p=0}^{n-1} \frac{1}{(\eta + p)^2} < 0,$$

the reduced log-likelihood is concave. This shows there is only one solution for eq. (5) in $(0, \infty)$; therefore, $\hat{\eta}$ satisfying this equation is the global maximum. It is also worthy noting that solving eq. (5) is a very easy numerical task.

Also note that $\mathbb{E}(-\partial^2 \ell(\mathbf{w}, \eta)/\partial \eta^2)$ gives the total Fisher information of the unknown parameter η . It can be readily seen that this information increases with n , the number of looks; this is consistent with the fact that the bigger the number of looks the better the signal-to-noise ratio in the image.

Cox and Snell [Cox and Snell 1968] provide the following formula for the second-order correction of the bias

$$\mathbb{E}(\hat{\eta}_N) - \eta = \frac{B_1(\eta, N)}{N} + \frac{B_2(\eta, N)}{N^2} + \dots,$$

of the estimator $\hat{\eta}_N$, based on N observations:

$$\frac{B_1(\eta, N)}{N} = K_2^{-2} \left(\frac{1}{2} K_3 + K_{2,1} \right),$$

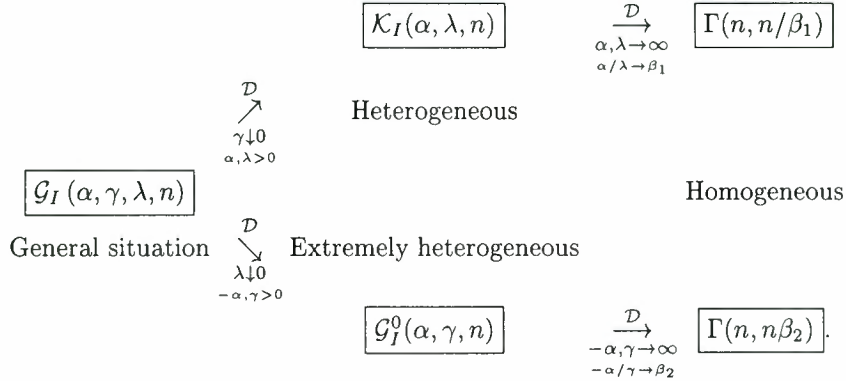


Figure 1: Limiting properties of intensity return distributions, and associated targets.

where

$$\begin{aligned}
 K_2 &= E\left(\frac{\partial^2 \ell(\mathbf{w}, \eta)}{\partial \eta^2}\right), \\
 K_3 &= E\left(\frac{\partial^3 \ell(\mathbf{w}, \eta)}{\partial \eta^3}\right), \\
 K_{2,1} &= E\left(\frac{\partial^2 \ell(\mathbf{w}, \eta)}{\partial \eta^2} \frac{\partial \ell(\mathbf{w}, \eta)}{\partial \eta}\right).
 \end{aligned}$$

For the considered case, the second-order correction is given by

$$B_1(\eta, N) = \frac{\sum_{p=0}^{n-1} (\eta + p)^{-3}}{\left(\sum_{p=0}^{n-1} (\eta + p)^{-2}\right)^2}. \quad (6)$$

Therefore, for one look data where $n = 1$, this correction reduces to $B_1(\eta, N) = \eta$.

4. SIMULATION RESULTS

We have performed two simulation studies in order to assess the adequacy of the G_I^0 distribution in fitting K_I distributed data for a very heterogeneous parameters space.

In both simulations the equivalent number of looks was set to $n = 4$ and the scale parameters λ and γ were fixed in 1. For the first simulation we used the homogeneity parameter $\alpha = 1/2$, and for the second, $\alpha = 1$ was chosen. Notice that, as presented in Fig. 1, these two situations are far from being homogeneous. Samples sizes of $N = 10000$ were used in both cases.

The methodology employed is as follows for each value of $\alpha = 1/2, 1$:

1. Generate $\mathbf{z} = (z_1, \dots, z_N)$, independent observations of the random variable $Z_I \sim K_I(\alpha, 1, 4)$.

2. Calculate $\hat{\alpha} = \hat{\alpha}(\mathbf{z})$, maximum likelihood estimator of the parameter α of the $G_I^0(\alpha, 1, 4)$ fitted distribution with eq. (5).
3. Draw in the same plot the densities of the true $K_I(\alpha, 1, 4)$ and the estimated $G_I^0(\hat{\alpha}, 1, 4)$ distributions.

Figs. 2 and 3 show the results of the aforementioned experiences, corresponding to $\alpha = 1/2$ and $\alpha = 1$, respectively. In both of these graphs the true density has zero mode. It can be seen from both graphs that for these small values of α , corresponding to extremely heterogeneous radar clutter models, the proposed technique seems to work very well in fitting the true K_I distribution by the estimated G_I^0 one.

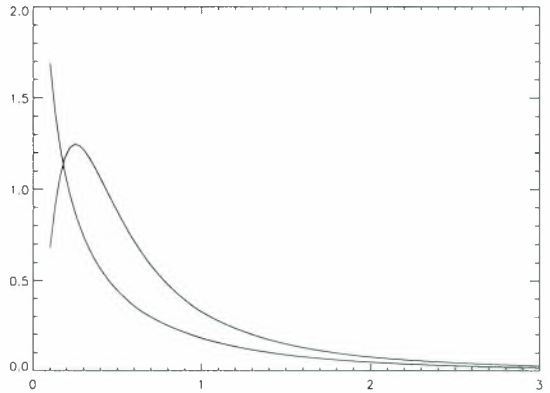


Figure 2: True $K_I(1/2, 1, 4)$ and estimated $G_I^0(\hat{\alpha}, 1, 4)$ densities.

5. CONCLUSIONS

A recent proposal for the intensity backscatter is the use of the generalized inverse Gaussian distribution.

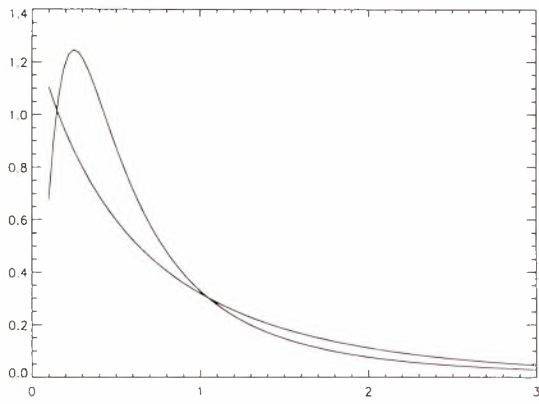


Figure 3: True $\mathcal{K}_I(1, 1, 4)$ and estimated $\mathcal{G}_I^0(\hat{\alpha}, 1, 4)$ densities.

This yields to a general distribution for the response, called Intensity \mathcal{G} distribution. We have discussed the particular case when the intensity backscatter can be modelled by an inverse Gamma distribution, leading to a special case of the Intensity \mathcal{G} which is the \mathcal{G}_I^0 distribution.

This \mathcal{G}_I^0 distribution has some nice properties, as being proportional to the classical Snedecor F distribution. We have derived the maximum likelihood estimator for a scaled version of the \mathcal{G}_I^0 distribution, and shown that this estimator can be easily obtainable as the only positive real root of a polynomial.

The second order bias correction for this estimator is also derived, and it is shown to be easily computed. This correction is important when the number of observations or the total information is relatively small.

Finally, we present some simulation results concerning the adaptability of the \mathcal{G}_I^0 distribution. In this study \mathcal{K}_I data with high heterogeneity is simulated and fitted by \mathcal{G}_I^0 distribution with success.

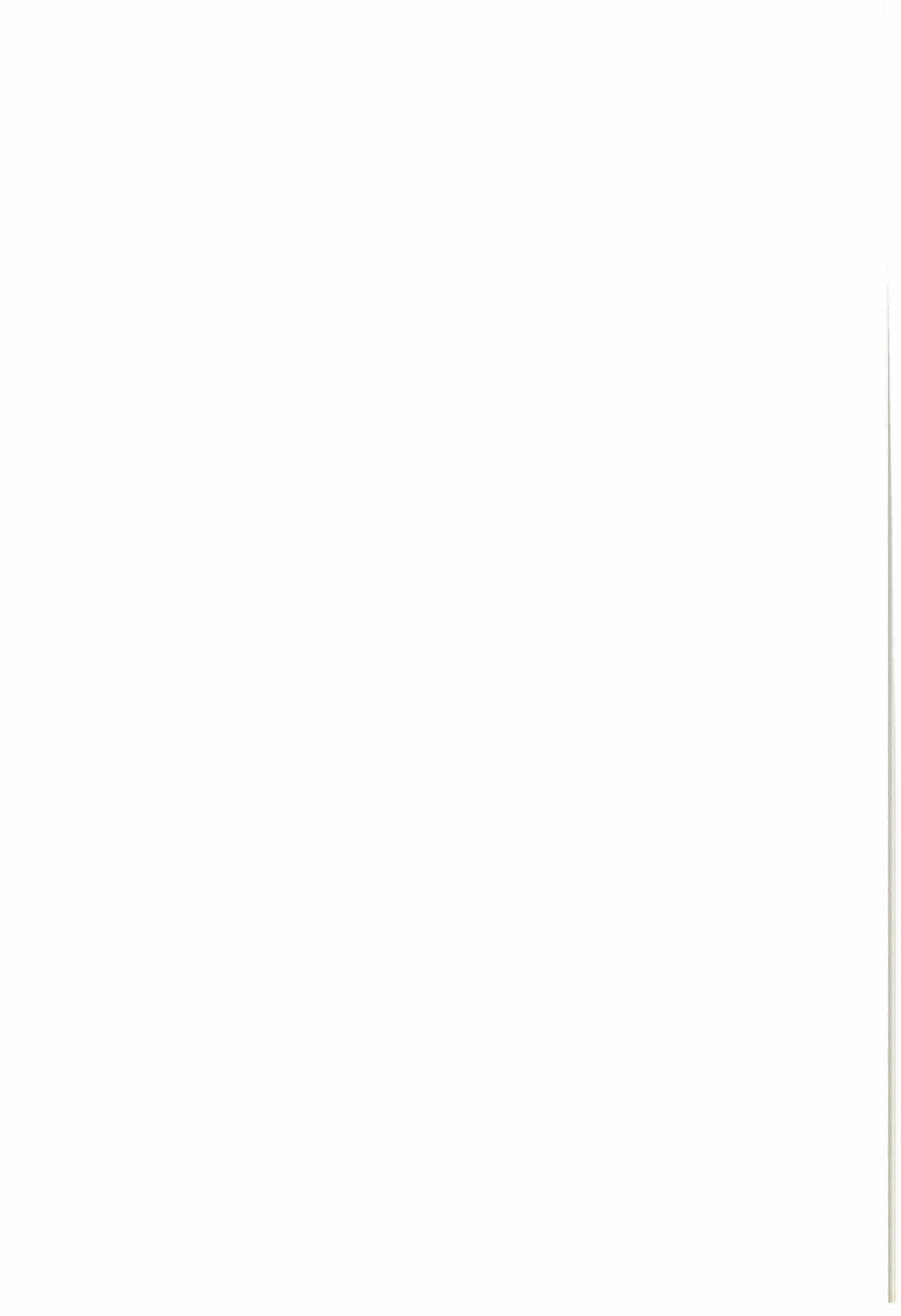
This work will proceed extending the presented results to the more general \mathcal{G}_I model and, if possible, for the amplitude and complex formats.

ACKNOWLEDGEMENTS

The authors are grateful to CNPq-Brazil that partially supported this work through project PROTECM-CC GEOTEC 680.061-94-0.

REFERENCES

- O. E. Barndorff-Nielsen and P. Blæsild. Hyperbolic distributions and ramifications: contributions to theory and applications. In C. Taillie and B. A. Baldessari, editors, *Statistical distributions in scientific work*, pages 19–44. Reidel, Dordrecht, 1981.
- D. R. Cox and E. J. Snell, “A general definition of residuals (with discussion),” *Journal of the Royal Statistical Society B*, vol. 30, pp. 248–275, 1968.
- A. C. Frery, H. J. Müller, C. C. F. Yanasse, and S. J. S. Sant’Anna. A model for extremely heterogeneous clutter. *IEEE Transactions on Geoscience and Remote Sensing*, 1996, in press.
- A. C. Frery, C. C. F. Yanasse, and S. J. S. Sant’Anna. Alternative distributions for the multiplicative model in sar images. In *Quantitative remote sensing for science and applications*, pages 169–171, Florence, Jul. 1995. IEEE. IGARSS’95 Proc.
- A. C. Frery, C. C. F. Yanasse, and S. J. S. Sant’Anna. Statistical characterization of SAR data: the multiplicative model and extensions. In *Latinoamérica evaluada desde el espacio*, pages 502–515, Mexico, Nov. 1995. SELPER.
- B. Jørgensen. *Statistical properties of the generalized inverse Gaussian distribution*, volume 9 of *Lecture Notes in Statistics*. Springer-Verlag, New York, 1982.
- I. R. Joughin, D. B. Percival, and D. P. Winebrenner. Maximum likelihood estimation of K distribution parameters for SAR data. *IEEE Transactions on Geoscience and Remote Sensing*, 31:989–999, 1993.
- P. Lombardo and C. J. Oliver, “Estimation of texture parameters in K-distributed clutter,” *IEE Proceedings in Radar, Sonar and Navigation*, vol. 141, no. 4, pp. 196–204, August 1994.
- R. S. Raghavan, “A method for estimating parameters of K-distributed clutter,” *IEEE Transactions on Aerospace and Electronic Systems*, vol. 27, no. 2, pp. 238–246, March 1991.
- M. Tur, K. C. Chin, and J. W. Goodman. When is speckle noise multiplicative? *Applied Optics*, 21:1157–1159, 1982.
- C. C. F. Yanasse, A. C. Frery, and S. J. S. Sant’Anna. Stochastic distributions and the multiplicative model: relations, properties, estimators and applications to SAR image analysis. Technical Report 5630-NTC/318, INPE, São José dos Campos, SP, Brazil, 1995.



Bitslice Noise Reduction using Mathematical Morphology

ANA LÚCIA BEZERRA CANDEIAS¹
ALEJANDRO C. FRERY²

¹DPI/INPE–Divisão de Processamento de Imagens
Instituto Nacional de Pesquisas Espaciais
Av. dos Astronautas, 1758 12227–010
São José dos Campos, SP, Brazil
phone: + 55 12 3256471 fax: + 55 123256460
analucia@dpi.inpe.br

²Departamento de Informática
Universidade Federal de Pernambuco
CP 7851, 50732–970
Recife, PE, Brazil
phone: + 55 812718430 fax: + 55812718438
frery@di.ufpe.br

ABSTRACT

This paper presents a noise reduction proposal based on the application of binary morphological operation to bitslices of images. The technique is applied to real and simulated synthetic aperture radar images, and it is evaluated with a methodology based on statistical measures. This nonlinear one step procedure is shown to reduce the high grey level noise.

1. INTRODUCTION

It is well known that synthetic aperture radar (SAR) images are corrupted by a signal dependent noise called speckle. Many filtering techniques have been proposed in literature (see, for instance, [Ref. 4]), and most of these filters are based on some statistical properties of the data. A complete account of the statistical properties of amplitude SAR data can be seen in [Ref. 2].

Mathematical Morphology is a non linear approach to signal processing, which proved its usefulness in image information extraction and in noisy data filtering. It is based on mappings between complete lattices in terms of some families of simple (*elementary*) transformations: dilations, erosions, anti-dilations, anti-erosions. Those mappings are built by combining these elementary transformations through the union, intersection and composition operations [Ref. 1].

Mathematical Morphology was initiated by G. Matheron and J. Serra at the École des Mines de Paris. It is called “Morphology” since it aims at analysing the shape of objects. It is “Mathematical” in the sense that this analysis is based on set theory, topology, lattices, etc. This theory ranges from binary (where the linear image processing approach was not efficient) to grey scale image analysis.

In this paper, binary morphological operations are applied to bitslices of images, aiming at reducing speckle noise. Instead of making a statistical approach to the observed grey levels, it is assumed that the noise creates small black (white resp.) spots over white (black resp.) fields, and binary operations are applied in order to reduce the extent and intensity of these spots before reconstructing the image.

There is a connection between this method and the statistical modelling of the data. It arises assuming that every bitslice is the outcome of a binary Markov random field (possibly an Ising model with a convenient neighbourhood structure) corrupted by binary noise. The “filter” is constructed looking for uncorrupted versions (estimators) of every bitslice. Though this approach will not be followed in this paper, it is interesting to bear in mind this connection.

2. DEFINITIONS AND NOTATION

Consider a finite rectangular lattice of the form $E = \{0, \dots, m-1\} \times \{0, \dots, n-1\}$. In every $s \in E$ a grey level $y(s) \in K = \{0, \dots, k-1\}$ is observed. Therefore, an image $\mathbf{y} = (y(s))_{s \in E}$ can be seen as a function $y : E \rightarrow K$ or an element of K^E . Consider f, g, f_n generic elements of K^E .

Assuming that every observed value is a byte, it can be represented as $y(s) = [b^7(s), \dots, b^0(s)]$, the bits (from most to least significative) forming the byte observed in s . Other usual image formats ($k = 2^{16}$ for instance) also lead to this representation.

The *bitslice* decomposition of the byte image \mathbf{y} consists of the eight binary images $b^p : E \rightarrow \{0, 1\}$, with $7 \geq p \geq 0$, given by the observed bits in every coordinate, denoted by $\mathbf{y} = [b^7, \dots, b^0]$, where $b^p = (b^p(s))_{s \in E}$.

Efficient algorithms for this bit image extraction are available in most programming languages, and an

arithmetic approach can be seen in [3]. Conversely, it is clear that restoring a grey level image from its bitslices is an easy task. This one-bit plane representation can be also used for image compression.

Figure 1 presents a greyscale image and its eight slices, ordered from most (b^7) to least (b^0) significative (bearing most to least information, respectively). The reader may notice that there is evident information up to the fourth bitslice, and with some effort some structure can be seen in the fifth.



Fig. 1 – Greyscale image and its eight bitslices (left to right, top to bottom most to least significative bit plane).

The methodology here proposed for noise reduction consists of restoring the bitslices using mathematical morphology binary transformations, and then reconstructing the “filtered” image by stacking the bit planes.

Denote the set of integers as Z , and let B be a subset of Z^2 called *structural element*. The translation of B by any vector $h \in Z^2$ is denoted by B_h and given by $B_h = \{s + h \in Z^2 : s \in B\}$. The transpose of B is denoted by B' and defined by $B' = \{-s \in Z^2 : s \in B\}$.

The *dilation of f by B* is the function $\delta_B(f) \in K^E$, given by, for any $s \in E$ by

$$\delta_B(f) = \max \{f(s) : s \in B_s \cap E\}.$$

The *erosion of f by B* is the function $\varepsilon_B(f) \in K^E$, given by, for any $s \in E$ by

$$\varepsilon_B(f) = \min \{f(s) : s \in B_s \cap E\}.$$

In these definitions the conventions $\max(\emptyset) = 0$ and $\min(\emptyset) = k$ were used.

The transformations γ_B and ϕ_B from K^E to K^E , given by the following compositions

$$\gamma_B = \delta_B \varepsilon_B, \text{ and}$$

$$\phi_B = \varepsilon_B \delta_B,$$

are called respectively, morphological opening and closing with respect to B . More details about these transformations can be seen in [Ref. 1].

An opening (closing, resp.) transformation removes small spurious regions of white (black, resp.) pixels in regions smaller than the size of B . These transformations are called morphological filters [Ref. 5], and this class of filters is very important because its members exhibit one-step convergence (they are idempotent operators).

3. METHODOLOGY

Let $f = [b^7, b^6, b^5, b^4, b^3, b^2, b^1, b^0]$ be the original image and its bitslice decomposition. Assume that it is desirable to reduce the noise present in f , and that morphological binary operations will be used to filter $[b^7, \dots, b^0]$. Amongst the many ways to tackle this task, two specifications have to be made:

1. Which bitslices will be filtered?
2. Which operations will be applied in order to filter the chosen bitslices?

The theoretical answer for both questions is beyond the scope of this work, and unknown to the authors.

The spurious noise in a slice is represented by small areas with black and white spots. Closing and opening transformations reduce small spurious regions of white and black pixels, so they are well adapted to solve this kind of problem. Remains open the question of the structuring element to be used.

Regarding which bitslices will be subjected to the filtering, it is intuitive that the more bitplanes filtered the smoother should be the final image, and that the computational effort is proportional to the number of filtered slices. Also, since most of the information lies in the most significant bitslices those are the *natural* candidates to be filtered. Figure 2 shows the general methodology representation.

An empirical approach is here proposed, based on the use of a simulated image. A true image (phantom) exhibiting two homogeneous areas, one dark one bright, is corrupted by one look amplitude speckle noise in a multiplicative manner [Ref. 2, 6]. The original and corrupted images are shown in Figure 3. The phantom here considered allows the simultaneous evaluation of noise reduction (over homogeneous areas) and the preservation of fine details (points and lines).

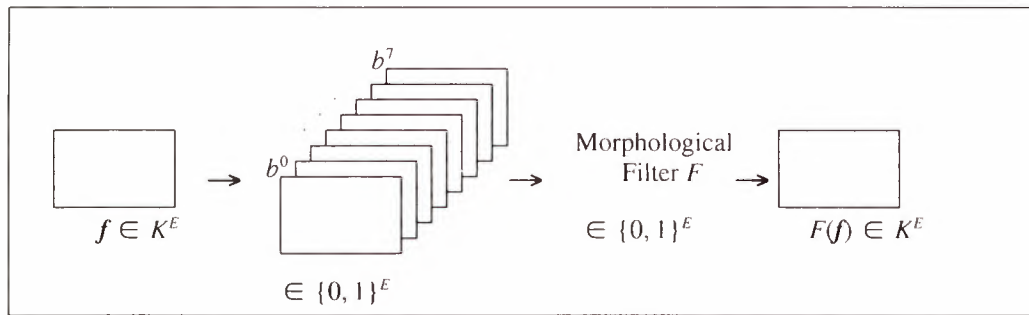


Fig. 2 – Representation of proposed methodology.

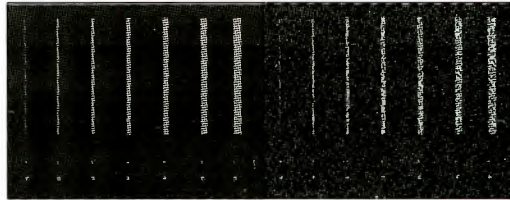


Fig. 3 – Phantom and one look amplitude corrupted phantom

It was decided to evaluate the bitslice image reconstruction provided by a opening closing filtering operation given by:

$$F = \gamma_B \phi_B, B = \begin{bmatrix} 1 & 1 & 1 \\ 1 & 1 & 1 \\ 1 & 1 & 1 \end{bmatrix}.$$

where “.” indicates where is the origin of structural element.

The “most filtered” image is that obtained by reconstructing (stacking) the eight filtered bitslices (i.e., $[F(b^7), \dots, F(b^0)]$, denoted here as f_8). The “second most filtered” image is that obtained by reconstructing the seven most significant filtered bitslices with the least significative left unaltered (i.e., $[F(b^7), \dots, F(b^1), b^0]$, denoted here as f_7). Proceeding in this way, the sequence of filtered images f_6, f_5, f_4, f_3, f_2 and $f_1 = [F(b^7), b^6, \dots, b^0]$ can be constructed, where the subscript denotes the number of filtered bitslices used in the reconstruction and where f_1 denotes the “least filtered” image. Figure 4 shows each bitslice of phantom and Figure 5 shows these bitslice filtered. Figure 6 shows one look amplitude corrupted phantom and result of three most significative bit plane bitslice filtered images.

As a measure of noise reduction the equivalent number of looks of the filtered images over both areas was calculated. Table I shows the equivalent number of looks (ENL) estimated over several filtered versions of corrupted phantom which, by construction, has one look noise. From this table the following conclusions can be draw:

- a) the quality of reconstruction increases, when measured by the equivalent numbers of looks, with the depth of the filtering.
- b) this growth is non-linear, and seems to be negligible after b^5 has been processed.
- c) the noise reduction is different for the dark and bright areas, being stronger for the latter.

A side effect of this technique is an increase in the mean of the areas, due to the fact that the transformation F starts with a closing transformation.

Table I – Equivalent number of looks of filtered images.

reconstruction	ENL	
	Dark	Bright
f_1	0.99	4.42
f_2	2.97	9.91
f_3	5.31	14.56
f_4	6.68	16.60
f_5	7.34	17.50
f_6	7.68	17.85
f_7	7.82	18.01
f_8	7.89	18.07

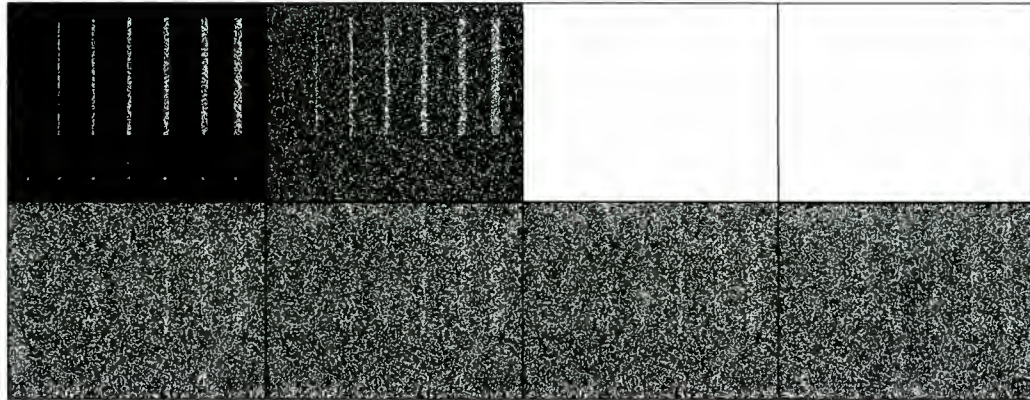


Fig. 4 – Bitslices $[b^7, \dots, b^0]$ from one look corrupted phantom.

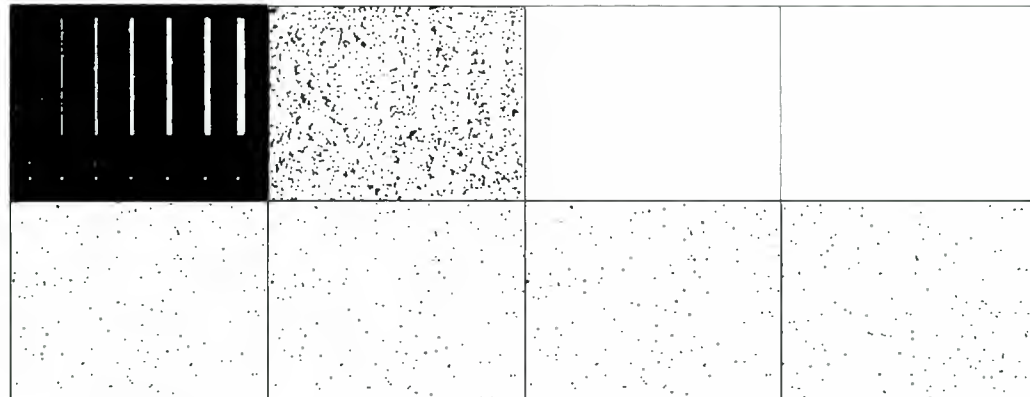


Fig. 5 – Filtered bitslices $[F(b^7), \dots, F(b^0)]$ from one look amplitude corrupted phantom.



Fig. 6 – One look amplitude corrupted phantom and result of its filtering three most significative bitslices.

4. RESULTS

The technique that consists of filtering the bitslices version of $f = [b^7, \dots, b^0]$ was applied to two SAR images, one obtained by the SAR580 sensor over Freiburg, Germany (image \mathbf{g}), and the other obtained by the JERS-1 sensor over Tapajós, Brazil (image \mathbf{h}).

Figure 7 shows the original \mathbf{g} image of Tapajós with approximately four looks and its bitslices. \mathbf{g} is one byte amplitude. Figure 8 shows the most significative bits-

lices of \mathbf{g} after filtering. Figure 9 shows the original image and the filtered version $\mathbf{g} = [F(b^7), F(b^6), F(b^5), b^4, b^3, b^2, b^1, b^0]$ images.

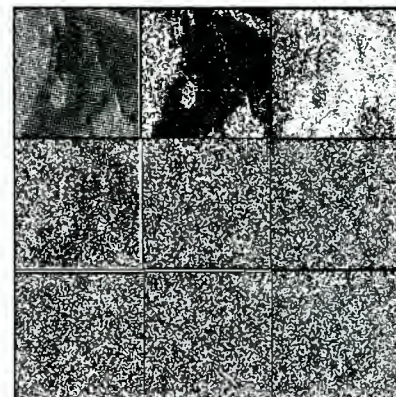


Fig. 7 – JERS-1 image over tapajós, and its filtered version.



Fig. 8 – Three most significative bitslices of Tapajós image after filtering.

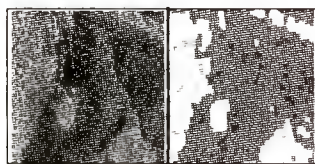


Fig. 9 –Original JERS-1 image over Tapajós and its filtered version.

Figure 10 shows the greyscale g image and its three most significante bit planes on the left side, top to bottom and their filtered versions are shown to the right. Figure 11 shows the original Freiburg image with approximately one look and the filtered result using the three most significante bit planes.

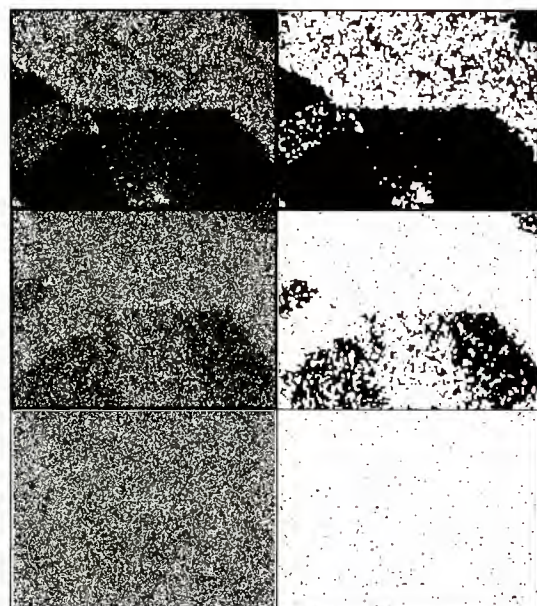


Fig. 10 – Bitslices [$b^7, b^6, b^5, b^4, b^3, b^2, b^1, b^0$] SAR-580 image over Freiburg.

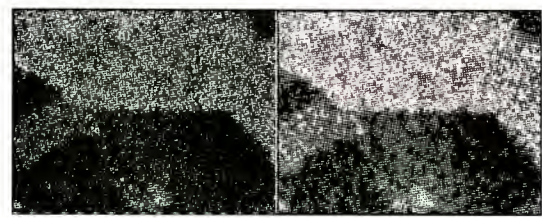


Fig. 11 – Original SAR-580 image over Freiburg and its filtered version.

5. CONCLUSIONS

Synthetic aperture radar (SAR) images are corrupted by speckle and many filtering techniques have been proposed in the literature. This paper presented a noise reduction based on binary morphologic application to bitslices of images.

Table I showed that the equivalente number of looks of morphological filtered image increases with the depth of the filtering and this increase is non-linear.

This methodology increases the mean and generates more homogeneous images (see Figure 6, Figure 9 and Figure 11).

The mean increases is due to the fact that the transformation F (morphological filter) starts with a closing transformation.

Some questions like which bitslice will be filtered and which operations will be applied are beyond the scope of this work and are not quite solved by the authors.

6. ACKNOWLEDGEMENTS

The authors are thankful to Prof. Pablo Ferrari (IME-USP, Brazil). We also thank PROTEM-CC/CNPq processes No. 680.061-94-0 (GEOTEC Project) and No. 680067/94-9 (AnIMoMat Project).

7. REFERENCES

- [1] J. Barrera, G. J. F. Banon e R. A. A. Lotufo. A mathematical morphology toolbox for the KHOROS system: specifications for Version 1.2b. *Workshop'95 de Morfologia matemática*, Campinas, mar., 1995. Available at <http://www.inpe.br/~banon/URLib2>, URLib repository: ime.usp.br/jb/1996/04.03.14.02, 1996.
- [2] A. C. Frery, H. J. Müller, C. C. Yanasse, and S. J. S. Sant'Anna. A model for extremely heterogeneous clutter. *IEEE Transactions on Geoscience and Remote Sensing*, 1996, in press.
- [3] A. K. Jain. *Fundamentals of digital image processing*. Prentice-Hall International Editions, englewoods Cliffs, NJ, 1989.
- [4] S. J. Sant'Anna. Avaliação do desempenho de filtros redutores de speckle em imagens de radar de abertura sintética. Master's thesis, Instituto Nacional de Pesquisas Espaciais, São José dos Campos, SP, Brazil, 1995.

- [5] J. Serra, *Image Analysis and Mathematical Morphology. Volume 2: Theoretical Advances*, Academic Press, London, 1988.
- [6] C. C. F. Yanasse, A. C. Frery, and S. J. S. Sant'Anna. Stochastic distributions and the multiplicative model: relations, properties, estimators and applications to SAR image analysis. Technical Report 5630–NTC/318, INPE, São José dos Campos, SP, Brazil, 1995.

DIGITAL FILTERING OF SAR IMAGES THROUGH LOCALIZATION OF MINIMUM SPECKLE INDEX REGIONS.

Pablo Daniel Ruiz
 Universidad Nacional de Salta, Argentina.
 e-mail ruizp@ciunsa.edu.ar
 phone: +54 87 230275

Héctor J. Rabal*
 Centro de Investigaciones Ópticas - La Plata
 e-mail postmaster@ciop.edu.ar
 phone: +54 21 840280, fax: +54 21 712771

* Also with the Faculty of Engeneering, Universidad Nacional de La Plata, Argentina

ABSTRACT

When a surface is iluminated with coherent light and its image is obtained by an optical system, it appears corrupted by speckle noise, that responds to a multiplicative noise model (for homogeneous regions in the image exists a linear relation between the standard deviation and the average value of intensity). A simple algorithm is presented to eliminate the speckle noise in SAR images. It is a modified version of a previous filter that had been used to eliminate additive gaussian noise. A minimum speckle index neighborhood area is selected around each pixel, and the average intensity level of the selected one replaces the corresponding pixel. The filter is compared with other ones such as the adaptive mean Lee's two sigma filter, the median and the Nagao & Matsuyama's filter. The parameters we used to compare the speckle reduction were the speckle index and the global entropy, and we used edge detectors to evaluate the edge preservation. Finally, it is observed that the presented filter allows a better separation of classes in the histogram of the images.

1. ORIGINAL FILTER PROPOSED BY NAGAO & MATSUYAMA

This filter was designed to remove additive gaussian noise without blurring edges and details in digitized images¹. It looks for the most homogeneous neighborhood around each point in a picture and then replaces each point by the average gray value of the selected neighborhood area. Noise is removed by the repeated usage of this method, while edges remain sharp. Nagao & Matsuyama improved a previous algorithm presented by Tsuji et al, redefining the size and geometry of the neighborhood areas, originally squares -figure 1 and 2-. Their improvement allowed the preservation of complex shaped edges.

The procedure of their edge preserving smoothing algorithm is as follows:

1. Define neighborhood areas arround a pixel (i,j).
2. Detect the area for which the variance of the gray level is minimum.
3. Asign the average gray level of the selected area to the point (i,j).
4. Apply 2 &3 for every pixel in the image.
5. Iterate the above process until the gray levels of almost all the pixels in the image do not change.

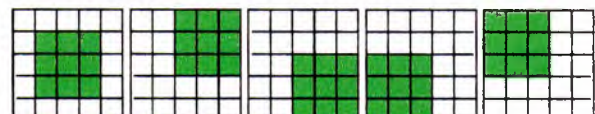


Figure 1. Tsuji et al.'s areas around the central pixel.

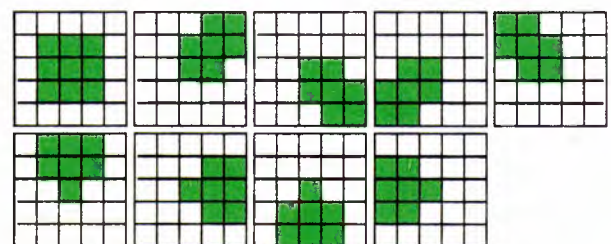


Figure 2. Nagao-Matsuyama's areas around the central pixel

In order to remove noise without blurring sharp edges averaging must not be applied to an area which contains an edge because it makes the edge blurred. That is why the most homogeneous area is to be found around the point to be smoothed.

The variance is used as the homogeneity measure of the gray level. When an edge is filtered, the variance value depends on the contrast of the bright and dark regions that defines the edge, being smaller the lower the contrast.

Let's suppose that a picture has two regions R1 & R2 with different means and variances defining an edge - see figure 3-. Let a point (x,y) belong to R1, and be far away from the edge.

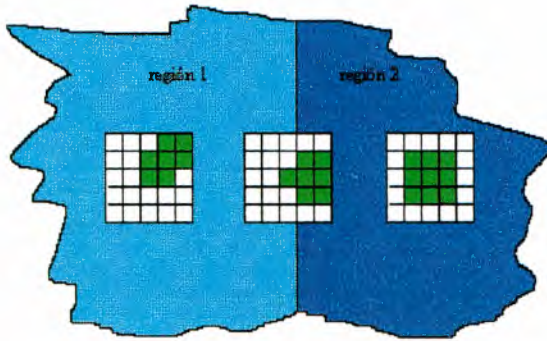


Figure 3. An edge defined by two regions. Near the edge, a neighborhood area totally included in R1 will be selected.

After some iterations of the filter its gray level will be blurred approaching the average level of R1. This also occurs if the point is in R2, far from the edge. But if (i,j) is just on the edge or very close to it, there are neighbour areas partially masking R1 and R2 while others are completely included in R1. For additive noise $\sigma_1^2 \approx \sigma_2^2$,

and it is reasonable to assume that the variance σ^2 of the shared area is bigger than σ_1^2 . That is $\sigma^2 > \sigma_1^2$ so the correct neighborhood is selected.

In order to reduce strongly the noise fluctuations the areas for averaging should be large, but this smooths out small details of the picture, and a blurred image is obtained.

Small neighborhoods of 5*5 pixels are defined arround each pixel and also seven pixels areas inside it to look for the minimun variance one.

We applied this filter to speckled images (SAR images & laboratory made ones illuminating flat objects with He-Ne laser light) and we found that the first iteration removed isolated speckles and preserved edges and details, appearing some kind of "tile" effect (little areas of homogeneous gray level).

Homogeneous regions of the image originally corrupted with speckle spot-noise are smoothed and high contrast edges are well preserved, but not low contrast ones. Nagao & Matsuyama suggested five iterations but

details 2 or 3 pixels wide are blurred out. This is due to the size defined for the neighborhood areas.

2. SPECKLE INDEX AS HOMOGENEITY MEASURE

We said that usually $\sigma_1^2 \approx \sigma_2^2$, but this is not the case when noise is multiplicative, as in speckle. In homogeneous areas, multiplicative noise has a linear relation between σ_z and \bar{z} (the local standard deviation and the local average gray level).

In a SAR image, Nagao & Matsuyama's filter gives high variance in high average gray level areas, and the minimum variance algorithm chooses the minimum average gray level area. Thus, dark areas become wider as the iteration goes on and tend to connect with each other.

Evidently, the cause of this effect is that the variance is not the right homogeneity measure for speckle noise. An indicator that considers both the noise fluctuations and the average level is the speckle index (or noise/signal ratio for speckle patterns) defined for a pixel (i,j) neighborhood as

$$SI = \frac{\sigma_{ij}}{\bar{z}_{ij}}$$

where σ_{ij} and \bar{z}_{ij} are the standard deviation and the average intensity value of the (i,j) pixel neighborhood respectively. This is a very useful measure to characterize speckle noise fluctuations. We improved Nagao & Matsuyama's filter by minimizing the speckle index instead of the variance and we used a procedure like the one described above.

We applied the filter obtained to some images and a better performance was obtained. It removed the noise better, blurring speckle fluctuations and preserving edges and lines of 2 or 3 pixels wide. Furthermore, no more connected dark areas appeared.

Figure 4 shows a SAR image a) Original, b) Median filtered, c) Adaptive mean Lee's two sigma filter d) Nagao & Matsuyama filtered and e) Improved method filtered.

It is noticed that high contrast edges are better preserved when the latter filter is used, but not the low contrast ones. The regions inside the white boxes in figure 5 were chosen to compare the different filters performances. Those are high contrast areas, to which we recorded the histograms -figure 6-. It is easy to recognize in figure 6 the performance of the filter for resolving the different modes or classes. The original speckled image has a very broad histogram, while the filtered ones tend to separate two different distributions, one corresponding to the bright areas and the other to the dark ones.

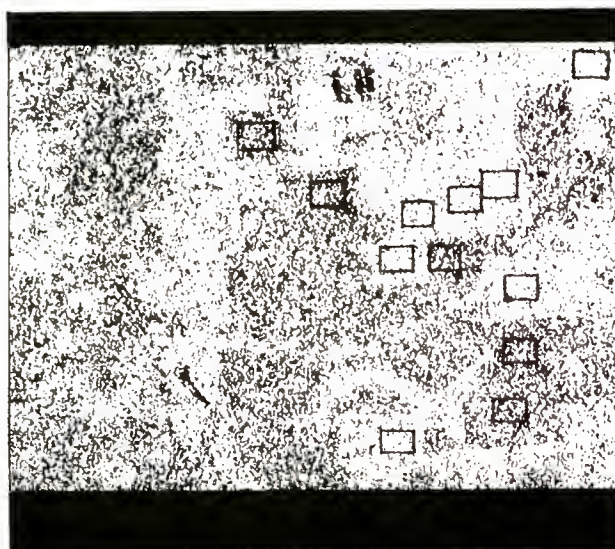


Figure 4a



Figure 4b



Figure 4c

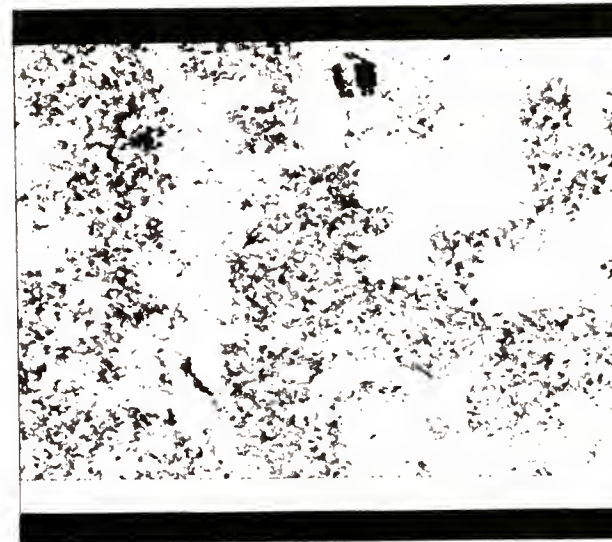


Figure 4d



Figure 4e

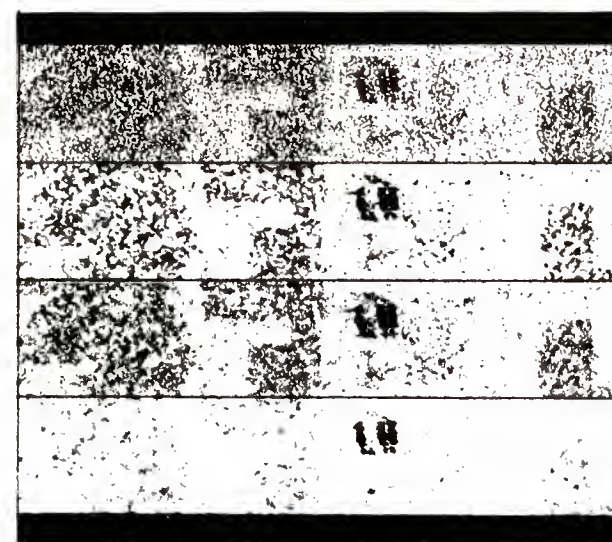


Figure 5.

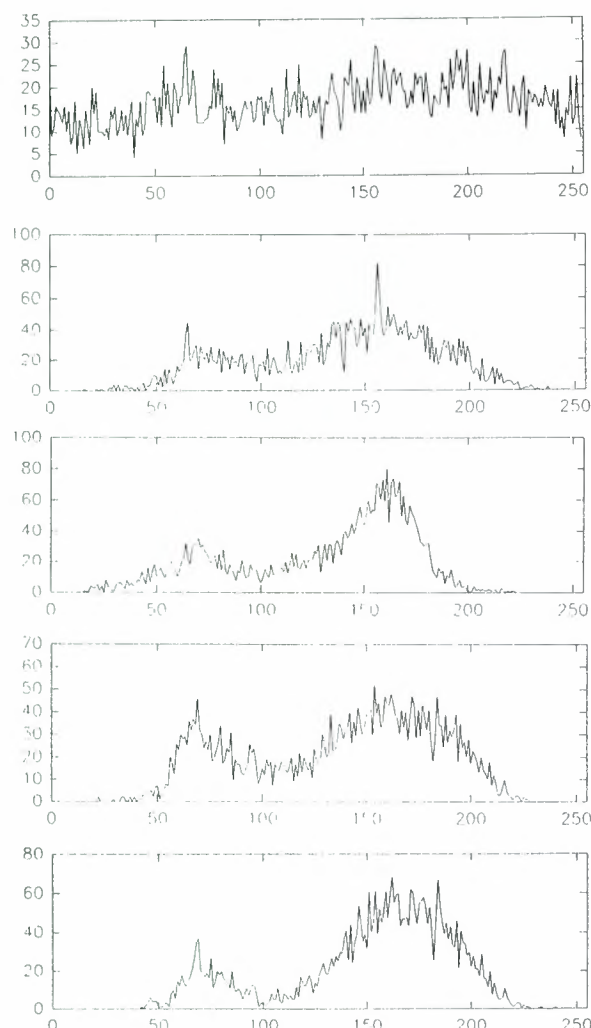


Figure 6. Corresponding histograms, from top to bottom: original image, median filtered (5×5 nucleus), adaptive mean Lee's two sigma filtered (5×5 nucleus)², Nagao & Matsuyama's filter of minimum variance neighborhood areas¹, improved version of minimum homogeneous areas.

In order to compare the performance of the filter we evaluated the speckle index defined as

$$SI = \frac{1}{KL} \sum_{i=1}^K \sum_{j=1}^L \frac{\sigma_{ij}}{\bar{z}_{ij}},$$

using 5×5 nuclei in a $K \times L$ image region, and the global entropy given by

$$H = - \sum_{x=1}^{256} p(x) \cdot \log_2 p(x)$$

where x refers to the gray levels in the histogram and $p(x)$ to their probabilities. Both parameters measure the homogeneity or noise reduction in the filtered images, and the results are shown in Table I.

Table I

image / filter	S.I.	H
original	0.4754	7.896
median	0.1918	7.258
Lee's adaptive mean (2sigma)	0.2358	7.238
Nagao & Matsuyama	0.1923	7.206
Improved	0.1327	6.781

In order to evaluate edge preservation we applied Robert's cross operator and Sobel's operator to the images in figure 5. The images obtained are shown in figure 7. The edges are better defined in the image filtered with the minimum speckle neighborhood areas algorithm.

The algorithm is computationally efficient when no more than two iterations are required.

We tested also another method, which consists in minimizing the speckle index in the same way described above but considering different neighborhood areas. Figure 8 shows the mask of 3 pixels area that we rotated over eight different positions. We considered the fractions of the masked pixels to calculate the speckle index. This algorithm resulted to be a low converging one because of the small number of pixels involved in each neighborhood area. It showed an effect like the "tiles" described in the Nagao & Matsuyama's filter but in this case they are bars one pixel wide and three or four pixels long. The filtered image remained noisy while fine details one pixel wide were well preserved in the four directions defined for the neighborhood areas (verticals, horizontals, and diagonals).

3. ACKNOWLEDGEMENTS

P.D.R gratefully acknowledges the financial support of the Consejo de Investigaciones de la Universidad Nacional de Salta, Argentina.

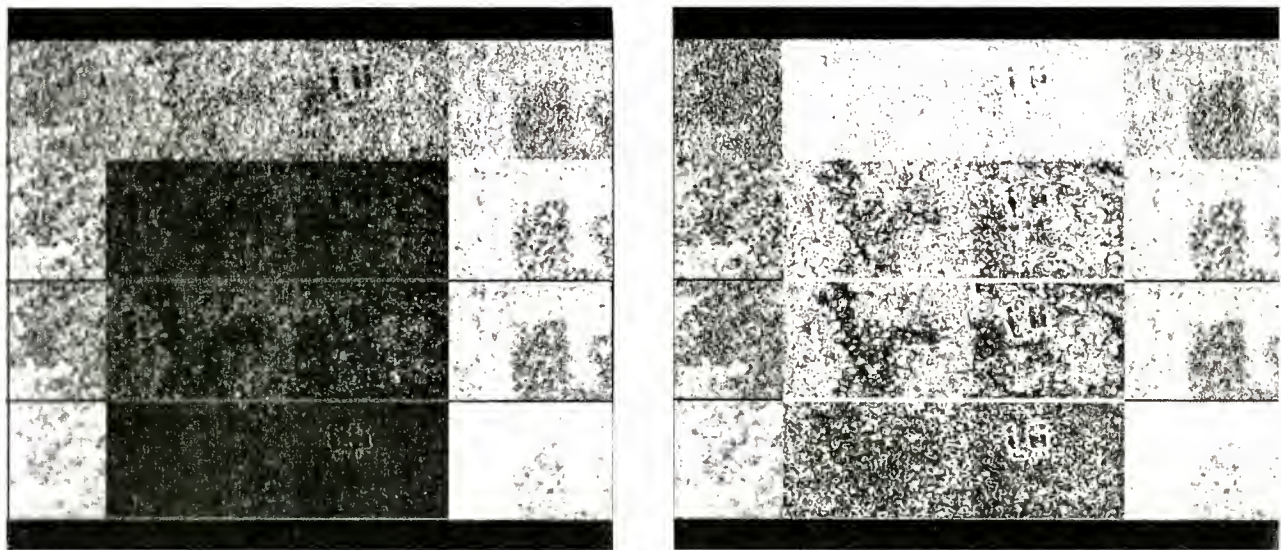


Figure 7. Robert's Cross operator and Sobel operator

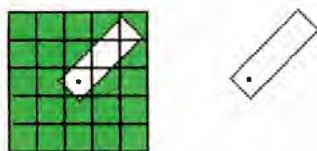
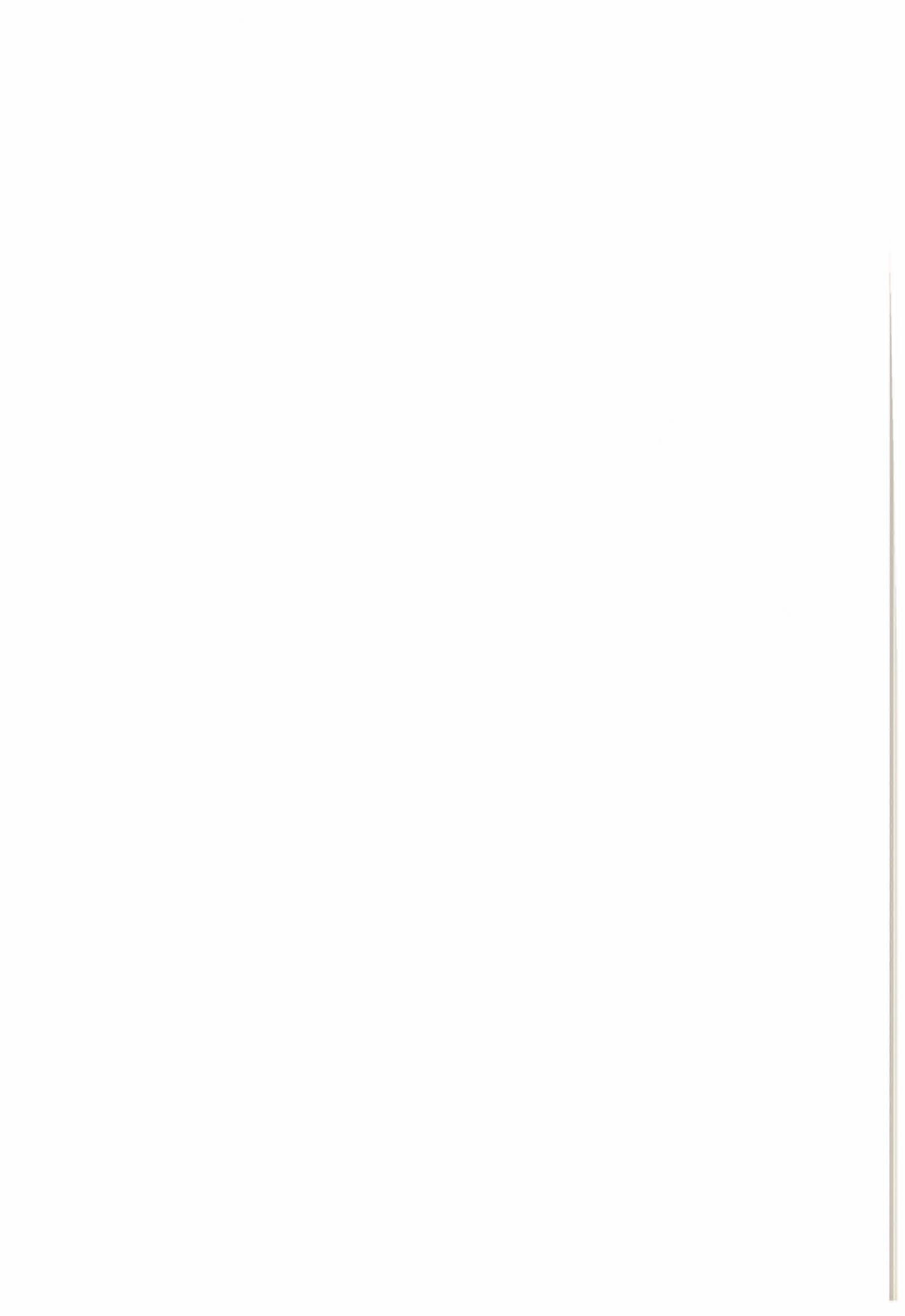


Figure 8. The mask where the speckle index is minimized

4. REFERENCES

- 1- M.Nagao and T Matsuyama, 1979, Edge preserving smoothing, *Comp. Graph. and Im. Proc.*, vol 9, 394-407.
- 2- Jong Seng Lee, 1986, Speckle suppression and analysis for synthetic aperture radar, *Opt. Eng.* 25, 636-643.
- 3- T. Asakura and J. Ohtsubo, 1976, Speckle patterns and entropy, *Optik* 46 , 19-25.



**INTEGRAÇÃO DE DADOS MULTIESPECTRAIS LANDSAT-5 TM COM IMAGENS SAR JERS-1,
PARA FINS CARTOGRÁFICOS**

Sérgio Monteiro Soares^{1,2}
 Sidnei João Siqueira Sant'Anna¹
 Gerardo Kuntschik¹

¹INPE - Instituto Nacional de Pesquisas Espaciais

e-mails:[msoares, sidnei, gerardo]@dpi.inpe.br

²DSG - Diretoria do Serviço Geográfico do Exército Brasileiro

e-mail: msoares@eme.eb.mil.br

Abstract

In several brazilian areas, mainly in some rain forest regions, where have cloud coverage trouble, all year long, the sistematic mapping is delay in time. In some those areas there aren't any cartographic document, in sistematic scales (1:500.000, 1:250.000, 1:100.000, 1:50.000 and 1:25.000) be able to represent them planialtimetricly. Those facts are due mainly by the following reasons: a) The absent of aerial photographics, because the wheather conditions, all year long, doesn't permit to take them; b) By the same reason, the analysis and interpretation of the satellites images, like LANDSAT-TM or SPOT, can not be performed for natural and artificial targets identification, on the surface of the Earth, to possibility the manufacturing the images-charts inside the visible spectrum; c) The only use of SAR images can not identify all the targets, cartographicly representable, on a image-chart, even though such SAR images have no inconvenient of cloud coverage.

The aim of this work is show what the digital images processing can efficiently do, thru Main Components proceedings, filtering, IHS Compositions, Resample of SAR data over TM data and visualization in RGB space to better geometric identification of targets, be able to build a image chart without clouds coverage, which one was removed by these digital operations, if the a specific algorithim was follow, like will be describe in this paper. In work by Sanabria (1995) before it, make the data integration with the same purpose using multispectrals SAR data by ERS-1. In this work, using the analog methodology, varying the type of data, sequence of procedures, type and sequence of filtering and incorporating a classification of the hibrid final product, was used SAR-images, in L band, polarization HH from JERS-1 Satellite. The choice for JERS-1 SAR-images in L band, against the SAR-images from ERS-1 in C band, was made by the higher penetration of the L band inside the canopy of the rain forests, permitting the better analysis of the geomorfology of the ground, in regions where cloud

coverage, all year long, doesn't permit the conventional cartographic methods.

The computational environment was made over the IDL and ENVI softwares, using graphical workstations. in all digital operations, since colect data from the tape devices, until creating the plotting files, as a final product, resulted of mixing TM data with SAR data, in all graphical formats, be able to build the base for production in large scale of images-charts, neither TM, nor SAR, but a composition of these data, removing the clouds effects from the TM data. These products can be used for paper image-chart or even for use like a data base for Geographical System Information, in geoprocessing analysis.

1 - Introdução

Em regiões caracteristicamente problemáticas quanto à cobertura de nuvens no Brasil, o mapeamento sistemático encontra-se defasado no tempo. Em algumas destas regiões inexiste qualquer documento cartográfico em escalas sistemáticas (1:500.000, 1:250.000, 1:100.000, 1:50.000, 1:25.000) capazes de representá-las planialtimetricamente. Este fato se deve, principalmente, às seguintes razões: a) A ausência de aerofotos, por condições atmosféricas desfavoráveis o ano inteiro, impedindo um mapeamento convencional por restituição aerofotogramétrica convencional; b) A excessiva cobertura de nuvens (mesmo em séries temporais de imagens) impossibilitando a identificação planimétrica dos diversos acidentes terrestres, impedindo a confecção de cartas imagem TM, ou outros sensores passivos do espectro óptico; c) O uso apenas de imagens SAR não permite uma perfeita identificação planimétrica dos diversos acidentes naturais e artificiais sobre a superfície da Terra para fins cartográficos. Apesar de não apresentar a inconveniência da influência de condições atmosféricas adversas, como no caso das imagens TM, devido à natureza de obtenção destas imagens e de um forte ruído chamado *speckle*, fornece como principal elemento classificador a textura da imagem, ou o efeito

coletivo dos *pixels*, dependendo da escala de observação.

O presente trabalho tem por objetivo mostrar a eficiência de ferramentas de processamento digital de imagens, através das técnicas de *Principais Componentes*, *Filtragens*, *Composições IHS*, *Reamostragens de imagens sobre outras imagens com tamanhos de pixels diferentes (representados no terreno)* e finalmente o retorno às composições coloridas **RGB**, para melhor visualização dos produtos do processamento digital, permitindo uma melhor definição geométrica de alvos sobre a superfície terrestre, notadamente para fins cartográficos.

Em trabalho anterior, Sanabria (1995) realizou a integração de dados multiespectrais com dados SAR/ERS-1. No presente trabalho, partindo-se de uma metodologia análoga, realizou-se um estudo com imagens multiespectrais LANDSAT-5 TM e imagens SAR JERS-1, estas últimas obtidas na polarização HH e na banda RADAR L.

A utilização de imagens SAR JERS-1 é justificada pelo fato da banda L, por ter comprimento de onda maior que a banda C (ERS-1), ter maior penetração em dosséis florestais, fornecendo maiores informações sobre a geomorfologia do relevo sub-florestal. Finalmente tentou-se uma classificação do produto híbrido TM-SAR, comparando-o com a classificação de uma imagem LANDSAT-5 TM pura, para avaliação dos resultados obtidos.

O ambiente computacional utilizado como base de desenvolvimento da pesquisa foi o *software ENVI* e sua linguagem IDL associada, em *workstations* gráficas. Neste ambiente realizaram-se os tratamentos digitais acima citados e a geração do produto final híbrido TM-SAR, em diversos formatos digitais. Estes estão numa estrutura que os faz passíveis de serem utilizados para a confecção de fotolitos *off-set*, destinados à impressão de cartas-imagens em grandes quantidades, ou mesmo dados digitais para fins de base geográfica de dados aplicados à Sistemas de Informações Geográficas, em geoprocessamento.

Em imagens LANDSAT-5 TM, situadas na faixa do espectro óptico de 300 a 2500 nm, existem basicamente duas fontes de desinformação: a cobertura de nuvens, e as sombras causadas por estas nuvens. A desinformação é causada pelo ângulo de iluminação solar, na hora da passagem do Satélite LANDSAT-5.

A sombra não consiste, de fato, uma fonte absoluta de desinformação. Ela, apesar de não refletir diretamente a luz solar, é composta por uma reflectância difusa, capaz de ser parcialmente recuperada, nas operações de *Principais Componentes*, como será descrito a seguir.

No entanto a cobertura de nuvens reflete completamente a luz solar, apresentando uma cor branca, em composições **RGB** com bandas TM 5, 4 e 3, respectivamente.

No caso de imagens de RADAR as nuvens, dependendo da sua espessura, são praticamente

transparentes ao sinal retroespelhado. desta forma, através de fusão de dados, pode-se utilizar estas imagens para tentar retirar parcialmente o efeito desta opacidade de nuvens dos acidentes sobre a superfície terrestre.

Existem outras técnicas para a redução do efeito de nuvens em imagens multiespectrais. Em Krug(1992), por exemplo, a radiometria dos *pixels* sob as nuvens foi estimada através de modelos de séries temporais, a partir de composições de séries de imagens multitemporais.

Contudo existem certas regiões no Brasil e no mundo, em que a cobertura de nuvens é quase permanente durante todo o ano, especialmente nos horários de passagem do Satélite LANDSAT. Uma coleta de dados temporais, poderia levar anos, até que por processos auto-regressivos demorados, se conseguisse resgatar tanto as informações planimétricas, quanto radiométricas, destas áreas em questão. O processo seria demorado e excessivamente caro, para a confecção de uma carta-imagem, capaz de representar com relativa fidelidade uma região de cobertura quase permanente de nuvens, como é o caso de certas regiões brasileiras tais como o litoral nordestino, na altura de Sergipe e Alagoas e os Estados como o Acre, Roraima, Amazonas, Amapá, Pará, ditos pertencentes à Amazônia Física, cuja nebulosidade impede tanto a cartografia convencional por aerofotogrametria quanto a confecção de cartas-imagens ópticas, pelo mesmo motivo.

Mas este fato é bastante comum no globo terrestre em todas as chamadas *rain forest*, como também em regiões de grandes altitudes como a Cordilheira dos Andes, por exemplo. Nesses casos, esta tentativa de fusão de dados multiespectrais, com imagens SAR, ganha importância, pois pode proporcionar uma relativa interpretabilidade destas regiões.

Neste estudo, não se pretendeu criar um software de integração de dados multiespectrais com dados SAR, mas sim, de posse de todas as ferramentas digitais, já desenvolvidas, num encadeamento lógico, gerar um fluxograma de aplicação destas ferramentas, otimizando sua utilização, para a geração de um produto híbrido, capaz de representar cartograficamente uma região, antes impossível por processos convencionais.

2 - Dados Utilizados

A área selecionada para o estudo foi a denominada FLONA (Floresta Nacional do Tapajós), situada ao sul de Santarém, no Estado do Pará, numa área abrangida pelas latitudes S02° 56' e 38" e S03° 23'e 28" e longitudes variando de W54° 49'36" e W55° 01' e 45", conforme mostrado na Figura 01.

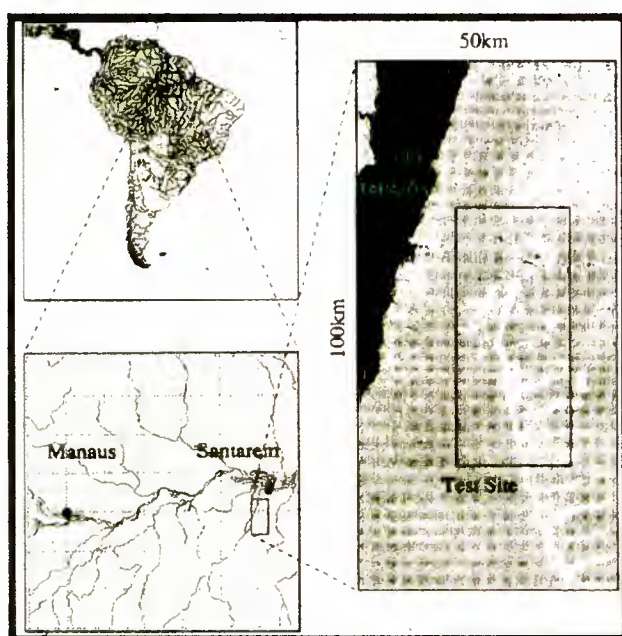


Figura 01 - Região de estudo

Esta região está situada ao longo da Rodovia Santarém-Cuiabá, tendo à Oeste a Floresta Nacional do Tapajós e à Leste, travessões de assentamento rural do Incra, ao Sul pela Rodovia Transamazônica e ao Norte pelo Rio Amazonas. Esta região é caracterizada pela exploração de madeiras nobres como o Mogno, Agelim e outros. Parte da região, anteriormente utilizada para pastos e agricultura, foram abandonados dando início a um processo de regeneração da floresta primária. Existem ainda, algumas áreas com solo exposto, preparados para cultura de Pimenta do Reino, ou novas formações de pasto para gado bovino.

Para fins de estudo na classificação digital foram escolhidas três classes distintas, Floresta primária, não-floresta ou rebrota ou cultura, e solo exposto. Foram ainda coletadas amostras de nuvens e sombras para evidenciar a falta de informação quando das operações digitais de classificação pelo classificador de máxima verossimilhança (*Likelihood*).

Desta área utilizaram-se as seguintes imagens:

1) Imagem LANDSAT-5 TM, nas bandas 1, 2, 3, 4, 5 e 7 correspondendo respectivamente aos seguintes comprimentos de ondas médios: banda 1 ($\lambda_m=0,48 \mu m$), correspondendo à cor azul; banda 2 ($\lambda_m=0,56 \mu m$), correspondendo à cor verde; banda 3 ($\lambda_m=0,66 \mu m$), correspondendo à cor vermelha; banda 4 ($\lambda_m=0,83 \mu m$), correspondendo ao infravermelho próximo ou refletido; banda 5 ($\lambda_m=1,65 \mu m$), correspondendo ao infravermelho médio, banda 7 ($\lambda_m=2,13 \mu m$), correspondendo ao infravermelho distante. A banda 6 ($\lambda_m=11,5 \mu m$) não foi utilizada por corresponder ao infravermelho termal, altamente

suscetível à absorção pela água da troposfera. Assim essa Banda introduz ruídos indesejáveis. Esta imagem é datada de 29 de Maio de 1993, com *pixels* de 30 metros de resolução geométrica, no terreno. Uma composição colorida RGB utilizando a banda 5 no canal R, a banda 4 no canal G e a banda 3 no canal B, pode ser vista na Figura 02.

2) Imagem SAR JERS-1 com órbita ponto 405/306, em amplitude, com um número de visadas ou *looks* igual à 3, de 16 bits, cada *pixel* com espaçamento geométrico de 12,5 metros. Esta imagem é da banda RADAR L (λ variando de 19 à 23 cm e freqüências de 1 à 3 GHz) na polarização HH. A imagem SAR JERS-1, da mesma região, já filtrado o *speckle*, pelo filtro de *Frost* e já registrada sobre a imagem LANDSAT TM, pode ser vista na Figura 03.

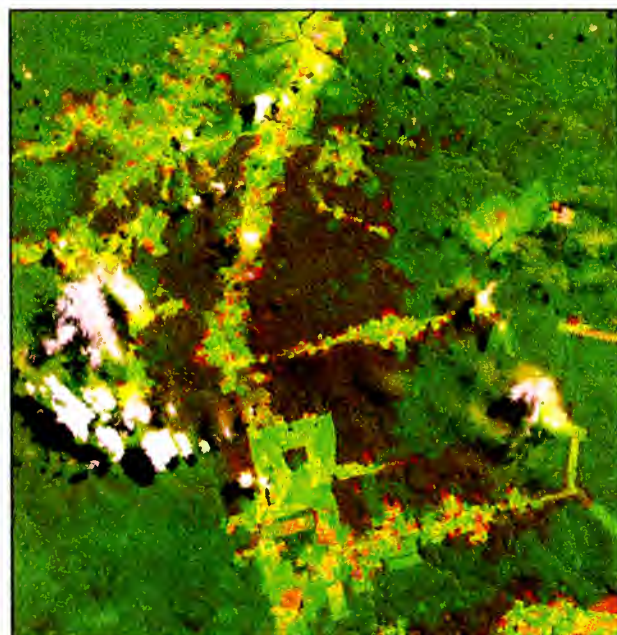


Figura 02 - Composição RGB da imagem LANDSAT TM com as bandas 5, 4 e 3 , respectivamente.

Na imagem LANDSAT TM (Figura 02), pode-se notar áreas cobertas com nuvens e suas respectivas sombras, sendo estas as fontes de desinformação que o algoritmo proposto tenta minimizar para construção de cartas-imagens híbridas TM-SAR. Embora exista uma grande parte da imagem descoberta, a área foi escolhida para teste de classificação entre a imagem híbrida e a imagem LANDSAT TM original.

Não se trata, aqui, da recuperação da radiometria original das áreas encobertas por nuvens e sombras, e sim a geração de uma imagem de atributos, cuja classificação espectral assemelhe-se à classificação de uma imagem com a radiometria original. Entende-se aqui *radiometria*, como sendo a resposta em níveis de cinza de um determinado alvo.

Em consequência, devido a alteração da radiometria, índices antes válidos para imagens

multiespectrais como, por exemplo, o NDVI (Índice Normalizado de Vegetação), por combinação linear entre as bandas 3 e 4 do sensor TM, naturalmente não são aplicáveis à imagem híbrida.



Figura 03 - Imagen SAR JERS-1, filtrada e registrada sobre a imagem LANDSAT TM.

Na imagem SAR JERS-1 (Figura 03) os acidentes planimétricos típicos de representação cartográfica não estão perfeitamente definidos. A falta de cores impede uma análise visual correta para a devida colocação das toponímias e simbologias cartográficas adequadas às escalas sistemáticas, relativas à vegetação, estradas, floresta primária, áreas de não-floresta, etc. Devido à natureza da imagem, a textura se torna o principal elemento pelo qual se poderia tentar uma classificação cartograficamente representável, apesar de não conter a indesejável cobertura de nuvens e suas sombras, como fontes de desinformação.

3 - Metodologia

Como mencionado na Introdução deste trabalho, não trata-se aqui de desenvolvimento de um *software* específico para a geração da fusão de dados multiespectrais com imagens RADAR. Versa sobre a correta utilização de ferramentas computacionais para tratamentos digitais de imagens, em diversos programas comerciais, numa ordem lógica, obtendo como resultado um produto capaz de ser utilizado para

a confecção de cartas-imagens, fugindo ao conceito tradicional da cartografia, qual seja a aerofotogrametria.

3.1 - Pré-processamento da imagem LANDSAT TM

Serão apresentados os procedimentos de pré-processamento da imagem LANDSAT TM, assim como os passos a serem seguidos, explicando-os quando não forem óbvios.

3.1.1 - Seleção da região com problemas meteorologicamente constatados por imagens temporais, não sendo passíveis de serem utilizados como cartas-imagens ópticas (TM ou SPOT, por exemplo), dentro do enquadramento do mapeamento sistemático, na escala escolhida.

3.1.2 - Execução do procedimento estatístico conhecido como *Principais Componentes*.

Principais Componentes:

Uma grande correlação inter-bandas em imagens multiespectrais é um problema frequentemente encontrado quando da análise destas imagens. A causa disto é que uma imagem obtida em diversos comprimentos de ondas do espectro eletromagnético (faixa conhecida como espectro óptico), muitas vezes torna um determinado alvo redundante em termos espectrais. A técnica de *Principais Componentes*, tem como objetivo estratificar estas informações redundantes em novas bandas espectrais, em ordem decrescente de quantidade de informações, reduzindo a *dimensionalidade*, dos dados. Desta forma, em uma imagem com n bandas espectrais, suas primeiras (1, 2, 3, dependendo da quantidade de Bandas), conterão a grande maioria das informações, sendo as últimas componentes consideradas resíduos ou percepção de radiação difusa. Em termos geométricos trata-se de uma rotação e translação de eixos espectrais de modo a orientar os novos eixos principais nas direções de máxima informação.

No caso em estudo, a imagem LANDSAT-5 TM possuía as bandas 1, 2, 3, 4, 5 e 7. Aplicando as operações estatísticas de *Principais Componentes*, foram geradas as seguintes novas bandas espectrais: PC1, PC2, PC3, PC4, PC5 e PC6.

Verificou-se que a PC1 continha mais de 90% da informação espectral das imagens. A fim de se avaliar quais das *Principais Componentes* apresentava o maior grau de informação da reflectância difusa (sombra das nuvens), foram feitas todas as combinações RGB possíveis com as *Principais Componentes*, fixando-se canal G (verde) sempre a PC1.

Analizando cada uma destas composições coloridas verificou-se que a composição **RGB** PC5-PC1-PC6, apresentava a maior quantidade de informações da reflectância difusa provocada pelas sombras das nuvens.

A fixação da PC1 no canal G (verde) deve-se ao fato desta componente traduzir mais de 90% do Albedo, o que corresponde à resposta da vegetação verde sadia (Floresta Amazônica). Assim para se tentar preservar um aspecto mais parecido com a realidade, fixou-se a *Principal Componente* PC1 no canal G nas combinações das composições **RGB**.

Analogamente foi feita a operação de *Principais Componentes* com as bandas TM 3, 4 e 5, obtendo-se as bandas PaC1, PaC2 e PaC3. A componente PaC1, continha mais de 90% das informações entre as Bandas espectrais 3, 4 e 5. Nesta *Principal Componente*, isenta dos resíduos difusos das sombras e contendo a maior resposta da vegetação será mais tarde útil na transformação inversa da composição **IHS** para **RGB**, para a tentativa de restauração dos atributos de níveis de cinza, correspondentes à radiometria original da cena TM.

3.1.3 - Transformação **IHS** da composição colorida **RGB**, eleita como a melhor representativa das informações da reflectância difusa das sombras das nuvens.

Uma forma alternativa de descrever as cores das imagens é no espaço **IHS** (**Intensity** ou Intensidade, **Hue** ou Matiz e **Saturation** ou Saturação). O Matiz é a medida do comprimento de onda médio da energia eletromagnética que ele reflete, o que determina a sua cor. A Intensidade é a quantidade de energia total refletida em todos os comprimentos de onda, o que define o brilho do alvo. A Saturação expressa o intervalo de comprimentos de onda ao redor do comprimento de onda médio, no qual a energia é refletida e corresponde à pureza da cor. Objetos com altos valores de saturação são vistos em cores espectralmente puras, enquanto que objetos com baixos valores de saturação são vistos em tons pastéis.

A transformação do espaço **RGB** para o **IHS** pode permitir maior controle sobre o realce das cores. Esta transformação é feita em várias etapas. Em primeiro termo escolhe-se um grupo de três bandas espectrais, calcula-se o matiz, intensidade e saturação para elas através de algoritmos que relacionam ambos espaços de cores. Como resultado obtém-se três novas imagens, cada uma das quais representam I, H e S. A seguir se efetua um aumento de contraste das imagens I e S. Finalmente se realiza a transformação inversa **IHS**→**RGB**. Isto fornece como consequência composições coloridas com reduzida correlação entre as bandas e, consequentemente, uma melhor utilização do espaço de cores.

Neste trabalho as bandas espectrais escolhidas para a transformação **RGB**→**IHS**, foram as formadoras da composição **RGB** PC5-PC1-PC6 da imagem

LANDSAT-5 TM computando-se as bandas obtidas através das *Principais Componentes*, a partir das bantas TM originais 1,2,3,4,5 e 7. Esta composição como descrito, representava a imagem que melhor realçava a reflectância difusa das sombras das nuvens..

Esta composição **IHS**, recém criada foi a chave para a introdução de uma banda RADAR na transformação inversa para o espaço **RGB**, como será descrito.

3.2 - Pré-processamento da imagem SAR JERS-1

A imagem SAR JERS-1 não é, à princípio, compatível com a imagem TM, nem em número de bits, representativos dos níveis de cinza de cada *pixel*, nem na resolução geométrica do *pixel* no terreno, 12,5 metros (radar) contra 30 metros (TM). É uma imagem monobanda, obtida em visada lateral, diferente da imagem LANDSAT TM, que é cônica em visada nadir.

Portanto é de se esperar grandes distorções no registro SAR JERS-1 sobre a LANDSAT TM, se uma região de dimensões compatíveis não for previamente selecionada.

3.2.1 - Filtragem do *Speckle*

Um ruído, característico de imagens SAR, chamado *speckle*, introduz uma textura adicional à textura original da imagem SAR, criando uma pigmentação. O efeito coletivo de uma imagem SAR é a textura da cena imageada misturada com a textura *speckle* (Ahren, 1994). Isto dificulta sobremaneira a interpretação, análise e classificação digital de uma imagem SAR.

Existem vários tipos de filtros de *speckle*, implementados em softwares comerciais. Neste trabalho optou-se pelo filtro de *Frost*, pela melhor definição das bordas da imagem filtrada, conforme demonstrou Sant'Anna (1995).

O filtro proposto por Frost et al. (1982) é convolucional linear, derivado da minimização do erro quadrático médio (critério MMSE - *Minimum Mean Square Error*) sobre o modelo multiplicativo, que representa o ruído *speckle*. Este filtro incorpora a dependência estatística do sinal original, já que considera uma função de correlação exponencial entre *pixels* vizinhos. É um filtro adaptativo que preserva a estrutura de bordas e é geral, não obstante seja baseado na detecção quadrática.

De posse da imagem SAR, descrita no item 2, foi executada a filtragem de toda a imagem, antes da reamostragem/registro desta sobre a imagem LANDSAT TM. Também não foi reduzido o número de bits de cada *pixel* de 16 para 8 bits, ou seja de inteiro para byte. Esta redução foi feita automaticamente executada, quando do registro da imagem SAR sobre a imagem TM.

3.2.2 - Registro da imagem SAR JERS-1 sobre a imagem LANDSAT TM, selecionada e já cortada para a região de interesse.

Este registro e concomitantemente a reamostragem da imagem SAR JERS-1 sobre a imagem LANDSAT TM, foi feita de modo linear, utilizando-se polinômios do primeiro grau e com interpolação pelo critério dos *pixels* vizinhos mais próximos.

Notou-se que a imagem inteira SAR JERS-1 mostrou-se consistentemente coincidente com a imagem LANDSAT TM na região de interesse, isto é, região em que foram coletados os pontos de controle, apresentando distorções nas bordas. Este fato era esperado, uma vez que os pontos de controle, coletados em ambas as imagens situavam-se na imagem LANDSAT TM cortada para a região de interesse.

Uma vez registrada e reamostrada a imagem SAR JERS-1 sobre a imagem LANDSAT TM, foi feito o corte da mesma, coincidindo *pixel a pixel* uma imagem sobre a outra, ajustando-se a representatividade do tamanho geométrico do *pixel* no terreno em ambas as imagens, bem como sendo a banda SAR representada no formato ponto flutuante (*float*).

Por necessidade do software utilizado (ENVI), tanto a imagem SAR JERS-1 como as PC1 e PaC1, foram transformadas no formato ponto flutuante num *range* variando entre zero e um (0.0 e 1.0), para a reversão da composição IHS para RGB (retorno).

3.3 - Fusão de dados SAR-TM

Conta-se agora com uma composição IHS formada pela transformação das *Principais Componentes* PC5-PC1-PC6 obtidas da imagem LANDSAT TM, nas 6 bandas disponíveis (1,2,3,4,5 e 7).

A transformação inversa desta composição IHS para o espaço RGB foi feita da seguinte forma:

a) Na componente I foi inserida a banda SAR *float*, num *range* de 0.0 a 1.0, à qual foi associada ao canal R, na transformação inversa IHS→RGB, representando a região sem o efeito das nuvens. Portanto era de se esperar que no lugar das nuvens uma textura amarelo-vermelhada aparecesse na composição RGB, produto final híbrido;

b) Na componente H foi inserida a banda espectral PaC1, obtida na operação de *Principais Componentes* entre as bandas TM 3, 4 e 5, associando-a ao canal G (verde) por representar o Albedo da região, cor dominante da região (Floresta Amazônica);

c) Na componente S foi inserida a PC1, obtida nas operações de *Principais Componentes* com todas as bandas TM, portanto contendo informações sobre a

reflectância difusa, associando-a ao canal B (azul) da composição RGB de retorno, esperando-se que as sombras aparecessem com cores azul-avermelhadas (magenta).

Com efeito, após a reversão da composição IHS original para o espaço RGB, obteve-se a composição colorida vista na Figura 04. Nesta imagem foram usados filtros lineares, gaussianos, quadráticos e manipulação manual nos histogramas RGB, para o produto final considerado aceitável.

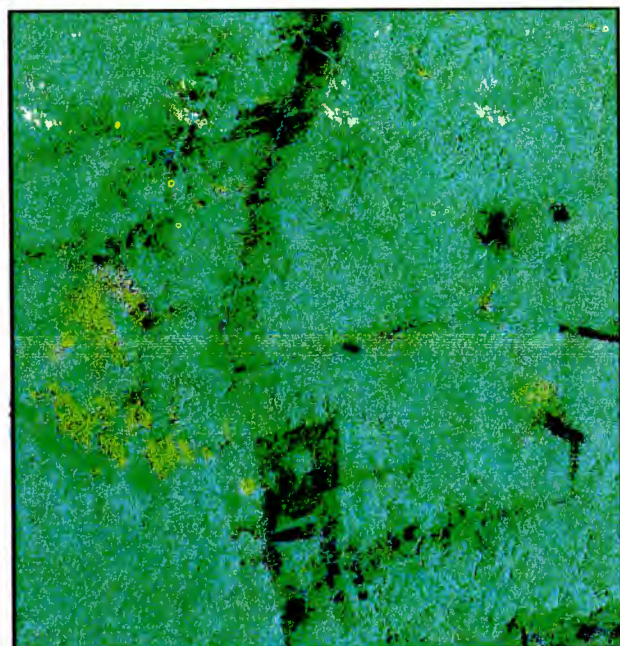


Figura 04 - Produto híbrido LANDSAT TM/SAR JERS-1

Nesta imagem, em comparação com a imagem contida na Figura 02, pode-se notar que a desinformação provocada pelas nuvens e sombras foi reposta pela textura SAR, em cores amarelo-vermelho-esverdeado. Contudo foi restaurada a informação planimétrica capaz de representar a região numa carta-imagem, em cores (radiometria ou atributos de cores) bem próximos da composição RGB original das bandas TM 5, 4 e 3, da Figura 02.

3.4 - Classificação Digital de Máxima Verossimilhança

Para que a imagem híbrida, possa finalmente ser usada como produto tipo carta-imagem, se faz necessária uma interpretação visual, entre as imagens originais SAR JERS-1 e LANDSAT TM, bem como uma classificação digital, que possa ser usada como *template*, para a colocação da toponímia e simbologia adequadas aos diversos acidentes naturais e artificiais,

sobre a superfície terrestre, de acordo com a escala de representação sistemática.

Foi escolhido o classificador de Máxima Verossimilhança pontual, pelo fato da imagem híbrida ter sido gerada com mais de 50% de informações da imagens LANDSAT TM.

Analogamente foi feita a mesma classificação sobre a imagem LANDSAT TM original comparando as classificações para a detecção de distorções aberrantes, porventura existentes.

Para estas classificações supervisionadas, foram coletadas amostras de treinamento para determinação dos parâmetros pelo classificador escolhido conforme mostrado na Figura 05.

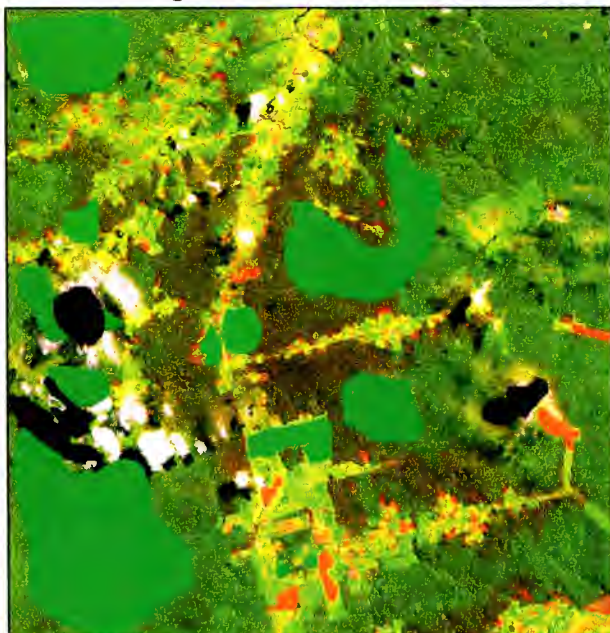


Figura 05 - Amostras coletadas para o treinamento do classificador de Máxima Verossimilhança

Pode-se notar através das regiões escolhidas como amostras que foram escolhidas 4 classes:

- a) Na cor **preta**: Amostras de nuvens e sombras;
- b) Na cor **verde escuro**: Amostras de floresta primária;
- c) Na cor **verde claro**: Amostras de não-floresta, incluindo, pastos sujos ou limpos, árvores de rebrota, áreas de utilizações agrícolas.
- d) Na cor **coral**: Áreas de solo exposto.

Embora as nuvens tenham reflectividade branca e as sombras tenham cor negra, na composição **RGB** da Figura 02, para fins de classificação foi escolhida a mesma cor **preta**, tanto para nuvens, quanto para sombras, com a finalidade de simbolizar o atributo de DESINFORMAÇÃO na imagem da composição colorida **RGB 543 - TM**.

Estas amostras, portanto, não tem caráter classificatório, tem apenas a finalidade de indicar as regiões onde não se pode determinar o que existe nas ditas regiões.

Os resultados destas classificações podem ser visualizadas nas imagens contidas nas Figuras 06 e 07.

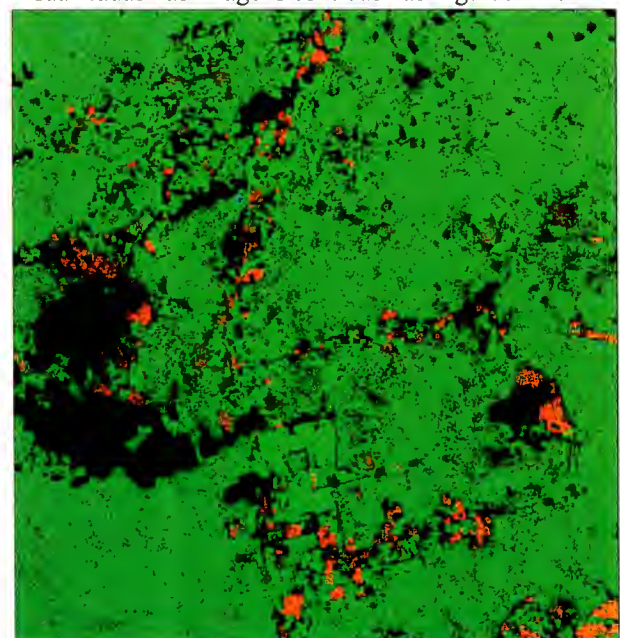


Figura 06 - Imagem da composição **RGB 543 - TM** classificada.

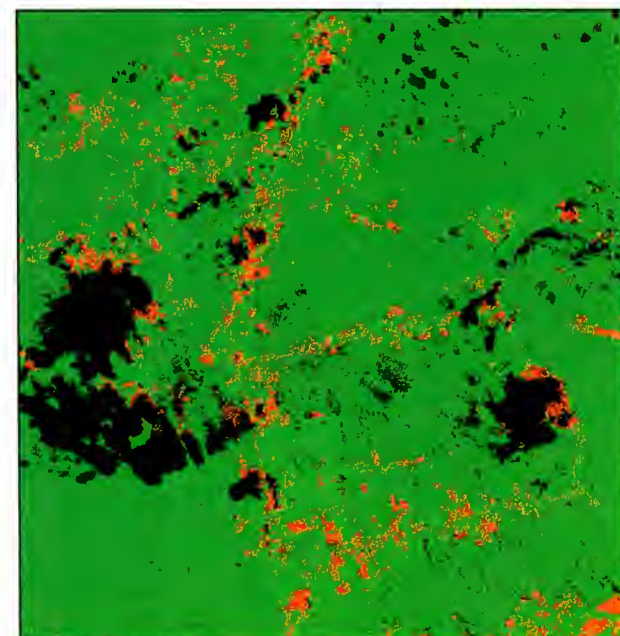


Figura 07 - Imagem LANDSAT TM classificada, filtrada pelo filtro da moda de dimensão *5X5 pixels*.

Nestas duas imagens, pode-se notar as manchas negras, regiões não classificadas, por opacidade ou sombras relativas às nuvens. A cor verde clara predomina sobre a cor coral, significando que foi considerado maior área de não floresta do que solo exposto.

Foram desconsideradas nessas imagens classificadas, o atributo bordas, por causa do tamanho da janela utilizada para a filtragem da moda.

Nas Figuras 08 e 09 a mesma classificação MAXVER, na imagem híbrida.

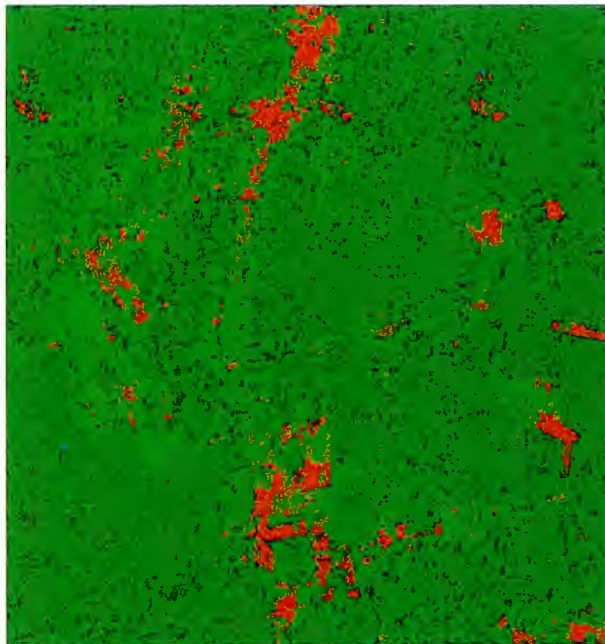
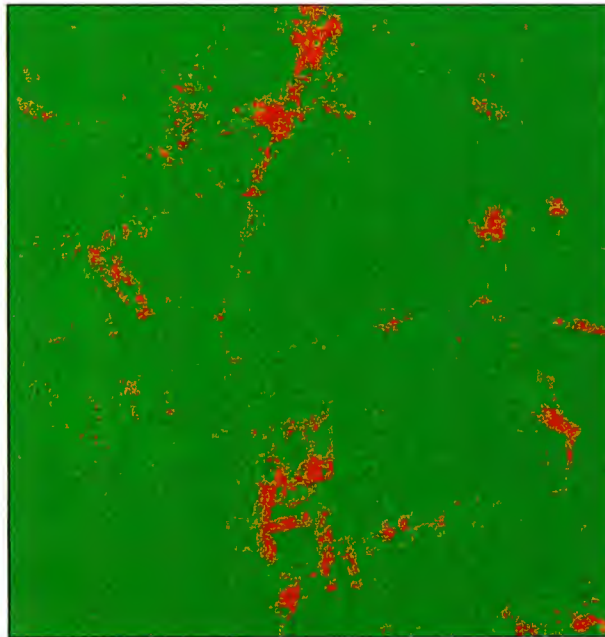


Figura 08 - Imagem híbrida TM/SAR classificada.



9 - Imagem híbrida classificada, filtrada com filtro da moda de dimensão 5X5 pixels.

É possível perceber que nas regiões onde a classificação da imagem LANDSAT TM havia áreas de desinformação, nas imagens classificadas do produto híbrido aparecem classificadas, embora com áreas de erro, onde nuvens foram tomadas como não floresta. Porém, apesar da radiometria original da imagem LANDSAT TM ter sido perdida tanto pelas operações de principais componentes, transformações IHS e inclusão de uma banda RADAR, a classificação da

imagem híbrida é bem próxima da original, tendo a vantagem de não haver áreas não classificadas. O fluxograma completo de toda a metodologia utilizada está descrito na Figura 10.

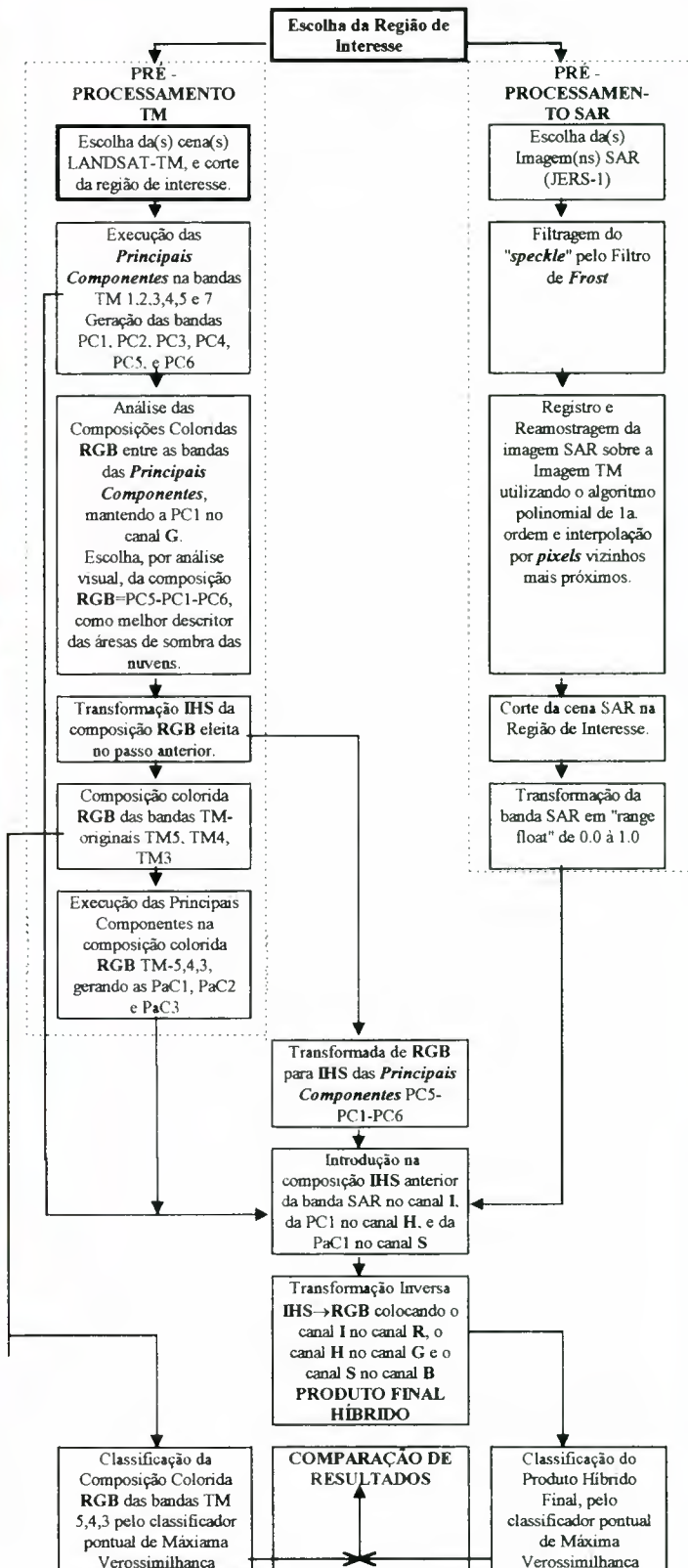


Figura 10 - Fluxograma da Metodologia da Integração de Dados TM/SAR

4 - Conclusão

O produto final híbrido mostrou-se satisfatório para a confecção de carta-imagem. Não obstante ter havido perda da radiometria da imagem LANDSAT TM (com todo o processamento efetuado), o resultado da classificação da imagem híbrida apresentou-se bem coerente com a verdade terrestre. Esta classificação servirá apenas como *template*, em combinação com a imagem SAR JERS-1 original, para quantificar e qualificar os acidentes naturais ou artificiais, passíveis de serem representados em uma carta-imagem. Possibilitando desta forma, a um custo muitíssimo menor quando comparada com a técnica de coleta multitemporal de dados de um mesmo sensor, na tentativa de compor uma imagem isenta de nuvens e sombras.

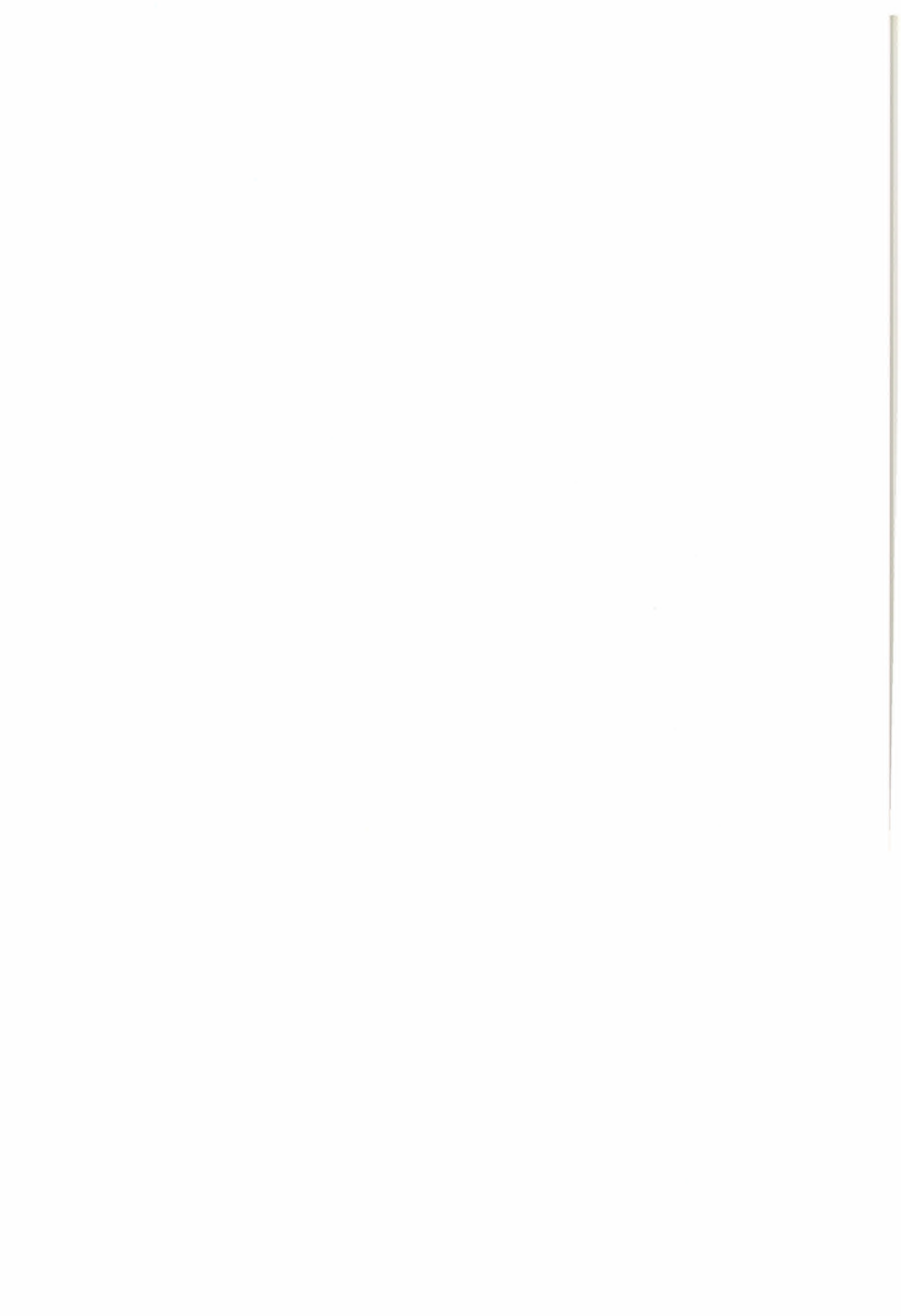
Tem, a vantagem ainda, de em regiões de parcial cobertura permanente de nuvens o ano inteiro, a confecção de cartas-imagens ou geração de produtos coloridos, próximos de uma composição colorida original, servir de base de dados para Sistemas de Informações Geográficas, em geoprocessamento.

AGRADECIMENTOS

Os autores são extremamente gratos ao Sr. MSc. ULF WALTER PALME, por todo o seu apoio e precisa orientação técnica e também ao CNPq, através do Projeto PROTEM-CC GEOTEC (Processo 680.061-94-0)

5 - Referências Bibliográficas.

- AHERN, F., J. *Basic Concepts of Imaging Radar, a Intensive Course*. Instituto Nacional de Pesquisas Espaciais, São José dos Campos, Outubro, 1994.
- BROCKWELL, P.J.; DAVIS, R. A. *Time series: theory and methods*. Berlin, Springer-Verlag, 1987.
- CROSTA, A. P. *Processamento Digital de Imagens de Sensoriamento Remoto*. Campinas, SP, UNICAMP, 1992, 170p.
- DUTRA, L. *Classificação de Texturas usando Modelos ARMA e Distâncias da Função de Autocorrelação*. (Tese de Doutorado em Computação Aplicada). Instituto Nacional de Pesquisas Espaciais, São José dos Campos, Abril 1990, 162 p. (INPE-5067-TDL/406).
- FRERY, L.V.; SANT'ANNA, S.J.S. *Non-adaptive robust filters for speckle noise reduction*. In: Simpósio Brasileiro de Computação Gráfica e Processamento de Imagens, 6., Recife, PE, 19-22 out. 1993. Anais. Recife, SBC/UFPB, out. 1993, pp. 165-174
- FROST, V.S.; STILES, J. A.; SHANMUGAN, K.S.; HOLTZMAN, J. C. *A model for radar images and its applications to adaptative digital filtering of multiplicative noise*. IEEE Trans. on Pattern Analysis Machine Intelligence, PAMI-4: 157-166, 1982.
- KRUG, T. *Statiscal approaches to the estimation of missing values arising in remotely sensed data*. (PhD Thesis) - University of Sheffield, 1992.
- LILLESAND T., M.; KIEFER, R. W. *Remote Sensing and Image Interpretation*. John Wiley & Sons, New York, NY, 1987.
- MARCHETTI, D. A.B.; GARCIA, G. J. *Princípios de Fotogrametria e Fotointerpretação*. São Paulo, Nobel, 1986, 264p.
- NETER, J.; WASSERMAN, W. *Applied Linear Statistical Models*. Richard D. Irwin Inc., Homewood, Illinois, 1974, 415p.
- PALME, U. W. *Radares geradores de imagens. Fundamentos*. Notas de curso. Fundación Instituto de Ingeniería. Caracas, Venezuela. 1995, 20 p.
- PORAT, B. *Digital Processing of Random Signals: Theory & Methods*. New Jersey, Englewood Cliffs, 1994, 449 p.
- RICHARDS, J. A. *Remote Sensing Digital Image Analysis*. Springer-Verlag, Berlim, 1986, 281 p.
- SANABRIA, Y. R., *Integracion de datos LANDSAT TM-5 y ERS-1, en el mapeamiento de unidades ecológicas en la Amazónia Brasileira-Colombiana (Tabatinga-Leticia)*, INPE, São José dos Campos, SP, Dezembro de 1995.
- SANT'ANNA, S.J.S. *Avaliação do desempenho de filtros redutores de "speckle" em imagens de RADAR de Abertura Sintética*. (Dissertação de Mestrado em Sensoriamento Remoto) - Instituto Nacional de Pesquisas Espaciais, São José dos Campos, SP, Novembro de 1995.
- SANT'ANNA, S. J. S.; DUTRA, L. *SAR Texture Discrimination using AR-2D models for Amazonian Land use classification*. Instituto Nacional de Pesquisas Espaciais, São José dos Campos, 1995.
- SLATER, N. P. *Remote Sensing: Optics and optical systems*. Addison-Wesley Publishing Company, London, 1980.



INTEGRAÇÃO DE DADOS DE RADAR ADQUIRIDOS COM DIFERENTES ÂNGULOS DE INCIDÊNCIA PARA ESTUDOS DE RESERVATÓRIO NA AMAZÔNIA.

Maycira Pereira de Farias Costa¹, Evelyn M.L. de M. Novo¹, Frank J. Ahern²

¹ INPE- Instituto Nacional de Pesquisas Espaciais.

tel:(012) 3526433, e-mail: maycira@ltid.inpe.br

² CCRS- Canada Center for Remote Sensing.

RESUMO

Dados SAR-C HH aero-transportado foram adquiridos em diferentes ângulos de incidência (43° , 66° , 76°) e direções de visada. Os dados foram integrados com o objetivo de estudar o efeito do ângulo de incidência da radiação de microondas na separabilidade de diferentes grupos de plantas aquáticas, floresta e água, no reservatório de Tucuruí, Amazônia.

As imagens digitais foram inicialmente calibradas radiometricamente e filtradas com filtro de média 3×3 , objetivando um balanço entre a redução do speckle, a preservação das bordas e a resolução do pixel. A correção geométrica foi realizada de acordo com o modelo de orto-retificação que considera a geometria de visada do sensor, as características da Terra e a projeção cartográfica. Mapas topográficos (1:100.000) e imagem TM/Landsat foram utilizados como base cartográfica. Fotografias aéreas (1:10.000) foram utilizadas para auxiliar no mapeamento dos temas de interesse. A Distância de Bhattacharya foi utilizada para determinar uma medida de separabilidade entre as diferentes classes, para os diferentes ângulos de incidência e combinação destes. Os resultados mostraram uma baixa separabilidade entre as classes quando se utilizou apenas um dado ângulo de incidência. Dados integrados com diferentes ângulos de incidência demonstraram um melhor índice de separabilidade entre as classes.

1. INTRODUÇÃO

O entendimento e monitoramento de alterações ambientais em reservatórios da Amazônia não é uma tarefa fácil, principalmente devido a grande extensão destas áreas e a dificuldade de acesso para coleta de dados. Técnicas de sensoriamento remoto podem ser utilizadas nestas regiões pois permitem uma visão sinóptica. Sistemas ópticos foram utilizados por algum tempo para estudo de monitoramento de plantas aquáticas (Abdon e Meyer, 1990) e qualidade da água (Braga, 1990; Pereira Filho, 1990; Steffen et al., 1993). Contudo, a cobertura de nuvens, praticamente constante na região, limita o uso de sistemas ópticos. Imagens de radar vêm se mostrando muito úteis para estudos de reservatórios na Amazônia, devido a sua

independência em relação a cobertura de nuvens e à capacidade de detecção de áreas inundadas sob uma cobertura vegetal.

Uma série de trabalhos tem mostrado a importante utilização de dados de radar para estudos de monitoramento de vegetação, quando o substrato é solo ou água. Outros trabalhos mostram o estudo de plantas aquáticas através de dados de radar. Para estudo da interação da radiação de microondas com a vegetação a geometria, o volume e o conteúdo de umidade da vegetação são os fatores que mais influenciam na profundidade de penetração da radiação, em uma certa freqüência. Sabe-se que um aumento no conteúdo de umidade da planta, acarreta uma diminuição na profundidade de penetração da radiação no meio e, consequentemente, aumenta o retroespalhamento da radiação. Trabalhos experimentais também têm demonstrado que o tipo e intensidade da resposta polarizada varia de acordo com a estrutura da vegetação. Por exemplo, para ondas incidentes polarizadas verticalmente, estruturas verticais tendem a exibir uma maior atenuação para polarização V do que para polarização H (NASA/JPL, 1986).

O ângulo de incidência da radiação também desempenha um papel importante no comportamento do retroespalhamento da radiação. Isto é particularmente verdade quando se considera o substrato em que está a vegetação, como por exemplo solo ou água, os quais primariamente produzem espalhamento de superfície. Porém, quando a interação é do tipo espalhamento de volume o retroespalhamento diminui muito lentamente com o aumento do ângulo de incidência. Ulaby et al. (1986) mostram que o retroespalhamento do substrato (solo) é mais importante para ângulos de incidência próximo do nadir (para menores freqüências), enquanto que para ângulos de incidência maiores, o espalhamento de volume da vegetação é o mais importante.

Vários autores têm mostrado que há um aumento do retroespalhamento da vegetação quando o substrato é a água (Richards et al., 1982; Ford e Casey, 1988; Hess et al., 1990, entre outros). Hess et al., (1990) discutiram a influência do ângulo de incidência, polarização e freqüência no coeficiente de

retroespalhamento de vegetação inundada. De acordo com os autores existem vários dados controversos, principalmente devido às diferenças nas estruturas da vegetação e à falta de dados calibrados. Contudo, os autores também mostram que o retroespalhamento da vegetação em pântanos é maior para ângulos de incidência menores. Ford e Casey (1988) explicaram que o retroespalhamento para regiões de pântanos com árvores é resultante de uma componente adicional da energia de microondas que penetra na vegetação, interage com a água/tronco, e retorna por reflexão por um efeito denominado "double-bounce". Os autores também observam uma diminuição do retroespalhamento com o aumento do ângulo de incidência da radiação, para áreas de pântano. Uma provável explicação seria: com o aumento do ângulo de incidência há um aumento nos 2 caminhos que a radiação percorre (incidência e retroespalhamento) sendo a radiação atenuada exponencialmente na vegetação, resultando em uma redução da componente de "double-bounce". Alguns trabalhos analisados por Hess et al., (1990) utilizando dados na banda L demonstraram que o contraste entre vegetação de pântano e vegetação de terra-firme é maior em polarização paralela (HH e VV) do que em polarização cruzada (HV e VH), e que a razão entre polarizações pode fornecer resultados interessantes.

Hess et al., (1995) apresentaram alguns dados do experimento SIR-C realizado na Amazônia. De acordo com os autores o efeito "double-bounce" é observado para plantas aquáticas para bandas C e L, e a banda C-HH não permite a discriminação entre plantas aquáticas e floresta inundada. Os autores também enfatizam que dados de multipolarização e multifreqüência permitem a discriminação entre plantas aquáticas, floresta, floresta inundada, pasto e água na área de estudo da Amazônia. Novo et al., (1995) analisando imagens SAR-C aerotransportado de polarização cruzada e polarização paralela da Amazônia mostram que plantas aquáticas podem ser separadas em pelo menos dois grandes grupos: as com forma de capim e as com folha espalmada. As análises destes mesmos dados também mostraram que o espalhamento de volume é o mecanismo primário de espalhamento para plantas aquáticas na banda C, durante a estação de cheia. Os mesmos dados mostraram que a composição de multipolarizações permite uma melhor separabilidade entre classes de plantas aquáticas (Costa, 1995; Costa et al., 1996). Imagem do satélite JERS-1 da mesma área mostrou uma melhor discriminação entre terra e água, e uma pior separabilidade entre plantas aquáticas, quando comparado com dados SAR-C HH aerotransportado (Novo e Costa, 1996).

Como vários autores citados anteriormente têm demonstrado, a utilização de dados de radar com multipolarização, multi-freequência ou multi-ângulo de

incidência é de grande importância para melhor caracterização dos alvos, devido a interação diferenciada destes com a radiação de microondas. Atualmente a disponibilidade de vários satélites (ERS, JERS1 e RADARSAT) com sensores operando na faixa de microondas permite o aproveitamento destas multi-características. Especificamente, o satélite RADARSAT com a possibilidade de aquisição de dados em diferentes ângulos de incidência vem a ser uma ferramenta importante no estudo e monitoramento de recursos terrestres. Porém, a integração de dados com multi-ângulo de incidência, e diferentes resoluções requer um pré-processamento dos dados considerando o método de filtragem e o algoritmo de retificação geométrica (Toutin, 1995; Crevier et al., 1996).

Dentro deste contexto, este trabalho apresenta uma breve descrição da integração de dados de radar aerotransportados adquiridos em diferentes ângulos de incidência e direções de visada, com o objetivo de estudar o efeito do ângulo de incidência da radiação de microondas na separabilidade de diferentes grupos de plantas aquáticas, floresta e água, no reservatório de Tucuruí, Amazônia.

2. ÁREA DE ESTUDO

A inundação de grandes áreas de florestas para a construção de reservatórios pode resultar em uma série de alterações ambientais, com por exemplo: alteração na qualidade da água; infestação por plantas aquáticas; alteração do ciclo de emissão de gases para a atmosfera; aumento de doenças tropicais; entre outras.

A hidroelétrica de Tucuruí ($2^{\circ}00'S/46^{\circ}00'W$ e $18^{\circ}00'S/55^{\circ}00'W$) na bacia dos rios Araguaia/Tocantins, é a quarta maior hidroelétrica do mundo, com uma atual capacidade de geração de energia de 4MW e com futura expansão de 8MW (Forattini et al., 1990).

Inundando uma área de aproximadamente 2430km², com profundidade média de 19m, uma série de alterações ambientais vem ocorrendo desde o enchimento do reservatório. O reservatório de Tucuruí é objeto de estudo para desenvolvimento de metodologia objetivando o monitoramento destas regiões com auxílio de dados de sensoriamento remoto.

O reservatório apresenta uma forma dendrítica e um tempo de residência da água entre 20 a 500 dias (Pereira Filho, 1990). A variação do fluxo sazonal, as características do reservatório e o tempo de retenção induz a infestação por macrófitas e a diminuição da qualidade da água.

De acordo com um levantamento realizado por Abdon e Meyer (1990), usando dados TM/Landsat, a área

coberta por plantas aquáticas tem diminuído desde o início das operações do reservatório, e durante a estação seca a área coberta pelas macrófitas representa 20% da superfície do reservatório. A cobertura de macrófitas durante a estação de cheia é desconhecida devido ao problema de nuvens.

As principais espécies de plantas aquáticas encontradas no reservatório são: *Eichhornia crassipes*, *Salvinia auriculata*, *Pistia stratiotes*, *Typha* sp, *Aninga* e *Scirpus* sp. Algumas características destas espécies são descritas por Novo et. al. (1995).

3. METODOLOGIA

3.1. Dados utilizados.

Os dados SAR utilizados (bra33HH - Fig. 1, bra34HH - Fig. 2, bra43HH - Fig. 3) neste estudo estão descritos na Tabela 1. Foram também utilizadas fotografias aéreas (1:10.000) e imagens TM/Landsat. As fotografias aéreas e imagens SAR foram adquiridas durante a mesma semana, em abril de 1992, sobre o canal do Pucuruizinho, como parte do projeto SAREX. A imagem Landsat foi adquirida em junho do mesmo ano, o que possibilitou a sua utilização para auxiliar a correção geométrica das imagens SAR.

Tabela 1. Descrição dos dados SAR.

Dado	bra33	bra34	bra43
Polarização	HH	HH	HH
Banda	C	C	C
cobertura (km)	55x18	350x60	55x10
direção de visada	direita	esquerda	esquerda
ângulo de incidênc.cia	~43°	~66°	~76°
tamanho do pixel (m)	4x4.31	4x4.31	15x6.9
resolução (m)	6x6	6x6	20x10
looks	7	7	7

3.2. Pré-processamento para integração dos dados.

Para integração dos dados SAR podemos separar o pré-processamento nas seguintes etapas: calibração radiométrica, filtragem para redução do “speckel” e correção geométrica.

A calibração geométrica é uma etapa necessária para correção do efeito de padrão de antena das imagens SAR. As imagens foram calibradas de acordo com os parâmetros de calibração sugeridos por Hawkins e Teany (1992).

Foi aplicado um filtro de média 3x3 considerando a redução do ruído multiplicativo “speckel”, a garantia do mesmo processamento em toda a imagem, a resolução dos dados e a preservação das bordas.

Após a filtragem das imagens SAR, procedeu-se à correção geométrica da imagem TM/Landsat, das fotografias aéreas no formato digital e das imagens SAR para a projeção cartográfica UTM. As imagens TM/Landsat e SAR foram orto-retificadas de acordo com o método de modelagem matemática desenvolvido por Toutin (1994, 1995). Este método pode ser utilizado para correção geométrica de imagens de sensores ópticos ou microondas, tanto aero-transportados como de satélites, utilizando dados de elevação do terreno. O modelo integra a geometria de visada, o que inclui a posição e a velocidade da plataforma, os parâmetros do sensor, as características da Terra e da projeção cartográfica. Um valor de altitude médio de 75m representativo da área foi utilizado gerando imagens orto-retificadas. A precisão média do modelo e da restituição para as imagens SAR foi de 16,5 e 30,1 metros, respectivamente. Considerando a precisão do modelo e a resolução dos dados originais foram geradas imagens com tamanho de pixel de 15x15 metros, utilizando-se o interpolador por convolução cúbica.

3.3. Determinação da separabilidade entre as classes.

3.3.1. Aquisição de amostras e determinação dos valores de retroespalhamento.

Para o teste de separabilidade espectral foram determinadas as seguintes classes: *Eichhornia* (**ech**), *Pistia* (**pst**), *Scirpus* (**scp**), *Salvinia* (**slv**), *Aninga* (**ani**) (grupos de plantas aquáticas), heterogênea (**htr**) (diferentes grupos de plantas aquáticas), “paliteiro” (**plt**) (tronco de árvores na água), água (**agu**) e floresta (**flt**). As amostras para determinação das classes foram identificadas nas imagens SAR com o auxílio do mosaico digital das fotografias aéreas.

Um número mínimo de 30 pixels para cada amostra foi considerado. Este valor corresponde a um número maior de amostra independente de “multi-look” do que o mínimo requerido (Laur et al., 1987; Touzi, 1995), e de acordo com os testes de homogeneidade realizados. Foram determinadas as médias de todas as classes para cada polarização e calculados os valores de retroespalhamento (**rs**) correspondentes de acordo com a seguinte equação de calibração:

$$rs = 10 \times \log_{10} DN + (F_{cal})$$

onde: DN é o valor digital médio para uma classe
rs é o valor de retroespalhamento médio para uma classe

F_{cal} é o fator de calibração médio fornecidos pelo CCRS.

3.3.2. Cálculo do índice de separabilidade entre as classes.

O método de Distância de Bhattacharya (DB) foi adotado para calcular a separabilidade entre as classes para um único dado com determinado ângulo de incidência e a combinação de dados com diferentes ângulos de incidência. Esta separabilidade matemática é calculada através das médias e matrizes de covariância das classes, resultando em uma distância que varia de 0 a 2 com os seguintes intervalos:

- 0 - 1.0 - separabilidade muito baixa
- 1 - 1.9 - separabilidade baixa
- 1.9 - 2.0 - boa separabilidade.

4. ANÁLISE DOS DADOS.

4.1. Análise dos valores de retroespalhamento.

A Tabela 2 apresenta os valores de retroespalhamento calculados para cada classe de interesse.

Tabela 2 - Coeficiente de retroespalhamento (CR)

Classes	33HH(43°)	34HH(66°)	43HH(76°)
ech	-15.38	-7.75	-10.34
pst	-13.72	-11.31	-13.26
scp	-10.96	-8.4	-11.13
agu	-28.37	-28.88	-25.66
het	-11.94	-9.31	-12.76
flt	-11.8	-10.07	-12.67
slv	-15.50	-15.01	-14.53
ani	-14.97	-10.93	-9.47
plt	-16.24	-13.81	-15.59

Em geral, variações no ângulo de incidência da radiação de microondas afeta a capacidade de penetração da radiação em alvos terrestres. Grandes ângulos de incidência resultam em longo trajeto para a radiação incidente atravessar um alvo denso, resultando em uma maior atenuação da radiação de microondas pelos constituintes do alvo. Para superfícies consideradas muito rugosas em relação ao comprimento de onda, os valores de retroespalhamento não são afetados seriamente com a variação do ângulo de incidência da radiação (Ulaby et al., 1986). De acordo com o critério de rugosidade de Fraunhofer, o comprimento de onda e o ângulo de incidência da radiação, as classes de vegetação em estudo são consideradas superfícies rugosas. Portanto, não são observados efeitos de "double-bounce" nem uma componente especular, o que pode indicar a predominância de interação do tipo espalhamento de volume para as classes de vegetação em estudo.

Os valores de retroespalhamento para classe água (agu) são tipicamente baixos para todos os ângulos de

incidência devido a reflexão especular. A classe "paliteiro" (plt) é representada por água e troncos de árvores resultando em uma aumento do retroespalhamento, quando comparado com a classe água, devido ao efeito de "double-bounce" entre o tronco e a água.

A classe floresta (flt) apresenta valores de retroespalhamento dentro do esperado (Ulaby e Dadson, 1989) resultante da componente de espalhamento dos galhos das árvores.

A análise da Tabela 2 mostra que existe uma diferença nos valores de retroespalhamento das diferentes classes de plantas aquáticas devido à variação nas estruturas e na distribuição espacial dos grupos, entre outros fatores.

As classes *Salvinia* e *Pistia* mostram valores de retroespalhamento baixos para todos os ângulos de incidência. Estes grupos podem ser considerados superfícies ligeiramente lisas e com alta constante dielétrica devido a proximidade da água, resultando em uma reflexão quase-especular. A classe *Scirpus* apresenta alto retroespalhamento devido a estrutura densa vertical deste grupo produzindo um alto efeito de espalhamento de volume. O mesmo pode ser considerado para classe heterogênea, composta basicamente de vegetação com a mesma estrutura do *Scirpus*. As classes *Eichhornia* e *Aninga* apresentam estruturas densas com folhas orientadas aleatoriamente sugerindo um efeito de volume de espalhamento, principalmente para os maiores ângulos de incidência, onde são observados altos valores de retroespalhamento quando comparado com a imagem 33HH (43°).

4.2. Análise dos índices de separabilidade entre as classes.

A Tabela 3 apresenta o resultado do índice de separabilidade entre as classes para cada ângulo de incidência e para a combinação dos 3 diferentes ângulos de incidência.

Para o cálculo do grau de separabilidade total (GST) para cada dado adotou-se o seguinte procedimento: 1) somou-se os índices de separabilidade entre o conjunto de classes para cada dado, resultando em 3 grupos de separabilidade: muito baixa, baixa, boa; 2) aplicou-se um peso a cada grupo de separabilidade e a soma destes resultou no grau de separabilidade total (GST) para um determinado dado. Os pesos aplicados a cada grupo de separabilidade obedeceram o seguinte critério:

- | | |
|--------------|--------|
| muito baixa: | peso 0 |
| baixa: | peso 1 |
| boa: | peso 2 |

Comparando o GST para os diferentes ângulos de incidência, observa-se que a imagem 43HH apresenta o mais baixo valor. As prováveis razões para este baixo valor são: a pior resolução (10x20m) e o mais alto ângulo de incidência (77°), diminuindo a separabilidade entre as classes. As imagens 33HH e 34HH apresentaram graus de separabilidade semelhantes, indicando que não existem diferenças na separabilidade entre as classes para ângulos de incidência de 43° e 66° .

Tabela 3. Separabilidade entre as classes de acordo com a Distância de Bhattacharya.

Grau de separabilidade(GS)	muito baixo	baixo	bom	total
33HH (43°)	22	11	3	17
34HH (66°)	22	11	3	17
43HH (76°)	28	8	0	8
33HH/34HH/43HH	11	17	8	33

A composição de multi-ângulo de incidência apresentou o mais alto GS total, indicando que para separabilidade dos alvos em estudo a possibilidade de utilização de dados adquiridos com ângulos de incidência diferentes vem a ser uma ferramenta importante.

5. CONCLUSÃO

Em preparação para utilização dos dados do satélite RADARSAT adquiridos com diferentes ângulos de incidência, o presente estudo sugere que:

1. A metodologia de pré-processamento para integração de dados SAR é satisfatória e importante.
2. O mecanismo de “double-bounce” ocorre provavelmente somente entre os paliteiros e a água. Um espalhamento quase-especular é observado para as classes de plantas aquáticas com tamanho inferior a 5cm. O espalhamento de volume deve ser o mecanismo primário de espalhamento para as demais classes. Para melhor compreensão dos mecanismos de espalhamento seriam necessárias mais informações sobre a estrutura das plantas, biomassa e conteúdo de água.
3. De acordo com a distância de Bhattacharya, a separabilidade entre classes é baixa para imagens individuais, e aumenta para a composição de diferentes ângulos de incidência. A mais baixa separabilidade entre as classes é observada para ângulos de incidência altos (77°). Este resultado parece indicar que para estudos com as mesmas características de alvos deste trabalho, os dados do satélite RADARSAT standard 6 ($41\text{--}46^\circ$ - Figura 5) ou combinação de diferentes modos de aquisição devem fornecer uma boa separabilidade entre alvos.

Agradecimentos: Os autores agradecem a ELETRONORTE pelo apoio de campo, a CIDA (Canadian International Development Agency) pelo suporte financeiro para desenvolvimento e oportunidade de apresentação deste trabalho.

REFERÊNCIAS

Abdon, M.M., Meyer, M. Variação temporal de áreas ocupadas por macrófitas aquáticas no reservatório de Tucuruí através de dados de satélite Landsat/TM. IN: Simpósio Brasileiro de Sensoriamento Remoto, 4., Jun., 24-29, Manaus. *Anais*. pp:545-548, 1990.

Braga, C.Z.F. Avaliação preliminar da produtividade primária na represa de Tucuruí, Pará, com utilização de imagens TM. In: Simpósio Brasileiro de Sensoriamento Remoto, 6., Jun., 24-29, Manaus. *Anais*. pp:826-832, 1990.

Costa, M.P.F. The effect of airborne SAR-C multipolarization and multiangle images in the backscattering separability of aquaticplants in the Brazilian Amazon basin. Technical Report. Canadian Center of Remote Sensing, 1995.

Costa, M.P.F.; Ahern, F; Novo, E.M.L.M.; Pietsch, R.W.; Noernberg, M.A. Separability of aquatic plants in the Brazilian Amazon using multi-polarization C-band SAR data. 26th International Symposium on Remote Sensing of Environment, Canada, 1996

Evans, D.L., Farr, T.G., Ford, J.P., Thompson W.T., Werner, C.L. Multipolarization radar images for geologic mapping and vegetation discrimination. *IEEE Transactions on Geoscience and Remote Sensing*. 24(2): 246-257, 1986.

Forattini, G.D., Barbosa, J.A. Aplicação de modelos matemáticos de qualidade de água na elaboração do plano de utilização do reservatório de Tucuruí. In: Hydrology and water management of the Amazon basin. *Proceedings*. Aug., 5-9, 1990, Manaus, AM, pp:3-15.

Ford, J.P., Casey, D.J. Shuttle radar mapping with diverse incidence angles in the rainforest of Borneo. *International Journal of Remote Sensing*. 9(5):927-943, 1988.

Hawkins, R.K., Teany, L.D. SAREX-92, Data calibration. Workshop-Sarex-92. *Proceedings*. Paris, 6-8, pp:41-53, 1993.

Hess, L.L., Melack, J.M., Simonett, D. Radar detection of flooding beneath the forest canopy: a review. *International Journal of Remote Sensing*. 11(7):1313-1325, 1990.

Junk, W.J., Nunes de Mello, J.A.S. Impactos ecológicos das represas hidroelétricas na bacia amazônica brasileira. *Estudos Avançados*. 4(8):126-143, 1987.

Laur, H., Le Toan, T., Lopes, A. Textural segmentation of SAR images using first order statistical parameters. In: *IGARSS'87 Symposium. Proceedings*. Ann Arbor, 18-21 May, pp:1463-1468, 1987.

NASA. Shuttle Imaging Radar-C Science Plan. Jet Propulsion Laboratory, Pasadena, CA. JPL publication 86-29, 1986.

Novo, M.L.M., Costa, M.P.F., Noernberg, M.A. Airborne SAR data to map Tucuruí reservoir (Amazon). In: *Workshop-Sarex-92, Proceedings*. Paris, 6-9, 1993, pp:71-86.

Novo, E.M.; Costa, M.P.; Noernberg, M.A., (1995), Relatório Preliminar do Projeto SAREX Tucuruí. INPE, (INPE - 5621-PRP/190), São José dos Campos.

Novo, E.M.L.M.; Costa, M.P.F. Radar detection of Macrophyte stands using L band and C band. *ISPRS*. Viena, 1996.

Pereira, A., Tassin, B., Jorgensen, S.E. A model for decomposition of the drowned vegetation in an amazonian reservoir. *Ecological Modelling*. 75/76: 447-458, 1994.

Pereira Filho, W. *Metódos de integração de dados de campo de sensoriamento remoto no estudo da influência de características de bacia de captação sobre a concentração de sedimentos em suspensão em reservatório*. Dissertação de mestrado em Sensoriamento remoto e aplicações. INPE, São José dos Campos, 1990.

Richards, J.A.; Woodgate, P.W.; Skidmore, A.K. An explanation of enhanced radar backscattering from flooded forest. *International Journal of Remote Sensing*. 8(7)1093-1100, 1987.

Steffen, C.A., Costa, M.P.F., Gama, F.F. Spectral reflectance of Tucuruí reservoir waters-Brazilian Amazon, In:*SPIE, Proceedings*, 14-15, Apr., 1993, Orlando, FL, pp:103-111.

Toutin, T. Multisource data intégration with an integrated and unified geometric modelling. In: *Sensors and Environment Applications of Remote Sensing. Proceedings*. Askne (ed.), Balkema, Rotterdam. pp:163-169, 1995.

Ulaby,F.T., Moore,R.K., Fung, A.K. *Microwave Remote Sensing*. vol., 1, 2 and 3. Dedham, MA, 1986.

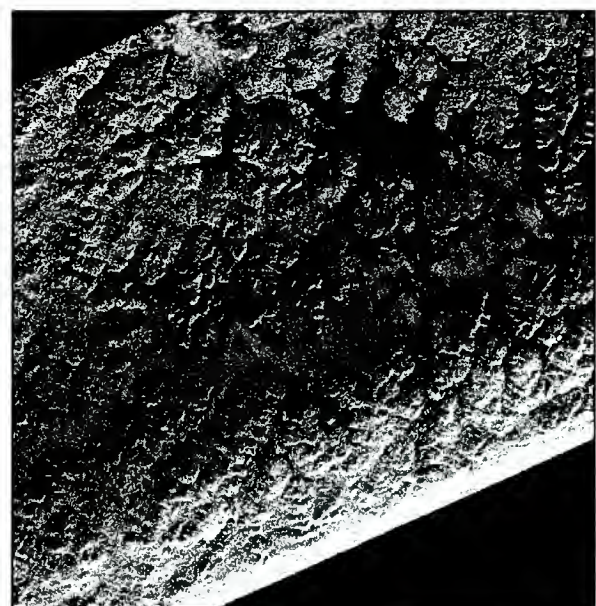


Figura 1. Imagem bra33HH - 43° ângulo de incidência.

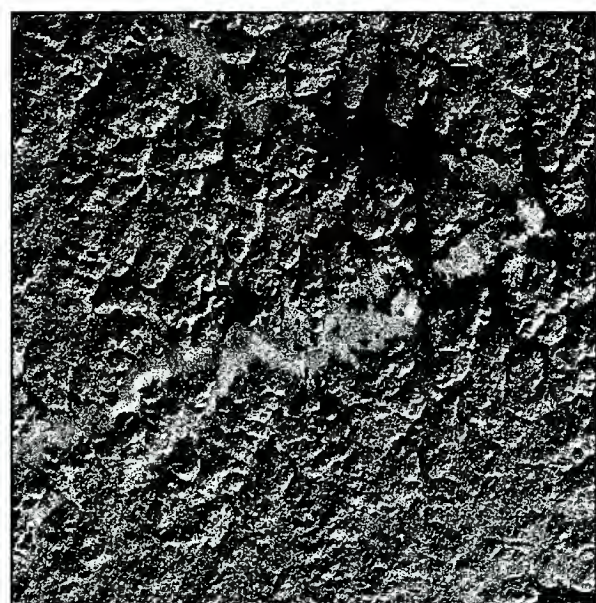


Figura 2. bra34HH - 66° ângulo de incidência



Figura 3. bra43hh - 76° ângulo de incidência.



Figura 5. Imagem RADARSAT - Standard 6, ascendente, 27 de Maio de 1996.

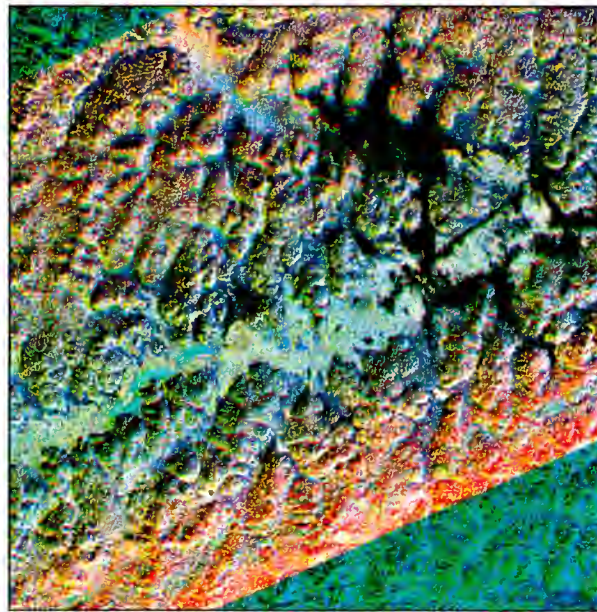


Figura 4. Composição colorida - 43°(R), 66°(G), 76°(B).

"APORTE EN LA INTERPRETACION VISUAL DEL USO DE LA TIERRA, DADO POR LA COMBINACION DEL SENSOR PASIVO TM, LANDSAT-4 Y EL SENSOR ACTIVO SAR ERS-1"

José Rafael Prieto Gómez.

**Instituto de Ingeniería
 Centro de Procesamiento Digital de Imágenes
 Apartado Postal 40.200
 Caracas, 1040-A
 Fax: +58-2-9420445
 Email: jprieto@conicit.ve**

RESUMEN

El siguiente trabajo expone la evaluación cualitativa en la interpretación visual del uso de la tierra y cobertura vegetal de la imagen combinada Landsat 4 TM / SAR ERS-1, comparándola con la realizada con el uso de la tradicional TM 4,5,3 en RGB del Landsat 4. La fusión se realizó con las bandas TM 4, TM 5 y SAR-C, en combinación RGB y composición IHS, con PCI. La interpretación se logró a través de un Procom-2, dando como resultado que las combinaciones obtenidas discriminaron el color, tono, textura y los bordes de los polígonos de la variable, mejor que con la combinación tradicional.

1.- INTRODUCCION

La combinación de imágenes de diferentes sensores se ha venido desarrollando desde el final de la década de los ochenta, alcanzando su mayor progreso en los años noventa, el objetivo propuesto en esas investigaciones, es el de complementar las resoluciones espectrales y espaciales de las imágenes resultantes. En particular, los sensores generalmente son complementarios, en cuanto al tamaño del pixel, región del espectro electromagnético donde trabajan, geometría en la obtención de la imagen, polarización y otros. El uso integrado de imágenes puede mejorar los estudios de temporalidad, para ello se combinan imágenes proveniente de sensores distintos en tomas de fechas diferentes.

Son muchos los trabajos desarrollados uniendo dos o más tipos de sensores y múltiples sus usos científicos, sin embargo en estos últimos años la unión de imágenes de Radares de Apertura Sintética (SAR) con sensores de tipo ópticos, ambos a bordo de satélites espaciales, han logrado la complementariedad de los datos, que en general, proporcionan óptimos resultado en cuanto a la interpretación.

La Combinación del sensor activo SAR con TM mejora la resolución espectral de la imagen resultante, las imágenes TM muestran información planimétrica multiespectral que discrimina muy bien la vegetación, el radar proporciona información del relieve como su orientación, discontinuidades y rugosidad, dada por su diferente condición de iluminación, (Rheault, M., et. al.

1991), la unión de muchas de éstas características arrojan como resultado, que éste tipo de combinación haya sido usado con múltiples fines cartográficos, en estudios de geología estructural, física, exploratoria, y en oceanografía, entre otros.

En cuanto a la interpretación del uso de la tierra, mediante éste tipo combinación, son pocos los estudios realizados, aún cuando, en algunos de los trabajos hechos con otros fines, destacan algunas bondades de estas imágenes, para el levantamiento de la actividad antrópica en el medio terrestre. La combinación por lo general realza la red de drenaje, agricultura (Yésou, H, et. al. 1993), diferencias entre cultivos, bosques, carreteras, ciudades, lugares de explotación minera y en fin, uso de la tierra (Rheault, M, op. cit.).

Para lograr la combinación de dos bases de datos provenientes de sensores de distinta naturaleza y con características contrastantes, se han utilizado varias técnicas, de las cuales las más usadas son la convencional combinación rojo-verde-azul (red-green-blue) RGB, las funciones aritméticas, el análisis por componentes principales (CPA) y la más utilizada en la actualidad la composición por intensidad, color o tono (Hue) y saturación (IHS).

La simple combinación RGB, generalmente tiende ha comprimir la saturación de colores (Gillespie, et. al. 1986), esta no se basa en la definición de atributos del color si no en su variación, obteniéndose un número de deficiencias implícitas en el procedimiento, aun cuando, producen buenos resultados manipulando correctamente los histogramas (Harris, J.R., et. al. 1990).

Las funciones aritméticas y el análisis por componentes principales, proporcionan a menudo información cualitativa y cuantitativa difícil de interpretar, así como manipulan las propiedades estadísticas de la imagen resultante, esto ocurre con mayor frecuencia en las imágenes obtenidas por componentes principales.

La composición IHS proporciona una conversión mecánica para exponer dos o tres base de datos independientes en una misma imagen (Daly, M., 1993), es una técnica que realza los atributos del color que están relacionados con la percepción del ojo humano

tales como, la intensidad que se refiere al brillo total del color, el tono o matiz referido al promedio de longitudes de ondas de luz constituyentes de un color y la saturación que es la pureza de un color relativa al gris (Harris, J. R., et. al., op. cit.).

Tanto la combinación RGB como la IHS han sido usadas como métodos para integrar información de diferentes sensores ópticos, activos-ópticos e incluso últimamente con mapas digitales (Harris, J. R., et. al., ident). Cuando se aplica composición IHS como técnica para la unión de SAR con TM se obtiene en un 80% excelentes características planimétricas para mapas 1:100.000 y escalas más pequeñas (Welch, R. et. al., 1988).

El objetivo general del presente trabajo fue el de obtener fusiones Landsat-TM y ERS-1 por medio de la combinación RGB y por composición IHS, para realizar interpretaciones del uso de la tierra, que permitieran comparar cualitativamente, los resultados del levantamiento de la información en forma tradicional (TM453) vs. el nuevo producto, con el fin de evaluar los aportes de éste último en cuanto a información visual, en el área de estudio y a escala 1:100.000.

2.- DELIMITACIÓN Y DESCRIPCIÓN DEL ÁREA DE ESTUDIO.

El área de estudio está representada por la región comprendida entre los $8^{\circ}32'00''$ y $8^{\circ}47'14,11''$ Norte, los $70^{\circ}04'06,3''$ y los $70^{\circ}23'22''$ Oeste, encontrándose en el territorio del estado Barinas en el occidente de la república de Venezuela, conformando un área de 1008 Km², estando políticamente formado por los municipios Barinas y Obispos del estado Barinas.

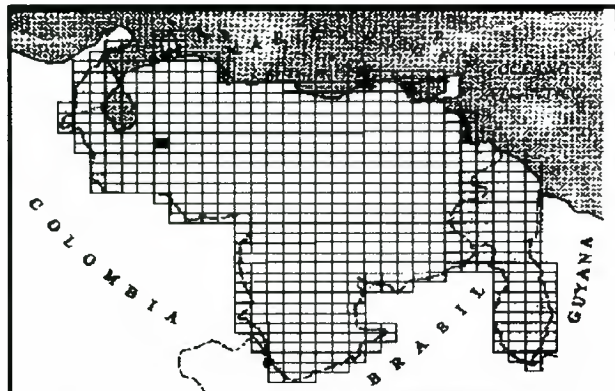


Figura N° 1: Situación relativa nacional del área de estudio.

Esta posee dos tipos de regiones características, el piedemonte andino y la planicie llanera.

El piedemonte andino posee un bioclima de bosque seco tropical de temperaturas medias de 25,5°C, precipitaciones anuales entre 1139 a 1822 mm. Litológicamente se constituye de roca Guanapa y la

Yuca del Pleistoceno, geomorfológicamente son medios deposicionales de piedemonte que forman terrazas, abanicos y glacis, con pendientes no mayores a el 8%. Los suelos son principalmente Haplustalfs y Tropaqualfs, estos constituyen las cuencas de los ríos Santo Domingo, Caldera, La Yuca y Maspalito.

La vegetación es en su gran mayoría bosque siempre verde y semi-deciduo con sabana tropical y sus asociaciones, el uso de la tierra que en el se desarrolla, es generalmente ganadería semi-intensiva, extensiva y agricultura de subsistencia.

La planicie llanera, posee un bioclima de bosque húmedo tropical, con temperaturas medias de 26°C y precipitaciones entre los 1850 a 3400 mm.



Figura N° 2: Situación relativa regional del área de estudio.

Litológicamente son aluviones cuaternarios cuyo relieve es plano, que no sobrepasan los 250 m.s.n.m. con pendientes promedios de 4%, son medios deposicionales en donde se explayan los ríos antes mencionados. Los suelos son Entisoles, Inceptisoles y Alfisoles, sobre los cuales se desarrolla una vegetación de sabana con sus asociaciones con matas, chaparrillos y ambas, bosque semideciduo y de galería asociado a los cursos de agua.

El uso característico de la planicie es la ganadería extensiva y la agricultura anual mecanizada, en esta región tiene asiento la ciudad de Barinas capital del estado del cual forma parte el área de estudio.

3.- MATERIALES Y MÉTODOS

3.1.- Materiales.

Para realizar el presente trabajo se utilizó:

Las imágenes Landsat-4 TM 006-054 del día 28 de enero de 1984 bandas 3, 4, 5 y ERS-1 SAR banda C del día 16 de julio de 1992, las cartas topográficas 1:100.000 de la Dirección de Cartografía Nacional, N° 6141 "Barinas" y N° 6142 "Barinitas", que cubren el área de estudio. El procesamiento digital se logró con el

programa canadiense PCI, versión 5.2 de octubre de 1993, que corre bajo ambiente SOLARIS en un Spar 10 SUN. La interpretación se efectuó con el uso de un Procom-2.

3.2.- Método

3.2.1.- Procesamiento digital de las Imágenes.

Debido a el recurso que posee el PCI para poder correlacionar una imagen corregida con otra no corregistradas, se escogió la banda TM4 para la georeferenciación y con ella se correlacionaron las bandas TM-5 y SAR-C.

Se tomó la banda SAR-C y se realizaron ajustes necesarios para su integración, de esta forma se aplicó un filtro tipo "Median Filter" para eliminar el ruido de la imagen (speckle), se llevó el tamaño del pixel a 25 x 25 metros de manera de hacerlo coincidir con el tamaño del pixel TM y por último se le aplicó una compresión de 16 a 8 bit con el fin de igualar su exposición en el rango de 0 a 256 niveles de gris, tal como en las bandas del TM.

Terminada la homogeneización del formato de las bases de datos, se procedió a realizar las composiciones RGB colocando las distintas bandas en diversos canales y mejorando el contraste a través de la manipulación de los histogramas, después de varias pruebas se escogieron las mejores combinaciones.

Con las bandas originales, es decir sin manipulación de los histogramas, se procedió a realizar la composición IHS, siguiendo la metodología propuesta por J. R. Harris y R. Murray, (Harris, J. R., et. al., op.cit.) en cuanto al uso de la IHS para integración de imágenes de radar con otros datos de sensores remotos y por R. Welch y M. Echlers, para unir la multiresolución del SPOT, HRS y datos del Landsat TM, (Welch, R., et. al., op. cit.).

De esa forma se colocaron las bandas TM en el siguiente orden TM-4 en el canal de intensidad, TM-5 en color-tono y nuevamente TM-5 en la saturación para correr el proceso IHS. Luego se reemplazó la saturación por la banda SAR-C y se aplicó la transformación RGB, obteniendo como resultado la combinación de bandas IHS transformadas en RGB, o sea SAR/TM.

3.2.2.- Interpretación visual de las Imágenes para la obtención de la variable uso de la tierra y cobertura vegetal.

Con los positivos resultantes de la impresión fotográfica de las imágenes se realizó la interpretación por medio del Procom-2, en primer lugar se interpretó el TM 4, 5, 3 y luego las combinaciones escogidas. Para dicha interpretación se utilizó una leyenda, establecida por el conocimiento previo del área de estudio.

Esta destaca las siguientes formaciones vegetales y usos:

Las formaciones arbóreas, representadas por los bosques siempre verde, semideciduo, y de galería; la formación arbustiva representada por el espinal y el matorral; la formación herbácea como los herbazales, la sabana abierta y por último las formaciones mixtas es decir, sabana con matas, chaparros y ambas.

Los usos son el agropecuario representado por la ganadería intensiva, semi-intensiva y extensiva, el uso agrícola dado por la agricultura anual mecanizada y la agricultura de subsistencia. El uso urbano fue dividido en residencial y agroindustrial.

4.- RESULTADOS.

Con la imagen TM 4, 5, 3, se realizó la primera interpretación visual del área de estudio con la cual se

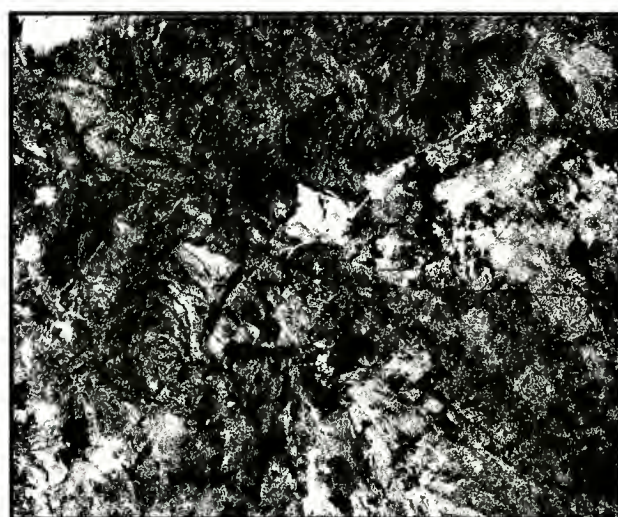


Figura N° 3: Muestra el resultado de combinar las bandas en RGB.

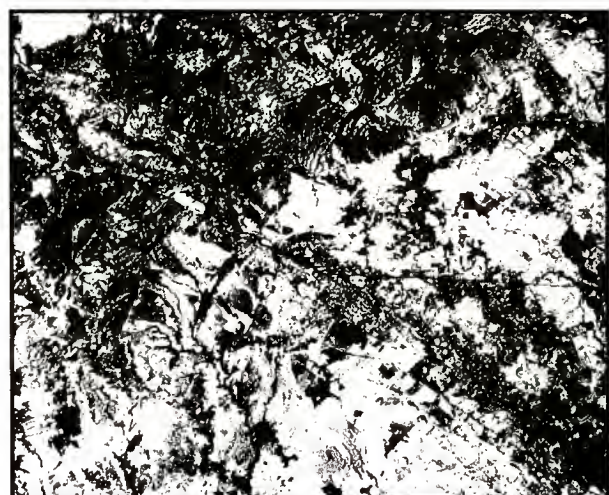


Figura N° 4: Muestra el resultado de combinar las bandas con IHS convertidas luego en RGB.

estableció un punto de partida en cuanto a la complejidad de la interpretación visual de las siguientes combinaciones:

Luego de la revisión de todas las posibles combinaciones RGB que se generaron, se escogió para ser interpretadas la combinación uno: banda TM-4 en el canal rojo (R) banda TM-5 en el canal verde (G) y banda SAR-C en el canal azul (B); la combinación dos: resultó de colocar en el canal rojo la banda TM-5, en el canal verde la banda TM-4 y en el canal azul continuó la banda SAR-C.

El resultado de la interpretación de ambas combinaciones fue comparado con el de la combinación TM 4, 5, 3, con el objeto de discriminar las bondades de cada una de ellas.

Luego, con la combinación resultante de las bandas IHS transformadas en RGB, tal como se explicó en el capítulo de metodología, se generó la interpretación de la variable estableciéndose conclusiones sobre el levantamiento temático con ese producto.

5.- CONCLUSIONES.

Realizada la interpretación visual de cada uno de los productos y comparando estos con la interpretación a través de las bandas TM 4, 5, 3, se puede llegar a la conclusión de que las imágenes resultantes del uso combinado de estos dos sensores mejora cualitativamente la interpretación visual del uso de la tierra, para el área de estudio y a escala 1:100.000.

Considerando el hecho que las imágenes combinadas son de diferentes fechas y que por tanto está implícita una componente temporal (cambios en el tipo de cultivos, el régimen de humedad, etapa de crecimiento de las plantas, cambios en el uso etc., las cuales deben ser cuidadosamente tratadas), éstas discriminan mucho más las texturas, tonos, color y límites de las diferentes clases interpretadas.

En el caso de la combinación uno, los bosques naturales resultaron resaltados con un fuerte color magenta, debido a la combinación del rojo dado por la banda TM 4 y el azul de la banda SAR-1 ya que la Banda TM 5 no aporta verde, debido a la absorción que éstos hacen, en esta región del espectro, por el contrario, las actividades antrópicas son bien resaltadas por tonalidades verdosas claras por aporte de las bandas TM, en estas regiones el radar discriminó más las texturas.

Las herbáceas aparecen con un fuerte tono azulado, debido a la mayor dispersión del radar en esa formación vegetal y por el hecho de ser oscuras en una de las bandas del TM.

En cuanto al uso urbano, la combinación permite una buena discriminación de la red de comunicación, un notable destaque en el área urbana, permitiendo la observación del áreas densamente pobladas y sus

diferencias con aquellas donde solamente se realizan actividades agro-industriales.

Los mismos efectos se repitieron en la combinación dos, solo que el cambio de la banda TM 5 al rojo generó tonos de cyan en los bosques naturales, más el grado de discriminación siguió siendo tan óptimo como en la anterior combinación. La diferencia fundamental entre ésta y la uno radica, por una parte, que la actividad antrópica aparece en una gran gama de tonos rojos, por tanto es más fácil de ser observada por el interprete, por otra, la red de vías de comunicación y el uso urbano fue bien destacado en la segunda combinación en comparación a las otras, incluyendo la combinación TM 4, 5, 3.

Las combinación resultante de las bandas IHS trasformadas en RGB, demostró ser excelente discriminatoria de los bosques naturales y de galería, pudiéndose observar mejor el grado de intervención que estos han tenido, se interpreta muy bien el patrón urbano así como, la red de comunicación.

Sin embargo en éste tipo de combinación utilizada, los límites de las clases de uso no son bien destacados, al contrario del resultado de las combinaciones RGB de las bandas sin tratamiento IHS. Este tipo de combinación destaca las formas del relieve, lo que justifica su uso para levantamientos geológicos y geomorfológicos, como ya ha sido mencionado en varias oportunidades.

Debe destacarse que la red de drenaje es bien realizada en todas las combinaciones realizada y en comparación con la imagen TM 4, 5, 3. En todas las combinaciones se pudo observar la mancha de quemas.

6.- RECOMENDACIONES.

El presente estudio se realizó para medir cualitativamente el aporte en la interpretación visual de las imágenes resultantes de la combinación de bandas TM 4,5 y SAR-C para el uso de la tierra y cobertura vegetal, la conclusiones exponen el óptimo resultado que éstas proporcionan, sin embargo, se recomienda realizar estudios de clasificación supervisada con estas imágenes, a fin de demostrar cuantitativamente la discriminación que éstas aportan en el levantamiento de dicha variable.

El uso de sensores de naturaleza distinta, es en realidad un complemento de sus resoluciones, con los cuales se generan productos óptimos para la interpretación del uso de la tierra, no obstante se debe combinar imágenes de fechas próximas, para evitar el análisis temporal que ello implica.

Se recomienda utilizar estas bandas para levantar la variable uso de la tierra, aun cuando, al ser éste un ámbito de investigación realmente novedoso, se deben realizar estudios con las restantes bandas del TM, de manera de observar su comportamiento en la discriminación de dicha variable.

A pesar de los resultados obtenidos, en el presente trabajo en cuanto a la respuesta de la combinaciones de las bandas IHS trasformadas en RGB, con fines de levantamiento de uso de la tierra, se debe dejar claro, que ésta fue el resultado de un tipo de combinación colocando la banda SAR-C en la saturación al realizar la transformación RGB, por tanto se recomienda realizar estudios del comportamiento de ese método, en otras combinaciones, tanto como en la posición del SAR como en cuanto a las bandas TM a utilizar.

El uso de PCI permitió de una manera rápida el combinar la imagen de radar con las bandas TM, en composición RGB, al igual que en IHS, demostrando ser un excelente programa para la realización de estudios como el presente.

7.- REFERENCIAS.

1. DALY, M., "Hue-Saturation-Intensity Split-Spectrum Processing of Seasat Radar Imagery". Photogrammetric Engineering & Remote Sensing, Vol. 49, Nº 3, marzo, pag. 349-355 (1983).
2. GILLESPIE, A., A. Kahale y R. E. Walker. "Color Enhancement of Highly Correlated Images. I. Decorrelation and IHS Contrast Stretches". Remote Sensing of Environment and Interdisciplinary Journal, Vol. 20, Nº 3 diciembre, pag. 209-235. (1986).
3. HARRIS, J. R. Murray R.; Hirose T. "IHS Transforma for the Integration of Radar Imagery With Other Remotely Sensed Data". Photogrammetric Engineering & Remote Sensing, Vol. 56, Nº 12, diciembre, pag. 1631-1641 (1990).
4. RHEAULT, M.; Simard, R.; Garneau, C.; Slaney, V. R. "SAR Landsat TM-Geophysical Data Integration Utility of Value-Added Products in Geological Exploration." Canadian Journal of Remote Sensing, Vol. 17, Nº 2, abril, pag. 185-190 (1991).
5. WELCH, R.; Ehlers, M. "Cartographic Feature Extraction With Integrated SIR-B and Landsat TM Images". International Journal of Remote Sensing, Vol. 9, Nº 5, mayo, pag. 873-889 (1988).

Segmentation, Classification, GIS

Chairmen/Presidentes:

Laura Frulla
Manuel Vierna Monteiro

SEGMENTATION AND CLASSIFICATION IN SAR IMAGERY

Shaun Quegan

Sheffield Centre for Earth Observation Science
 University of Sheffield
 Hicks Building
 Hounsfield Road
 Sheffield S3 7RH UK

phone: +44 114 22 23778 fax: +44 114 22 23759 email: s.quegan@sheffield.ac.uk

ABSTRACT

The need for segmentation as an image analysis tool for agriculture and forestry is demonstrated and related to classification strategies. Methods to compare segmentation algorithms are described and shown to suggest that segmentation based on global maximum a posteriori (MAP) recruitment provides the best approach currently.

Segmentation of multi-channel imagery as a single entity is shown to confer advantages over combined single channel methods. Attempts to classify and segment tropical forest regions for forest discrimination are seen to be closely related to methods for change detection. The MAP classifier for multi-channel data is displayed; currently this does not yield good results, and more ad hoc methods appear superior, perhaps due to inadequate descriptions of the class identifier.

I. INTRODUCTION

When human beings see an image, they automatically see structure, recognising regions, lines and edges. Segmentation is the process by which we try to derive and store such structure when handling images by computer. It consists of a labelling of pixels meeting two conditions:

- pixels with the same label form a connected region (segment);
- label changes occur at a discontinuity in one or more measured parameters (an edge).

A third condition which may be applied is that segments should be internally homogeneous. The weakness in this condition is that regions with gradual changes may be perceived by a human being as forming a single segment but will fail the homogeneity test. Nonetheless, some condition regarding the integrity of a region (for example, no internal edges) needs to be enforced to ensure conformity with our intuition. In

fact, the whole question of how we represent (or transcend) human perception in machine segmentation is unresolved.

Segmentation provides the computer with a means to handle objects in the image as single entities. It is **not** an *a priori* classification, simply a recognition of image structure. However, the two processes are closely linked. The existence of segments allows regions to be classified making use of the whole population of pixels within the segment. This is particularly important for SAR, where speckle causes great variability in single pixel measurements. Also, pixel classification (normally after filtering) provides a possible method to recognise similar pixels and regions within the image, and hence can lead to a segmentation. An example of this approach will be illustrated in Section 5.

This paper will discuss the connections between segmentation and classification in the context of agriculture and forestry. In Section 2 we survey the empirical data, which strongly suggests that segmentation is critical to monitoring agriculture (particularly in temperate climates). Section 3 addresses the important question of how we can compare segmentation schemes: are there objective tests which allow us to select the best from the range of possible approaches? Global statistical tests which provide a limited answer to this question are given and shown to provide clear guidance when comparing two current segmentation methods, for single channel, single date images. The extension of existing methods to multiple channels (polarimetric or multi-temporal) is discussed in Section 4. Both the value of the multi-channel approach and weaknesses in current methods are displayed. Comparison of methods in the context of forest discrimination forms the topic of Section 5. In Section 6 the maximum a posteriori (MAP) classifier for multi-channel SAR data is derived. While making the need for segmentation even clearer, problems which arise in using MAP classification are identified. We conclude in Section 7 with a summary of the current status of methods.

2. SEGMENTATION AND CLASSIFICATION IN AGRICULTURAL MONITORING

The major needs in agricultural monitoring are mapping of crop area, identification of crop state, integration with other information (such as farmers' crop declarations within the EU) and yield forecasting. SAR has a role to play in the first two of these (the second two serve to remind us that it should be viewed as only part of an information handling system). At present, the most influential data in this context are from the ERS satellites, because of their high calibration accuracy and the existence of long multi-temporal sequences of measurements. Several studies [see Ref. 1 and References therein] have demonstrated that for these data the important information is carried by the temporal behaviour of σ^o , averaged over fields. The use of per field averaging is important because there is much scatter at a given time, due to natural variation. Enough samples must be averaged to reduce further uncertainty due to speckle, and to preserve the shape of temporal curves. The field is the preferred object on which to base pixel averaging since this is how crops are organised (at least in temperate climates). Pixel-based methods would require very good speckle reduction which preserves σ^o if temporal curves are to be tracked. Even then, the computational burden would be very high and is much reduced by treating whole fields as single entities for tracking.

Three situations arise when using a field-based approach:

- (a) Field boundaries are known, based on maps, GIS, visual inspection or comparison with, for example, optical data.
- (b) Boundaries are imperfectly known; for example, last year's field map may be available, but will not contain information on changes in field structure, farming practice, etc.
- (c) There is no a priori data on field boundaries, just the image itself.

In practice, almost all studies up to the present have used manual segmentation of images to define field boundaries. This is slow, subjective, dependent on the image display and may not be able to cope with high dimensional data (see Section 4). The use of imperfect data is a current research area which can make extensive use of tools developed to tackle problem (c), which we will refer to as **blind segmentation**. This has attracted most attention [Ref. 2-5] and there has been a steady development of improved algorithms, to the extent that their use in applications is now becoming

viable. However, any application should be based on the best available methods and means to identify such methods are therefore needed.

3. QUANTITATIVE COMPARISON OF SEGMENTATION ALGORITHMS

An extended treatment of the theory on which this section is based is given in [Ref. 6]; only a summary of the principles and conclusions is given here. It is based on a 'cartoon' model for the image, in which the underlying scene consists of regions of constant σ^o with abrupt edges. Each such region comprises a uniform extended target, in which the pixel intensities, I , will obey a gamma distribution, with probability density function

$$p(I) = \frac{L^L I^{L-1} e^{-LI/\mu}}{\Gamma(L)\mu^L} \quad (1)$$

Here L is the number of looks and μ is the mean intensity in the region. For a calibrated system, μ is proportional to σ^o .

For an image represented correctly by the cartoon model, a perfect segmentation would locate all the edges in the right place and would assign the correct value of μ to each segment. The ratio of the original image and this perfect segmentation would consist of pure speckle of mean 1. Assume, then, that we have performed a segmentation. Since we can ensure that adjacent segments are statistically different by merging [Ref. 6], we need to test that segments are homogeneous. This can be achieved by using the squared coefficient of variation within segment k , defined by

$$CV_k^2 = m_k = \frac{n_k}{n_k - 1} \left(\frac{\bar{I}_k^2}{\bar{I}_k^2} - 1 \right) \quad (2)$$

where n_k is the number of pixels in segment k , \bar{I}_k denotes the intensity of a pixel in segment k and $\bar{\cdot}$ denotes an average of the quantity over segment k . Exact expressions for the mean and variance of m_k are known [Ref. 6], hence the deviation of any given segment from homogeneity can be tested.

This single segment measure can be related to a global measure of homogeneity through the ratio image, r . To form r we assign to each pixel the mean value of the segment within which it lies and divide the original by this segmented image. The sample variance of the ratio image is then defined by

Segmentation (p_m)	Real image	Simulations (10 images)		
		mean	SD	normalised difference
Original	-	0.1988	0.00217	-
ANNEAL (2×10^{-2})	0.2231	0.2259	0.01095	2.37
RWSEG (2×10^{-2})	0.3239	0.2420	0.01298	3.24
ANNEAL (10^{-4})	0.2376	0.2307	0.01047	2.93
RWSEG (10^{-4})	0.3484	0.2476	0.01304	3.65

Table 1. Measured values of s_r^2 , the sample variance of the ratio image.

$$s_r^2 = \frac{n}{n-1} \left(\bar{r^2} - \bar{r}^2 \right) = \sum_{k=1}^M \frac{n_k - 1}{n-1} m_k. \quad (3)$$

Here n denotes the total number of pixels in the image, there are M segments and $\bar{\cdot}$ denotes an average over the whole ratio image. The mean and variance of s_r^2 are known, providing a means of testing the homogeneity of the whole image. Analogous measures based on maximum likelihood can also be derived and again depend on properties of the ratio image [Ref. 6].

These measures have been applied to both simulated and real images. Figure 1 shows an example of (a) an ERS-1 PRI image; (b) a simulated image formed by segmenting Figure 1(a) and assigning the appropriate mean value to each segment; (c) the edge map corresponding to Figure 1(b); (d) a simulated image formed by multiplying each pixel of Figure 1(b) by an independent speckle realisation from 5-look unit mean speckle (i.e. Equation (1) with $L = 5$, $\mu = 1$). Here 5-look speckle is used because the original ERS-1 data is first 2×2 averaged to reduce spatial correlation. This leads to data which is close to 5-look. The simulated images produced in this way have a range of segment shapes and brightness differences similar to the real image.

The advantage of simulated images is that we know they obey the data model. Hence marked failure of a segmentation on such data would indicate an algorithm of little value. Tests of a large number of algorithms are under way, but we here present results from just two algorithms, ANNEAL and RWSEG. ANNEAL uses simulated annealing techniques to locate the global maximum a posteriori reconstruction of the image. RWSEG is an iterative edge detection and segment growing algorithm which progressively ‘learns’ the image. Detailed descriptions of these algorithms are given in [Refs. 2-4 and 6].

Table 1 summarises our findings. ANNEAL and RWSEG both depend on a merging parameter p_m , which controls average segment size. With $p_m = 2 \times 10^{-2}$, the mean segment size for the simulated data is about 145 pixels for both algorithms, growing to 200 pixels when $p_m = 10^{-4}$. On real data the corresponding mean segment size is reduced by approximately 50% in both cases. The values given for simulation are the average values over 10 simulated images; there is, of course, only a single real image. The first row in the Table indicates results from an ideal segmentation imposed using the edge map given as Figure 1(c). In this case the theoretical values for the mean value and standard deviation of s_r^2 are 0.1988 and 0.0024, which are very close to those observed.

Performance clearly deteriorates when blind segmentation is used, with significantly increased values of the mean value of s_r^2 . (The average departure from the expected value in units of one standard deviation is given in the last column as ‘normalised difference’). The most important conclusions to extract from Table 1 are:

1. ANNEAL performs a little better than RWSEG on simulated data, but markedly better on real data.
2. The performance of ANNEAL is comparable on real and simulated data, but RWSEG degrades drastically on real data.
3. Despite segments being ~30% bigger, ANNEAL with $p_m = 10^{-4}$ gives better performance than RWSEG with $p_m = 2 \times 10^{-2}$. Hence ANNEAL finds larger homogeneous regions than RWSEG, which is a very desirable property of the algorithm.

The overall conclusion is that global MAP estimation provides the better of the two approaches. Current work comparing a number of algorithms reinforces the conclusion that ANNEAL is the best of the currently available methods.

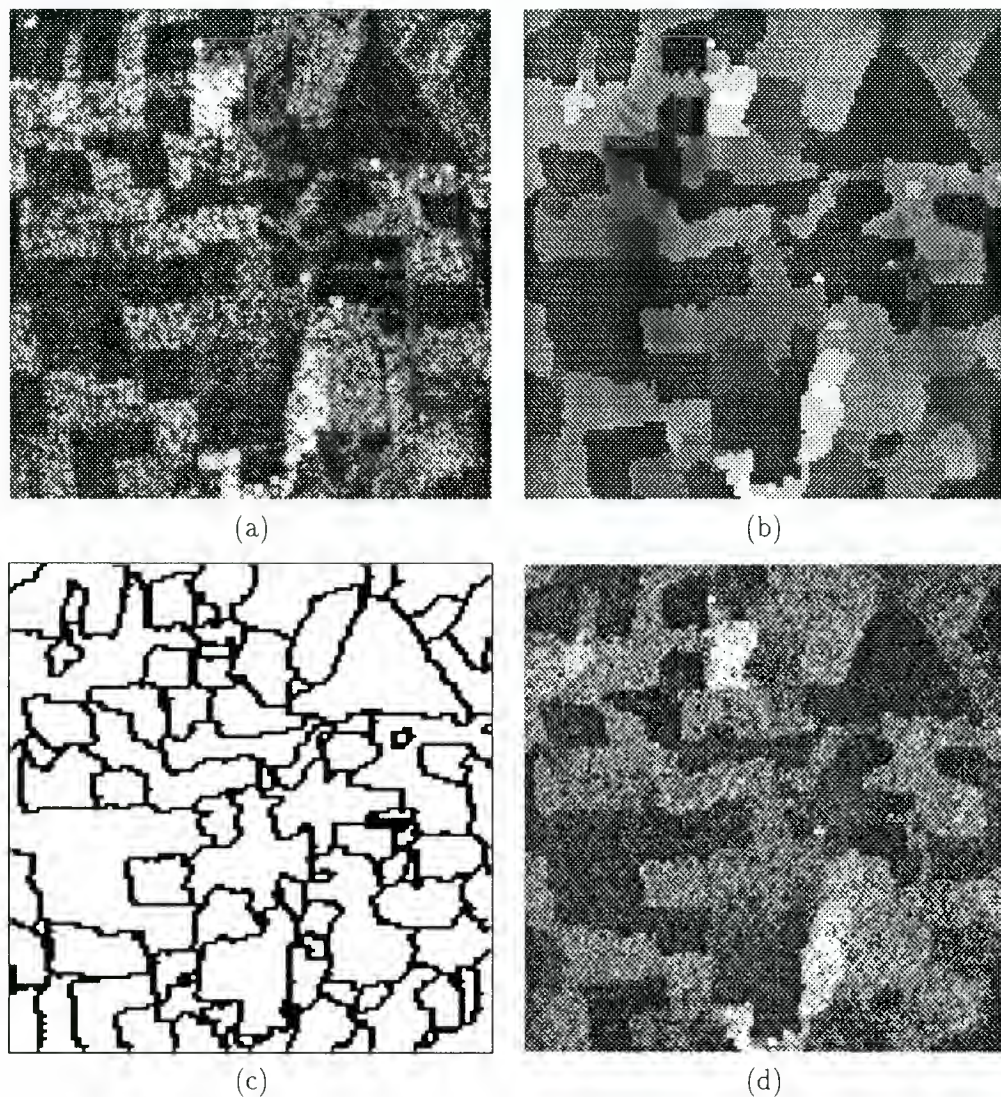


Figure 1: (a) ERS-1 PRI image of Feltwell, UK; (b) simulated RCS; (c) edge map corresponding to (b); (d) simulated 5-look image. The images are 128×128 pixels in size and are displayed in amplitude.

Note that the statistical approach to comparing segmentations described above can only recognise departures from homogeneity in the segments. Other relevant concerns are segment shape and oversegmentation. Measures of shape have been developed and are in process of being tested on a range of segmentation algorithms. Detection of oversegmentation is more problematical. A possible approach is to use merging to relax an over-detailed segmentation to the point where there is a clear departure from homogeneity within segments, but little work has been done on this as yet.

4. MULTI-CHANNEL SEGMENTATION

The previous section has demonstrated methods for comparing segmentations of single images of single channel data. However, as argued in Section 2, the more important problem is segmentation of a sequence of images. This is particularly so since true scene structure often only emerges over time [Ref. 7]. The problem of segmenting a multi-temporal sequence of images can be generalised to include any multi-channel collection of images of a given scene, provided the geometry of the different channels is identical. We will consider this more general case, which allows us to adopt a unified approach to multi-temporal data and the multi-frequency polarimetric data provided by the new generation of airborne SAR sensors and the SIR-C mission.

The most general case is well exemplified by single channel polarimetric data, in which we need to consider not only the channel powers but also quantities formed by combinations of channels. For calibrated data from natural targets, the measurements from a polarimetric SAR can be described by the complex 3-vector

$$\mathbf{S} = (S_{hh}, S_{hv}, S_{vv})' \equiv (S_1, S_2, S_3)' \quad (4)$$

where h and v refer to horizontal and vertical polarisations. This is known as scattering matrix data, although other forms are possible [Ref. 8]. For distributed targets, the random vector \mathbf{S} in many cases obeys a Gaussian distribution,

$$p(\mathbf{S}) = \frac{1}{\pi^3 \det(C)} \exp(-\mathbf{S}' C^{-1} \mathbf{S}) \quad (5)$$

where C is the co-variance matrix of \mathbf{S} ,

$$C(i,j) = \langle S_i S_j^* \rangle, \quad (6)$$

† denotes conjugate transpose, $\langle . \rangle$ denotes expectation and $*$ denotes conjugate. (This data model has limitations, especially at high resolutions and long wavelengths [Ref. 9 and Refs. therein] but we will ignore these complications here.) From (5), it is clear that all the information about a distributed target is contained in the covariance matrix, C , which can be written

$$C = \begin{pmatrix} \sigma_1 & \sqrt{\sigma_1 \sigma_2} \rho_{12} & \sqrt{\sigma_1 \sigma_3} \rho_{13} \\ \sqrt{\sigma_1 \sigma_2} \rho_{12}^* & \sigma_2 & \sqrt{\sigma_2 \sigma_3} \rho_{23} \\ \sqrt{\sigma_1 \sigma_3} \rho_{13}^* & \sqrt{\sigma_2 \sigma_3} \rho_{23}^* & \sigma_3 \end{pmatrix} \quad (7)$$

Here $\sigma_i = \langle |S_i|^2 \rangle$, $1 \leq i \leq 3$, is the mean intensity of channel i and

$$\rho_{ij} = \frac{\langle S_i S_j^* \rangle}{\sqrt{\sigma_i \sigma_j}} \quad (8)$$

is the complex correlation coefficient of channels i and j .

In principle, there are therefore 9 real parameters available from a distributed target (3 channel intensities and the 3 phases and amplitudes of the complex correlation coefficients). However, target symmetries can significantly reduce these degrees of freedom; for example, for an azimuthally symmetric target the like and cross-polarised channels are uncorrelated, so that $\rho_{12} = \rho_{23} = 0$ and only 5 parameters are available to carry information about the target.

The availability of several information-bearing parameters suggests that a segmentation should try to detect changes in any one of them in order to locate edges. In practice, this creates difficulties, largely because of the sampling properties of the terms arising from the correlation coefficients. The maximum likelihood estimators of all the terms in the covariance matrix are well-known, but only the estimates of the σ_i have an easily manipulable form, viz. the well-known gamma distribution given as Eq. (1). Also, the images of the amplitude and phase of the correlation coefficients tend to be quite noisy for natural scenes, requiring considerable amounts of averaging to achieve reasonable estimates. Hence they do not readily fit into the local methods preferred for image segmentation. As a result, the most useful approach to multi-channel segmentation uses only the channel powers, σ_i . This being the case, multi-temporal, multi-frequency and

polarimetric images can all be handled in the same way.

Given a set of intensity images of the same scene provided by different channels, there are two approaches to using the dataset to recover structural information. We could segment each channel separately and combine the segmentations by preserving all edges found in any of the separate segmentations. This approach is illustrated by Figure 2(a)-(g). Figures 2(a), (c) and (e) are 16-look HH, HV and VV AirSAR L-band images of an agricultural area near Feltwell, UK. The corresponding edge maps produced by single channel segmentation using RWSEG are shown as Figure 2(b), (d) and (f), while Figure 2(g) shows the HH image overlaid with these edges, combined using a logical OR operation. Very obvious is the thickening and excessive complexity of edges caused by the fact that edges found in each channel are subject to a speckle induced 'jitter'.

The second approach is to treat the set of images as a single multi-dimensional entity and to segment the combined data. In Figure 2(h) we show the result of this approach using multi-dimensional RWSEG, in which the edge-detection, segment growing and convergence criterion for halting iteration all make use of a least squares approach combining information from all channels. This obviously produces a 'cleaner' segmentation, without edge-thickening and apparently producing a good representation of image structure. Note, however, limitations in this approach. By design, it will lose weak edges found in only a single channel (necessary to remove the 'jitter' effect). The least squares criterion for combining information is arbitrary and other criteria may be more appropriate. Perhaps most telling is that at present the only useful multi-dimensional segmentation algorithm uses RWSEG, while in Section 3 we have indicated the likely superiority of methods based on ANNEAL. These are currently being developed. What is not clear for either algorithm is how to account rigorously for the inter-channel correlation which will be present in polarimetric data. This will not be an issue for multi-frequency or multi-temporal data (unless the time separation in the latter case is short enough to allow significant inter-channel correlation, as would be exploited by interferometry).

As well as providing an improved field boundary map, multi-channel segmentation has two obvious uses. Firstly, it provides a means to compare information present in different channels. From the edge map of Figure 2(h), we can establish whether there is evidence for a given edge in each of the separate channels. This then provides information on the relative values of the different channels for extracting scene structure.

Secondly, once the field boundaries are determined, field averaging provides a method to 'sharpen up' the noisy information carried by the correlation coefficients in polarimetric data. In the case of the data displayed in Figure 2, this helps to establish a number of regions where the correlation of the like and cross-polarised channels is significant at L band. For C band data, only the correlation of the like polarised channels is useful.

Although the example in Figure 2 is from single frequency polarimetric data, the same methods have been successfully applied to multi-frequency and multi-temporal images. However, neither a large scale application of these methods nor a demonstration that they permit tracking of the multi-temporal behaviour of regions with sufficient accuracy for crop identification (see Section 2) has yet been performed.

Finally, note that the requirements for tropical agriculture with very diverse field structures and no annual crop calendar may require different methods. For example, change detection has been demonstrated as a potentially important technique for measuring acreage of wetland rice [Ref. 10]. We explore its relevance in forestry in the next section.

5. FOREST CLASSIFICATION AND SEGMENTATION USING CHANGE DETECTION

As in agriculture, mapping of forest areas and discrimination of forest types are important aims for remote sensing, although radar also offers numerous other possibilities, such as estimation of tree density, gappiness, tree height and above ground biomass. A potentially very important use of radar is in mapping forest cover in tropical forests, which are frequently cloud-covered and inaccessible to optical sensing. Here we illustrate the use of the ERS-1 C band SAR for this purpose, but in the context of comparing approaches to classification and segmentation, rather than as the preferred sensor. This is because longer wavelengths are better for forest sensing, as discussed in [Ref. 11].

An extensive set of SAR, optical and ground data has been assembled for the Tapajos National Forest in Brazilian Amazonia; here we make use of three ERS-1 PRI images acquired on 22 May, 31 July and 18 December 1992, together with a cloud-free TM image obtained on 29 July 1992. A fuller description of the dataset and the methods involved is available in [Ref. 12].

An obvious feature of the imagery is that the apparent structure changes markedly with time. Very little detail can be seen in the May and July images, but the December image shows regions related to roads and associated agricultural activity (Figure 3). Modelling

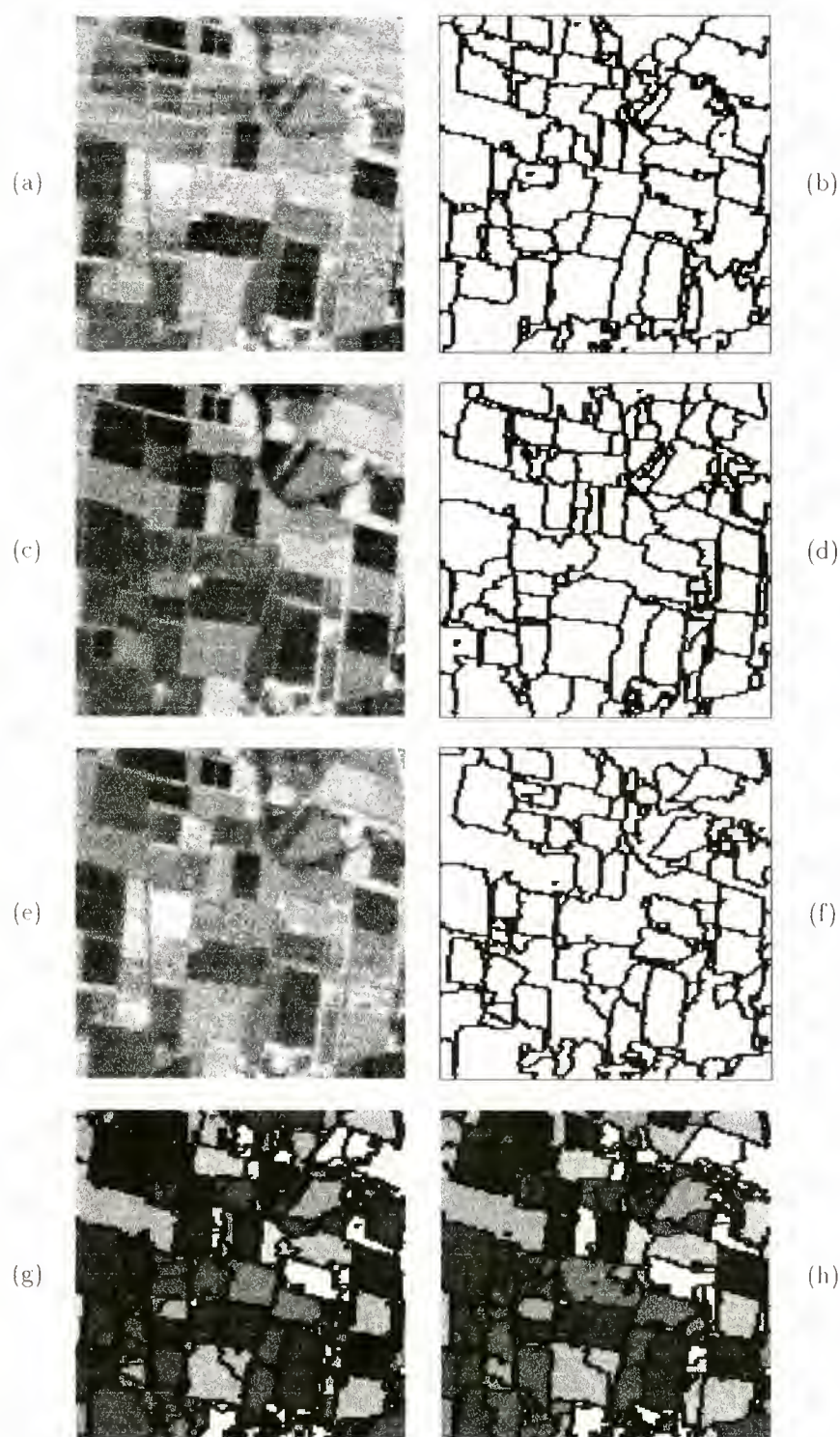
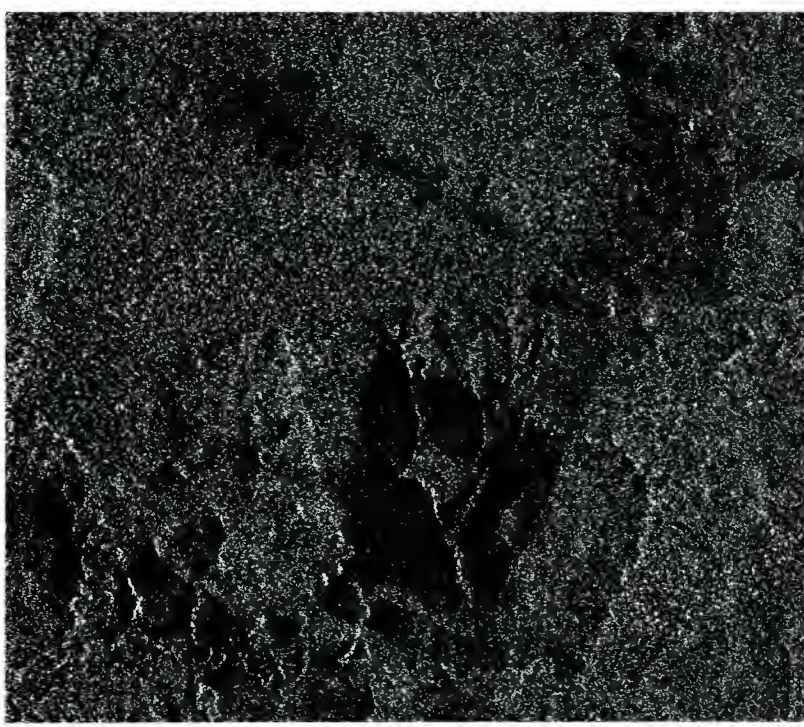


Figure 2: Segmentation results, from 16-look AirSAR data of an area near Feltwell, UK. (a) HH power image; (b) associated edge map produced by single channel segmentation, (c) and (d) are the corresponding images for the HV channel; (e) and (f) are the corresponding images for the VV channel; (g) edge map produced by combining single channel segmentations, i.e. an OR operation applied to (b), (d) and (f); (h) edge map produced by multi-channel segmentation.



(a)



(b)

Figure 3: ERS-1 PRI images of an area bordering the Tapajos Natural Forest. Images were acquired on (a) 31 July 1992 (b) 18 December 1992.

and ground survey suggests that the changes are caused by soil moisture effects. These have little effect on the backscattering coefficient of the forest canopy but marked effects in bare soil or areas of low vegetation. Although the ensuing differences between areas in the December image could be used as a forest discriminant, methods based on image ratios (and hence changes in backscattering coefficient) are more attractive because they remove topographic and calibration effects. This makes the analysis more general since in many regions of the world (though not Tapajos) tropical forest is found in hilly areas.

A simple ratio of the December and July images is of little value for forest discrimination because of speckle, and some pre-processing of the images is required. Four methods were considered, based on block averaging [Ref. 13], local (gamma MAP) filtering [Ref. 14], global MAP [Ref. 4] and segmentation (see Section 4). In the first three cases, single images were pre-processed before forming the ratio; in the last case, two-dimensional segmentation was carried out using the July and December images. After pre-processing and ratioing the resulting images were thresholded, giving rise to the one-bit images shown as Figure 4(a)-(d), where the white areas indicate a decrease exceeding 1.5 dB from July to December. For comparison, the ratio of the two original PRI images is shown as Figure 4(e) and a threshold applied to band 5 of the TM data as Figure 4(f); the latter provides a reasonable estimate of the true forest cover. While all techniques pick out the main features (a large area of pasture with enclosed woodland at the bottom centre, forest disturbance along the road running down the image and two parallel side roads) there are clear differences between them. The large window (18×18) needed to produce good discrimination using averaging causes loss of detail and small areas (Figure 4(a)). In Figure 4(b) we see that GMAP produces a noisy image with many small non-forest detections in the forest areas, unlike the other methods. ANNEAL and RWSEG lead to Figures 4(c) and 4(d), which both preserve edge structure well, ANNEAL doing slightly better.

A more quantitative analysis based on comparison of the radar results with the forest map inferred from the TM data supports the conclusion that ANNEAL is the most accurate method of those compared. (However, the results do not support the value of ERS-1 as a forest discrimination tool, with less than 50% of the non-forest regions being detected. This is almost certainly due to low vegetation cover being enough to mask the soil moisture signal driving the change in backscattering coefficient [Ref. 12]. Better results are possible at the L band wavelength used by JERS-1 [Ref. 13]). We note that ANNEAL again provides the most

accurate means of image analysis, the conclusion this time being based on experimental rather than theoretical grounds. Notice that in this case a forest/non-forest classification also provides a segmentation even in those cases not explicitly using RWSEG.

6. MAXIMUM A POSTERIORI CLASSIFICATION

Based on the approach in [Ref. 15], it can be readily shown that if we have L independent observations from N -channel data obeying the Gaussian model described by Equation (5), the maximum likelihood estimator of the covariance matrix C is given by the single covariance matrix

$$A = (1/L) \sum_{k=1}^L S^{(k)} S^{(k)*} \quad (9)$$

Here the superscript k denotes the k th observation. Although Equation (8) refers to single look polarimetric data, it is readily generalised to include multi-frequency and multi-temporal data. Hence our use here of the general case of N channels.

Since C carries all the information about the region, A is a key quantity. It has a related vector

$$\begin{aligned} A &= \\ (A_{11}, \dots, A_{NN}, \operatorname{Re} A_{12}, \operatorname{Im} A_{12}, \dots, \operatorname{Re} A_{N-i,N}, \operatorname{Im} A_{N-i,N})' \end{aligned} \quad (10)$$

which is equivalent to the Hermitian matrix A . The probability density function of A is given by

$$p(A|C) = \frac{(\det A)^{L-N} \exp\{-L\operatorname{Tr}(C^{-1}A)\}}{K(L, N)(\det C)^L} \quad (11)$$

where $K(L, N) = \pi^{N(N-1)/2} \Gamma(L - N + 1) L^{-NL}$ and Tr denotes trace.

Given Q classes each with covariance matrix C_q and observed covariance data A , it is readily shown using Bayes rule:

$$p(q|A) \propto p(A|q)p(q) \quad (12)$$

that the maximum a posteriori classifier minimises

$$d_q = -\ln p(A|q) - \ln p(q) \quad (13)$$

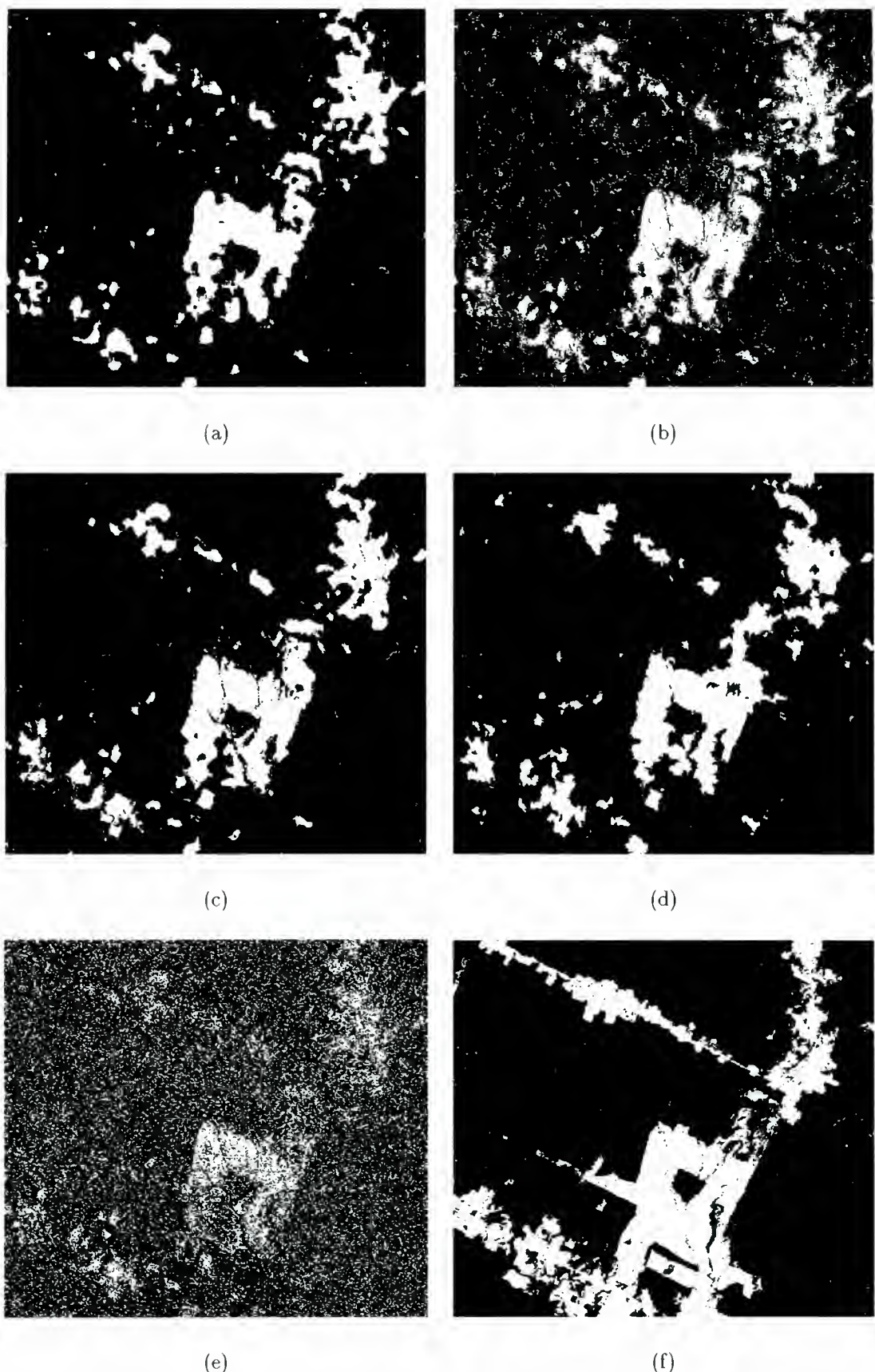


Figure 4: (a) - (e) ratio images thresholded at 1.5 dB; (a) Smoothed over 18 by 18 pixel window; (b) GMAP filtered over a 15 by 15 pixel window; (c) Annealed; (d) Segmented; (e) Unprocessed ERS-1 data; (f) Landsat Thematic Map per (Band 5).

leading, for multi-channel SAR data, to

$$d_q = -\ln p(q) + L \left\{ \text{Tr} \left(C_q^{-1} A \right) + \ln \left[\det(C_q) \right] \right\} \quad (14)$$

A key point here is that the prior probability $p(q)$ (normally poorly known) becomes less important as L increases. Hence, it is advantageous to average over as many samples as possible from the same population in carrying out the classification. Hence as large as possible homogeneous segments provide the best route to accurate classification.

Despite this analysis, our current evaluation of the classifier given by (14) has given poor results over agricultural areas. This is still being evaluated, but a problem may lie in the assumption of a single representative covariance matrix for each class. In fact, these covariance matrices show considerable variability, increasing with wavelength [Ref. 9].

7. SUMMARY

Segmentation is essential to carrying out agricultural and forestry applications of SAR. At present, single channel methods based on global MAP using annealing appear on objective and empirical grounds to give the best results, although they need to be extended to operate on multi-dimensional data.

MAP classification indicates the advantage of taking a segment based approach, although current tests do not yield good results over agricultural regions, possibly because of large variability of covariance behaviour within classes. More ad hoc methods based, for example, on change detection appear at present to deliver superior performance.

Acknowledgements. People who have helped in this work include R. Caves, M.I. Preston and K.D. Grover of SCEOS and C.C.F. Yanasse of INPE. Thanks are given to DRA Malvern and NA Software, Liverpool for permission to use algorithms, to ESA for ERS data and to NASA/JPL for AirSAR data.

REFERENCES

- [1] Wooding M.G. et al 1995. Satellite radar in agriculture: Experience with ERS-1, ESA SP-1185.
- [2] White R.G. 1994. A simulated annealing algorithm for radar cross-section estimation and segmentation. *Proc. Applications of Artificial Neural Networks*, ((Orlando, USA)), SPIE.
- [3] White R.G. 1991. Change detection in SAR imagery. *Int. J. Remote Sensing*, vol.12, 339-360.
- [4] White R.G. 1994. Cross-section estimation by simulated annealing. *Proc. IGARSS '94*, ((Pasadena, USA)), 2188-2190, IEEE.
- [5] Cook R., McConnell I. and Oliver C.J., 1994. MUM (Merge Using Moments) segmentation for SAR images, Proc. SPIE, Vol 2316, 92-103.
- [6] Caves R., Quegan S. and White R.G., 1997. Quantitative comparison of the performance of SAR segmentation algorithms, *IEEE Trans IP*. (submitted).
- [7] Quegan S., Caves R.G., Grover K.D. and White R.G. 1992. Segmentation and change detection in ERS-1 images over East Anglia. *Proc. First ERS-1 Symposium: Early Results*, ((Cannes, France)), 617-622.
- [8] Ulaby F.T. and Elachi C. 1990. Radar Polarimetry for Geoscience Applications, Artech House.
- [9] Quegan S. and Rhodes I. 1995. Statistical models for polarimetric data: consequences, testing and validity. *Int. Jnl. Remote Sensing* 16, 1183-1210.
- [10] Ribbes F. et al. 1995. On the retrieval of rice crop parameters from SAR data, Proc. Symp. on Retrieval of bio- and geophysical parameters from SAR data for land applications, Toulouse.
- [11] Quegan S. and Grover K.D. 1996. Quantitative estimation of tropical forest cover by SAR. *Proc. SBRS*. Salvador, Brazil.
- [12] Grover K.D., Quegan S. and Yanasse C.C.F. 1997. Use of C band SAR for quantitative estimation of tropical forest cover - methods and limitations. *IEEE GRS* (submitted).
- [13] Rignot E.J. M. and van Zyl J.J. 1993. Change detection techniques for ERS-1 SAR data. *IEEE Transactions on Geoscience and Remote Sensing*, 31(4): 896-906.
- [14] Lopes et al. 1993. Structure detection and adaptive speckle filtering in SAR images. *International Journal of Remote Sensing*, 14, 1735-1758.
- [15] Goodman N.R. 1963. Statistical analysis based on a certain multivariate gaussian distribution (an introduction), *Ann. math. Stat.* 34, 152-177.

Morphology of Segmented Regions in SAR Images by Means of a Region Growing Algorithm*

J. Lira¹, L. Frulla², D. Chavira¹, R. Pastrana¹

1.- Instituto de Geofísica-UNAM,
A.P. 22-560, 14091 México D.F., México.

e-mail: labpr@tonatiuh.igeofcu.unam.mx

2.- Satellite Radiometry Division - CONICET,
Julián Alvarez 1218, (1414) Buenos Aires, Argentina.
e-mail: laura@caerce.edu.ar

ABSTRACT

Synthetic Aperture Radar (SAR) images present a great geomorphological information content. Due to the particular operation of this sensor the geomorphologic features of the earth surface are enhanced, hence providing valuable detail related to texture of terrain.

In this work, speckle reduction in SEASAT/SAR images is considered first by applying selected filters to the original image. The goodness of the filtering was qualitatively evaluated for the whole image, and quantitatively estimated on selected smooth and rough texture areas. The quantitative evaluation was done by calculation of image parameters such as contrast, edge sharpening and speckle reduction. This analysis indicated that the geometric filter perform the best for SEASAT images. The filtered image was input into an automated region growing algorithm that produced segmented texture objects. The texture model and the parameters of the algorithm are based upon the co-occurrence matrix. From this, a new texture distance is introduced. This distance is used to quantify the optimal parameters of the automated algorithm and to determine the goodness of the segmentation.

Once the image is segmented the morphology of texture regions is obtained, this comprises the following parameters: area, perimeter, and fractal dimension. A texture distance between regions is calculated as well in order to estimate the texture separation of these regions. A series of examples is provided to illustrate the methodology proposed in this research.

1.- Introduction

The concept of texture is a subjective and qualitative idea developed by the psicovision in human beings. This concept is structured with limited capacity in the psicovision since textures differing farther than the second statistical moment are not distinguished (Gotlieb and Kreyszig, 1990) by a human. In a digital image, texture manifests itself as an organized spatial phenomenon. Therefore, before attempting a detection of texture objects the construction of a texture model is required that quantifies and delimits the idea stored in the psicovision. To detect an object a texture model is needed, and to quantify the goodness of the segmentation, a texture distance is required to measure the separation among the various objects recognized in this detection process.

On the other hand, the coherent interaction of the phased electromagnetic pulses with the surface under study gives rise to a granularity aspect in the image known as speckle noise (Lee, 1986). The reduction of this noise by digital techniques is required before a texture analysis is carried on the radar image.

The texture models reported in the literature (Reed and du Buf, 1993) may be classified in three broad categories: structured-based, feature-based and model-based. In the first category the existence of detectable primitive elements is assumed; a condition not generally fulfilled by radar images of natural scenes. In the feature-based methods regions of constant and predetermined texture characteristics are sought, while in a model-based technique the textures are conceived as the result of an underlying stochastic process. When model parameters are employed as texture features, the model-based techniques may be considered as a subcategory of the feature-based methods. In the present

* Work supported by project IN101994 of DGAPA-UNAM

work a model-based texture approach was selected, utilizing the entropy descriptor for the co-occurrence matrix that is evaluated on a window in the image. The segmentation of a specific texture object is carried out by means of an automated region growing algorithm.

The nature of a region growing algorithm (Zucker, 1976; Morel and Solimini, 1995) is appropriate for detection (segmentation) of texture objects. A number of results have been reported in the literature. Raafat and Wong (1988) constructed a texture model and a texture distance based on the gradient magnitude and gradient directionality. In this work the region initiation is achieved through the use of resolution dependent texture information measures. The region growing process is then directed by the texture distances between image texture blocks; a good but a rather coarse segmentation is obtained with this procedure. Considering a region growing scheme, Kay and Muller (1991) segmented multispectral satellite imagery generating thematic maps of unidentified spectral features. The growing of the regions was conducted using a local absolute brightness difference as a threshold provided by the user in combination with edge information derived from the image itself. This proved to be useful in segmenting low contrast satellite data.

In this paper, a model-based texture approach was selected. The results of this research on segmentation of texture objects and a new texture distance by means of a region growing algorithm are presented. The parameters involved in this algorithm, i.e., the window size and the threshold are optimized according to the texture model and to the texture distance in order to obtain the best separation among the segmented objects. Once an optimum segmentation is achieved the morphology of each segmented region is evaluated so the spatial structure of texture objects may be estimated. Hence the objective of this work is twofold: a).- To design and construct an automated region growing algorithm, and b).- To measure the spatial structure of specific segmented texture objects. In the following sections details about speckle reduction, the texture model, the texture distance, and the region growing algorithm are provided.

2.- Speckle Reduction in SAR Images

The antenna of a SAR system produces a wavetrain of coherent phased electromagnetic pulses that interact with the Earth surface. In the instantaneous field of view irradiated by these pulses, there is a certain set of objects that perform as scatterers when their size is

comparable to the wavelength of the radar. Those objects backscatter the incoming radiation in different directions and phases generating a constructive and destructive ondulatory phenomenon. This interference phenomenon is known as speckle coherence effect, visually appearing in the image as a random granularity formed by pixels of various brightness. In this sense the speckle noise appears with a well defined structure: very narrow spikes with positive and negative intensities superimposed to the general profile of the image. Hence, from the family of speckle filters (Nagao and Matsuyama, 1980; Kuan et al., 1985; Frost et al., 1982), it is considered that the noise structure is adequate for the application of a geometric filter (Crimmins, 1985) based on a Hit or Miss (Pratt, 1991) morphological transformation. Thus, this filter was applied to the SAR image and compared to the Median and the Lee Multiplicative filters (Lee et al., 1994). The comparison included the change in contrast (cf), retention of mean value (μ), change of standard deviation (σ), and a speckle factor given by σ/μ . A qualitative comparison was done as well. This included the modification of a selected profile, preservation of edges and texture details, overall sharpness, and general image quality. The modification of these parameters (quantitative and qualitative) through several iterations of the filters was observed. This permits to conclude that the geometric filter applied with one iteration is the most suitable speckle reduction procedure for SEASAT/SAR images.

3.- Texture Model and Texture Distance

The texture image and the speckle noise are assumed to be the result of a stochastic process, resulting in two hierarchical random fields (Nguyen and Cohen, 1993), at the higher level is the texture image and at the lower level is the speckle process. The speckle process is assumed stationary with a Rayleigh density function resulting from the average of independent realizations (Derin et al., 1990) of single-look intensity observations. Four looks intensity images were regularly produced by the SEASAT SAR system. A Rayleigh density function was experimentally observed for the images analyzed in the present work: both original speckled and filtered. Therefore, let $z = \{z(i,j)\}$ defined over the domain $D = \{(i,j), 1 \leq i \leq N, 1 \leq j \leq M\}$, be a specific speckled textural image. The image z is a realization of a bidimensional random field $Z = \{Z(i,j)\}$, hierarchically defined in terms of an underlying random field $X = \{X(i,j)\}$ characterizing the partition of the domain D into regions of different texture type. The random variable $X(i,j)$ may take value in one of a set of labels

representing a set of texture regions. In each of these regions a texture object is assumed to be the result of a homogeneous random field. Then, the region growing based segmentation may be stated as follows: given the speckled textural image $\mathbf{z} = \{z(i,j)\}$, estimate the partition $\hat{\mathbf{x}} = \{\hat{x}(i, j)\}$ that best correspond to a similarity criterion applied to \mathbf{z} . This criterion is derived from the texture model itself.

The texture model is based on the co-occurrence matrix defined as follows: let δ be a compact and convex set established in the image space as and odd sized rectangular window and let β be a vector position operator relating the relative spatial location of a pair of pixels in the window. The co-occurrence matrix C is the estimated probability of having a pair of pixel values (λ_p, λ_q) in the relative position given by β ; the elements of this matrix are then given by

$$c(\lambda_p, \lambda_q, \beta, \delta) = \frac{\sigma(\{r | r + \beta \in \delta, g(r) = \lambda_p, g(r + \beta) = \lambda_q\})}{\sigma(\{r | r + \beta \in \delta\})} \quad (1)$$

where $g(r)$ is the radar image, $\sigma(\delta)$ is a translation isometry over the window, σ is the order of the set, and $r = (i, j)$ is the vector position of a pixel in the image. The dimension of the co-occurrence matrix is equal to the allowable pixel values: 256 for most radar images. The influence of this quantization level on texture evaluation has been studied (Marceau et al., 1990) on multispectral satellite images. Considering this work, the quantization level was reduced to 64 since no significant loss of information is observed, resulting in a manageable co-occurrence matrix with less computational load. In addition to this, since the correlation between neighboring pixels falls off rapidly (Li, 1988) the magnitude of β was taken to consider only 8-connected pixels.

To characterize the texture information content of the co-occurrence matrix the entropy criterion (Haralick, 1979; Gotlieb and Kreyszig, 1990; Reed and du Buf, 1993) was utilized

$$\mathcal{E} = - \sum_{p=0}^{63} \sum_{q=0}^{63} c_{pq} \log c_{pq} \quad (2)$$

where c_{pq} are the elements of the co-occurrence matrix for a given β and δ . Four directions of β were selected: $0^\circ, 45^\circ, 90^\circ$ and 135° , an average value is obtained over these directions.

3.1.- Automated region growing algorithm

The region growing algorithm requires two parameters to initiate a segmentation: a window size and a threshold. A window is associated to each seeded pixel where initial texture values are estimated. It is assumed that an optimum size window exists that differentiates the most the texture values related to each seeded pixel windows. To decide if a pixel is aggregated to a region a texture difference between the tested pixel window and the initial one is obtained; if this value does not exceed a certain threshold the tested pixel is incorporated into the region. It is assumed as well that an optimum threshold exists that differentiate the best the different texture regions signaled by the seeded pixels. To optimize the above parameters a texture distance is required. This distance is constructed on the grounds of the texture model, for this, a joint entropy for pairs of windows is now introduced. Let consider two texture classes t and s , for which a window of size $n \times n$ is associated to each seeded pixel. First, a joint co-occurrence matrix for pairs of pixels $(\lambda_p^s, \lambda_q^t)$ that occur in the same relative position in each window is obtained. If two equally smooth (or rough) textures are present in the two windows, the resulting matrix shall have a single element, and the joint entropy

$$\mathcal{E}_n^{st} = - \sum_p \sum_q c_{pq}^{st} \log [c_{pq}^{st}] \quad (3)$$

will be zero, i.e., the texture distance is null, and reaches a maximum when the textures s and t are totally different. From equation (3) a texture distance matrix for pairs of classes is obtained. The optimum window size is estimated when the average value

$$\bar{\mathcal{E}}_n = \frac{2}{N_c(N_c - 1)} \sum_{s=1}^{N_c-1} \sum_{t=s+1}^{N_c} \mathcal{E}_n^{st} \quad (4)$$

is maximum, where N_c is the number of considered classes. Where $\mathcal{E}_n^{st} = \mathcal{E}_n^{ts}$, if $t \neq s$, and $\mathcal{E}_n^{st} = 0$, if $t = s$. It is worth while to mention that a texture object defines a patch of a class and a region in the image.

It is assumed that there is an optimum threshold value for the growing of each region class. The estimation of this threshold is based upon the texture distance among classes and the texture distribution of the window's pixels that compose the initial window class. Let consider the group of $n \times n$ windows centered on each of the pixels of the initial window's classes. For each pixel

member of this collection of window's classes a set of $n \times n$ entropy values is obtained

$$E_n^\alpha = \{E_n^1, E_n^2, \dots, E_n^{n \times n}\}^\alpha \quad (5)$$

where α represents the set of defined texture classes. Each set of distribution entropy values E_n^α has associated a standard deviation σ_n^α . The texture distance between these distributions is given by E_n^{st} , $\forall s \neq t$. The average distance (Gong and Howarth, 1992) between two entropy distributions is defined by

$$d^{st} = \frac{1}{n \times n} \sum_{i=1}^{n \times n} \frac{|E_n^s(i) - E_n^t(i)|}{\sigma_n^s + \sigma_n^t}, \forall s \neq t \quad (6)$$

This expression measures the average similarity or dissimilarity of two texture objects. Once the optimum window is established, the mean (μ_n^t) and standard deviation (σ_n^t) of each of them is calculated. Hence a pixel is aggregated into a region if its entropy related value (E_p) does not differ from this mean by a certain percentage. Therefore an optimum threshold is fixed as follows

$$\varepsilon^\alpha = 2\sigma_n^\alpha \quad (7)$$

Expression (7) measures the existence of a textural border for a given class α , and indicates the percentage of variation with respect to the mean. A tested pixel p is then aggregated into class t if its associated entropy value E_p is close enough to the entropy mean of the initial window for this class, thus

$$p \rightarrow \text{class } t : |E_p^t - \mu_n^t| \leq \varepsilon \quad (8)$$

Two objects may be physically or texturally close, expressions (4) and (7) are employed to minimize a possible overlap, and expression (6) is used to measure the texture distance between them. In brief, equations 4 - 7 are used to grow a region as much as needed but maintaining a possible overlap as minimum as possible.

4.- Results and Discussion

A portion of a SEASAT image (fig. 2) was selected to apply the methods proposed in this work. This radar image covers the eastern portion of the Obayos anticline, about 100 km to the North of the city of Monclova in northern México. The dimension of this subimage is

998 pixels by 998 lines. The original SEASAT/SAR image was registered in 1978, it is the result of a 4-look process with a pixel depth of 8-bits, and a pixel size of $25 \times 25 \text{ m}^2$ for nominal ground resolution both in range and azimuth. This subimage (fig. 1) was selected due to the richness content in different textural features.

Firstly, the mentioned subimage was filtered to minimize the effect of speckle. A set of selected filters was applied to the data and a qualitative and quantitative evaluation was performed to identify the best filter. The tested filters were: Median, Lee multiplicative and geometric (Lee et al., 1994); for each of them, a set of parameters (table 1) was estimated and a visual inspection on the image was carried out. The Median and Lee multiplicative were applied using a 3×3 window, the later with an experimental standard deviation of noise of 0.26. For the set of filters three iterations were performed. The quantified parameters were: a contrast factor ($cf = [p_{\max} - p_{\min}] / [p_{\max} + p_{\min}]$) averaged over a set of 3×3 windows, the mean (μ), the standard deviation (σ), and a speckle factor (σ/μ), all of them evaluated for areas where smooth and rough textures are present. The qualitative inspection included: the analysis of the modification of a selected image profile (fig. 2), preservation of edges and texture details, overall sharpness and contrast, and general image quality, both for original and filtered images. As explained in section 2, on the grounds of a global evaluation of the above, the filter that best reduces the speckle, preserving texture details, is the geometric filter with one iteration. The aim of this filtering is to prepare the image for an optimum texture segmentation task.

A series of digital experiments was worked out on the filtered image (fig. 3) with the aim to evaluate the morphology of selected texture objects employing an automated region growing algorithm as described earlier. Three texture objects were visually identified in the radar image: smooth (upper part of image), medium (center of image), and rough (bottom of image). From suitable pixels belonging to these objects, a region growing process was initiated with optimized window and threshold (table 2) according to the method already described and stated in expressions 4 - 7. In this process three texture objects were segmented, the result of which is depicted in figure 4. The morphology of these texture objects is given in table 3, where the optimum window ($n \times n$), the optimum threshold (ε), the mean of entropy values for initial window (μ_n^t), the standard deviation of entropy values for initial window (σ_n^t), the average entropy of the region (μ_e), the area of the region (A), the

perimeter of the region (P), and the fractal dimension of the region (D) are provided.

A texture map was generated (fig. 5) to compare with the segmentation achieved in the region growing process. This map was prepared as follows: an entropy value was associated to each pixel of the filtered image. This value was obtained by calculating the co-occurrence matrix in a pixel centered window with the same size as that used in the region growing algorithm. This process generated an entropy image whose values were clustered in six classes by employing a k-means clustering algorithm. Three patches out of these six classes compare favorably (table 4) with the texture objects segmented in the region growing algorithm. A texture class may manifest itself in several patches but a texture object in only one patch.

5.- Conclusions

An automated region growing algorithm working with optimized parameters is presented in this work. The optimization of these parameters is done by means of a new texture distance defined through a joint class co-occurrence matrix. With this algorithm an optimum segmentation of selected texture objects is achieved. Based on these results a characterization of the morphology of the objects is possible. The morphology is characterized by evaluating the area, the perimeter, the fractal dimension, and the number of pixels of each texture object. A texture map is prepared by clustering the entropy values associated to each pixel of the radar image. Three patches of three classes of this map compare favorably, both visually and morphologically, to the texture objects identified by the region growing algorithm. The texture classes obtained in this way may be used as a reference to seed pixels in suitable positions for texture object segmentation.

7.- References

- T. R. Crimmins (1985). Geometric Filter for Speckle Reduction, *Applied Optics*, Vol. 24, pp.1438-1443.
- H. Derin, P.A. Kelly, G. Vézina and S.G. Labitt (1990). Modeling and Segmentation of Speckled Images Using Complex Data, *IEEE Transactions on Geoscience and Remote Sensing*, Vol. 28, pp. 76-86.
- P. Gong and P.J. Howarth (1992). Frequency-Based Contextual Classification and Gray-Level Vector Reduction for Land-Use Identification, *Photogrammetric Engineering & Remote Sensing*, Vol. 58, pp. 423-437.
- C.C. Gotlieb and H.E. Kreyszig (1990). Texture Descriptors Based on Co-occurrence Matrices, *Computer Vision, Graphics, and Image Processing*, Vol. 51, pp. 70-86.
- R.M. Haralick (1979). Statistical and Structural Approaches to Texture, *Proceedings of the IEEE*, Vol. 67, pp. 304-322.
- L. Kai and J.P. Muller (1991). Segmenting Satellite Imagery: A Region Growing Scheme, *Proceedings, International Geoscience and Remote Sensing Symposium*, Helsinki University of Technology, Espoo, Finland, June 3-6, 1991.
- J.S. Lee (1986). Speckle Suppression and Analysis for Synthetic Aperture Radar Images, *Optical Engineering*, Vol. 25, pp. 636-643.
- J.S. Lee, I. Jurkevich, P. Dewaele, P. Wambacq and A. Oosterlinck (1994). Speckle Filtering of Synthetic Aperture Radar Images: A Review, *Remote Sensing Reviews*, Vol. 8, pp. 313-340.
- Ch. Li (1988). Two Adaptive Filters for Speckle Reduction in SAR Images by Using the Variance Ratio, *International Journal of Remote Sensing*, Vol. 9, pp. 641-653.
- D.J. Marceau, P.J. Howarth, J.M.M. Dubois, and D.J. Gratton (1990). Evaluation of the Grey-Level Co-Occurrence Matrix Method for Land-Cover Classification Using SPOT Imagery, *IEEE Transactions on Geoscience and Remote Sensing*, Vol. 28, pp. 513-518.
- J.M. Morel and S. Solimini (1995). *Variational Methods in Image Segmentation*, Birkhauser, Woodbine, NJ.
- H.H. Nguyen and P. Cohen (1993). Gibbs Random Fields, Fuzzy Clustering, and the Unsupervised Segmentation of Textured Images, *CVGIP: Graphical Models and Image Processing*, Vol. 55, pp. 1-19.
- W.K. Pratt (1991). *Digital Image Processing*, Wiley Interscience, New York.
- H.M. Raafat and A.K.C. Wong (1988). A Texture Information-Directed Region Growing Algorithm for Image Segmentation and Region Classification, *Computer Vision, Graphics, and Image Processing*, Vol. 43, pp. 1-21.
- T.R. Reed and J.M.H. du Buf (1993). A review of Recent Texture Segmentation and Feature Extraction Techniques, *CVGIP: Image Understanding*, Vol. 57, pp. 359-372.
- S.W. Zucker (1976). Region Growing: Childhood and Adolescence, *Computer Graphics and Image Processing*, Vol. 5, pp. 382-399.

Tables

Table 1a.- Evaluation parameters related to a smooth texture area.

Filter \Parameter	cf	μ	σ	σ/μ
Original	245	23.187	7.884	0.340
Median	198	22.862	4.841	0.212
Lee Multiplicative	203	23.183	4.999	0.215
Geometric	180	24.229	4.061	0.167

Table 1b.- Evaluation parameters related to a rough texture area.

Filter \Parameter	cf	μ	σ	σ/μ
Original	247	34.860	20.325	0.583
Median	230	33.909	15.829	0.467
Lee Multiplicative	231	34.784	16.812	0.483
Geometric	223	35.597	17.049	0.479

Table 2.- Average of joint entropy for a series of window sizes.

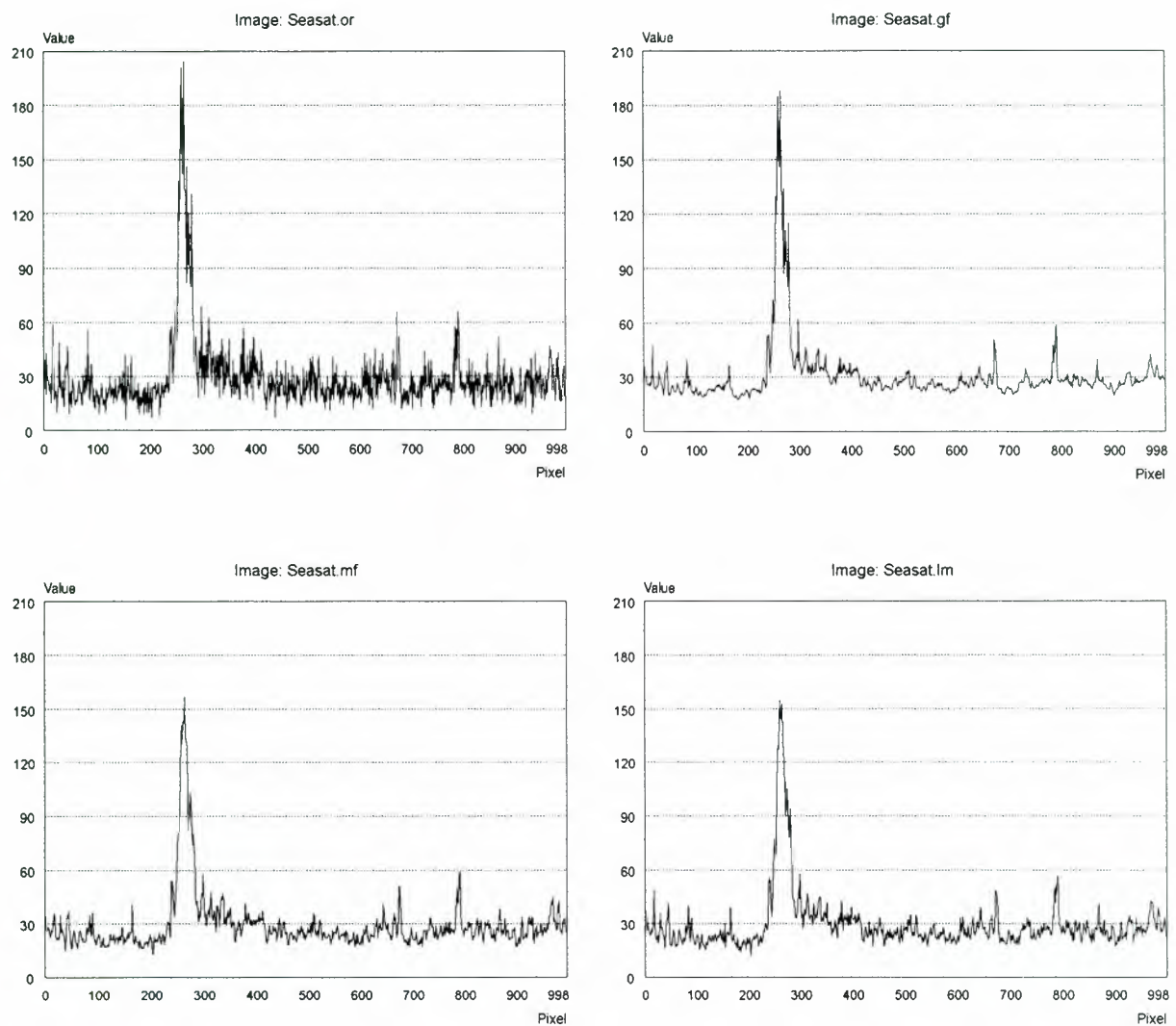
Window size	Average entropy	Window size	Average entropy
23 x 23	4.1404	43 x 43	4.1966
25 x 25	4.1774	45 x 45	4.1950
27 x 27	4.1671	47 x 47	4.1838
29 x 29	4.1567	49 x 49	4.1684
31 x 31	4.1431	51 x 51	4.1518
33 x 33	4.1375	53 x 53	4.1414
35 x 35	4.1433	55 x 55	4.1347
37 x 37	4.1614	57 x 57	4.1345
39 x 39	4.1725	59 x 59	4.1418
41 x 41	4.1893	61 x 61	4.1414

Table 3.- Morphological parameters of texture class objects segmented by region growing.

Class (t)	n x n	ϵ	μ_n^t	σ_n^t	μ_ϵ	A	P	D
Smooth	43 x 43	27	1.64	0.22	1.78	73,324	3,612	1.215
Medium	43 x 43	8	3.14	0.13	3.11	67,177	8,634	1.381
Rough	43 x 43	10	4.42	0.22	4.29	16,958	1,586	1.229



Fig. 1.- Original SEASAT subimage.



a	b
c	d

Fig. 2.- Selected image line profile (row 260) of: a) original subimage, b) geometric filter, c) median filter and d) Lee multiplicative filter.



Fig. 3.- Filtered subimage with the geometric filter, one iteration.

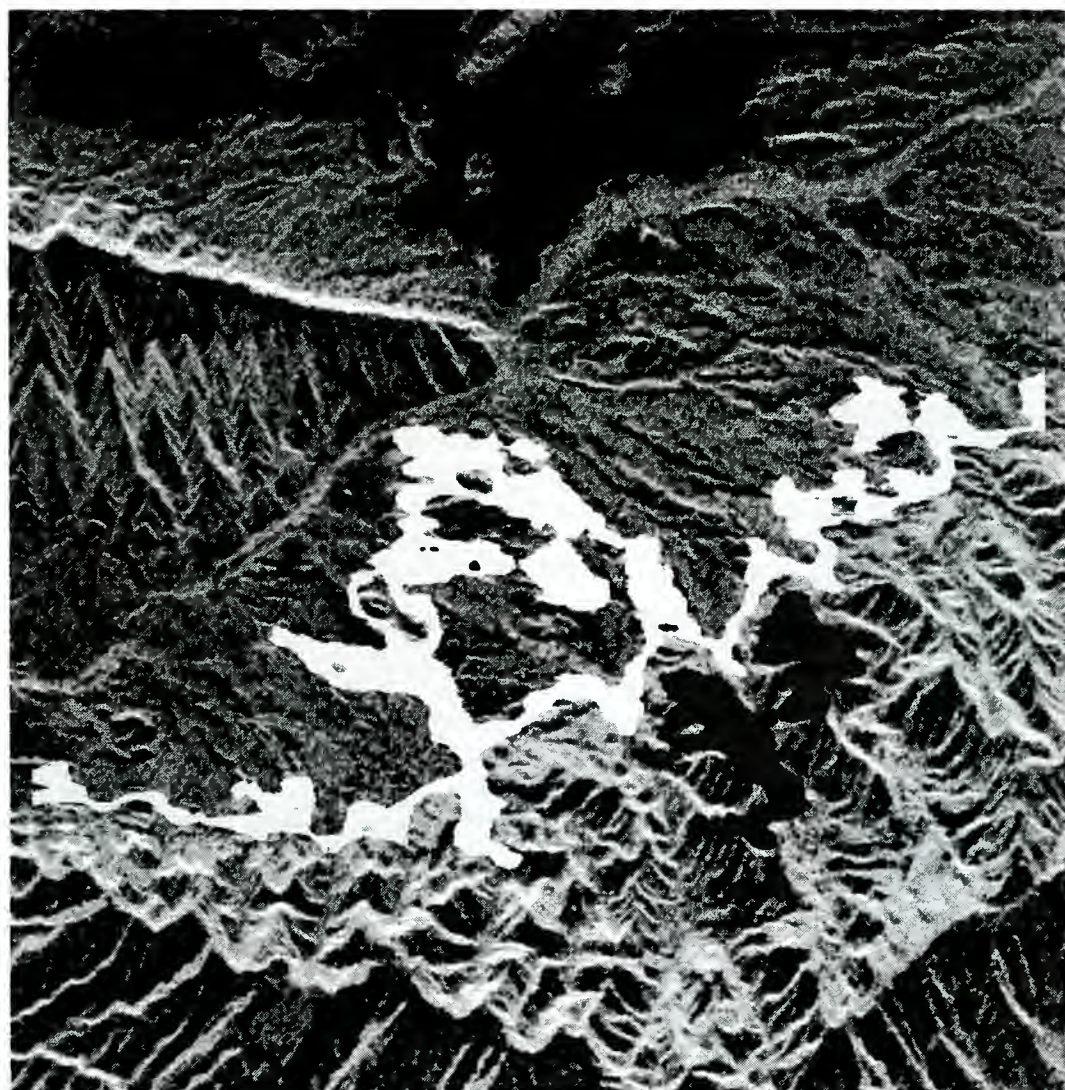


Fig. 4.- Segmentation of three texture objects.

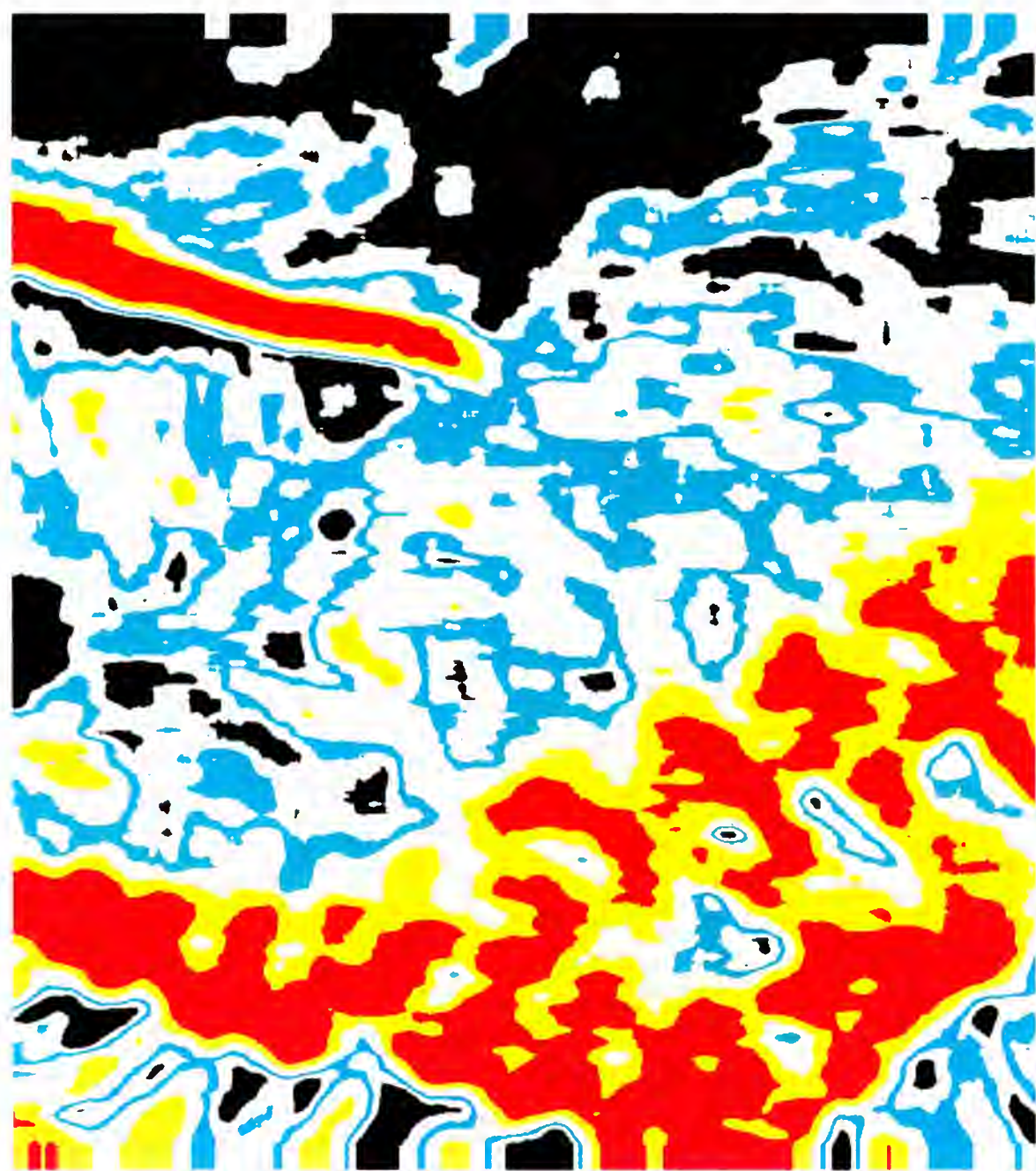
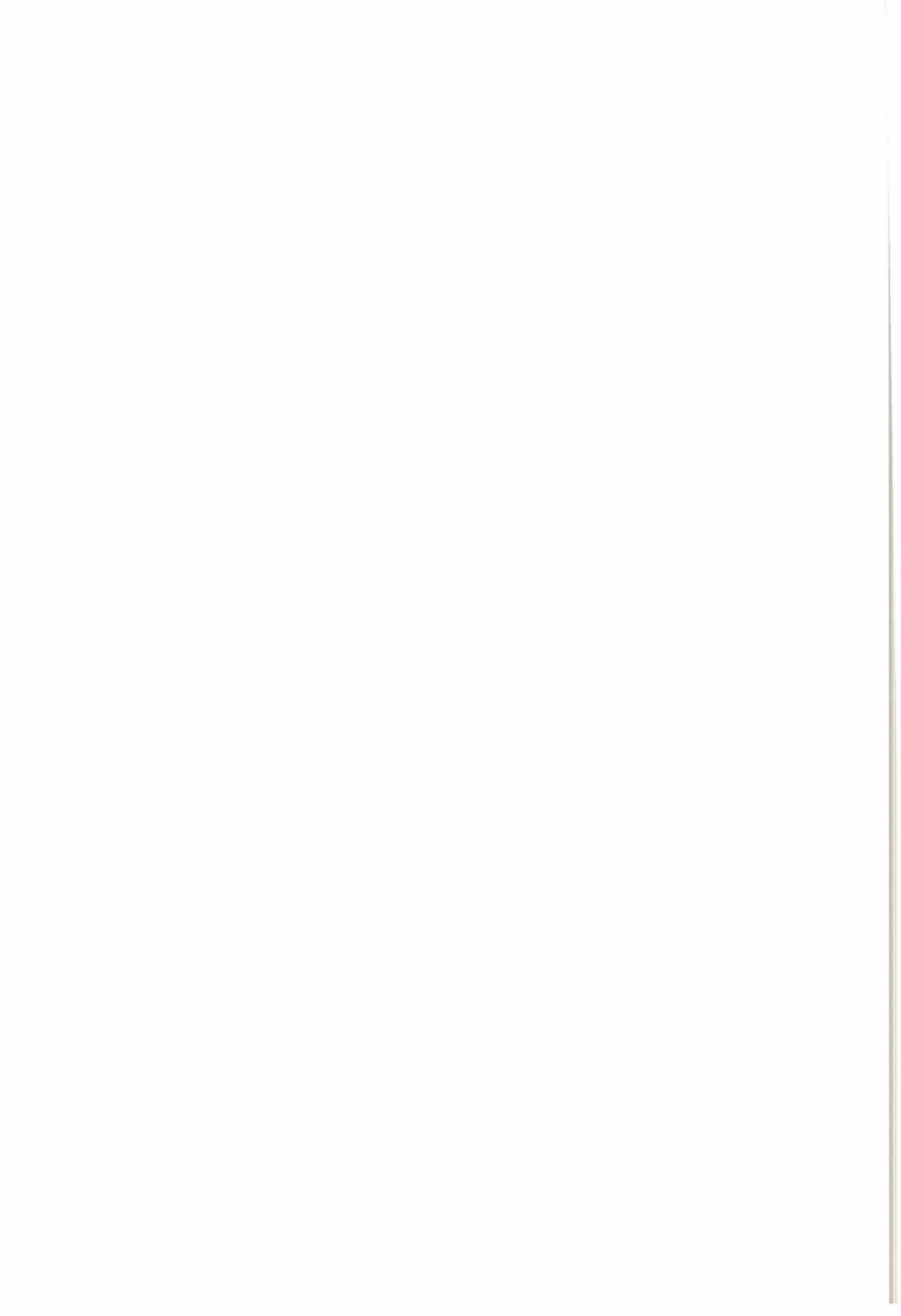


Fig. 5.- Texture map indicating various texture classes.



Classificação de culturas irrigadas na região de Bebedouro, PE, Brasil, usando a informação polarimétrica das imagens da missão SIR-C/X-SAR

Sueli Pissarra Castellari Ribeiro
 Luciano Vieira Dutra
 Camilo Daleles Rennó
 João Viane Soares

INPE - Instituto Nacional de Pesquisas Espaciais
 DPI - Divisão de Processamento de Imagens
 Av. dos Astronautas, 1758
 12227-010 São José dos Campos, SP, Brasil
 sueli,dutra@dpi.inpe.br
 camilo,viane@ltid.inpe.br

ABSTRACT

This paper investigates the use of polarimetric information extracted from SIR-C/X-SAR complex polarimetric images for crop discrimination in Bebedouro region, Pernambuco state, Brasil. In addition to widely used modulus of complex channels (amplitude) another two channels, modulus and phase from complex correlation coefficient between HH and VV complex channels were also used. The phase of correlation coefficient is a smoothed version of phase difference information between HH and VV, and was used in lieu of it. Five classes; corn, soya beans, stubble, bare soil and "caatinga" were defined. To assess the discrimination power of the extracted features confusion matrix of maximum likelihood per point classification and Jeffreys-Matusita distance were calculated for three classes. Results showed that phase information can greatly improve the classification accuracy and the modulus of correlation coefficient carries also discrimination power.

1. Introdução

Sistemas polarimétricos de radar multifreqüência representam uma nova geração de sensores de microondas ainda em avaliação para aplicação sistemática em sensoriamento remoto. As características de multifreqüência e polarimetria destes sensores tornam possível não só a aquisição de informação sobre a superfície dos objetos, mas também sobre as características estruturais, dielétricas e volumétricas dos mesmos. O potencial na aplicação destes dados, particularmente na banda L, tem aumentado o interesse pelo seu uso em problemas de discriminação de culturas e florestas, avaliação de desflorestamento e deteção de mudanças.

Neste trabalho pretende-se investigar o uso das imagens de radar polarimétricas, obtidas pela missão SIR-C em abril de 1994 (esta missão foi repetida em

outubro de 1994), na classificação de diferentes tipos de cobertura através da extração de atributos dessas imagens e utilizando-as em combinação com os dados polarimétricos originais.

2. Dado polarimétrico e definições

A informação polarimétrica pode ser obtida através da decomposição do sinal do radar em dois sinais ortogonais, um horizontal e outro vertical, que são recebidos e processados em canais separados independentemente. A informação de polarização completa para cada pixel da cena imageada é descrita pela matriz de espalhamento [S], definida por

$$[S] = \begin{pmatrix} S_{hh} & S_{hv} \\ S_{vh} & S_{vv} \end{pmatrix} \quad (1)$$

onde os subscritos **h** e **v** correspondem aos componentes do campo elétrico de transmissão e recepção polarizados na horizontal e na vertical, respectivamente. Cada elemento da matriz de espalhamento é uma função da freqüência e dos ângulos de espalhamento e iluminação.

O dado polarimétrico também pode ser expresso em termos da matriz de Stokes [M]. Esta representação consiste de combinações lineares dos produtos cruzados dos 4 elementos da matriz de espalhamento [1].

$$[M] = \begin{pmatrix} S_{hh}S_{hh}^* & S_{hv}S_{hv}^* & S_{hh}S_{hv}^* & S_{hv}S_{hh}^* \\ S_{vh}S_{vh}^* & S_{vv}S_{vv}^* & S_{vh}S_{vv}^* & S_{vv}S_{vh}^* \\ S_{hh}S_{vh}^* & S_{hv}S_{vv}^* & S_{hh}S_{vv}^* & S_{hv}S_{vh}^* \\ S_{vh}S_{hh}^* & S_{vv}S_{hv}^* & S_{vh}S_{hv}^* & S_{vv}S_{hh}^* \end{pmatrix} \quad (2)$$

3. Procedimentos para extração de atributos

Este trabalho usa como base a matriz de Stokes para definição dos atributos discriminantes, através da combinação dos seus elementos. Nesta seção serão introduzidos os seguintes procedimentos de extração de atributos : diferença de fase e coeficiente de correlação complexa. Outros procedimentos, tais como razões normalizadas entre canais, autocorrelação "lag1" e coeficiente de variação, entre outros, serão objetos de estudo futuro.

3.1 Diferença de fase

A diferença de fase entre canais com ondas copolarizadas (hh - vv) é definida por

$$\phi_{hh-vv} = \tan^{-1} \left[\frac{\Im \langle S_{hh} S_{vv}^* \rangle}{\Re \langle S_{hh} S_{vv}^* \rangle} \right] \quad (3)$$

onde \Im e \Re representam as partes real e imaginária, respectivamente. Diferenças de fase também podem ser calculadas entre canais com polarização cruzada.

3.2 Coeficiente de correlação complexa

O coeficiente de correlação complexa entre os elementos co-polarizados da matriz de Stokes é definido por

$$\rho_{hhvv} = \frac{\langle S_{hh} S_{vv}^* \rangle}{\sqrt{\langle S_{hh} S_{hh}^* \rangle \langle S_{vv} S_{vv}^* \rangle}} \quad (4)$$

de onde se obtém o módulo e a fase. Tal definição também pode ser estendida para canais com polarização cruzada.

4. Região de estudo e obtenção das imagens

A área de estudo (figura 1) compreende o Projeto de Irrigação de Bebedouro (PIB) localizado na região do Sub-médio São Francisco ($9^{\circ}07'S$, $40^{\circ}18'W$), a aproximadamente 40 km à nordeste do município de Petrolina, estado de Pernambuco [2].

4.1 Descrição da região

O PIB está dividido em 2 partes, denominadas PIB I e PIB II, com área total aproximada de 3500 ha e 2000 ha, respectivamente. O PIB I é formado por

pequenas propriedades de 5 a 12 ha, áreas maiores destinadas a pequenas empresas privadas, áreas de reserva de vegetação natural e pequenos núcleos habitacionais. O PIB II possui uma área destinada a empresas privadas e outra destinada ao Serviço de Produção de Sementes Básicas (SPSB) da EMBRAPA.

Foi analisada a região do PIB II, especificamente a região composta por 4 pivôs com classes de milho, soja, restolho e solo preparado, pertencente ao Serviço de Produção de Sementes Básicas da Embrapa, além da classe caatinga, (ver figura 1).

Esta região foi visitada por ocasião da coleta de imagens e os dados referentes ao plantio das diversas culturas foram anotados.

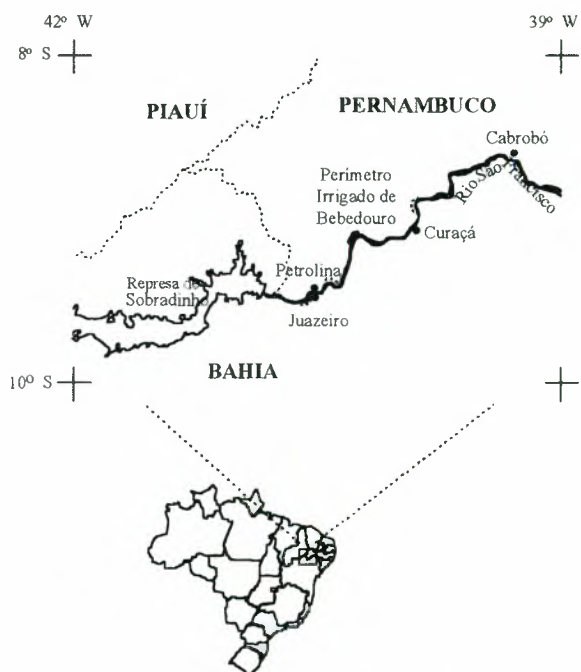


Figura 1 - Descrição da região estudada

4.2 Parâmetros das imagens utilizadas

As imagens foram adquiridas através da missão space shuttle SIR-C/X-SAR em abril de 94. A tabela I mostra os principais parâmetros destas imagens.

Tabela I - Parâmetros da imagem

Freqüência	L(1,254 Ghz) C(5,304 Ghz)
Polarização	HH, HV, VV, VH
Ângulo de incidência	37,97°
Altitude da plataforma	219,38 Km
Direção da órbita	descendente
Tipo do produto	Matriz de Stokes - 16 looks
Representação geométrica	Ground range
Espaçamento pixel	rgn 12,5m / az 12,5m

5. Metodologia

O objetivo principal deste trabalho é avaliar o desempenho do uso da informação polarimétrica, com a utilização dos canais originais em combinação ou não com os canais transformados, na discriminação de culturas. Aqui foram usadas apenas imagens da banda L, em 3 polarizações (HH, HV, VV), totalizando 3 imagens originais na forma complexa. A figura 2 mostra uma imagem com polarização HH da região estudada e as classes de interesse. A tabela II apresenta os tipos de classes utilizadas e os respectivos número de amostras e número de pixels.

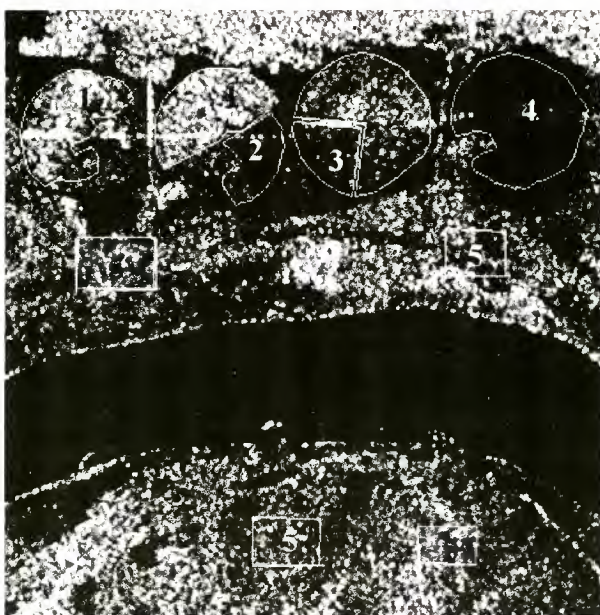


Figura 2 - Banda L, polarização HH, classes de interesse 1 - milho, 2 - soja, 3 - restolho, 4 - solo preparado, 5 - caatinga

Tabela II - Classes estudadas

Classes	Número de amostras	Número total de pixels
milho	2	6245
soja	2	6635
restolho	1	1498
solo preparado	1	5592
caatinga	4	5245

As combinações utilizadas para mensuração do poder discriminatório dos atributos, considerando-se as classes já definidas foram :

- 3 bandas originais em amplitude HH, HV e VV (aqui não existe a informação de fase dos atributos complexos).

- 2 bandas extraídas da correlação complexa, a saber : módulo e ângulo. A banda ângulo do coeficiente de correlação complexa é basicamente a informação diferença de fase da equação (3), filtrada quanto ao efeito do ruído “speckle” sobre a fase, por causa da operação média necessária para o cálculo da equação (4) em janelas 5x5 em torno de cada pixel da imagem. Aqui não existe a informação relativa a HV.
- o conjunto das 5 bandas acima.

Considera-se que os atributos em questão seguem uma distribuição gaussiana conjunta por causa do alto número de “looks” dos canais originais e adicionalmente do efeito de média no cálculo do módulo do coeficiente de correlação complexa. A fase para valores relativamente altos do coeficiente de correlação complexa também possuem distribuição semelhante à gaussiana [3].

A avaliação das contribuições dessas combinações de canais na discriminação das culturas é feita de duas formas :

1. comparando-se os resultados dos índices de desempenho médio (DM) e confusão média (CM), calculados sobre matrizes de classificação de áreas de treinamento e para as três combinações. Classificador utilizado : máxima verossimilhança pontual (seção 5.1).
2. através da comparação entre distâncias estatísticas entre distribuições (seção 5.2) avaliadas para as classes em estudo e para as três combinações de canais assinalados.

Esse método tem a vantagem de ser independente do algoritmo de classificação a ser utilizado.

5.1. Classificador pontual de máxima verossimilhança

O já bem conhecido classificador pontual de máxima verossimilhança [4], [5], é usado para classificar as áreas de treinamento das classes envolvidas.

Levanta-se uma matriz de classificação para cada combinação de canais. O desempenho médio (DM) é calculado pela média da percentagem de classificação correta para cada classe ponderada pelo número de pontos de cada classe. A abstenção média (AM) é calculada pela média das percentagens de pontos não classificados por classe ponderada pelo número de partes de cada classe. A confusão média (CM) é calculada como $CM = 1 - (DM + AM)$.

5.2. Distância J-M

A distância de Jeffries-Matusita entre duas distribuições é definida por

$$J_{ij} = \left\{ \int \left[\sqrt{p(x|w_i)} - \sqrt{p(x|w_j)} \right]^2 dx \right\}^{1/2} \quad (5)$$

onde $p(x|w_i)$ e $p(x|w_j)$ são os valores da distribuição da i-ésima e j-ésima classe. No caso de distribuições gaussianas a equação (5) assume a forma

$$J_{ij} = \left[2 \left(1 - e^{-\alpha} \right) \right]^{1/2} \quad (6)$$

onde

$$\alpha = \frac{1}{8} (\mu_i - \mu_j)^t \left\{ \frac{\Sigma_i + \Sigma_j}{2} \right\}^{-1} (\mu_i - \mu_j) + \frac{1}{2} \ln \left\{ \frac{\left| \Sigma_i + \Sigma_j \right|}{\left[\left| \Sigma_i \right| \cdot \left| \Sigma_j \right| \right]^{1/2}} \right\} \quad (7)$$

A distância JM pode ser usada para medir a separabilidade em conjuntos fixos de canais ou dado um conjunto de atributos, possibilita escolher um subconjunto deles, com certo número de canais, de tal forma que se maximize a distância JM média entre todos os pares de classes ou que se escolha o subconjunto de canais que maximize a menor distância JM entre pares de classes.

6. Resultados

6.1. Classificação pontual

As 3 bandas correspondentes às polarizações HH, HV e VV em amplitude chamaremos de canais originais. Na classificação usando estes dados obteve-se um desempenho médio (DM) de 61,4%, (ver Tabela III), e uma confusão média de 38,6%. A abstenção média (AM) nesta e nas tabelas seguintes foi nula porque o limiar de classificação foi ajustado para classificar todos os pontos. Considerando-se as classes individualmente nota-se que a classe de solo preparado teve um resultado bem acima da média, de 89,21%, enquanto a classe soja comportou-se de maneira oposta, tendo um resultado abaixo da média, de 34,05%, confundindo-se quase que na mesma proporção entre as classes de restolho e de caatinga. Este comportamento deve-se ao fato das médias destas classes estarem bem próximas como pode ser observado através da Tabela IV. As demais classes tiveram um resultado próximo ao desempenho médio.

Tabela III - Matriz de classificação

Atributos : Amplitude HH, HV e VV

\ áreas classes\	milho	soja	restolho	solo preparado	caatinga
milho	65,56 %	8,12 %	14,46 %	1,32 %	10,52 %
soja	6,86 %	34,05 %	29,14 %	9,60 %	20,32 %
restolho	5,80 %	8,41 %	65,02 %	19,75 %	1,00 %
solo preparado	1,00 %	0,59 %	9,17 %	89,21 %	0,01 %
caatinga	9,28 %	25,07 %	6,93 %	0,57 %	58,13 %

Desempenho médio (DM) : 61,4 %

Confusão média (CM) : 38,6 %

Tabela IV - Média e desvio padrão

Atributos Amplitude - Banda L

		milho	soja	restolho	solo preparado	caatinga
HH	μ	0,3453	0,2514	0,2104	0,1363	0,2864
	σ	0,1129	0,1012	0,0718	0,0539	0,0832
HV	μ	0,1116	0,1022	0,0642	0,0336	0,1449
	σ	0,0328	0,0425	0,0212	0,0133	0,0440
VV	μ	0,4074	0,2207	0,2078	0,1524	0,2598
	σ	0,1422	0,0809	0,0924	0,0606	0,0783

A Tabela V mostra o resultado da classificação quando são usados o módulo e o ângulo do coeficiente de correlação complexa. O desempenho médio melhora em relação a classificação anterior de 61,4% para 69,1%. As classes de milho e soja também tiveram uma melhora significativa, de 65,5% para 87% e de 34% para 45,8%, respectivamente. O fator preponderante na melhoria da separabilidade da classe milho é a informação de fase que registra o valor de $\sim -\left(\frac{\pi}{2}\right)$ entre HH e VV (ver Tabela VI).

Tabela V - Matriz de classificação

Atributos : Módulo e ângulo do coeficiente de correlação complexa

\ áreas classes\	milho	soja	restolho	solo preparado	caatinga
milho	87,00 %	9,37 %	0,19 %	0,00 %	3,42 %
soja	2,76 %	45,89 %	6,61 %	0,22 %	34,50 %
restolho	0,06 %	0,00 %	60,08 %	29,17 %	10,68 %
solo preparado	0,00 %	0,00 %	12,41 %	87,41 %	0,17 %
caatinga	3,20 %	22,36 %	17,21 %	0,01 %	57,19 %

Desempenho médio (DM) : 69,1 %

Confusão média (CM) : 30,9 %

O módulo de correlação é também bem distinto nesse caso. No caso da soja, diminuiu a confusão com

a classe restolho, mas aumentou em relação à classe caatinga. Este resultado pode ser explicado pelas médias dessas classes em se tratando do atributo módulo do coeficiente de correlação complexa (ver Tabela VI), neste caso as médias da classe soja ($\mu=0,2556$) e da classe restolho ($\mu=0,6239$) diferenciaram-se bem, ao contrário do caso anterior. A classe restolho diminuiu o desempenho em 5% e aumentou a confusão com a classe solo preparado em 10%. A classe caatinga manteve o mesmo índice de desempenho, melhorou a confusão com a classe milho e piorou em relação à classe restolho. Apesar de alguns resultados isolados não serem satisfatórios, o uso da combinação do dado polarimétrico neste caso, melhorou a classificação de uma maneira geral, sem o uso do canal HV.

Tabela VI- Média e desvio padrão

Atributos Módulo e ângulo do coeficiente de correlação complexa

	milho	soja	restolho	solo preparado	caatinga
Módulo	μ	0,4590	0,2556	0,6239	0,7897
	σ	0,1397	0,1313	0,1359	0,0823
Ângulo	μ	-1,6939	-0,4557	0,1430	0,1608
	σ	0,5418	1,3094	0,2523	0,1351
					0,8240

O uso conjunto das bandas usadas nas duas classificações mencionadas anteriormente, melhora o desempenho da classificação, para todas as classes, como pode ser visto na Tabela VII. A melhora é de 18,1% em relação à primeira classificação e de 10,4% em relação à segunda.

Tabela VII - Matriz de classificação

Atributos :Amplitude HH, HV, VV +
Módulo e ângulo do coeficiente de correlação complexa

\áreas classes\	milho	soja	restolho	solo preparado	caatinga
milho	87,15 %	10,09 %	0,46 %	0,00 %	2,27 %
soja	7,59 %	66,19 %	5,66 %	0,11 %	20,43 %
restolho	0,20 %	2,46 %	83,51 %	12,28 %	1,53 %
solo preparado	0,05 %	0,00 %	7,42 %	92,47 %	0,05 %
caatinga	2,32 %	22,45 %	4,38 %	0,00 %	70,82 %

Desempenho médio : 79,5 %

Confusão média : 20,5 %

O desempenho individual da classe milho manteve o mesmo índice da segunda classificação, enquanto as classes de soja e restolho melhoraram em torno de 20% e as classes solo preparado e caatinga em 5% e 13% respectivamente. A confusão da classe

soja com a classe caatinga manteve o mesmo índice observado na primeira classificação.

6.2 Distâncias entre distribuições

No caso da comparação das distâncias entre distribuições foi analisado cada procedimento realizado nas classificações anteriores. A Tabela VIII mostra as distâncias JM mínima e média da análise de cada procedimento em separado. Os resultados desta análise confirmam os resultados obtidos anteriormente.

Tabela VIII - Distância JM mínima e média

	Amplitude HH, HV, VV	Módulo e ângulo coef. cor. compl	Amplitude HH,HV,VV Módulo e ângulo do coef.correl.compl
JM min	0,364460	0,568256	0,673633
JM med	0,895871	1,06852	1,31420

Como forma adicional de medir a importância dos diversos atributos aqui usados, usou-se a distância JM para escolher 3 canais entre 5 do conjunto completo. A Tabela IX apresenta todas as combinações possíveis de 3 canais considerando-se todas as classes definidas.

Tabela IX - Distância JM mínima e média das 5 bandas em combinações 3 a 3

	JM min	JM med
1 B1/B2/B3	0,60	1,12
2 B1/B2/B4	0,57	1,16
3 B1/B2/B5	0,57	1,13
4 B1/B3/B4	0,63	1,18
5 B1/B3/B5	0,59	1,20
6 B1/B4/B5	0,57	1,19
7 B2/B3/B4	0,33	0,74
8 B2/B3/B5	0,24	0,75
9 B2/B4/B5	0,17	0,79
10 B3/B4/B5	0,36	0,89
B1 - Ângulo do coeficiente de correlação complexa		
B2 - Módulo do coeficiente de correlação complexa		
B3 - Amplitude HH		
B4 - Amplitude HV		
B5 - Amplitude VV		

Os melhores desempenhos são das combinações do ângulo do coeficiente de correlação complexa com pares de amplitude HH e HV, HH e VV e HV e VV (seleções 4, 5 e 6). Foram realizadas classificações usando esses três conjuntos de atributos e os resultados são mostrados na Tabela X, assim como os resultados das classificações realizadas anteriormente.

Tabela X - Desempenho médio das classificações

Atributos	Desempenho médio
Amplitude HH, HV, VV	61,4 %
Módulo e ângulo do coeficiente de correlação complexa	69,1 %
Amplitude HH, HV, VV + Módulo e ângulo do coeficiente de correlação complexa	79,5 %
Ângulo do coeficiente de correlação complexa	67,6 %
Amplitude HH, VV	
Ângulo do coeficiente de correlação complexa	71,1 %
Amplitude HH, HV	
Ângulo do coeficiente de correlação complexa	73,7 %
Amplitude HV, VV	

(Dissertação submetida para a obtenção do grau de Mestre em Sensoriamento Remoto).

[3] J.S. Lee, K.W. Hoppel, S.A. Mango and A.R. Miller, "Intensity and Phase Statistics of Multilook Polarimetric and Interferometric SAR Imagery," IEEE Trans. Geosci. Remote Sensing, vol. 32 pp. 1017-1028, Sept. 1994.

[4] K. Fukunaga, "Introduction to Statistical Pattern Recognition", Academic Press, Inc, 1990.

[5] N.D.A. Mascarenhas e F.R.D. Velasco, "Processamento Digital de Imagens," IV EBAI 1989.

7. Conclusões

A principal conclusão que se pode derivar destes resultados é que a informação de fase (entre HH e VV) é importante e não deve ser descartada em classificações utilizando-se dados polarimétricos complexos. Esta conclusão é reforçada ao se verificar que na tabela X todas as combinações com fase mostraram JM médias consistentemente maior que as sem fase.

O canal correlação também pode fornecer separabilidade para diversos casos, basta observar o que foi explicado na seção 6.1 com respeito às classes soja e restolho.

O presente trabalho vai continuar testando outros atributos e procurando estabelecer necessárias ligações com as propriedades estruturais das diversas classes de vegetação ou culturas.

8. Agradecimentos

Este trabalho foi parcialmente financiado pelo Projeto Temático CNPq Geotec (Processo Institucional n. 680.061/940)

Referências

- [1] J.J.van Zyl, H.A. Zebker, and C. Elachi, "Imaging Radar Polarization Signatures: Theory and Observations," *Radio Science*, vol. 22, pp. 529-543, 1987.
- [2] C.D. Rennó, "Avaliação de Medidas Texturais na Discriminação de Classes de Uso Utilizando Imagens SIR-C/X-SAR do Perímetro Irrigado de Bebedouro, Petrolina, PE." INPE, São José dos Campos, 1995.

UTILIZAÇÃO DE MEDIDAS TEXTURAIS NA DISCRIMINAÇÃO DE CLASSES DE USO DO SOLO DO PERÍMETRO IRRIGADO DE BEBEDOURO, PERNAMBUCO, BRASIL, UTILIZANDO-SE IMAGENS SAR.

Camilo Daleles Rennó
João Vianei Soares

INPE - Instituto Nacional de Pesquisas Espaciais
Caixa Postal 515, 12201-970 São José dos Campos, SP, Brasil
{camilo, vianei }@ltid.inpe.br

RESUMO

A textura é uma importante característica utilizada na interpretação visual de imagens. Dessa forma, sua utilização pode melhorar o desempenho de classificadores digitais, principalmente em imagens com alta resolução espacial. Muitas medidas de textura podem ser encontradas na literatura mas, no entanto, não há um consenso na definição deste termo, nem tampouco uma formulação matemática única e precisa. A escolha das medidas de textura a serem utilizadas numa determinada análise é feita quase sempre de forma empírica. Este trabalho vem apresentar uma metodologia de seleção de medidas de textura baseada na maximização da discriminação de classes de uso em imagens SAR. Foram utilizadas imagens provenientes da missão SIR-C/X-SAR, bandas L e C, polarizações HH, HV e VV, de abril de 1994 sobre o Perímetro Irrigado de Bebedouro, Petrolina - PE, Brasil. Foram analisadas um total de 24 medidas de textura de primeira e segunda ordem. Os resultados mostraram que classificações baseadas apenas na média tonal obtiveram valores de kappa pouco acima de 0,50. O uso de medidas de textura resultaram numa melhoria da classificação, obtendo-se valores de kappa superiores a 0,90 quando 15 medidas foram utilizadas simultaneamente, considerando uma análise conjunta de todas as bandas e polarizações. Mesmo quando apenas uma imagem (uma banda, uma polarização) foi utilizada, conseguiu-se, em geral, valores de kappa superiores a 0,85 com a utilização de mais de 20 medidas de textura. Os resultados comprovaram que a informação textural presente em imagens de radar podem ajudar na discriminação de classes de uso de solo.

1. INTRODUÇÃO

A textura é uma importante característica utilizada na interpretação visual de imagens e por esta razão, o uso de medidas de textura pode aumentar o desempenho de classificadores digitais, principalmente em imagens com alta resolução espacial. No entanto, a textura de uma imagem é muito difícil de ser quantificada, uma

vez que não há um consenso na definição deste termo, nem tampouco uma formulação matemática precisa. Ao contrário da informação espectral, que descreve a variação do nível de cinza de um *pixel*, a textura contém informações sobre a distribuição espacial dos níveis de cinza de uma região da imagem (Ulaby et al., 1986; Marceau et al., 1989).

Muitos autores têm tentado quantificar a textura. Métodos de análise de textura têm sido desenvolvidos usando-se padrões de freqüência (Chen, 1990), estatísticas de primeira ordem (Hsu, 1978; Irons e Petersen, 1981) e estatísticas de segunda ordem (Haralick et al., 1973; Welch et al., 1990).

O objetivo geral deste trabalho é avaliar o desempenho de medidas de textura na discriminação de alvos agrícolas utilizando-se imagens de radar. Para tanto, serão utilizados dois métodos de seleção que maximizam a discriminação obtidas a partir da missão SIR-C/X-SAR.

2. MEDIDAS DE TEXTURA

Entre as medidas mais utilizadas, destacam-se aquelas baseadas na matriz de co-ocorrência (Haralick et al., 1973). Cada elemento $P(i, j)_{\Delta x, \Delta y}$ da matriz de co-ocorrência representa a freqüência com que dois *pixels* vizinhos (separados por uma distância de Δx colunas e Δy linhas) ocorrem na imagem, um com o nível de cinza i e o outro com o nível de cinza j . A principal desvantagem no uso de medidas texturais baseadas na matriz de co-ocorrência é a grande exigência em memória e tempo computacional. Como alternativa, pode-se trabalhar com vetores soma e diferença de níveis de cinza (Weszka et al., 1976; Unser, 1986; Welch et al., 1990). Neste trabalho estão sendo avaliadas as seguintes medidas de Haralick: uniformidade (energia), entropia, contraste, homogeneidade, correlação, chi-quadrado, média do vetor soma, variância do vetor soma, uniformidade do vetor soma, entropia do vetor soma, média do vetor diferença, variância do vetor diferença, uniformidade do vetor diferença e entropia do vetor diferença.

Além das medidas baseadas na matriz de co-ocorrência, outra medida de segunda ordem que reflete, de certo modo, a textura de uma imagem, é a autocorrelação espacial que indica a relação espacial existente entre os *pixels* desta imagem. Neste trabalho, estão sendo testadas as autocorrelações de *lag* (0,1), (1,0) e (1,1).

Outros métodos utilizados para caracterizar a textura de imagens baseiam-se em parâmetros estatísticos de primeira ordem, ou seja, que não levam em consideração a distribuição espacial dos níveis de cinza de uma região da imagem. As medidas de primeira ordem analisadas neste estudo são: variância, coeficiente de variação, assimetria, assimetria da média em relação à mediana e curtose.

Estas medidas de textura, assim como as baseadas em estatísticas de segunda ordem, não são específicas para imagens de radar, uma vez que não consideram nenhum modelo matemático que explique a variação encontrada na imagem. Yanasse et al. (1993), estudando as propriedades estatísticas de imagens SAR, testaram diversas distribuições (K amplitude *multilook*, gamma, raiz da gamma, log-normal, entre outras) para determinar aquelas para as quais seus dados mostraram melhor ajuste. Analisando as estimativas dos parâmetros de algumas distribuições, concluíram que estas poderiam ser utilizadas para discriminar áreas de floresta e não floresta. Particularmente, o parâmetro α da distribuição K amplitude *multilook* parece expressar a variação de textura entre estas duas classes e desta forma pode também ser usado como uma medida de textura. Altos valores de α são indicativos de homogeneidade. Duas estimativas estão sendo avaliadas, uma baseada na distribuição K amplitude *multilook* e outra na distribuição K intensidade *multilook*.

3. MATERIAL E MÉTODOS

A área de estudo compreende o Projeto de Irrigação de Bebedouro (PIB) localizado na região do Sub-médio São Francisco ($9^{\circ}07'S$, $40^{\circ}18'W$ Gr), Petrolina, Pernambuco, Brasil. O PIB constitui um mosaico de culturas anuais e perenes com propriedades de 5 a 12 ha (Soares et al., 1988).

Neste trabalho, foram analisadas as imagens referentes a 2 passagens do SIR-C obtidas durante o primeiro experimento (abril de 1994). A Tabela 1 resume as principais características destas imagens. GR1 e GR2 são imagens *ground range* e SR *slant range*.

Inicialmente, as imagens SR sofreram um processamento *multilook* a fim de reduzir o speckle e obter elementos de resolução correspondentes a cada *pixel* da imagem mais ou menos quadrados (12,57 x 13,32 m). Cada conjunto é composto por 6 imagens

amplitude discretizadas em 256 níveis de cinza (bandas L e C, polarizações HH, HV e VV).

Tabela 1 - Características das imagens SAR

	GR1	GR2	SR
Data	09/04/94	13/04/94	13/04/94
Bandas	L e C	L e C	L e C
Polarizações	HH, HV e VV	HH, HV e VV	HH, HV e VV
Projeção	<i>Ground</i> <i>Range</i>	<i>Ground</i> <i>Range</i>	<i>Slant</i> <i>Range</i>
Âng. de incid.	47,77°	37,97°	37,97°
Esp. na linha	12,5 m	12,5 m	4,19 m
Esp. na coluna	12,5 m	12,5 m	13,32 m
Altitude	220,37 km	219,38 km	219,38 km

Simultaneamente ao imageamento feito pelo SIR-C/X-SAR, foi realizado o trabalho de campo visando o levantamento do uso da terra, utilizado como verdade terrestre. Uma legenda foi definida levando-se em consideração a área, a distribuição e a importância de cada classe de uso. Dessa forma, foram definidas 7 classes de uso: uva, melão/melancia, tomate, solo preparado, pasto limpo, pasto sujo/pousio e manga.

Para cada propriedade, foi obtido um *overlay* (tendo o mapa topográfico do PIB como base), que posteriormente, foi digitalizado e registrado às imagens. Este procedimento garantiu que nenhuma distorção nos níveis de cinza fosse gerada, conservando as imagens em seu formato original.

Em seguida, para cada amostra de cada imagem foram determinadas 25 medidas (14 medidas de Haralick; 3 autocorrelações espaciais; 5 medidas baseadas em estatísticas de primeira ordem; 2 estimadores de α ; e a média), totalizando 150 medidas para cada conjunto de imagens analisadas. A Tabela 2 apresenta a relação de todas as medidas testadas, assim como a abreviatura adotada para cada uma destas medidas.

A utilização de todas as medidas texturais na caracterização de um alvo é impraticável e desnecessária uma vez que a demanda computacional para a extração destas informações seria extremamente elevada.

O desempenho de um conjunto de variáveis pode ser avaliado, por exemplo, através da classificação de amostras. Um conjunto ótimo de variáveis seria aquele que classificasse todas as amostras corretamente. Comumente empregam-se medidas de divergência (distâncias) ou de similaridade no processo de classificação.

Entre as diversas medidas de distância encontradas na literatura, a de uso mais geral (por não considerar qualquer forma específica para a distribuição das variáveis) é a distância euclidiana.

Quando as variáveis são normalmente distribuídas, pode-se utilizar a distância de Mahalanobis ao invés da euclidiana. O uso da distância de Mahalanobis na classificação normalmente traz melhores resultados pois esta avalia não somente a média, mas também a variância e a covariância entre as variáveis envolvidas.

Tabela 2 - Variáveis analisadas

Abreviatura	Nome da variável
con	contraste
cor	correlação
chi	chiquadrado
ent	entropia
hom	homogeneidade
uni	uniformidade
mvs	média do vetor soma
vvs	variância do vetor soma
univs	uniformidade do vetor soma
entvs	entropia do vetor soma
mdv	média do vetor diferença
vvd	variância do vetor diferença
univd	uniformidade do vetor diferença
entvd	entropia do vetor diferença
aut01	autocorrelacao espacial lag 0,1
aut10	autocorrelacao espacial lag 1,0
aut11	autocorrelacao espacial lag 1,1
v	variância
cv	coeficiente de variação
ass	assimetria
assm	assimetria da média em relação à mediana
cur	curtose
alfaa	α estimado pela K amplitude <i>multilook</i>
alfai	α estimado pela K intensidade <i>multilook</i>
m	média

Caso se conheça a verdadeira classe a que pertence cada amostra, pode-se construir uma matriz que relaciona as classes às quais foram atribuídas as amostras com a verdadeira classe a que pertence cada amostra. Esta matriz é conhecida como matriz de confusão ou matriz de erro. Os elementos da diagonal desta matriz representam as amostras corretamente classificadas.

Usualmente, uma classificação é avaliada pela proporção de amostras corretamente classificadas, denominada precisão total, que corresponde à razão entre a soma da diagonal da matriz de confusão (amostras corretamente classificadas) e a soma de todos os elementos desta matriz (número de amostras classificadas). Como alternativa, pode-se avaliar uma classificação através do coeficiente kappa (Rosenfield e Fitzpatrick-Lins, 1986; Hudson e Ramm, 1987; Foody, 1992). Este coeficiente tem a vantagem de levar em consideração todos os elementos da matriz de confusão e não somente os elementos da diagonal.

O kappa assume valores menores ou iguais a 1, podendo inclusive assumir valores negativos. Quando todas as amostras são corretamente classificadas, o coeficiente kappa possui valor 1. Valores de kappa pequenos indicam que a classificação não obteve bons resultados (Landis e Koch, 1977).

Devido às imagens GR1, GR2 e SR não serem co-registradas, fez-se uma análise e seleção de medidas para cada conjunto de imagens separadamente. Dessa forma, o procedimento é descrito apenas uma vez, mas é válido para qualquer um dos 3 produtos utilizados.

Cada conjunto é composto por 6 imagens: 2 bandas e 3 polarizações. Para cada imagem, foram determinadas 25 medidas (14 medidas de Haralick, 3 autocorrelações espaciais, 5 medidas baseadas em estatísticas de primeira ordem, 2 estimadores de α , e a média), resultando em 150 variáveis para cada conjunto de imagens analisado. Como as variáveis apresentam diferentes grandezas, procedeu-se à padronização das mesmas, ou seja, para cada valor foi subtraída a média e o resultado dividido pelo desvio padrão. Desta forma, todas as variáveis passaram a possuir média nula e variância unitária.

Primeiramente, o poder discriminante de cada variável foi determinado adotando-se o coeficiente kappa obtido a partir da classificação das amostras de acordo com cada variável. A variável com maior kappa individual foi a primeira a ser selecionada. Em seguida, buscou-se, entre as 149 restantes, a variável que juntamente com a primeira selecionada apresentou maior kappa. Selecionadas as duas variáveis, procurou-se entre as demais, a que, juntamente com as duas primeiras, apresentou maior kappa. Este processo foi repetido até que um coeficiente kappa igual ou superior a 0,90 foi encontrado. É importante salientar que após a introdução de uma nova variável, combinações entre as já selecionadas eram testadas a fim de verificar se alguma destas variáveis poderia ser eliminada sem, no entanto, diminuir o valor do kappa.

Pode-se observar que, por esta metodologia, um grande número de combinações deve ser testado até que se selecione o melhor conjunto de variáveis, sem a garantia de que esta combinação seja a melhor seleção a utilizar.

Como o poder discriminante de uma variável depende do modo como os seus valores se distribuem nas diferentes classes analisadas, é possível supor que variáveis com alta variância entre grupos possuam maiores taxas de acerto e portanto maiores valores de kappa. A variância entre grupos é definida por

$$VAR_{entre} = \frac{\sum_i n_i (\bar{x}_i - \bar{x})^2}{N},$$

onde \bar{x}_i é a média da variável para a classe i , n_i é o número de amostras que compõem a classe i , \bar{x} é a média geral da variável e N é o número total de amostras. Como todas as variáveis foram padronizadas, a média \bar{x} é nula e portanto a variância entre grupos reduz-se a

$$VAR_{entre} = \frac{\sum_i n_i \bar{x}_i^2}{N}.$$

Com base na variância entre grupos, pôde-se promover uma pré-seleção de modo a reduzir o número de variáveis testadas. Numa primeira etapa, ordenaram-se as variáveis de acordo com a variância entre grupos apresentada por cada uma delas. A seleção iniciou-se pela variável com maior variância entre grupos. A cada variável selecionada, foram reclassificadas as amostras e determinado o coeficiente kappa. A seleção foi encerrada quando um kappa igual a 1 foi obtido. Em seguida, procedeu-se à seleção das variáveis do mesmo modo que já havia sido proposto, com a vantagem de não ser necessário testar todas as 150 variáveis.

4. RESULTADOS E DISCUSSÃO

Apesar de algumas variáveis não poderem ser consideradas como sendo normalmente distribuídas, adotou-se a distância de Mahalanobis como regra de decisão no processo de classificação, uma vez que testes preliminares indicaram que o uso da distância euclidiana apresentava resultados muito inferiores aos da distância de Mahalanobis.

O próximo passo foi realizar a seleção das variáveis que melhor discriminaram as classes de uso estudadas. Os dois métodos foram então testados. O primeiro método selecionou as variáveis de acordo com o coeficiente kappa obtido a partir da classificação das amostras. O segundo método fez uma pré-seleção das variáveis, selecionando aquelas que apresentaram alta variância entre grupos. Esta pré-seleção reduziu para cerca de um terço o número de variáveis analisadas (64 para GR1, 55 para GR2 e 54 para SR). A classificação, considerando todas estas variáveis pré-selecionadas, apresentou kappa igual a 1. A seleção propriamente dita foi feita do mesmo modo que para o primeiro método.

A Figura 1 apresenta uma comparação entre os métodos adotados para seleção das variáveis. O desempenho de cada conjunto de variáveis selecionadas é avaliado pelo kappa correspondente à classificação das amostras segundo estas variáveis. Ambos os métodos são comparados com o desempenho de classificação quando somente as médias tonais são consideradas. Pode-se notar que, em alguns casos, quando um pequeno número de variáveis é selecionado,

as médias apresentam melhor desempenho. No entanto, como cada conjunto de imagens é composto por apenas 6 imagens, tem-se, no máximo, 6 médias selecionadas (1 média para cada amostra de cada imagem) resultando num kappa máximo de pouco mais que 0,5. Este kappa indica uma classificação cuja precisão pode ser considerada apenas moderada (Landis e Koch, 1977). Quando medidas de textura são avaliadas, pode-se chegar a valores de kappa superiores a 0,90 para os casos em que se consideram mais do que 15 medidas simultaneamente.

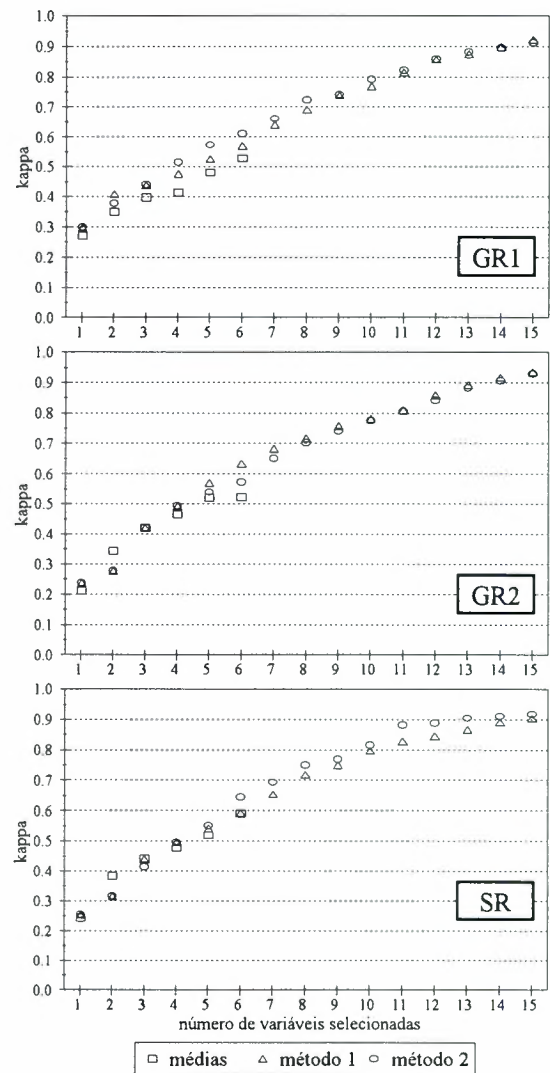


Fig. 1 - Desempenho da classificação.

Os dois métodos de seleção apresentaram desempenho muito semelhante, com leve vantagem para o segundo método nas imagens *slant range* (SR). É importante salientar que as variáveis selecionadas por cada um dos métodos não são necessariamente as mesmas. De acordo com estes resultados, pode-se eleger o segundo método como o melhor uma vez que este compara um número menor de variáveis, sendo cerca de 3 vezes mais rápido que o primeiro método. A

partir daqui, os comentários serão feitos considerando apenas os resultados obtidos pelo método 2.

A Figura 2 mostra a relação existente entre a variância entre grupos e o kappa de cada uma das variáveis. Também é indicado, nestas figuras, o valor mínimo de variância entre grupos apresentado pelas variáveis pré-selecionadas. A classificação feita utilizando-se todas estas variáveis pré-selecionadas apresentou kappa igual a 1. Note que grande parte das variáveis é descartada nesta fase. Os maiores valores de kappa e variância entre grupos individuais são provenientes de imagens da banda L. Isto demonstra que pela textura (e também a média) desta banda consegue-se separar melhor as classes de uso estudadas.

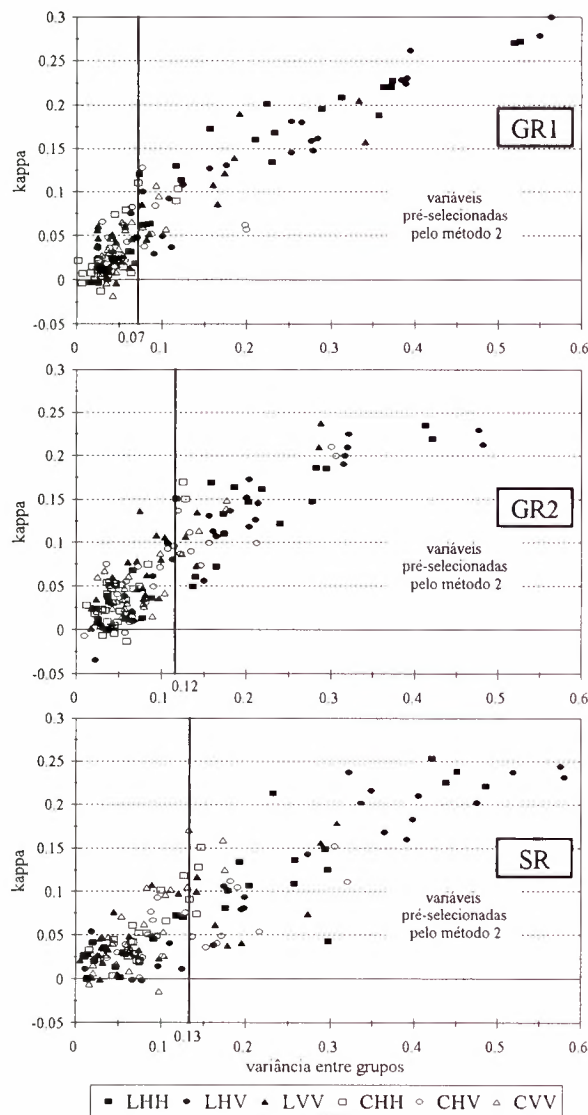


Fig. 2 - Relação entre variância entre grupos e o kappa individual.

Por outro lado, quando apenas as variáveis selecionadas são mostradas (Figura 3), pode-se observar que o melhor conjunto de variáveis selecionado não corresponde às variáveis com maior kappa

individual, daí o motivo pelo qual, na fase de pré-seleção, não se deve fazer o descarte de um grande número de variáveis.

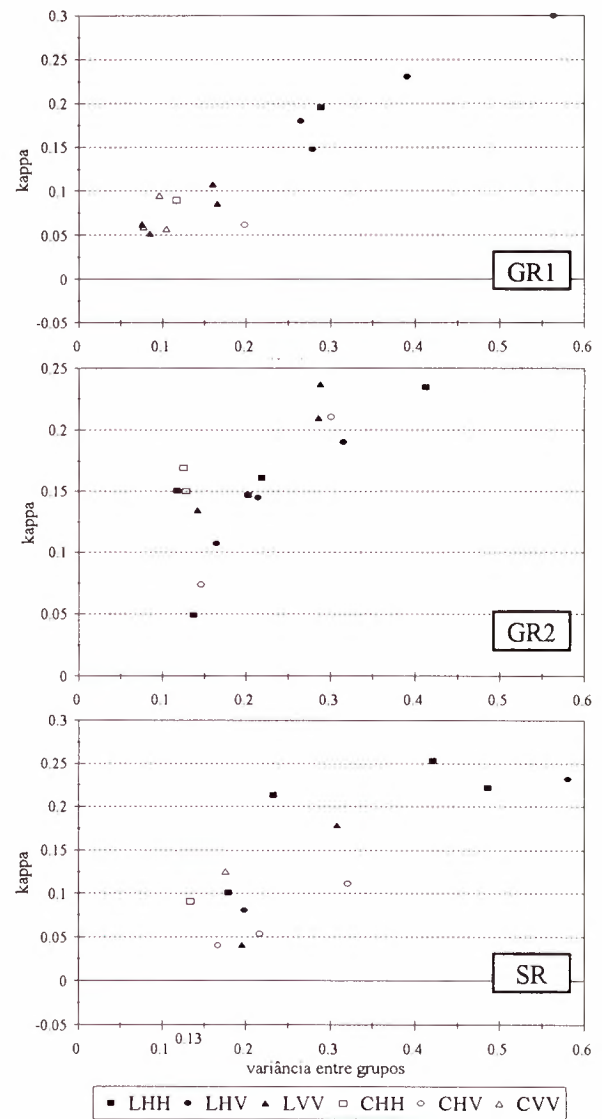


Fig. 3 - Kappa e variância entre grupos das variáveis selecionadas.

Todas as imagens contribuíram com pelo menos 1 variável (com exceção da imagem CVV do produto GR2), sendo que as imagens da banda L, de modo geral, foram as que tiveram o maior número de variáveis selecionadas. Para o produto GR1, a maior contribuição textural foi dada pela polarização VV, enquanto que esta mesma polarização para os produtos GR2 e SR foi a que menos contribuiu.

A Tabela 3 apresenta a relação das variáveis selecionadas por produto. Pode-se observar que, para as classes de uso analisadas, a média foi uma medida muito importante na discriminação, sendo que quase todas as imagens estão representadas pela sua média. Cada produto tem um conjunto distinto de variáveis

selecionadas, mas, no entanto, há algumas variáveis altamente correlacionadas: *m* e *mvs*, *entvd* e *mvd*, *univd* e *chi*, *con* e *m*, *vvs* e *v*, entre outras.

Tabela 3 - variáveis selecionadas

GR1	GR2	SR
<i>chiLHH</i>	<i>corLHH</i>	<i>conLHH</i>
<i>entvsLHV</i>	<i>chiLHH</i>	<i>homLHH</i>
<i>entvdLHV</i>	<i>mLHH</i>	<i>mvsLHH</i>
<i>mLHV</i>	<i>assmLHH</i>	<i>curlLHH</i>
<i>vLHV</i>	<i>curlLHH</i>	<i>mvsLHV</i>
<i>conLVV</i>	<i>conLHV</i>	<i>assLHV</i>
<i>chiLVV</i>	<i>vvsLHV</i>	<i>mvsLVV</i>
<i>homLVV</i>	<i>mvdLHV</i>	<i>vvdLVV</i>
<i>cvLVV</i>	<i>mvsLVV</i>	<i>vvdCCH</i>
<i>mCCHH</i>	<i>univdLVV</i>	<i>univdCHV</i>
<i>mvsCHV</i>	<i>mLVV</i>	<i>mCHV</i>
<i>mvsCVV</i>	<i>mvsCCH</i>	<i>cvCHV</i>
<i>univdCVV</i>	<i>mCHH</i>	<i>mvsCVV</i>
<i>entvdCVV</i>	<i>mvsCHV</i>	
<i>cvCVV</i>	<i>assmCHV</i>	

A fim de verificar se os diferentes conjuntos de variáveis selecionadas possuem uma relação implícita, procedeu-se à classificação de cada produto utilizando-se todos os 3 conjuntos de variáveis selecionadas. O resultado desta classificação, apresentado na Tabela 4, mostra que, de modo geral, um conjunto de variáveis selecionado a partir de um dos produtos pode ser utilizado para classificar outro produto com características distintas e, ainda assim, conseguir um bom resultado. Segundo Landis e Kock (1977), valores de kappa entre 0,61 e 0,80 correspondem a uma boa precisão na classificação.

Tabela 4 - Classificação dos produtos utilizando os três conjuntos de variáveis selecionadas

	kappa		
	GR1	GR2	SR
variáveis de GR1	0,91	0,81	0,80
variáveis de GR2	0,82	0,91	0,85
variáveis de SR	0,75	0,82	0,90

Até aqui, considerou-se uma análise conjunta de imagens de 2 bandas e 3 polarizações. No entanto, na prática raramente se dispõe de dados SAR multipolarimétricos e em mais que uma banda. Dessa forma, procedeu-se a uma análise de cada imagem separadamente. É importante observar que, agora, há no máximo 25 medidas de textura para cada imagem. A Figura 4 mostra o desempenho apresentado por cada imagem quando um determinado número de variáveis é selecionado. Os resultados mostram que mesmo utilizando-se uma imagem de uma banda e polarização, as medidas de textura conseguem discriminar as classes de uso estudas, conseguindo valores de kappa

superiores a 0,85, independentemente da freqüência e polarização utilizada.

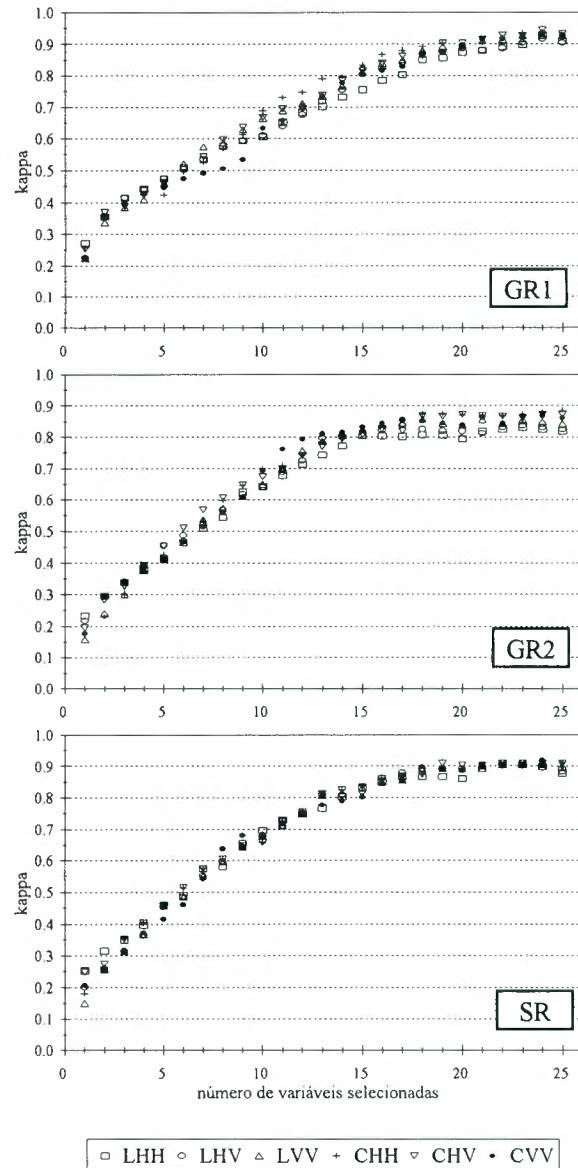


Fig. 4 - Desempenho da classificação, considerando as imagens separadamente.

5. CONCLUSÃO

Os resultados deste trabalho comprovaram que as medidas de textura melhoram significativamente a precisão da classificação de imagens SAR. No entanto, não há um conjunto destas medidas que se possa generalizar como sendo ideal para estudos de discriminação de alvos agrícolas. Foi mostrado que, pelo menos para o caso estudado, as características próprias de cada produto testado (projeção e ângulo de incidência) pouco influenciaram na seleção das medidas de texturas, uma vez que um conjunto selecionado para um determinado produto pode ser

aplicado, com resultados muito bons, nos demais produtos.

A utilização de medidas de textura em imagens adquiridas em uma freqüência e polarização trouxe resultados surpreendentes. Neste tipo de imagem, que caracteristicamente apresenta baixos índices de acerto quando são utilizados classificadores baseados apenas na informação tonal, pode-se observar, em alguns casos, valores de kappa superiores a 0,90.

Ficou evidente que também a informação tonal foi muito importante para a discriminação das classes de uso, visto que, praticamente em todos os casos, houve a seleção das médias (ou outras variáveis altamente correlacionadas a estas) de todas as imagens testadas.

AGRADECIMENTOS

Os autores agradecem o apoio do CNPq através do projeto PROTEM-CC GEOTEC (Processo 682.061-94-0)

REFERÊNCIAS

Chen, C.H. Texture unit, texture spectrum, and texture analysis **IEEE Transactions on Geoscience and Remote Sensing**, 28(4):509-512, July 1990.

Foody, G.M. On the compensation for chance agreement in image classification accuracy assessment. **Photogram. Eng. & Rem. Sen.**, 58(10):1459-1460, Oct. 1992.

Haralick, R.M.; Shanmugan, K.; Dinstein, I. Texture features for image classification. **IEEE Trans. Systems, Man and Cybernetics**, SMC-3(6):610-621, Nov. 1973.

Hsu, S.Y. Texture-tone analysis for automated land-use mapping. **Photogram. Eng. & Rem. Sen.**, 44(11):1393-1404, Nov. 1978.

Hudson, W.D.; Ramm, C.W. Correct formulation of the kappa coefficient of agreement. **Photogram. Eng. & Rem. Sen.**, 53(4):421-422, Apr. 1987.

Irons, J.R.; Petersen, G.W. Texture transforms of remote sensing data. **Rem. Sen. Env.**, 11(5):359-370, Nov. 1981.

Landis, J.R.; Koch, G.G. The measurements of observer agreement for categorical data. **Biometrics**, 33:159-174, Mar. 1977.

Marceau, D.; Howarth, P.J.; Dubois, J.M. Automated texture extraction from high spatial resolution satellite imagery for land-cover classification: concepts and application. In: IGARSS'89 - Canadian Symposium on Remote Sensing, 12., Vancouver, July 10-14, 1989. **Proceedings**. IEEE, 1989, v. 5, p. 2765-2768.

Rosenfield, G.H.; Fitzpatrick-Lins, K. A coefficient of agreement as a measure of thematic classification accuracy. **Photogram. Eng. & Rem. Sen.**, 52(2):223-227, Feb. 1986.

Soares, J.V. et al. **Microwave remote sensing from a spaceborne platform as a tool to monitor the hydrologic cycle of a floodplain area (várzea) at northeast Brazil**. São José dos Campos, INPE, 1988. (INPE-4741-RPE/579)

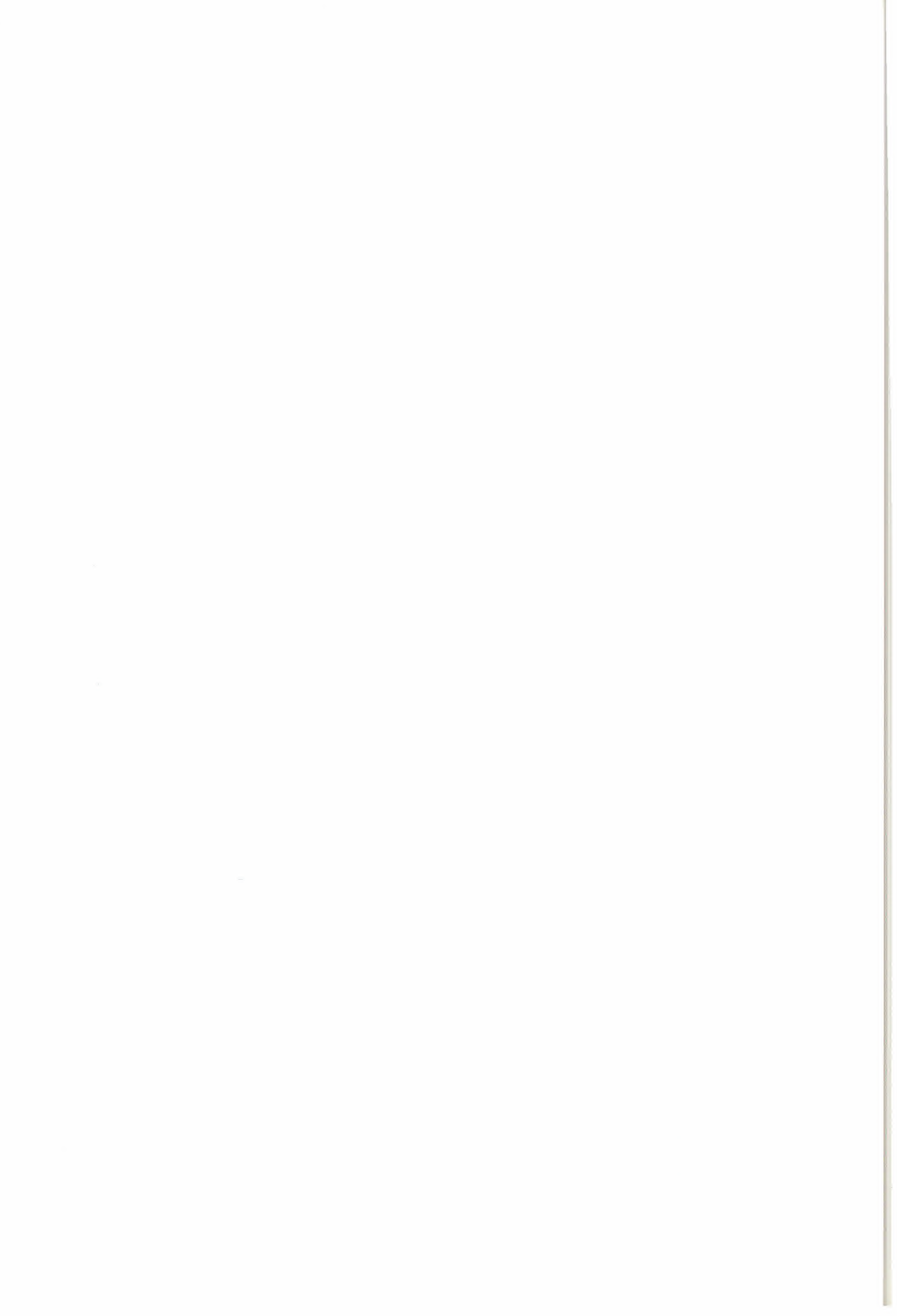
Ulaby, F.T.; Kouyate, F.; Brisco, B.; Lee Williams, T.H. Textural Information in SAR Images. **IEEE Trans. on Geosc. and Remote Sensing**, 24(2):235-245, Mar. 1986.

Unser, M. Sum and difference histograms for texture classification. **IEEE Trans. Pattern Anal. Mach. Intell.**, PAMI-8(1):118-125, Jan. 1986.

Welch, R.M.; Kuo, K.; Sengupta, S.K. Cloud and surface textural features in polar regions. **IEEE Trans. on Geosc. and Remote Sensing**, 28(4):520-528, July. 1990.

Weszka, J.S.; Dyer, C.R.; Rosenfeld, A. A comparative study of texture measures for terrain classification. **IEEE Trans. Syst. Man. Cybern.**, SMC-6(4):269-285, Apr. 1976.

Yanasse, C.C.F.; Frery, A.C.; Sant'Anna, S.J.S.; Hernandes, P.F.; Dutra, L.V. Statistical analysis of SAREX data over Tapajós - Brazil. In: SAREX-92: South American Radar Experiment, ESA, Paris, Dec. 6-8, 1993. **Workshop Proceedings**. Paris, ESA, 1993, p. 25-40.



UM SISTEMA DE ANÁLISE E CLASSIFICAÇÃO ESTATÍSTICAS PARA IMAGENS SAR

Pedro Ronalt Vieira†
 Corina da C. F. Yanasse†
 Alejandro C. Frery‡
 Sidnei J. S. Sant'Anna‡

†INPE – Instituto Nacional de Pesquisas Espaciais
 DPI – Divisão de Processamento de Imagens
 Avenida dos Astronautas, 1758
 12227-010 São José dos Campos, SP, Brasil

‡UFPE – Universidade Federal de Pernambuco
 DI – Departamento de Informática
 CP 7851
 50732-970 Recife, PE, Brasil

ABSTRACT

The objective of this paper is to present an integrated system for Synthetic Aperture Radar (SAR) data processing, classification and analysis, based on the statistical properties of SAR data. The classification is performed using the Maximum Likelihood (MaxVer) classifier and the Iterated Conditional Modes (ICM) contextual classifier. The system showed to be very efficient for the classification of images from two different sensors. The classification results indicate that a more precise classification is achieved using the distributions which are suitable for SAR data, when compared with classical methods that use Gaussian distributions. It is also shown that the ICM classifications present results that are usually twice higher than those obtained using the MaxVer method.

Keywords: classification; SAR; statistical modelling.

1. INTRODUÇÃO

Com o advento de novos sensores, pode-se dispor cada vez mais de um grande volume de imagens de sensoriamento remoto. Torna-se, portanto, necessário processar-se imagens de forma rápida, e obter-se de maneira precisa a informação procurada. Uma das técnicas mais úteis no processamento de imagens é a da classificação automática. Ela permite automatizar tarefas associadas à interpretação visual de imagens, diminuindo assim o tempo entre a aquisição dos dados e a sua análise, criando um referencial isento das subjetividades dos intérpretes humanos.

Embora existam várias técnicas de classificação automática de imagens, poucas delas são adequadas para os problemas particulares que apresentam as imagens SAR. A grande maioria dos procedimentos para a análise e classificação de imagens disponíveis em sistemas comerciais se baseia na hipótese dos dados serem normalmente distribuídos, hipótese esta raramente observada nas imagens

SAR. As propriedades estatísticas das imagens SAR dependem de parâmetros dos sistema imageador (comprimento de onda, polarização, ângulo de incidência, número de visadas, tipo de detecção, etc.), como também de parâmetros do alvo a ser imageado.

Verifica-se, assim, a necessidade de se desenvolver técnicas e procedimentos estatísticos específicos para a análise e classificação de imagens SAR, e de que os mesmos sejam disponibilizados em um sistema amigável para os usuários de imagens SAR. Tal sistema deve ser capaz de permitir ao usuário:

- escolher e gerenciar amostras;
- analisá-las estatisticamente;
- poder estabelecer, para cada alvo, aquelas propriedades estatísticas que mais se adequam a ele;
- dispor de algoritmos de classificação automática de fácil utilização baseados nessas propriedades estatísticas;
- poder avaliar a qualidade destas classificações.

Recentemente foi desenvolvido no INPE um sistema para a classificação e análise de imagens SAR, baseado em propriedades estatísticas específicas para este tipo de imagens [Vieira 1996]. O objetivo deste trabalho é apresentar os conceitos básicos em que se baseia este sistema, e mostrar alguns resultados obtidos para imagens SAR de dois diferentes sensores. Este sistema está implementado em linguagem IDL e, a princípio, permite que se trabalhe com imagens em amplitude de uma única banda. Os classificadores foram implementados na estrutura de um sistema baseado em interfaces gráficas que, além de possuir as operações auxiliares para se executar as tarefas de classificação, permite a incorporação de novas ferramentas.

2. MODELOS ESTATÍSTICOS PARA DADOS SAR

O modelo multiplicativo é comumente adotado para a explicação do comportamento estatístico de dados obtidos com radiação coerente, como é o caso das imagens SAR. Este modelo supõe que o valor observado em cada *pixel* é a ocorrência de uma variável aleatória $Z = X \cdot Y$, onde X representa a variável aleatória referente ao retroespalhamento do pulso incidente na superfície terreste (*backscatter*), e Y representa a variável aleatória referente ao ruído associado à radiação coerente (*speckle*).

Diferentes distribuições para X e Y acarretam diferentes distribuições para a variável aleatória Z .

Em recente publicação [Frery et al. 1996], foi proposto o uso da distribuição Raiz Quadrada da Gaussiana Inversa Generalizada para a modelagem do *backscatter* (X) para dados em amplitude. Diz-se que a variável aleatória X possui uma distribuição Raiz Quadrada da Gaussiana Inversa Generalizada, com parâmetros α , γ e λ , denotada por $X \sim \mathcal{N}^{-1/2}(\alpha, \gamma, \lambda)$, se a sua densidade for dada por:

$$f_X(x) = \frac{(\lambda/\gamma)^{\alpha/2}}{K_\alpha(2\sqrt{\lambda\gamma})} x^{2\alpha-1} \exp\left(-\frac{\gamma}{x^2} - \lambda x^2\right), \quad x > 0,$$

onde K_α denota a função de Bessel modificada de terceiro tipo e ordem α . O espaço de parâmetros é dado por:

$$\begin{cases} \gamma > 0, \quad \lambda \geq 0 & \text{if } \alpha < 0 \\ \gamma > 0, \quad \lambda > 0 & \text{if } \alpha = 0 \\ \gamma \geq 0, \quad \lambda > 0 & \text{if } \alpha > 0 \end{cases}. \quad (1)$$

As propriedades estatísticas do *speckle* são bem conhecidas e reportadas na literatura [Frery et al. 1996; Goodman 1982]. Para dados em amplitude supõe-se que o ruído *speckle* (Y) possua uma distribuição Raiz Quadrada da Gama com parâmetro n , denotada por $Y \sim \Gamma^{1/2}(n, n)$, onde n é o número equivalente de visadas. Neste caso, a densidade de Y é dada por:

$$f_Y(y) = \frac{2n^n}{\Gamma(n)} y^{2n-1} \exp(-ny^2), \quad y, n > 0.$$

Pode-se provar [Frery et al. 1996] que se $X \sim \mathcal{N}^{-1/2}(\alpha, \gamma, \lambda)$ e $Y \sim \Gamma^{1/2}(n, n)$, então $Z = X \cdot Y$ possui uma distribuição denominada G-Amplitude com parâmetros $\alpha, \gamma, \lambda, n$, denotada por $\mathcal{G}_A(\alpha, \gamma, \lambda, n)$, cuja densidade é caracterizada por:

$$f_Z(x) = \frac{2n^n (\lambda/\gamma)^{\alpha/2}}{\Gamma(n) K_\alpha(2\sqrt{\lambda\gamma})} x^{2n-1} \left(\frac{\gamma + nx^2}{\lambda}\right)^{\frac{\alpha-n}{2}} K_{\alpha-n}\left(2\sqrt{\lambda(\gamma + nx^2)}\right), \quad x \in \mathbb{R}, \quad (2)$$

e o espaço de parâmetros é dado em (1).

Seus momentos de ordem r são dados por:

$$E(Z^r) = \left(\frac{\gamma}{n^2 \lambda}\right)^{r/4} \frac{K_{\alpha+r/2}(2\sqrt{\gamma\lambda}) \Gamma(n+r/2)}{K_\alpha(2\sqrt{\gamma\lambda}) \Gamma(n)}.$$

A distribuição \mathcal{G}_A possui como casos especiais as seguintes distribuições:

1. a distribuição $\mathcal{K}_A(\alpha, \lambda, n)$, quando $\gamma \rightarrow 0$ com $\alpha, \lambda > 0$, cuja densidade é dada por:

$$f_Z(x) = \frac{4\lambda nx}{\Gamma(\alpha)\Gamma(n)} (\lambda nx^2)^{(\alpha+n)/2-1} \cdot K_{\alpha-n}\left(2x\sqrt{\lambda n}\right), \quad \alpha, \lambda, n, x > 0; \quad (3)$$

2. a distribuição $\mathcal{G}_A^0(\alpha, \gamma, n)$, quando $\lambda \rightarrow 0$ com $-\alpha, \gamma > 0$, cuja densidade é dada por:

$$f_{Z_A}(x) = \frac{2n^n \Gamma(n-\alpha) \gamma^{-\alpha} x^{2n-1}}{\Gamma(n)\Gamma(-\alpha)(\gamma + nx^2)^{n-\alpha}}, \quad -\alpha, \gamma, n, x > 0. \quad (4)$$

3. a distribuição $\Gamma^{1/2}$, que tanto pode vir de (3), quando $\alpha, \lambda \rightarrow \infty$, com $\alpha/\lambda \rightarrow \beta_1$, quanto de (4), quando $-\alpha, \gamma \rightarrow \infty$, com $-\alpha/\gamma \rightarrow \beta_2$.

Tem-se observado [Frery et al. 1996], que a distribuição \mathcal{G}_A^0 modela bem dados provenientes de áreas extremamente heterogêneas (como é o caso de áreas urbanas), enquanto que as distribuições \mathcal{K}_A e $\Gamma^{1/2}$ são utilizadas para a modelagem de áreas heterogêneas (floresta, por exemplo) e homogêneas (solo exposto, pastagem, culturas agrícolas, etc), respectivamente. O grau de homogeneidade está associado, entre outros fatores, aos parâmetros do sensor.

As relações acima mencionadas podem ser resumidas na Figura 1.

Além destas distribuições existem outras que, embora não decorrentes do modelo multiplicativo, ajustam-se bem aos dados SAR [Vieira 1996; Yanasse et al. 1993]. Como exemplos pode-se citar as distribuições Log-Normal, Beta e Weibull.

O sistema acima mencionado permite que se defina, para cada classe da imagem, a distribuição que mais se adequa aos dados dela provenientes. Para auxiliar o usuário nesta escolha, o sistema dispõe do teste de aderência χ^2 . A estimativa dos parâmetros das distribuições é efetuada utilizando-se, sempre que possível, os estimadores de Máxima Verossimilhança ou os estimadores obtidos pelo Método dos Momentos, quando os primeiros forem de difícil implementação.

A Figura 2 mostra a saída que o sistema fornece como resultado do teste χ^2 para o ajuste de uma distribuição a um conjunto de dados.

3. CLASSIFICAÇÃO POR MÁXIMA VEROSSIMILHANÇA

A classificação por Máxima Verossimilhança (MaxVer) é uma das técnicas de classificação supervisionada comumente utilizada em dados de Sensoriamento Remoto [Richards 1986]. Os principais passos para efetuar esta classificação são:

- decidir, entre os possíveis conjuntos de classes da cobertura terreste, aquele que será utilizado para particionar a imagem a ser classificada;

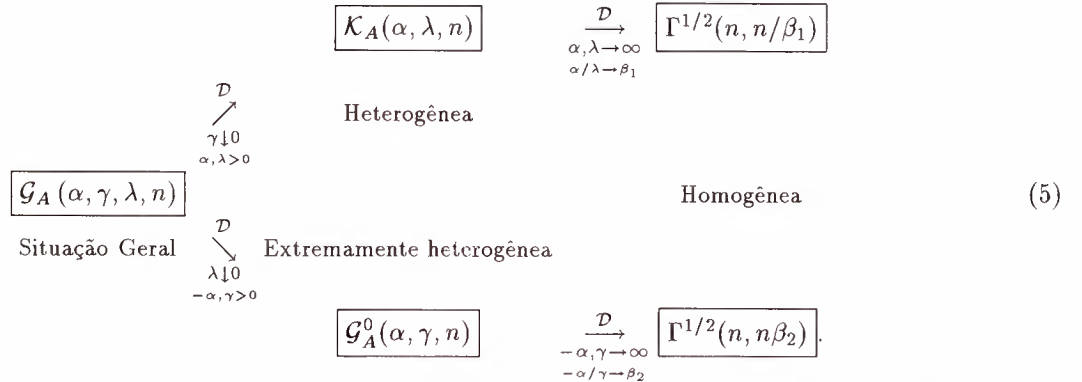


Figura 1: Sumário das relações entre as distribuições decorrentes do modelo multiplicativo para dados em formato de amplitude.

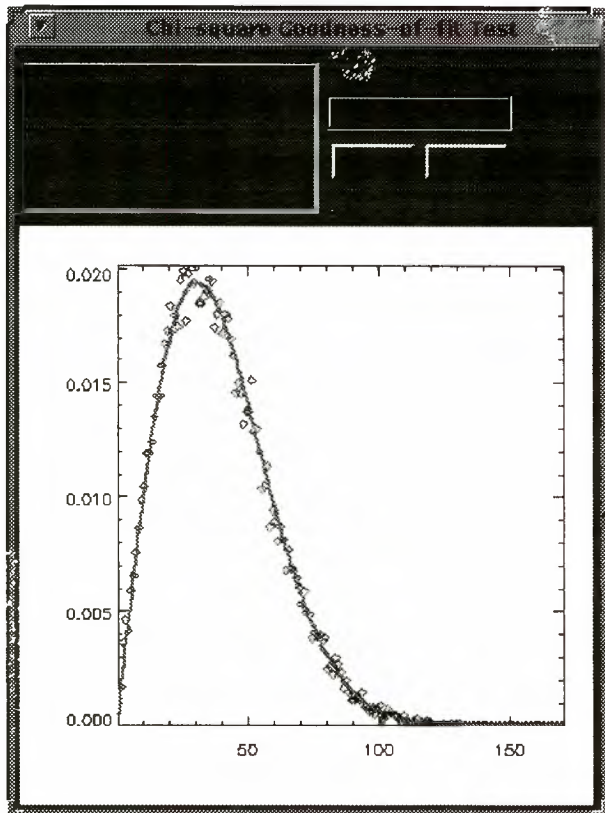


Figura 2: Saída gráfica do resultado do teste χ^2 .

- associar uma distribuição a cada classe;
- selecionar e retirar amostras de regiões representativas de cada classe na imagem;
- estimar os parâmetros das distribuições associadas a cada classe;
- opcionalmente, pode-se testar o ajuste das distribuições associadas a cada classe;
- classificar a imagem, atribuindo cada pixel da imagem à classe com maior verossimilhança.

A Figura 3 ilustra uma interface do sistema, ativada quando a classificação por Máxima Verossimilhança é efetuada.

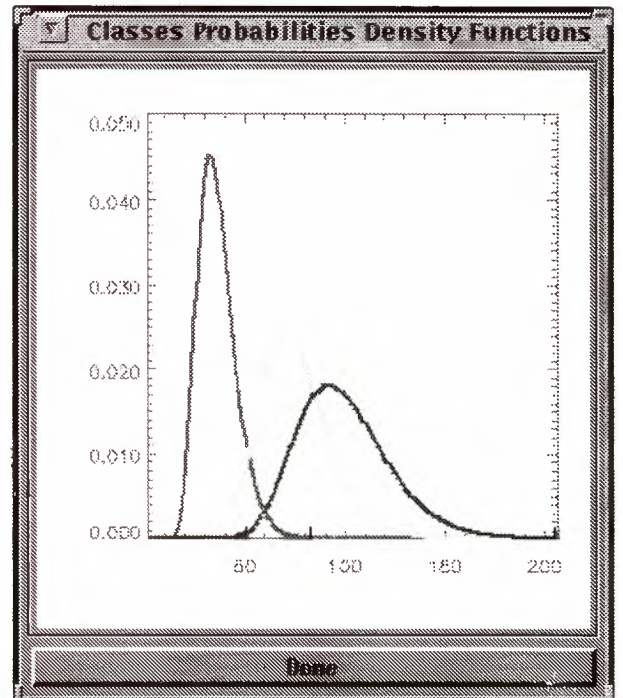


Figura 3: Melhores densidades para a modelagem das classes.

tuada. Esta interface permite visualizar as funções densidade de probabilidade das distribuições associadas às classes escolhidas. Na seção 6. são mostrados resultados de classificações MaxVer para duas imagens SAR.

4. CLASSIFICAÇÃO ICM

Tal como mencionado na seção anterior, o critério de Máxima Verossimilhança é o de maximizar uma função que somente depende da radiometria observada e do modelo (densidade) escolhido para cada classe. Esse critério não leva em consideração a informação contextual, já que supõe que as radiometrias dadas as classes são eventos independentes.

Existem na literatura várias propostas para incorporar a informação contextual [Besag 1989], mas a grande mai-

ria delas leva a algoritmos computacionalmente muito dispendiosos e difíceis de serem usados. Em [Frery 1993] é mostrada uma versão de um algoritmo de classificação contextual que apresenta boas características de desempenho e de facilidade de uso. Essa técnica, o algoritmo ICM (*Iterated Conditional Modes*), foi melhorada em [Vieira 1996] e aplicada a várias imagens de radar.

O algoritmo ICM é um método iterativo de refinamento de classificações que consiste em substituir a classe associada a cada coordenada por aquela classe que maximiza um certo critério. Esse critério é a distribuição a posteriori da classe, dadas a radiometria (componente MaxVer) e as classes vizinhas (componente de contexto). A influência das classes vizinhas é quantificada por um parâmetro real, que é estimado iterativamente supondo um modelo para a distribuição espacial das classes. No sistema aqui descrito, a influência de oito vizinhos é considerada para classificar cada coordenada.

Para detalhes sobre esta técnica, recomenda-se a leitura das três referências acima mencionadas. Na seção 6. são mostrados resultados de classificações ICM para duas imagens SAR.

5. FUNÇÕES ADICIONAIS DO SISTEMA

Além das características mencionadas nas seções anteriores, o sistema dispõe das seguintes funções:

Filtros redutores de speckle: Os seguintes filtros estão disponíveis: Lee, da mediana e qualquer um definível através de convoluções.

Estimação do número equivalente de visadas:

O número equivalente de visadas é um dos parâmetros das distribuições provenientes do modelo multiplicativo (ver seção 2.). No sistema mencionado, este parâmetro é estimado uma única vez para toda a imagem, com o uso dos dois primeiros momentos amostrais de amostras selecionadas e coletadas em regiões homogêneas da imagem [Yanasse et al. 1993], isto é, em regiões cujos dados em amplitude proviriam de uma distribuição Raiz Quadrada da Gama. O módulo implementado permite a captura de várias amostras, as quais são testadas pelo teste de aderência χ^2 quanto ao ajuste desta distribuição. As amostras com baixo p -valor podem ser rejeitadas e as amostras remanescentes podem ser novamente testadas para um certo número equivalente de visadas médio ou inserido via teclado.

Conversões de imagens: Permite a conversão entre imagens em amplitude, intensidade e complexa.

Decorrelação de amostras: Permite que as amostras sejam decorrelacionadas, para um dado fator de reamostragem nas direções horizontal e vertical. Esta função tem como objetivo tornar a amostra constituída de pixels não correlacionados para a aplicação do teste de aderência χ^2 .

Operações unárias de imagens: Permite que cada pixel da imagem seja adicionado, subtraído, multiplicado e dividido por um escalar. Permite também a aplicação de algumas funções matemáticas à imagem, e gerar a imagem de histograma equalizado.

Operações entre imagens: Permite realizar a adição, subtração, multiplicação e divisão entre imagens.

Teste de classificação: O resultado da classificação pode ser avaliado através da matriz de confusão, calculada com o uso das amostras selecionadas para teste ou de uma imagem verdade registrada em relação à imagem classificada, e também pelo coeficiente de concordância Kappa [Bishop et al. 1975; Congalton and Mead 1983].

6. APLICAÇÕES DO SISTEMA A IMAGENS REAIS

Nesta seção são apresentados os resultados da classificação de imagens SAR de dois sensores distintos, usando os classificadores MaxVer e ICM.

É mostrado que para as imagens utilizadas há uma melhora significativa na classificação quando se utiliza o classificador MaxVer com as distribuições adequadas aos dados, quando comparada ao classificador MaxVer clássico que utiliza a distribuição Gaussiana. Mostra-se também que o classificador ICM sempre produz resultados significativamente melhores que o MaxVer.

Para a realização das classificações foram utilizadas as seguintes imagens:

1. Imagem SAR-580: Imagem obtida por sensor aero-transportado, em amplitude, banda L, com número nominal de visadas igual a um, de tamanho 512×512 pixels, da região de Freiburg, Alemanha;
2. Imagem JERS-1: Imagem do satélite JERS-1, órbita/ponto D405/306, em amplitude, com número nominal de visadas igual a três, espaçamento entre pixels de 12.5×12.5 m, banda L, polarização HH, de 26/06/1993, de tamanho 1600×2400 pixels, da região da Floresta Nacional de Tapajós, Pará, Brasil.

6.1. Resultados com a imagem SAR-580

A imagem SAR-580 é apresentada na Figura 4a. Apesar desta imagem possuir o número de visadas igual a um, valor este que foi atribuído ao parâmetro n no decorrer da análise, o número equivalente de visadas foi estimado para comprovar a eficiência deste módulo no sistema. Foram coletadas quatro amostras em regiões homogêneas, com tamanhos variando de 1163 a 3119 pixels. Os p -valores obtidos no teste χ^2 variaram de 71% a 99%, e o valor médio estimado para o número equivalente de visadas foi de 1.00968, coerente com o valor original.

Foram selecionadas três classes distintas na imagem, denominadas aqui Cultura 1, Cultura 2, e Floresta, das quais foram retiradas amostras, com número total de pixels igual a 21456, 7312 e 21652, respectivamente. Estas amostras foram decorrelacionadas com fator de amostragem 2 tanto na horizontal quanto na vertical, para o uso do teste χ^2 . Este fator foi escolhido baseado na análise da funções de autocorrelação espacial estimadas nestas duas direções.

O teste χ^2 foi aplicado para todas as distribuições mencionadas na seção 2., para cada amostra das classes. A distribuição que mais se ajustou à classe Cultura 1 foi a

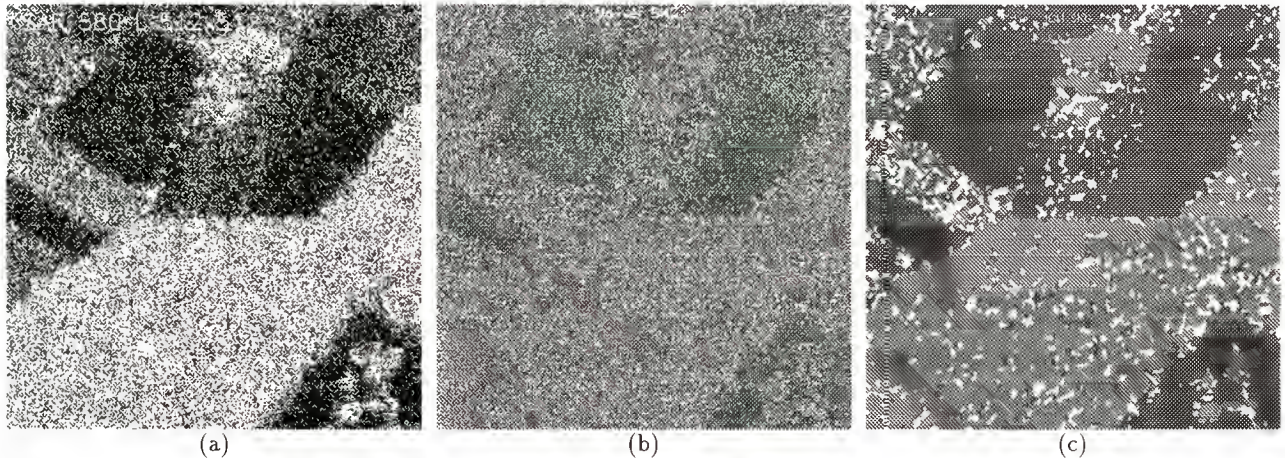


Figura 4: Imagem SAR-580 original (a), classificada pelo método MaxVer (b) e classificada pelo método ICM (c).

Raiz Quadrada da Gama (ou, neste caso onde $n = 1$, a distribuição Rayleigh), à classe Cultura 2 foi a \mathcal{K}_A , e à classe de Floresta foi a \mathcal{G}_A^0 . Os p -valores obtidos foram 0.15, 0.80 e 0.53, respectivamente.

Foram obtidas as classificações MaxVer e ICM, tanto sob a hipótese da normalidade para as classes, quanto sob a hipótese da distribuição mais ajustada para cada classe. As classificações ICM foram iniciadas com as classificações MaxVer, tendo sido estabelecido como critério de parada o percentual de trocas de *pixels* classificados inferior a 0.1% em relação à classificação obtida na iteração anterior.

A Tabela 1 apresenta, para cada classificação, os valores estimados do coeficiente de concordância Kappa ($\hat{\kappa}$), e das respectivas variâncias ($\hat{\sigma}_{\hat{\kappa}}^2$), obtidos através de amostras de teste.

Tabela 1: Valores estimados do coeficiente de concordância Kappa ($\hat{\kappa}$), e de suas variâncias ($\hat{\sigma}_{\hat{\kappa}}^2$)

Classificação	$\hat{\kappa}$	$\hat{\sigma}_{\hat{\kappa}}^2$
MaxVer Gaussianas	0.3859	7.296×10^{-5}
MaxVer Ajustadas	0.4060	6.206×10^{-5}
ICM Gaussianas	0.7222	3.321×10^{-5}
ICM Ajustadas	0.7688	2.895×10^{-5}

Os testes para a igualdade dos coeficientes de concordância Kappa foram efetuados para todos os pares de classificações. Estes testes foram todos estatisticamente significativos para níveis de significância acima de 10%.

Portanto, pode-se afirmar que para a imagem SAR-580:

- a classificação MaxVer com o uso das distribuições mais ajustadas às classes apresenta um resultado de melhor qualidade, quando comparada à MaxVer com o uso de distribuições Gaussianas. Pelos resultados apresentados na Tabela 1 é possível verificar que houve uma melhora de 5.2% para o $\hat{\kappa}$ da classificação MaxVer ao se utilizar as distribuições mais ajustadas;
- a classificação ICM com o uso das distribuições mais ajustadas às classes apresenta um resultado de melhor qualidade, quando comparada à ICM com o uso

de distribuições Gaussianas. Através da Tabela 1 é possível verificar que houve uma melhora de 6.5% para o $\hat{\kappa}$ da classificação ICM ao se utilizar as distribuições mais ajustadas;

- a classificação ICM é superior à classificação MaxVer. Pelos resultados apresentados na Tabela 1 pode-se verificar que houve uma melhora média de 88.3% para o $\hat{\kappa}$ ao se utilizar a classificação ICM em substituição à MaxVer.

As Figuras 4b e 4c apresentam os resultados da classificações MaxVer e ICM, respectivamente, da imagem SAR-580 com o uso das distribuições mais ajustadas para as classes. As classes Cultura 1, Cultura 2 e Floresta estão representadas pelas cores cinza escuro, branco e cinza claro, respectivamente. Estas figuras evidenciam a superioridade da classificação ICM quando comparada à classificação MaxVer.

6.2. Resultados com a imagem JERS-1

A área de estudo da imagem JERS-1 é apresentada na Figura 5a. O número equivalente de visadas da imagem foi estimado em 2.83522. Este valor, como esperado, é menor que o número nominal de visadas (três) em virtude da correlação existente entre os *pixels* da imagem.

As classes de uso da terra de interesse são solo exposto e pastagem, regeneração (floresta secundária) e floresta primária. Foram selecionadas amostras, para inferência e teste, destas três classes. O número total de *pixels* destas amostras foram de 2636 (solo exposto e pastagem), 13940 (regeneração), e 20740 (floresta primária). Estas amostras foram decorrelacionadas com fator 2 nas direções horizontal e vertical. Este fator foi escolhido baseado na análise da funções de autocorrelação estimadas nestas duas direções. Após esta decorrelação aplicou-se o teste de aderência χ^2 às distribuições mencionadas na seção 2.. A distribuição que mais se ajustou aos dados foi a \mathcal{G}_A^0 , para todas as três classes de interesse. Os p -valores do teste foram 0.32 (solo exposto e pastagem), 0.42 (regeneração) e 0.27 (floresta primária).

As classificações MaxVer e ICM foram obtidas, tanto sob a suposição de normalidade dos dados, quanto sob a suposição da distribuição mais ajustada à cada classe. Os

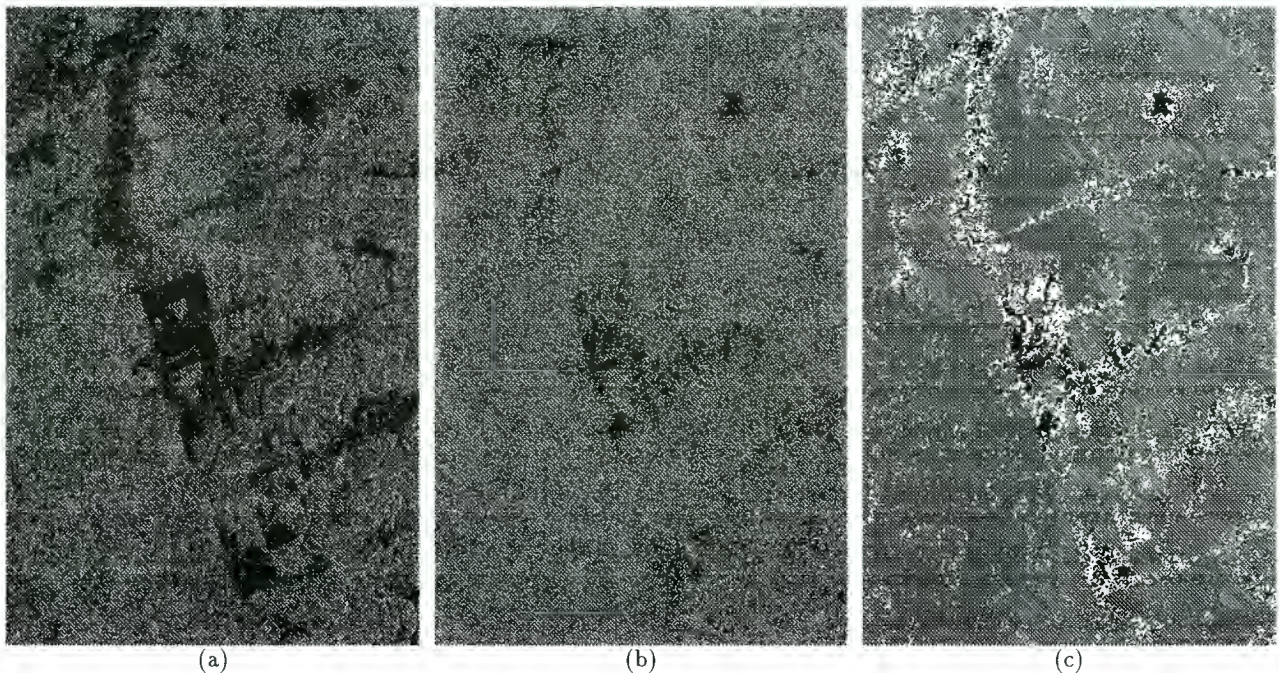


Figura 5: Imagem JERS-1 original (a), classificada pelo método MaxVer (b) e classificada pelo método ICM (c).

coeficientes de concordância Kappa foram estimados para cada classificação, através das respectivas matrizes de confusão obtidas das amostras de teste. A Tabela 2 apresenta os valores estimados do coeficiente de concordância Kappa ($\hat{\kappa}$), e de suas respectivas variâncias ($\hat{\sigma}_{\hat{\kappa}}^2$).

Tabela 2: Valores estimados do coeficiente de concordância Kappa ($\hat{\kappa}$), e de suas variâncias ($\hat{\sigma}_{\hat{\kappa}}^2$)

Classificação	$\hat{\kappa}$	$\hat{\sigma}_{\hat{\kappa}}^2$
MaxVer Gaussianas	0.3283	1.030×10^{-4}
MaxVer Ajustadas	0.3728	9.789×10^{-5}
ICM Gaussianas	0.6559	8.717×10^{-5}
ICM Ajustadas	0.7388	6.779×10^{-5}

Os testes para a igualdade dos coeficientes de concordância Kappa foram efetuados para todos os pares de classificações. Os p -valores destes testes foram aproximadamente iguais a zero, indicando que os coeficientes de concordância Kappa são estatisticamente diferentes para todos os pares de classificação, para níveis de significância de ordem prática.

Portanto, pode-se afirmar que para a imagem JERS-1 utilizada:

- a classificação MaxVer com o uso das distribuições mais ajustadas às classes apresenta um resultado de melhor qualidade quando comparada à MaxVer obtida com o uso de distribuições Gaussianas. Pelos resultados apresentados na Tabela 2 pode-se verificar que houve uma melhora de 13.6% para o $\hat{\kappa}$ da classificação MaxVer ao se utilizar as distribuições mais ajustadas aos dados SAR;
- a classificação ICM com o uso das distribuições mais ajustadas às classes é de melhor qualidade quando

comparada à classificação ICM com o uso de distribuições Gaussianas, havendo uma melhora de 12.6% para o valor $\hat{\kappa}$.

- a classificação ICM é superior à classificação MaxVer, havendo uma melhora média de 99% para o valor $\hat{\kappa}$ ao se utilizar a classificação ICM em substituição à MaxVer.

As Figuras 5b e 5c apresentam os resultados da classificações MaxVer e ICM, respectivamente, da imagem JERS-1 com o uso das distribuições mais ajustadas para as classes. As classes estão representadas pelas cores branco (solo exposto e pastagem), preto (regeneração) e cinza (floresta). Estas figuras evidenciam a superioridade da classificação ICM quando comparada à classificação MaxVer.

7. CONCLUSÕES

Neste artigo foram apresentadas as principais características de um sistema, implementado na linguagem IDL, para o processamento, a classificação e a análise de imagens SAR, baseado em propriedades estatísticas específicas para este tipo de imagens.

Este sistema permite que se estabeleça, para cada classe da imagem, a distribuição que mais se adeque aos dados. Os parâmetros destas distribuições são estimados e as classificações de Máxima Verossimilhança e ICM podem ser facilmente utilizadas pelo usuário. Além destas funções, o sistema permite a aplicação de filtros redutores de *speckle*, estimação do número equivalente de visadas, operações unárias e binárias de imagens, conversão de imagens, decorrelação de amostras, e avaliação das classificações.

O sistema mostrou-se eficiente para a classificação de imagens de dois diferentes sensores: SAR-580 e JERS-1. Os

principais resultados destas classificações são:

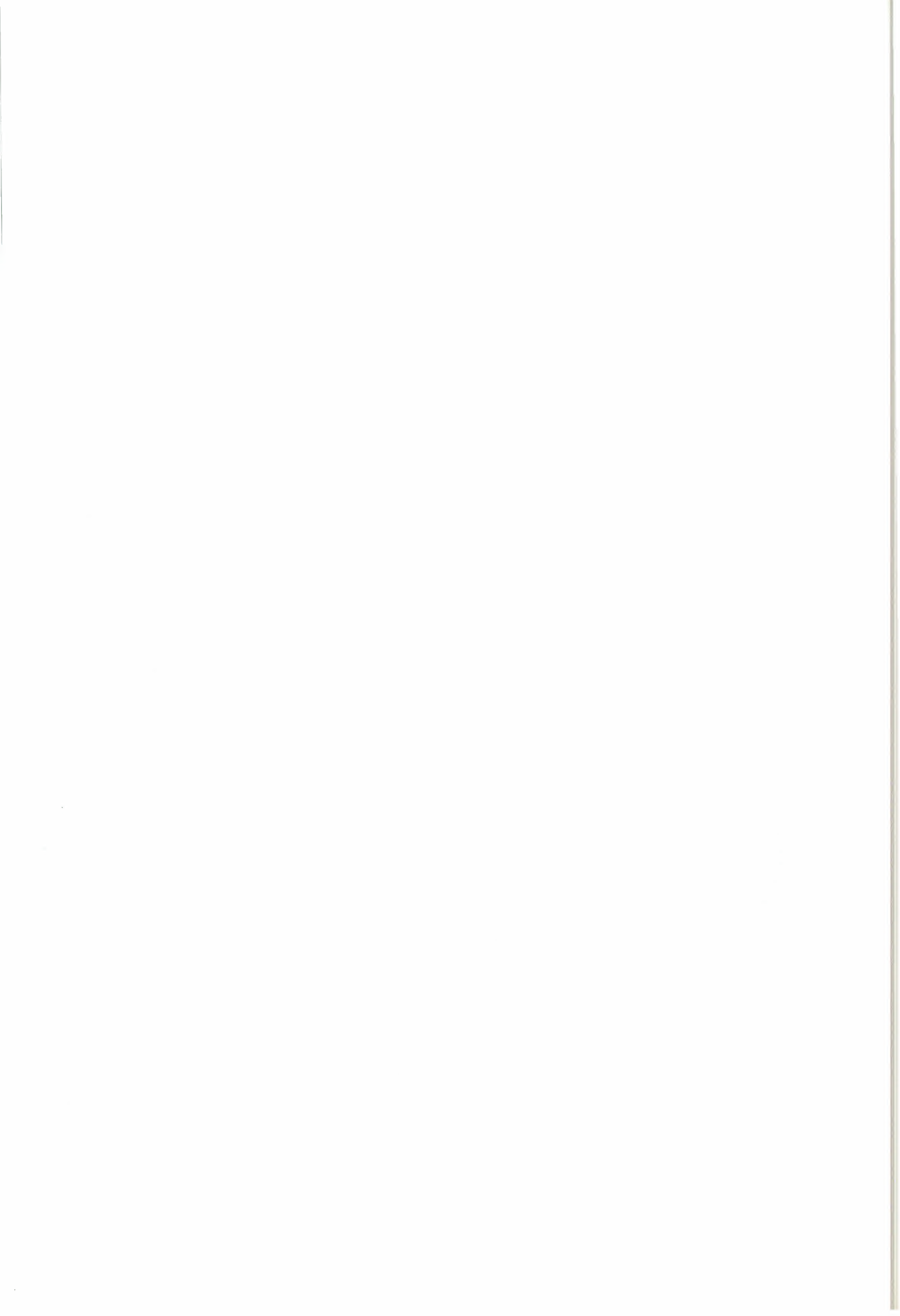
- o uso das distribuições mais ajustadas para os dados apresentam resultados de qualidade superior, quando comparadas aos obtidos utilizando-se as distribuições Gaussianas. Quando comparadas pelo coeficiente de concordância Kappa esta melhora é, em média, de aproximadamente 6% para as classificações MaxVer e de 13% para as ICM.
- o uso da informação contextual (através do algoritmo ICM), acrescentado ao uso das melhores distribuições, permite a obtenção de resultados, em média, 94% melhores quando comparados com as classificações MaxVer através do coeficiente de concordância Kappa.

AGRADECIMENTOS

Os autores agradecem o apoio do CNPq através do projeto PROTEM-CC GEOTEC (Processo 680.061-94-0).

REFERÊNCIAS

- J. Besag. Towards Bayesian image analysis. *Journal of Applied Statistics*, 16(3):395–407, 1989.
- Y. M. Bishop, S. E. Feinberg, and P. W. Holland. *Discrete multivariate analysis: theory and practice*. MIT Press, Cambridge, MA, 1975.
- R. C. Congalton and R. A. Mead. A quantitative method to test for consistency and correctness in photointerpretation. *Photogrammetric Enginnering and Remote Sensing*, 49(1):69–74, 1983.
- A. C. Frery. *Algumas ferramentas estatísticas na síntese, análise e processamento de imagens de radar de abertura sintética*. Tese de Doutorado, Instituto Nacional de Pesquisas Espaciais, São José dos Campos, SP, Brasil, 1993.
- A. C. Frery, H. J. Müller, C. C. F. Yanasse, and S. J. S. Sant'Anna. A model for extremely heterogeneous clutter. *IEEE Transactions on Geoscience and Remote Sensing*, 1996, in press.
- J. W. Goodman. Statistical properties of laser speckle patterns. In J. C. Dainty, editor, *Laser speckle and related phenomena*, chapter 2. Springer-Verlag, Berlin, 1982.
- J. A. Richards. *Remote sensing digital image analysis: an introduction*. Springer-Verlag, Berlin, 1986.
- P. R. Vieira. Desenvolvimento de classificadores de máxima verossimilhança pontuais e ICM para imagens de radar de abertura sintética. Dissertação de Mestrado, Instituto Nacional de Pesquisas Espaciais, São José dos Campos, SP, Brasil, 1996.
- C. C. F. Yanasse, A. C. Frery, S. J. S. Sant'Anna, P. F. Hernandez, and L. V. Dutra. Statistical analysis of SAREX data over Tapajós - Brazil. In M. Wooding and E. Attema, editors, *SAREX-92: South American Radar Experiment*, pages 25–40, Paris, 1993. ESA.



ESTUDO COMPARATIVO DE ALGUNS CLASSIFICADORES UTILIZANDO-SE IMAGENS RADARSAT DA REGIÃO DE TAPAJÓS

Sidnei J. S. Sant'Anna†
Corina da C. F. Yanasse†
Alejandro C. Frery‡

†INPE – Instituto Nacional de Pesquisas Espaciais
DPI – Divisão de Processamento de Imagens
Avenida dos Astronautas, 1758
12227-010 São José dos Campos, SP, Brasil

‡UFPE – Universidade Federal de Pernambuco
DI – Departamento de Informática
CP 7851
50732-970 Recife, PE, Brasil

ABSTRACT

The digital classification is a very important procedure used in remote sensing applications. Several classification techniques had been developed and tested for optical data. With respect to radar data, the development, evaluation and testing of digital classifiers have been a subject of study in last decades. The objective of this article is to compare the classification results of a SAR image, obtained using three different supervised classifiers. A RADARSAT image from the Tapajós National Forest was used for this purpose. The original image was processed in one-look amplitude. This image was degraded obtaining a nine nominal look image. The degraded image was filtered by the Frost filter in order to analyse the influence of the speckle reduction on the classification. The effect of textural information was analysed by filtering the image by the sample coefficient of variation and by an estimated parameter of the amplitude K distribution. The classifiers used were the Maximum Likelihood, Iterated Conditional Modes, and a region classifier based on the Bhattacharrya distance. The image was classified in three classes: "Bare Soil and Pasture", "Regeneration" (Secondary Forest), and "Primary Forest". The classification was evaluated by the Kappa coefficient of agreement and by the corresponding confusion matrices, using samples obtained from a field work.

Keywords: classification; SAR, ICM.

1. INTRODUÇÃO

A classificação digital é uma das técnicas de processamento de imagens mais utilizadas no sensoriamento remoto para o mapeamento de alvos na superfície terrestre. Ela consiste na partição do espaço de atributos e na atribuição dos pixels ou regiões a cada classe correspondente.

Os métodos de classificação se dividem em métodos su-

pervisionados e não supervisionados. No primeiro extraíse das classes, previamente selecionadas (treinamento), informações com as quais pode-se construir critérios utilizáveis na relação de pertinência dos pixels ou regiões às classes. Já no segundo método verifica-se a existência de grupos de pixels ou regiões com certas características semelhantes, não havendo a fase de treinamento.

A maioria das técnicas de classificações digitais existentes foi desenvolvida para imagens ópticas. Nos últimos anos as imagens SAR vêm sendo usadas mais intensamente em sensoriamento remoto para mapear classes de uso do solo, florestas, etc. Desta forma, como a adequação das técnicas tradicionais nem sempre se verifica, tem-se estudado e implementado técnicas de classificações específicas para imagens SAR [Vieira 1996].

O objetivo deste trabalho é comparar três classificadores digitais: um classificador pontual de Máxima Verossimilhança (MaxVer), um contextual de Modas Condicionais Iterativas (Iterated Condicional Modes - ICM) e um por regiões. Os dois primeiros classificadores foram projetados especificamente levando-se em consideração as propriedades estatísticas dos dados de radar e o classificador por regiões utiliza uma distância estocástica entre vetores de atributos (distância de Bhattacharrya).

A avaliação dos classificadores foi realizada comparativamente. Para isto computou-se, para amostras de teste, as matrizes de confusão e o estimador do coeficiente de concordância $Kappa (\hat{\kappa})$ [Congalton and Mead 1983] obtidos pelos classificadores quando aplicados a uma imagem RADARSAT (banda C) na região de Tapajós.

Na seções seguintes descreve-se de forma suscinta os classificadores avaliados, apresenta-se os dados utilizados e a metodologia empregada, os resultados alcançados e finalmente as conclusões obtidas.

2. CLASSIFICADORES

O classificador de Máxima Verossimilhança (MaxVer) utilizado foi implementado de modo que se possa associar diferentes distribuições às distintas classes. Por se tratar de dados de radar, as distribuições passíveis de uso são aquelas que mais se adequam a este tipo de dados, tais como \mathcal{K} , \mathcal{G}^0 , Γ , $\Gamma^{1/2}$, Log-Normal, Weibull, Beta, etc.

O classificador ICM (*Iterated Conditional Modes*) é um algoritmo iterativo e contextual de refinamento de classificações. Ele se baseia na substituição da classe associada a cada coordenada por aquela classe que maximiza a distribuição a posteriori da classe, dadas a radiometria (componente MaxVer) e as classes vizinhas (componente de contexto). A influência das classes vizinhas é quantificada por um parâmetro real, que é estimado iterativamente supondo um modelo para a distribuição espacial das classes. Ao leitor interessado em mais detalhes sobre esta técnica, recomenda-se a leitura de [Besag 1989; Frery 1993 e Vieira 1996].

As implementações dos classificadores MaxVer e ICM utilizadas neste trabalho foram as descritas em [Vieira 1996 e Vieira et al 1996].

O classificador por regiões parte de um particionamento prévio, da imagem a ser classificada, em segmentos denominados regiões. Dadas esta imagem segmentada e amostras de treinamento, cada região é atribuída a uma classe segundo uma medida de distância entre classes. O classificador por regiões utilizado neste trabalho é o implementado no Sistema de Processamento de Informações Georreferenciadas (SPRING) [Câmara et al 1996], o qual faz uso da distância de Bhattacharrya como medida de separabilidade entre as distribuições (Gaussianas) associadas a cada classe.

3. DADOS E METODOLOGIA

A área selecionada para o estudo fica situada em Tapajós ao sul da cidade de Santarém no estado do Pará e é denominada FLONA (Floresta Nacional de Tapajós). Esta área possui coordenadas geográficas W 55° 01' 45", S 02° 56' 38", e W 54° 49' 36", S 03° 23' 28".

A imagem utilizada neste trabalho é proveniente do RADARSAT, datada de 3 de maio de 1996, na banda C, na polarização HH, com uma visada nominal, *fine mode processing*, em amplitude, com ângulo de incidência variando de 45° a 48°, com espaçamento entre pixels de 6.25m, com 13766 linhas por 12166 colunas e no formato inteiro (16 bits por pixel). A resolução espacial da imagem foi degradada computando-se a raiz quadrada da média de 9 pixels em intensidade. Isto é, a cada conjunto de 3 × 3 pixels calculou-se a média que gerava um novo valor de radiometria, aumentando-se assim o número de visadas nominal e diminuindo-se o número de linhas e colunas para 4589 e 4056, respectivamente. Na imagem degradada também realizou-se uma transformação linear para a conversão do formato de inteiro para byte (8 bits por pixel), de forma a não alterar a classe de distribuição dos dados. Desta imagem extraiu-se uma área de 1000 × 1000 pixels para o estudo, a qual pode ser vista na Figura 1a.

O efeito do ruído *speckle* na imagem degradada ainda é evidente. Portanto a fim de reduzi-lo, bem como verificar

seu efeito na separabilidade entre os alvos, fez-se uso do filtro de Frost com janela de processamento de 5 × 5 pixels (Figura 1b). Na imagem filtrada pode-se observar que o contraste geral é aumentado com relação a imagem degradada. Assim, se espera que um classificador que utilize apenas o atributo radiometria como discriminador tenha um resultado melhor na imagem filtrada.

A textura em imagem de radar é um atributo de grande importância na identificação e discriminação de alvos [Dutra 1990; Sant'Anna e Dutra 1995], o que pode ser verificado por uma simples inspeção visual nas Figuras 1a e 1b. Desta forma gerou-se duas novas imagens, uma do coeficiente de variação amostral (Figura 1c) e outra do estimador do parâmetro α da distribuição \mathcal{K} de amplitude (Figura 1d), a partir da imagem degradada. A parametrização da distribuição \mathcal{K} de amplitude utilizada neste trabalho é a mesma adotada em [Frery et al 1996]. O cálculo destes dois parâmetros foram obtidos com janelamento de 7 × 7 e de 11 × 11 pixels, respectivamente, ou seja, trocou-se o valor do pixel central das janelas pelas respectivas estimativas destes parâmetros.

Para efeito de classificação considerou-se apenas as classes dominantes na imagem, que são:

Solo Nu e Pastagem: que aparece na Figura 1b com tonalidade mais escura e com textura mais lisa;

Regeneração: ou floresta secundária, que aparece na Figura 1b com tonalidade mais clara e com textura moderada; e

Floresta Primária: que aparece na Figura 1b com tonalidade clara e com textura rugosa.

Na fase de treinamento dos classificadores foram selecionadas amostras das três classes acima, contendo 44489, 7715 e 15164 pixels para as classes de floresta, regeneração e solo nu, respectivamente. Para efetuar os testes χ^2 de aderência com as distribuições comumente utilizadas para dados de radar, essas amostras foram decorrelacionadas por fatores de reamostragem nas direções horizontal e vertical, obtidos por inspeção visual da função de autocorrelação espacial das amostras de cada classe, para cada uma das quatro imagens.

Na Tabela 1 são apresentadas as distribuições que melhor se ajustaram aos dados e que foram utilizadas para os classificadores MaxVer e ICM. Nesta tabela estão representadas as distribuições Log-Normal, \mathcal{G}^0 de amplitude, \mathcal{K} de amplitude e Gaussiana, que são denotadas por \mathcal{LN} , \mathcal{G}_A^0 , \mathcal{K}_A e \mathcal{N} , respectivamente. Convém observar que os dados da imagem filtrada pelo parâmetro α da distribuição \mathcal{K} de amplitude não foram ajustados por nenhuma das distribuições usadas. Desta forma escolheu-se utilizar a distribuição Gaussiana para as três classes nesta imagem.

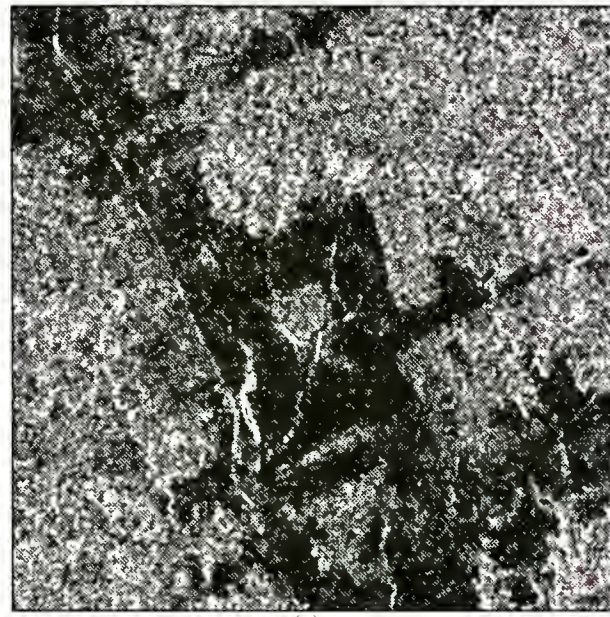
A avaliação dos classificadores foi efetuada através das matrizes de confusão e do estimador do coeficiente de concordância κ , utilizando-se amostras de teste. Esta amostras continham 41648, 3589 e 19195 pixels para as classes de floresta, regeneração e solo nu, respectivamente. Tanto as amostras de treinamento quanto as amostras de teste foram escolhidas baseadas em verdade terrestre, a partir de informações coletadas em trabalho de campo.



(a)



(b)



(c)



(d)

Figura 1: Imagem RADARSAT (a) degradada, (b) filtrada pelo algoritmo de Frost, (c) filtrada pelo coeficiente de variação e (d) filtrada pelo parâmetro α da distribuição \mathcal{K} de amplitude.

Tabela 1: Distribuições ajustadas as classes.

Imagen/Classes	Solo Nu	Regener.	Floresta
Degrada	\mathcal{LN}	\mathcal{LN}	\mathcal{G}_A^0
Frost	K_A	\mathcal{LN}	K_A
Coef. Var.	\mathcal{LN}	\mathcal{LN}	\mathcal{LN}
α	\mathcal{N}	\mathcal{N}	\mathcal{N}

4. AVALIAÇÃO DO DESEMPENHO DOS CLASSIFICADORES

Os resultados das classificações das quatro imagens (degradada, filtrada pelo algoritmo de Frost, filtrada pelo coeficiente de variação e filtrada pelo parâmetro α) são apresentados nas Figuras 2, 3, 4 e 5, respectivamente. As classes floresta, regeneração e solo nu estão representadas pelas cores cinza médio, branco e cinza escuro, respectivamente.

Na Tabela 2 são apresentados os valores estimados do coeficiente de concordância κ para cada imagem classificada. Os melhores resultados de classificação para cada imagem estão ressaltados em negrito nesta tabela.

Tabela 2: Valores estimados do coeficiente de concordância κ ($\times 100$).

Classif./Imag.	Degrad.	Frost	CV	α
MaxVer	5.14	9.52	46.35	63.04
ICM	11.50	13.00	54.30	70.72
Regiões	42.04	54.24	36.48	52.15

Através da análise visual destas classificações, das matrizes de confusão, não apresentadas aqui, e do coeficiente de concordância κ , pode-se concluir que:

- para as imagens degradada e filtrada pelo algoritmo de Frost há muita confusão entre as classes, especialmente entre floresta e regeneração;
- a maior parcela de erro nas classificações MaxVer e ICM das imagens degradada e filtrada pelo algoritmo de Frost ocorre em pixels da classe floresta que são classificados como regeneração;
- a maior parcela de erro na classificação por regiões das imagens degradada e filtrada pelo algoritmo de Frost ocorre em pixels da classe regeneração que são classificados como floresta;
- os resultados obtidos na classificação da imagem filtrada pelo algoritmo de Frost são melhores que aqueles obtidos com a imagem degradada, independentemente do classificador utilizado;
- usando a imagem degradada ou filtrada pelo algoritmo de Frost o melhor resultado de classificação é obtido pelo classificador de regiões, seguido pelo ICM e MaxVer;
- para as classificações efetuadas utilizando informação textural (imagens filtradas pelo coeficiente de variação ou pelo parâmetro α) há muita confusão entre solo nu e regeneração;

- com a informação textural é possível separar as classes floresta e não floresta (regeneração e solo nu);
- a maior parcela de erro na classificação por regiões da imagem filtrada pelo coeficiente de variação ocorre em pixels da classe solo nu que são classificados como regeneração. Este erro é minimizado quando o parâmetro α é utilizado;
- usando a imagem filtrada pelo coeficiente de variação ou pelo α , o melhor resultado de classificação é obtido pelo classificador ICM, seguido pelo MaxVer e pelo de regiões;
- a melhor classificação ocorre quando o ICM é utilizado sobre a imagem filtrada pelo parâmetro α .

Convém notar que durante o processo de classificação observou-se que o classificador por regiões utilizado é fortemente dependente da segmentação prévia.

5. AVALIAÇÃO DO DESEMPENHO DOS CLASSIFICADORES CRUZADAS

Como foi observado anteriormente, as imagens classificadas usando a radiometria apresentam muita confusão entre as classes floresta e regeneração, e as imagens classificadas usando a informação textural apresentam muita confusão entre solo nu e regeneração. Isto evidencia a necessidade da utilização de ambos atributos para obter-se bons resultados de classificação. Uma opção seria utilizar classificadores multicanais. Esta opção não foi utilizada, pois os classificadores MaxVer e ICM foram implementados para uma única banda (por utilizarem diferentes distribuições para cada classe). Outra opção, utilizada neste trabalho, é o cruzamento entre as classificações através de operações lógicas (operações Booleanas). Estas operações foram aplicadas em pares de imagens classificadas, a primeira obtida através de uma imagem de radiometria (imagens degradada ou filtrada pelo algoritmo de Frost), e a segunda de uma imagem de textura (imagens filtradas pelo coeficiente de variação ou pelo parâmetro α). A Tabela 3 apresenta as regras utilizadas nesta operação.

Tabela 3: Regras utilizadas para a obtenção das classificações cruzadas.

Im. Degr. ou Frost	Im. CV ou α	Im. Cruzada
Floresta	Floresta	Floresta
Regeneração	Floresta	Floresta
Solo Nu	Floresta	Floresta
Floresta	Solo Nu	Regeneração
Regeneração	Solo Nu	Regeneração
Solo Nu	Solo Nu	Solo Nu
Floresta	Regeneração	Regeneração
Regeneração	Regeneração	Regeneração
Solo Nu	Regeneração	Solo Nu

Os resultados, para cada classificador, dos cruzamentos entre imagens (degradada \times CV, degradada \times α , Frost \times CV, Frost \times α) são apresentados nas Figuras 6, 7, 8 e 9, respectivamente. Na Tabela 4 são apresentados os valores estimados do coeficiente de concordância κ para cada uma destas imagens classificadas. Nesta tabela os

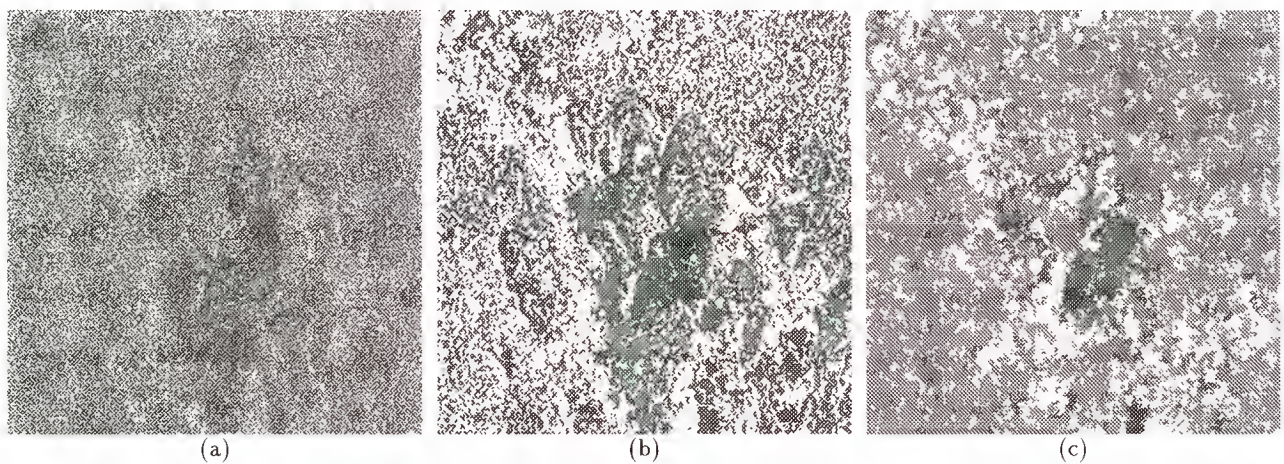


Figura 2: Imagem degradada classificada (a) MaxVer, (b) ICM e (c) Regiões.

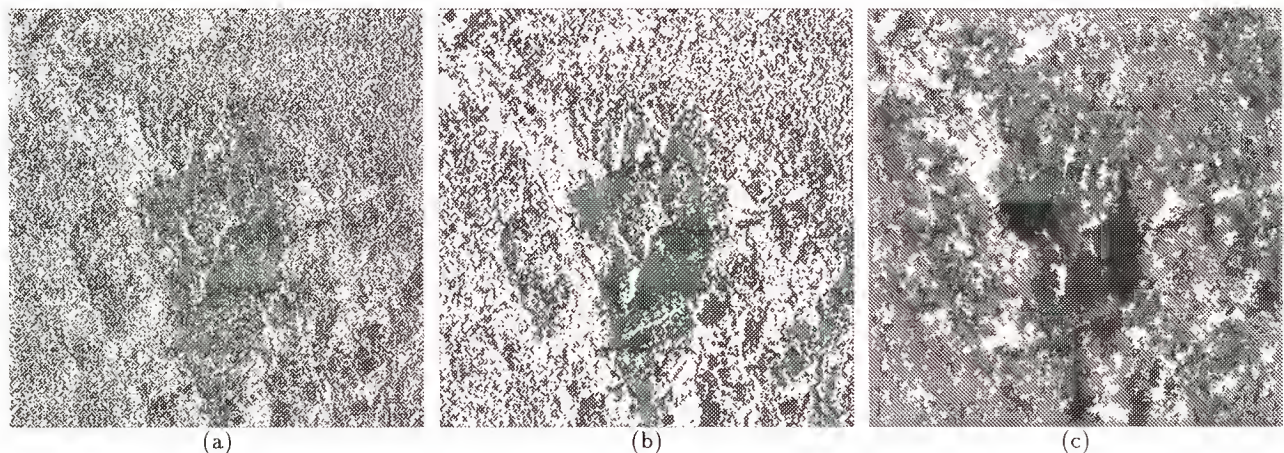


Figura 3: Imagem filtrada pelo algoritmo de Frost classificada (a) MaxVer, (b) ICM e (c) Regiões.

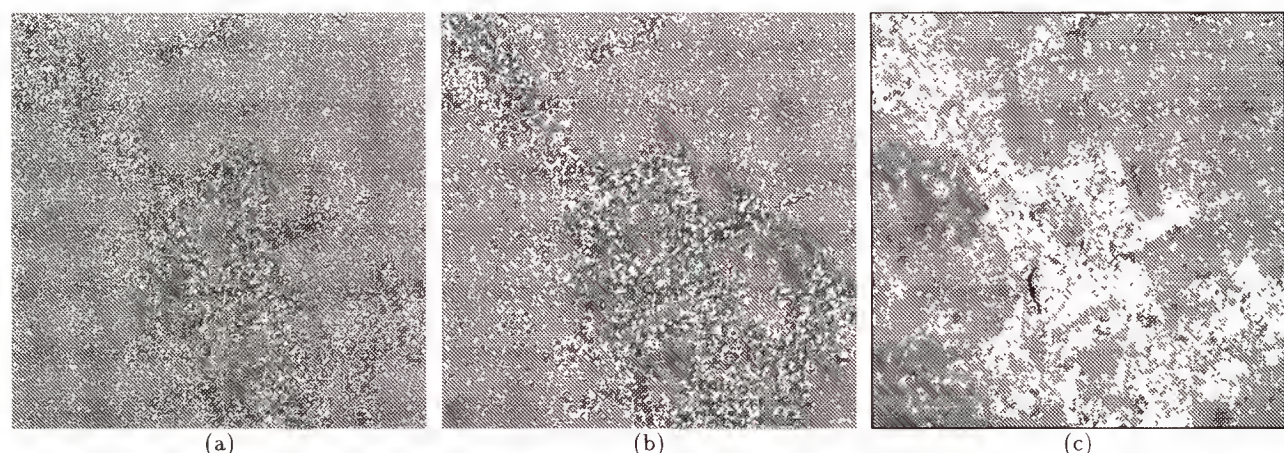


Figura 4: Imagem filtrada pelo coeficiente de variação classificada (a) MaxVer, (b) ICM e (c) Regiões.

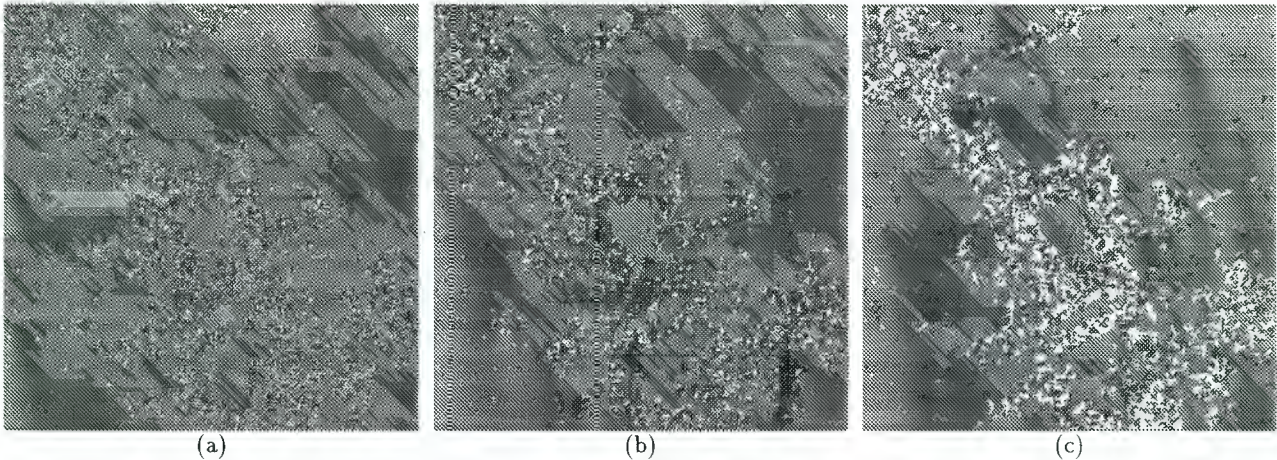


Figura 5: Imagem filtrada pelo parâmetro α classificada (a) MaxVer, (b) ICM e (c) Regiões.

melhores resultados de classificação para cada imagem estão ressaltados em negrito.

Tabela 4: Valores estimados do coeficiente de concordância κ ($\times 100$).

Clas./Img.	Dg \times CV	Fr \times CV	Dg \times α	Fr \times α
MaxVer	43.85	51.36	56.73	64.54
ICM	61.41	64.08	69.12	71.76
Regiões	48.34	64.04	54.73	71.20

Através da análise visual destas classificações, das matrizes de confusão, não apresentadas aqui, e do estimador do coeficiente de concordância κ pode-se concluir que:

- as classificações em que foi utilizada a imagem classificada baseada no parâmetro α apresentaram melhores resultados do que as baseadas no coeficiente de variação, evidenciando a relevância do uso deste parâmetro em classificadores;
- as classificações em que foi utilizada a imagem classificada baseada no filtro de Frost apresentaram melhores resultados do que as baseadas na imagem original degradada, evidenciando a importância de filtros redutores de *speckle* nas classificações;
- o classificador que apresentou melhores resultados foi o ICM, independentemente dos pares de imagens utilizados;
- o melhor resultado de classificação foi obtido utilizando-se as imagens classificadas baseadas no filtro de Frost e no parâmetro α , na classificação ICM;
- a classificação baseada no cruzamento Frost \times α proporcionou um melhora de 1.5% em relação à classificação ICM utilizando somente a imagem filtrada pelo parâmetro α , mostrando que o maior conteúdo de informação está contido neste parâmetro.

6. CONCLUSÕES

Neste trabalho avaliou-se o desempenho de três classificadores supervisionados: MaxVer, ICM e um por regiões.

Para a análise dos resultados de classificação e partindo-se de uma imagem RADARSAT (uma visada e banda C) geraram-se quatro imagens, uma degradada, uma filtrada pelo algoritmo de Frost, uma filtrada pelo coeficiente de variação amostral e outra filtrada por uma estimativa do parâmetro α da distribuição \mathcal{K} de amplitude. A avaliação dos resultados obtidos foi realizada através das matrizes de confusão e do estimador do coeficiente de concordância κ .

As conclusões deste trabalho referem-se sempre as três classes (Solo Nu, Regeneração e Floresta) utilizadas nas classificações e são as seguintes:

- Verificou-se que todas as estimativas encontradas para o coeficiente de concordância κ foram estatisticamente diferentes entre si;
- Pode-se observar que os resultados da classificação ICM é sempre superior aos da classificação MaxVer, mostrando a relevância do contexto quando se classifica imagens de radar;
- Para as três classes utilizadas nas classificações destas imagens notou-se a fundamental importância da informação textural;
- Quando somente as radiometrias (imagem degradada e a filtrada pelo algoritmo de Frost) foram usadas o classificador que apresentou os melhores resultados foi o por regiões;
- Quando somente os parâmetros texturais (imagem do coeficiente de variação e do parâmetro α) foram usados o classificador que obteve os melhores desempenhos foi o ICM;
- A segmentação prévia influencia fortemente nos resultados obtidos com o classificador por regiões;
- O melhor resultado de classificação foi obtido cruzando-se as classificações ICM das imagens filtrada pelo algoritmo de Frost e pelo estimador do parâmetro α ;
- O resultado da classificação cruzada ICM (Frost \times α) proporcionou um incremento de apenas 1.5% em relação a classificação ICM obtida com a imagem do parâmetro α , evidenciando que a informação textural é a maior responsável pelo alto desempenho da classificação.

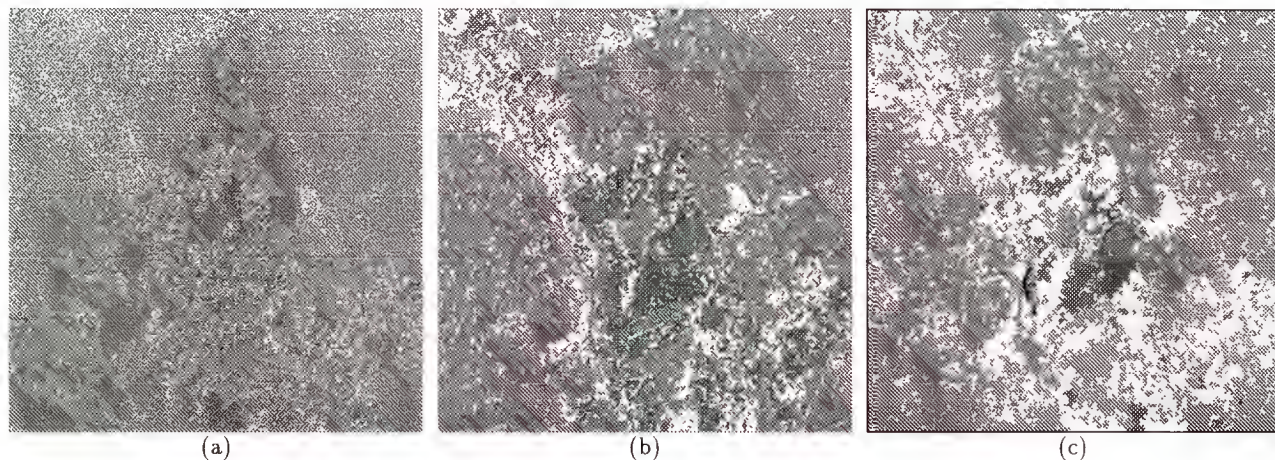


Figura 6: Imagem classificada resultante do cruzamento entre as imagens degradada e do coeficiente de variação (a) MaxVer, (b) ICM e (c) Regiões.

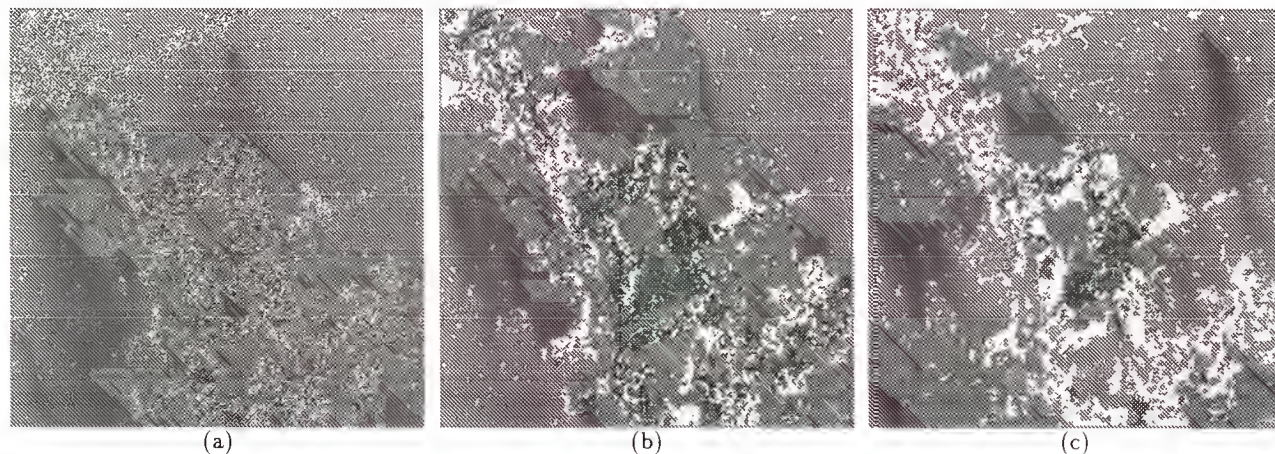


Figura 7: Imagem classificada resultante do cruzamento entre as imagens degradada e do parâmetro α (a) MaxVer, (b) ICM e (c) Regiões.

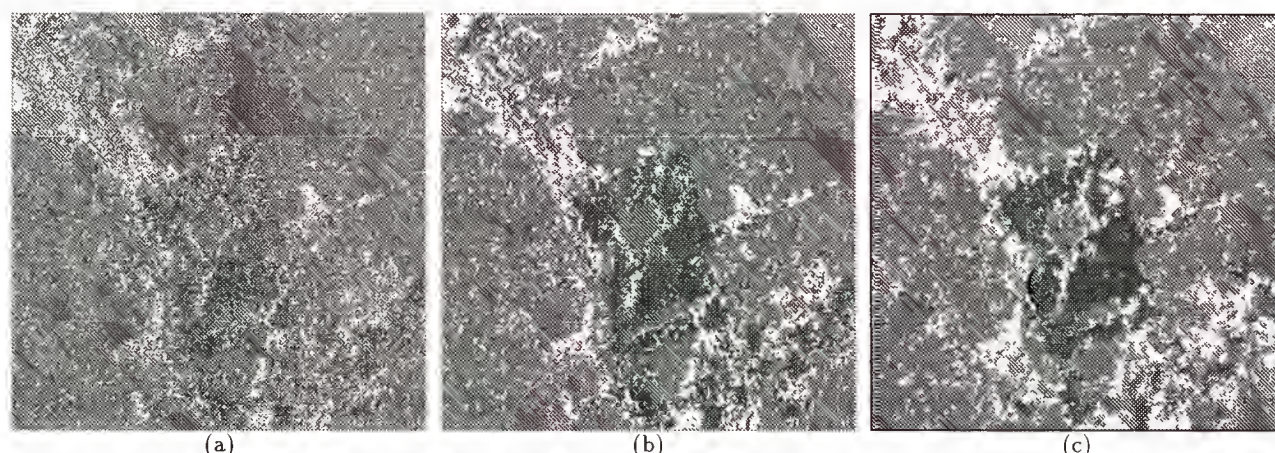


Figura 8: Imagem classificada resultante do cruzamento entre as imagens filtradas pelo algoritmo de Frost e pelo coeficiente de variação (a) MaxVer, (b) ICM e (c) Regiões.

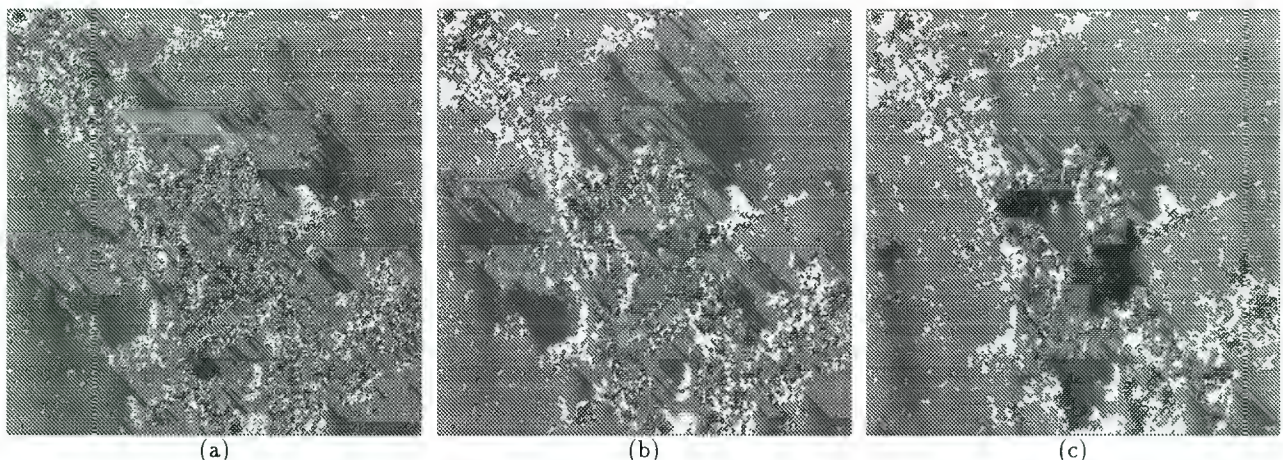


Figura 3: Imagem classificada resultante do cruzamento entre as imagens filtradas pelo algoritmo de Frost e pelo parâmetro α (a) MaxVer, (b) ICM e (c) Regiões.

AGRADECIMENTOS

Os autores agradecem o apoio do CNPq através do projeto PROTEM-CC GEOTEC (Processo 680.061-94-0).

P. R. Vieira, C. C. F. Yanasse, A. C. Frery, S. J. S. Sant'Anna. Um sistema de análise e classificação estatísticas para imagens SAR. In: Primeras Jornadas Latinoamericanas de Percepción Remota por Radar: Técnicas de Procesamiento de Imágenes. Buenos Aires, Argentina, Dez. 1996.

REFERÊNCIAS

- J. Besag. Towards Bayesian image analysis. *Journal of Applied Statistics*, 16(3):395–407, 1989.
- G. Câmara, R. C. M. Souza, U. M. Freitas, J. Garrido. SPRING: Integrating remote sensing and GIS by object-oriented data modelling. *Comput. & Graphics*, 20(3):395–403, 1996.
- R. C. Congalton and R. A. Mead. A quantitative method to test for consistency and correctness in photointerpretation. *Photogrammetric Enginnering and Remote Sensing*, 49(1):69–74, 1983.
- L. V. Dutra. Classificação de texturas usando modelos ARMA e distâncias da função de autocorrelação. Tese de Doutorado, Instituto Nacional de Pesquisas Espaciais, São José dos Campos, SP, Brasil, 1990.
- A. C. Frery. *Algumas ferramentas estatísticas na síntese, análise e processamento de imagens de radar de abertura sintética*. Tese de Doutorado, Instituto Nacional de Pesquisas Espaciais, São José dos Campos, SP, Brasil, 1993.
- A. C. Frery, H. J. Müller, C. C. F. Yanasse, and S. J. S. Sant'Anna. A model for extremely heterogeneous clutter. *IEEE Transactions on Geoscience and Remote Sensing*, 1996, in press.
- S. J. S. Sant'Anna and L. V. Dutra. SAR texture discrimination using AR-2D models for amazonian land use classification. In Simpósio de Especialistas Latinoamericanos em Percepción Remota, (SELPER) VII, Puerto Vallarta, México, Oct. 1995, pages 516–523.
- P. R. Vieira. Desenvolvimento de classificadores de máxima verossimilhança pontuais e ICM para imagens de radar de abertura sintética. Dissertação de Mestrado, Instituto Nacional de Pesquisas Espaciais, São José dos Campos, SP, Brasil, 1996.

Soil moisture retrieval from active microwave remote sensing.

João Vianei Soares
Camilo Daleles Rennó

Instituto Nacional de Pesquisas Espaciais - INPE
Caixa Postal 515, CEP 12201-970
São José dos Campos, SP, Brasil
{vianei;camilo}@ltid.inpe.br

Keywords. soil moisture, SAR, surface, scattering, model, empiric, polarization

Abstract. It is well known that microwave reflectivity of agricultural targets is primarily associated with soil roughness, soil dielectric properties and the presence of vegetation. The dielectric constant of a completely dry soil is around 3 and that of pure water approaches 80. Then, as the wetness of the soil top layer increases the reflectivity will also rise. On the other hand there is a dichotomy: rough and dry soils could produce a higher backscatter (scatter in the receiving antenna direction) than smooth wet soils, since most of the fields could experience specular reflection away from the radar. This paper briefly reviews the theory and methods of retrieving soil moisture from remote active microwave systems, its application, conditions of validity and limitations as practical use is concerned. Methods based on a simple linear regression between radar backscatter and soil moisture as well as those based on the inversion of surface scattering models are presented. The validity conditions are discussed. Finally, we introduce the preliminary results on the inversion of a semi-empirical surface scattering model to retrieve top layer (first few centimeters) soil moisture using the SIR-C L and C band multipolarization imagery acquired over the Bebedouro Irrigation Project test site, in the semi-arid São Francisco river valley in the northeast Brazil. "In situ" soil moisture and soil roughness for some bare and low vegetated fields, were measured simultaneously with the radar data acquisition during the first flight of the SIR-C/X-SAR mission in April 1994.

Introduction

Estimates of soil moisture are of great importance in numerous environmental studies, including hydrology, meteorology, irrigation control, water resources systems planning and agriculture forecasting. In spite its importance, soil moisture information is not widely used in resource monitoring or prediction because it is difficult and costly to obtain "in situ" measurements on a routine basis over large areas (Wang et al., 1986). From theory, the dielectric constant of a completely dry soil is around 3 and that of pure water approaches 80. Then, as the wetness of the soil top layer increases the reflectivity will also rise. Based on that, there has been various experiments including aircraft, ground level truck mounted scatterometers and even satellites, showing that one can relate radar backscatter to soil top layer moisture (see for example, Ulaby et al., 1976; Ulaby et al., 1978; Wang et al., 1986; Soares et al., 1988; Bernard et al.; 1986).

Because radar backscatter is also affected by surface roughness and vegetation, such that any practical application of radar must be able to account for all three of these target features. As matter of fact, there is a dichotomy: rough and dry soils could produce a higher backscatter (scatter in the receiving antenna direction) than smooth wet soils, since most of the fields could experience specular reflection away from the radar. Thus, if one were interested in monitoring soil moisture over a mixed area, the effects of surface roughness and plant canopy would have to be subtracted from the measurements of radar backscatter in order to isolate soil moisture modulation on the radar

measured signal. Earlier results of several investigators (for example, Ulaby et al., 1978, Soares et al., 1988) showed that, at small incidence angles (between 10° and 20°), soil surface roughness effects on the received radar scatter are minimized. On the other hand, these results have also pointed out that the linear relationships found between soil moisture and radar backscatter were not the same for different sites, and the optimal incidence angle to minimize roughness also fell in a rather big range. This variability suggests that many algorithms are site-specific and that there exists a need to develop portable algorithms that do not require fitting to specific site properties. Furthermore, methods that are limited to small incidence angles narrow the application of remote radar imagery to the near range of the swath. This is of course an important drawback of the technique since most SAR measurements from space generally range from 15° to 55° in incidence angle, implying that any operational algorithm to retrieve soil moisture should be able to provide good estimates over an as wide as possible incidence angle range. This paper briefly reviews the theory and methods of retrieving soil moisture from remote active microwave systems, its application, conditions of validity and limitations as practical use is concerned.

Soil moisture retrieval from active microwave systems.

- ***Linear relationship between radar backscatter and soil moisture***

Ulaby and Batlivala, (1976), studied the radar response to soil moisture for three bare field plots with considerably different surface roughnesses at eight frequencies in the 2-8 GHz range for VV and HH polarizations, using a truck mounted antenna located 20 m above the ground. They concluded that the effect of roughness on the radar backscattering coefficient can be minimized by proper choice of the radar parameters. An optimal combination of sensor parameters is defined such that σ^0 of the ground is almost independent of surface roughness while retaining an acceptable sensitivity to soil moisture. Their data led them to recommend the best radar parameters for an operational soil moisture system as being C band (4 GHz), both HH and VV operating at a range of incidence angles of 7-15°.

Soares et al. (1988), following Ulaby and Batlivala recommendation, established a linear relationship between soil moisture (m_s , $\text{cm}^3 \text{cm}^{-3}$) and absolute radar backscatter (σ^0 , $\text{dB m}^2 \text{m}^{-2}$ measured with an accuracy of about 0.5 dB), using a 5.3 GHz C band scatterometer onboard an helicopter pointed at 12° incidence angle. Their data is synthesized in figure 1. The regression line is:

$$w_g = 0.015\sigma^0 + 0.30 \quad (1)$$

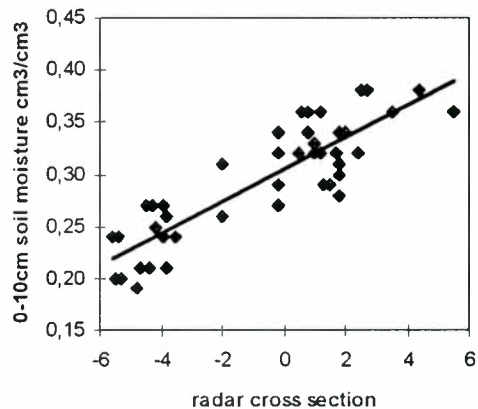


Figure 1. Radar Calibration curve against surface soil moisture, using either bare or low vegetated soils (From Soares et al., 1988).

Cognard et al. (1995, reported on the evaluation of the ERS-1 SAR capability to estimate soil moisture. ERS-1 SAR operates in C Band with an incidence angle of 23°, what makes it unlikely to sense soil moisture at field scale using a simple universal linear algorithm, as those established in the pioneering work of Ulaby's team at the University of Kansas. They acquired SAR scenes during 1992 and 1993, concurrently with point measurements of soil moisture in the fields using both automatic tools and the gravimetric method. They found out that on a field scale the correlation between the radar signal and the surface soil moisture depends strongly on the type of cover: correlation was poor for the different cultures except for wheat. On a basin scale, they figured out that, for a period of low vegetation, there is a linear relationship between the mean radar data and the point automatic measurements, a result that open the way to hydrological applications.

The following general considerations are to be made:

1. The sensitivity of radar backscatter to soil moisture is very clear.
2. The conditions imposed as to minimize roughness effects (incidence angle) make it not practical for operational use in most cases.
3. As the incidence angle increases, the vegetation canopy attenuation of the radar power goes up, such that the sensitivity of the radar to moisture, such as expressed in equation (1), is no longer assured.
4. As stated above, the linear relationships found by many authors are site-specific.
5. Speckle noise in imaging systems is another source of uncertainty, specially for field scale.
6. Finally, one has to make sure to proceed an absolute calibration of the radar (really knowing about σ^0 in dB m⁻²), for every radar data set, to produce accurate estimates of soil moisture. Scatterometers are easier to calibrate than imaging systems.

- ***Measuring Soil Moisture with Polarimetric Imaging Radar***

1. Surface scattering models

The interaction between electromagnetic waves and bare soil can be approximately described as a surface scattering problem. The scattering of electromagnetic waves by rough surfaces has been studies for many years, but no exact close-form solutions have been obtained. Numerical solutions can be used to compute the exact solution, but in general they are computationally prohibitive and are only used in evaluating the accuracy and range of validity of approximate models (Chen and Fung, 1988). When dealing with practical applications, simpler approximate models are the ones of choice. The main drawback is: they are valid only within a limited range of roughness. Three scattering models are used (Ulaby et al., 1986):

- The small perturbations method when the variations in surface height are small relative to the wavelength and the surface slope is small;
- The Kirchoff model under scalar approximation (*physical optics*), when the radius of curvature is

large and the *rms* surface slope is small relative to the wavelength;

- The Kirchoff model under stationary-phase approximation (*geometrical optics*), when the roughness is large relative to the wavelength.

The validity conditions for all the three models are summarized in Table 1 (from Ulaby et al. 1986).

Table 1. Validity conditions for surface scattering models.

$$k = 2\pi / \lambda$$

s = *rms* surface height

l = correlation length

m = *rms* surface slope

Model	validity conditions
Perturbation	$ks < 0.3$ and $m < 0.3$
Physical Optics	$m < 0.25$ and $kl > 6$
Geometrical Optics	$(2ks\cos\theta)^2 > 10$ and $l^2 > 2.76 s\lambda$

Since surface scattering is a function of reflectivity and surface roughness, all models above can be represented as a product of dielectric and surface roughness functions:

$$\sigma_{pp}(f, \theta_i) = D(f, p, \theta_i) \times S(f, \theta_i, s, l) \quad (2)$$

where *pp* indicates polarization, *f* is frequency, *s* is the *rms* height and θ_i is incidence angle.

For the *small perturbations model*, the dielectric functions can be described as follows:

$$D(hh, \theta_i) = \left| \frac{\epsilon_r - 1}{\left(\cos\theta_i + (\epsilon_r - \sin^2\theta_i)^{1/2} \right)^2} \right|^2 \quad (3)$$

and

$$D(vv, \theta_i) = \left| \frac{(\epsilon_r - 1)(\epsilon_r(1 + \sin^2\theta_i) - \sin^2\theta_i)}{\left(\epsilon_r \cos\theta_i + (\epsilon_r - \sin^2\theta_i)^{1/2} \right)^2} \right|^2 \quad (4)$$

where ϵ_r is the relative dielectric constant. The surface roughness function at given frequency f and incidence angle θ_i is given by:

$$S(f, \theta_i, W) = 8\kappa^4 \cos^4 \theta_i W(2\kappa \sin \theta_i) \quad (5)$$

where $W(2\kappa \sin \theta_i)$ is the normalized roughness spectrum, which is given (for the Gaussian correlation function) by:

$$W(2\kappa \sin \theta_i) = \frac{1}{2} l^2 \exp[-(\kappa l \sin \theta_i)^2] \quad (6)$$

For the *physical optics model*, the coherent part can be neglected for incidence angles that are not near the normal. When we consider the non-coherent term only, the dielectric functions become:

$$D(f, pp, \theta_i) = |R_{pp}(\theta_i)|^2 \quad (7)$$

where

$$R_{vv}(\theta_i) = \frac{(\epsilon_r - 1)(\epsilon_r \cos^2 \theta_i - \sin^2 \theta_i)}{\left(\epsilon_r \cos \theta_i + (\epsilon_r - \sin^2 \theta_i)^{1/2}\right)^2} \quad (8)$$

and R_{hh} is the same as in equation (3).

When one considers the backscattering from both the non-coherent term and the one due to slope, the equations are:

$$D(f, pp, \theta_i) = |R_{pp}(\theta_i)|^2 (1 + \sin^2 \theta_i) + \operatorname{Re}[R_{pp}(\theta_i) R_{ppl}^*(\theta_i)] \sin 2\theta_i \quad (9)$$

where,

$$R_{hh}(\theta_i) = -\frac{2 \sin \theta_i R_{hh}(\theta_i)}{\cos \theta_i + (\epsilon_r - \sin^2 \theta_i)^{1/2}} \quad (10)$$

and

$$R_{vvl}(\theta_i) = \frac{\sin \theta_i [R_{vv}(\theta_i)(\epsilon_r + 1) - \epsilon_r + 1]}{\epsilon_r \cos \theta_i + (\epsilon_r - \sin^2 \theta_i)^{1/2}} \quad (11)$$

Assuming again a Gaussian correlation form, the surface roughness function is as follows:

$$S(f, \theta_i, \sigma, l) = (\kappa l)^2 \exp(-K_0) \times \sum_{n=1}^{\infty} \frac{(K_0)^n}{n n!} \exp\left(-\frac{(\kappa l \sin \theta_i)^2}{n}\right) \quad (12)$$

where $K_0 = 4k^2 s^2 \cos^2 \theta_i$.

For both the perturbation and physical optics models, the dielectric formulation include the dependence on incidence angle, frequency, polarization and the dielectric properties themselves. They do not depend on the correlation function and *rms* roughness. The surface roughness parameterization are a function of frequency, incidence angle, surface roughness correlation form and *rms* surface height. They are independent of polarization. The measured ratio expressed by equation (13) (see bellow), is expected to be independent of the surface roughness function.

$$\frac{\sigma_{hh}^o}{\sigma_{vv}^o} = \frac{D(f, hh, \theta_i)}{D(f, vv, \theta_i)} \quad (13)$$

Since single surface scattering models physics indicate that the relative phase difference between HH and VV polarizations approaches 0, the imaginary part of the dielectric function is very small. Therefore, one can either use the magnitude of the dielectric constant to replace the complex dielectric constant or express the dielectric function as a function of the incidence angle θ_i and the refractive angle θ_t at a given frequency and polarization through Snell's law, as in Shi et al., (1992). For example, for the perturbation model the dielectric function ratio between the HH and VV polarizations can be written as:

$$\frac{\sigma_{hh}^o(f, \theta_i)}{\sigma_{vv}^o(f, \theta_i)} = \frac{\cos^4(\theta_i - \theta_t)}{\sin^2 \theta_i + \cos^2 \theta_t} \quad (14)$$

Then, the refractive angle is the only unknown in the ratio and can be easily solved for. Consequently, the magnitude of dielectric constant can be obtained through Snell's law, and finally volumetric soil moisture can be derived following the dependence of the soil dielectric constant on soil type and the volumetric constant (see, for example, appendix E of Ulaby et al., 1986).

Regarding the geometrical optics model, the dielectric and surface roughness functions are given by:

$$D(f) = |R_{hh}(0)|^2 = |R_{vv}(0)|^2 = \frac{\epsilon_r^{1/2} - 1}{\epsilon_r^{1/2} + 1} \quad (15)$$

and

$$S(\theta_i) = \frac{1}{2m^2 \cos^4 \theta_i} \exp\left(-\frac{\tan^2 \theta_i}{2m^2}\right) \quad (16)$$

which show that the dielectric function depends only on the dielectric properties of the surface at a given frequency. It is independent of both polarization and incidence angle. The surface roughness formula is done as a function of incidence angle and mean random surface slope. It is independent on both polarization and frequency. In this case, the ratio of co-polarization signals does not provide any information about surface dielectric properties and roughness because both functions are the same for the co-polarization signals.

Shi et al., (1992), have attempted to use these surface scattering models using data collected during an experiment carried out in 1989 with the NASA/JPL AIRSAR in an agricultural area near Fresno, Ca. Soil moisture measurements were obtained for three plots, showing low values corresponding to dielectric constant within the 3.0 - 5.5 range. They were assumed to represent the whole area because all the fields were flat, essentially uniform in texture, none of them had been irrigated for several weeks, the weather conditions were high temperatures and low humidity. Based on the "a priori" condition that the roughness function $S(f, \theta, s, l)$ is independent of polarization, they used the ratio of co-polarization channels to indicate which surface scattering model should be used as follows:

- For the small perturbation model the ratio $\sigma_{hh}^\rho / \sigma_{vv}^\rho$ is always less than one except at near-normal incidence.
- For the physical optics model, the ratio is greater than one, except at near nadir incidence.
- For the geometrical optics model, the ratio is always equal to one.

Therefore, one can "say" something about the surface roughness condition using the co-polarization ratio and automatically choose the model to be applied for each pixel (or plot). Their results showed that the co-polarization ratio has good potential for measuring soil moisture for bare fields, particularly when soil moisture was less 30% in volume and incidence angle is above 40°. The inversion algorithm performed well at L Band but not at C Band. The geometric model could not be evaluated because the validity conditions were not met.

The main drawbacks of using the purely analytical surface scattering models are:

- The validity conditions are hardly met in the practical world;
- The co-polarization ratio is very noisy on a pixel by pixel basis;
- Absolute calibration is needed.

2. Semi-empirical models

Oh et al., (1992,1994), developed semi-empirical expressions for the two co-polarized backscattering coefficients σ_{hh}^ρ and σ_{vv}^ρ and the cross-polarized backscattering coefficient, σ_{hv}^ρ , as a function of the incidence angle θ , the radar wavelength λ , and two soil parameters, the relative dielectric constant ϵ_s and the *rms* surface roughness. The models, valid over the angular range defined by $20^\circ \leq \theta \leq 70^\circ$, are given by:

$$\sigma_{vv}^\rho = \frac{g \cos^3 \theta_i}{p^{1/2}} [\Gamma_v(\theta) + \Gamma_h(\theta)] \quad (17)$$

$$\sigma_{hh}^\rho = p \sigma_{vv}^\rho \quad (18)$$

$$\sigma_{hv}^\rho = q \sigma_{vv}^\rho \quad (19)$$

$$p = \left[1 - \left(\frac{2\theta}{\pi} \right)^{[0.314/\Gamma_o]} \cdot \exp(-\kappa s) \right]^2 \quad (20)$$

$$q = 0.25 (\Gamma_o)^{1/2} (0.1 + \sin^{0.9} \theta_i) \cdot [1 - \exp[-(1.4 - 1.6 \Gamma_o) \kappa s]] \quad (21)$$

$$g = 0.7 \left[1 - \exp(-0.65 (\kappa s)^{1.8}) \right] \quad (22)$$

$$\Gamma_o = \left| \frac{\epsilon_s^{1/2} - 1}{\epsilon_s^{1/2} + 1} \right|^2 \quad (23)$$

$$\Gamma_h(\theta_i) = \left| \frac{\cos \theta_i - (\epsilon_s - \sin^2 \theta_i)^{1/2}}{\cos \theta_i + (\epsilon_s - \sin^2 \theta_i)^{1/2}} \right|^2 \quad (24)$$

$$\Gamma_v(\theta_i) = \left| \frac{\epsilon_s \cos \theta_i - (\epsilon_s - \sin^2 \theta_i)^{1/2}}{\epsilon_s \cos \theta_i + (\epsilon_s - \sin^2 \theta_i)^{1/2}} \right|^2 \quad (25)$$

and is the relative complex dielectric constant of the soil:

$$\epsilon_s = \epsilon'_s - j\epsilon''_s \quad (26)$$

According to this surface scattering model, the three magnitude quantities measured by a polarimetric radar, σ_{hh}^o , σ_{vv}^o and σ_{hv}^o , provide three measured quantities, from which it should be possible to determine the *rms* height s and the dielectric constant ϵ_s , since θ_i and κ are known. The dielectric constant is in turn a function of the soil volumetric moisture m_v and the soil type. Using this model, Ulaby et al., (1995) provide two algorithms for estimating s and ϵ_s from polarimetric radar observations:

- The first one, the p - q Inversion Algorithm uses the equations (17)-(26). The advantage of this algorithm is that it is insensitive to absolute calibration of σ_{hh}^o , σ_{vv}^o and σ_{hv}^o , relying only on good relative calibration one to each other. Its potential disadvantage is when vegetation is present since whereas σ_{hh}^o and σ_{vv}^o are only weakly sensitive to the presence of modest vegetation, σ_{hv}^o (and q) is quite sensitive to vegetation cover.
- The second one is the p - σ_{hh}^o inversion algorithm that does not use the cross-polarized channel, but requires good absolute calibration of the co-polarized channels.

Ulaby et al., (1995) compared radar-estimated surface roughness and soil moisture using JPL AIRSAR data with ground truth data, and obtained

very good agreements with correlation coefficients as high as 0.96.

Dubois et al., (1995), developed an algorithm that also employs only the co-polarized channels to estimate s and m_v . Their equations are:

$$\sigma_{hh}^o = 10^{-2.75} \frac{\cos^{1.5} \theta_i}{\sin^5 \theta_i} 10^{0.028 \epsilon \tan \theta_i} \cdot (\kappa s \sin \theta_i)^{1.4} \lambda^{0.7} \quad (27)$$

$$\sigma_{vv}^o = 10^{-2.35} \frac{\cos^3 \theta_i}{\sin^3 \theta_i} 10^{0.046 \epsilon \tan \theta_i} \cdot (\kappa s \sin \theta_i)^{1.1} \lambda^{0.7} \quad (28)$$

Here ϵ is the real part of the complex dielectric constant. According to the authors, the algorithm is optimized to work at a frequency between 1.5 and 11 GHz and gives best results for $\kappa s \leq 2.5$, $m_v \leq 35\%$, and $\theta \geq 30^\circ$. They used a simple criteria based on the $\sigma_{hv}^o / \sigma_{vv}^o$ ratio to select the areas where the inversion is not impaired by the vegetation. To test their algorithm, they used several SAR data sets taken between 1991 and 1994 from airborne (AIRSAR) and spaceborne (SIR-C) for bare surfaces, under a large range of sampling conditions. They found an RMS error in the estimated soil moisture to be less than 4.2%.

The following general statements can be made:

- The models require polarimetric data, not always available;
- The models work better at lower frequencies (L band);
- Absolute calibration accuracy is a problem, since the model is quite sensitive to uncertainties in the backscattering;
- The models are of a semi-empirical nature, such that a lot of independent data throughout the world must be tested for before being certified as operational.

The Bebedouro SIR-C Hydrology Supersite

We introduce here the preliminary results of testing the empirical model of Dubois et al., (1995), over

the Bebedouro SIR-C/X-SAR Supersite (JPL Publication 93-29). The area is located on the left bank ($9^{\circ}07'S$, $40^{\circ}18'W$) of the São Francisco River, a major north-south trending flowing river system. The river crosses a vast semi-arid region in northeast Brazil, where a government sponsored development program will irrigate over 1 million hectares for agriculture, of which 200,000 have already been irrigated. In the Bebedouro Irrigation Project, BIP, individual farms range from 5 to 12 ha and the total irrigated area is 1750 ha (Soares et al., 1988). Crops and orchards in the BIP include mango, vine, tomato, melon and water melon. Other types of land cover (found at the time of the SIR-C April'94 flight) are pasture, pasture with bushes, and bare soil. We used a total of 6 scenes taken on April 9, April 10, April 13, April 14 (two, ascending and descending) and April 15.

Soil moisture and roughness measurements were taken over 13 fields scattered all over the test site. Soil moisture sampling were done at two layers: 0-5 cm and 5-10 cm, on a daily basis, during the SIR-C/X-SAR April'94 flight. Four sampling points were done for each field, with five repetitions each. Over 2000 samples were collected, weighted, dried out and weighted again. There was a rainfall of 80 mm the night before the first SIR-C overpass (April, 8, 1994), and it did not rain for the rest of the experiment. Because top 30 cm of the dominant soil are sandy, some fields were irrigated for planting 5 days after the rainfall. Surface roughness was estimated using photographs of a gridded panel oriented both parallel and perpendicular to radar swaths. Photographs were digitized and the *rms* height was calculated.

We tested the inversion of equations (27) and (28) to derive both *rms* height and the dielectric constant ϵ and compared them with the "in situ" measured values. Soil moisture was calculated from dielectric constant using soil texture information as in Hallikainen et al., (1985). The results for soil moisture obtained from using both co-polarized L Band channels are plotted in figure 2 against the measured values. Only the averages are used in this case. Although the sensitivity of radar backscatter is very clear, the derived values are in general underestimated and the correlation coefficient is only moderate, indicating that this empirical model could not be used to map soil moisture with an acceptable accuracy. On the other hand if the *rms* height is previously known, we could use only one

co-polarized data set (either equation (27) or (28)). This situation is realistic in many cases, for which no agricultural practices are happening to change the surface roughness. Also, in the near future, for technical reasons, multipolarimetric spaceborne SAR are not likely to fly, what brings the problem of "a priori" knowledge of soil roughness if one are interested in estimating soil moisture. Figure 3 displays the comparison between model derived and measured values, using L band VV polarization (equation (28)). In this case, the underestimation is minimized and the correlation coefficient is higher. One can notice that the variance tends to be higher when m_v is higher than 25% in volume, which is in agreement with the findings of Dubois et al., (1985). There may be situations where realistic estimates of roughness could be done over a stable region, after days of continuous rainfall that saturates the soil; in this case soil moisture is an input and *rms* height is obtained from inversion of equation (28). On the other hand, when the HH polarization is used (figure 4), the correlation coefficient is smaller indicating that there may be problems of fitting for equation (27). Dubois et al., (1995) did not compare VV and HH polarization for their sensitivity to soil moisture. It appears, though, from this preliminary results, that the VV polarization are less sensitive to uncertainties on *rms* height, a result to be investigated as a follow up of this survey. To confirm these results, we show, in figures 4 and 5, the plots of the theoretical values for σ_{vv}^o and σ_{hh}^o corresponding to a range of m_v going from 0 to 40% and two *rms* height (0.3 to 1.4 cm). When *rms* height is 0.3 cm, σ_{vv}^o goes from -24 to -14 dB σ_{hh}^o varies between -27 and -21 dB as m_v changes from 0 to 40%. If the *rms* height of 1.4 cm is used, σ_{vv}^o goes from -17 to -7 dB and σ_{hh}^o varies between -18 and -11 dB in the same range of m_v . Ulaby et Siquiera, (1995), show that, for their model, σ_{vv}^o rises from -23 to -13 dB as soil moisture goes from 0 to 40% in volume, a 10 dB change, while σ_{hh}^o increases from -23 to -18, a 5 dB change (1.25 GHz, $s=1.5\text{cm}$, $\theta_i=40^\circ$). It is clear that, for both semi-empirical models, σ_{vv}^o is approximately twice as much sensitive to volumetric moisture variation.

Measured "in situ" *rms* height used in our tests were between 0.33 and 1.4 cm. They correspond to

ks from 0.087 and 0.37 for L band and from 0.37 and 1.57 for C band.

According to Dubois et al.,(1995), the science requirements for the SIR-C Calibration accuracy at both L and C bands are ± 2.0 dB / ± 0.4 dB for absolute and relative calibration, respectively. It is obvious that, since as much as 4 dB change could happen due only to calibration problems (in the worst case), absolute calibration errors are an important source of scattering in the cluster. Obviously, since the *hh* polarization is less sensitive to soil moisture changes, it is more affected by absolute calibration inaccuracy.

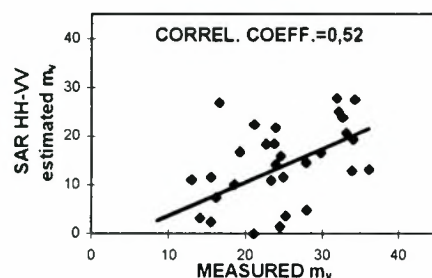


Figure 2. SAR derived soil moisture using the two co-polarized bands (L Band) versus measured soil moisture.

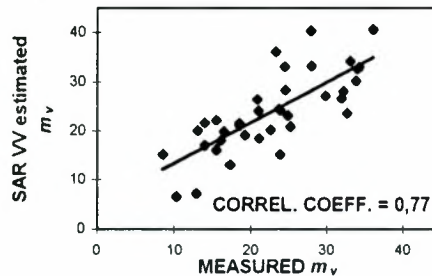


Figure 3. SAR derived soil moisture using the one co-polarized band (VV, L Band) versus measured soil moisture.

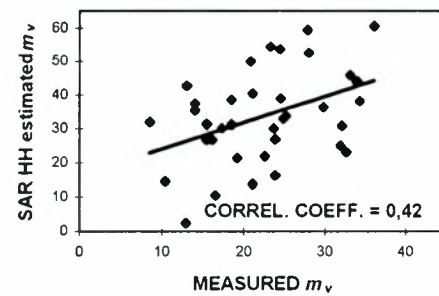


Figure 4. SAR derived soil moisture using the one co-polarized band (HH, L Band) versus measured soil moisture.

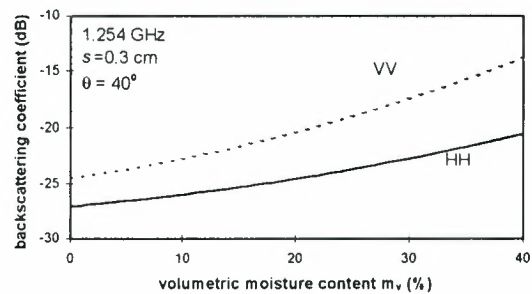


Figura 5. Plots of σ_{vv}^0 and σ_{hh}^0 as a function of m_v (L band, $s=0.3$ cm, $\theta=40^\circ$).

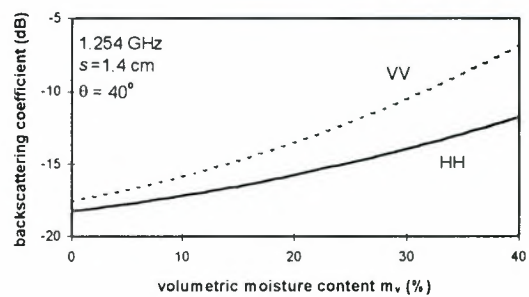


Figura 6. Plots of σ_{vv}^0 and σ_{hh}^0 as a function of m_v (L band, $s=1.4$ cm, $\theta=40^\circ$).

Acknowledgment

The authors would like to thank the "Conselho Nacional de Desenvolvimento Científico e Tecnológico", CNPq, through the project PROTEM-CC GEOTEC Nº 680.061-94-0

References

- Hallikainen, M. T. & al, 1985, Microwave dielectric behavior of wet soil - part I: empirical models and experimental observations, *IEEE Trans. G. Rem Sens*, 23, 25-34
- Dubois, P. C. & al, 1985, Measuring soil moisture with imaging radars, *IEEE Trans. G. Rem Sens*, 33, 915-926
- Ulaby, F. T. & Batlivala, P.P., 1976, Optimum radar parameters for mapping soil moisture, *IEEE Trans. Electronics*, GE-14, 81-93
- Ulaby, F.T. & al, 1978, Microwave backscatter dependence on surface roughness, soil moisture and

soil texture: part I - bare soil, *IEEE Trans. Electronics*, GE-16, 286-295

Ulaby et al., 1986, Microwave remote sensing: active and passive, 3, from theory to applications, Dedham, MA, Artech House, 1065-2162

Ulaby, F.T. & Siquiera, P., 1995, Polarimetric SAR soil moisture inversion algorithms, University of Michigan, Technical Memorandum 95-12

Wang, J. R. & al 1986, The SIR-B observations of microwave backscatter dependence on soil moisture, surface roughness, and vegetation covers, *IEEE Trans. G. Rem Sens*, GE-24, 510-516

Soares et al 1988, Estimation of bare soil evaporation from airborne measurements, *Journal of Hydrology*, 99, 281-296.

Bernard et al 1986, Differential bare field drainage properties from airborne microwave observation. *W. Res Research*, 17, 869-875.

Cognard et al 1995, Evaluation of the ERS 1/Synthetic Aperture radar capacity to estimate surface soil moisture: two-year results over the Naizin watershed, *W. Res Research*, 31, 975-982.

Chen, M. F. & Fung A. K., 1988, A numerical study of the regions of validity of the Kirchhoff and small-perturbation rough surface scattering models, *Radio Science*, 23, 163-170.

Shi, J., et al., 1992, Development of soil moisture retrieval algorithm for L-Band SAR measurements, IGARSS'92, Houston, TX, EUA.

Oh, Y. & al 1992, An empirical model and an inversion technique for radar scattering from bare soil surfaces, *IEEE Trans. G. Rem Sens*, 30, 370-381.

Oh, Y. et al 1994, An Inversion algorithm for retrieving soil moisture and surface roughness from polarimetric radar observations, IGARSS'94, Pasadena, Ca, USA.

SPECKLE REDUCTION IN SAR IMAGES BY USING DISCRETE WAVELET TRANSFORM

Saturnino Leguizamón

CONAE - Gerencia Gestión Tecnológica
C.C. 131, 5500 Mendoza, Argentina
Phone: +54-61-288654, Fax: +54-61-288565
e-mail: ntcricyt@arcriba.edu.ar

ABSTRACT

SAR (Synthetic Aperture Radar) images are affected by the presence of a multiplicative noise, called the *speckle*. This noise gives these sort of images the typical "salt and pepper" aspect. When this information is used in combination with optical images (e.g. TM, SPOT images) this feature of radar images is a drawback. Therefore, assuming some statistical properties of the speckle, different types of spatial filters are being used to overcome this problem. In the last decade Wavelet Transform (WT) has an increasing interest in the field of remote sensing due to its advantage in the analysis of non-stationary signals and other advantages in respect of Fourier analysis. In this paper we explore the application of WT to reduce the speckle. Wavelet transform provides a complete description of the image at all available scales by means of the multiresolution analysis (MRA). Using this technique, which is a pyramidal analysis, the image under study can be decomposed in lower resolution images representing the general structure of it, and images with high frequency features in which the speckle is included. The approach used here operates on the decomposed image by reducing or modifying some of the high frequency components and, after that, reconstructing the filtered new image. Some experiments have been conducted using this approach on different radar images. The preliminary results of these experiences show that this approach offers a promising future.

1. INTRODUCTION

Synthetic Aperture Radar (SAR) images are characterized by the presence of a granular noise, called speckle noise, of a multiplicative nature which stems from the manner in which the images are formed.

Due to this noise, the interpretation of the image, as well as the performance of some processes, are difficult. Reducing the speckle would improve the discrimination among different land features. It would also make easier the fusion between optical and radar images, and it would make the classifiers of radar images more efficient.

To achieve that goal one needs to make use of a certain class of filters. According to Lopes *et al.* (1990) the desirable characteristic of despeckling filters should be: in the case of homogeneous areas (agricultural areas, for example), the filters should preserve the backscattering coefficient value (the radiometric information) and edges between different areas. For textured areas (forest for example), the filters should preserve the spatial variability. (textural information).

Along the years, many efforts have been made to overcome this inherent problem in radar images. A number of different programs have been written using a variety of algorithms to despeckle noisy images. Filters based on the statistical properties of the image, such as Lee or Frost, are very popular. Adaptive filters also seem to be suitable for preserving radiometric and textural information (Frery *et al.*, 1993). The problem, however, is still present.

The wavelet transform is a mathematical tool developed in the late 1980's to deal with the analysis of nonstationary signals. It can be interpreted as a scale invariant transform which makes it suitable to deal with fractal or complex signals (Chui, 1992). The purpose of this paper is to present the potentialities of the WT to deal with some difficult problems presented in radar image processing.

The application of wavelets to reduce speckle is not new. Ranchin *et al.* (1993) and Caneau *et al* (1993) used the wavelet decomposition to reduce the speckle by using the Wiener filter approach. There are, however, few papers using this technique or reporting some experiences in this field.

The approach considered in this paper intends to point out the inherent properties of the WT and not in the design, or application, of sophisticated filters. To that end, a simple filter such as the median filter was applied to the resulting sub-images of a WT decomposition. The filtering was applied at different resolution levels of two radar images. For the assessment of the results a simple parameter, the coefficient of variation, was used.

The paper is organized as follows: Section 2 describes the

fundamentals of WT and its application in the multiresolution analysis of images. Section 3 explains the despeckling procedure and gives details of the experiences carried out on radar images by using the WT. Section 4 presents the conclusions.

2.-FUNDAMENTALS OF WAVELET TRANSFORM

2.1.- The Continuous Wavelet Transform

The Continuous Wavelet Transform (CWT) is a mathematical tool developed in late 1980's to deal with the analysis of nonstationary signals (Grossman and Morlet, 1984). Daubechies (1990, 1992) showed that there are functions ψ , called *mother* wavelets, whose translations and dilations are orthonormal bases of $L^2(\mathbb{R})$, which is the vector space of the measurable, square integrable 1-d function $f(x)$. In the one dimensional case, this family of functions can be expressed as,

$$\psi^{a,b}(x) = \frac{1}{\sqrt{a}} \psi\left(\frac{x-b}{a}\right) \quad a, b \in \mathbb{R}, a \neq 0 \quad (1)$$

In Eq. 1, a is a scaling parameter, while b is a shift parameter. The *mother* wavelet has to satisfy $\int \psi(x) dx = 0$, which implies at least some oscillations. The condition on ψ , known as admissibility condition, can also be expressed as $\int |\Psi(\omega)|^2 |\omega^{-1}| d\omega < \infty$, where $\Psi(\omega)$ is the Fourier transform of $\psi(t)$. The basic idea of the wavelet transform is to represent any arbitrary function f as a superposition of wavelets. Any such superposition decomposes f into different scale levels, where each level is then further decomposed with a resolution adapted to the level.

2.2.- The Discrete Wavelet Transform

The Discrete Wavelet Transform (DWT) is an extension of the wavelet series for finite-length discretized signals. The DWT is applicable to sampled continuous time signals. It is derived by quantizing the scale and the shift parameters. As with the CWT, it decomposes a function into a series of wavelet basis functions which are dilated and translated. The wavelet decomposition of f is then written as:

$$f = \sum c_{m,n}(f) \psi_{m,n} \quad (2)$$

$$\psi_{m,n}(x) = a_0^{-m/2} \psi(a_0^{-m}x - nb_0) \quad (3)$$

where $a = a_0^m$, $b = nb_0a_0^m$, $m, n \in \mathbb{Z}$, and $a_0 > 1$, $b_0 > 0$ fixed.

For practical reasons, in such decompositions the values $a_0=2$, and $b_0=1$ are used. In this case, the coefficients $c_{m,n}$ can be written as in Eq. (4).

$$c_{m,n}(f) = \langle \psi_{m,n}, f \rangle = \int \psi_{m,n}(x) f(x) dx \quad (4)$$

2.3.- Multiresolution Analysis

In a multiresolution analysis (MRA) (Mallat, 1989), the mother wavelet ψ and a *scaling function* ϕ can be chosen in such a manner that the translations and dilating of ϕ form a basis for a vector space denoted as V_m . Letting m vary, it results in a sequence of successive approximations spaces,

$$\dots V_2 \subset V_1 \subset V_0 \subset V_{-1} \subset V_{-2} \dots \quad (5)$$

V_m is said to have a resolution of 2^{-m} . Translations of ψ span a vector space W_m that is the complement of V_m in V_{m-1} .

The approximation of an arbitrary input function f at a resolution 2^{-m} (denoted as $A_m(f)$) is given by the projection of f onto the vector space V_m . The information lost when going from an approximation of f at resolution 2^{-m} to the coarser approximation $A_{m+1}(f)$ with resolution $2^{-(m+1)}$, is referred to as the error, or *detail* signal $D_{m+1}(f)$.

Let h and g be the impulse responses for decomposition (or analysis) low-pass and high-pass filters, respectively. Given the approximation of f at a resolution 2^{-m} (i.e., $A_m(f)$), $A_{m+1}(f)$ and $D_{m+1}(f)$ can be computed by filtering $A_m(f)$ with h and g and then keeping every other sample of the output. This algorithm is illustrated by the block diagram shown in Fig. 1.a. Approximations at lower resolutions are obtained by repeated application of this algorithm.

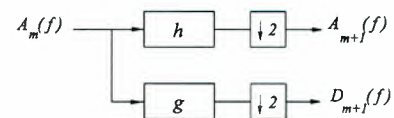


Fig.1.a.- Wavelet decomposition

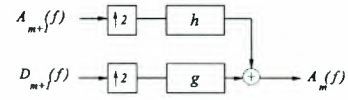


Fig.1.b.- Wavelet reconstruction

On the other hand, given $A_{m+1}(f)$, $D_{m+1}(f)$ and the necessary functions ψ and ϕ (wavelet and scaling functions), $A_m(f)$ can be perfectly reconstructed by interpolating $A_{m+1}(f)$ and $D_{m+1}(f)$ by a factor of two and filtering the resulting signals with h and g , respectively.

The block diagram shown in Fig. 1.b illustrates this algorithm. Observing Figs. 1.a and 1.b, it is easy to derive that the DWT is essentially a subband decomposition systems. Hence, the terms *subband decomposition* and *wavelet decomposition* are used interchangeably in the wavelet literature (Vetterli *et al.*, 1992).

In the case of 2-D signals, which is the case of images, the decomposition can be obtained by successive 1-D processing along the rows and columns of an image. Fig.2 shows the resulting set of sub-images after two steps of a WT decomposition.

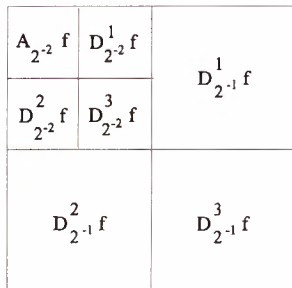


Fig.2.- Wavelet representation, pyramid structure

3. DESPECKLING PROCEDURE

3.1. Filtering of Images by WT

From the frequency point of view, the direct WT of an image is a decomposition of a bidimensional signal in subbands of different frequencies. After this decompositon, one can operate on the resulting components. The filtering method consists of modifications or elimination of some of the components. After that, the application of the inverse WT is necessary in order to obtain the filtered image. In this sense, filtering by WT can be considered similar to Laplace transform or other transformations dealing with the frequency components of a signal. WT has, however, some properties from which advantages can be taken. One of this properties, after the application of a multiresolution process, is the possibility of operate on images at different scales. In this way selected components, at different scales, can be modified or filtered. The general procedure to perform the mentioned task is presented in Fig.3.

3.2.- Materials and Methodology

In our study we used one SAR image obtained from the ERS-1 satellite covering the city of Mar del Plata (in Argentina) and its nearby agricultural areas. In our study we used two portions of the SAR image of 512 x 512 pixels. In this paper they are referred as Image 1 (Fig.4) and Image 2 (in the upper left corner of Fig. 6).

As Fig. 3 shows, the despeckling procedure presented here relies on three steps: (1) the decomposition of the speckled

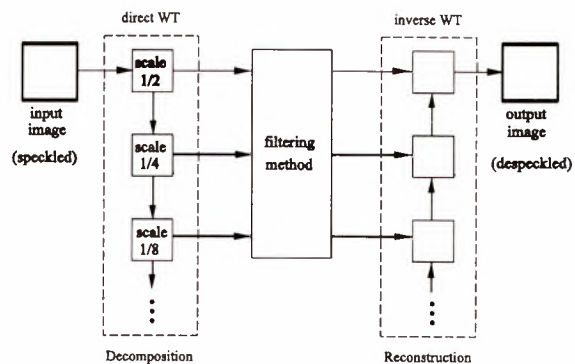


Fig.3.- General despeckling method by using wavelet transform

image by using the MRA algorithm, (2) application of filtering to all of the details components in any, or some, resolution levels, and (3) application of the inverse WT for the reconstruction of the processed image.

Even though the process is conceptually simple, there are some questions to answer, particularly related to steps 1 and 2. Some of these questions are:

- how many resolution levels may be considered in the decomposition stage.
- which filter should be used.
- on which component, or components, may be applied the filter process for a more efficient result.

There is, however, other important question to answer in the application of the WT: which wavelet performs better for the desired goal. In our work the 4 coefficient Daubechies wavelet was used (Daubechies, 1990).

Observing the results obtained in the experiences conducted on different images, the number of resolution levels should not be greater than 3. The best results of despeckling were obtained by applying filtering only in the first or second resolution step. Referring to the filter, we used a simple median 3x3 filter which performed well for the despeckling operation.

3.3.- Operations on image 1.

As previously mentioned, three resolution levels were performed on image 1. This implies that 3 direct WT and 3 inverse WT are needed. If three resolution steps of a multiresolution decomposition are performed, and if no filtering is applied, the original image is recovered at the end of the process. To achieve a despeckling effect, at least one filtering operation at one resolution level, has to be carried out.

In our experience, the filtering operation was applied to all



Fig.4.- Image 1, SAR image of the ERS-1 satellite of Mar del Plata (Buenos Aires), Argentina.

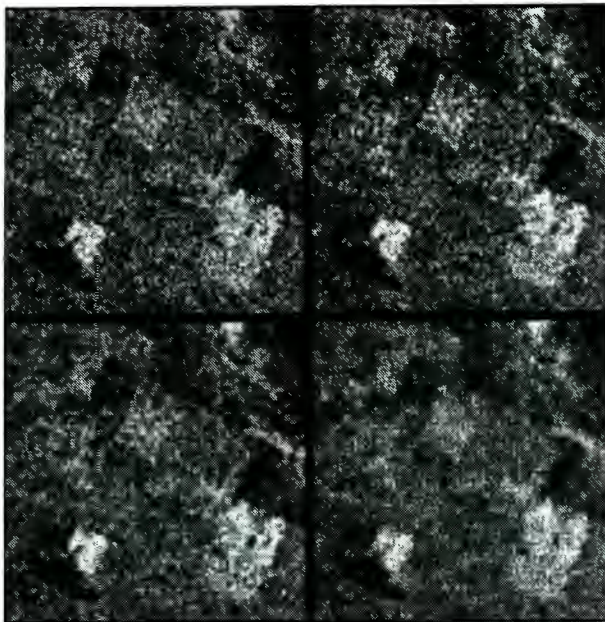


Fig. 5.- From top to bottom and from left to right, sub-images of: Image 1, IIf-1, IIf-2 and IIf-3.

3 high frequency components (detail sub-images) of a decomposition. But this procedure was applied to the combinations of one, two or the tree resolution levels.

The application of 3 resolution steps gives place to 7 different combinations of filtering and, as a consequence, 7 processed images were obtained.

For the assessment of the filtering process the coefficient of variation (CV) measured on the same 4 homogeneous sections of the processed images was used. It is considered that the despeckling effect is better when the CV measured

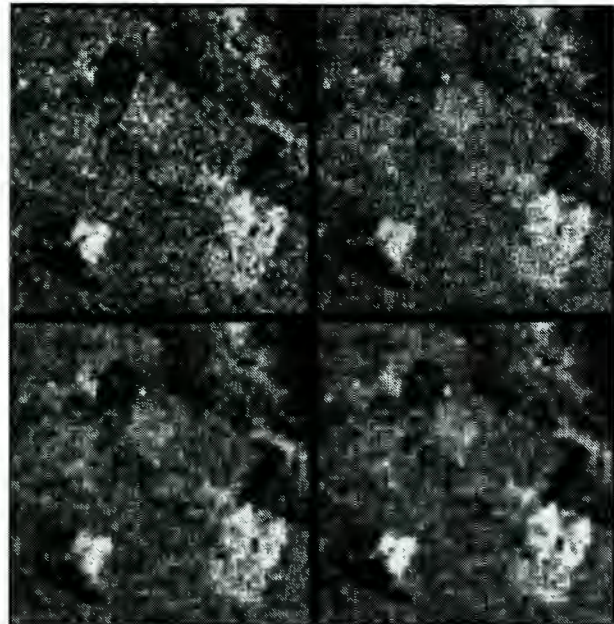


Fig. 6.- From top to bottom and from left to right, sub-images of: Image 1, IIf12, IIf-13, IIf-23 and IIf-123.

on the processed image is lower than the CV measured on the unfiltered image. The CV is one of the simplest and most popular parameters to measure the performance of a despeckling filters (Ranchin *et al.*, 1993). In our experience, however, it has been found that this parameter is not good enough to measure some undesirable characteristics appearing because of the use of WT decomposition.

Tabla 1.- Coefficient of variation calculated in 4 sectors of Image 1 and the derived images.

Image	sector 1	sector 2	sector 3	sector 4
Image 1	0.3258	0.3557	0.3849	0.3828
IIf-1	0.2859	0.3207	0.3555	0.3478
IIf-2	0.2670	0.2959	0.3321	0.3366
IIf-3	0.2873	0.3217	0.3559	0.3492
IIf-12	0.2113	0.2494	0.2931	0.2931
IIf-13	0.2364	0.2791	0.3205	0.3116
IIf-23	0.2180	0.2511	0.2963	0.2897
IIf-123	0.1432	0.1937	0.2522	0.2378

The evaluation of the process was applied to the 7 resulting images of the despeckled images. The CV values of each image, measured on 4 selected sectors of the processed image are presented in Table 1. Fig. 5 shows the graphical behaviour of the CV parameter.

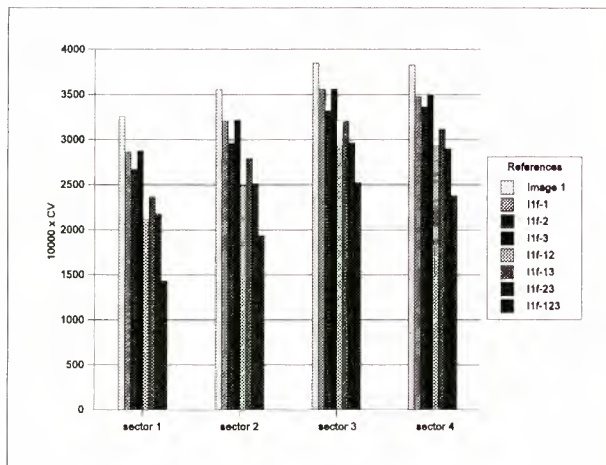


Fig. 7.- Coefficient of variation (CV) of 4 sectors in each image obtained after processing Image 1.

From the information provided by Table 1 and Fig. 7, and based only on the values taken by the CV, it is possible to see that filtering of the image at least in a single resolution step, produces an improvement of CV values. However, the visual observation of the resulting images may be not as good as one may desire. The application of filtering in all 3 resolution levels, for example, gives the lowest CV values, but it provides an image too much "smoothed". The processed resulting images can be observed in Fig. 5 and Fig. 6.

3.4.- Operations on Image 2

The process applied to image 1 was also applied to Image 2. Image 2 was chosen because it presents an airport runway clearly visible in the upper right corner of the image (see Fig. 8). This is useful because it allows the evaluation of the despeckling process in the presence of sharp edges.

After the despeckling process was applied to Image 2 the following images were obtained:

- Image **I2f-1**, filtering in step 1
- Image **I2f-2**, filtering in step 2
- Image **I2f-12**, filtering in steps 1 and 2
- Image **I2f-23**, filtering in steps 2 and 3
- Image **I2f-123**, filtering in steps 1, 2 and 3

Table 2 shows the CV values measured in 4 selected sectors of Image 2. According to Table 2 the best result should be obtained by the process which takes into account the third resolution level. In this case the image I2f-23 should be the best because it has the lowest CV value. However, this result is not good because strong distortions of the original scene have been produced.

The deformation, produced by filtering in the third resolution step, is easily seen in image I2f-23 of Fig. 8. To show more clearly the visual effects of the **Tabla 2**

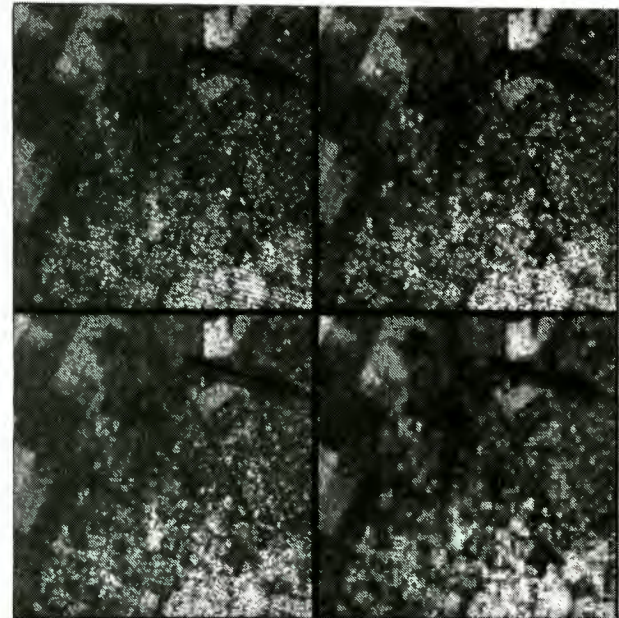


Fig.8.- From top to bottom and from left to right, Image 2, I2f-12, I2f-2 and I2f-23.

..- Coefficient of variation calculated in 4 sectors of Image 2 and derived images.

Image	sector 1	sector 2	sector 3	sector 4
Image 2	0.4294	0.3965	0.4993	0.4860
I2f-1	0.3988	0.3678	0.4446	0.4609
I2f-2	0.3902	0.3597	0.4252	0.4494
I2f-12	0.3531	0.3236	0.3910	0.4213
I2f-23	0.3648	0.3234	0.3689	0.4047
I2f-123	0.3252	0.2830	0.3267	0.3710

of the despeckling operations on Image 2, a sector of each image of Fig.8 is presented in Figs. 9,10,11 and 12.

4.- CONCLUSIONS

The purpose of this paper is to present the potentialities of the Wavelet Transform (WT) to deal with the speckle noise reduction in radar images. Although many techniques have been developed to perform this task, they are not completely satisfactory and the exploration of new tools to face this problem is mandatory.

The approach considered in this paper intends to emphasize the use of the inherent properties of the WT and not the properties of a sophisticated filter. To that end, a simple median filter has been applied to one or several sub-images arisen in a WT decomposition.



Fig. 9.- Sector of Image 2



Fig. 11- Sector of Image I2f-2.



Fig. 10.- Sector of image I2f-12



Fig. 12.- Sector of image I2f-23.

The methodology was applied to two images and after the visual evaluation of the results, and the assessment of the process by means of a simple parameter: the coefficient of variation, the following conclusions were obtained: 1) The wavelet transform is a promising tool to deal with speckle reduction. 2) Satisfactory results of the method were accomplished working on sub-images with resolution levels not lower than 2.

The filtering of images of lower resolutions introduces modifications to the original structure of the scene. 3) For further studies, new types of wavelet need to be explored.

5. REFERENCES

- Chui, C.K.**, 1992, *An Introduction to Wavelets*, Academic Press.
- Daubechies I.**, 1990, *The Wavelet Transform, Time-Frequency Localization , and Signal Analysis*, IEEE Trans. Inform. Theory, vol. 36, No. 9, pp. 961-1005.
- Daubechies, I.**, 1992, *Ten Lectures on Wavelets*, CBMS-NSF Regional Conference Series in Applied Mathematics, SIAM.
- Frery, A, and S. Sant'Anna**, 1993, *Non-Adaptive Robust Filters for Speckle Noise Reduction*, Proc. of the Simposio Brasileiro de Comp. Grafica e Proc. de Imagens, Recife, PE., Brasil.

Grossman A. and J. Morlet, 1984, *Decomposition of Hardy Functions into Square Integrable Wavelets of Constant Shape*", SIAM Journal of Mathematical Analysis, vol. 15, pp. 723-736.

Lee, J.S., 1980, *Digital Image Enhancement and Noise Filtering by Use of Local Statistics*, IEEE Trans. on Patt. Anal. and Mach. Intell. vol. PAMI-2, No2, pp. 165-168.

Lopes, R.Touzi and E. Nezry (1990), *Adaptive Speckle Filters and Scene Heterogeneity*, IEEE Trans. on Geosc. and Rem. Sens., vol. 28, No. 6, pp. 992-1000.

Mallat, S.G. , 1989, *A Theory for Multiresolution Signal Decomposition*, IEEE Trans. on Pattern Analysis and Machine Intell., vol. 11, pp. 674-693.

Ranchin, T. and L. Wald, 1993, *The Wavelet Transform for the Analysis of Remotely Sensed Images*, Int. J. Remote Sensing, vol. 14, No.3, pp. 615-619.

Ranchin T. and F. Caneau, 1993, *Speckle Reduction in Synthetic Aperture Radar Imagery using Wavelets*, Proc. of the SPIE's 1993 Internat. Symp. on Optics and Instrument. San Diego Cal., USA, vol 2034, pp. 432-441.

Vetterli M. and C. Herley, 1992, *Wavelet and Filter Banks: Theory and Design*, IEEE Trans. on Signal Proc., vol. 40, pp. 2207-2231.

ACKNOWLEDGMENTS

Thanks to ESA for the provision of ERS-1 SAR images and to Dr. T. Ranchin who encourages to me to work in this subject.

**REDE NEURAL NÃO SUPERVISIONADA BASEADA EM TRANSFORMADA
KARHUNEN-LOÈVE PARA PROCESSAMENTO, COMPRESSÃO E RECONHECIMENTO DE
IMAGENS**

João Fernando Marar[†]
Edson Costa de Barros Carvalho Filho[‡]
José Dias dos Santos[‡]

[†]UNESP – Universidade Estadual Paulista
Laboratório de Sistemas de Tempo Real
Faculdade de Ciências - Depto de Computação
Bauru, SP, Brasil

[‡]UFPE – Universidade Federal de Pernambuco
DI – Departamento de Informática
50732-970, CP 7851, Recife, PE, Brasil
{jfm,ecdbcf,jds}@di.ufpe.br

ABSTRACT

The merit of the Karhunen-Loève transform is well known. Since its basis is the eigenvector set of the covariance matrix, a statistical, not functional, representation of the variance in pattern ensembles is generated. By using the Karhunen-Loève transform coefficients as a natural feature representation of a character image, the eigenvector set can be regarded as an feature extractor for a classifier.

Keywords: Karhunen-Loève Transform; Pattern Recognition; Neural Networks.

1. Introdução

Para o poderoso e complexo sistema visual humano, uma simples imagem engloba uma vasta quantidade de informações. A grande maioria dessas informações são difíceis de serem expressadas com igual concisão, precisão e flexibilidade através de mecanismos artificiais. O cérebro humano, por sua vez, é capaz de extrair características essenciais de uma imagem em um simples relance, registrando o específico padrão, bem como, ele consegue reconhecer padrões mesmo na presença de ruídos, transformações geométricas, movimento, entre outros.

A ciência, em todo seu contexto, procura meios de desvendar os mistérios cerebrais associados a visão e outras habilidades humanas, com a finalidade de construir dispositivos artificiais que realizem tais tarefas com tamanha perfeição. Durante as últimas décadas, a área de processamento de imagens têm dedicado muita pesquisa na elaboração de modelos matemáticos para o processamento, descrição e classificação de imagens [COO 65],[OPP 75], [PRO 88],[GON 92].

Atualmente, em processamento de imagens tem ocorrido um razoável investimento em pesquisas para o desenvolvimento de novas técnicas e métodos que possam ser em-

pregados em um amplo domínio de aplicações [GON 92]. Uma das preocupações básicas diz respeito com a transformação adequada de sinais, de modo que os mesmos possam ser analisados e formas comportadas de sua representação possam ser extraídas, economizando o espaço de memória necessário para o armazenamento e a diminuição da demanda computacional exigida.

O objetivo deste artigo é apresentar a transformada Karhunen-Loève como uma rede neural não supervisionada para processamento, compressão e reconhecimento de imagens localizadas em uma retina de pixels. Na realidade, o método apresentado trata-se de uma técnica matemática que possibilita a extração de um conjunto de características mensuráveis das imagens (padrões) que serão tratadas através de um classificador linear, onde um conjunto de padrões será apresentado para o reconhecimento. A base desta técnica reside na utilização da transformada Karhunen-Loève [CAM 71],[STA 88],[CHE 91], que corresponderá a parte de extração das principais componentes, onde cada imagem (padrão) é representado por um vetor de características e o reconhecimento do padrão é realizado através de medidas realizadas no espaço de características das classes existentes.

Nas seções que se seguem, trataremos de maneira mais geral sobre o espaço de características, transformadas ortogonais, conjunto de dados para a realização dos experimentos, compressão e reconstrução de imagens, reconhecimento de padrões e as conclusões.

2. Espaço de características via Transformadas Ortogonais

A idéia central desta seção é a transformação do espaço original dos padrões para outro com dimensão menor. De maneira que, esta nova representação dos padrões esteja livre de informações redundantes. Em geral, para se obter uma transformação adequada, adota-se um critério

de otimização, entre eles destacam-se o *mínimo erro quadrado* e a *entropia*. Estes critérios associados as transformações tem por objetivo auxiliar a discriminação das classes existentes, de maneira a maximizar as distâncias inter-classes e a minimização das distâncias intra-classes, em problemas de classificação.

Dentre as transformações mais utilizadas, destacamos a transformada de *Fourier* [COO 65],[OPP 75],[BLA 87] a transformada *Walsh-Hadamard* [HUT 75],[GON 92], a transformada *Haar*, a transformada *Karhunen-Loève* e mais recentemente as *Wavelets* [DAU 88], [MAL 89],[DAU 90]. A transformada Karhunen-Loève (KLT) é ótima em relação ao critério de mínimo erro quadrado. Este método conhecido como análise das principais componentes (PCA) tem sido muito utilizado em aplicações onde a redução de dimensionalidade, torna-se necessária.

As transformações mencionadas acima são denominadas transformadas ortogonais, na seção seguinte, as descreveremos de maneira mais técnica.

3. Transformadas Ortogonais

As transformadas ortogonais constituem uma poderosa ferramenta matemática para representar funções extremamente complexas através de outras mais simples. Imagens podem ser vistas como funções. Uma importante aplicação desta técnica é a redução de dimensionalidade ou compressão de dados [AHM 75],[WOM 77]. Estas transformadas podem ser divididas em duas classes, segundo as funções básicas utilizadas. Desta forma, temos a classe baseada em funções não senoidais e a de funções senoidais, tendo esta última como única representante a transformada de Fourier.

Em geral, aplica-se esta técnica a um conjunto de dados obtidos experimentalmente, cujo objetivo é encontrar uma lei de formação para a função. Detalhes sobre a representação de funções através desta técnica serão expostas a seguir, bem como apresentaremos a transformada Karhunen-Loève, como uma das inúmeras representante da classe das transformadas ortogonais que são definidas através funções básicas não senoidais.

3.1. Extração de Características via Transformadas Ortogonais

Seja $\Psi = \{\psi_0(t), \psi_1(t), \dots, \psi_n(t), \dots\}$ um conjunto de funções reais e contínuas,(utilizamos funções reais por conveniência), será dito ortogonal no intervalo (t_0, t_0+T) se:

$$\int_{t_0}^{t_0+T} \psi_m(t)\psi_n(t)dt = \begin{cases} c_n & \text{se } m = n \\ 0 & \text{se } m \neq n \end{cases} \quad (1)$$

Para o caso onde $c_n = 1$, o conjunto Ψ é chamado ortonormal. Seja $x(t)$ uma função de valores reais, definida em um intervalo (t_0, t_0+T) , e suponha que $x(t)$ possa ser escrita na forma :

$$x(t) = \sum_{n=0}^{\infty} a_n \psi_n(t) \quad (2)$$

então os coeficientes a_n podem ser obtidos da seguinte forma : multiplicamos ambos os lados da equação 3 por ψ_m e integramos o resultado no intervalo (t_0, t_0+T) , onde obteremos :

$$\int_{t_0}^{t_0+T} x(t)\psi_m(t)dt = \int_{t_0}^{t_0+T} \sum_{n=0}^{\infty} a_n \psi_n(t)\psi_m(t)dt \quad (3)$$

Como ψ_m e ψ_n são ortogonais, temos :

$$a_m = \frac{1}{c_n} \int_{t_0}^{t_0+T} x(t)\psi_m(t)dt, \quad m = 0, 1, 2, \dots$$

Um conjunto de funções ortogonais é chamado fechado ou completo se for verificada a seguinte condição:

Para qualquer parte contínua de $x(t)$ com :

$$\int_{t_0}^{t_0+T} x^2(t)dt < \infty$$

Qualquer que seja $\epsilon > 0$, existe N tal que seja possível representar uma aproximação de $x(t)$ por uma expansão finita :

$$\int_{t_0}^{t_0+T} |x(t) - \hat{x}(t)|^2 dt < \epsilon$$

onde :

$$\hat{x}(t) = \sum_{n=0}^{N-1} a_n \psi_n(t)$$

Pelo desenvolvimento acima, é visível que por uma expansão em funções ortogonais, sempre será possível representar $x(t)$ por um conjunto infinito, mas enumerável $\{a_0, a_1, a_2, \dots\}$. Entretanto, quando Ψ for completo torna-se possível uma aproximação de $x(t)$ através de um conjunto finito $\{a_0, a_1, \dots, a_{N-1}\}$.

3.2. Extração de Características via Transformadas Karhunen-Loève

Seja $\{X\}$ um conjunto de vetores, obtidos por amostragem, de uma classe de sinais aleatórios, podendo ser um conjunto de imagens. Um representante de $\{X\}$ é dado por $x_j = (x_{j,1}, x_{j,2}, \dots, x_{j,N})$. A amostra x_j pode ser aproximada por 4:

$$x_j = y_{j,1}\psi_1 + y_{j,2}\psi_2 + \dots + y_{j,K}\psi_K = \sum_{i=1}^K y_{j,i}\psi_i \quad K < N \quad (4)$$

$$y_{j,i} = x_j^t \psi_i \quad i = 1, 2, \dots, K \quad (5)$$

onde N é o número total de componentes da amostra e K é o número de componentes utilizadas na aproximação.

Por definição, o mínimo erro quadrado, ε , é dado pela expressão 6:

$$\varepsilon = (\sum_{i=1}^N y_{j,i}\psi_i - \sum_{i=1}^K y_{j,i}\psi_i)^2 = \sum_{i=K+1}^N \psi_i^t R_X \psi_i \quad (6)$$

onde R_X corresponde a matriz de covariância do conjunto $\{X\}$. Dada por $R_x = \frac{1}{V} \sum_{j=1}^V (x_j - \bar{X})(x_j - \bar{X})^t$, onde V representa o número total de elementos do conjunto $\{X\}$ e \bar{X} é o vetor médio do referido conjunto.

Quando $\{\psi_i\}$ constituem a base ortogonal de Karhunen-Loève, os elementos ψ_i são determinados a partir dos autovetores de R_X , de acordo com a equação 7:

$$R_X \psi_i = \lambda_i \psi_i \quad (7)$$

onde λ_i são os autovalores da matriz de covariância.

De maneira que, o erro de truncamento da equação 6 é minimizado pela equação 8

$$\text{Min}_{\{\psi_i\}} \varepsilon = \sum_{i=K+1}^N \lambda_i \quad (8)$$

Isto significa que, se utilizarmos apenas K auto-vetores para a representação de funções, o erro de truncamento será a soma dos auto-valores da matriz de covariância, sendo dado pela equação 8. A equação 4, escrita em termos dos auto-vetores da matriz de covariância, é denominada expansão Karhunen-Loève. A Figura 1 ilustra a transformada Karhunen-Loève.

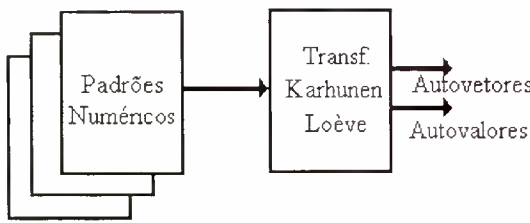


Figura 1: Extração dos Autovalores e Autovetores da matriz de covariância.

A correspondente transformação ortogonal inversa, na equação 5, é chamada transformada Karhunen-Loève [CHE 91].

4. Base de Imagens

Para investigarmos as propriedades fundamentais e a qualidade do método proposto, utilizamos a base de dados do *British Post Office* que possui um conjunto de dados alfanuméricos extraídos de envelopes de cartas. Este conjunto constitui-se de 34 classes de padrões, i.e., caracteres alfabeticos de A-Z e caracteres numéricos de 0-9.

Cada classe contém 300 amostras de padrões digitalizados e normalizados através de 384 pontos em preto e branco, sobre uma matriz de 24 linhas e 16 colunas. Nossa experimento baseou-se nas classes constituídas dos caracteres numéricos de 0-9, totalizando 3.000 padrões divididos em 10 classes. A figura 2 ilustra alguns dos melhores padrões existentes na base de dados.

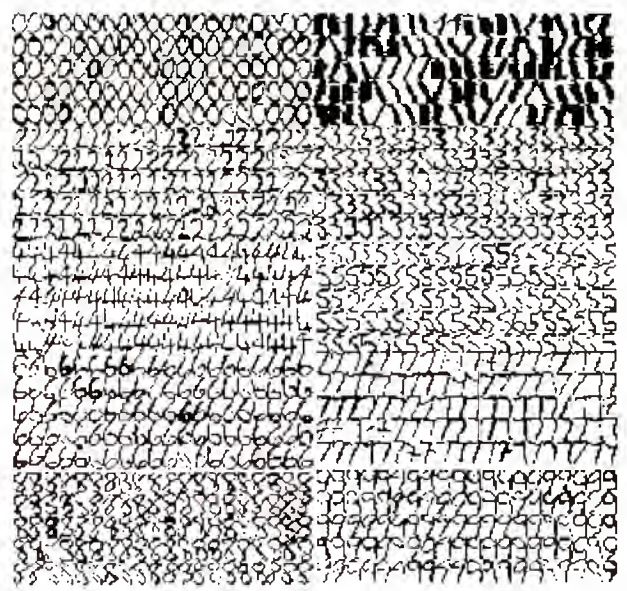


Figura 2: Exemplos de 100 amostras por classes de numerais existentes na base de imagens.

5. Compressão e Reconstrução de Imagens via Transformada Karhunen-Loève

Compressão de imagens é basicamente motivada pela redução de dados para o armazenamento, transmissão de imagens e reconstrução. Muitos métodos convencionais, incluindo a transformada rápida de Fourier, transformada coseno, transformada Walsh-Hadamard, transformada Wavelets, entre outros são disponíveis na prática [GON 92]. Nesta seção trataremos a teoria associada a transformada Karhunen-Loève para a compressão e reconstrução de imagens. A Figura 3 ilustra o modelo para a decomposição e reconstrução dos numerais.

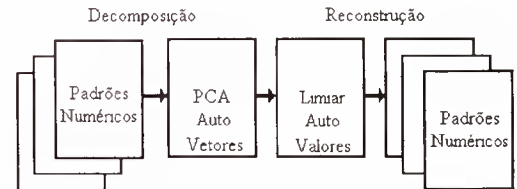


Figura 3: Método para decomposição e reconstrução de imagens baseado em limiares.

Sob o ponto de vista teórico, o mínimo erro quadrado é dado Equação 8. Neste contexto, vamos apresentar uma técnica de reconstrução de imagens numéricas baseada no conceito de função limiar extraída diretamente da Equação 8. Definimos uma função limiar, dada pela Equação 9 :

$$y_i = \begin{cases} 1 & \text{se } y_i > \text{limiar} \\ 0 & \text{se } y_i \leq \text{limiar} \end{cases} \quad (9)$$

onde limiar corresponde a soma de todos os autovalores associados as componentes que foram negligenciadas para a reconstrução.

A partir desta função, realizamos experimentos baseados na extração das principais componentes das primeiras 90 imagens do numeral zero, ilustrados na Figura 2. O gráfico da magnitude dos autovalores extraídos das imagens é ilustrado pela Figura 4.

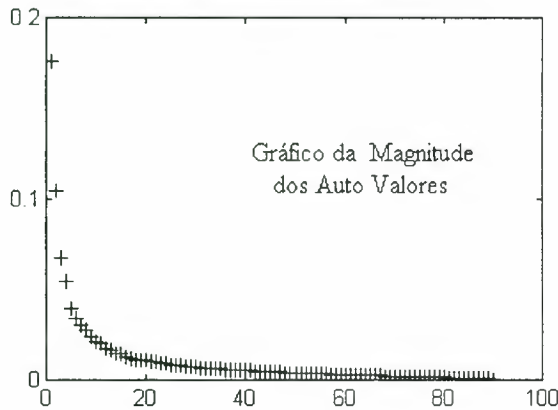


Figura 4: Valores normalizados dos autovalores para os 90 primeiros caracteres zeros da base de imagens.

Estabelecemos duas estratégias para a reconstrução das imagens. A primeira é a reconstrução de imagens utilizadas no processo da transformada Karhunen-Loéve. Dentre as 90 possíveis, escolhemos as imagens de números 1, 2, 3, 4 e 5. O outro experimento, testamos a reconstrução de imagens que não foram utilizadas no processo da transformada, onde selecionamos as imagens de números 91, 92, 93, 94 e 95. Os resultados obtidos são ilustrados na Figura 5.

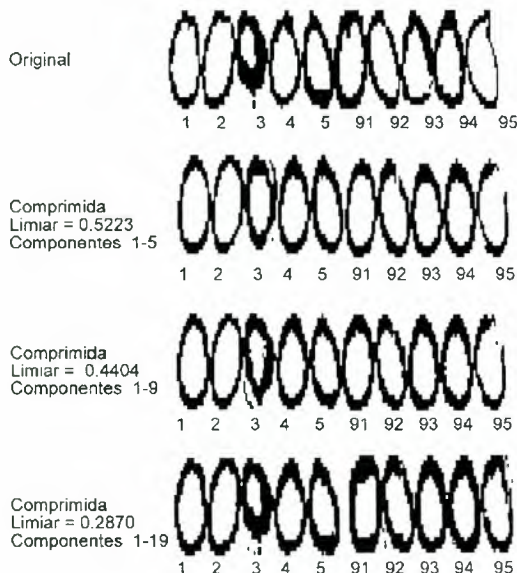


Figura 5: Resultados obtidos para a reconstrução de imagens numéricas através da função limiar.

6. Reconhecimento de Padrões

O estudo de reconhecimento de padrões pode ser dividido em duas áreas principais : *extração de características*

e *projeto do classificador*, como podemos observar na Figura 6.

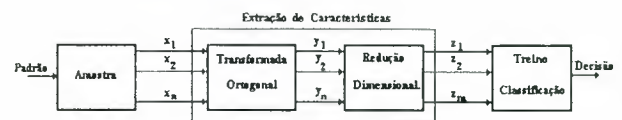


Figura 6: Representação gráfica do processo de Reconhecimento de Padrões.

O processo de amostragem, basicamente, fornece uma sequência de valores que definem o padrão dado. Após este processo, o padrão de entrada é tratado como um vetor N -dimensional.

6.1. Processo de Extração de Características e Redução de Dimensionalidade

Obtido o vetor, correspondente ao padrão de entrada, inicia-se o processo de extração de características. O primeiro estágio, consiste em uma transformação ortogonal dos valores de entrada (o padrão amostrado). Neste trabalho, utilizamos a transformada K-L , esta provê um mapeamento um para um, transformando a sequência de entrada $X,(x_1, x_2, \dots, x_n)$, em outra $Y,(y_1, y_2, \dots, y_n)$, de mesma dimensão.

Na prática, a dimensão dos padrões , N , é muito grande, sendo necessário sua redução. Por exemplo, neste trabalho, a dimensão dos padrões é $N = 384$. Utilizando-se das propriedades inerentes da transformada K-L, reduziremos a dimensionalidade. Desta forma, o segundo estágio do processo de extração de características é a escolha das componentes mais significativas do padrão de entrada. A saída deste módulo será um vetor $Z,(z_1, z_2, \dots, z_K)$, com K componentes de Y , tal que $K \ll N$. Esta redução de dimensionalidade é alcançada segundo os critérios que norteam a transformada Karhunen-Loëve, de maneira que o erro seja tão pequeno quanto se deseja e facilmente calculado através da equação 8. Sob outro ponto de vista, esta técnica pode ser tratada como uma rede neural com aprendizagem não supervisionada. A Figura 7 ilustra este processo.

O algoritmo de aprendizagem para este tipo de rede neural é dado por uma regra Hebbiana, definida pela Equação 10:

$$Pesos_{t+1} = Pesos_t + \delta(R_x.Pesos_t) \quad (10)$$

onde δ é a taxa de aprendizagem, R_x é a matriz de covariância e $Pesos_{t+1}$ são os elementos adaptativos da rede neural, o símbolo t significa o estado anterior e $t + 1$ o estado atual dos pesos.

O passo seguinte, consiste em classificar o padrão de entrada. Na realidade, o processo de classificação consiste inicialmente de um treinamento e posteriormente a classificação. A classificação é somente uma tomada de decisão, que nos informa qual a classe a que pertence o padrão dado.

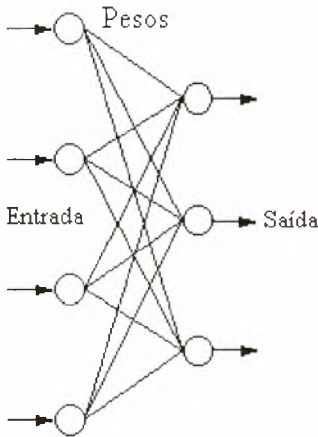


Figura 7: A transformada Karhunen-Loéve vista como uma rede neural linear.

6.2. Projeto do Classificador

Nosso desejo é construir e treinar um classificador que seja capaz de localizar automaticamente a classe a que pertence um determinado padrão Z , escrito através das funções básicas K-L e com dimensionalidade reduzida.

Projetaremos um classificador baseado no critério de mínima distância quadrada, este é definido a partir da seguinte regra:

Um padrão Z é dito pertencente a classe C_i se Z é mais próximo a \bar{Z}_i , onde C_i corresponde a classe i e \bar{Z}_i é o vetor médio da classe C_i .

A figura 8 ilustra o processo de classificação para três classes (C_1, C_2, C_3). Neste caso, o padrão Z será reconhecido como elemento pertencente a classe C_2 .

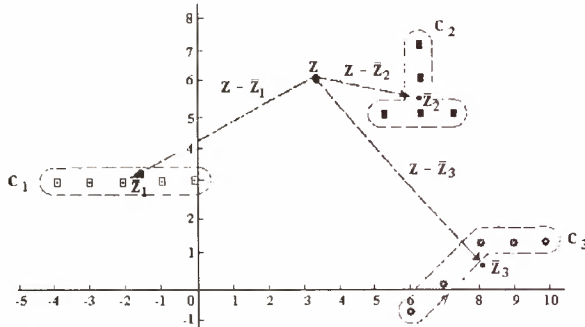


Figura 8: Representação geométrica de um classificador de mínima distância quadrada para três classes

Denotaremos por D_i^2 a distância quadrada entre Z e os \bar{Z}_i s. A fórmula para o cálculo da distância é dada por :

$$D_i^2 = |Z - \bar{Z}_i|^2 = (Z - \bar{Z}_i)(Z - \bar{Z}_i)^t \quad i = 1, \dots, r \quad (11)$$

onde Z é o padrão a ser classificado e \bar{Z}_i é o vetor médio da classe i , r é a quantidade de classes.

Reescrevendo a equação 11, temos :

$$D_i^2 = |Z|^2 - 2(Z \cdot \bar{Z}_i) + |\bar{Z}_i|^2 \quad i = 1, \dots, r \quad (12)$$

Observando a equação acima, D_i^2 é mínimo quando o termo $(Z \cdot \bar{Z}_i) - \frac{1}{2} |\bar{Z}_i|^2$ é o máximo. Assim, o classificador baseado na mínima distância deve calcular as distâncias do padrão para cada uma das classes, isto é, calcular D_i^2 da equação 12. Note que não é necessário calcular toda a expressão; basta apenas calcular o termo $(Z \cdot \bar{Z}_i) - \frac{1}{2} |\bar{Z}_i|^2$. Desta maneira, podemos descrever o classificador pela seguinte função de discriminação:

$$g_i(Z) = Z \cdot \bar{Z}_i - \frac{1}{2} |\bar{Z}_i|^2 \quad i = 1, \dots, r \quad (13)$$

onde o termo $\frac{1}{2} |\bar{Z}_i|^2$ é conhecido por limiar.

O classificador calculará "r" valores reais $g_1(Z), g_2(Z), \dots, g_r(Z)$ como mostra a Figura 9, e os compara. De maneira que, Z pertence a classe C_i quando $g_i(Z)$ for maior valor encontrado entre os $g_i(Z)$ para $i = 1, 2, \dots, r$. A implementação geral para este tipo de classificador é ilustrado na figura 9. Mostrando para r -classes.

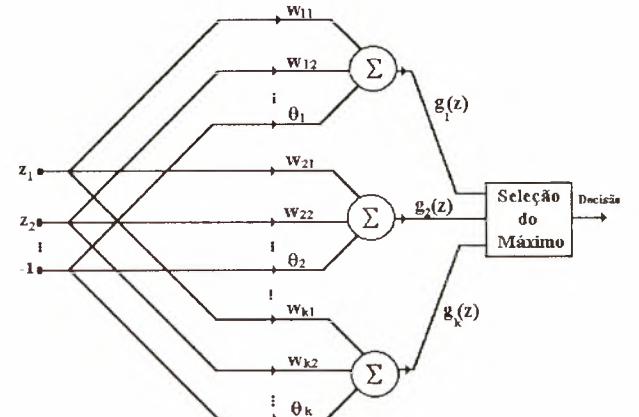


Figura 9: Classificador de mínima distância quadrada para k classes

Em nosso experimento, utilizamos para este classificador de 10-classes a seguinte função discriminadora :

$$g_i(Z) = Z \cdot \bar{Z}_i - \frac{1}{2} |\bar{Z}_i|^2 \quad i = 1, 2, \dots, 10 \quad (14)$$

onde \bar{Z}_i é o vetor padrão médio da classe C_i . Dado que $Z = (z_1, z_2, \dots, z_k)$, a função discriminação assume a seguinte forma :

$$g_i(Z) = w_{i,1}z_1 + w_{i,2}z_2 + \dots + w_{i,k}z_k - \theta_i, \quad i = 1, 2, \dots, 10$$

onde $\theta_i = \frac{1}{2} |\bar{Z}_i|^2$, $(w_{i,1}, w_{i,2}, \dots, w_{i,k})$ é o padrão médio da classe. A implementação desta técnica está baseado na figura 9

7. Conclusões

O trabalho demonstrou a utilização da transformada Karhunen-Loève como uma boa ferramenta para a extração e redução de características de padrões numéricas. A metodologia empregada, pode ser generalizada para padrões quaisquer em uma retina de pontos.

A transformada Karhunen-Loève foi aplicada a um conjunto de dados, com o objetivo de investigar sua adequabilidade e desempenho. Nos experimentos realizados, a técnica apresentou níveis de reconhecimento da ordem de 96.80%, demonstrando assim, sua viabilidade no processo de extração de características, redução de dimensionalidade em sistemas de reconhecimento de padrões.

Agradecimentos

Os autores agradecem o suporte financeiro da CAPES-PICD e CNPQ.

8. Referências

- [MAL 89] S.G. Mallat, *A Theory for Multiresolution Signal Decomposition : The Wavelet Representation*, IEEE Transactions on Pattern Analysis and Machine Intelligence, July 1.989, Vol. 11, Nro. 7, p 674-693.
- [OPP 75] A.V. Oppenheim, R.W. Schafer, *Digital Signal Processing*, Prentice-Hall international, Inc., London, 1.975.
- [PRO 88] J.G. Proakis, D.G. Manolakis, *Introduction to Digital Signal Processing*, Macmillan Publishing Company, New York, 1.988.
- [STA 88] J.C. Stapleton, S.C. Bass, *Synthesis of Musical Tones Based on the Karhunen-Loéve Transform*, IEEE Transactions on Acoustics, Speech and Signal Processing, Vol. 36, Nro. 3, March 1.988, p 305-319.
- [WOM 77] M.E. Womble, J.S. Halliday, S.K. Mitter, M.C. Lancaster, J.H. Triebwasser, *Data Compression for Storing and Transmitting*, Proceedings of the IEEE, Vol 65, Nro 5, May 1.977, p 702-706.
- [AHM 75] N. Ahmed, P.J. Milne, S.G. Harris, *Eletrocardiographic Data Compression Via Orthogonal Transforms*, IEEE Transactions on Biomedical Engineering, vol.bme-22,Nro 6, November 1.975, p 484-487.
- [BLA 87] R.E. Blahut, *Fast Algorithms for Digital Signal Processing*, Addison-Wesley Publishing Company, Reading, MA, 1.987.
- [CAM 71] S.J. Campanella, G.S. Robinson, *A Comparison of Orthogonal Transformations for Digital Speech Processing*, IEEE Transactions on Communication Technology, Vol.Com-19, Nro 6, December 1.971, p 1045-1049.
- [CHE 91] C.S. Chen, K.S. Huo, *Karhunen-Loève Method for Data Compression and Speech Synthesis*, IEE Proceedings-I, Vol. 138, Nro. 5, October 1.991, p 377-380.
- [COO 65] J.W. Cooley, J.W. Tukey, *An Algorithm for the Machine Calculation of Complex Fourier Series*, Mathematics of Computation, Vol 19, Nro 90, Publication National Academy of Sciences - National Research Center by The Americam Mathema tical Society, April 1.965, p 297-301.
- [DAU 88] I. Daubechies, *Orthonormal Basis of Compactly Supported Wavelets*, Comm. Pure Applied Math., 1.988, Vol. 41, p 909-996.
- [DAU 90] I. Daubechies, *The Wavelets Transform, Time-Frequency Localization and Signal analysis*, IEEE Transactions on Information Theory, September 1.990, Vol. 36, Nro. 5, p 961-1005.
- [GON 92] R.C. Gonzales, R. E. Woods, *Digital Image Processing*, Addison Wesley Publishing Company, Inc, New York, 1.992.
- [HUT 75] B.A. Hutchins, *Applications of a real-time Hadamard Transform Network to sound synthesis*, Journal of Audio Engineering Society,Vol 23, Nro 7, September 1975, p 558-562.

Participants

Category	Number of Participants	Percentage
Male	10	50.0
Female	10	50.0
Total	20	100.0

Table 1. Demographic characteristics of participants.

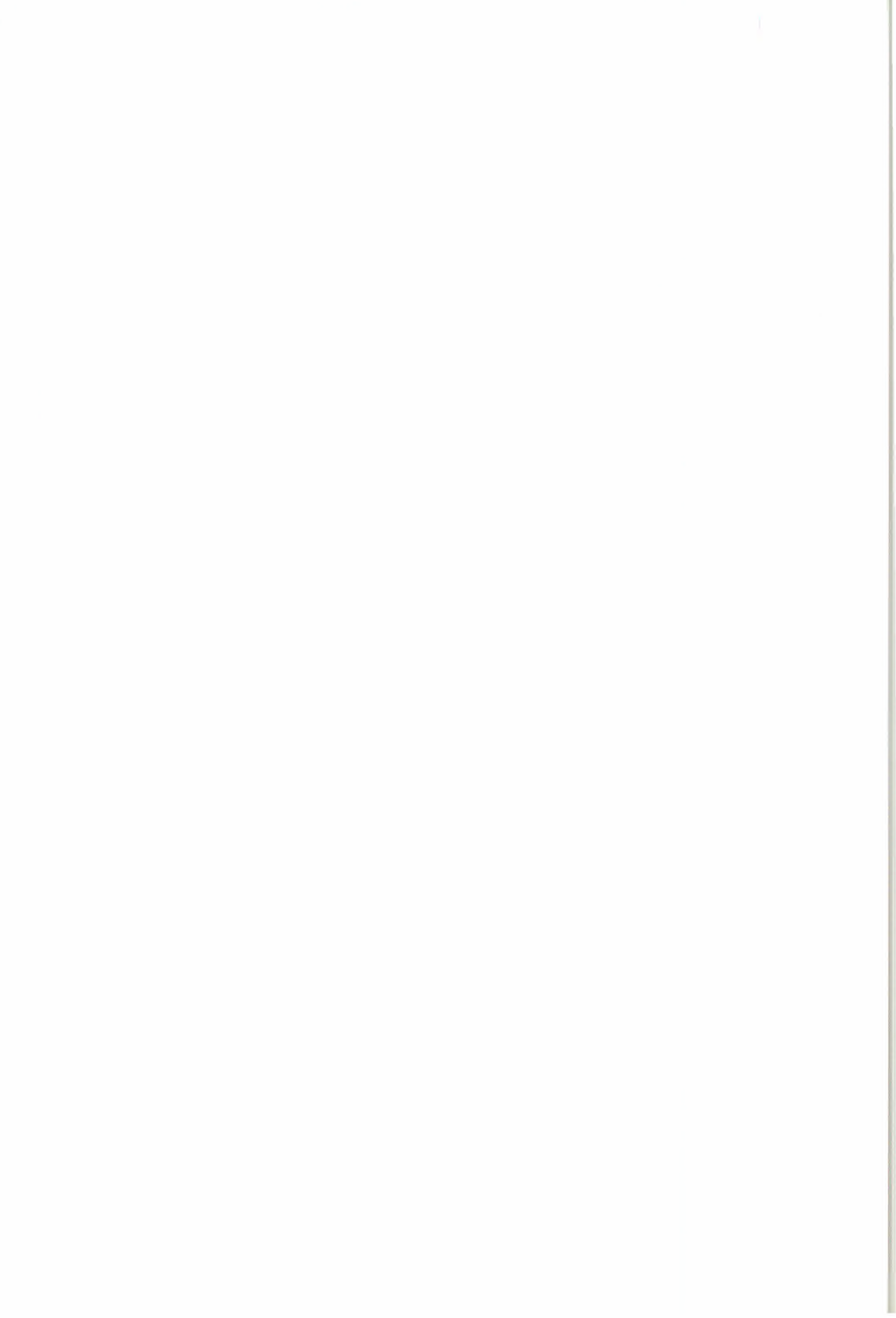
Note: The mean age of the participants was 25.0 years (SD = 2.5). The mean education level was 12.5 years (SD = 1.5).

Table 2. Descriptive statistics of the total sample and gender differences in the total sample.

Note: The mean age of the participants was 25.0 years (SD = 2.5). The mean education level was 12.5 years (SD = 1.5).

Table 3. Descriptive statistics of the total sample and gender differences in the total sample.

Note: The mean age of the participants was 25.0 years (SD = 2.5). The mean education level was 12.5 years (SD = 1.5).



Mercedes L. Acosta
 Instituto de Sensores Remotos Universidad del
 Salvador
 Rodriguez Peña 670 - 5. piso
 0 Capital Federal
 Argentina

César Augusto Aguirre
 Facultad de Ciencias Agropecuarias Universidad
 Nacional de Entre Ríos
 0 Parana Entre Ríos
 Argentina

Carlos Gabriel Asato
 Dirección Nacional del Servicio Geológico
 Av. J.A. Roca 651, 8 , Sector I
 1322 Capital Federal
 Argentina

Virginia Ballarín
 Departamento de Electrónica Facultad de Ingeniería
 Universidad Nacional de Mar del Plata
 J.B.Justo 4302
 7600 Mar del Plata Pcia. de Buenos Aires
 Argentina

Daniel R. Bari
 IHEM Facultad de Ciencias Médicas Universidad
 Nacional de Cuyo
 5500 Mendoza
 Argentina

Enrique Bozzarello
 Dirección de Aplicación de Imágenes Satelitales
 Av. 7, N 1267, piso 2
 1900 La Plata Pcia. de Buenos Aires
 Argentina

Oscar Bustos
 FAMAF Universidad Nacional de Córdoba
 Ciudad Universitaria
 5000 Córdoba
 Argentina

Martín Héctor Afflitto
 Afferes SRL
 Esmeralda 155, 2 11
 0 Capital Federal
 Argentina

Osvaldo J. Arango
 IHEM Facultad de Ciencias Médicas Universidad
 Nacional de Cuyo
 5500 Mendoza
 Argentina

Diego Andrés Azcurra
 FIUBA
 Virrey del Piro, 2604 - 4. piso
 0 Capital Federal
 Argentina

Daniela Barbera
 Facultad de Ingeniería Universidad Nacional de La
 Plata
 Calle 1 y 47
 1900 La Plata Capital Federal
 Argentina

Julio Jacobo Berlles
 Dep.Computación, Ftad Cs. Exactas, Físicas y Natur.
 UBA
 Ciudad Universitaria
 1428 Capital Federal
 Argentina

Marcelo Brun
 Departamento de Electrónica Facultad de Ingeniería
 Universidad Nacional de Mar del Plata
 J.B.Justo 4302
 7600 Mar del Plata Pcia. de Buenos Aires
 Argentina

Maria Gabriela Calvetty Ramos
 Universidad Nacional de La Plata
 481 N 1381
 1896 City Bell-La Plata Pcia de Buenos Aires
 Argentina

Juan Carlos Candiani
Mineria de La Nación
Poeta Lugones, 161
5000 Cordoba
Argentina

Luis Romulo Coll
CEMIC
Las Heras 2867 1 A
0 Capital Federal
Argentina

Carlos G. Cotlier
Programa de Desarrollo Tecnológico Area
Teledetección y SIG Universidad Nacional de Rosario
Entre Ríos 1019, 4 piso "A"
2000 Rosario Santa Fe
Argentina

Carlos M. Dons Blaedel
Instituto Nacional de Investigación y Desarrollo
Pesquero
Paseo Victoria Ocampo N 1 - Escollera Norte
7600 Mar del Plata Pcia. de Buenos Aires
Argentina

Marta Alicia Fernandez
Servicio Meteorologico Nacional
Av. de los Constituyentes, 3454
1427 Capital Federal
Argentina

Elena M. Fernandez-Berdagner
CONICET
Av. Alvarez Thomas, 2820 - 18A
0 Capital Federal
Argentina

Silvia Flaherty
Servicio Meteorológico Nacional
Av. Constituyentes 3454
0 Capital Federal
Argentina

Juan Carlos Caretti
CONAE
Ruta C45, Km 8
5000 Falda del Carmen Córdoba
Argentina

Raúl Colomb
CONAE
Director
Paseo Colón 751
1063 Capital Federal
Argentina

Hector Del Valle
CENPAT-CONICET
Paquebote Santa Teresa, 54 -
9120 Puerto Madryn, Chubut
Argentina

Martin España
CONAE
Paseo Colón 751, 3 piso
1063 Capital Federal
Argentina

Rodolfo Fernández
INVAP
Bdo. De Yrigoyen 230, 2° C
1072 Capital Federal
Argentina

Guillermo Luis Ferraris
Instituto Universitário Aeronautico - IUA
Av. Fuerza Aérea, KM 6 1/2
5000 Cordoba
Argentina

Ana Flesia
FAMAF Universidad Nacional de Córdoba
Dr. Haya de la Torre e Ing. Medina Allende
0 Ciudad Universitaria Córdoba
Argentina

Laura Frulla
CONICET
Julián Alvarez 1218
1414 Capital Federal
Argentina

Antonio Gagliardini
CONAE
Paseo Colón 751
1063 Capital Federal
Argentina

Omar Garcia
INFOSAT-PCI
Luis María Campos 1464, 6 B
1426 Capital Federal
Argentina

Ana María Garra
CAC UBA CONSUDEC-INDEC
Gallo 1421, piso 14, Dto. C
0 Capital Federal
Argentina

Daniel Gonzalo Gestal
CONAE
Av. Paseo Colon 751, 4 piso
1063 Falda del Carmen Córdoba
Argentina

Mirta Alicia Giachino
Dto Hidrometeorología Servicio Meteorológico Nacional
25 de mayo 658
1002 Capital Federal
Argentina

Alberto Giraldez
SENID
Av. del Libertador 327
1368 Vicente López Pcia. de Buenos Aires
Argentina

Miguel Giraut
Dirección Nacional de Recursos Hídricos INCYTH
Ministerio de Obras y Servicios Públicos
Hipólito Yrigoyen N 250, piso 11, of. 1109
1310 Capital Federal
Argentina

Juan Carlos Gomez
Aerofotogeología Facultad de Ciencias Naturales
UNLP
Museo de la Plata, Paseo del Bosque, s/n
1900 La Plata Pcia. de Buenos Aires
Argentina

Francisca Celia Gonzalez
Lab. de Fotointerpretación - UNS Universidad
Nacional del Sur
San Andres, 850
8000 Bahía Blanca Pcia. de Buenos Aires
Argentina

María Alejandra González
Dirección Nacional del Servicio Geológico
Av. Roca 651, piso 8
1322 Capital Federal
Argentina

Jose L. Griffa
CONAE
Ruta C45, Km 8
5000 Cordoba
Argentina

Pedro Schmitz Gualterio
Servicio Meteorológico Nacional
Av. de los Constituyentes, 3454
1427 Capital Federal
Argentina

María Marta Guevara
CIFOT Facultad de Filosofía y Letras Universidad
Nacional de Cuyo
Centro Univers. P. Gral. San Martín
5500 Mendoza
Argentina

Chris Hartley
 Anite Systems
 Alvarez Igarzabal , 915 - Urca
 5000 Cordoba
 Argentina

Alicia Hartley
 Anite Systems
 Alvarez Igarzabal, 915
 5009 Cordoba
 Argentina

Rodrigo Henao
 Centro de Investigaciones Opticas
 Casilla de Correo 124
 1900 La Plata Pcia. de Buenos Aires
 Argentina

Jorge A. Izaurralde
 U.N.C.
 Terragona 1408 - C.P. 5014
 5000 Cordoba
 Argentina

Carlos Alberto Jimenez
 INDEC
 Av. Julio A. Roca 609 7 piso of. 704
 1067 Capital Federal
 Argentina

Gorki Jover
 Teledetección Dto. de Meteorología Servicio de
 Hidrografía Naval
 Av. Comodoro Py 2055, piso 15, of. 1
 1104 Capital Federal
 Argentina

Patricia Kandus
 Gr. Proces. Imágenes-Dto. de Computación
 Ftad. Ciencias Exactas, Físicas y Naturales - UBA
 Pabellón I, Ciudad Universitaria
 1428 Capital Federal
 Argentina

Haydée Karszembaun
 CONICET
 M. Galvez 220, 3 6
 1155 Capital Federal
 Argentina

Saturnino Leguizamón
 CONAE-Gerencia de Gestión Tecnológica
 C.C. 131
 5500 Mendoza
 Argentina

Fernando Lopez
 Instituto Nacional de Investigacion y Desarrollo
 Pesquero
 Paseo victoria Ocampo N 1
 7600 Mar del Plata Pcia. de Buenos Aires
 Argentina

Miguel Angel López
 Armada Argentina
 Comodoro Py 2055
 1104 Capital Federal
 Argentina

Luis Eduardo López
 Comisión Nacional de Energía Atómica
 Av. del Libertador, 8250
 1428 Buenos Aires Capital Federal
 Argentina

Beatriz Lorenzo
 Teledetección Dto. de Meteorología Servicio de
 Hidrografía Naval
 Av. Comodoro Py 2055, piso 15, of. 1
 1104 Capital Federal
 Argentina

María Magdalena Lucini
 FAMAF Universidad Nacional de Córdoba
 Angel Suarez 1353
 5010 Córdoba
 Argentina

Maria Ines Lund
 Centro de Fotogrametria Cartografia y Catastro - UNSJ
 Lapida 1130 (0)
 5400 San Juan
 Argentina

Daniela Marchionni
 INREMI Universidad Nacional de La Plata
 Calle 47 N 522
 1900 La Plata Pcia. de Buenos Aires
 Argentina

Jorge Marconi
 Armada Argentina
 Comodoro Py 2055 - 7. piso
 1104 Capital Federal
 Argentina

Graciela Marín
 Dirección Nacional del Servicio Geológico
 Av. J.A. Roca 651, 8 , Sector I
 1322 Capital Federal
 Argentina

Natalia Marlenko
 Facultad de Filosofía y Letras Universidad Nacional de
 Buenos Aires
 Larrea 1050, 5 B
 1117 Capital Federal
 Argentina

Ana G. Medico
 CONAE
 Paseo Colón 751
 1063 Capital Federal
 Argentina

Marta Mejail
 Dto.Computación, Ftad. Ciencias Exactas, Físicas y
 Naturales -UBA
 Ciudad Universitaria. Pabellón 1
 1428 Capital Federal
 Argentina

Antonio Menescardi
 CONAE
 Ruta C45, Km 8
 5000 Falda del Carmen Córdoba
 Argentina

Pablo Mercuri
 Instituto Clima y Agua INTA
 Las Cabañas y Los Reseros
 1712 Castelar Pcia. de Buenos Aires
 Argentina

Jorge A. Milovich
 CONICET
 Julián Alvarez 1218
 1414 Capital Federal
 Argentina

Priscilla Minotti
 Consultora en medio ambiente
 H. Yrigoyen 1337
 1638 Vicente López Pcia. de Buenos Aires
 Argentina

Emilce Moler
 Departamento de Electrónica Facultad de Ingeniería
 Universidad Nacional de Mar del Plata
 J.B.Justo 4302
 7600 Mar del Plata Pcia. de Buenos Aires
 Argentina

Jorge A. Monsú
 CONAE
 Ruta C45, Km 8
 5000 Falda del Carmen Córdoba
 Argentina

Celina Montenegro
 Dirección de Recursos Forestales Nativos Secretaría
 de Recursos Naturales y Ambiente Humano
 San Martín 459, 2 piso
 1004 Capital Federal
 Argentina

Alejandro Movia
 Departamento de Ciencias de la Atmósfera
 Universidad Nacional de Buenos Aires
 Ciudad Universitaria
 1428 Capital Federal
 Argentina

Carlos Ninci
 Comisión Nacional de Energía Atómica
 Av. del Libertador 8250
 1429 Capital Federal
 Argentina

José Miguel Nuñez
 Servicio Meteorológico Nacional
 25 de mayo 658
 1002 Capital Federal
 Argentina

Patricia Padrón
 Universidad Nacional de Luján
 Billinghurst 2138 PB "A"
 1425 Capital Federal
 Argentina

Fernando Pérez Serrano
 INVAP S.E.
 Esmeralda 356
 1035 Capital Federal
 Argentina

Diego Pieres
 Afferes SRL
 Esmeralda 155, 2 11
 0 Capital Federal
 Argentina

Mónica Rabolli
 CONAE
 Paseo Colón 751
 1063 Capital Federal
 Argentina

Carlos Emilio Moyano
 CONAE
 Paseo Colón 751
 1063 Capital Federal
 Argentina

Ida Nöllmann
 CONAE
 Paseo Colón 751
 1063 Capital Federal
 Argentina

Silvia María Ojeda
 FAMAF Universidad Nacional de Córdoba
 Av. Arenales 990, TD1 7 F, Bo. Juniors
 5000 Córdoba
 Argentina

Víctor Raúl Pérez
 Servicio Meteorológico Nacional
 Av. Constituyente 3454
 0 Capital Federal
 Argentina

Manuel Hipólito Picasso
 Servicio Meteorológico de la Armada
 Edificio Libertad, piso 15-23 - Comodoro Py 2055
 1104 Capital Federal
 Argentina

Hector Rabal
 Centro de Investigaciones Ópticas
 CC 124
 1900 La Plata Pcia. de Buenos Aires
 Argentina

Raúl Reta
 INIDEP
 Pasaje Victoria Ocampo N 1
 7600 Mar del Plata Pcia. de Buenos Aires
 Argentina

Alberto Ridner
CONAE
Paseo Colón 751
1063 Capital Federal
Argentina

Claudia Mabel Roldán
Universidad de Luján
Ecuador 482
1714 Ituzaingó Pcia. de Buenos Aires
Argentina

Pablo D. Ruiz
Departamento de Física Facultad de Ciencias Exactas
Universidad Nacional de Salta
Buenos Aires 177
4400 Salta
Argentina

Marcela Sagardoy
Universidad Nacional de La Plata
1900 43 N. 725 172 - "C" e/ayio
1900 La Plata Pcia. de Buenos Aires
Argentina

Héctor Armando Salgado
Teledetección Dto. de Meteorología Servicio de
Hidrografía Naval
Av. Comodoro Py 2055, piso 15, of. 1
1104 Capital Federal
Argentina

Graciela Salinas de Salmuni
Saavedra 125 (N)
5400 Rivadavia San Juan
Argentina

Guillermo Sampallo
Facultad de Ciencias exactas Universidad Nacional del
Nordeste
Guastavino 1621
3400 Corrientes
Argentina

Klaas Jan Sant
SAPYA-PROSAP
Del Ombú 1949
1712 Castelar Pcia. de Buenos Aires
Argentina

Gladys Lilian Sauer
Armada Argentina
Comodoro Py 2055
1104 Capital Federal
Argentina

Alicia Sedeño
Centro de Sensores Remotos Fuerza Aerea Argentina
Av. Dorrego 4018
1426 Capital Federal
Argentina

Maria Cristina Serafini
Universidad de Luján
Secretaría Académica
Ruta 7, km. 65
6700 Luján Pcia. de Buenos Aires
Argentina

Luis Somoza
CONAE
Paseo Colón 751
1063 Capital Federal
Argentina

Mabel Haydée Strada
Dirección de Recursos Forestales Nativos Secretaría de
Recursos Naturales y Ambiente Humano
San Martín, 459
1429 Capital Federal
Argentina

José M. Suriano
Dirección Nacional del Servicio Geológico
Av. Roca 651, piso 8
1322 Capital Federal
Argentina

Alicia Leonor Tejerina Puch
 Servicio Meteorológico
 25 de mayo 658
 C Capital Federal
 Argentina

Edda Claudia Valpreda
 CIFOT Facultad de Filosofía y Letras Universidad
 Nacional de Cuyo
 5500 Mendoza
 Argentina

Inés Velasco
 Cs. de la Atmósfera Universidad Nacional de Buenos
 Aires
 Cdad. Universitaria
 1428 Capital Federal
 Argentina

Daniel Alejandro Vila
 Servicio Meteorológico Nacional
 Pola 451, 5 F
 0 Capital Federal
 Argentina

Alberto B. Viola
 Aeroterra
 Gorostiaga 2465
 1426 Capital Federal
 Argentina

José Francisco Zelasco
 Facultad de Ingeniería - UBA
 Bolívar 1224, 2 C
 0 Capital Federal
 Argentina

Glauber Acunha Goncalves
 Dep. de Física - Universidad Federal de Rio Grande
 CP 474
 Av. Italia, km 8
 96201-900 Rio Grande RS
 Brasil

Sandra Torrusio
 Dirección de Aplicación de Imágenes Satelitales
 Av. 7, N 1267, piso 2
 1900 La Plata Pcia. de Buenos Aires
 Argentina

César Daniel Vara
 SENID
 Av. del Libertador 327
 1638 Vicente López Pcia. de Buenos Aires
 Argentina

Roberto Vignoni
 LEICI Facultad de Ingeniería Universidad Nacional de
 La Plata
 Calle 1 y 47
 1900 La Plata Pcia. de Buenos Aires
 Argentina

Eduardo C. Viola
 Aeroterra
 Gorostiaga 2465
 1426 Capital Federal
 Argentina

Carlos M. Viola Binaghi
 Aeroterra S.A.
 Vice Presidente Ejecutivo
 Gorostiaga 2465
 1426 Capital Federal
 Argentina

Oscar Galvez
 Av. Martín de la Rocha # 1427
 Cochabamba
 Bolivia

Silvana Amaral
 INPE
 Av. dos Astronautas 1758
 12227-010 San José dos Campos SP
 Brasil

Ana Lucía Bezerra Candeias
 INPE
 Av. dos Astronautas 1758
 12227-010 San José dos Campos SP
 Brasil

Mateus Biriato de Azevedo
 COMGAR
 Superior (Eng. Civ. Urbanista)
 Anexo do M. Aer
 70.045-900 Brasilia, DF
 Brasil

Terezinha Botelho
 INPE
 Av. dos Astronautas 1758
 12227-010 San José dos Campos SP
 Brasil

Corina da Costa Freitas Yanasse
 INPE
 Av. dos Astronautas 1758
 12227-010 San José dos Campos SP
 Brasil

Camilo Daleles Renó
 INPE
 Av. dos Astronautas 1758
 12227-010 San José dos Campos SP
 Brasil

Alejandro C. Frery
 Depto. de Informática Universidad Federal de
 Pernambuco
 Caixa Postal 7581
 50732-970 Recife PE
 Brasil

Glauber Acunha Goncalves
 Campus Carreiros Universidade do Rio Grande
 Av. Itália, Km 8
 9,6E+07 Rio Grande - RS
 Brasil

Thelma Krug
 INPE
 Coordinadora- Observación de la Tierra
 Av. dos Astronautas 1758
 12227-010 San José dos Campos SP
 Brasil

Joao Fernando Marar
 Departamento de Informática UNESP Universidad
 Federal de Pernambuco
 Rua María Magina Pontual 260, Apto 104
 51021-510 Recife PE
 Brasil

Sergio Monteiro Soares
 INPE
 Av. dos Astronautas 1758
 12227-010 San José dos Campos SP
 Brasil

José Claudio Mura
 INPE
 Av. dos Astronautas 1758
 12227-010 San José dos Campos SP
 Brasil

Ulf Palme
 INPE-FUNCATE
 Av. Brig. Faria Lima, 3305
 CEP 12225-000 San José dos Campos SP
 Brasil

Maycira Pereira de Farias Costa
 INPE
 Av. dos Astronautas 1758
 12227-010 San José dos Campos SP
 Brasil

Sidnei Joao Siqueira Sant'Anna
 INPE
 Av. dos Astronautas 1758
 12227-010 San José dos Campos SP
 Brasil

Germano Vasconcelos
 Universidade Federal de Pernambuco
 Av. Prof. Luiz Freire, s/n - C.P. 7851
 0 Recife - PE
 Brasil

Carlos Alberto Vettorazzi
 ESALQ/USP
 Av. Pdua Dias, 11
 Piracicaba SP 13418-900
 Brasil

Joao Viane Soares
 INPE
 Av. dos Astronautas 1758
 12227-010 San José dos Campos SP
 Brasil

Antonio Miguel Vieira Monteiro
 INPE
 Av. dos Astronautas 1758
 12227-010 San José dos Campos SP
 Brasil

Fred Campbell
 Canadian Center for Remote Sensing
 Director Business and Management
 588 Booth St, Room 335
 K1A 0Y7 Ottawa Ontario
 Canada

Alain Kahil
 Intermap Technologies Ltd.
 Suite 900 - 645-7th Ave. S.W.
 T2P 4G8 Calgary Alberta
 Canada

Michael Manore
 Canada Center for Remote Sensing Coordinator, Ice
 Applications
 588 Booth St.
 K1A 0Y7 Ottawa Ontario
 Canada

J. Bryan Mercer
 Intermap Technologies Ltd.
 Suite 900 - 645-7th Ave. S.W.
 T2P 4G8 Calgary Alberta
 Canada

Eugenio Pettigiani
 Seaconsult Marine Research
 8805 Osler Street - V6P 4G1
 Vancouver, BC
 Canada

Hector Allende
 Universidad Técnica Federico Santa María
 Casilla 110-Y
 Valparaíso
 Chile

Jorge Galbiati
 Universidad Católica de Valparaíso
 Casilla 4059
 Valparaíso
 Chile

Carlos Patillo B.
 Progr. Percepc. Remota y SIG, Uni. Católica de Chile
 Casilla 306
 Av. Vicuña Mackenna, 4860 - Correo Int. 906
 22 Santiago de Chile
 Chile

María Elena Pezoa Solís
 Facultad de Agronomía Universidad Católica de Chile
 Casilla 306
 Av. Vicuña Mackenna, 4860 - Correo Int. 906
 22 Santiago de Chile
 Chile

Raúl E. Truffat
 SEASPACE CORPORATION
 Marketing Coord. for Latin America & the Caribbean
 Av. dos Astronautas 1758
 12227-010
 Costa Rica

João Moreira
 Aerosensing Radar Systeme Managing Director
 Oberpfaffenhofen
 D-82234 Wessling
 Germany

Osvaldo Peinado
 CONAE-AGF
 Luisenstrasse 37
 80794 München
 Germany

Maurizio Fea
 ESA-ESRIN Earth Observation Promotion
 via Galileo Galilei
 Casella Postale 64
 00044 Frascati
 Italy

Henri Laur
 ESA-ESRIN
 Via Galileo Galilei
 CP 64
 00044 Frascati
 Italy

Fabio Rocca
 Politecnico de Milano Dipartimento di elettronica ed
 Informazione Professor of Digital Signal Processing
 Piazza L. da Vinci 32
 20133 Milano
 Italy

Jorge Lira
 Instituto de Geofísica Univ.Nac.Autonoma de Mexico -
 UNAM
 Delegación Tlalpan
 14091 Mexico DF
 Mexico

Petr Bares
 Anite Systems
 Plaza M. Gutierrez, 4 - Cobeña
 28863 Madrid
 Spain

Ralph Cordey
 GEC-MARCONI Research Centre
 Great Baddow, Chelmsford
 UK

Shaun Quegan
 Sheffield Center for Earth Observation The University
 of Sheffield
 Hicks Building, Houndsfield Road
 S3 7RH Sheffield
 UK

Maria Magdalena Blanco
 Facultad de Ciencias Universidad de la Republica
 Tristan Naruaja, 1674
 11200 Montevideo
 Uruguay

Gabriel Carballo
 Facultad de Ingenieria Universidad de la República
 Julio Herrera y Reissig, 565, p. 5
 11300 Montevideo
 Uruguay

John R. Apel
 Global Ocean Associates
 PO Box 12131
 20908 Silver Spring Maryland
 USA

Regulo A. Osorio Moreno
 Instituto de Ingeniería
 Apdo. 40200
 Caracas 1040-A D.F.
 Venezuela

European Space Agency
Agence spatiale européenne

Contact: *ESA Publications Division*
c/o ESTEC, PO Box 299, 2200 AG Noordwijk, The Netherlands
Tel (31) 71 565 3400 - Fax (31) 71 565 5433